The implementation and application of dynamic finite element analysis to geotechnical problems

A thesis submitted to the University of London

for the degree of Doctor of Philosophy and for the Diploma of

the Imperial College of Science, Technology and Medicine

By

Stuart Hardy

Department of Civil and Environmental Engineering

Imperial College of Science, Technology and Medicine

London, SW7 2BU

March 2003

BRI. LO IN. UNIV.

This thesis is dedicated to the memory of Myo Min Thaung

ABSTRACT

The thesis details the development work that was undertaken to make dynamic analyses possible with the pre-existing static geotechnical finite element program ICFEP (Imperial College Finite Element Program). The changes were then validated against known closed form solutions.

The possibility of analysing dynamic problems opens up a massive potential for new research topics. For this study two where chosen.

The first of these concerns the use of bender element tests to measure the stiffness of soils at very small strains. Their use is the laboratory has grown over recent years due mainly to their low cost and the ease by which they can be incorporated in other existing laboratory equipment. Ambiguity still remains surrounding their use and several researchers have tried to remove this ambiguity by comparing experimental data with results obtained using dynamic finite element analyses. All the data published so far in the literature assumes two dimensional plane strain conditions, were as in reality the problem is a truly three dimensional one.

In this thesis two and three dimensional analyses are presented for an extensive range of input frequencies. Both types of analyses suggest that there is a small error involved in the one dimensional assumption of shear wave propagation through the sample. A numerical study is also presented for continuously cycled bender element tests which have recently been proposed to remove the ambiguity surrounding the use of bender element tests. The results show a large and input frequency dependant error in the shear modulus calculated using this method.

The second topic researched considers the behaviour of a deep foundation subjected to an earthquake loading. Current seismic design practice relies on the use of a reduced bearing capacity calculated using the limit equilibrium technique. This assumes that the inertial forces induced in the ground are taken into consideration by applying a pseudo static horizontal force. Previous pseudo static finite element analysis has shown that the assumed failure mechanism may not be correct.

Pseudo static finite element results are compared with dynamic finite element results assuming a variety of different recorded earthquakes. The behaviour in both a qualitative and quantitative sense is found to be considerably different, with the results from the dynamic analyses found to be more consistent with the behaviour observed in the field.

ACKNOWLEDGEMENTS

The work presented in this thesis was sponsored by an Engineering and Physical Science Research Council (EPSRC) case studentship in collaboration with the Geotechnical Consulting Group.

My first thanks must go to my supervisors, Dave Potts and Lidija Zdravković. Their patience and dedication to this work knew no bounds during the completion of this thesis. Thanks for giving me this chance and always guiding me in the right direction. Thanks are also due to Dr. Sarma who was always there to discuss dynamics when I had exhausted my supervisors.

The support, financial or otherwise, from the Geotechnical Consulting Group is gratefully acknowledged. Particular thanks are due to Barry New for pointing me towards some of the closed form solutions presented in this thesis and Kelvin Higgins for his constant support. Without Kelvin I would never have got into this position, and if he wasn't there at the end I may never have got out of it. You are one in a million.

Research is a long and arduous task and without the support from my fellow students it would not have been possible. The research group in the Soil Mechanics section at Imperial College is unique in its diversity and quality. Thanks are due to the members of the research group, past and present, for making such an enjoyable work environment. In addition to the students, the section simply would not be the same without Sue Feller, Graham Keefe and John Baxter. Special thanks are due to the usual suspects, Felix Schroeder, Niki Franzius, Reinaldo Rolo and Kostis Geordiadis. I hope what we have now is just the beginning of a life long friendship. Good luck to Stavroula Kontoe for carrying on the dynamic finite element analysis.

The largest and most personal thanks must be saved for the people dearest to me, my Mum and Dad and Angeliki (Τζέλι μου). How grateful I am for the love and support you offered me during my research cannot be expressed here. I hope I make you proud.

TABLE OF CONTENTS

ABSTRACT 3

ACKNOWLEDGEMENTS 5

LIST OF FIGURES 12

LIST OF TABLES 23

LIST OF SYMBOLS 25

Chapter 1

INTRODUCTION 32

1.1 General Introduction 32

1.2 Scope of Research 33

1.3 Layout of Thesis 34

Chapter 2

FINITE ELEMENT THEORY 37

2.1 Introduction 37

2.2 General Formulation 38

2.3 Geotechnical Considerations 45

2.3.1 Pore Fluid – Soil Interaction 45

2.3.2 Special Elements Required to Model Geotechnical Problems 47

2.4 Non-Linear Finite Element Theory 49

2.5 Consolidation Theory 52

2.6 Fourier Series Aided Finite Element Analysis 57
2.6.1 Introduction 57
2.6.2 Theory 58
2.7 Summary 62

Chapter 3

DYNAMIC FINITE ELEMENT THEORY 64
3.1 Introduction 64
3.2 Dynamic Finite Element Formulation 65
3.2.1 Two and Three Dimensional Analyses 65
3.2.2 Fourier Series Aided Finite Element Analysis 68
3.3 Nature and Evaluation of the Element Mass and Damping Matrices 71
3.4 Time Discretisation 75
3.4.1 The Central Difference Method 75
3.4.2 The Houbolt Method 78
3.4.3 The Linear Acceleration Method 79
3.4.4 The Wilson θ Method 85
3.4.5 The Newmark Method 86
3.4.6 Other Schemes 89
3.4.7 Choice of Scheme 90
3.5 Boundary Conditions 91
3.6 Dynamic Pore Fluid Interaction 93
3.7 Summary 99
3.8 Implementation 100

Chapter 4

VALIDATION EXERCISES 103
4.1 Introduction 103

4.2 Validation of the modified Newmark time discretisation scheme 103

4.3 Validation of the Finite Element Code: Original Newmark Method 114

4.3.1 Introduction 114

4.3.2 Analysis of a compression wave propagating through a cylindrical bar 114

4.3.3 Analysis of a shear wave propagating through a one dimensional column 122

4.3.4 Analysis of an impulse loading in a spherical cavity 125

4.3.5 Investigations using the Newmark method 128

4.4 Validation of the Finite Element Code: Quadratic Acceleration Method 135

4.4.1 Introduction 135

4.4.2 Analysis of an impulse loading in a spherical cavity 135

4.4.3 Discussion 139

4.5 Validation of pore fluid compressibility and coupled dynamic analyses. 140

4.5.1 Introduction 140

4.5.2 The validation problem 140

4.6 Conclusions 146

Chapter 5

LABORATORY MEASUREMENT OF SMALL STRAIN STIFFNESS 148

5.1. Introduction 148

5.2. Laboratory Techniques 149

5.2.1 Resonant Column Test 149

5.2.2 Bender Element Tests 151

5.2.3 Other Dynamic Soil Tests 152

5.2.4 Measuring Anisotropy with Piezoelectric Devices 154

5.3 Analysis of Bender Element Tests 156

5.3.1 Introduction 156
5.3.2 Strain Level 156
5.3.3 Wave Travel Distance 156
5.3.4 Wave Travel Time 157
5.3.5 Finite Element Analysis of Bender Element Tests 161
5.3.6 Further Studies of the Sanches-Salinero Solution 164
5.3.7 Inertial Coupling 169

5.4 Continuously Cycled Bender Element Tests 170
5.4.1 Introduction 170
5.4.2 Description of the Method 170

5.5 Numerical Analyses Undertaken 172
5.5.1. Introduction 172
5.5.2 Geometry Assumed in the Analyses 173
5.5.3 Plane Strain Analyses 174
5.5.3.1 Material Properties 174
5.5.3.2 Details of the Bender Element Analyses 178
5.5.3.3 Newmark Parameters 180
5.5.3.4 Finite Element Mesh 181
5.5.3.5 Time Step 182
5.5.3.6 Drainage Conditions 184
5.5.3.7 Estimate of G_{max} by First Shear Wave Arrival 186
5.5.3.8 Measurement of G_{max} by the Phase Sensitive Detection Method 191
5.5.4 Fourier Series Aided Finite Element Analyses 196
5.5.4.1 Estimate of G_{max} by First Shear Wave Arrival 198
5.5.4.2 Estimate of G_{max} by the Phase sensitive Detection Method 201

5.6 Discussion 203
5.6.1 First Shear Wave Arrival Technique 203
5.6.2 Phase Sensitive Detection Method 205

5.7 Results of Continuously Cycled Tests 211

Chapter 6

FINITE ELEMENT MODELLING OF THE SEISMIC BEHAVIOUR OF DEEP FOUNDATIONS 222

6.1 Introduction 222

6.2 The Behaviour of Foundations Subjected to Seismic Loads 223

6.2.1 Foundations in Clay 223

6.2.2 Foundations in Residual Soils and Sands 227

6.2.3 Summary 229

6.3 Current Design Practice for Foundations Subjected to Seismic and Cyclic Loads 230

6.3.1 The Design of Foundations for Cyclic Loading 231

6.3.2 The Seismic Design of Foundations 231

6.4 Summary 245

6.5 Finite Element Analyses 246

6.5.1 Introduction 246

6.5.2 Description of analysis 246

6.6 Calculation of Foundation Capacity 248

6.6.1 Static Capacity 249

6.6.2 Seismic Capacity 250

6.6.3 Finite Element Analysis of the Static Bearing Capacity 252

6.6.4 Working Load 253

6.7 Description Input Earthquake (Athens 7/9/1999) 254

6.8 Results of Dynamic Finite Element Analysis 258

6.8.1 Introduction 258

6.8.2 Results 259

6.8.2.1 During the Earthquake 259

6.8.2.2 After the Earthquake 269

6.8.3 Discussion 273

6.8.4 Analyses Using Wider Mesh 274

6.8.5 Analysis Including Structural Mass 275

6.9 Dynamic Finite Element Analysis Results using Different Input Earthquakes 277
6.9.1 Introduction 277
6.9.2 Description of Earthquake Records 277
6.9.3 Results 281
6.10 Analyses on Foundations at Different Working Loads 290
6.10.1 Introduction 290
6.10.2 Description of Analyses 290
6.11 Large Displacement Analyses 294
6.11.1 Introduction 294
6.11.2 Description of Analyses 296
6.11.3 Summary 301
6.12 Summary 302

Chapter 7

CONCLUSIONS AND RECOMMENDATIONS 306
7.1 Introduction 306
7.2 Finite Element Implementation 306
7.3 Validation 307
7.4 Problems Analysed 308
7.4.1 Comparison of the Problems Analysed 308
7.4.2 Conclusions from the Bender Element Analyses 310
7.4.3 Conclusions from the Deep Foundation Analyses 313
7.5 Recommendations for Further Research 315
7.5.1 Implementation 316
7.5.2 Research Topics 317
7.5.2.1 Bender Element Analyses 317
7.5.2.2 Deep Foundation Analyses 317

REFERENCES 320

LIST OF FIGURES

Chapter 2

Figure 2.1: Eight noded isoparametric solid element.....39
Figure 2.2: Three noded isoparametric beam element.....48
Figure 2.3: Graphical representation of the modified Newton-Raphson scheme.....51
Figure 2.4: Axi-symmetric coordinate system and associated displacements.....58

Chapter 3

Figure 3.1: Comparison of mass matrices 72
Figure 3.2: Damping as a function of frequency (after Bathe (1996)).....74
Figure 3.3: Finite difference grid.....76
Figure 3.4: Graphical representation of the linear acceleration method.....80
Figure 3.5: Schematic representation of incremental load vector.....83
Figure 3.6: Schematic representation of the differential of the incremental load vector 84
Figure 3.7: Graphical representation of the Wilson θ method 85
Figure 3.8: Graphical representation of the Newmark method 88
Figure 3.9: Percentage period elongations and amplitude decays (after Bathe (1996)) 91

Chapter 4

Figure 4.1: Single degree of freedom problem..... 105
Figure 4.2: Single degree of freedom analysis using original Newmark scheme..... 107
Figure 4.3: Single degree of freedom analysis using quadratic acceleration scheme 107
Figure 4.4: Single degree of freedom analysis using quadratic acceleration scheme (thrust calculated using Equation 4.8)..... 108
Figure 4.5: Single degree of freedom analysis using quadratic acceleration scheme t=40–60 seconds (thrust calculated using Equation 4.8) 109

Figure 4.6: Single degree of freedom analysis using quadratic acceleration scheme t=40–60 seconds 109
Figure 4.7: Closed form solution to single degree of freedom problem with no damping 110
Figure 4.8: Discretised solution to single degree of freedom problem with no material damping 111
Figure 4.9: Discretised solution to single degree of freedom problem with no material damping ($\gamma = 1.05$) 112
Figure 4.10: Discretised solution to single degree of freedom problem with no material damping ($\delta = 0.34$) 112
Figure 4.11: Discretised solution to single degree of freedom problem with no material damping ($\alpha = 0.1$) 113
Figure 4.12: Analysis arrangement for modelling compression wave propagation 115
Figure 4.13: Bar analysis results: Increment 70 116
Figure 4.14: Bar analysis results: Increment 120 116
Figure 4.15: Bar analysis results: Increment 220 – wave propagation after reflection from the fixed end 117
Figure 4.16: Bar analysis results: Increment 275 – wave reaching the free end after being reflected from the fixed end 118
Figure 4.17: Bar analysis results: Increment 320 – wave propagation after reflecting from the free end 118
Figure 4.18: Analysis arrangement for propagation of a compression wave through a bar with two different material types 119
Figure 4.19: Analysis results at Increment: 60 120
Figure 4.20: Analysis results at Increment: 115 120
Figure 4.21: Analysis results at Increment: 150 120
Figure 4.22: Analysis results at Increment: 240 121
Figure 4.23: Analysis arrangement for the propagation of a shear wave 123
Figure 4.24: Shear wave analysis results Increment: 50 123
Figure 4.25: Shear wave analysis results Increment: 150 124
Figure 4.26:Analysis arrangement for cavity problem 126
Figure 4.27: Displacement normal to cavity, $r = 2.17$ m 127
Figure 4.28: Displacement normal to cavity, $r = 5.29$ m 127
Figure 4.29: Displacement normal to cavity, $r = 10.36$ m 128

Figure 4.30: bar analysis with different meshes: Increment 85 129
Figure 4.31: bar analysis with different meshes: Increment 210 130
Figure 4.32: Displacement normal to cavity (damped analysis), $r = 2.17$ m..... 131
Figure 4.33: Displacement normal to cavity (damped analysis), $r = 5.29$ m..... 131
Figure 4.34: Displacement normal to cavity (damped analysis), $r = 10.36$ m 132
Figure 4.35: Mass matrices calculated using different orders of integration 133
Figure 4.36: Displacement normal to cavity, $r = 2.17$ m..... 134
Figure 4.37: Displacement normal to cavity, $r = 5.29$ m..... 134
Figure 4.38: Displacement normal to cavity, $r = 10.36$ m..... 134
Figure 4.39: Results of analysis using the quadratic acceleration method with original parameters ($\gamma = 1.0$, $\delta = 1/3$ and $\alpha = 1/12$) $r = 2.17$ m 136
Figure 4.40: Results of analysis using the quadratic acceleration method with damped parameters ($\gamma = 1.0$, $\delta = 0.35$ and $\alpha = 0.1$) $r = 2.17$ m..... 137
Figure 4.41: Results of analysis using the quadratic acceleration method with damped parameters ($\gamma = 1.0$, $\delta = 1/3$ and $\alpha = 0.2$) $r = 2.17$ m 138
Figure 4.42: Results of analysis using the quadratic acceleration method with damped parameters ($\gamma = 1.0$, $\delta = 0.5$ and $\alpha = 1/12$) $r = 2.17$ m 138
Figure 4.43: Soil layer subjected to periodic loading..... 141
Figure 4.44: ICFEP results compared to closed form solution for different values of Π_1..... 143
Figure 4.45: Validation of dynamic coupled analyses $\Pi_1 = 0.1$ 145
Figure 4.46: Validation of dynamic coupled analyses $\Pi_1 = 1.0$..... 145
Figure 4.47: Zones of applicability of various assumptions (after Zienkiewicz *et al.* (1980))..... 146

Chapter 5

Figure 5.1: Schematic representation of stiffness against strain curve 148
Figure 5.2: Piezoelectric bender element (after Kramer (1996)) 151
Figure 5.3: Compression Transducer (after Brignoli *et al.* (1996)) 152
Figure 5.4: Shear Plate Transducer (after Brignoli *et al.* (1996)) 154
Figure 5.5: Arrangement of External Piezoelectric Transducers to Measure Soil Anisotropy (after Fioravante (2000))..... 155

Figure 5.6: Relationship between travel time and sample length (after Viggiani and Atkinson (1995)) 157
Figure 5.7: Typical input and output waves from bender element test 158
Figure 5.8: Notation for three-dimensional motion of points (after Jovičić *et al.* (1996)) 159
Figure 5.9: Analytical solution of the motion at the monitoring point (after Sanches-Salinero *et al.* (1986)) 160
Figure 5.10: Finite element analysis of bender element test (after Jovičić *et al.* (1996)) 162
Figure 5.11: Ratio of Group Velocity and Bulk Velocity Against R_d (after Arroyo *et al.* (2002)) 166
Figure 5.12: Stokes Propagation of a distorted Sine Wave (after Arroyo *et al.* (2002)) 167
Figure 5.13: Near Field Effect for Different Signal Types (after Arroyo *et al.* (2002)) 168
Figure 5.14: Influence of Near Field on First Arrival Estimate of V_s (after Arroyo *et al.* (2002)) 168
Figure 5.15: Traditional time of flight method, using a square wave input (after Blewett *et al.* (1999)) 171
Figure 5.16: Results from phase sensitive detection method (after Blewett *et al.* (1999)) 171
Figure 5.17: Mesh used to investigate one dimensional wave propagation 175
Figure 5.18: Recorded motion of reference point A 176
Figure 5.19: Result of analyses with different increment size 178
Figure 5.20: Finite element mesh and boundary conditions used in bender element analyses 179
Figure 5.21: Analysis to investigate the influence of the Newmark parameters 180
Figure 5.22: Analyses comparing different mesh densities 182
Figure 5.23: Motion of receiving bender element for different size time steps 183
Figure 5.24: Enlarged view of shear wave arrival for analyses with different time steps 183
Figure 5.25: Comparing first shear wave arrival assuming drained, undrained and coupled behaviour 185

Figure 5.26: Recorded motion of receiving bender element for R_d = 4 (2D analysis) 187
Figure 5.27: Recorded motion of receiving bender element for R_d = 1 (2D analysis) 188
Figure 5.28: Recorded motion of receiving bender element for R_d = 2 (2D analysis) 188
Figure 5.29: Recorded motion of receiving bender element for R_d = 3 (2D analysis) 188
Figure 5.30: Recorded motion of receiving bender element for R_d = 5 (2D analysis) 189
Figure 5.31: Recorded motion of receiving bender element for R_d = 6 (2D analysis) 189
Figure 5.32: Recorded motion of receiving bender element for R_d = 7 (2D analysis) 189
Figure 5.33: Recorded motion of receiving bender element for R_d = 8 (2D analysis) 190
Figure 5.34: Input and output waves for continuously cycled test, R_d = 2 (2D) 192
Figure 5.35: Cross correlation coefficient for R_d = 2, 2D analysis 193
Figure 5.36: Input and time shifted output waves R_d = 2 194
Figure 5.37: Measured and theoretical relationship between input frequency and R_d (2D analysis) 196
Figure 5.38: Finite element mesh and equivalent model for Fourier series aided three dimensional analysis 197
Figure 5.39: Recorded motion of receiving bender element for R_d = 1 (FS analysis) 198
Figure 5.40: Recorded motion of receiving bender element for R_d = 2 (FS analysis) 198
Figure 5.41: Recorded motion of receiving bender element for R_d = 3 (FS analysis) 199
Figure 5.42: Recorded motion of receiving bender element for R_d = 4 (FS analysis) 199
Figure 5.43: Recorded motion of receiving bender element for R_d = 5 (FS analysis) 199

Figure 5.44: Recorded motion of receiving bender element for R_d = 6 (FS analysis) 200
Figure 5.45: Recorded motion of receiving bender element for R_d = 7 (FS analysis) 200
Figure 5.46: Recorded motion of receiving bender element for R_d = 8 (FS analysis) 200
Figure 5.47: Measured and theoretical relationship between input frequency and R_d (FS analysis) 202
Figure 5.48: Results of phase sensitive detection method for two and three dimensional analyses 205
Figure 5.49: Experimental results of continuously cycled tests 206
Figure 5.50: Fast Fourier transform for two dimensional analysis with R_d = 1 207
Figure 5.51: Fast Fourier transform for two dimensional analysis with R_d = 2 207
Figure 5.52: Fast Fourier transform for two dimensional analysis with R_d = 3 207
Figure 5.53: Fast Fourier transform for two dimensional analysis with R_d = 4 208
Figure 5.54: Fast Fourier transform for two dimensional analysis with R_d = 5 208
Figure 5.55: Fast Fourier transform for two dimensional analysis with R_d = 6 208
Figure 5.56: Fast Fourier transform for two dimensional analysis with R_d = 7 209
Figure 5.57: Fast Fourier transform for two dimensional analysis with R_d = 8 209
Figure 5.58: Input and output waves for continuously cycled test, R_d = 1 (2D) 211
Figure 5.59: Cross correlation coefficient for R_d = 1, 2D analysis 211
Figure 5.60: Input and output waves for continuously cycled test, R_d = 3 (2D) 212
Figure 5.61: Cross correlation coefficient for R_d = 3, 2D analysis 212
Figure 5.62: Input and output waves for continuously cycled test, R_d = 4 (2D) 212
Figure 5.63: Cross correlation coefficient for R_d = 4, 2D analysis 213
Figure 5.64: Input and output waves for continuously cycled test, R_d = 5 (2D) 213
Figure 5.65: Cross correlation coefficient for R_d = 5, 2D analysis 213
Figure 5.66: Input and output waves for continuously cycled test, R_d = 6 (2D) 214
Figure 5.67: Cross correlation coefficient for R_d = 6, 2D analysis 214
Figure 5.68: Input and output waves for continuously cycled test, R_d = 7 (2D) 214
Figure 5.69: Cross correlation coefficient for R_d = 7, 2D analysis 215
Figure 5.70: Input and output waves for continuously cycled test, R_d = 8 (2D) 215
Figure 5.71: Cross correlation coefficient for R_d = 8, 2D analysis 215
Figure 5.72: Input and output waves for continuously cycled test, R_d = 1 (FS) 216

Figure 5.73: Cross correlation coefficient for $R_d = 1$, FS analysis..... 216
Figure 5.74: Input and output waves for continuously cycled test, $R_d = 2$ (FS)..... 216
Figure 5.75: Cross correlation coefficient for $R_d = 2$, FS analysis..... 217
Figure 5.76: Input and output waves for continuously cycled test, $R_d = 3$ (FS)..... 217
Figure 5.77: Cross correlation coefficient for $R_d = 3$, FS analysis..... 217
Figure 5.78: Input and output waves for continuously cycled test, $R_d = 4$ (FS)..... 218
Figure 5.79: Cross correlation coefficient for $R_d = 4$, FS analysis..... 218
Figure 5.80: Input and output waves for continuously cycled test, $R_d = 5$ (FS)..... 218
Figure 5.81: Cross correlation coefficient for $R_d = 5$, FS analysis..... 219
Figure 5.82: Input and output waves for continuously cycled test, $R_d = 6$ (FS)..... 219
Figure 5.83: Cross correlation coefficient for $R_d = 6$, FS analysis..... 219
Figure 5.84: Input and output waves for continuously cycled test, $R_d = 7$ (FS)..... 220
Figure 5.85: Cross correlation coefficient for $R_d = 7$, FS analysis..... 220
Figure 5.86: Input and output waves for continuously cycled test, $R_d = 8$ (FS)..... 220
Figure 5.87: Cross correlation coefficient for $R_d = 8$, FS analysis..... 221

Chapter 6

Figure 6.1: Settlements on the Impulsora Bridge foundation (after Mendoza et al. (2000b))..... 226
Figure 6.2: Failure of building foundations due to liquefaction during Niigata earthquake, Japan 1964 (after Zienkiewicz *et al.* (1999))..... 228
Figure 6.3: Large gap induced by liquefaction-induced ground settlement in Port Island, Kobe (after Tokimatsu *et al.* (1996))..... 229
Figure 6.4: Cyclic interaction diagram from Haga tension pile tests (after Jardine, (1991))..... 231
Figure 6.5: General footing-soil interaction for bearing capacity equations for strip footings (after Bowles (1988))..... 232
Figure 6.6: A deep strip foundation subjected to a horizontal acceleration $k.g$ (after Potts (2000))..... 235
Figure 6.7: The inclined loading condition (after Potts (2000))..... 236
Figure 6.8: Geometry of critical slip surface for general case (after Sarma and Iossifelis (1990))..... 237

Figure 6.9: Bearing capacity factors as a function of horizontal acceleration and angle of internal friction (after Sarma and Iossifelis (1990)) 237
Figure 6.10: Failure mechanism of a deep strip foundation in horizontal ground (after Potts (2000)) 238
Figure 6.11: Seismic reduction factor $i_{\gamma e}$ for a deep foundation for φ = 30°, c = 0, D = 5B (after Chen (1997)) 240
Figure 6.12: Finite element mesh used in pseudo static analyses 241
Figure 6.13: The effects of φ and δ on the limiting value of the seismic coefficient (k) (after Potts (2000)) 242
Figure 6.14: Vectors of incremental displacement at failure for φ =30° and δ = 15° 243
Figure 6.15: Degree of strength mobilisation at failure for pseudo static analysis . 243
Figure 6.16: Calculation of degree of shear strength mobilisation (after Potts (2000)) 244
Figure 6.17: Active and passive pressures on foundation at failure (φ = 30°, δ = 15°) 244
Figure 6.18: Figure showing mesh and boundary conditions assumed in dynamic analyses 247
Figure 6.19: Arrangement of standard deep foundation 249
Figure 6.20: Load-displacement curve for standard foundation 252
Figure 6.21: Degree of strength mobilisation around foundation at working load 253
Figure 6.22: Original East-West component of Athens earthquake (7/9/1999) ... 254
Figure 6.23: Fourier spectra of original East-West component of Athens earthquake (7/9/1999) 254
Figure 6.24: Equivalent displacement history from original East-West component of Athens earthquake (7/9/1999) 256
Figure 6.25: Frequency components passed by filter 256
Figure 6.26: Athens earthquake record scaled to 0.2g maximum acceleration and filtered 257
Figure 6.27: Equivalent displacement time history from Athens earthquakes after filtering 258
Figure 6.28: Degree of strength mobilisation around foundation after 2.0 seconds 259

Figure 6.29: Degree of strength mobilisation around foundation after 4.1 seconds 260
Figure 6.30: Degree of strength mobilisation around foundation after 4.2 seconds 260
Figure 6.31: Degree of strength mobilisation around foundation after 35.0 seconds 260
Figure 6.32: Expanded view of the total displacement time history for Athens 0.2*g* record, highlighting important analysis increments 262
Figure 6.33: Vectors of incremental displacement at time 3.41 seconds 262
Figure 6.34: Vectors of incremental displacement at time 3.87 seconds 263
Figure 6.35: Vectors of incremental displacement at time 4.25 seconds 263
Figure 6.36: Vectors of incremental displacement at time 4.46 seconds 263
Figure 6.37: Vectors of incremental displacement at time 5.60 seconds 264
Figure 6.38: Stress path for element adjacent to foundation 265
Figure 6.39: Horizontal stress history for Gauss point adjacent to foundation..... 266
Figure 6.40: Vertical stress history for Gauss point adjacent to foundation 266
Figure 6.41: Stress path for element below foundation 267
Figure 6.42: Horizontal stress below foundation during earthquake 267
Figure 6.43: Vertical stress below foundation during earthquake 268
Figure 6.44: Horizontal stress on side of foundation during earthquake 269
Figure 6.45: Areas of mesh showing an increase in horizontal stress 270
Figure 6.46: Areas of mesh showing a significant increase in vertical stress..... 270
Figure 6.47: Horizontal stress distribution before and after earthquake 271
Figure 6.48: Vertical stress distribution before and after earthquake 271
Figure 6.49: Displacement vectors due to earthquake motion 272
Figure 6.50: Vertical displacement history of point A 272
Figure 6.51: Settlement history for point A subjected to 0.2*g* Athens earthquake . 275
Figure 6.52: Detail of mesh used in analysis including structural mass..... 276
Figure 6.53: Settlement history of point A subjected to Athens 0.2*g* earthquake with and without structural mass 276
Figure 6.54: Kocaeli earthquake acceleration record scaled to 0.2*g* 278
Figure 6.55: Kocaeli earthquake displacement record 279
Figure 6.56: Kocaeli earthquake Fourier spectrum 279
Figure 6.57: Tabas earthquake acceleration record scaled to 0.2*g* 279

Figure 6.58: Tabas earthquake displacement record 280
Figure 6.59: Tabas earthquake Fourier spectrum 280
Figure 6.60: Spitak earthquake record scaled to 0.2*g* 280
Figure 6.61: Spitak earthquake displacement record 281
Figure 6.62: Spitak earthquake Fourier spectrum 281
Figure 6.63: Settlement of point A for different earthquakes scaled to 0.2*g* 282
Figure 6.64: Earthquake induced settlement for the four earthquakes scaled to different peak ground accelerations 283
Figure 6.65: AS parameter against earthquake induced settlement 286
Figure 6.66: VS parameter against earthquake induced settlement 286
Figure 6.67: DS parameter against earthquake induced settlement 286
Figure 6.68: AA parameter against earthquake induced settlement 287
Figure 6.69: AV parameter against earthquake induced settlement 287
Figure 6.70: AD parameter against earthquake induced settlement 287
Figure 6.71: Expanded view of the displacement time history for Spitak 0.5*g* record, highlighting important analysis increments 288
Figure 6.72: Vectors of incremental displacement at time = 12.43 seconds 289
Figure 6.73: Vectors of incremental displacement at time = 12.93 seconds 289
Figure 6.74: Earthquake induced displacement vectors for Spitak 0.5*g* earthquake289
Figure 6.75: Load-displacement curve with different working loads illustrated 291
Figure 6.76: Settlement history for the standard foundation at different working loads 292
Figure 6.77: Earthquake induced settlement for Athens 0.3*g* record with different working loads 293
Figure 6.78: Total Lagrangian system (after Izzuddin (1991)) 295
Figure 6.79: Updated Lagrangian system (after Izzuddin (1991)) 295
Figure 6.81: Displacement history of point A for Spitak 0.5*g* earthquake for large and small displacement analyses 297
Figure 6.82: Vectors of incremental displacement at time = 12.43 seconds 297
Figure 6.83: Vectors of incremental displacement at time = 12.93 seconds 298
Figure 6.84: Final mesh configuration around the foundation for large displacement analysis of the Spitak 0.5*g* earthquake 298
Figure 6.85: Displacement vectors around foundation for Spitak 0.5*g* earthquake 299
Figure 6.86: Earthquake induced settlement for Athens earthquake 299

Figure 6.87: Earthquake induced settlement for Kocaeli earthquake..... 300
Figure 6.88: Earthquake induced settlement for Tabas earthquake..... 300
Figure 6.89: Earthquake induced settlement for Spitak earthquake..... 300
Figure 6.90: Figure illustrating the different amounts of shear stress required to induce plastic strains at different foundation depths..... 301

LIST OF TABLES

Chapter 2

Table 2.1: Weighting coefficients and location of integration points for Gaussian integration 44

Chapter 4

Table 4.1: Single degree of freedom analysis parameters 106
Table 4.2: Summary of cylindrical bar analyses 129
Table 4.3: Parameters for the closed form solution of a soil column subjected to a periodic load 143
Table 4.4: Parameters for the finite element analysis of the soil column subjected to a periodic load 143

Chapter 5

Table 5.1: Input wave parameters and interpreted shear wave velocities from first shear wave arrival plane strain bender element analyses 190
Table 5.2: Input wave parameters and interpreted shear wave velocities from continuously cycled plane strain bender element analyses 195
Table 5.3: Input wave parameters and interpreted shear wave velocities from first shear wave arrival plane strain bender element analyses (FS analysis) 201
Table 5.4: Input wave parameters and interpreted shear wave velocities from continuously cycled Fourier series aided bender element analyses 202

Chapter 6

Table 6.1: Summary of bearing capacities and factors of safety for each combination of φ and δ 241
Table 6.2: Bearing capacity of standard foundation by different methods 249
Table 6.3: Seismic bearing capacity of standard foundation by different methods 250

Table 6.4: Details of earthquake records used in study 278
Table 6.5: Summary of results for 0.2*g* earthquakes 282
Table 6.6: Summary of analyses undertaken at different working loads 291
Table 6.7: Seismic bearing capacity of standard foundation subjected to 0.3*g* earthquake 293
Table 6.8: Predicted earthquake induced settlement for a foundation designed using limit equilibrium methods 294

LIST OF SYMBOLS

A and B	Parameters used in evaluating the Rayleigh damping matrix.
B	Width of foundation.
$[B]$	Matrix containing the derivatives of the shape functions.
B' and L'	Reduced dimension of deep foundation due to applied moment given by $B' = B - 2e$ *and* $L' = L - 2e$.
c	Damping coefficient for single degree of freedom problem given by $c = 2\lambda m\omega_D$.
c'	Cohesion intercept of a soil.
$[C_E]$	Elemental damping matrix.
$[C_G]$	Global damping matrix.
d/λ	Ratio of element size d, and input loading wavelength λ.
d_γ d_q and d_c	Correction factors for depth for self weight, surcharge and cohesion bearing capacity factors respectively.
D	Bulk modulus of soil skeleton.
$[D]$	Total stress constitutive matrix.
$[D_f]$	Stiffness matrix of pore fluid.
$[D']$	Effective stress constitutive matrix.
E	Young's modulus.
$[E]$	Vector containing the derivatives of the pore fluid shape functions.

f	Bender element excitation input frequency.
f_{min}	Minimum input frequency for a bender element test to avoid the near field effect.
FOS	Factor of safety of foundation.
G	Shear modulus.
G_{max}	Shear modulus of a soil at very small strains, which is assumed to be its maximum value.
$[G]$	Pore fluid inertia matrix.
h	Height of resonant column sample.
$[h]$	Pressure head of pore fluid.
i	Equivalent ground inclination angle for deep foundation subjected to horizontal loading given by $i = \tan^{-1}(k)$.
i_γ i_q and i_c	Correction factors for load inclination for self weight, surcharge and cohesion bearing capacity factors respectively.
$i_{\gamma e}$	Seismic reduction factor for a deep foundation proposed by Chen (1997).
$\{i_G\}$	Unit vector parallel, but in the opposite direction to gravity.
I	Mass polar moment of inertia of a resonant column sample.
I_0	Mass moment of inertia for the loading system for a resonant column test.
J	Polar moment of inertia of a resonant column sample.
$[J]$	Jacobian matrix, used to transform parent coordinate system to the global coordinate system.

k	Applied horizontal acceleration as a proportion of gravitational acceleration.
$[k]$	Matrix of soil permeability.
K_0	Coefficient of earth pressure at rest.
K_a and K_p	Active and passive coefficients of earth pressure present during the application of horizontal loading.
K_e	Equivalent bulk modulus of pore fluid.
K_f	Bulk modulus of pore fluid.
K_s and K_n	Shear and normal stiffness of interface elements.
K_s	Bulk modulus of soil skeleton.
$[\overline{K}]$	Effective stiffness matrix, including contributions from the global mass and damping matrices.
$[K_E]$	Elemental stiffness matrix.
$[K]$	Global stiffness matrix
L	Length of foundation.
$[L]$	Off diagonal multiplying matrix in coupled equations.
$[m]^T$	Multiplying vector equal to $[1 \quad 1 \quad 1 \quad 0 \quad 0 \quad 0]$.
M_a	Earthquake magnitude measure based on wave amplitude.
M_e	Earthquake magnitude measure based on energy content.
M_s	Earthquake magnitude measure based on surface wave energy.
$[M_E]$	Elemental mass matrix.
$[M]$	Global mass matrix.

n	Soil porosity.
$[n]$	Right hand side load vector for pore fluid equilibrium equation.
N	Number of wavelengths between the bender element tips for a continuously cycled bender element test.
$\lfloor N_p \rfloor$	Shape functions for pore pressure degrees of freedom.
N_n	Isoparametric shape function for node n.
$[N]$	Matrix of all element shape functions.
$\overline{N}$	Substitute shape function for beam element.
N_γ, N_q and N_c	Bearing capacity factors for self weight, surcharge and cohesion respectively.
$P(t)$	Forcing function.
$\mathcal{Q}$	Represents any sinks and/or sources of flow.
$\mathcal{Q}_{av}$	Average permanent loading on foundation.
$\mathcal{Q}_b$	Vertical load on foundation.
$\mathcal{Q}_{cyclic}$	Cyclic amplitude of loading on foundation.
$\mathcal{Q}_{max.static}$	Static loading capacity foudantion.
R_d	Ratio of distance between the bender element tips d, and the input wavelength λ. This ratio represents the number of wavelengths present between the bender element tips.
$[S]$	Pore fluid compressibility matrix.
t	Current time in any analysis.
t	Thickness of element.

T	Inertial torque of a resonant column test.
T	Time period of loading
T/T_a	Ratio of current time T, to theoretical shear wave arrival time T_a for a bender element analysis.
T_1	Fundamental natural frequency of a soil column.
T_n	Smallest natural period of a system with n degrees of freedom.
u and v	Displacement components for an isoparametric element.
v	Poisson's ratio
V_c, V_{comp} and v_p	Velocity of propagation for a compression wave.
V_{hh}, v_{hh}	Velocity of propagation for a shear wave initiated and propagating in the horizontal direction.
V_{hv}, v_{hv}	Velocity of propagation for a shear wave initiated in the vertical direction but propagating in the horizontal plane.
V_{shear}, V_s and v_s	Velocity of propagation of a shear wave.
w_x, w_y and w_z	Components of the superficial velocity of the pore fluid.
α and δ.	Newmark parameters (after Bathe (1996)), equivalent to the parameters β and γ respectively, introduced by Newmark (1959).
β	Integration parameter introduced to indicate how the pore pressure is assumed to vary during an increment.
γ	Parameter introduced to the modified Newmark method to allow the choice of a time discretisation scheme in which the acceleration is assumed to vary according to a quadratic expression.
γ_f	Bulk unit weight of the pore fluid.

δ_a and δ_p	Interface angle of friction between the foundation shaft and the soil on the active and passive sides respectively.
$\{\Delta d\}^T$	Vector of displacement components given by $\{\Delta d\}^T = \{\Delta u, \Delta v\}$.
$\{\Delta F\}^T$	Vector of body forces given by $\{\Delta F\}^T = \{\Delta F_x, \Delta F_y\}$.
Δp_f	Applied incremental pore pressure.
$\{\Delta \dot{p}\}$	Derivative of incremental pore pressure with respect to time.
ΔR_i	Iterative load vector.
$\{\Delta \dot{R}\}$	Differential of the loading vector with respect to time.
$\{\Delta \overline{R}\}$	Effective right hand side load vector, including known values from the previous time step.
$\{\Delta R_E\}$	Elemental right hand side load vector.
Δt	Incremental time step.
Δt_{cr}	Critical time step required to ensure a time scheme remains stable.
$\{\Delta T\}^T$	Vector of surface tractions given by $\{\Delta T\}^T = \{\Delta T_x, \Delta T_y\}$.
$\{\Delta u\}$	Vector containing incremental values for u and v.
$\{\Delta \dot{u}\}$	Vector of incremental velocities.
$\{\Delta \ddot{u}\}$	Vector of incremental accelerations.
$\{\Delta \dddot{u}\}$	Vector containing incremental values of the third derivative of displacement with respect to time, or jerk.
$\Delta \varepsilon_v$	Incremental volumetric strain.

$\Delta\varepsilon_x$, $\Delta\varepsilon_y$ and $\Delta\gamma_{xy}$	Horizontal, vertical and shear strain components within an element.
$\Delta\sigma$	Change in total stress.
$\Delta\sigma'$	Change in effective stress.
$\Delta\sigma_f$	Change in pore fluid pressure.
λ	Damping fraction for single degree of freedom problem.
μ and λ	Lame's constants.
ρ_f	Fluid density.
ρ	Material density.
τ/τ_f	Ratio of current shear stress to the shear stress at failure.
φ'	Angle of internal shearing resistance of a soil.
$[\phi]$	Permeability submatrix in consolidation stiffness matrix.
ψ	Angle of dilation.
ψ_i	Out of balance force for iteration *i*.
ω_D	Damped natural frequency of single degree of freedom problem.
ω_n	Natural circular frequency of soil sample.

Chapter 1:

INTRODUCTION

1.1 General Introduction

Dynamic forces are present in every engineering problem although they are only considered to be significant in a few specific scenarios. The most high profile situation is when an engineered structure is subjected to earthquake induced loading. The design and response of structures to earthquake loading is important in areas of high seismicity, such as Southern Europe, the West coast of the USA and South East Asia. In regions of low seismicity such as the UK, certain critical structures such as nuclear power stations and quay walls have to be designed to resist a characteristic earthquake loading.

Although it is important to be able to analyse the response of geotechnical structures to these dynamic loads, it is often not possible due to the complexity of the problem. Closed form solutions are rare, and those that do exist often have to assume an idealised geometry and material behaviour. As well as these simplifications, many dynamic analyses only consider a total stress response. This is a gross over simplification and the phenomena of weakening and liquefaction can only be reproduced by considering a two-phase coupled response.

There are other situations where dynamic forces become important which are less dramatic than the analysis of earthquakes. For example the foundation pressures from reciprocating machinery, the process of pile driving and the passage of traffic on a bridge.

In contrast to the devastation caused by earthquakes, the propagation of elastic shear waves has been turned to the advantage of the geotechnical engineer with the development of dynamic soil tests. These include in-situ and laboratory based examples such as the cross borehole, resonant column and bender element tests. All these tests rely on the user exciting the soil and measuring either the natural

frequency of the sample in the case of the resonant column or the shear wave travel time for the crosshole and bender element tests. The motivation for performing these tests is the relationship between these dynamic characteristics and the fundamental elastic soil properties.

Finite element analysis is a powerful analysis tool which has grown in popularity over the last twenty years due to its increased ability to analyse realistic problems and achieve good predictions. Dynamic analyses are less widespread but are becoming more important as the pressure of urban expansion in developed countries and economic progress in the third world requires the development of land in seismic areas. Finite element analysis is increasingly being used to design high profile developments due to the flexibility that this analysis tool offers in terms of accurately modelling the geometry of a problem and its ability to replicate some of the key features of soil behaviour.

1.2 Scope of Research

The main aim of this research was to investigate, implement and then validate the changes that must be made to the existing static geotechnical finite element program ICFEP (Imperial College Finite Element Program) to make dynamic analyses possible. ICFEP has been developed at Imperial College by Prof. David Potts for over twenty years and has many features designed specifically to analyse geotechnical problems.

This was achieved by conducting a literature review of the most commonly used time marching schemes available in the literature and then recommending the most appropriate algorithm for our application. The chosen time discretisation scheme was a modified version of the standard Newmark method. The addition of an extra parameter allowed further flexibility of including a higher order approximation in which the acceleration was assumed to vary during an increment of the analysis according to a quadratic function.

Upon the recommendations of the student, the coding was performed by Professor David Potts. The subsequent debugging and validation were performed by the research student.

The implementation of the modified Newmark method was then validated by analysing problems which have well known closed form solutions and then comparing the results. The dynamic version of ICFEP was then used to investigate two problems that were chosen to demonstrate the diversity of situations in which dynamic forces are significant.

The first of these was the use of bender elements to measure the small strain stiffness of soils in the laboratory. Two dimensional and Fourier series three dimensional analyses were undertaken to investigate the accuracy of the traditional time of the flight method and the recently developed phase sensitive detection method.

The second research topic concerned the behaviour of deep foundations when subjected to earthquake loading. Traditional design methods take earthquake induced forces into account by reducing the static bearing capacity of the foundation either by replacing the earthquake forces with an equivalent inclined load or by using pseudo static limit equilibrium analyses. The dynamic version of ICFEP was used to investigate the response of a deep foundation when subjected to a range of real earthquake records.

1.3 Layout of Thesis

The work presented in this thesis is divided into the following chapters:

Chapter 2 presents the finite element theory necessary to analyse static geotechnical problems. This includes the derivation of the finite element equilibrium equations for the solid phase and the pore fluid and then demonstrates how these are combined to analyse a coupled problem. As well as presenting the derivation for two dimensional analyses, the theory is also presented for the Fourier series aided three dimensional analyses. The theory for interface and beam elements is also presented as these are important for analysing geotechnical problems.

Chapter 3 presents a literature review of the available time discretisation methods. A comparison of these methods is then made and a decision regarding which is most suitable for our application reached. The implementation of this time discretisation

method is then described for two dimensional and Fourier series aided three dimensional analyses. The dynamic considerations are presented for the pore fluid equilibrium equation and the interface and beam elements which have been derived particularly for geotechnical analyses.

Chapter 4 presents the results of the validation exercises undertaken once the implementation of the theory presented in Chapter 3 had been completed. The analyses are validated in a qualitative sense by analysing the simplest possible problem of a longitudinal wave travelling through a cylindrical rod. Quantitative validation is achieved for total stress analyses by analysing a spherical cavity subjected to an impulse loading and coupled analyses are validated by considering a fully saturated soil column subjected to cyclic loading at the surface. A brief investigation is undertaken to determine some of the fundamental properties of dynamic finite element analyses. The dependence of the analysis accuracy upon the number of the elements per wavelength and the unsuitability of the higher order time discretisation scheme are illustrated.

Chapter 5 presents the results from the investigation into the use of bender elements to measure the small strain stiffness of soils. A parametric study is undertaken to determine the properties of the analysis which are required to give accurate and reliable results. This included the mesh density, time step and the type of drainage assumed in the soil. An investigation was then carried out into the accuracy of the traditional time of flight method and the recently developed phase sensitive detection method for a range of input frequencies.

Chapter 6 presents the results of the investigation into the behaviour of deep foundations when subjected to earthquake loading. First the traditional design methods for the design of deep foundations are reviewed and then the modifications required to include the effects of earthquake loading are presented. A standard foundation is then defined and its dynamic capacity determined using the previously described design methods. This foundation is then subjected to a series of earthquake records and its behaviour analysed using dynamic finite element analysis. The behaviour is then compared with that predicted by the traditional design methods, pseudo static analyses and the general behaviour of deep foundations observed in the field.

Chapter 7 presents a summary of the work presented in this thesis and compares the two main problems chosen for investigation. Conclusions are then drawn regarding each topic and suggestions made for the direction of future research in terms of finite element implementation and the two researched topics.

Chapter 2:

FINITE ELEMENT THEORY

2.1 Introduction

This chapter details the theory that underlies static finite element analysis. Whilst ICFEP supports a wide range of features, only those used in this thesis will be detailed here. In the first section the equations of equilibrium are formulated for the displacement based finite element method. This section also includes the algorithms that are required to numerically integrate the element stiffness matrix and to invert the global system of equations.

Up to this point the theory is generic and is applicable to the analysis of any solid mechanics problem. The next section presents the theory that is particularly required for the analysis of geotechnical problems. This includes the calculation of pore fluid pressures and the formulation of special elements to model structural features, such as retaining walls or tunnel linings, and interface elements that allow relative movement between adjoining solid elements.

The next section presents the theory that is required for the solution of non-linear problems. This includes a discussion of the modified Newton-Raphson scheme used to obtain the results presented in this thesis.

The theory presented in the second section for calculating the pore fluid pressure response is only valid if the response of the soil is undrained, that is no overall volume change is allowed. If, however, the pore fluid is allowed to flow within the soil matrix, then the deformation behaviour of the soil and the pore pressure response are interdependent or coupled together. The next section gives details of how this behaviour is modelled by finite element theory.

The final section explains the theory behind Fourier series aided finite element analysis. This is a novel method for analysing three dimensional problems in a

fraction of the time and with substantially less computational resources than standard three dimensional analyses. The method can be used for problems that have an axi-symmetric geometry but non-axi-symmetric boundary conditions and/or material properties. The mesh is still two dimensional, but the displacements and loads are varied in the out of plane direction as a Fourier series.

The theory presented in this chapter reflects the approach taken in ICFEP. There are examples presented in this chapter where more than one option is available for achieving the same goal. An example of this is the non-linear iterative solver. The modified Newton-Raphson method is by default used by ICFEP, although other options do exist, for example the tangent stiffness method, the visco-plastic method and the original Newton-Raphson method. For this and any other examples the reasons for this choice will not be presented in this thesis. Full details for these choices and other numerical investigations can be found in Potts and Zdravković (1999).

2.2 General Formulation

The process of finite element analysis begins with dividing the solution domain into discrete regions, termed finite elements, that are interconnected at nodal points. The manner in which this is performed according to accuracy requirements, although some geometric features, such as a boundary between two geological strata, may influence the geometry of the mesh. Consideration also has to be made regarding alterations to the mesh geometry that may occur during the analysis. If, for example a tunnel excavation is to be modelled, then the geometry of the final excavated shape must be included in the original mesh.

Once geometric considerations have been taken into account, the number of elements and their distribution is often left to engineering judgement. However, the manner in which this is undertaken will have a major influence on the validity of the results obtained. For example, having a very fine regular mesh would give accurate results but would take a long time to analyse. A very coarse mesh would take less time to run, but the results would be less reliable. The objective is to have as few elements as possible to reduce the analysis run time, but to refine the mesh at locations where the greatest stress concentrations occur to give an accurate result.

Some rules of thumb exist for the number of elements required for accuracy requirements, although commonly the mesh design is based on previous experience.

The most common type of element used in ICFEP is the eight noded isoparametric solid element. Such an element has two unknown displacements (i.e. degrees of freedom) at each node. An example is shown in Figure 2.1.

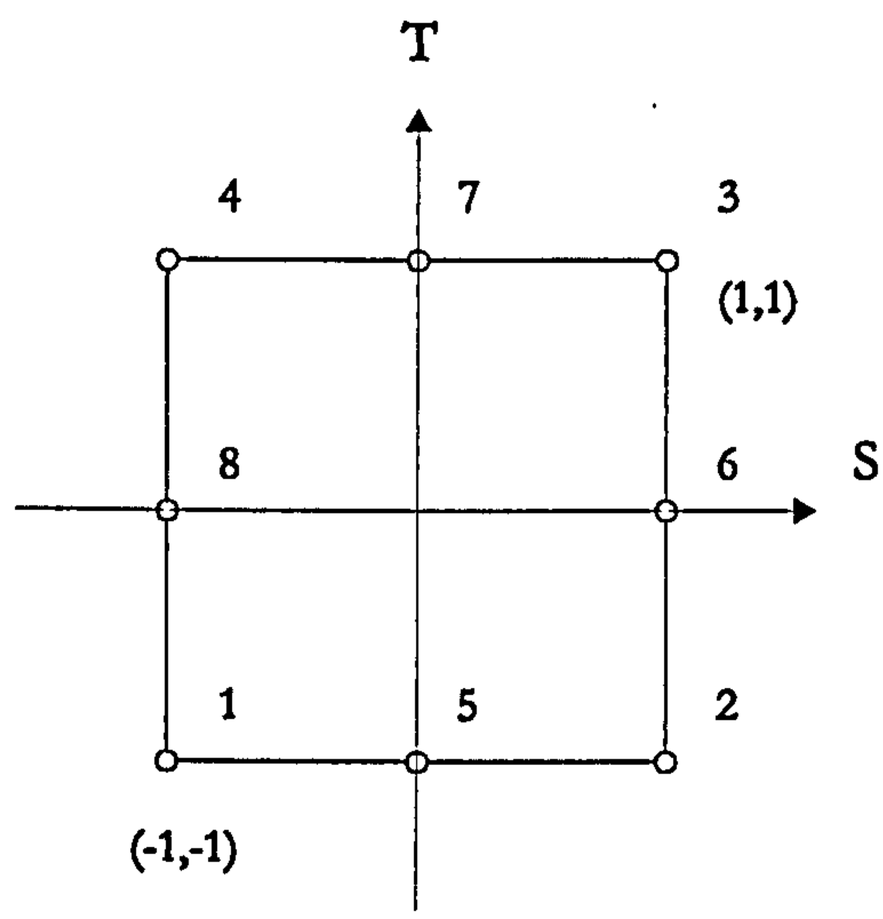

Figure 2.1: Eight noded isoparametric solid element

The basic assumption in the displacement based finite element approach is to establish a set of functions that are chosen so that they uniquely define the state of displacement within each element in terms of its nodal values. In this way the number of degrees of freedom becomes finite, and any other displacement within an element can be interpolated using these so called shape functions and the known nodal values. The shape functions for a typical corner node, node 1, and a typical mid-side node, node 5, of the element shown in Figure 2.1 are given in terms of natural coordinates S and T by Equations 2.1a and 2.1b.

$$N_1 = \tfrac{1}{4}(1-S)(1-T) - \tfrac{1}{4}(1-S^2)(1-T) - \tfrac{1}{4}(1-S)(1-T^2) \qquad (2.1a)$$

$$N_5 = \tfrac{1}{2}\left(1-S^2\right)(1-T) \qquad (2.1b)$$

Similar shape functions can be found for the remaining nodes ensuring that the value of the shape function for node n must be unity at node n and zero at the other nodes. The displacement components u and v at any point within an element can now be expressed in terms of their values at the nodes.

$$\begin{Bmatrix} u \\ v \end{Bmatrix} = [N] \begin{Bmatrix} u \\ v \end{Bmatrix}_{nodes} \tag{2.2}$$

This type of element is called isoparametric because the same matrix of shape functions [*N*], is used to map the global coordinates of each element (in terms of x and y) to the natural coordinates (in terms of S and T) and to describe the variation of the unknown displacements within an element. The advantage of defining the displacement variation in terms of the natural coordinates S and T is that a standard procedure can be used to evaluate the integrals that make up each term in the stiffness matrix.

The approximation of the displacements by Equation 2.2 makes it possible to formulate the equilibrium equation for each element, which can then be used to describe its deformational behaviour. Assuming plane strain conditions apply, the strains within the element are related to the nodal displacements by Equation 2.3.

$$\Delta\varepsilon_x = \frac{\partial(\Delta u)}{\partial x}, \Delta\varepsilon_y = \frac{\partial(\Delta v)}{\partial y}, \Delta\gamma_{xy} = \frac{\partial(\Delta u)}{\partial y} + \frac{\partial(\Delta v)}{\partial x}$$

$$\Delta\varepsilon_z = \Delta\gamma_{xz} = \Delta\gamma_{zy} = 0; \ \{\Delta\varepsilon\}^T = \{\Delta\varepsilon_x \Delta\varepsilon_y \Delta\gamma_{xy}\} \tag{2.3}$$

Replacing the displacements by the approximations given by Equation 2.2, the following relationship is found.

$$\{\Delta\varepsilon\} = [B] \begin{Bmatrix} \Delta u \\ \Delta v \end{Bmatrix}_{nodal} = [B]\{\Delta d\}_{nodal} \tag{2.4}$$

where the matrix [*B*] contains the derivatives of the shape functions *N*.

The stresses can now be determined using the chosen constitutive relationship:

$$\{\Delta\sigma\} = [D]\{\Delta\varepsilon\} \tag{2.5}$$

where $\{\Delta\sigma\}$ is a vector containing the stress components and [*D*] is the constitutive matrix.

For a single element the primary variable, displacement, has now been related to the two secondary variables, stress and strain. These relationships can then be used to calculate the incremental potential energy of a single element, which is defined as:

$$\textit{Incremental potential energy } (\Delta E) = \textit{Incremental Strain energy } (\Delta W) - \textit{Incremental work done by applied loads } (\Delta L) \tag{2.6}$$

The incremental strain energy in an element and the incremental work done by external loads are given by Equations 2.7 and 2.8 respectively.

$$\Delta W = \frac{1}{2}\int \{\Delta\varepsilon\}^T \{\Delta\sigma\} dVol \tag{2.7}$$

$$\Delta L = \int_{Vol} \{\Delta d\}^T \{\Delta F\} dVol + \int_{Surface} \{\Delta d\}^T \{\Delta T\} dSurface \tag{2.8}$$

where $\{\Delta d\}^T = \{\Delta u, \Delta v\}$ = displacements

$\{\Delta F\}^T = \{\Delta F_x, \Delta F_y\}$ = body forces

$\{\Delta T\}^T = \{\Delta T_x, \Delta T_y\}$ = surface tractions

Equilibrium requires that a body's potential energy is a minimum. The condition when this occurs can be found by differentiating the expression for incremental potential energy and setting it to zero. The stress and strain terms in Equation 2.7 can now be replaced by the approximations found previously and the resulting expression along with Equation 2.8 substituted into Equation 2.6 to give the potential energy in terms of the unknown nodal displacements. The minimum potential energy is then found by summing up the potential energy of all the individual elements and then differentiating this expression with respect to the nodal displacements. The result is Equation 2.9, which becomes zero when the expression in square brackets is equal to zero. This expression, when written in the form of Equation 2.10, represents the equilibrium equation for the finite element assemblage.

$$\delta\Delta E = \sum_{i=1}^{N}\left(\{\delta\Delta d\}_n^T\right)_i \begin{bmatrix} \int_{Vol}[B]^T[D][B]dVol\{\Delta d\}_n - \\ \int_{Vol}[N]^T\{\Delta F\}dVol - \int_{Surface}[N]^T\{\Delta T\}dSurface \end{bmatrix}_i = 0 \qquad (2.9)$$

$$\sum_{i=1}^{N}[K_E]_i(\{\Delta d\}_n)_i = \sum_{i=1}^{N}\{\Delta R_E\} \qquad (2.10)$$

where $[K_E] = \int_{Vol}[B]^T[D][B]dVol$ = Element stiffness matrix

$\{\Delta R_E\} = \int_{Vol}[N]^T\{\Delta F\}dVol + \int_{Surface}[N]^T\{\Delta T\}dSurface$ = Right hand side load vector

$\{\Delta d\}_n$ = vector of unknown displacements.

As mentioned previously, the matrix of shape functions [*N*], and therefore its derivatives [*B*], are given in terms of the natural coordinate system, *S* and *T*, however the integrals shown in Equation 2.9 must be calculated in terms of the global coordinates *x* and *y*. The volume integral in Equation 2.9 can be transformed into the global coordinate system by using the determinant of the Jacobian matrix. Assuming the element to have a thickness *t* (which is taken as unity for plane strain problems), the transformed integral is given by Equation 2.11.

$$dVol = t\,dxdy = t|J|dS\,dT \qquad (2.11)$$

where [*J*] is the Jocobian matrix:

$$[J] = \begin{bmatrix} \frac{\partial x}{\partial S} & \frac{\partial y}{\partial S} \\ \frac{\partial x}{\partial T} & \frac{\partial y}{\partial T} \end{bmatrix} \qquad (2.12)$$

and hence:

$$|J| = \frac{\partial x}{\partial S}\frac{\partial y}{\partial T} - \frac{\partial y}{\partial S}\frac{\partial x}{\partial T} \qquad (2.13)$$

Therefore the stiffness matrix of a single element can be calculated in terms of the natural coordinates S and T by Equation 2.14.

$$[K_E] = \int_{-1}^{1}\int_{-1}^{1} t[B]^T [D][B] J|dSdT \tag{2.14}$$

The overall stiffness matrix of the finite element mesh can then be found by summing the contribution of each individual element.

Before integrating Equation 2.14, the [B] matrix which contains the derivatives of the shape functions must be transformed into the natural coordinate system. This requires the use of the chain rule.

$$\left\{\frac{\partial N_i}{\partial S}\frac{\partial N_i}{\partial T}\right\}^T = [J]\left\{\frac{\partial N_i}{\partial x}\frac{\partial N_i}{\partial y}\right\}^T \tag{2.15}$$

Equation 2.15 can then be inverted to give the derivative of the shape functions in terms of the natural coordinates:

$$\begin{Bmatrix}\dfrac{\partial N_i}{\partial x}\\ \dfrac{\partial N_i}{\partial y}\end{Bmatrix} = \frac{1}{|J|}\begin{bmatrix}\dfrac{\partial y}{\partial T} & -\dfrac{\partial y}{\partial S}\\ -\dfrac{\partial x}{\partial T} & \dfrac{\partial x}{\partial S}\end{bmatrix}\begin{Bmatrix}\dfrac{\partial N_i}{\partial S}\\ \dfrac{\partial N_i}{\partial T}\end{Bmatrix} \tag{2.16}$$

The integrations required to find the right hand side load vector can be transformed into the natural coordinate system in a similar fashion.

Explicitly evaluating the integrals given by Equation 2.14 is only possible for a limited number of simplified cases. For the general case it is therefore necessary to use a form of numerical integration to perform this task. Although many options are available, ICFEP uses Gaussian integration due to its high degree of accuracy for relatively few computations. For a function *f(x)*, its integration between the limits -1 and +1 is approximated by Equation 2.17.

$$\int_{-1}^{1} f(x)dx \approx \sum_{j=1}^{n} A_i f_i \tag{2.17}$$

where A_i is a weighting coefficient, n is the integration order and f_i is the expression $f(x)$ evaluated at a given value of x_i. Depending on what order of integration is required, the values of these weighting coefficients and the values of x at which the function $f(x)$ must be evaluated are given in Table 2.1.

Integration Order	Evaluation Points	Weighting Coefficients
2	$\pm 1/\sqrt{3}$	1
3	0 $\pm\sqrt{3/5}$	8/9 5/9
4	$\pm\sqrt{(15-\sqrt{120})/35}$ $\pm\sqrt{(15+\sqrt{120})/35}$	0.6521451549 0.3478548451

Table 2.1: Weighting coefficients and location of integration points for Gaussian integration

The approximation becomes more accurate as the value of n increases at the expense of greater computational effort. Gaussian integration of order n can accurately integrate a polynomial of order $2n$-1. The option exists in ICFEP for using 2×2, 3×3 or 4×4 Gaussian integration. The default option is 2×2 Gaussian integration which is referred to as reduced integration due to potential numerical difficulties being encountered when using 3×3 or full integration with undrained problems. This issue, and its influence on dynamic finite element analyses, will be returned to later in this chapter.

It is now possible to evaluate the global stiffness matrix for a given finite element mesh. The final stage of the analysis procedure is the application of appropriate boundary conditions and the subsequent solution of the global set of equations. Boundary conditions fall into two distinct categories and affect different parts of the equilibrium equation. The first set affects the right hand side load vector and includes the effect of body forces and the application of point loads and surcharges. The second set of boundary conditions affect the list of nodal displacements. It is necessary to prescribe the movement for no less than three degrees of freedom, with at least one in each direction. In a mathematical sense this is to ensure that the

global stiffness matrix does not become singular and thus unsolvable. In an engineering sense it is to guarantee that rigid body motion of the mesh is not possible. The application of boundary conditions to geotechnical problems can cause some difficulties, as most geotechnical problems occur in the infinite earth. The solution most commonly adopted is to place zero displacement conditions along the sides and bottom of a mesh which themselves are located at a great enough distance so their location does not affect the behaviour of the areas of significant interest. This is again a matter of balancing the need for an accurate result whilst minimising the analysis run time.

Now that the global stiffness matrix has been formed and the boundary conditions applied, the system of equations must be solved to give the list of unknown nodal displacements. Many mathematical algorithms have been developed to invert large matrices. The default option used in ICFEP is LU factorisation or triangular decomposition, as it can be coupled with the column-profile storage scheme which reduces the computational memory requirement (see Potts and Zdravković (1999)). Once the primary variable, displacement, has been found, the secondary variables, stress and strain, can be calculated using Equations 2.4 and 2.5.

2.3 Geotechnical Considerations

The finite element theory presented in the previous section is applicable to any static mechanics problem. However, there are some features particular to geotechnical engineering that must be added to the theory before any real problems can be analysed.

2.3.1 Pore Fluid – Soil Interaction

The most significant difference between soil and other engineering materials is that it is composed of two separate phases, the soil skeleton and the fluid which fills the pores between the individual soil particles. If the soil begins to de-saturate, the inclusion of air in the soil matrix adds another possible phase to the material, although this will not be considered in this thesis. This difference requires the finite element program to include the presence of the pore fluid in the equilibrium

equations. This is made possible by invoking the principle of effective stress which splits the total stress into an effective stress component and the pore fluid pressure.

$$\{\Delta\sigma\} = \{\Delta\sigma'\} + \{\Delta\sigma_f\} \tag{2.18}$$

where $\{\Delta\sigma\}$ is the change in total stress

$\{\Delta\sigma'\}$ is the change in effective stress

$\{\Delta\sigma_f\}^T = \{\Delta p_f \quad \Delta p_f \quad \Delta p_f \quad 0 \quad 0 \quad 0\}$ and $\{\Delta p_f\}$ is the change in pore fluid pressure

Two extreme cases can be identified in geotechnical engineering. The first assumes drained conditions in which the change in total stress is assumed to be equal to the change in effective stress. For this case the theory presented in Section 2.2 will suffice. The second is the undrained case in which there is no overall volume change allowed. For this case the stiffness of the pore fluid $[D_f]$ must be added to the stiffness of the soil skeleton $[D']$ to create a new constitutive matrix $[D]$.

$$[D] = [D'] + [D_f] \tag{2.19}$$

The pore fluid stiffness matrix is related to the bulk modulus of the pore fluid, K_f, by considering a unit volume of soil with porosity n. The pore fluid occupies a volume n and the soil particles a volume $1\text{-}n$. If K_s is the bulk modulus of the solid soil particles, the application of an increment of pore pressure, Δp_f, would cause a change in volume given by:

$$\Delta\varepsilon_v = \frac{n}{K_f}\Delta p_f + \frac{(1-n)}{K_s}\Delta p_f \tag{2.20}$$

When this is rearranged it gives the following expression for the equivalent bulk modulus of the pore fluid (i.e. $\Delta p_f / \Delta\varepsilon_v$):

$$K_e = \left(\frac{n}{K_f} + \frac{(1-n)}{K_s}\right)^{-1} \tag{2.21}$$

As K_s is often large compared to K_f, Equation 2.21 can be simplified to:

$$K_e = \frac{K_f}{n} \tag{2.22}$$

If however the exact value of the bulk modulus is unimportant, it may be convenient to assume $K_f = K_s$, in which case Equation 2.21 simplifies further to Equation 2.23.

$$K_e = K_f \tag{2.23}$$

The stiffness matrix can then be evaluated by the addition of the solid stiffness matrix, calculated in the manner described in Section 2.2, to the pore fluid stiffness matrix. The solution procedure then continues as before, with the only difference arising when calculating the stresses. To find the change in pore pressure, $[D_f]$ is used with the calculated strains, and $[D']$ is used to find the change in effective stresses.

2.3.2 Special Elements Required to Model Geotechnical Problems

Two types of special element were used during the research for this thesis. The first allows structural components to be modelled by a simplified two dimensional beam element that is conveniently formulated in terms of axial, bending and shear strains. Whilst it may be possible to model, for example a retaining wall, by solid elements, this would produce results in the form of plane and out of plane strains which are much less convenient. In addition to this problem, many solid elements would be required to maintain a reasonable aspect ratio. This would increase the overall number of elements in the mesh and hence increase computational demand. The finite element formulation of an isoparametric curved Mindlin beam element with 3 nodes was developed for use in ICFEP and will be briefly described here. An example of one of these elements is shown in Figure 2.2.

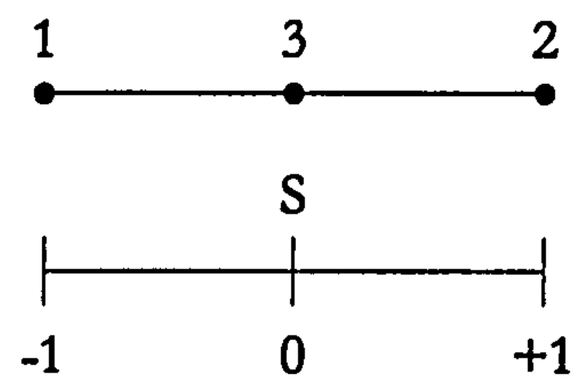

Figure 2.2: Three noded isoparametric beam element

Each node has three degrees of freedom, two displacements and one rotation. In a similar fashion to the solid elements described in Section 2.2, the overall deformational behaviour of the element is assumed to be given by a product of a shape function and the values of the degrees of freedom at the nodes. The shape function for node 1 of the element shown in Figure 2.2 is given by Equation 2.24.

$$N_1 = \frac{1}{2}S(S-1) \tag{2.24}$$

A similar procedure to that explained in Section 2.2 for the solid elements is then performed to derive the element stiffness matrix. The result is Equation 2.25.

$$[K_E] = \int_{-1}^{1} t[B]^T[D][B]|J|ds \tag{2.25}$$

where t is the element thickness and $|J|$ is the determinant of the Jacobian matrix given by Equation 2.26.

$$|J| = \left[\left(\frac{dx}{dS}\right)^2 + \left(\frac{dy}{dS}\right)^2\right]^{\frac{1}{2}} \tag{2.26}$$

and $[B]$ is a matrix containing the derivatives of the shape functions. Problems arise when using 3×3 Gaussian integration for the evaluation of the integral given by Equation 2.25. The membrane axial and shear forces tend to 'lock up', resulting in numerical instability. To overcome this problem substitute strain shape functions were used for some of the terms in the $[B]$ matrix. The substitute function for node 1 shown in Figure 2.2 is given by Equation 2.27 (see Potts and Zdravković (1999)).

$$\overline{N} = \frac{1}{2}\left(\frac{1}{3} - S\right) \tag{2.27}$$

Note that the substitute strain shape function has the same value as the original shape function at the location of the integration points for 2×2 Gaussian integration ($S = \pm 1/\sqrt{3}$). This makes the evaluation of these terms in the element stiffness matrix equivalent to using 2×2 integration irrespective of what is used for the remaining terms, thus ensuring numerical stability.

The second type of special element used is a zero thickness interface element which allows the relative movement of two adjoining elements. One of the fundamental requirements of finite element analysis is that continuity is maintained between connected nodes. However, in practice discontinuities may develop within the ground. Examples of this are a tension crack forming behind a retaining wall, at the top of a slope or behind a pile subjected to lateral loading. To overcome this problem without invalidating the continuity requirement, zero thickness elements have been developed that can open up when their tensile strength is exceeded. This does of course rely on the user predicting where a discontinuity may occur and placing interface elements at that location. Whilst it may be obvious where a shear failure may occur around a pile, predicting the location of a tension crack in a slope is considerably more difficult. The material properties assigned to these interface elements also cause complications. Due to the nature of their formulation, the material properties have different units to the surrounding solid elements. This causes difficulties because the interface elements are trying to replicate the deformational behaviour of the surrounding soil and therefore some investigation is required before choosing the shear stiffness and normal stiffness of the interface elements.

Full details of the formulation for both the beam and interface elements and their implementation and performance in ICFEP can be found in Day (1990) and Potts and Zdravković (1999), (2001).

2.4 Non-Linear Finite Element Theory

The finite element theory presented in Section 2.2 is only valid if the soil behaviour is assumed to be linear. It has been well established experimentally that real soil behaviour is far from linear and that soil stiffness is stress and strain level

BIBL. LOND. UNIV.

dependant and irrecoverable, or plastic strains develop upon loading and unloading. The way in which the soil behaves depends upon many factors, some of which are not yet fully understood. Over the years many different soil models have been developed to capture some of the most important features of soil behaviour. Whilst they all differ considerably in their approach they all have one thing in common and that is that they invoke a non-linear soil response. Therefore their implementation into a finite element code introduces the need for a numerical scheme to accommodate such behaviour. Exact solutions can only be found for very simple problems with a limited number of degrees of freedom, therefore an incremental/iterative solution scheme must be used to home in on the true solution. In this section the method introduced into ICFEP and used in this thesis to solve the non-linear response of the soil will be described.

Many techniques have been proposed for the solution of non-linear finite element analyses. One thing they all have in common is that to overcome the constantly changing behaviour of the soil, the analysis is discretised into a series of increments. The most popular techniques are the tangent stiffness (Britto and Gunn (1987)), the visco-plastic and the Newton-Raphson methods. The first two methods are generally thought to be inferior, as the results obtained when using them depend on the size of the increment assumed in the analysis. The Newton-Raphson method is relatively insensitive to the increment size and is the default non-linear solution technique used in this thesis. For the first increment the technique begins by solving the global system of equations assuming the initial global stiffness matrix is determined in the same manner as described in Section 2.2. If the material behaviour was linear elastic the solution found would be correct as the stiffness matrix would be constant during the increment. However, for the general case the material behaviour is not linear elastic and therefore the solution will not be correct because the material properties will have varied during the increment. The nodal displacements, and therefore the element strains calculated from the stiffness assumed for the first iteration will not satisfy the constitutive model. The constitutive model is then integrated along the incremental strain paths to obtain an estimate of the stress changes. These stress changes are added to the stresses at the beginning of the increment and then integrated to give equivalent nodal forces which are then compared to the externally applied loads. Because the first iteration did not give the correct solution, equilibrium will not be satisfied and there will be a

finite difference. This difference, known as the out of balance forces, is then added to the right hand side load vector. The stiffness matrix is then recevaluated and the system of equations solved again including the out of balance forces found from the previous iteration. This technique is repeated until the correct solution is found. It is possible to make the technique more efficient by using the same stiffness matrix for each iteration. This saves a considerable amount of computation effort as for each increment the stiffness matrix has to be evaluated and inverted only once, at the expense of possibly having to use more iterations to converge on the correct solution. The technique, known as the modified Newton-Raphson method, is illustrated graphically in Figure 2.3.

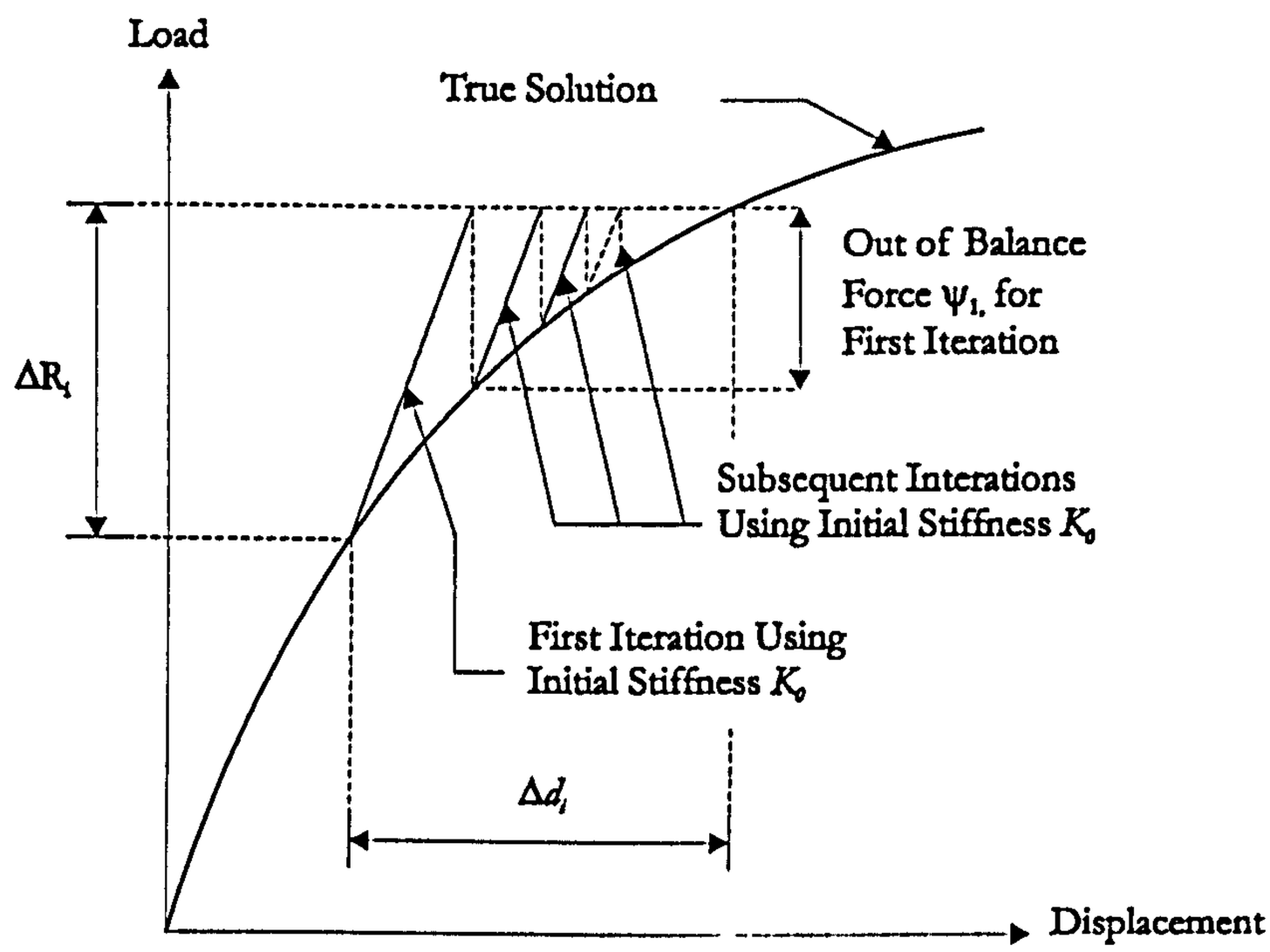

Figure 2.3: Graphical representation of the modified Newton-Raphson scheme

The accuracy of the Newton-Raphson method is dependent upon the precision with which the incremental stresses are determined. Performing this calculation is not straight forward as the way in which the material properties, and hence the stresses and strains, vary during an increment are not known. The mathematical procedure that performs this task is called a stress point algorithm and there are many available in the literature. The technique implemented into ICFEP is a sub-stepping stress point algorithm in which the strains are assumed to vary linearly during the increment and are then divided into smaller sub-steps. For each sub-step the stresses are found by integrating the constitutive equations using a numerical integration scheme. The default option in ICFEP and chosen for the analyses

presented in this thesis is the modified Euler method. The overall stress change during an increment is then found by summing the stress changes found from each sub-step.

Due to the iterative nature of the solution technique required to solve non-linear finite element problems, the results will never correspond exactly to the correct solution. The Newton-Raphson method described in the previous section could iterate indefinitely but may never reach the true solution. For this reason it is necessary to define a convergence criteria, that when satisfied tells the algorithm that the solution found is accurate to an acceptable degree and the analysis can now move on to the next increment. Of course the true solution is not known and therefore ICFEP sets a limit on the relative size of the iterative displacements ($\{\Delta d_{it}\}$) and the out of balance forces ($\{\psi\}$). As both of these quantities are vectors, their relative magnitude can be determined by evaluating their scalar norms:

$$\|\{\Delta d_{it}\}\| = \sqrt{\{\Delta d_{it}\}^T \{\Delta d_{it}\}} \tag{2.28}$$

$$\|\{\psi\}\| = \sqrt{\{\psi\}^T \{\psi\}} \tag{2.29}$$

The magnitude and tendency of these norms gives an indication of the convergence of the solution. If either value is seen to increase the solution has begun to diverge from the true solution and the analysis should be aborted. If their values continue to reduce, an absolute convergence criterion is determined by comparing the norms of the incremental and accumulated nodal displacements to the norm of the iterative displacements. When its value falls below a certain percentage of these values the solution is said to have converged. A similar limit is set for the norm of the out of balance forces compared to the norms of the incremental and accumulated right hand side load vector.

2.5 Consolidation Theory

The issue of modelling the presence of a fluid in the soil pores has been addressed in Section 2.3.1. Two extreme cases were identified. The first assumed that any change in total stress would be matched by a change in effective stress.

This occurs when the permeability of a soil is very high and/or the application of a loading boundary condition is very slow. The second case assumes that no change in overall volume is allowed. This occurs when the permeability of a soil is very low and/or a loading boundary condition is applied rapidly. These two extreme types of response are termed drained and undrained respectively, and for any case that exists between them the time dependent nature of the pore fluid response must be modelled. To be able to model this behaviour it is necessary to combine or 'couple' together the equations that govern the flow of the pore fluid with those that control the mechanical behaviour of the soil skeleton. The consequence of this is the introduction of pore fluid pressure as a new degree of freedom.

As mentioned in section 2.3.1, the mechanical behaviour of a saturated porous media is divided into the response of the pore fluid and the soil skeleton by the principle of effective stress, given by Equation 2.30.

$$\{\Delta\sigma\} = \{\Delta\sigma'\} + \{\Delta\sigma_f\} \tag{2.30}$$

where $\{\Delta\sigma\}$ is the change in total stress

$\{\Delta\sigma'\}$ is the change in effective stress

$\{\Delta\sigma_f\}^T = \{\Delta p_f \quad \Delta p_f \quad \Delta p_f \quad 0 \quad 0 \quad 0\}$ and $\{\Delta p_f\}$ is the change in pore fluid pressure

The finite element equations derived in Section 2.2 must now be altered to include the principle of effective stress. This is achieved by changing Equation 2.5 to include the change in pore fluid pressure as a new variable.

$$\{\Delta\sigma\} = [D']\{\Delta\varepsilon\} + \{\Delta\sigma_f\} \tag{2.31}$$

where $[D']$ is the constitutive matrix in terms of effective stress.

To proceed with the finite element formulation, the variation of the pore fluid pressure over an element is approximated by a shape function in the same manner as the displacement degrees of freedom.

$$\{\Delta p_f\} = [N_p]\{\Delta p_f\}_n \tag{2.32}$$

where $\{\Delta p_f\}$ is the change in pore fluid pressure, $[N_p]$ is the matrix of shape functions and $\{\Delta p_f\}_n$ is the change in nodal pore fluid pressure. The matrix $[N_p]$ is similar to the matrix of shape functions $[N]$ used in Section 2.2 for the finite element formulation of the equilibrium equations. If the same order shape function is assumed for the pore pressure degrees of freedom and the displacement degrees of freedom an inconsistency arises when determining the effective stress within an element. If, for example, the displacements vary quadratically across an element (as they would for an eight nodded element), the strains and therefore the stresses vary linearly. If the pore pressures also vary quadratically an inconsistency arises when determining the effective stresses (Potts and Zdravković (1999)). To overcome this the pore pressure shape functions used in this thesis where assumed to be linear, and therefore pore pressure degrees of freedom only exist at the corner nodes of an eight nodded element. The finite element formulation can now proceed in a similar fashion to that described in Section 2.2. The incremental strain energy ΔW is given by Equation 2.33.

$$\Delta W = \frac{1}{2}\int \{\Delta\varepsilon\}^T \{\Delta\sigma\} dVol \tag{2.33}$$

Using the principle of effective stress, the incremental stress is divided into effective stress and pore fluid components.

$$\Delta W = \frac{1}{2}\int \left[\{\Delta\varepsilon\}^T [D']\{\Delta\varepsilon\} + \Delta p_f . \Delta\varepsilon_v\right] dVol \tag{2.34}$$

The work done by external loads remains unchanged and is therefore still given by Equation 2.8. Equilibrium is again found by minimising the potential energy of the body in the same manner as described in Section 2.2. The result is Equation 2.35, the finite element equilibrium equation in terms of effective stresses.

$$[K]\{\Delta d\} + [L]\{\Delta p_f\} = \{\Delta R\} \tag{2.35}$$

where $$[K] = \sum_{i=1}^{N} [K_E]_i$$

$$[K_E] = \int_{Vol} [B]^T [D][B] dVol$$

$$\{\Delta R\} = \sum_{i=1}^{N} \{\Delta R_E\}$$

$$\{\Delta R_E\} = \int_{Vol} [N]^T \{\Delta F\} dVol + \int_{Surface} [N]^T \{\Delta T\} dSurface$$

$$[L] = \int_{vol} \{m\} [B]^T [N_p] dVol,$$

$$\{m\}^T = \{1 \quad 1 \quad 1 \quad 0 \quad 0 \quad 0\}$$

At this point the solution of Equation 2.35 is not possible because it has two unknowns, the vector of nodal displacements $\{\Delta d\}$, and the vector of nodal pore pressures $\{\Delta p_f\}$. Therefore another set of equations that governs the flow of the pore fluid is required to solve the complete problem. The solution to the problem of pore fluid movement in a saturated media was first found by Biot (1941). The solution begins by considering the flow of pore fluid in and out of a cube of unit dimensions. Conservation of mass requires that the derivative of the volumetric strain with respect to time is equal to the sum of the velocities in the coordinate directions plus the volume of fluid added by any sources and minus the volume of fluid taken by any sinks. This is summarised by Equation 2.36.

$$\frac{\partial w_x}{\partial x} + \frac{\partial w_y}{\partial y} + \frac{\partial w_z}{\partial z} - Q = -\frac{\partial \varepsilon_v}{\partial t} \tag{2.36}$$

where w_x, w_y and w_z are the components of the superficial velocity of the pore fluid, and Q represents any sources and/or sinks. Using the principle of virtual work Equation 2.36 can be written as:

$$\int_{Vol} \left[\{w\}^T \left\{ \nabla \{\Delta p_f\} \right\} + \frac{\partial \varepsilon_v}{\partial t} \{\Delta p_f\} \right] dVol - Q\{\Delta p_f\} = 0 \tag{2.37}$$

The seepage velocity $\{w\}$ of a fluid through a porous media is related to the pressure head $\{h\}$ by the well known Darcy's law:

$$\{w\} = -[k]\{\nabla h\} \tag{2.38}$$

Where $[k]$ is the permeability matrix of the soil. To be consistent with Equation 2.35, equation 2.37 must be expressed in terms of pore fluid pressure which is related to the hydraulic head by Equation 2.39.

$$h = \frac{p_f}{\gamma_f} + \left(x i_{Gx} + y i_{Gy} + z i_{Gz} \right) \tag{2.39}$$

where $\{i_G\}$ is a unit vector parallel, but in the opposite direction to gravity and γ_f is the bulk unit weight of the pore fluid. Substituting these relationships into Equation 2.37 and approximating $\partial \varepsilon_v / \partial t$ as $[B]\{\Delta d\}/\Delta t$, the final finite element equation can be rewritten as Equation 2.40.

$$[L]^T \left\{ \frac{\Delta d}{\Delta t} \right\} - [\phi]\{p_f\} = [n] + Q \tag{2.40}$$

Where

$$[\phi] = \int_{vol} \frac{1}{\gamma_f} [E]^T [k][E] dvol$$

$$[n] = \int_{vol} [E]^T [k]\{i_G\} dvol$$

$$[E] = \left[\frac{\partial N_p}{\partial x}, \frac{\partial N_p}{\partial y}, \frac{\partial N_p}{\partial z} \right]^T$$

To solve Equations 2.35 and 2.40 a time marching process is adopted. If the solution $\left(\{\Delta d\}_{nG}, \{p_f\}_{nG} \right)_1$ is known at time t_1, then the solution $\left(\{\Delta d\}_{nG}, \{p_f\}_{nG} \right)_2$ at time $t_2 = t_1 + \Delta t$ is sought. To proceed it is necessary to assume:

$$\int_{t1}^{t2} \{p_f\} dt \approx \left[\{p_f\}_1 + \beta \left(\{p_f\}_2 - \{p_f\}_1 \right) \right] \Delta t = \left[\{p_f\}_1 + \beta \{\Delta p_f\} \right] \Delta t \tag{2.41}$$

where β is an integration parameter introduced to indicate how the pore pressure is assumed to vary during the increment. Substitution of Equation 2.41 into Equation 2.40 yields the final finite element equation.

$$[L]^T \{\Delta d\} - \beta \Delta t [\Phi]\{\Delta p_f\} = [n]\Delta t + Q\Delta t + [\Phi]\{p_f\}_1 \Delta t \tag{2.42}$$

All of the terms on the right hand side of Equation 2.42 are known and the unknown variables on the left hand side are the vector of incremental nodal displacements $\{\Delta d\}$ and the vector of incremental nodal pore fluid pressures $\{\Delta p_f\}$. That is they are the same as the unknowns in Equation 2.35 and therefore allow the solution of the overall problem by solving the two constitutive equations for the two unknowns. Therefore the coupled behaviour of the soil skeleton and pore fluid can be modelled by solving the system of simultaneous equations represented by Equation 2.43.

$$\begin{bmatrix} [K] & [L] \\ [L]^T & -\beta\Delta t[\phi] \end{bmatrix} \begin{bmatrix} \{\Delta d\} \\ \{\Delta p_f\} \end{bmatrix} = \begin{bmatrix} \{\Delta R\} \\ \left[[n]+Q+[\phi]\{p_f\}\right]\Delta t \end{bmatrix} \tag{2.43}$$

Hydraulic boundary conditions must be prescribed at every node that appears on the boundary of the mesh. This is usually assumed to be a zero flow boundary condition, although it is possible to prescribe a nodal flow or pore fluid pressure.

Once the matrices shown in Equation 2.43 have been evaluated in their natural coordinates using the numerical integration technique shown in Section 2.2 and the hydraulic and displacement boundary conditions have been specified, the solution of the resulting simultaneous equations can then be undertaken to give the nodal displacements and pore pressures.

2.6 Fourier Series Aided Finite Element Analysis

2.6.1 Introduction

The time and computational demands of three dimensional analysis often mean that its use in practice is restricted to academic studies. Considerable savings in both storage requirements and analysis run times can be made for a particular set of three dimensional problems using the Fourier series aided finite element method. Whilst all problems in reality are three dimensional, the geometry can often be simplified to two dimensions by assuming that the displacements do not vary in one direction. For example, a long embankment can often be simplified to a plane strain two dimensional problem because very little movement will occur in the out of

plane direction. A vertically loaded circular pile can be modelled by an axi-symmetric two dimensional mesh because there is no movement in the circumferential direction. A novel method has been developed that represents the out of plane displacements, boundary conditions and material properties as Fourier series and thus allows three dimensional analyses to be performed with a two dimensional mesh. Whilst it is possible to formulate the Fourier series aided finite element method for a Cartesian coordinate system, ICFEP only has the option of using cylindrical coordinates as this is considered most useful for geotechnical problems. The following section will outline the theory that underlies the Fourier series finite element method as implemented into ICFEP. For further details, see Ganendra (1993) and Potts and Zdravković (1999).

2.6.2 Theory

The coordinate system for an axi-symmetric geometry is shown in Figure 2.4.

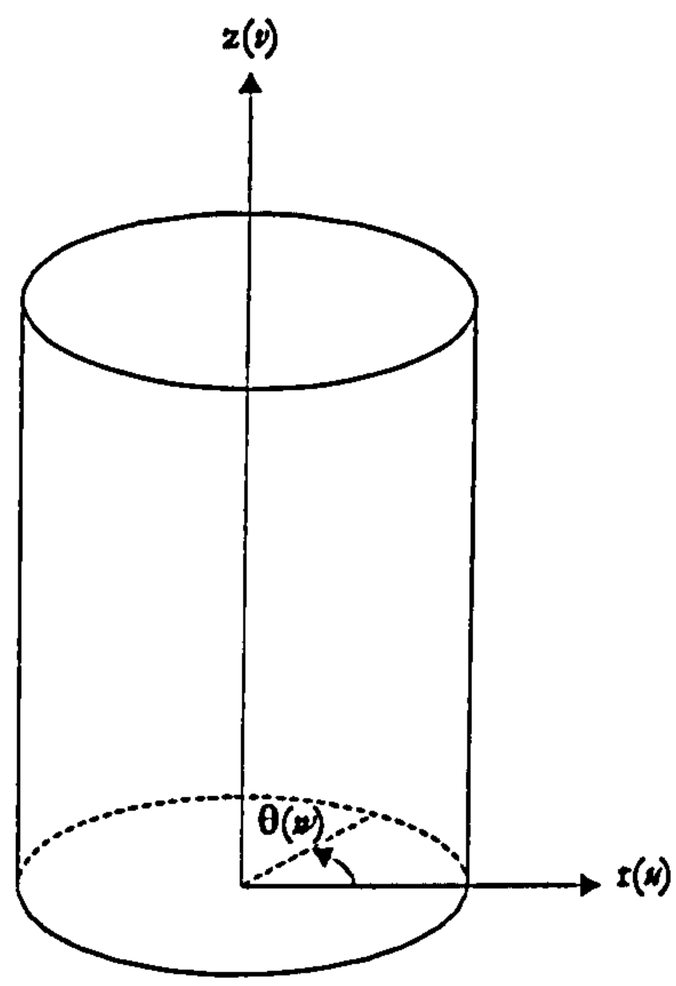

Figure 2.4: Axi-symmetric coordinate system and associated displacements

For a typical axi-symmetric analysis the theory presented in Section 2.2 could be used with the appropriate boundary conditions. To allow the out of plane motion (in this case the θ direction) to be modelled and to create a three dimensional analysis, the solution variables are replaced by a Fourier series. Any variable x in the

analysis can be replaced by a Fourier series in terms of the out of plane coordinate θ. An example of this type of function is given by Equation 2.44.

$$x = x^0 + \sum_{l=1}^{L} \overline{x^l} \cos l\theta + \overline{\overline{x^l}} \sin l\theta \tag{2.44}$$

where x^0, $\overline{x^l}$ and $\overline{\overline{x^l}}$ are the zeroth, the lth order cosine and the lth order sine harmonic coefficients and L is the number of harmonics used to represent the variable. The larger the number of harmonics, l, the better the accuracy of the solution. Once the variables in the finite element formulation have been replaced by Fourier series, the analysis is then performed in terms of the harmonic coefficients rather than the variables themselves.

In a similar fashion to the conventional finite element derivation, each of the nodal displacement components can be represented in terms of their nodal values by using shape functions.

$$\Delta u = \begin{Bmatrix} \Delta u \\ \Delta v \\ \Delta w \end{Bmatrix} = \sum_{i=1}^{n} \begin{bmatrix} N_i \left(\sum_{l=0}^{L} \overline{u_i^l} \cos l\theta + \overline{\overline{u_i^l}} \sin l\theta \right) \\ N_i \left(\sum_{l=0}^{L} \overline{v_i^l} \cos l\theta + \overline{\overline{v_i^l}} \sin l\theta \right) \\ N_i \left(\sum_{l=0}^{L} \overline{w_i^l} \cos l\theta + \overline{\overline{w_i^l}} \sin l\theta \right) \end{bmatrix} \tag{2.45}$$

where N_i is the shape function for node i. In terms of cylindrical coordinates, the strains within an element are given by Equation 2.46.

$$\{\Delta\varepsilon\} = \begin{Bmatrix} \Delta\varepsilon_r \\ \Delta\varepsilon_z \\ \Delta\varepsilon_\theta \\ \Delta\varepsilon_{rz} \\ \Delta\varepsilon_{r\theta} \\ \Delta\varepsilon_{z\theta} \end{Bmatrix} = -\begin{Bmatrix} \dfrac{\partial(\Delta u)}{\partial r} \\ \dfrac{\partial(\Delta v)}{\partial z} \\ \dfrac{\Delta u}{r} + \dfrac{1}{r}\dfrac{\partial(\Delta w)}{\partial \theta} \\ \dfrac{\partial(\Delta u)}{\partial z} + \dfrac{\partial(\Delta v)}{\partial r} \\ \dfrac{1}{r}\dfrac{\partial(\Delta r)}{\partial \theta} + \dfrac{\partial(\Delta w)}{\partial r} - \dfrac{\Delta w}{r} \\ \dfrac{1}{r}\dfrac{\partial(\Delta v)}{\partial \theta} + \dfrac{\partial(\Delta w)}{\partial z} \end{Bmatrix} \tag{2.46}$$

The substitution of the displacement approximations into Equation 2.46 results in an expression that can conveniently be split into two components, illustrated by Equation 2.47.

$$\{\Delta\varepsilon\} = \sum_{i=1}^{n}\sum_{l=0}^{L}\left(\begin{bmatrix} [B1_i^l]\cos l\theta \\ [B2_i^l]\sin l\theta \end{bmatrix}\{\Delta d_i^{l*}\} + \begin{bmatrix} [B1_i^l]\sin l\theta \\ -[B2_i^l]\cos l\theta \end{bmatrix}\{\Delta d_i^{l**}\}\right) \tag{2.47}$$

where:

$$[B1_i^l] = -\begin{bmatrix} \dfrac{\partial N_i}{\partial r} & 0 & 0 \\ 0 & \dfrac{\partial N_i}{\partial z} & 0 \\ \dfrac{N_i}{r} & 0 & \dfrac{lN_i}{r} \\ \dfrac{\partial N_i}{\partial z} & \dfrac{\partial N_i}{\partial r} & 0 \end{bmatrix} \text{ and } \{\Delta d_i^{l*}\} = \begin{Bmatrix} \overline{u_i^l} \\ \overline{v_i^l} \\ \overline{\overline{w_i^l}} \end{Bmatrix}$$

$$[B2_i^l] = \begin{bmatrix} -\dfrac{lN_i}{r} & 0 & \left(\dfrac{\partial N_i}{\partial r} - \dfrac{N_i}{r}\right) \\ 0 & -\dfrac{lN_i}{r} & \dfrac{\partial N_i}{\partial z} \end{bmatrix} \text{ and } \{\Delta d_i^{l**}\} = \begin{Bmatrix} \overline{\overline{u_i^l}} \\ \overline{\overline{v_i^l}} \\ \overline{-w_i^l} \end{Bmatrix}$$

Therefore the $[B]$ matrix and the incremental displacements for each harmonic l, has been divided into two components, $[B1_i^l]$ and $\{\Delta d_i^{l*}\}$ which represent the

displacements that exhibit parallel symmetry and $\left[B2_i^l\right]$ and $\left\{\Delta d_i^{l**}\right\}$ which represent displacements that have orthogonal symmetry. Parallel symmetry terms consist of cosine harmonic coefficients of radial and vertical incremental displacements and sine harmonic coefficients of circumferential incremental displacements. Conversely, orthogonal symmetric terms consist of sine harmonic coefficients of radial and vertical incremental displacements and cosine harmonic coefficients of circumferential incremental displacements. A similar division can then be made of the constitutive matrix [D].

$$\begin{Bmatrix} \Delta\sigma_1 \\ \Delta\sigma_2 \end{Bmatrix} = \begin{bmatrix} [D_{11}] & [D_{12}] \\ [D_{21}] & [D_{22}] \end{bmatrix} \begin{Bmatrix} \Delta\varepsilon_1 \\ \Delta\varepsilon_2 \end{Bmatrix} \tag{2.48}$$

where $\{\Delta\sigma_1\} = \{\Delta\sigma_r, \Delta\sigma_z, \Delta\sigma_\theta, \Delta\sigma_{rz}\}^T$, $\{\Delta\sigma_2\} = \{\Delta\sigma_{r\theta}, \Delta\sigma_{z\theta}\}^T$ and

$$\{\Delta\varepsilon_1\} = \{\Delta\varepsilon_r, \Delta\varepsilon_z, \Delta\varepsilon_\theta, \Delta\varepsilon_{rz}\}^T, \ \{\Delta\varepsilon_2\} = \{\Delta\varepsilon_{r\theta}, \Delta\varepsilon_{z\theta}\}^T$$

Now that the primary variable displacement, and the secondary variables stress and strain have successfully been formulated in terms of the Fourier series approximation, the finite element formulation can then proceed using the principle of minimising the potential energy of a body in the same manner described for the standard finite element formulation in Section 2.2.

The result of the finite element formulation process is a system of simultaneous equations representing the equilibrium of each harmonic term. This is illustrated by Equation 2.49.

$$\begin{bmatrix} K^0 & 0 & 0 & 0 & 0 & 0 & 0 & 0 & 0 \\ 0 & K^1 & 0 & 0 & 0 & 0 & 0 & 0 & 0 \\ 0 & 0 & \dots & 0 & 0 & 0 & 0 & 0 & 0 \\ 0 & 0 & 0 & \dots & 0 & 0 & 0 & 0 & 0 \\ 0 & 0 & 0 & 0 & K^l & 0 & 0 & 0 & 0 \\ 0 & 0 & 0 & 0 & 0 & \dots & 0 & 0 & 0 \\ 0 & 0 & 0 & 0 & 0 & 0 & \dots & 0 & 0 \\ 0 & 0 & 0 & 0 & 0 & 0 & 0 & K^{L-1} & 0 \\ 0 & 0 & 0 & 0 & 0 & 0 & 0 & 0 & K^L \end{bmatrix} \begin{Bmatrix} \Delta d^0 \\ \Delta d^{1*}, \Delta d^{1**} \\ \dots \\ \dots \\ \Delta d^{l*}, \Delta d^{l**} \\ \dots \\ \dots \\ \Delta d^{L-1*}, \Delta d^{L-1**} \\ \Delta d^{L*}, \Delta d^{L**} \end{Bmatrix} = \begin{Bmatrix} \Delta R^0 \\ \Delta R^{1*}, \Delta R^{1**} \\ \dots \\ \dots \\ \Delta R^{l*}, \Delta R^{l**} \\ \dots \\ \dots \\ \Delta R^{L-1*}, \Delta R^{L-1**} \\ \Delta R^{L*}, \Delta R^{L**} \end{Bmatrix} \tag{2.49}$$

For each harmonic component, the stiffness matrix K^l couples together the parallel and orthogonal symmetric displacements in the form shown below.

$$\begin{bmatrix} [K^l]^p & [K^l]^{po} \\ [K^l]^{op} & [K^l]^o \end{bmatrix} \begin{Bmatrix} \{\Delta d^{l*}\} \\ \{\Delta d^{l**}\} \end{Bmatrix} = \begin{Bmatrix} \{\Delta R^{l*}\} \\ \{\Delta R^{l**}\} \end{Bmatrix} \tag{2.50}$$

This is further simplified if the off diagonal terms, $[D_{12}]$ and $[D_{21}]$, of the constitutive matrix $[D]$ are zero, for example with a linear elastic isotropic material. In this case the terms $[K^l]^{po}$ and $[K^l]^{op}$ become zero, leaving two independent sets of equations for $\{\Delta d^{l*}\}$ and $\{\Delta d^{l**}\}$. The solution procedure described in Section 2.2 can then be carried out for each harmonic component and the overall displacement determined by summing these together using Equation 2.45. By uncoupling the response of each harmonic component, the Fourier series finite element method has reduced the computational demand. This is because inverting several small matrices is computationally less intensive then inverting one large stiffness matrix that would result from constructing a three dimensional mesh.

Whilst here only the representation of the displacements by Fourier series has been described, for the solution to be made possible all other input details and solution variables must also be approximated by a Fourier series. In this way it is possible to include boundary stresses and/or material properties that vary in the out of plane direction and include the effect of the presence of a pore fluid in the finite element analysis. Full details of the formulation can be found in Potts and Zdravković (1999).

2.7 Summary

The first part of the chapter detailed the derivation and implementation of the finite element theory for linear materials. The results obtained are applicable to the analysis of any static mechanics problem.

Attention then focused on the changes to this standard theory that are required to analyse geotechnical problems. The most fundamental difference between soils and other engineering materials is the presence of a fluid in the pores that exist between individual soil particles. Three different types of possible soil response were

identified: the fully drained case in which the pore fluid response is zero and can be analysed using the standard finite element theory, the fully undrained case which can be dealt with by including the pore fluid stiffness in the overall element stiffness matrix and finally the situation in between these two extremes that must model the coupled response of the pore fluid and soil skeleton. For each of these three cases the theory necessary to analyses a problem of this nature has been presented.

Another feature of soils is that their material behaviour is not linear. Many models have been presented in the literature to capture as closely as possible the true behaviour of soils and in this chapter the theory that is required to solve the resulting non-linear (i.e. elasto-plastic) equilibrium equations was presented.

The final section presented the theory that lies behind the Fourier series aided finite element method. This is a novel technique that allows the analysis of a three dimensional problem with axi-symmetric geometry but non-axi-symmetric boundary conditions and/or material properties in a fraction of the analysis run time and with substantially less computer memory requirements of standard three dimensional analysis.

All of the theory presented so far allows the analysis of static geotechnical problems. In reality all events are dynamic, that is they occur over a certain period of time. If the time period of the loading event is significantly greater than the time period of the fundamental frequency of the body, then the assumption of no time dependence is valid. If however the input period is similar to or less than the period of the fundamental frequency then inertia effects become significant and the time dependent nature of the response must be taken into account. The theory presented in the next chapter allows such dynamic finite element analyses to be undertaken with ICFEP.

Chapter 3:

DYNAMIC FINITE ELEMENT THEORY

3.1 Introduction

The theory presented in Chapter 2 is sufficient to allow the analysis of most static geotechnical problems. In reality all problems are dynamic, that is they vary with time. For example, the construction of an embankment does not occur instantaneously, rather it is constructed in layers over a certain period of time. The way in which we deal with this in finite element analysis is to divide the construction sequence into stages or increments and then consider the equilibrium of the system at the end of each increment. The overall response is then found by adding together the individual increments. This approach is valid if the events occur slowly and thus the inertia forces remain low. If however the inertia forces become significant, then they must be included in the analysis. Inertia forces are generally considered to become important when the frequency of loading is equal to or greater than the natural frequency of the body under consideration.

The purpose of this chapter is to introduce the techniques available for incorporating the effects of inertia forces into finite element analysis. As usual in numerical analyses, due to its approximate nature there are many different techniques proposed in the literature for achieving the same effect. In the derivation of the static finite element theory these options were not discussed because this theory had already been implemented into ICFEP and the discussion could be found elsewhere. This chapter on dynamic finite element theory differs, as it was the purpose of this thesis to implement dynamic capabilities into ICFEP and therefore each option is carefully considered before a choice is made regarding which option to take.

The first part of the chapter gives details of the changes that are required to the basic equilibrium equations for standard two and three dimensional analyses for all

the element types reviewed in Chapter 2. The dynamic theory is then extended to the Fourier series aided finite element method.

The next section of the chapter discusses some of the different options available for the finite element formulation of the dynamic equilibrium equation. This includes a comparison of the most popular time discretisation schemes available in the literature and also the nature and evaluation of the mass and damping matrices. Based on this discussion the reasons for the choices made in ICFEP are given.

As well as the changes required in the solid equilibrium equations, those equations governing the flow of the pore fluid derived in Section 2.5 also have to include the effects of inertia forces. The next section in the chapter first details the changes to the flow equations and then discusses the choices that are available for its finite element implementation. Based on the reasons given in this discussion, a choice is made regarding it implementation into ICFEP.

The final section of the chapter summarises the techniques that where implemented into ICFEP and discusses the overall solution strategy adopted for linear and non-linear dynamic problems.

3.2 Dynamic Finite Element Formulation

3.2.1 Two and Three Dimensional Analyses

Assuming that the solution domain has been divided into a finite element mesh in the same manner as described in Section 2.2, the dynamic formulation must begin by redefining the incremental potential energy of a single element. Using d'Alemberts principle, Equation 2.6 can be modified to include the incremental inertial energy (ΔI).

$$\textit{Incremental potential energy } (\Delta E) = \textit{Incremental strain energy } (\Delta W) +$$

$$\textit{Incremental inertial energy } (\Delta I) - \textit{Incremental work done by applied loads } (\Delta L) \quad (3.1)$$

Newton's second law states that the force applied to a body is equal to the rate of change of momentum. This reduces to inertial force equals mass times acceleration

if the bodies mass does not change. Therefore, using the principle of virtual work the incremental inertial energy is given by Equation 3.2:

$$\Delta I = \int \{\Delta u\} \rho \{\Delta \ddot{u}\} \, dVol \tag{3.2}$$

where ρ is the material density and $\{\Delta u\}$ and $\{\Delta \ddot{u}\}$ are the incremental displacements and accelerations respectively. In addition to this inertial force, experimental observations have identified that, when subjected to dynamic excitations, objects tend to dissipate energy. This is usually taken into account by introducing a damping force (ΔD) into the equilibrium equation.

Incremental potential energy (ΔE) =

Incremental strain energy (ΔW) +*Incremental inertial energy* (ΔI) +

Incremental damping energy (ΔD) – *Incremental work done by applied loads* (ΔL) (3.3)

If the damping force is assumed to be velocity dependent, and again using the principle of virtual work, the incremental damping energy is given by Equation 3.4.

$$\Delta D = \int \{\Delta u\} \kappa \{\Delta \dot{u}\} \, dVol \tag{3.4}$$

where $\{\Delta \dot{u}\}$ is the incremental velocity and κ is a constant representing the damping characteristics of the material. Representing a material's damping characteristics with a single parameter is a gross oversimplification. The options available to overcome this problem will be discussed later in this chapter. To formulate the finite element equations the displacements, velocities and accelerations must be approximated in terms of their nodal values. This is achieved using the same shape functions described in Section 2.2.

$$\begin{aligned} \{u\} &= [N]\{u\}_{nodes} \\ \{\dot{u}\} &= [N]\{\dot{u}\}_{nodes} \\ \{\ddot{u}\} &= [N]\{\ddot{u}\}_{nodes} \end{aligned} \tag{3.5}$$

It is now possible to formulate the dynamic finite element equations using the same procedure as in Chapter 2

1. Substitute the expressions for ΔW, ΔI, ΔD and ΔL into Equation 3.3.
2. Substitute the approximations given by Equation 3.5 into the resulting expression for the incremental potential energy.
3. Differentiate this expression with respect to the list of nodal displacements.
4. Set this expression equal to zero to find the equilibrium equation.

The result of this process is Equation 3.6:

$$\delta\Delta E = \sum_{i=1}^{N}\left(\{\delta\Delta u\}_n^T\right)_i \left[\begin{array}{c} \int_{Vol}[B]^T[D][B]dVol\{\Delta u\}_n + \\ \int_{Vol}[N]^T\rho[N]dVol\{\Delta\ddot{u}\}_n + \int_{Vol}[N]^T\kappa[N]dVol\{\Delta\dot{u}\}_n - \\ \int_{Vol}[N]^T\{\Delta F\}dVol - \int_{Surface}[N]^T\{\Delta T\}dSurface \end{array}\right]_i = 0 \quad (3.6)$$

This is more conveniently expressed by Equation 3.7:

$$\sum_{i=1}^{N}[M_E]_i\left(\{\Delta\ddot{u}\}_n\right)_i + \sum_{i=1}^{N}[C_E]_i\left(\{\Delta\dot{u}\}_n\right)_i + \sum_{i=1}^{N}[K_E]_i\left(\{\Delta u\}_n\right)_i = \sum_{i=1}^{N}\{\Delta R_E\} \quad (3.7)$$

Where $[M_E] = \int_{Vol}[N]^T\rho[N]dVol$ = Element mass matrix

$[C_E] = \int_{Vol}[N]^T\kappa[N]dVol$ = Element damping matrix

$[K_E] = \int_{Vol}[B]^T[D][B]dVol$ = Element stiffness matrix

$\{\Delta R_E\} = \int_{Vol}[N]^T\{\Delta F\}dVol + \int_{Surface}[N]^T\{\Delta T\}dSurface$ = Right hand side load vector

The general formulation is applicable to any element with a matrix of shape functions [N]. Special care has to be taken when formulating the equilibrium equations for the elements specially derived to allow the analysis of geotechnical problems. First consider the interface elements mentioned in Chapter 2 and detailed

in Potts and Zdravković (1999). These elements are introduced to allow relative movement between two adjacent elements without invalidating the basic requirement of continuity. These elements do not represent anything that exists in reality and therefore it is important that they do not contribute to the dynamic behaviour of the mesh. This is ensured as the elements have zero thickness and therefore zero mass.

3.2.2 Fourier Series Aided Finite Element Analysis

Extending the theory presented in Chapter 2 for the Fourier series aided finite element analysis to allow dynamic problems to be analysed is a simple matter. First the new variables, velocity and acceleration are approximated to vary in the out of plane direction as a Fourier series and then expressed in terms of their incremental nodal values using the matrix of shape functions [*N*].

$$\Delta\dot{u} = \begin{Bmatrix} \Delta\dot{u} \\ \Delta\dot{v} \\ \Delta\dot{w} \end{Bmatrix} = \sum_{i=1}^{n} \begin{bmatrix} N_i\left(\sum_{l=0}^{L} \overline{\dot{u}_i^l} \cos l\theta + \overline{\overline{\dot{u}_i^l}} \sin l\theta\right) \\ N_i\left(\sum_{l=0}^{L} \overline{\dot{v}_i^l} \cos l\theta + \overline{\overline{\dot{v}_i^l}} \sin l\theta\right) \\ N_i\left(\sum_{l=0}^{L} \overline{\dot{w}_i^l} \cos l\theta + \overline{\overline{\dot{w}_i^l}} \sin l\theta\right) \end{bmatrix} \tag{3.8}$$

$$\Delta\ddot{u} = \begin{Bmatrix} \Delta\ddot{u} \\ \Delta\ddot{v} \\ \Delta\ddot{w} \end{Bmatrix} = \sum_{i=1}^{n} \begin{bmatrix} N_i\left(\sum_{l=0}^{L} \overline{\ddot{u}_i^l} \cos l\theta + \overline{\overline{\ddot{u}_i^l}} \sin l\theta\right) \\ N_i\left(\sum_{l=0}^{L} \overline{\ddot{v}_i^l} \cos l\theta + \overline{\overline{\ddot{v}_i^l}} \sin l\theta\right) \\ N_i\left(\sum_{l=0}^{L} \overline{\ddot{w}_i^l} \cos l\theta + \overline{\overline{\ddot{w}_i^l}} \sin l\theta\right) \end{bmatrix} \tag{3.9}$$

where L is the number of harmonics and n is the number of nodes. The discretised form of the equilibrium equation is of the same form as that derived for the standard two and three dimensional analyses:

$$\sum_{i=1}^{N} [M_E]_i \left(\{\Delta\ddot{u}\}_n\right)_i + \sum_{i=1}^{N} [C_E]_i \left(\{\Delta\dot{u}\}_n\right)_i + \sum_{i=1}^{N} [K_E]_i \left(\{\Delta u\}_n\right)_i = \sum_{i=1}^{N} \{\Delta R_E\} \tag{3.10}$$

where N is the total number of elements. The evaluation of the mass and damping matrices is not as straight forward as with the standard two and three dimensional cases. In Chapter 2 the displacements were divided into two components, parallel symmetry terms and orthogonal symmetry terms, and therefore the same must be done to the velocities and accelerations before the mass and damping matrices can be evaluated. The derivation will be presented for the element mass matrix, although the same principles apply to the evaluation of the damping matrix. First consider the displacement vectors that represent the parallel and orthogonal displacement components:

$$\left\{\Delta d_i^{l*}\right\} = \begin{Bmatrix} \overline{u_i^l} \\ \overline{v_i^l} \\ \overline{\overline{w_i^l}} \end{Bmatrix} \text{ and } \left\{\Delta d_i^{l**}\right\} = \begin{Bmatrix} \overline{\overline{u_i^l}} \\ \overline{\overline{v_i^l}} \\ \overline{-w_i^l} \end{Bmatrix} \tag{3.11}$$

The acceleration vectors must have a similar form:

$$\left\{\Delta \ddot{d}_i^{l*}\right\} = \begin{Bmatrix} \overline{\ddot{u}_i^l} \\ \overline{\ddot{v}_i^l} \\ \overline{\overline{\ddot{w}_i^l}} \end{Bmatrix} \text{ and } \left\{\Delta \ddot{d}_i^{l**}\right\} = \begin{Bmatrix} \overline{\overline{\ddot{u}_i^l}} \\ \overline{\overline{\ddot{v}_i^l}} \\ \overline{-\ddot{w}_i^l} \end{Bmatrix} \tag{3.12}$$

The approximation given by Equation 3.9 must now be rearranged to give the acceleration as a sum of the parallel and orthogonal acceleration components.

$$\left\{\Delta \ddot{u}\right\} = \sum_{i=1}^{n}\sum_{l=0}^{L} \begin{bmatrix} \begin{Bmatrix} N_i \cos l\theta & 0 & 0 \\ 0 & N_i \cos l\theta & 0 \\ 0 & 0 & N_i \sin l\theta \end{Bmatrix} \begin{Bmatrix} \overline{\ddot{u}_i^l} \\ \overline{\ddot{v}_i^l} \\ \overline{\overline{\ddot{w}_i^l}} \end{Bmatrix} + \\ \begin{Bmatrix} N_i \sin l\theta & 0 & 0 \\ 0 & N_i \sin l\theta & 0 \\ 0 & 0 & -N_i \cos l\theta \end{Bmatrix} \begin{Bmatrix} \overline{\overline{\ddot{u}_i^l}} \\ \overline{\overline{\ddot{v}_i^l}} \\ \overline{-\ddot{w}_i^l} \end{Bmatrix} \end{bmatrix} \tag{3.13}$$

This can then be expressed in a simpler form by Equation 3.14:

$$\{\Delta\ddot{u}\} = \sum_{i=1}^{n}\sum_{l=0}^{L}\left(\begin{bmatrix}[N1_i^l]\cos l\theta \\ [N2_i^l]\sin l\theta\end{bmatrix}\{\Delta\ddot{d}_i^{l*}\} + \begin{bmatrix}[N1_i^l]\sin l\theta \\ -[N2_i^l]\cos l\theta\end{bmatrix}\{\Delta\ddot{d}_i^{l**}\}\right) \quad (3.14)$$

Where $[N1_i^l] = \begin{bmatrix} N_i & 0 & 0 \\ 0 & N_i & 0\end{bmatrix}$ and $[N2_i^l] = [0 \quad 0 \quad N_i]$

This form can then be used to derive the global mass matrix:

$$[M_G] = \sum_{i=1}^{n}\int_{Vol}[N]^T \rho [N]\, dVol = \text{global mass matrix} \quad (3.15)$$

$$\int[N]^T \rho [N] =$$

$$\int\sum_{i=1}^{n}\left[\sum_{l=0}^{L}\begin{bmatrix}[N1_i^l]\cos l\theta \\ [N2_i^l]\sin l\theta\end{bmatrix} + \begin{bmatrix}[N1_i^l]\sin l\theta \\ -[N2_i^l]\cos l\theta\end{bmatrix}\right]^T \cdot \rho \cdot \quad (3.16)$$

$$\sum_{j=1}^{n}\left[\sum_{k=0}^{L}\begin{bmatrix}[N1_j^k]\cos k\theta \\ [N2_j^k]\sin k\theta\end{bmatrix} + \begin{bmatrix}[N1_j^k]\sin k\theta \\ -[N2_j^k]\cos k\theta\end{bmatrix}\right] r\, dArea$$

In a similar fashion to the evaluation of the stiffness matrix, many of the cross multiplied terms become zero when integrated between the limits $-\pi$ and $+\pi$. The remaining integrals take a value of either π or 2π. The resultant simplified mass matrix is given by Equation 3.17:

$$\pi\int\begin{bmatrix}\sum_{i=1}^{n}\sum_{j=1}^{n}\left[\left[2[N1_i^0]^T \rho [N1_j^0] + 2[N2_i^0]^T \rho [N2_j^0]\right] + \right. \\ \sum_{l=1}^{L}\left[[N1_i^l]^T \rho [N1_j^l] + [N2_i^l]^T \rho [N2_j^l]\right] + \\ \left.\sum_{l=1}^{L}\left[[N1_i^l]\rho[N1_j^l] + [N2_i^l]\rho[N2_j^l]\right]\right]\end{bmatrix} r\, dArea \quad (3.17)$$

This formulation assumes that the density of the soil is constant in the θ direction. It is however possible to formulate the mass matrix with the material density varying in the θ direction as a Fourier series.

3.3 Nature and Evaluation of the Element Mass and Damping Matrices

In addition to the stiffness matrix $[K]$, the mass matrix $[M]$ and the damping matrix $[C]$ must now be evaluated for each element. First consider the evaluation of the mass matrix using Equation 3.18.

$$[M_E] = \int_{Vol} [N]^T \rho [N] \, dVol \tag{3.18}$$

The matrix of shape functions $[N]$ is given in terms of the natural coordinate system (S and T) and therefore to evaluate the mass matrix, the integral variables must be transformed from the global system (in terms of x and y) to the natural coordinate system. This is achieved using the determinant of the Jacobian matrix, as shown in Equation 3.19.

$$[M_E] = \int_{-1}^{+1}\int_{-1}^{+1} t [N]^T \rho [N] |J| dS dT \tag{3.19}$$

where t is the element thickness. This integral can then be evaluated using the Gaussian integration technique described in Chapter 2.

Using the original isoparametric shape functions for the evaluation of Equation 3.19 results in a so called consistent mass matrix which is fully populated and models the distributed nature of the element mass. The need to reduce the amount of information that must be stored by the computer led early analysts to try and find ways of reducing the number of terms in the element mass matrix. By using substitute shape functions it is possible to eliminate the off-diagonal terms in the element mass matrix. The difference between this type of lumped mass matrix and the consistent mass matrix for a parent four noded two dimensional element is illustrated by Figure 3.1.

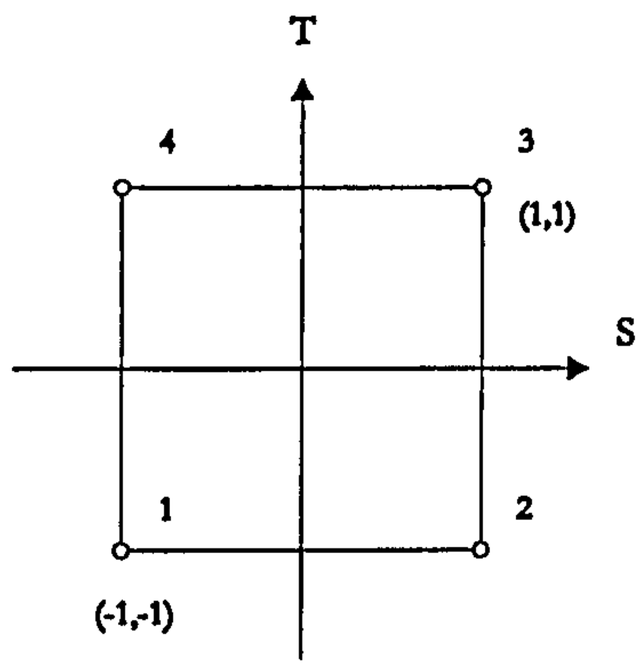

$$M = \rho \begin{bmatrix} 1 & 0 & 0 & 0 \\ 0 & 1 & 0 & 0 \\ 0 & 0 & 1 & 0 \\ 0 & 0 & 0 & 1 \end{bmatrix} \qquad M = \frac{\rho}{9} \begin{bmatrix} 4 & 2 & 1 & 2 \\ 2 & 4 & 2 & 1 \\ 1 & 2 & 4 & 2 \\ 2 & 1 & 2 & 4 \end{bmatrix}$$

Four Noded Two-Dimensional Element	Lumped Mass Matrix	Distributed (Consistent) Mass Matrix

Figure 3.1: Comparison of mass matrices

The principle advantage of using a lumped mass matrix is found when it is combined with the central difference time discretisation scheme, which will be introduced later in this chapter. In the absence of a damping matrix, the solution of the equations of equilibrium become explicit in time and are therefore significantly less expensive to solve. This saving in terms of analysis run time comes at the expense of numerical stability. For reasons that will be explained later in this chapter the central difference scheme will not be implemented into ICFEP and therefore this perceived advantage is lost. It is clear that assuming the mass of the element is concentrated at each node reduces the amount of computer memory required to store the element mass matrix. However, as mentioned previously the distributed nature of the element mass is no longer taken into account. Although some commercial codes utilise this option (Brinkgreve and Vermeer (1998)), the benefits of employing a lumped mass matrix appear to be of less importance than during the early days of finite element analysis. The global mass matrix created by using the isoparametric shape functions is sparsely populated and banded to the same degree as the global stiffness matrix. Therefore when the global mass matrix is combined with the global stiffness matrix (for reasons that will be seen later) it will not increase the number of terms that need to be stored and hence does not increase the storage memory requirements. For these reasons and to maintain consistency, the choice that will be implemented into ICFEP is to use the original isoparametric shape functions to obtain the global mass matrix in dynamic analyses.

As mentioned previously, experimental results led to the observation that energy is lost from a body as it vibrates. This so called damping originates from three different mechanisms (Ghanooni (1994)):

1. Hysteretic damping: This type of damping is independent of the frequency of vibration and is caused by frictional loss and the non-linearity of the stress strain relationship of the material.
2. Radiation damping: For problems in the ground, energy is lost as the waves and hence the energy propagate into the surrounding soil.
3. Viscous damping: Caused by the viscosity of the fluid flow within the pores of the soil matrix. The energy loss is proportional to the velocity and is also dependent on the frequency of the vibration.

Including all these features in a finite element analysis is extremely difficult. The problem of radiation damping cannot easily be dealt with and will be returned to later. A non-linear elasto-plastic soil model should be sufficient to reproduce the energy loss due to hysterisis, whilst including the presence of the pore fluid in the equilibrium equations should model the energy loss due to viscous damping. If however, an elastic soil model is to be used to simplify the analysis and the presence of the pore fluid is not to be included, it may be necessary to add a damping matrix to approximate the energy loss from these two sources. A mentioned previously, modelling viscous and hysteretic damping with a single constant κ as indicated by Equation 3.7 is a vast simplification of what is a complex phenomenon, and in this way cannot model the frequency dependent nature of the energy loss. The most popular assumption made to improve the performance of the damping matrix is to use Rayleigh damping. This method assumes that the damping matrix $[C]$ is made of a linear combination of the mass matrix $[M]$ and the stiffness matrix $[K]$, i.e.

$$[C] = A[M] + B[K] \tag{3.20a}$$

During a non-linear analysis the stiffness matrix is constantly changing and therefore to overcome the problem, Rayleigh damping is not allowed to be prescribed for elements which have a non-linear constitutive model. This assumption is considered to be more consistent as Rayleigh damping is generally introduced to model the energy loss through hysteretic damping which should be recreated by a non-linear soil model. Generally the performance of damping

matrices is not adequate as they fail to capture the true frequency and amplitude dependent nature of energy loss that has been observed in practice.

To demonstrate the variation of the material damping ratio with frequency observed when Rayleigh damping is introduced into an analysis, the example given by Bathe (1996) will be repeated here. The level of damping ξ_i, for any frequency ω_i, is given by Equation 3.20b in terms of the Rayleigh parameters A and B.

$$\xi_i = \frac{A + B\omega_i}{2\omega_i} \tag{3.20b}$$

For details of this derivation, refer to the original text. This relationship is illustrated in Figure 3.2 for the parameters A=0.01498 and B=0.01405.

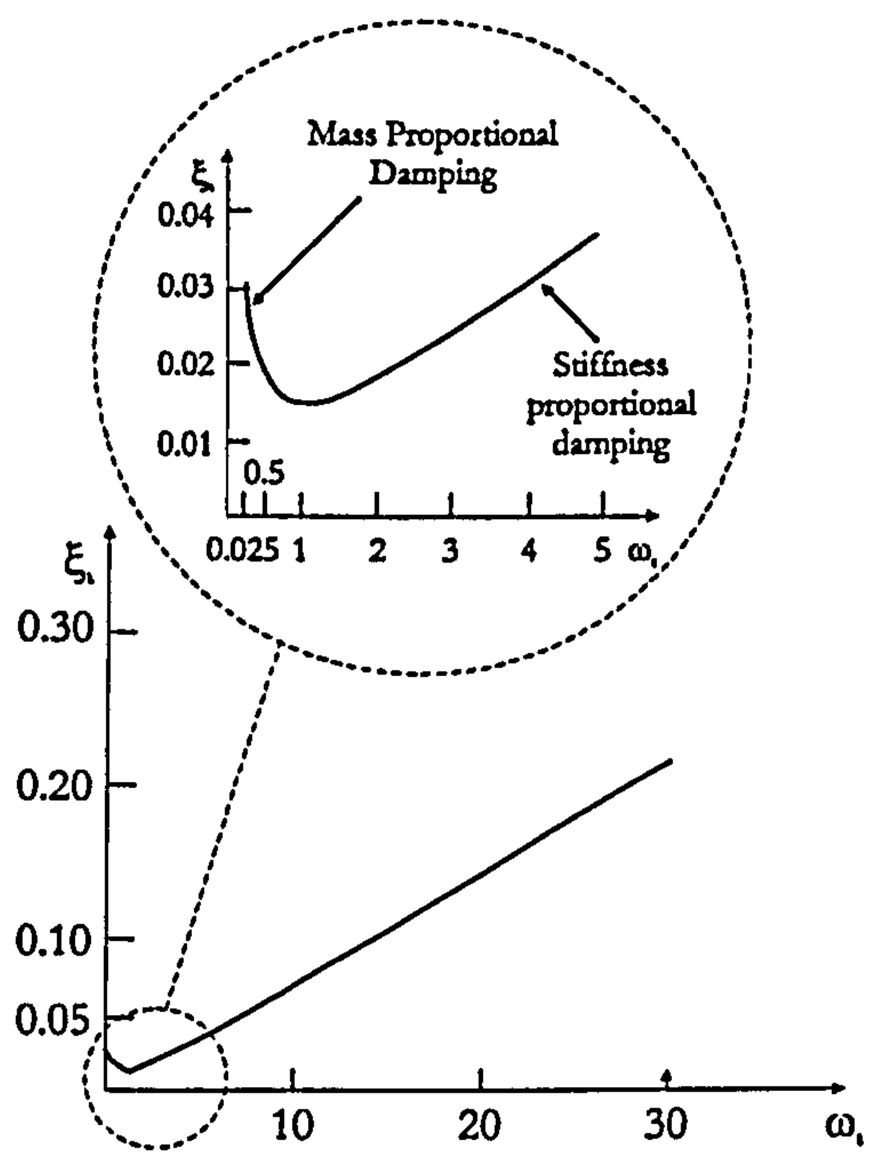

Figure 3.2: Damping as a function of frequency (after Bathe (1996))

When using Rayleigh damping the level of damping cannot be related to strain level and is heavily dependant on the frequency of vibration. These two features illustrate the unsuitability of Rayleigh damping when trying to model the response of soils to dynamic loading. The ultimate goal is to model hysteric damping by using an appropriate cyclic soil model and to model the presence of the pore fluid to include the effects of viscous damping. However, to allow investigations to be carried out

and because it involves evaluating no extra matrices, the option of including Rayleigh damping in an analysis was implemented into ICFEP.

3.4 Time Discretisation

The matrix form of the equilibrium equation represents n simultaneous equations, where n is the number of nodal displacement degrees of freedom. There are however $3n$ unknown quantities. These are the nodal displacements, nodal velocities and nodal accelerations. Therefore Equation 3.7 in its present form is unsolvable and further assumptions must be made before an analysis can be performed. The assumptions are involved in the choice of the time discretisation scheme. The most popular schemes are presented in the following sections. Only those that involve direct integration are reviewed as the alternatives (mode superposition, spectral analysis and frequency domain analysis) are restricted to linear problems (Tsatsanifos (1982)). In these equilibrium is considered at discrete time intervals Δt apart. To achieve this, some form for the variation of displacements, velocities and accelerations must be assumed within each time interval Δt. It is principally these assumptions that distinguish each method and determine the accuracy, stability and efficiency of the solution procedure. The relative merits of each method are then considered and the method implemented into ICFEP identified. The most important property of a time discretisation scheme is its stability. An integration method is said to be unconditionally stable if the solution for any initial conditions does not grow without bound for any time step Δt. The method is only conditionally stable if the above holds provided that Δt is smaller than or equal to a certain value. The solutions found by unstable time discretisation schemes become unbounded because inaccuracies in initial conditions or values stored from previous increments, which may be due to rounding off errors in the computer, grow uncontrolled during the integration. An example of how a stability analysis is performed using spectral decomposition is given in Bathe (1996).

3.4.1 The Central Difference Method

The fundamental relationships between the three nodal quantities, displacement, velocity and acceleration are:

$$Displacement = u\,,\ Velocity = \frac{\partial u}{\partial t} = \dot{u}\,,\ Acceleration = \frac{\partial^2 u}{\partial t^2} = \ddot{u} \qquad (3.21)$$

Some approximation must be made to relate these three quantities and hence reduce the number of variables to one. The simplest approximation for relating the first and second derivatives of a variable to the variable itself is a common finite difference approximation called the "central difference scheme". This technique uses a truncated form of Taylor's expansion to approximate the differentials over a finite difference grid. Consider the displacement u at the finite difference grid points t, $+\Delta t$ and $-\Delta t$ shown in Figure 3.3.

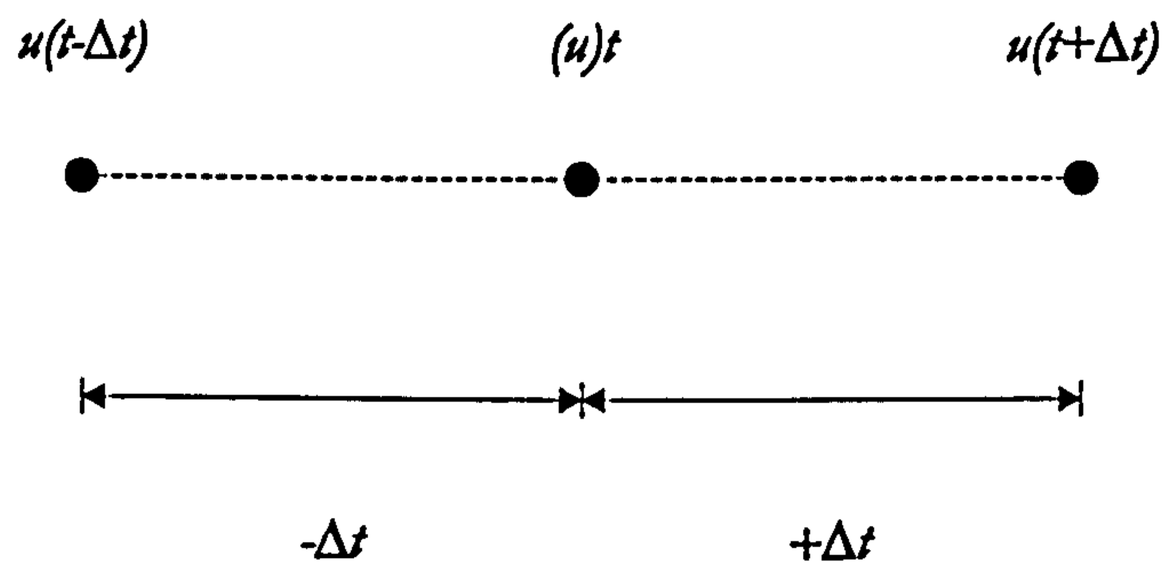

Figure 3.3: Finite difference grid

The first three terms of the Taylor's series expansion for the displacements at time $t=t-\Delta t$ and $t=t+\Delta t$ are given by Equations 3.22 and 3.23 respectively:

$$u(t+\Delta t) = u(t) + \Delta t \frac{du}{dt} + \Delta t^2 \frac{1}{2}\frac{d^2u}{dt^2} \qquad (3.22)$$

$$u(t-\Delta t) = u(t) - \Delta t \frac{du}{dt} + \Delta t^2 \frac{1}{2}\frac{d^2u}{dt^2} \qquad (3.23)$$

These approximations can then be combined to derive estimates of the first and second order derivatives of displacement with respect to time. Subtracting Equation 3.23 from Equation 3.22 leaves the following expression:

$$u(t+\Delta t) - u(t-\Delta t) = 2\Delta t \frac{du}{dt} \qquad (3.24)$$

This can then be rearranged to give an approximate expression for the velocity in terms of the displacement at the two time stations.

$$\frac{du}{dt}=\frac{1}{2\Delta t}\left(u(t+\Delta t)-u(t-\Delta t)\right) \tag{3.25}$$

By adding Equations 3.22 and 3.23 the terms involving the first derivative of displacement with respect to time cancel out, making it possible to derive an approximate relationship for the acceleration in terms of displacement, given by Equation 3.26.

$$\frac{d^2u}{dt^2}=\frac{1}{\Delta t^2}\left(u(t+\Delta t)-2u(t)+u(t-\Delta t)\right) \tag{3.26}$$

Now that approximate relationships have been derived for the velocity and acceleration in terms of displacement, the number of variables has been reduced to one, namely the nodal displacement. The solution procedure begins by substituting Equations 3.25 and 3.26 into the equilibrium equation. The result is Equation 3.27:

$$\begin{gathered}[M]\frac{1}{\Delta t^2}\{u(t+\Delta t)-2u(t)+u(t-\Delta t)\}+\\ [C]\frac{1}{2\Delta t}\{u(t+\Delta t)-u(t-\Delta t)\}+[K]\{u(t)\}=\{R\}\end{gathered} \tag{3.27}$$

Assuming that the displacements are known at times $t=t$ and $t=t\text{-}\Delta t$, the solution at time $t=t+\Delta t$ can be found by rearranging Equation 3.27 so that all of the known terms are on the right hand side, leaving only $u(t+\Delta t)$ on the left.

$$\begin{gathered}\left(\frac{1}{\Delta t^2}[M]+\frac{1}{2\Delta t}[C]\right)\{u(t+\Delta t)\}=\{R(t)\}-\left([K]-\frac{2}{\Delta t^2}[M]\right)\{u(t)\}-\\ \left(\frac{1}{\Delta t^2}[M]-\frac{1}{2\Delta t}[C]\right)\{u(t-\Delta t)\}\end{gathered} \tag{3.28}$$

This system of equations can then be solved in a similar manner to the static equilibrium equations and the nodal velocities and accelerations calculated by using Equations 3.25 and 3.26. A disadvantage of this method is the need for a special starting procedure. Whilst the initial conditions should be specified at time $t=0$, the solution for $t=+\Delta t$ requires knowledge of the displacements at $t=\text{-}\Delta t$, which do not exist. To overcome this problem the initial values of the velocity and accelerations must be used to calculate these fictitious displacement values. Solving Equations 3.25 and 3.26, the following expression is found:

$$u(-\Delta t) = u(0) - \Delta t\dot{u}(0) + \frac{\Delta t^2}{2}\ddot{u}(0) \tag{3.29}$$

The principle advantage of the central difference scheme is that when it is combined with a lumped mass matrix, and in the absence of a damping matrix, the solution to the equilibrium equation becomes explicit. Unlike the implicit schemes that will be presented later in this chapter, explicit schemes do not require the solution of a system of simultaneous equations. This means that the solution is less expensive in terms of computational steps and therefore analysis run time. Generally explicit schemes are only conditionally stable. This means that the size of the time step employed in an analysis must be smaller than a critical value given by Equation 3.30 to maintain numerical stability.

$$\Delta t \leq \Delta t_{cr} = \frac{T_n}{\pi} \tag{3.30}$$

Where T_n is the smallest period of the finite element assemblage with n degrees of freedom (Bathe (1996)). This criterion requires the user to determine the smallest natural period of the finite element assemblage by performing an eigenvector analysis before the finite element analysis can begin proper. The formulation of the central difference method presented here does not allow the size of the time step to be altered during an analysis. To reduce the overall analysis run time it is common in finite element analyses to use larger time steps during period of the analysis in which the variables are changing slowly. This is a common problem for time discretisation schemes which extend over more than one time step, but can be overcome by using a single time step scheme such as one of those that will be presented later in this chapter. The scheme also requires additional information to be stored at time $t = t$-Δt.

3.4.2 The Houbolt Method

This method also employs a finite difference scheme to approximate the velocities and accelerations in terms of the displacements. To improve accuracy and stability, additional values from previous time steps are used. The expressions for the acceleration and velocity are given by Equations 3.31 and 3.32.

$$\ddot{u}(t+\Delta t)=\frac{1}{\Delta t^2}\left(2u(t+\Delta t)-5u(t)+4u(t-\Delta t)-u(t-2\Delta t)\right) \tag{3.31}$$

$$\dot{u}(t+\Delta t)=\frac{1}{6\Delta t}\left(11u(t+\Delta t)-18u(t)+9u(t-\Delta t)-2u(t-2\Delta t)\right) \tag{3.32}$$

Details of the derivation can be found in the original paper (Houbolt (1950)), and will not be repeated here. Substituting these expressions into the equilibrium equation yields the following expression:

$$\begin{aligned}\left(\frac{2}{\Delta t^2}[M]+\frac{11}{6\Delta t}[C]+[K]\right)\{u(t+\Delta t)\}=\{R(t+\Delta t)\}+\\ \frac{1}{\Delta t^2}[M]\{5u(t)-4u(t-\Delta t)+u(t-2\Delta t)\}+\\ \frac{1}{\Delta t}[C]3\left\{u(t)-\frac{3}{2}u(t-\Delta t)+\frac{1}{3}u(t-2\Delta t)\right\}\end{aligned} \tag{3.33}$$

This method also suffers due to the need for a special starting procedure. The solution of $u(t+\Delta t)$ requires the knowledge of $u(t)$, $u(t-\Delta t)$ and $u(t-2\Delta t)$. Therefore to find the solution for the first time step, the displacements at two imaginary time intervals must be found. This is not possible using the Houbolt method and therefore in practice the central difference method is used for the first two increments and than the Houbolt method thereafter. The principal advantage that the Houbolt scheme has over the central difference scheme is that it is unconditionally stable and in general a larger time step than that given by Equation 3.30 can be used to achieve the same degree of accuracy. Due to the time discretisation scheme approximating the velocity and acceleration over many time steps, the size of the time step cannot be altered during the analysis, in a similar fashion to the central difference method.

3.4.3 The Linear Acceleration Method

As the name suggests, this method assumes that the acceleration varies linearly over the given time step. This is illustrated by Figure 3.4.

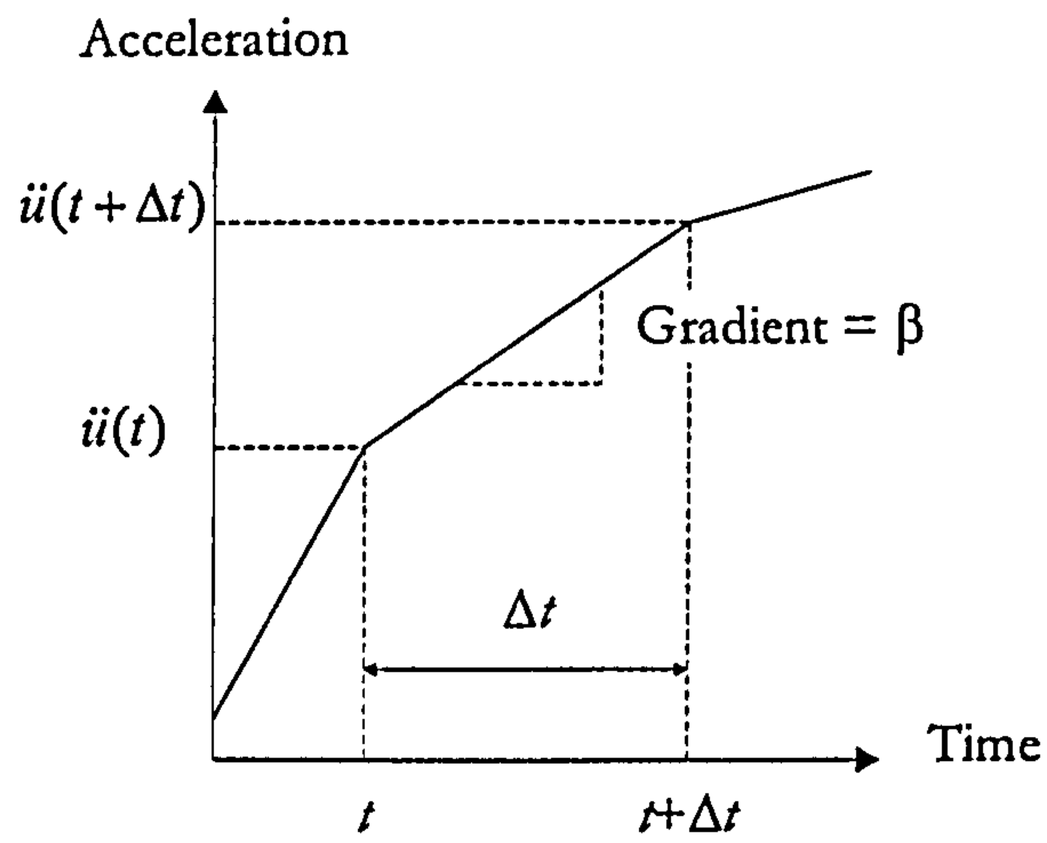

Figure 3.4: Graphical representation of the linear acceleration method

The acceleration is assumed to vary linearly during the increment with a gradient of say β. Using this assumption it is possible to find the acceleration at the end of the time step using Equation 3.34.

$$\ddot{u}(t+\Delta t) = \ddot{u}(t) + \beta\Delta t \tag{3.34}$$

An approximation of the velocity can then be found by integrating this expression with respect to t over the time interval Δt.

$$\dot{u}(t+\Delta t) = \dot{u}(t) + \int_0^{\Delta t} \left(\ddot{u}(t) + \beta t\right) dt \tag{3.35}$$

$$\dot{u}(t+\Delta t) = \dot{u}(t) + \left(\ddot{u}(t)t + \beta\frac{t^2}{2}\right)\Bigg|_0^{\Delta t} \tag{3.36}$$

$$\dot{u}(t+\Delta t) = \dot{u}(t) + \ddot{u}(t)\Delta t + \beta\frac{\Delta t^2}{2} \tag{3.37}$$

This expression can then be integrated again with respect to t to find an approximate relationship for the displacement.

$$u(t+\Delta t) = u(t) + \int_0^{\Delta t} \left(\dot{u}(t) + \ddot{u}(t)t + \beta\frac{t^2}{2}\right) dt \tag{3.38}$$

$$u(t+\Delta t)=u(t)+\left(\dot{u}(t)t+\ddot{u}(t)\frac{t^2}{2}+\beta\frac{t^3}{6}\right)\Bigg|_0^{\Delta t} \tag{3.39}$$

$$u(t+\Delta t)=u(t)+\dot{u}(t)\Delta t+\ddot{u}(t)\frac{\Delta t^2}{2}+\beta\frac{\Delta t^3}{6} \tag{3.40}$$

The finite element formulation is carried out in terms of incremental nodal displacements and therefore the term β must be eliminated from Equations 3.34 and 3.37 and Δu made the primary unknown. This is achieved by rearranging Equation 3.40 to give β in terms of Δu and then substituting this expression into the equations for the velocity and acceleration. The results are Equations 3.41 and 3.42.

$$\dot{u}(t+\Delta t)=-2\dot{u}(t)-\frac{\Delta t}{2}\ddot{u}(t)+\frac{3}{\Delta t}\Delta u \tag{3.41}$$

$$\ddot{u}(t+\Delta t)=-2\ddot{u}(t)-6\frac{\dot{u}(t)}{\Delta t}+6\frac{\Delta u}{\Delta t^2} \tag{3.42}$$

This kind of scheme does not suffer from any starting problems as only information from the previous time step is required. Substituting Equations 3.41 and 3.42 into the equilibrium equation and rearranging to put all the known values on the right hand side gives the following expression:

$$\begin{gathered}\left(\frac{6}{\Delta t^2}[M]+\frac{3}{\Delta t}[C]+[K]\right)\{\Delta u\}=\{\Delta R\}+\\ [M]\left\{3\ddot{u}(t)+6\frac{\dot{u}(t)}{\Delta t}\right\}+[C]\left\{3\dot{u}(t)+\frac{\Delta t}{2}\ddot{u}(t)\right\}\end{gathered} \tag{3.43}$$

This can then be more conveniently expressed in a similar form to the static equilibrium equations:

$$\left[\bar{K}\right]\{\Delta u\}=\left\{\Delta\bar{R}\right\} \tag{3.44}$$

where $\left[\bar{K}\right]=\frac{6}{\Delta t^2}[M]+\frac{3}{\Delta t}[C]+[K]$ the effective stiffness matrix.

$\left[\Delta\bar{R}\right]=\{\Delta R\}+[M]\left\{3\ddot{u}(t)+6\frac{\dot{u}(t)}{\Delta t}\right\}+[C]\left\{3\dot{u}(t)+\frac{\Delta t}{2}\ddot{u}(t)\right\}$ is the effective right hand side load vector.

Whilst the time step used in an analysis that employs the linear acceleration method can be varied because the approximations only extend over one time increment, it is still only conditionally stable. The critical time step to ensure numerical stability is given by Equation 3.45 (Newmark (1959)).

$$\Delta t \leq \Delta t_{cr} = 0.551T_n \tag{3.45}$$

The most obvious improvement that can be made to the linear acceleration method is to represent the variation of the acceleration within an increment by a higher order polynomial. If, for example, the acceleration is represented by a quadratic equation, it implies that the third derivative of displacement with time, which from this point onwards will be called the thrust, varies linearly.

$$\dddot{u}(t+\Delta t)=\dddot{u}(t)+\beta\Delta t \tag{3.46}$$

This expression can then be integrated with respect to time to yield the following expressions for acceleration, velocity and displacement.

$$\ddot{u}(t+\Delta t)=\ddot{u}(t)+\dddot{u}(t)\Delta t+\beta\frac{\Delta t^2}{2} \tag{3.47}$$

$$\dot{u}(t+\Delta t)=\dot{u}(t)+\ddot{u}(t)\Delta t+\dddot{u}(t)\frac{\Delta t^2}{2}+\beta\frac{\Delta t^3}{6} \tag{3.48}$$

$$u(t+\Delta t)=u(t)+\dot{u}(t)\Delta t+\ddot{u}(t)\frac{\Delta t^2}{2}+\dddot{u}(t)\frac{\Delta t^3}{6}+\beta\frac{\Delta t^4}{24} \tag{3.49}$$

Equation 3.49 can then be used to eliminate β from the other expressions and the resulting relationships are substituted into the equilibrium equation. When rearranged this yields Equation 3.50.

$$\begin{gathered}\left(\frac{12}{\Delta t^2}[M]+\frac{4}{\Delta t}[C]+[K]\right)\{\Delta u\}=\{\Delta R\}+\\ [M]\left\{12\frac{\dot{u}(t)}{\Delta t}+6\ddot{u}(t)+\dddot{u}(t)\Delta t\right\}+[C]\left\{4\dot{u}(t)+\ddot{u}(t)\Delta t+\dddot{u}(t)\frac{\Delta t^2}{6}\right\}\end{gathered} \tag{3.50}$$

It has however been found in practice that Equation 3.46 is not sufficient to calculate the incremental thrust. This will be practically demonstrated in Chapter 4 but can be explained by considering dynamic equilibrium which is given by Equation 3.51.

$$[M]\{\Delta\ddot{u}\}+[C]\{\Delta\dot{u}\}+[K]\{\Delta u\}=\{\Delta R\} \tag{3.51}$$

where all the terms have their usual meaning. If each term is differentiated once with respect to time, the result is the following equation:

$$[M]\{\Delta\dddot{u}\}+[C]\{\Delta\ddot{u}\}+[K]\{\Delta\dot{u}\}=\{\Delta\dot{R}\} \tag{3.52}$$

Whilst this must hold in general, it only becomes relevant with a time discretisation scheme that relies on the incremental thrust being calculated (i.e. the quadratic acceleration method derived previously). If the load vector $\{\Delta R\}$ is assumed to vary linearly during the increment as shown in Figure 3.5, the derivative of the load vector becomes discontinuous, as shown in Figure 3.6.

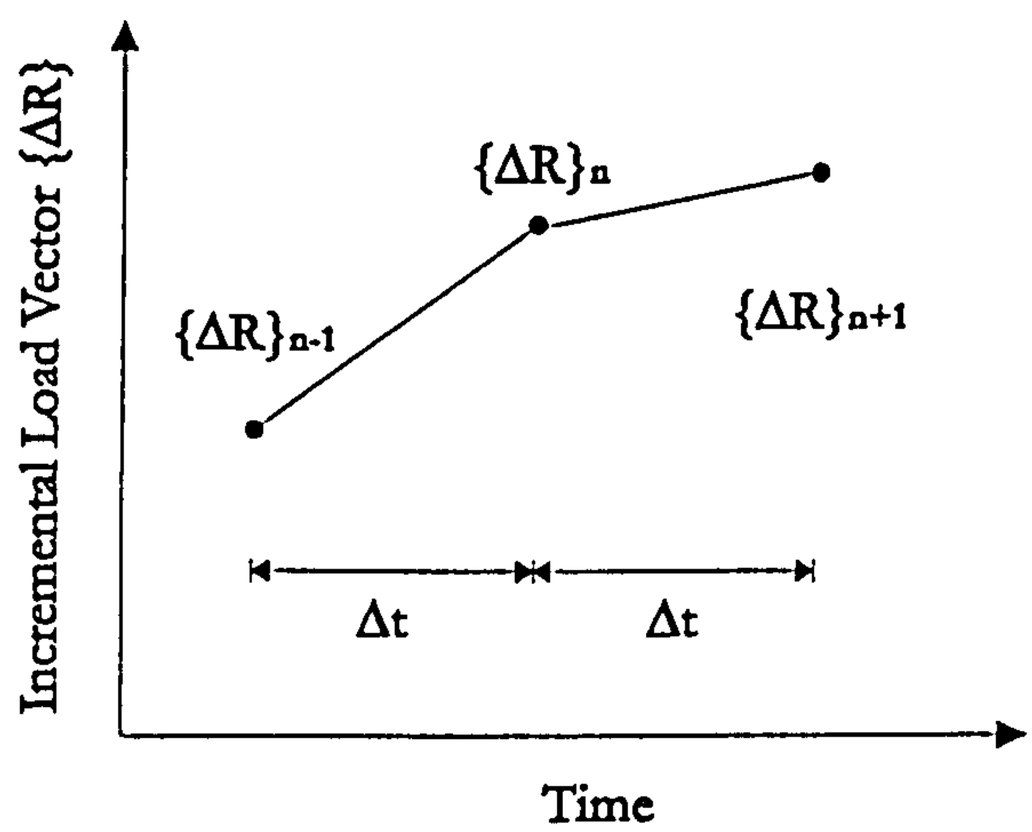

Figure 3.5: Schematic representation of incremental load vector

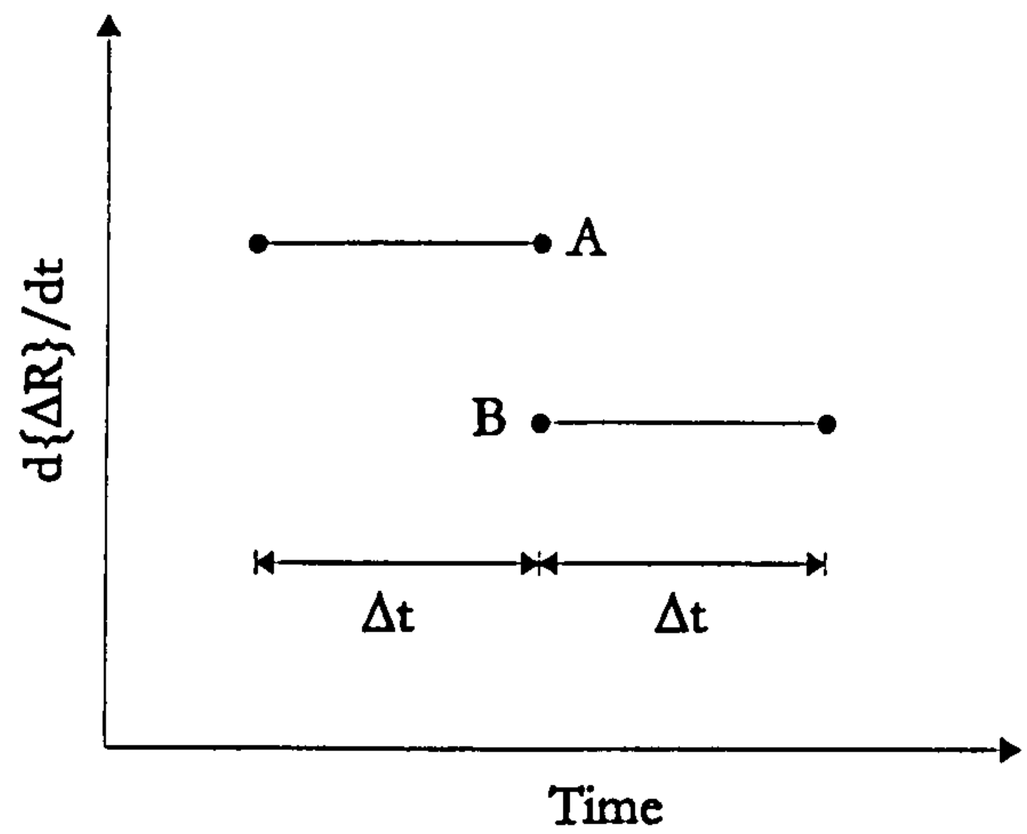

Figure 3.6: Schematic representation of the differential of the incremental load vector

The incremental thrust obtained from Equation 3.46 is equivalent to the equilibrium condition shown by point A in Figure 3.6. For the correct solution to be found for the next increment, equilibrium must be satisfied by the condition equivalent to point B. This can be achieved by rearranging Equation 3.52 and obtaining the incremental thrust from equilibrium conditions at the end of the increment. This is not an issue for schemes that do not include differentials above the order of acceleration (i.e. the linear acceleration method) as they do not require the differential of the load vector to be a continuous function.

The incremental thrust is therefore found from Equation 3.53:

$$\{\Delta\ddot{u}\} = [M]^{-1}\left(\{\Delta\dot{R}\} - [C]\{\Delta\ddot{u}\} - [K]\{\Delta\dot{u}\}\right) \tag{3.53}$$

where $[M]^{-1}$ is the inverse of the mass matrix. The values calculated for the incremental velocities and accelerations can then be used in Equation 3.53, although a further expression is required to approximate the differential of the load vector. The simplest possible approximation is given by Equation 3.54.

$$\{\Delta\dot{R}\} = \frac{\{\Delta R(t+\Delta t)\} - \{\Delta R(t)\}}{\Delta t} \qquad (3.54$$

By approximating the variation of the acceleration with a higher order polynomial it is hoped that this will more accurately match the true variation at the expense of having to calculate and store in the computer memory an additional variable, the

thrust. The length of the time step can be changed during an analysis as the approximation is only made over a single increment, although Tsatsanifos (1982) found that the scheme was unstable in absence of any hysteretic damping.

3.4.4 The Wilson θ Method

To improve the stability characteristics of the linear acceleration method, Wilson *et al.* (1973) proposed a new method in which equilibrium is first considered at a time outside the original time increment and then the solution at the point of interest is found by extrapolating backwards. Consider the variation of acceleration with time shown in Figure 3.7.

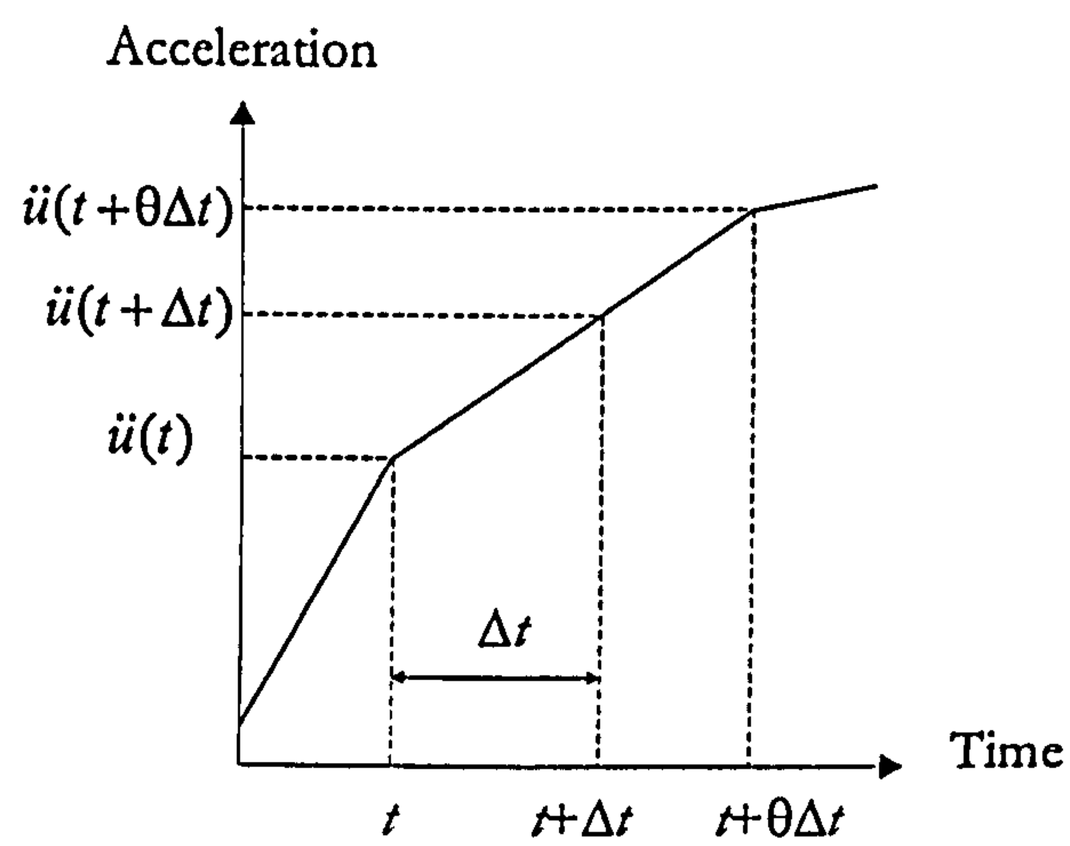

Figure 3.7: Graphical representation of the Wilson θ method

The acceleration is assumed to vary linearly in the time interval t to $t+\theta\Delta t$, where θ is a constant greater than or equal to unity. The acceleration at any time in the interval $0 \le \tau \le \theta\Delta t$ can then be found using Equation 3.55.

$$\ddot{u}(t+\tau) = \ddot{u}(t) + \frac{\tau}{\theta\Delta t}\left(\ddot{u}(t+\theta\Delta t) - \ddot{u}(t)\right) \tag{3.55}$$

This expression can then be integrated in a similar fashion to that employed in the linear acceleration method to yield expressions for the velocity and displacement at any time in the interval $0 \le \tau \le \theta\Delta t$.

$$\dot{u}(t+\tau) = \dot{u}(t) + \ddot{u}(t)\tau + \frac{\tau^2}{2\theta\Delta t}\left(\ddot{u}(t+\theta\Delta t) - \ddot{u}(t)\right) \tag{3.56}$$

$$u(t+\tau)=u(t)+\dot{u}(t)\tau+\frac{1}{2}\ddot{u}(t)\tau^2+\frac{\tau^3}{6\theta\Delta t}\left(\ddot{u}(t+\theta\Delta t)-\ddot{u}(t)\right) \qquad (3.57)$$

Substituting $\tau=\theta\Delta t$ into the above expressions gives the velocities and displacements at the projected point in the future:

$$\dot{u}(t+\theta\Delta t)=\dot{u}(t)+\frac{\theta\Delta t}{2}(\ddot{u}(t+\theta\Delta t)+\ddot{u}(t)) \qquad (3.58)$$

$$u(t+\theta\Delta t)=u(t)+\theta\Delta t\dot{u}(t)+\frac{\theta^2\Delta t^2}{6}\left(\ddot{u}(t+\theta\Delta t)+2\ddot{u}(t)\right) \qquad (3.59)$$

These expressions can then be substituted into the equilibrium equation to find the solution to the problem at time $t=t+\theta\Delta t$. Due to equilibrium being considered at some time in the future, a linearly extrapolated load vector must be used.

$$R(t+\theta\Delta t)=R(t)+\theta\left(R(t+\Delta t)-R(t)\right) \qquad (3.60)$$

The required solution variables at time $t=t+\Delta t$ can then be found using Equations 3.55, 3.56 and 3.57 and substituting $\tau=\Delta t$. It is found that the scheme is unconditionally stable if θ is greater than or equal to 1.37, although Wilson *et al.* (1973) report the best performance with a value of 1.4. If θ is assumed to be unity then the scheme reverts to the linear acceleration method.

3.4.5 The Newmark Method

This technique is essentially an extension of the linear acceleration method. The Newmark expressions for the velocity and displacement at the end of an increment are similar in form to those derived assuming the acceleration varies linearly over the increment, although some of the coefficients have been replaced with two parameters α and δ.

$$\dot{u}(t+\Delta t)=\dot{u}(t)+(1-\delta)\ddot{u}(t)\Delta t+\delta\ddot{u}(t+\Delta t)\Delta t \qquad (3.61)$$

$$u(t+\Delta t)=u(t)+\dot{u}(t)\Delta t+\left(\tfrac{1}{2}-\alpha\right)\ddot{u}(t)\Delta t^2+\alpha\ddot{u}(t+\Delta t)\Delta t^2 \qquad (3.62)$$

Newmark (1959) stated that the two parameters α and δ are introduced to indicate how much of the acceleration at the end of the interval enters into the relations for velocity and displacement at the end of the interval. Equations 3.61 and 3.62 can then be rearranged and combined to give expressions for the incremental velocity and acceleration in terms of the incremental displacements:

$$\Delta\dot{u} = \frac{\delta}{\alpha\Delta t}\Delta u - \frac{\delta}{\alpha}\dot{u}(t) + \left(1 - \frac{\delta}{2\alpha}\right)\Delta t\ddot{u}(t) \tag{3.63}$$

$$\Delta\ddot{u} = \frac{1}{\alpha\Delta t^2}\Delta u - \frac{1}{\alpha\Delta t}\dot{u}(t) - \frac{1}{2\alpha}\ddot{u}(t) \tag{3.64}$$

These relationships can then be substituted into the equilibrium equation and rearranged to give Equation 3.65:

$$\begin{gathered}\left[\frac{1}{\alpha\Delta t^2}[M] + \frac{\delta}{\alpha\Delta t}[C] + [K]\right]\{\Delta u\} = \{\Delta R\} + \\ [M]\left\{\frac{\dot{u}(t)}{\alpha\Delta t} + \frac{1}{2\alpha}\ddot{u}(t)\right\} + [C]\left\{\frac{\delta\dot{u}(t)}{\alpha} + \Delta t\left(\frac{\delta}{2\alpha} - 1\right)\ddot{u}(t)\right\}\end{gathered} \tag{3.65}$$

The choice of the Newmark parameters α and δ determines the characteristics of the time discretisation scheme. The δ parameter determines the amount of numerical damping that is added to the analysis. If δ is less than 0.5, then negative damping results and the analysis becomes unstable. If δ is set to 0.5 then no damping is added and accordingly a value greater than 0.5 adds positive numerical damping. The value chosen for the parameter α determines how the acceleration is assumed to vary during the time interval. Whilst any value can be set for α, certain values correspond to a variation of acceleration during the increment which can be understood physically. For example, setting α equal to 1/6 is equivalent to assuming the acceleration varies linearly during the time increment. This can be shown by substituting values of 0.5 and 1/6 for δ and α respectively into Equations 3.63 and 3.64 and thus retrieving the same expressions for the incremental velocity and acceleration as given by the linear acceleration method. An α value of 1/4 corresponds to a uniform value of acceleration during the increment equal to the mean of the initial and final values of the acceleration and an α value of 1/8 is equivalent to a step function that has the value of the initial acceleration for the first

half of the increment and then has the final value of the acceleration for the second half. These differences are illustrated by Figure 3.8.

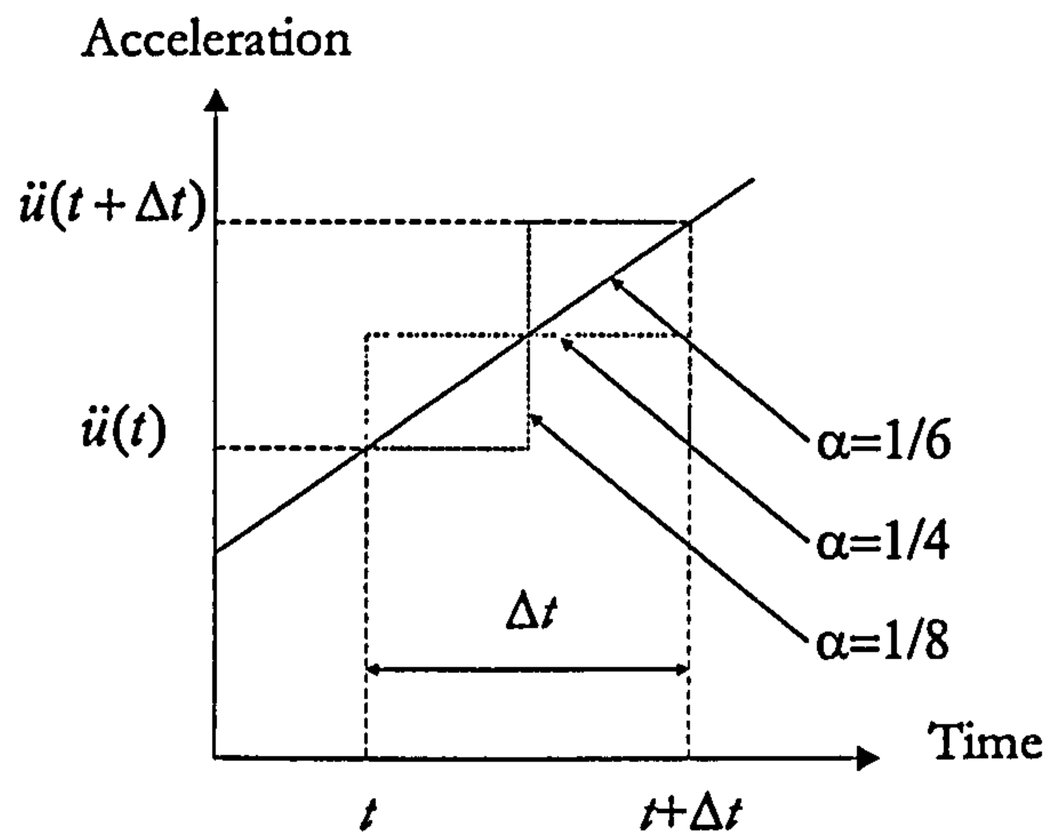

Figure 3.8: Graphical representation of the Newmark method

The most attractive feature of the Newmark method is that by choosing parameters that satisfy the following criteria it is possible to create an unconditionally stable scheme (Bathe (1996)):

$$\delta \geq 0.5 \tag{3.66a}$$

$$\alpha \geq 0.25(0.5+\delta)^2 \tag{3.66b}$$

Therefore Newmark's so called constant average acceleration scheme with an α value of 0.25 and δ equal to 0.5 is unconditionally stable. If however, a conditionally stable scheme is to be used that does not satisfy Equation 3.66b, the critical time step is given by Equation 3.67 (Newmark (1959)).

$$\Delta t \leq \Delta t_{cr} = \frac{1}{\pi\sqrt{1-4\alpha}} T_n \tag{3.67}$$

If an additional term, γ, is added to the original Newmark scheme to take account of the third derivative of displacement with time (or thrust), the Newmark method can be made to incorporate the quadratic acceleration scheme derived in Section 3.4.3. Equations 3.68 and 3.69 show the changes that are required to the standard Newmark equations to incorporate the higher order assumption. Equation 3.70

gives the incremental thrust, which, as mentioned previously, must be calculated using the equilibrium condition at the end of the increment.

$$\Delta\dot{u} = \frac{\delta}{\alpha\Delta t}\Delta u - \frac{\delta}{\alpha}\dot{u}(t) + \left(1 - \frac{\delta}{2\alpha}\right)\Delta t\ddot{u}(t) - \frac{\gamma}{6}\Delta t^2\dddot{u}(t) \tag{3.68}$$

$$\Delta\ddot{u} = \frac{1}{\alpha\Delta t^2}\Delta u - \frac{1}{\alpha\Delta t}\dot{u}(t) - \frac{1}{2\alpha}\ddot{u}(t) - \gamma\Delta t\dddot{u}(t) \tag{3.69}$$

$$\{\Delta\dddot{u}\} = [M]^{-1}\left(\Delta\dot{R} - [C]\{\Delta\ddot{u}\} - [K]\{\Delta\dot{u}\}\right) \tag{3.70}$$

where $$\{\Delta\dot{R}\} = \frac{\{\Delta R(t+\Delta t)\} - \{\Delta R(t)\}}{\Delta t}$$

By setting $\gamma = 1$, $\delta = 1/3$ and $\alpha = 1/12$ the quadratic acceleration scheme derived in section 3.4.3 is retrieved. If γ is set to zero then the equations revert to the original Newmark form. Upon substitution into the equilibrium equation the following general expression is found:

$$\begin{aligned}\left(\frac{1}{\alpha\Delta t^2}[M] + \frac{\delta}{\alpha\Delta t}[C] + [K]\right)\{\Delta u\} = \{\Delta R\} + \\ [M]\left\{\frac{\dot{u}(t)}{\alpha\Delta t} + \frac{1}{2\alpha}\ddot{u}(t) + \gamma\dddot{u}(t)\Delta t\right\} + \\ [C]\left\{\frac{\delta}{\alpha}\dot{u}(t) + \Delta t\left(\frac{\delta}{2\alpha} - 1\right)\ddot{u}(t) + \frac{\gamma}{6}\dddot{u}(t)\Delta t^2\right\}\end{aligned} \tag{3.71}$$

With this slight modification it is possible to expand the Newmark method to include another time discretisation scheme with one general equilibrium equation.

3.4.6 Other Schemes

The principle drawback of the Newmark method is the excessive numerical damping introduced into the lower modes of vibration when the α parameter is set to a value above 0.25. The numerical damping is introduced to reduce the influence of the higher modes of vibration, as these are not accurately modelled by the finite element assemblage and contribute little to the overall behaviour. As a by-product, the lower modes, which dominate the overall behaviour of the analysis, also suffer

some level of numerical damping. Hilbert *et al.* (1977) proposed a new three parameter time discretisation scheme which claimed to damp out the higher modes of vibration but not affect the lower modes too strongly. The time discretisation scheme is an extension of the Newmark method, which can be retrieved by setting the additional parameter to zero. This scheme will not be considered for implementation in this thesis but does offer an obvious direction for research in the future. This subject will be returned to in Chapter 7.

3.4.7 Choice of Scheme

The central difference and Houbolt methods can both be discarded immediately. The need for a special starting procedure renders both of these schemes impractical.

This then only leaves the linear acceleration, quadratic acceleration, Wilson θ method and the modified Newmark method. The quadratic and linear acceleration methods can be discarded as they are just special cases of the modified Newmark method. This then only leaves the Wilson θ method and the modified Newmark method. The distinct advantage of the Wilson method is that if θ is greater than or equal to 1.37 the scheme is unconditionally stable. The same can be said of the modified Newmark method with the parameters chosen to satisfy Equation 3.66a and 3.66b. To choose between these two schemes one must consider their respective accuracy. A comparative study of a single degree of freedom problem was undertaken by Bathe (1996) to examine the accuracy of each time discretisation scheme. The accuracy of each scheme could be illustrated with two characteristics, namely the period elongation and the amplitude decay. The results are shown in Figure 3.9.

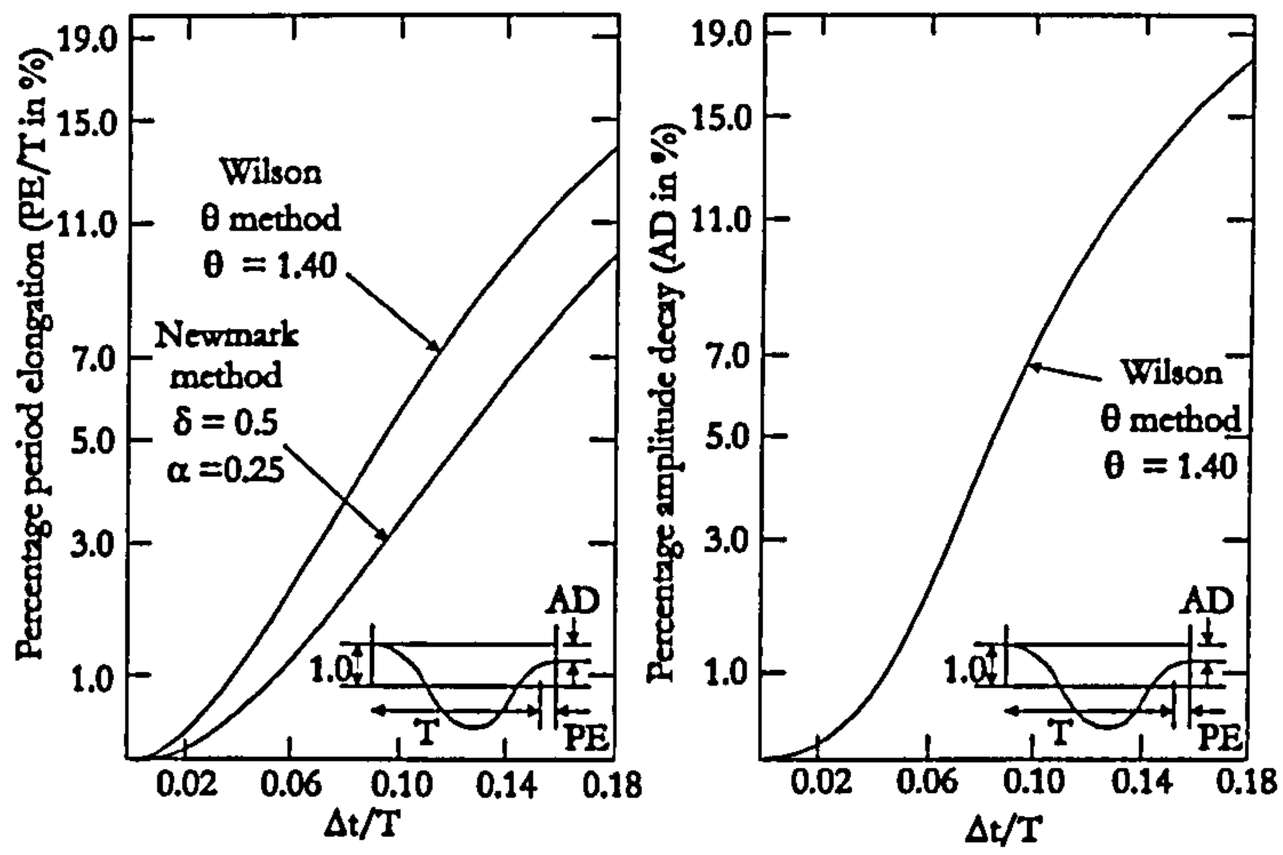

Figure 3.9: Percentage period elongations and amplitude decays (after Bathe (1996))

Only the results' using the constant average acceleration parameters of the group of Newmark schemes has been presented. It is clear from the results that as the ratio of the time step to the natural period increases all of the schemes become less accurate, although of the two presented here the Newmark scheme introduces the least period elongation. With regard to amplitude decay the Wilson method suffers from significant amplitude loss when the ratio $\Delta t / T$ is above 0.05, while the constant average acceleration scheme mentioned in Section 3.4.5 does not introduce any additional numerical damping and therefore does not cause any amplitude decay. These advantageous properties and the potential flexibility that the modified Newmark method offers, make this scheme clearly the most superior among those considered in this thesis. Consequently this is implemented into ICFEP.

3.5 Boundary Conditions

As mentioned in Section 2.2, boundary conditions fall into two categories. The first affects the right hand side load vector and consists of applied surcharges and point loads and the second affects some of the nodal displacements. The specification of a certain number of boundary conditions of the second type is necessary to make the solution of the system of finite element equations possible. Due to most geotechnical problems occurring in the earth there is no obvious location of where to place the outer boundaries of the finite element mesh. The choice of their location is often based on experience, as an artificial zero

displacement boundary condition too close to the areas of interest of an analysis will unrealistically influence the results. Conversely, if the boundary is placed too far away it will increase the analysis run time without improving the quality of the results. In addition to specifying boundary conditions to the solid phase of the soil, if a coupled analysis is to be undertaken then either a nodal pore pressure or fluid flow must be specified at each boundary node. This will not be altered by the inclusion of dynamic capabilities and therefore from henceforth any mention of boundary conditions will mean only those that apply to the solid phase.

In addition to applying displacement boundary conditions, in dynamic finite element analysis it must also be possible to apply velocity and acceleration boundary conditions. However, due to the finite element formulation being performed in terms of incremental displacements, whatever form the boundary condition is specified in, it must first be converted into an equivalent incremental displacement. It is natural to perform this transformation using the same time discretisation scheme that has been implemented into the equilibrium equations. Being able to apply a boundary condition in the form of acceleration is of particular importance as it allows the response of a finite element mesh to an earthquake record to be modelled. It is not possible to apply two different types of boundary conditions (i.e. acceleration and displacement) to the same node in the same direction, unless they result in the same incremental nodal displacement. Applying a dynamic point load or surcharge follows the same procedure as that required for a static analysis. The application of the load must now be discretised into a series of load increments, with the desired input frequency taken into account by choosing the size of the time step and the appropriate number of increments.

The application of a displacement boundary condition, either by itself or converted from an acceleration or velocity input causes additional problems for dynamic finite element analysis. Consider, for example, the analysis of a one dimensional soil column subjected to a single sinusoidal displacement boundary condition by finite elements. The sine wave is specified in terms of displacement at the base of the mesh and the wave then propagates through the soil column and a zero displacement boundary condition is then applied to the base of the mesh to prevent rigid body motion. The wave reaches the surface and reflects back into the soil column due to the zero stress boundary condition at the surface. This is correct as it

would occur in reality. When the wave reaches the base of the mesh it is again reflected into the column due to the zero displacement boundary condition. If there is no stiff base rock present in reality this reflection would not occur and the wave energy would be dissipated through the infinite extent of the earth. To realistically model the situation where no rigid bedrock exists, a special boundary condition must be employed that allows the incoming wave to enter the problem and also allows reflected waves to leave. This problem will not be addressed in this thesis and any analyses that encounter this problem must assume the presence of a stiff bedrock. Methods to address the issue of reflecting boundaries will be returned to in Chapter 7 where recommendations for future research are discussed.

3.6 Dynamic Pore Fluid Interaction

It was demonstrated in Chapter 2 that three cases can be identified when analysing the combined behaviour of a soil matrix and pore fluid. The first two are the limiting cases of drained and undrained behaviour and the third is the intermediate case which requires the use of coupled analysis to fully model the two phase behaviour. To model a dynamic problem with one of the two extreme types of behaviour requires no additional consideration than that outlined in Chapter 2. The fully drained case is unchanged because the response of the pore fluid is assumed to be zero. The question of whether this is ever a realistic assumption to make for a dynamic analysis, except in totally dry conditions, is another issue but fundamentally it requires no extra changes to be made. When the assumption of totally undrained behaviour is made this inherently implies that no relative movement of the pore fluid is allowed and therefore no dynamic or inertia effects can affect the pore fluid phase. Effectively the soil matrix and the pore fluid move as one body and therefore the only change that must be made is to use the saturated density. When considering the intermediate case, extra consideration must be made regarding the effects that dynamics may have on the equilibrium of the soil and pore fluid mix. It is this issue that will be considered in this section.

The consolidation theory presented in Chapter 2 was extended by Biot in 1956 (Biot (1956a), Biot (1956b)) to include the effects of inertia loading. To begin the derivation, the equilibrium equation must be derived for each phase of the material.

The discretised form of the dynamic equilibrium equation for the solid phase is given by Equation 3.72.

$$[M]\{\Delta\ddot{u}\}+[C]\{\Delta\dot{u}\}+[K]\{\Delta u\}=\{\Delta R\} \tag{3.72}$$

where $[M]=\sum_{i=1}^{N}\int_{Vol}[N]^T\rho[N]dVol$ = global mass matrix

$[C]=\sum_{i=1}^{N}\int_{Vol}[N]^T\kappa[N]dVol$ = global damping matrix

$[K]=\sum_{i=1}^{N}\int_{Vol}[B]^T[D][B]dVol$ = global stiffness matrix

$\{\Delta R\}=\int_{Vol}[N]^T\{\Delta F\}dVol+\int_{Surface}[N]^T\{\Delta T\}dSurface$ = Right hand side load vector

$\{\Delta u\}$, $\{\Delta\dot{u}\}$ and $\{\Delta\ddot{u}\}$ are the nodal displacement, velocity and acceleration vectors respectively.

In a similar fashion to that described in Section 2.5, the principle of effective stress can be used to divide the stiffness matrix into an effective stress and a pore fluid component.

$$[M]\{\Delta\ddot{u}\}+[C]\{\Delta\dot{u}\}+[K]\{\Delta u\}+[L]\{\Delta p_f\}=\{\Delta R\} \tag{3.73}$$

where $[K]=\sum_{i=1}^{N}\int_{Vol}[B]^T[D'][B]dVol$ = the stiffness matrix in terms of effective stress parameters

$[L]=\sum_{i=1}^{N}\int_{vol}\{m\}[B]^T[N_p]dVol$ = coupling matrix

$\{m\}^T=\{1 \quad 1 \quad 1 \quad 0 \quad 0 \quad 0\}$

$\{\Delta p_f\}$ is the vector of nodal pore pressures.

An approximation has already been made in the derivation of Equation 3.73. The original Biot derivation contained an additional term in the equilibrium equation relating to the acceleration of the pore fluid relative to the soil matrix. This term has been omitted from the derivation presented here as its inclusion would significantly alter the finite element implementation and has been found to be insignificant for earthquake analysis of engineering structures such as dams and foundations (Zienkiewicz *et al.* (1980)).

The equation of continuity for the pore fluid is given by Equation 3.74:

$$\frac{\partial w_x}{\partial x}+\frac{\partial w_y}{\partial y}+\frac{\partial w_z}{\partial z}-\frac{\partial p_f}{\partial t}\frac{n}{K_f}-Q=-\frac{\partial \varepsilon_v}{\partial t} \tag{3.74}$$

Equation 3.74 is the same as the equation of continuity derived in Chapter 2 with the addition of an extra term to include the compressibility of the pore fluid. The consolidation theory presented previously assumed that the pore fluid was incompressible. This is a reasonable assumption when the compressibility of the pore fluid is compared to that of the soil skeleton. This is generally accepted for static geotechnical analyses, although the same assumption may not apply to dynamic problems. Therefore to investigate the importance of this term to dynamic problems it has been included in the equation of continuity.

Darcy's law is not valid for dynamic events and therefore cannot be used to relate the pore fluid velocity $\{w\}$, to the hydraulic gradient $\{\nabla h\}$. In place of Darcy's law, the more general momentum balance equation, given by Equation 3.75, must be used.

$$-\{\nabla h\}-[k]^{-1}\{w\}+\frac{1}{g}\{\ddot{u}\}=0 \tag{3.75}$$

where g is the acceleration due to gravity

$[k]$ is the permeability matrix.

If the third term (which represents the inertia in the pore fluid) is ignored, Equation 3.75 reduces to Darcy's law.

To be consistent with the equilibrium equation for the solid phase, Equation 3.75 does not include the effect of the acceleration of the pore fluid relative to the soil matrix. As mentioned previously, the inclusion of this term changes the nature of finite element implementation. If the acceleration of the pore fluid relative to the soil matrix $\{\dot{w}\}$, were to be included in Equation 3.75, it could no longer be used to uniquely relate the pore fluid velocity $\{w\}$ to the hydraulic gradient $\{\nabla h\}$ and hence eliminate the pore fluid velocity term in the continuity equation. In practical terms this means that the analysis would have to be undertaken using the momentum balance equation for both phases of the material and the equation of continuity. This results in three coupled equations that must be solved simultaneously to fully describe the problem. However, the fluid acceleration relative to the soil matrix is often small in real engineering problems (Zienkiewicz *et al.* (1999)) and can therefore be ignored allowing the elimination of the velocity term in the continuity equation using the momentum balance for the pore fluid given by Equation 3.75. The range of problems over which this assumption is valid is discussed in detail in Zienkiewicz *et al.* (1980). This assumption is referred to as the *u-p* approximation as the only variables considered are the displacement of the soil phase (*u*) and the pore fluid pressure (*p*). On the other hand, using the complete set of equations is called the *u-w-p* theory as the velocity of the pore fluid (*w*) is also considered. By adopting the *u-p* approximation, the equation for the solid phase remains unchanged from that derived in Section 2.2. The changes that are required to the equation of continuity shall now be given. The hydraulic gradient $\{\nabla h\}$ is related to the pore pressure by Equation 3.76 in a similar fashion to that described in Section 2.5.

$$h = \frac{p_f}{\gamma_f} + \left(x i_{Gx} + y i_{Gy} + z i_{Gz}\right) \tag{3.76}$$

where $\{i_G\} = \{i_{Gx} \quad i_{Gy} \quad i_{Gz}\}^T$ is the unit vector parallel, but in the opposite direction to gravity. The momentum balance of the fluid phase is now given by Equation 3.77:

$$\{\nabla p_f\} + [k]^{-1} \gamma_f \{w\} + \frac{\gamma_f}{g}\{\ddot{u}\} + \gamma_f \{i_G\} = 0 \tag{3.77}$$

This expression can then be rearranged to give the pore fluid velocity in terms of the pressure head and the acceleration of the soil-fluid mixture.

$$\{w\} = [k]\left[-\frac{1}{\gamma_f}\{\nabla p_f\} - \{i_G\} - \frac{1}{g}\{\ddot{u}\}\right] \tag{3.78}$$

Equation 3.78 can then be used to eliminate the pore fluid velocity term in the equation of continuity, which in turn can then be converted to the finite element form using the principle of virtual work.

$$\int_{Vol}\left[\begin{array}{c}\left[-\frac{1}{\gamma_f}\{\nabla p_f\} - \{i_G\} + \frac{1}{g}\{\ddot{u}\}\right][k]\{\nabla p_f\} \\ +\frac{\partial \varepsilon_v}{\partial t}\Delta p_f - \frac{\partial p_f}{\partial t}\frac{n}{K_f}\Delta p_f\end{array}\right] dVol - Q\Delta p_f = 0 \tag{3.77}$$

Approximating $\partial\varepsilon_v/\partial t$ as $[B]\{\Delta d\}/\Delta t$ and $\partial p_f/\partial t$ as $\{\Delta p_f\}/\Delta t$, the final finite element equations can be rewritten as Equation 3.78.

$$[L]^T\left\{\frac{\Delta d}{\Delta t}\right\} + [G]\left\{\frac{\Delta \ddot{u}}{\Delta t}\right\} - [\phi]\{p_f\} - [S]\left\{\frac{\Delta p_f}{\Delta t}\right\} = [n] + Q \tag{3.78}$$

Where

$$[\phi] = \int_{vol}\frac{1}{\gamma_f}[E]^T[k][E]dvol$$

$$[n] = \int_{vol}[E]^T[k]\{i_G\}dvol$$

$$[G] = \int_{Vol}\frac{1}{g}[N]^T[k][E]dvol$$

$$[S] = \int_{Vol}\frac{n}{K_f}[N_p]^T[N_p]dvol$$

$$[E] = \left[\frac{\partial N_p}{\partial x}, \frac{\partial N_p}{\partial y}, \frac{\partial N_p}{\partial z}\right]^T$$

Using the time marching scheme described in Chapter 2 and replacing the acceleration term with the appropriate modified Newmark approximation, the final coupled dynamic finite element formulation is given by Equation 3.79.

$$\begin{bmatrix} [\bar{K}] & [L] \\ [L]^T + \frac{1}{\alpha\Delta t}[G] & -[S] - \beta\Delta t[\phi] \end{bmatrix} \begin{bmatrix} \{\Delta u\} \\ \{\Delta p_f\} \end{bmatrix} = \begin{bmatrix} \{\Delta\bar{R}\} \\ \left[[n] + Q + [\phi]\{p_f\} + [G]f(u)\right]\Delta t \end{bmatrix} \quad (3.79)$$

Where $$f(u) = \frac{1}{\alpha\Delta t}\{\dot{u}(t)\} + \frac{1}{2\alpha}\{\ddot{u}(t)\} + \gamma\Delta t\{\dddot{u}(t)\}$$

If the quadratic acceleration scheme is to be used with a coupled analysis, a slight modification must be made to calculate the incremental thrust. The dynamic solid equilibrium equation is now given by Equation 3.80:

$$[M]\{\Delta\ddot{u}\} + [C]\{\Delta\dot{u}\} + [K]\{\Delta u\} + [L]\{\Delta p\} = \{\Delta R\} \quad (3.80)$$

When this expression is differentiated with respect to time, the result is Equation 3.81.

$$[M]\{\Delta\dddot{u}\} + [C]\{\Delta\ddot{u}\} + [K]\{\Delta\dot{u}\} + [L]\{\Delta\dot{p}\} = \{\Delta\dot{R}\} \quad (3.81)$$

When rearranged this gives:

$$\{\Delta\dddot{u}\} = [M]^{-1}\left(\{\Delta\dot{R}\} - [L]\{\Delta\dot{p}\} - [C]\{\Delta\ddot{u}\} - [K]\{\Delta\dot{u}\}\right) \quad (3.82)$$

Therefore the differential of the pore pressure term with respect to time must also be approximated in the same manner as the differential of the load vector:

$$\{\Delta\dot{p}\} = \frac{\{\Delta p(t+\Delta t)\} - \{\Delta p(t)\}}{\Delta t} \quad (3.83)$$

The only modifications that are required to the overall finite element formulation are the inclusion of the pore fluid compressibility and the inertia term in the equilibrium equation for the pore fluid. Zienkiewicz *et al* (1999) chose to neglect the inertia term in the pore fluid equation as it renders the system of equations non-symmetric. Chan (1988) found that the influence of this term was insignificant within the frequency range that the *u-p* approximation was valid, although he did comment that to overcome the problem of a non-symmetric matrix, the term could be moved to the right hand side load vector and then dealt with in an iterative fashion.

Due to the recommendations made by Chan (1988) it has been decided that only the pore fluid compressibility matrix will be added to the overall finite element formulation. There is however the option of adding the inertia term into the pore fluid equilibrium equation in the future and then investigating its importance to real engineering problems.

3.7 Summary

The work presented in this chapter can be summarised as follows:

- It was found that to include the effects of dynamic loading it was necessary to include inertia forces.
- It has also been noted experimentally that when a body vibrates it tends to lose energy. This is commonly taken into account by including a damping force that is proportional to a body's velocity.
- Using d'Alembert's principle the equilibrium equation for dynamic problems was derived.
- The body's displacement, velocity and acceleration were approximated to be equal to the element matrix of shape functions multiplied by the nodal values.
- Using the principle of minimising a body's potential energy, the finite element formulation in terms of the nodal values was derived.
- In addition to the element's stiffness matrix, it was found necessary to evaluate the element's mass and damping matrices.
- It was decided to evaluate a consistent element mass matrix using the isoparametric shape functions and to allow the option of having a Rayleigh damping matrix for linear elastic elements.
- The equilibrium equation is in terms of three unknowns, the acceleration, the velocity and the displacement. Some approximation is required to relate these three variables. These relationships are known as time discretisation schemes.
- A series of possible time discretisation schemes was discussed. Of these the most flexible and accurate was the Newmark method.

- The Newmark method was therefore implemented into ICFEP with a slight modification that includes the option of using a time discretisation scheme that assumes a quadratic variation of acceleration during the increment.
- Acceleration and velocity boundary conditions can now be applied. This is achieved by first converting them into an equivalent incremental displacement and then specifying the values in the displacement list in the same fashion as in static analyses.
- With regard to the dynamic pore fluid–soil skeleton interaction, it was decided to use the so called *u-p* approximation without the inertia term in the pore fluid equation.
- The only modification required to achieve this was to include the pore fluid compressibility in the equation of continuity.

3.8 Implementation

The computational steps required to perform a dynamic finite element analysis will be now outlined.

Assemble the stiffness, damping and mass matrices $[K]$, $[C]$ and $[M]$

Define the initial conditions (u_0, $\dot{u}_0$, $\ddot{u}_0$ and $\dddot{u}_0$) and the required time step Δt.

Choose the Newmark parameters:

$\gamma = 0$, $\delta = 1/2$, $\alpha = 1/6$ Linear Acceleration Method

$\gamma = 0$, $\delta = 1/2$, $\alpha = 1/4$ Constant Acceleration

$\gamma = 1$, $\delta = 1/3$, $\alpha = 1/12$ Quadratic Acceleration

Calculate the modified stiffness matrix

$$[\bar{K}] = [K] + \frac{\delta}{\alpha \Delta t}[C] + \frac{1}{\alpha \Delta t^2}[M]$$

And the modified right hand side vector

$$\{\Delta\bar{R}\} = \{\Delta R\} + [M]\left\{\frac{\dot{u}(t)}{\alpha\Delta t} + \frac{1}{2\alpha}\ddot{u}(t) + \gamma\dddot{u}(t)\Delta t\right\} +$$
$$[C]\left\{\frac{\delta}{\alpha}\dot{u}(t) + \Delta t\left(\frac{\delta}{2\alpha} - 1\right)\ddot{u}(t) + \frac{\gamma}{6}\dddot{u}(t)\Delta t^2\right\}$$

Take any prescribed boundary conditions in terms of acceleration and/or velocity and convert them into an equivalent incremental displacement.

Take these boundary conditions and any actually prescribed displacements and then solve the modified set of simultaneous equations for $\{\Delta u\}$ and $\{\Delta p_f\}$.

$$\begin{bmatrix} [\bar{K}] & [L] \\ [L]^T + \frac{1}{\alpha\Delta t}[G] & -[S] - \beta\Delta t[\phi] \end{bmatrix} \begin{bmatrix} \{\Delta u\} \\ \{\Delta p_f\} \end{bmatrix} = \begin{bmatrix} \{\Delta\bar{R}\} \\ \left[[n] + Q + [\phi]\{p_f\} + [G]f(u)\right]\Delta t \end{bmatrix}$$

Where $$f(u) = \frac{1}{\alpha\Delta t}\{\dot{u}(t)\} + \frac{1}{2\alpha}\{\ddot{u}(t)\} + \gamma\Delta t\{\dddot{u}(t)\}$$

For all nodes calculate $$\Delta\dot{u} = \frac{\delta}{\alpha\Delta t}\Delta u - \frac{\delta}{\alpha}\dot{u}(t) + \left(1 - \frac{\delta}{2\alpha}\right)\Delta t\ddot{u}(t) - \frac{\gamma}{6}\Delta t^2\dddot{u}(t)$$

$$\Delta\ddot{u} = \frac{1}{\alpha\Delta t^2}\Delta u - \frac{1}{\alpha\Delta t}\dot{u}(t) - \frac{1}{2\alpha}\ddot{u}(t) - \gamma\Delta t\dddot{u}(t)$$

$$\{\Delta\dddot{u}\} = [M]^{-1}\left(\Delta\dot{R} - [L]\{\Delta\dot{p}\} - [C]\{\Delta\ddot{u}\} - [K]\{\Delta\dot{u}\}\right)$$

where $$\{\Delta\dot{R}\} = \frac{\{\Delta R(t+\Delta t)\} - \{\Delta R(t)\}}{\Delta t}$$

$$\{\Delta\dot{p}\} = \frac{\{\Delta p(t+\Delta t)\} - \{\Delta p(t)\}}{\Delta t}$$

To invert the mass matrix the same subroutine used to invert the overall stiffness matrix can be used.

Update the stored values $$u(t+\Delta t) = u(t) + \Delta u$$

$$\dot{u}(t+\Delta t) = \dot{u}(t) + \Delta\dot{u}$$

$$\ddot{u}(t+\Delta t) = \ddot{u}(t) + \Delta\ddot{u}$$

$$\dddot{u}(t+\Delta t) = \dddot{u}(t) + \Delta\dddot{u}$$

$$p_f(t+\Delta t) = p_f(t) + \Delta p$$

Iterate until convergence criteria has been satisfied for non-linear problems. If the original Newton-Raphson method is used for iterating towards the correct solution, the stiffness matrix and therefore the effective stiffness matrix must be revaluated for each iteration.

Move on to the next time step.

If a non-linear analysis is to be undertaken the theory presented in Chapter 2 is still valid. Although inertia and damping forces are taken into consideration in dynamic analyses, these are expressed in terms of the incremental nodal displacement by the time discretisation scheme. Therefore there is no need to check convergence of the nodal velocities and accelerations because this is inherently included with the convergence of the nodal displacements. The only modification that must be made is when the out of balance forces are calculated. The iterative accelerations and velocities must be used to calculate the approximated inertial and damping forces. These are then taken into account when comparing the forces found from the stress point algorithm to the applied loads.

With these modifications it is now possible to analyses dynamic problems with ICFEP. To ensure that the theory is indeed correct and that the implementation has been performed correctly, the results obtained from dynamic ICFEP analyses must now be validated. In the next chapter some closed form solutions to dynamic problems are presented and then compared with equivalent ICFEP analyses.

Chapter 4:

VALIDATION EXERCISES

4.1 Introduction

The dynamic finite element theory detailed in Chapter 3 was implemented into the existing ICFEP framework. To ensure the theory was correct and implemented accurately it is necessary to conduct validation exercises. The results of these validation exercises are the main focus of this chapter.

The changes that must be validated can be summarised as follows:

- The formulation of the modified Newmark time discretisation scheme.
- The implementation of the modified Newmark scheme into the ICFEP code.
- The addition of the compressibility term into the equation of continuity for the pore fluid.

In addition to these validations a number of investigations will be undertaken to determine some general features of the behaviour of dynamic finite element analyses.

4.2 Validation of the modified Newmark time discretisation scheme

The method chosen to discretise the time domain was a modified form of the standard Newmark scheme. The addition of an extra parameter allowed the inclusion of the quadratic acceleration method into the range of schemes already available within the Newmark framework. This scheme has been specially derived for this thesis and therefore its formulation must be validated before it can be

implemented into the finite element code. The modified form of the equilibrium equation using the new scheme is given by Equation 4.1.

$$\left([K]+\frac{\delta}{\alpha\Delta t}[C]+\frac{1}{\alpha\Delta t^2}[M]\right)\{\Delta u\}=\{\Delta R\}+$$
$$[M]\left\{\frac{\dot{u}(t)}{\alpha\Delta t}+\frac{1}{2\alpha}\ddot{u}(t)+\gamma\dddot{u}(t)\Delta t\right\}+ \tag{4.1}$$
$$[C]\left\{\frac{\delta}{\alpha}\dot{u}(t)+\Delta t\left(\frac{\delta}{2\alpha}-1\right)\ddot{u}(t)+\frac{\gamma}{6}\dddot{u}(t)\Delta t^2\right\}$$

where $[K]$ is the global stiffness matrix.

$[C]$ is the global damping matrix.

$[M]$ is the global mass matrix

Δt is the incremental time step

The parameters α, δ and γ are chosen to give the desired time scheme:

$\gamma = 0,\ \delta = 1/2,\ \alpha = 1/6$ Linear Acceleration Method

$\gamma = 0,\ \delta = 1/2,\ \alpha = 1/4$ Constant Acceleration

$\gamma = 1,\ \delta = 1/3,\ \alpha = 1/12$ Quadratic Acceleration

The updated solution variables are then calculated using equations 4.2-4.4:

$$\Delta\dot{u}=\frac{\delta}{\alpha\Delta t}\Delta u-\frac{\delta}{\alpha}\dot{u}(t)+\left(1-\frac{\delta}{2\alpha}\right)\Delta t\ddot{u}(t)-\frac{\gamma}{6}\Delta t^2\dddot{u}(t) \tag{4.2}$$

$$\Delta\ddot{u}=\frac{1}{\alpha\Delta t^2}\Delta u-\frac{1}{\alpha\Delta t}\dot{u}(t)-\frac{1}{2\alpha}\ddot{u}(t)-\gamma\Delta t\dddot{u}(t) \tag{4.3}$$

$$\{\Delta\dddot{u}\}=[M]^{-1}\left(\Delta\dot{R}-[C]\{\Delta\ddot{u}\}-[K]\{\Delta\dot{u}\}\right) \tag{4.4}$$

Where $$\{\Delta\dot{R}\}=\frac{\Delta R(t+\Delta t)-\Delta R(t)}{\Delta t} \tag{4.5}$$

The time discretisation scheme can be validated by using it to solve a single degree of freedom problem for which there is a known closed form solution. Consider the problem shown in Figure 4.1.

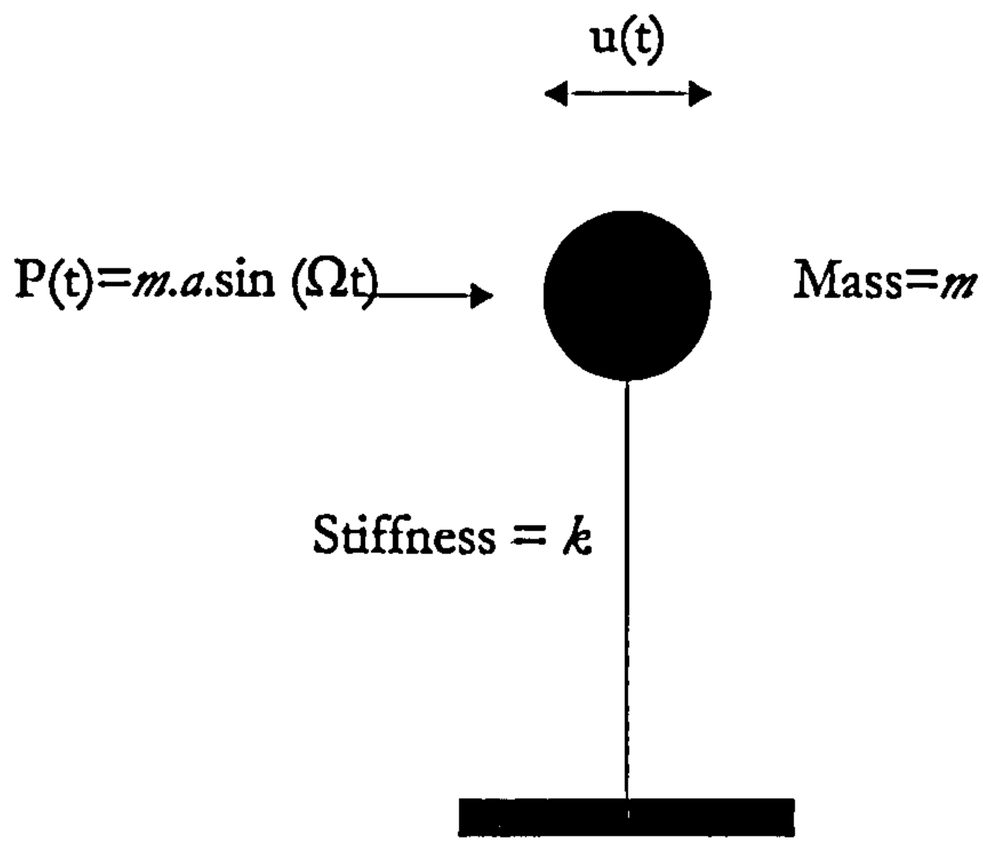

Figure 4.1: Single degree of freedom problem

The closed form solution for a harmonically forced single degree of freedom is given by Equation 4.6 (e.g. Sarma (1994)).

$$u(t)=\frac{a}{\omega^2}M\left[\frac{\alpha}{\sqrt{1-\lambda^2}}e^{-\lambda\omega t}\sin\left(\omega_D t+\theta\right)+\sin\left(\Omega t-\psi\right)\right] \qquad (4.6)$$

where

$$M=\left(\left(1-\alpha^2\right)^2+4\lambda^2\alpha^2\right)^{-\frac{1}{2}}$$

$$\tan\psi=\frac{2\lambda\alpha}{\left(1-\alpha^2\right)}$$

$$\tan\theta=\frac{2\lambda\left(\sqrt{1-\lambda^2}\right)}{\alpha^2-1+2\lambda^2}$$

$$\omega=\sqrt{\frac{k}{m}}=\text{ natural frequency of the system}$$

$$\alpha=\frac{\Omega}{\omega}$$

$$\omega_D = \omega\left(\sqrt{1-\lambda^2}\right) = \text{ damped natural frequency}$$

$$\lambda = \text{ damping fraction}$$

The displacement of the body, given by Equation 4.6, is made up of two components. The first represents the transient part of the motion and therefore reduces with time and the second represents the steady state oscillations. To check the validity of the time discretisation scheme developed in Chapter 3, the same problem was solved on a spreadsheet using the modified Newmark method and then compared with the exact solution. The overall equilibrium for the single degree of freedom problem shown in Figure 4.1 is given by Equation 4.7 in incremental form:

$$m\Delta\ddot{u} + c\Delta\dot{u} + k\Delta u = a \cdot m \cdot \left(\sin\left(\Omega\left(t+\Delta t\right)\right) - \sin\left(\Omega t\right)\right) \qquad (4.7)$$

where $c =$ damping coefficient given by $c = 2\lambda m\omega_D$

The following parameters were assumed for the validation exercise:

a(N)	Ω(rad/s)	λ	m(kg)	c (kg rad/s)	k (N/m^2)	ω (rad/s)	ω_D (rad/s)
100	10	0.05	1	0.5	25	5	4.9937

Table 4.1: Single degree of freedom analysis parameters

Equation 4.1 can now be used to solve the single degree of freedom problem. For the first comparison the constant average acceleration scheme was used with the following parameters: $\gamma = 0$, $\delta = 0.5$ and $\alpha = 0.25$. Figure 4.2 compares the results of the analysis with a time step of 0.1 seconds with the closed form solution:

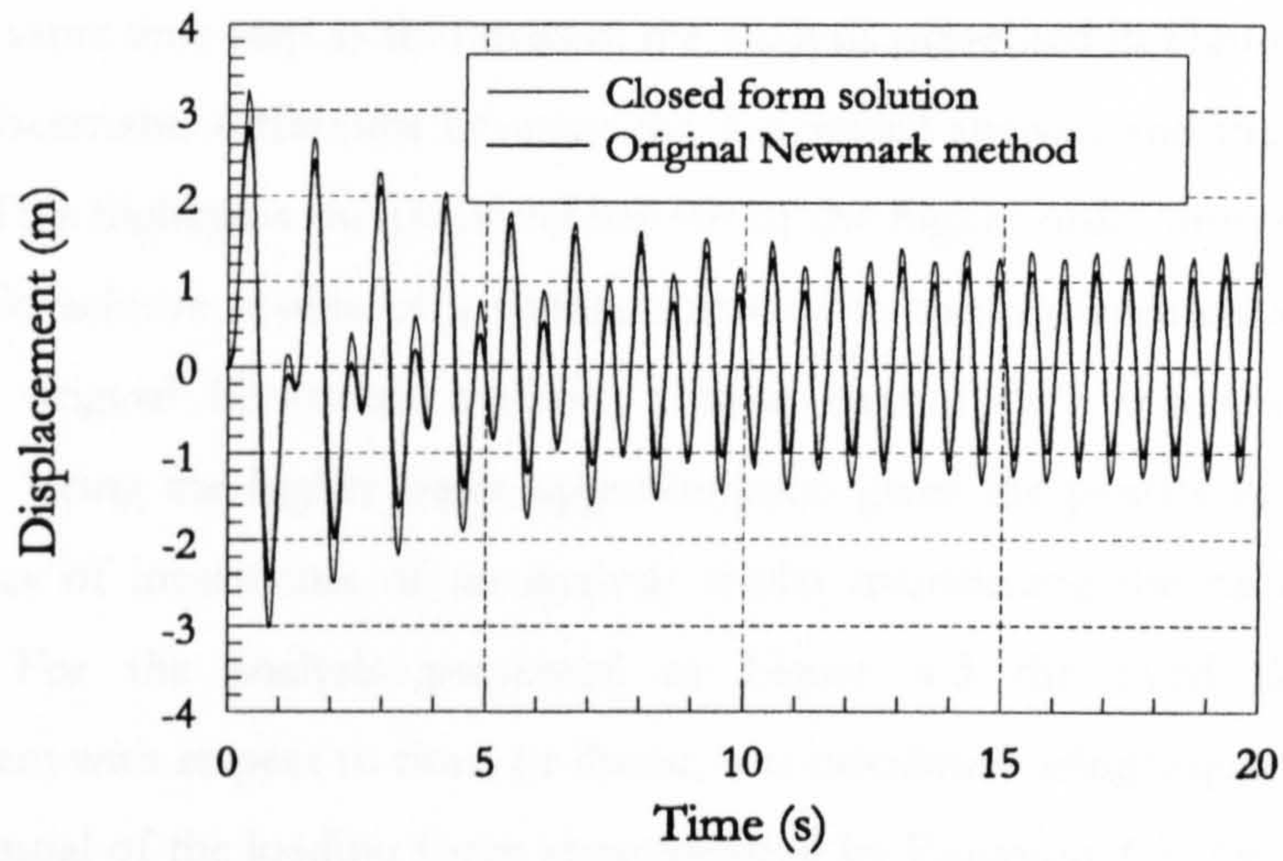

Figure 4.2: Single degree of freedom analysis using original Newmark scheme

The transient component of the response is clearly visible until a time of approximately 10 seconds. After this the displacement oscillates with a constant frequency which represents steady state conditions. The approximate solution found using the constant average acceleration Newmark scheme follows the closed form solution accurately. The transient motion at the start of the analysis is well represented, however generally the peak displacements are smaller than the closed form solution.

The same problem was then be analysed using the quadratic acceleration method ($\gamma = 1.0$, $\delta = 1/3$ and $\alpha = 1/12$) and the same time step of 0.1 seconds. The results are compared with the closed form solution in Figure 4.3.

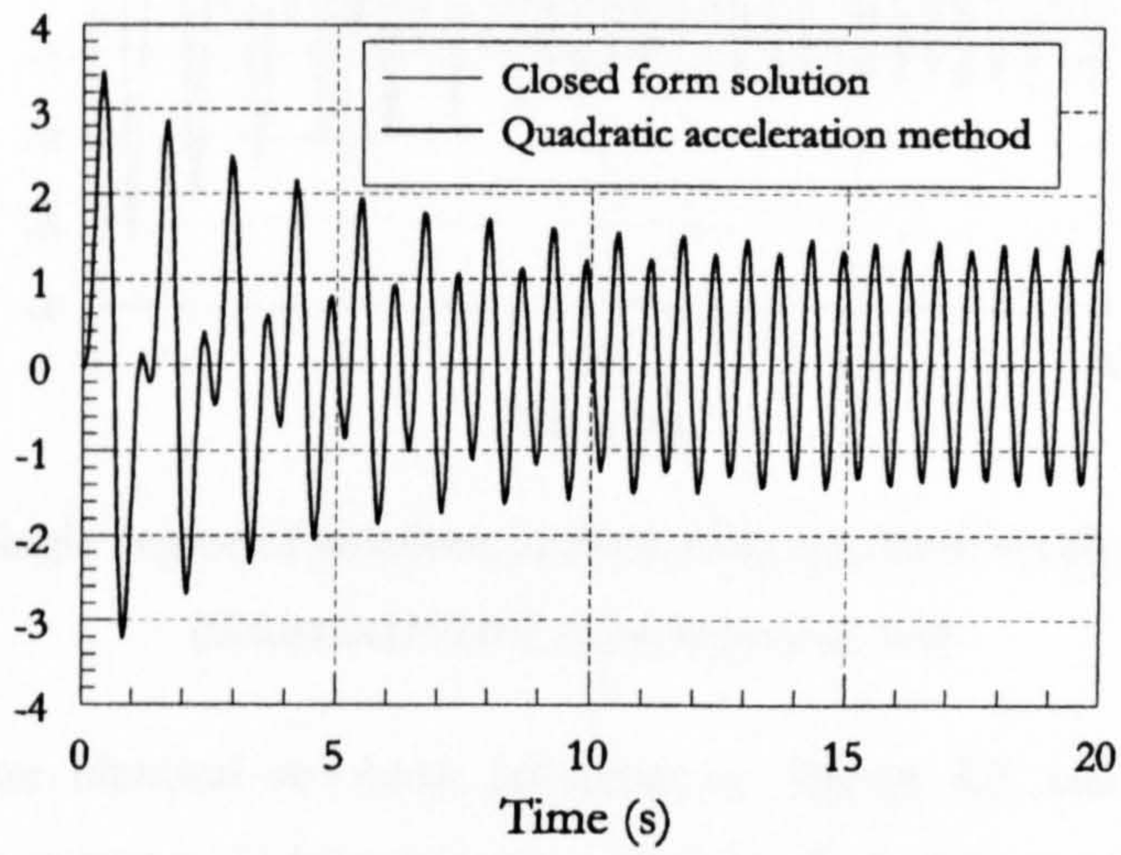

Figure 4.3: Single degree of freedom analysis using quadratic acceleration scheme

Using the same time step as that used in the analysis presented in Figure 4.2, there is now no discernable difference between the discretised analysis and the closed form solution. This highlights the potential benefit of the higher order time discretisation scheme. To achieve results of a similar accuracy to those presented in Figure 4.3 using the original Newmark method, a time step if 0.01 seconds had to be employed. Using the higher order approximation gives the possibility of reducing the number of increments of an analysis whilst maintaining the same degree of accuracy. For the analysis presented in Figure 4.3 the third derivative of displacement with respect to time, or thrust, was calculated using Equation 4.4, with the differential of the loading force approximated by Equation 4.5. To demonstrate that it is necessary to calculate the thrust in this manner the same single degree of freedom problem was analysed using the quadratic acceleration method, but calculating the thrust from the incremental displacement using Equation 4.8.

$$\Delta\dddot{u} = \frac{2}{\alpha\Delta t^3}\Delta u - \frac{2}{\alpha\Delta t^2}\dot{u}_t - \frac{1}{\alpha\Delta t}\ddot{u}_t - \frac{\delta}{\alpha}\dddot{u}_t \tag{4.8}$$

This equation has been derived in a similar fashion to the equations for velocity and acceleration. The results of the analysis are presented in Figure 4.4.

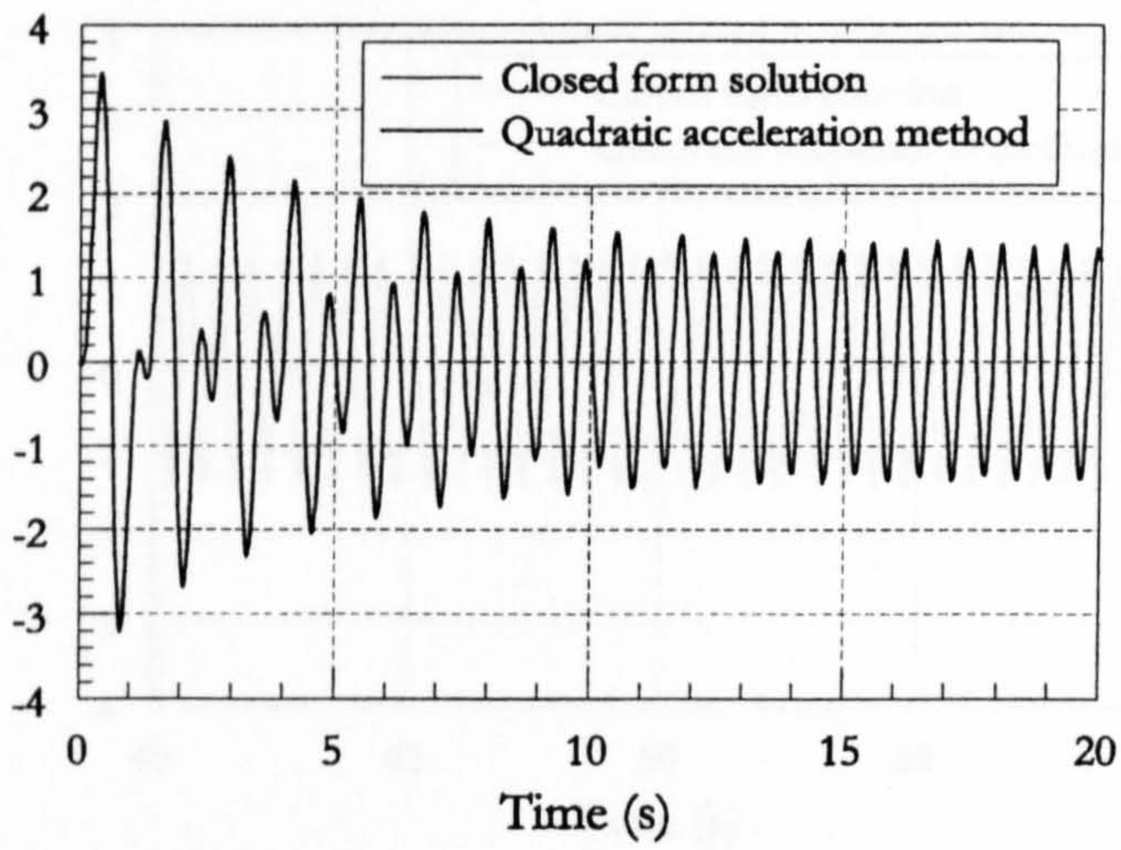

Figure 4.4: Single degree of freedom analysis using quadratic acceleration scheme (thrust calculated using Equation 4.8)

The results are identical to those presented in Figure 4.3 and no numerical instabilities are apparent. If however the analysis is allowed to run for a further 20

seconds, it becomes unstable. The results of the analysis within the time interval 40-60 seconds are shown in Figure 4.5.

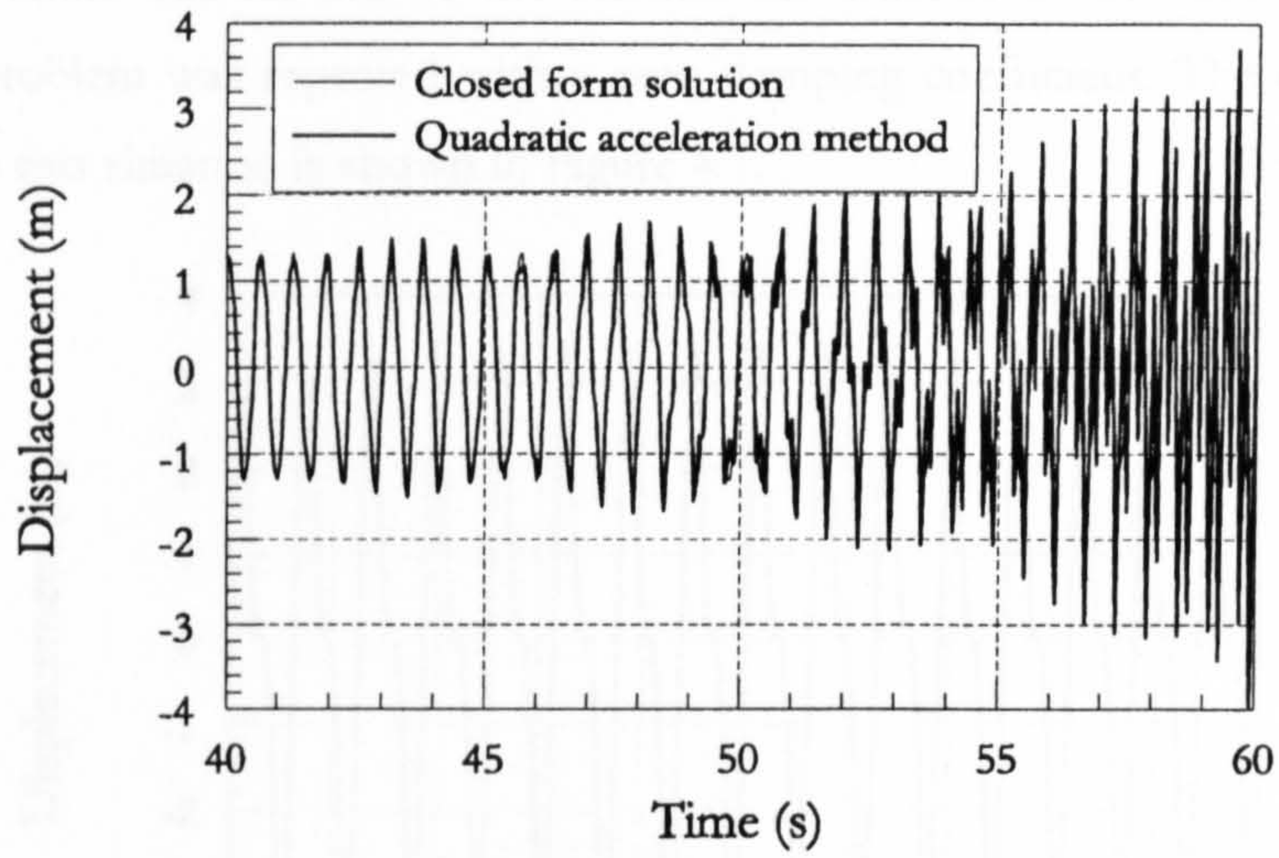

Figure 4.5: Single degree of freedom analysis using quadratic acceleration scheme t=40–60 seconds (thrust calculated using Equation 4.8)

This problem is overcome if the thrust is calculated using Equation 4.4. To illustrate this, the results of the analysis within the time interval 40-60 seconds using this technique are shown in Figure 4.6.

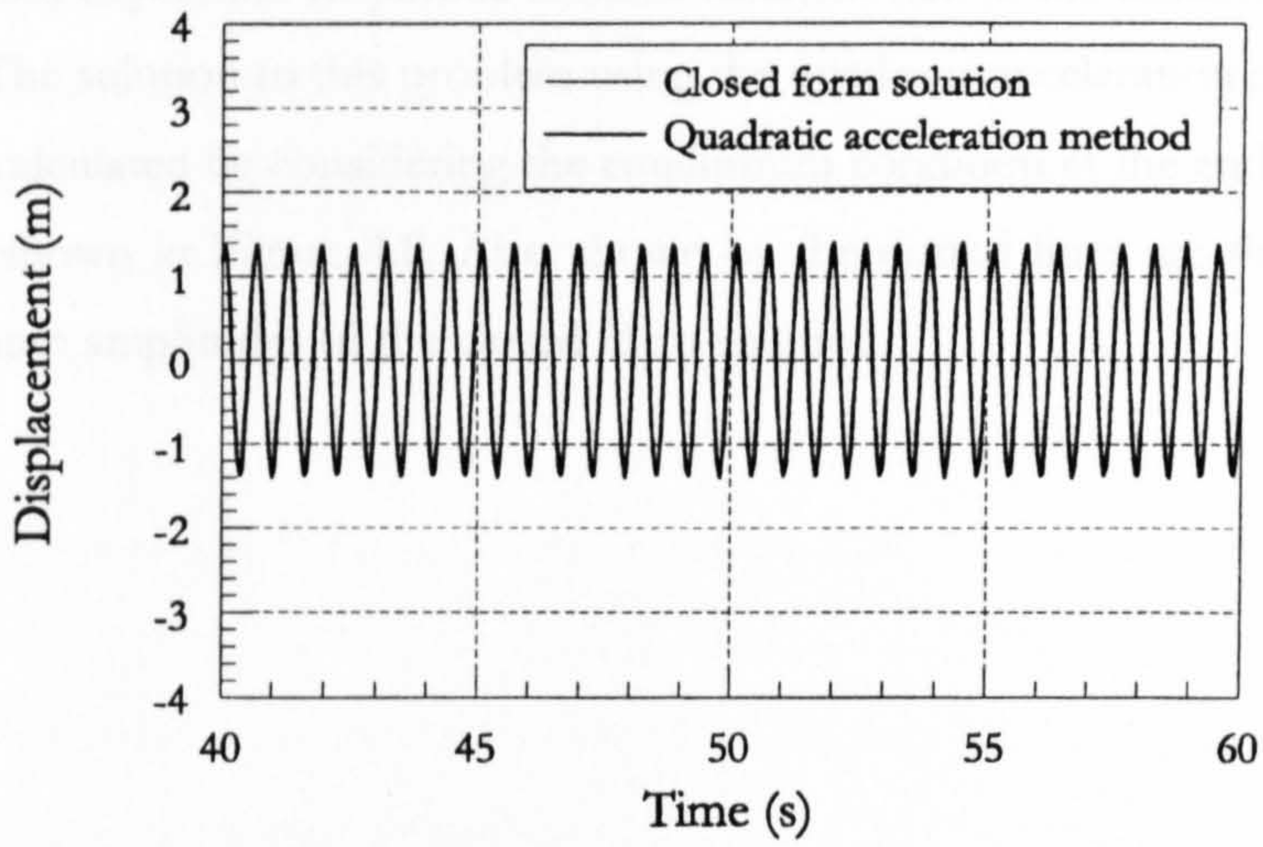

Figure 4.6: Single degree of freedom analysis using quadratic acceleration scheme t=40–60 seconds

There is no evidence of numerical instability within the time range shown in Figure 4.6. The analysis was continued up to a time of 1000 seconds and no evidence of stability was observed.

As mentioned in Chapter 3, Tsatsanifos (1982) found that without any form of damping the higher order quadratic acceleration method is unconditionally unstable. To demonstrate this feature of the scheme the analysis of the single degree of freedom problem was repeated with a zero damping coefficient. The closed form solution to this situation is shown in Figure 4.7.

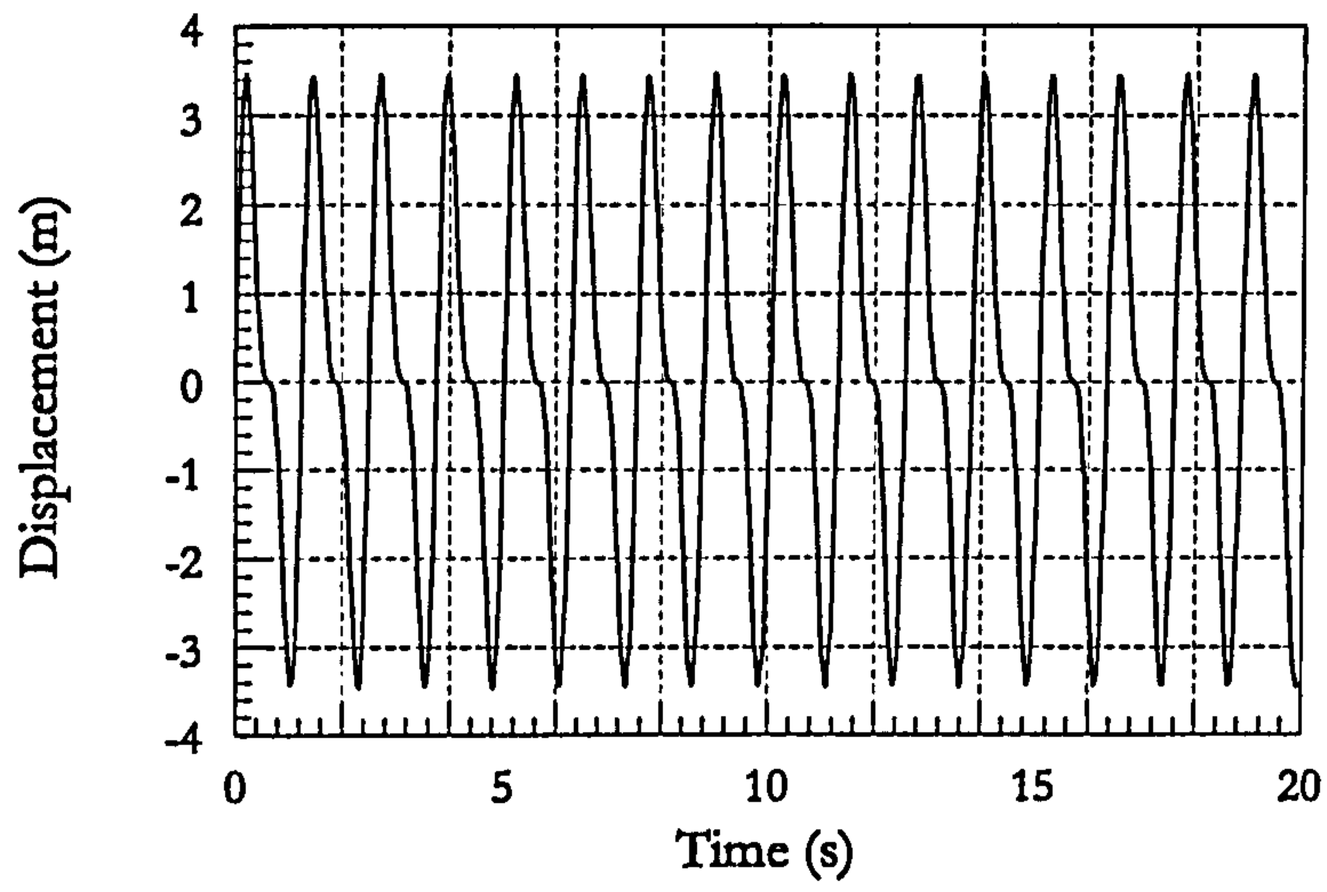

Figure 4.7: Closed form solution to single degree of freedom problem with no damping

As one would expect the amplitude remains constant due to the absence of material damping. The solution to this problem using the quadratic acceleration method with the thrust calculated by considering the equilibrium condition at the end of the time interval is shown in Figure 4.8. Also shown by the dotted lines are the minimum and maximum amplitudes of the closed form solution.

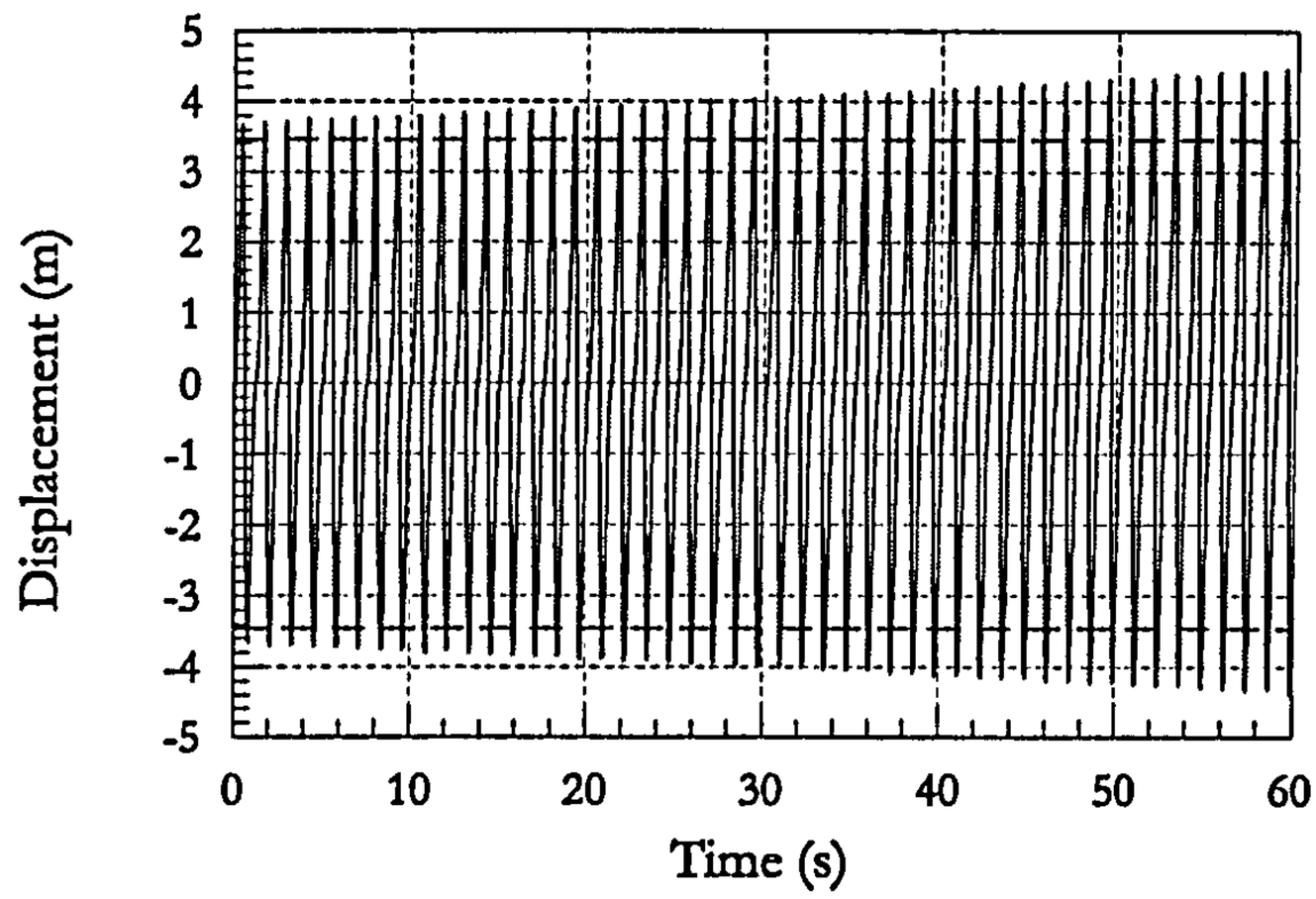

Figure 4.8: Discretised solution to single degree of freedom problem with no material damping

It is clear that the amplitude of the oscillations is slowly increasing above the amplitude of the closed form solution. If the analysis is allowed to continue the amplitude keeps on growing indefinitely. This feature of the analysis demonstrates the presence of negative damping in the discretisation scheme and renders it unconditionally unstable in the absence of any material damping. It was found during this research that changing the modified Newmark parameters α, δ and γ can introduce numerical damping to the scheme which is sufficient to make it stable. This is similar to the numerical damping that can be introduced into the original Newmark method by increasing the δ parameter. The single degree of freedom problem was analysed again with the quadratic acceleration scheme, but with non standard values for the parameters α, δ and γ. To achieve the exact quadratic acceleration scheme the following values must be taken for the modified Newmark scheme: $\gamma = 1$, $\delta = 1/3$, $\alpha = 1/12$. Each parameter was varied in turn to determine how this affects the schemes stability and level of numerical damping. Figure 4.9 shows the results of the analysis with $\gamma = 1.05$, $\delta = 1/3$, $\alpha = 1/12$.

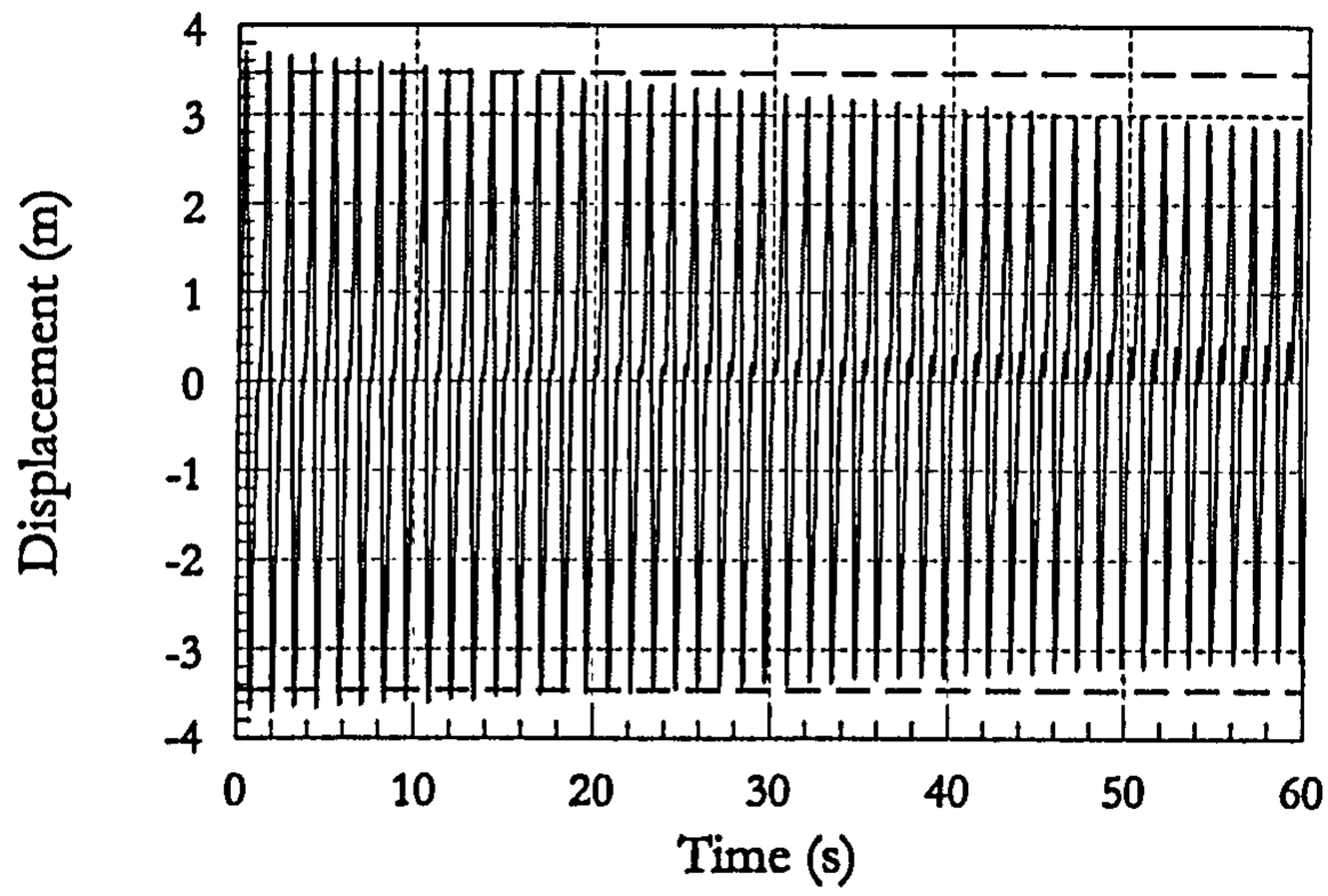

Figure 4.9: Discretised solution to single degree of freedom problem with no material damping ($\gamma = 1.05$)

The numerical damping introduced by increasing the γ parameter to 1.05 appears to be sufficient to ensure the time discretisation scheme remains stable. However, there does appear to be a slight reduction in the amplitude of the oscillations caused by the numerical damping. The next analysis will assume a δ value of 0.34 and the standard values for the remaining parameters ($\gamma = 1.0$, $\alpha = 1/12$). The results are shown in Figure 4.10.

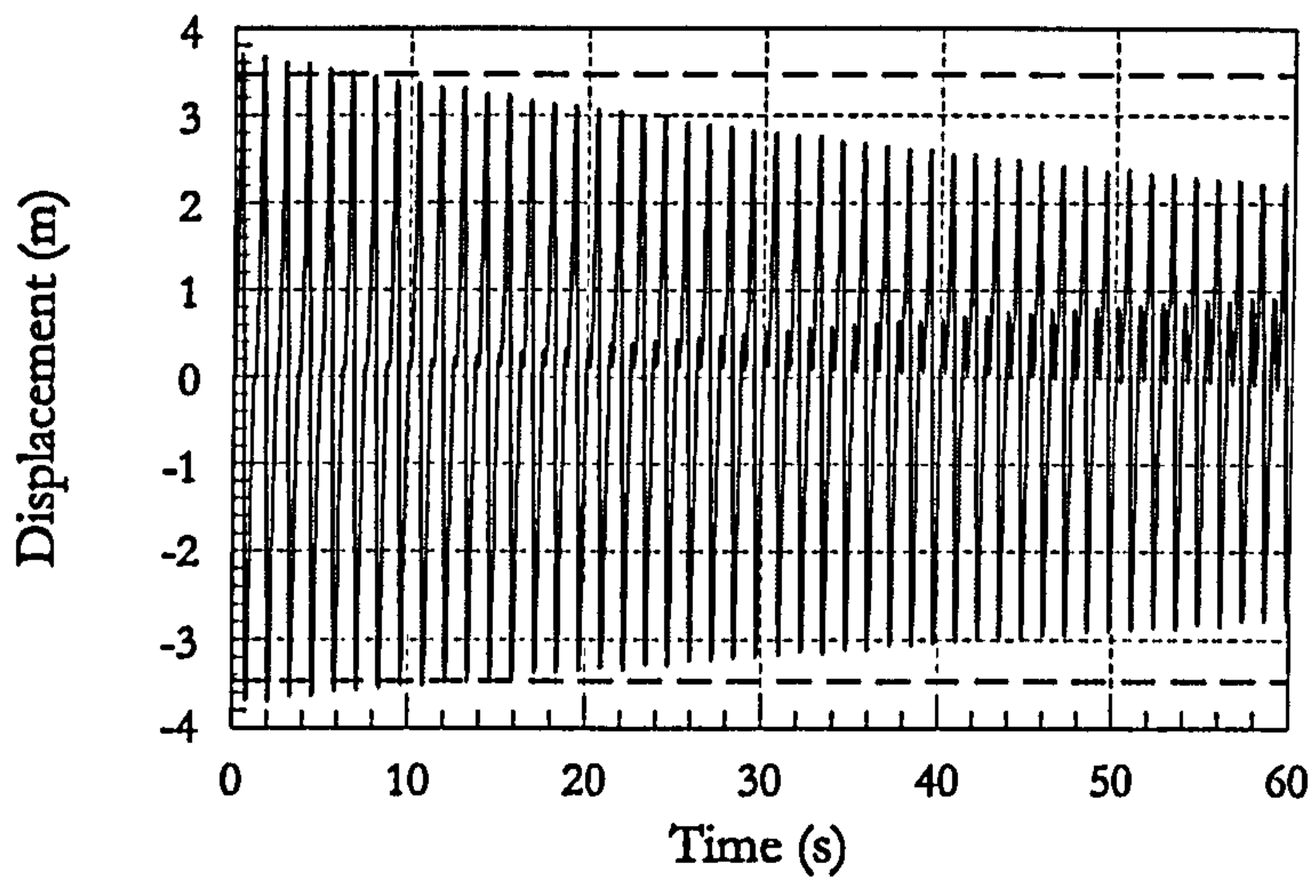

Figure 4.10: Discretised solution to single degree of freedom problem with no material damping ($\delta = 0.34$)

The scheme is now stable but the numerical damping introduced by using $\delta = 0.34$ significantly reduces the amplitude of the oscillations. The last analysis used $\alpha = 0.1$. The results of the analysis are shown in Figure 4.11.

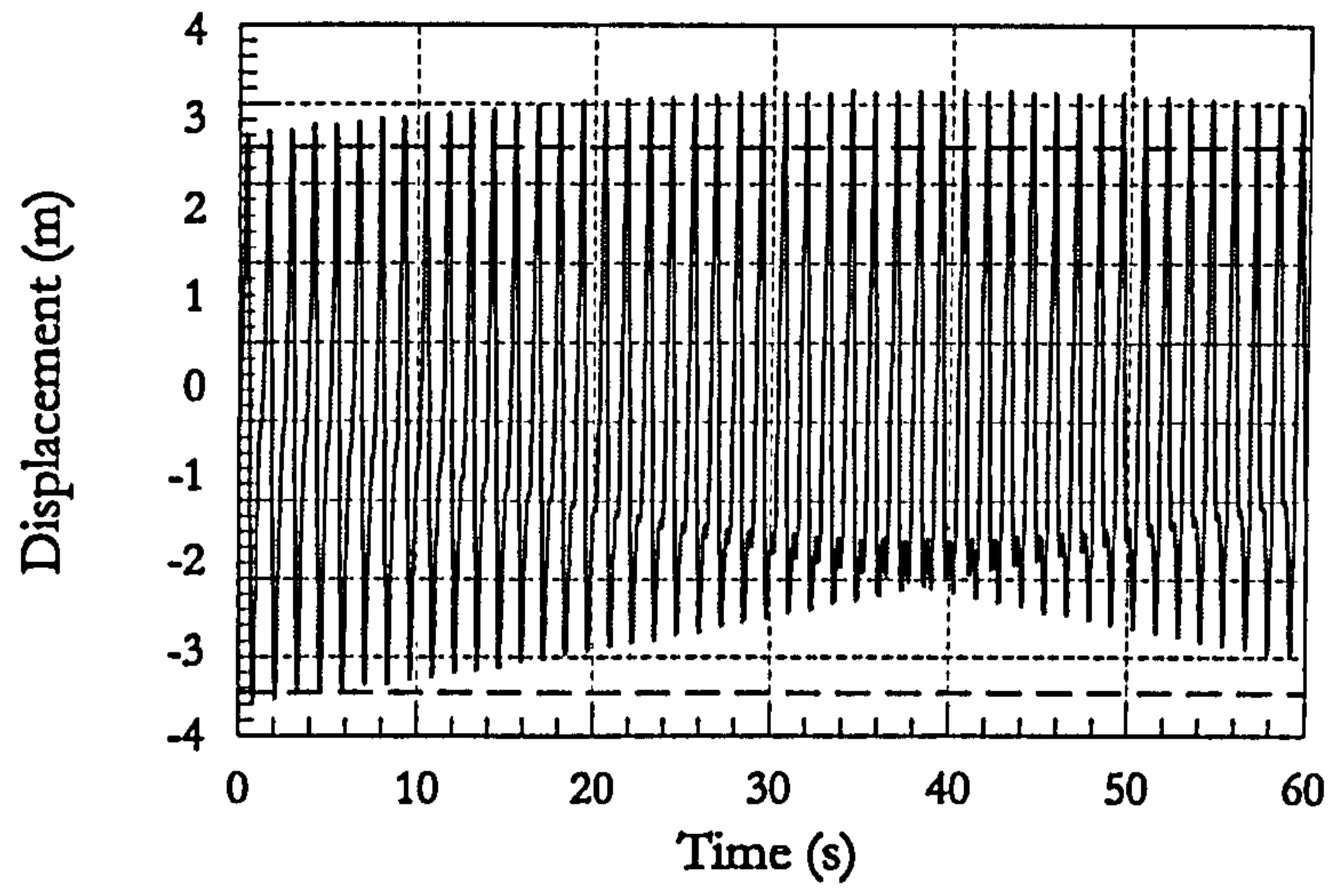

Figure 4.11: Discretised solution to single degree of freedom problem with no material damping ($\alpha = 0.1$)

The scheme appears to be stable although increasing the value of α to 0.1 has caused the solution to oscillate at a secondary frequency which is lower than the natural frequency of the system.

The results of this parametric study show that in the absence of any material damping the quadratic acceleration scheme is unconditionally unstable. It has been shown that increasing the modified Newmark parameters α, δ or γ can introduce sufficient numerical damping to ensure the time discretisation scheme remains stable. Increasing the values of γ or δ can introduce a considerable amount of numerical damping which can cause a significant reduction in the amplitude of the oscillations of the single degree of freedom problem. Increasing the value of α does not appear to significantly reduce the amplitude of oscillation whilst ensuring the time discretisation scheme remains stable. It does however introduce spurious oscillations in the results that are not present in the closed form solution. To investigate the accuracy and stability of the quadratic acceleration scheme when analysing a problem with multiple degrees of freedom, a full finite element analysis was undertaken. The results of this investigation are presented later in the chapter.

4.3 Validation of the Finite Element Code: Original Newmark Method

4.3.1 Introduction

The work presented in Section 4.2 demonstrated that the modified Newmark method in the form derived in Chapter 3 is capable of modelling dynamic events. The analysis of the single degree of freedom problem using the original Newmark method which can be retrieved by setting γ to zero, demonstrated that the results obtained using this method are reasonably accurate and numerically stable. The aim of this section is to validate the implementation of the original Newmark method into the existing ICFEP framework. The implementation of the quadratic acceleration scheme is validated in the next section.

4.3.2 Analysis of a compression wave propagating through a cylindrical bar

The validation of the Newmark method is performed in two phases. The first examines qualitatively how the dynamic finite element analysis behaves and the second compares quantitatively the results of dynamic finite element analyses with a known closed form solution.

First consider the propagation of a compression wave along a cylindrical bar. If the diameter of the bar is considerably smaller than the wavelength of the applied load, then Kolsky (1953) gives the one-dimensional equation of motion as Equation 4.9a.

$$\frac{\partial^2 u}{\partial t^2} = V_c \frac{\partial^2 u}{\partial x^2} \tag{4.9a}$$

where $V_c = \sqrt{\frac{E}{\rho}}$

E = Young's Modulus

ρ = Material Density

The general form of the solution to Equation 4.9a is given by Equation 4.9b.

$$u(x,t) = f(V_c t + x) \tag{4.9b}$$

Where f is an arbitrary function of $(V_c\ t + x)$ that satisfies Equation 4.9a. The solution of Equation 4.9b describes a wave travelling in the x direction with velocity V_c that does not change its shape as it propagates.

The most basic validation of the finite element code is to model the propagation of a compression wave through a thin cylindrical bar and compare the measured velocity with that predicted by Equation 4.9. The analysis of a 100 meter long bar with a radius of 0.25 meters was undertaken, utilising the axi-symmetry of the problem. The mesh was divided into 200 equi-sized elements along its length and one element across its width. To initiate the compression wave a sinusoidal boundary stress was applied at one end of the bar. The opposite end was restricted from moving in both the horizontal and vertical directions and the side boundaries were assumed to be stress free. The arrangement of the analysis is shown in Figure 4.12.

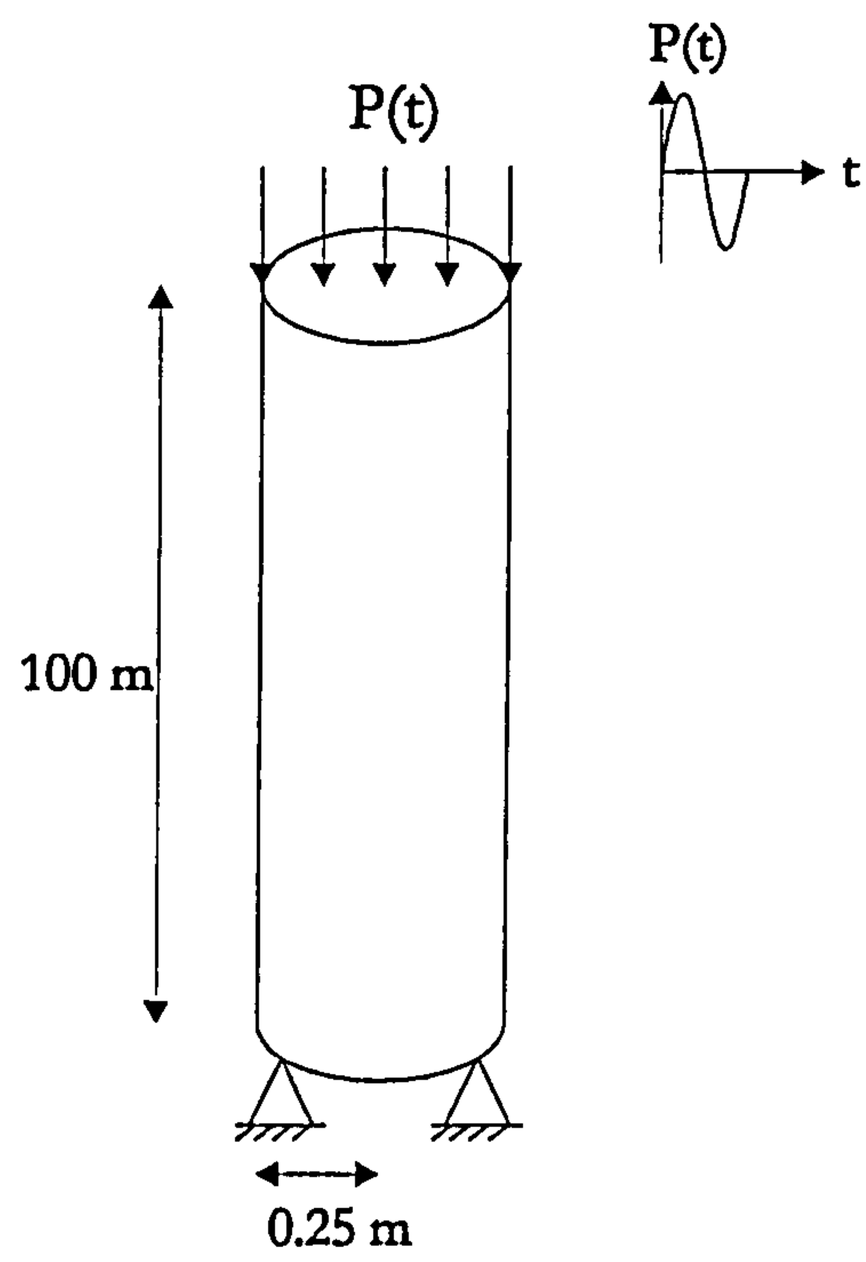

Figure 4.12: Analysis arrangement for modelling compression wave propagation

The sinusoidal loading was discretised into 50 increments with a time step of 0.001 seconds. The material properties chosen for the analysis were as follows:

$$E = \text{Young's modulus} = 6.4\times10^{8}\ \text{N/m}^2$$

v = Poisson's ratio = 0.2

ρ = Material density = 1000 kg/m^3

These parameters give a compression wave velocity of 800 m/s and therefore an input wavelength of 40 meters. After the first 50 increments of the analysis the wave has fully entered the bar and travelling towards the fixed end of the bar. The position of the wave in the bar at some intermediate increments 70 and 120 are shown in Figure 4.13 and Figure 4.14.

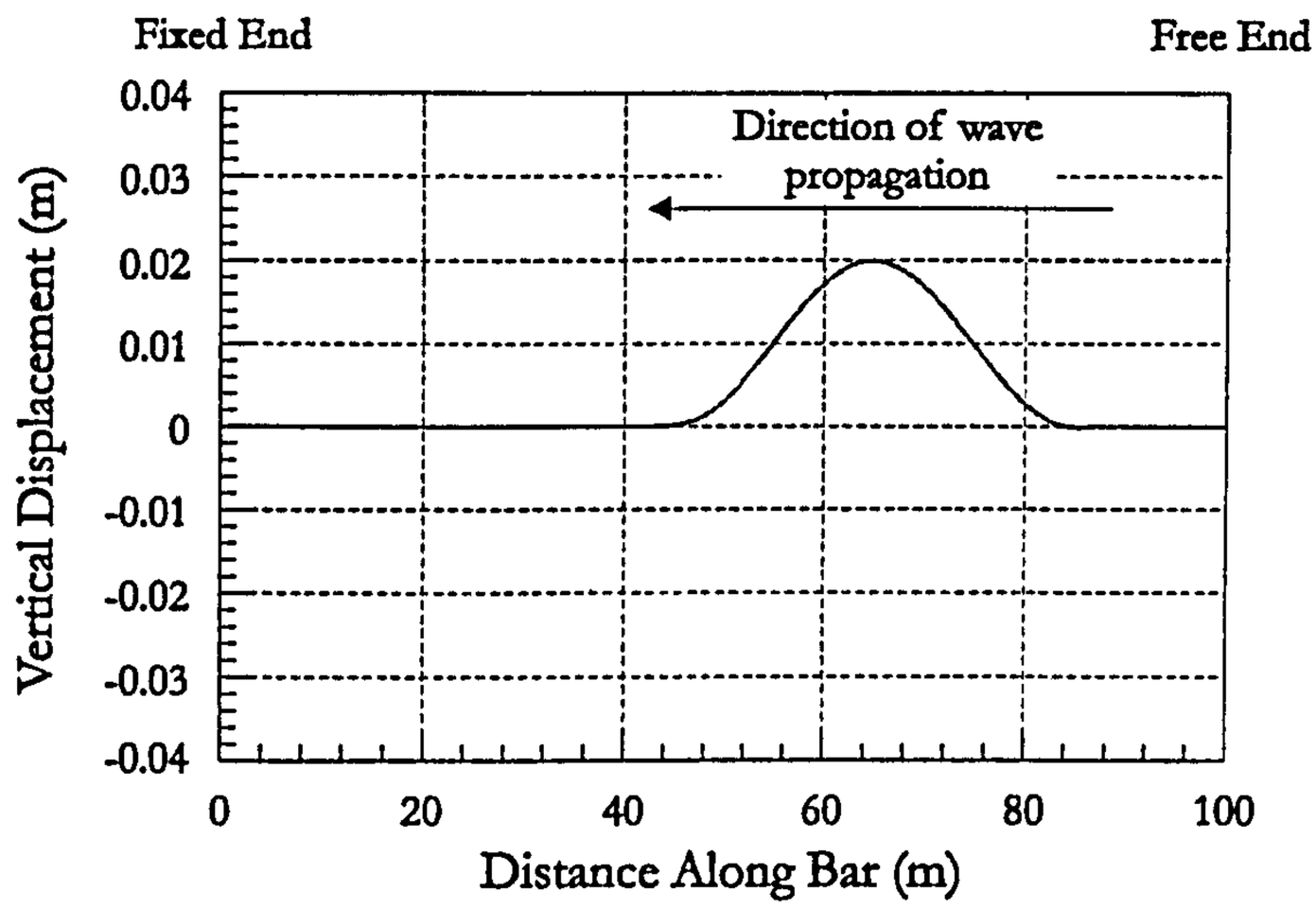

Figure 4.13: Bar analysis results: Increment 70

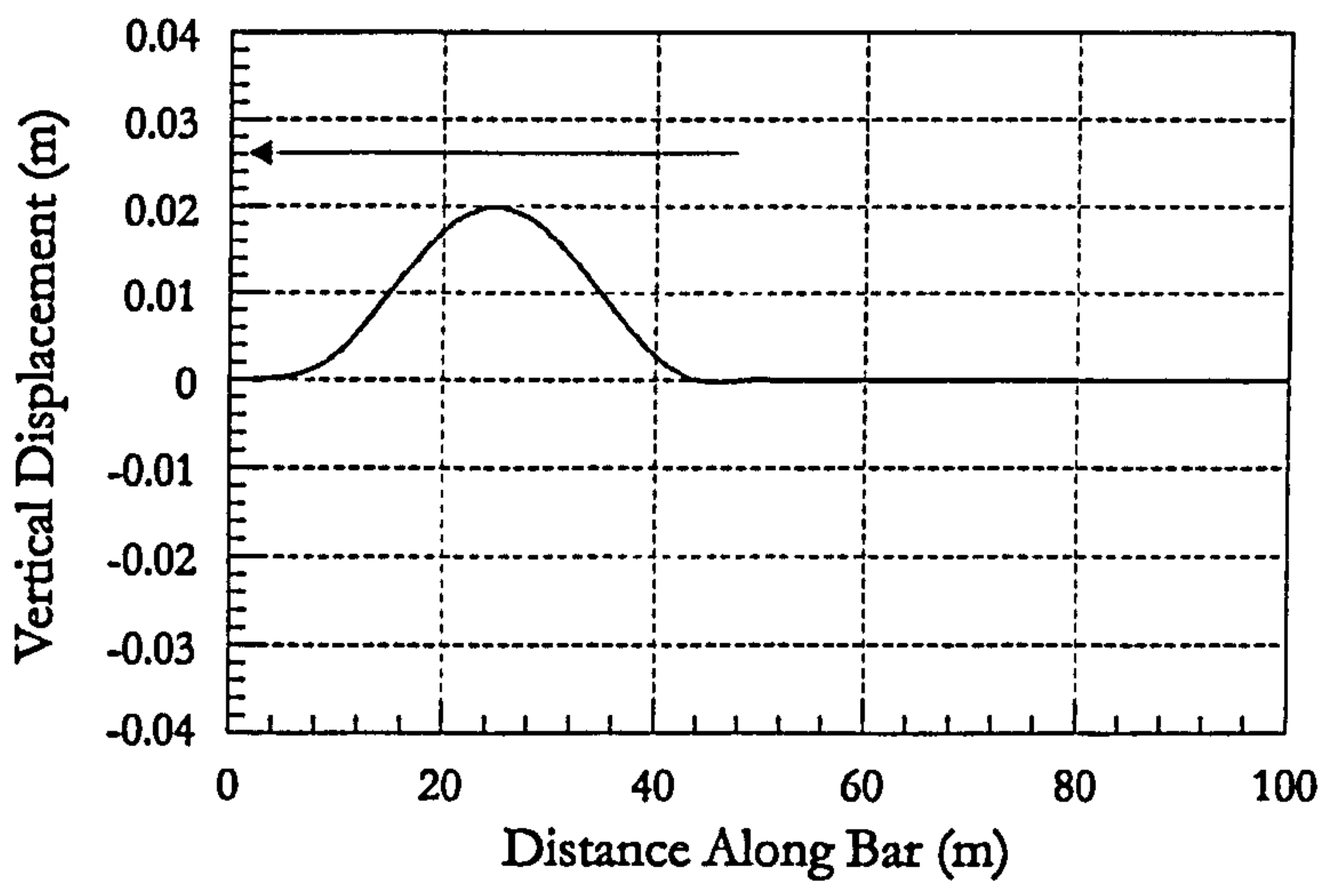

Figure 4.14: Bar analysis results: Increment 120

The results shown in Figure 4.13 and Figure 4.14 represent a wave travelling in the x direction that does not change its shape, as predicted by Equation 4.9b. To check

the velocity of the wave is correctly represented, the distance the peak of the wave travels between the two increments can be measured and used to calculate the velocity of wave propagation. Between the increments 70 and 120 the peak of the wave travelled from 65 to 25 meters from the fixed end of the bar. Knowing the time step of the analysis the velocity of the compression wave can be calculated:

$$Velocity = \frac{Distance}{Time} = \frac{(65-25)}{0.001\times(120-70)} = 800\,m/s$$

This is equal to the compressive wave velocity predicted from the material properties used in the analysis and therefore confirms that a compressive wave can be modelled propagating through a thin elastic bar. The analysis was continued to examine some other qualitative features of wave propagation. The results from some of these increments are shown in the following figures.

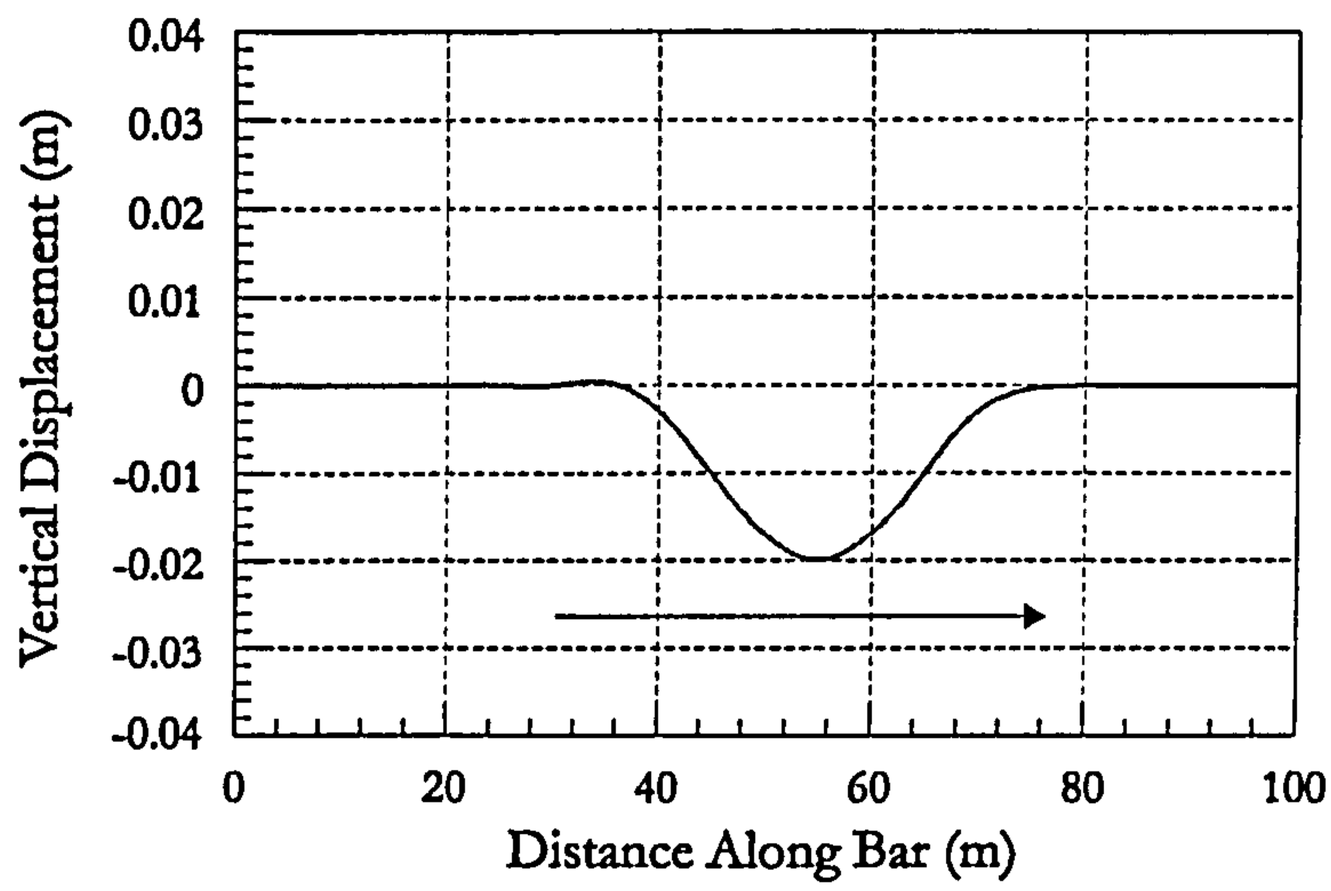

Figure 4.15: Bar analysis results: Increment 220 – wave propagation after reflection from the fixed end

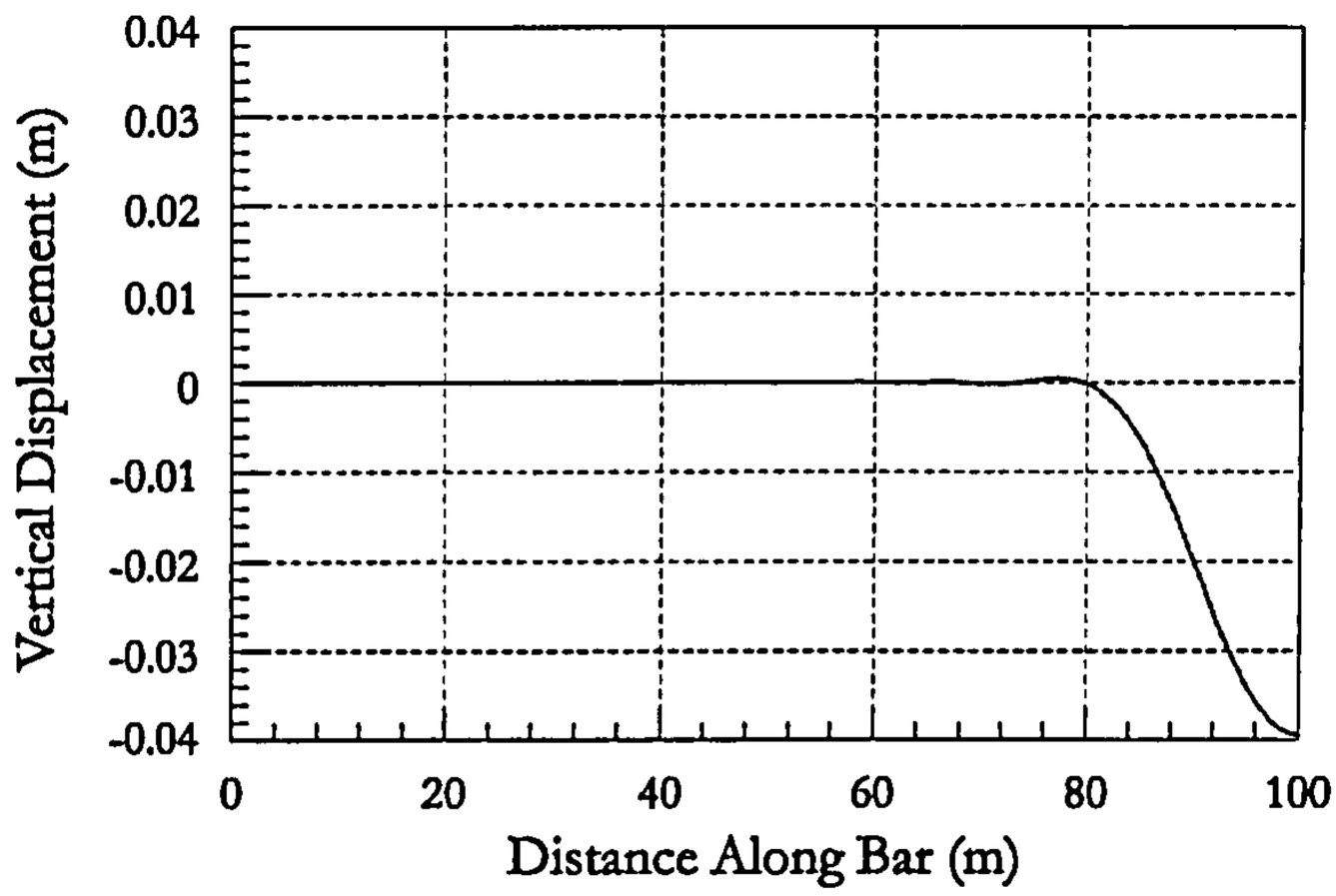

Figure 4.16: Bar analysis results: Increment 275 – wave reaching the free end after being reflected from the fixed end

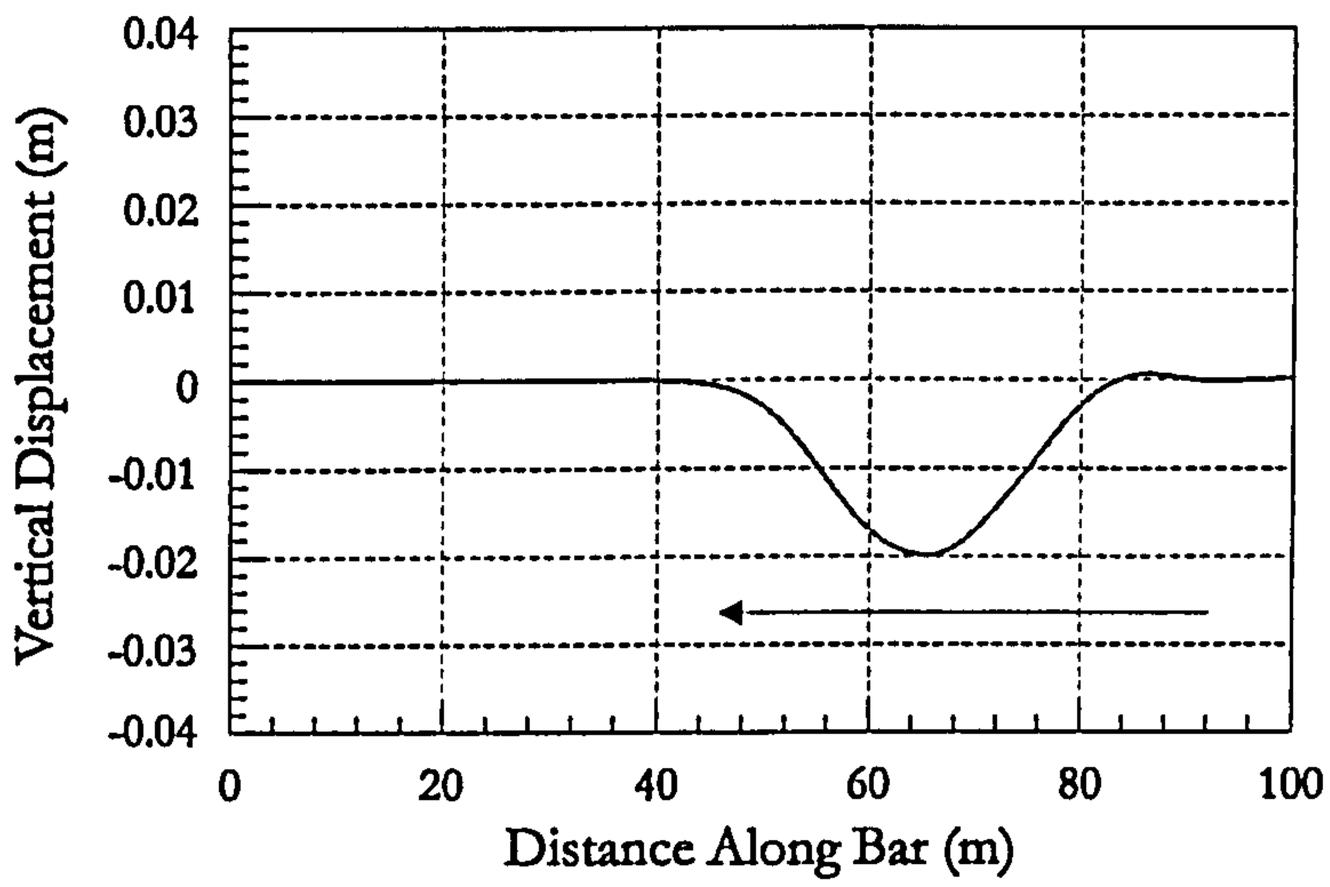

Figure 4.17: Bar analysis results: Increment 320 – wave propagation after reflecting from the free end

Figure 4.15 shows the position of the wave after 220 increments of the analysis. When the wave reached the fixed end of the bar it was reflected back into the bar with the opposite sign. At increment 275 the wave has reached the free end of the bar. Due to the stress free condition the amplitude of the wave doubles and is again reflected back into the bar but with the same displacement sign. This is shown in Figure 4.16 and Figure 4.17. From this point onwards the wave was observed to travel through the bar indefinitely due to the assumption of linear elastic behaviour. These features are consistent with classic wave propagation theory and in a qualitative sense validate the most basic dynamic property of an elastic material.

A further qualitative test of the propagation of a compression wave is to observe its behaviour when it passes through a boundary of two different material types. The same arrangement of the cylindrical bar was used as before, except the material properties of the second half of the bar were changed to the following:

E = Young's modulus = 1.6×10^8 N/m^2

ν = Poisson's ratio = 0.2

ρ = Material density = 1000 kg/m^3

This gives a compression wave velocity of 400 m/s for the lower half of the cylindrical bar. The analysis arrangement is shown in Figure 4.18.

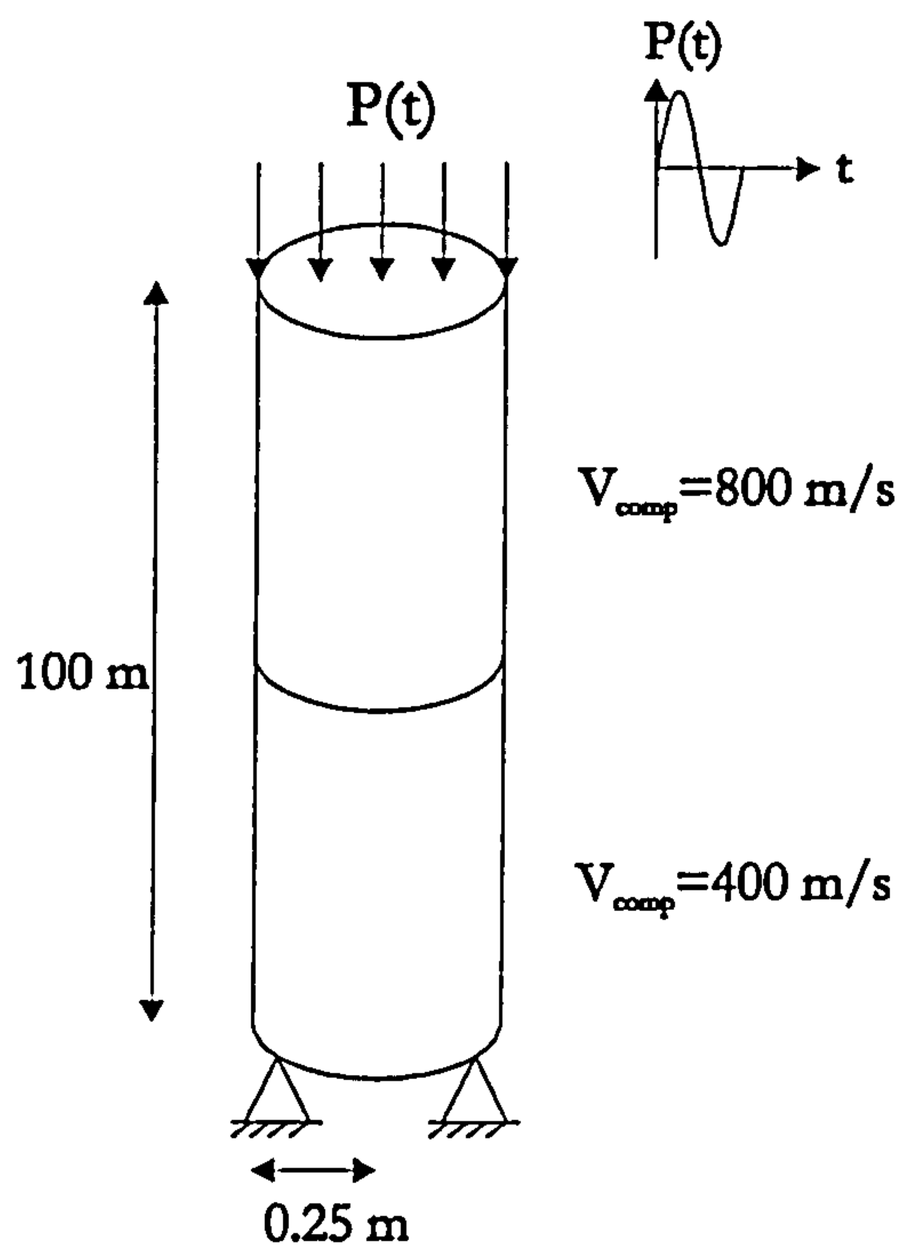

Figure 4.18: Analysis arrangement for propagation of a compression wave through a bar with two different material types

Again, the wave was input into the bar over the first 50 increments. The results of the analysis at certain increments afterwards are shown in the following figures.

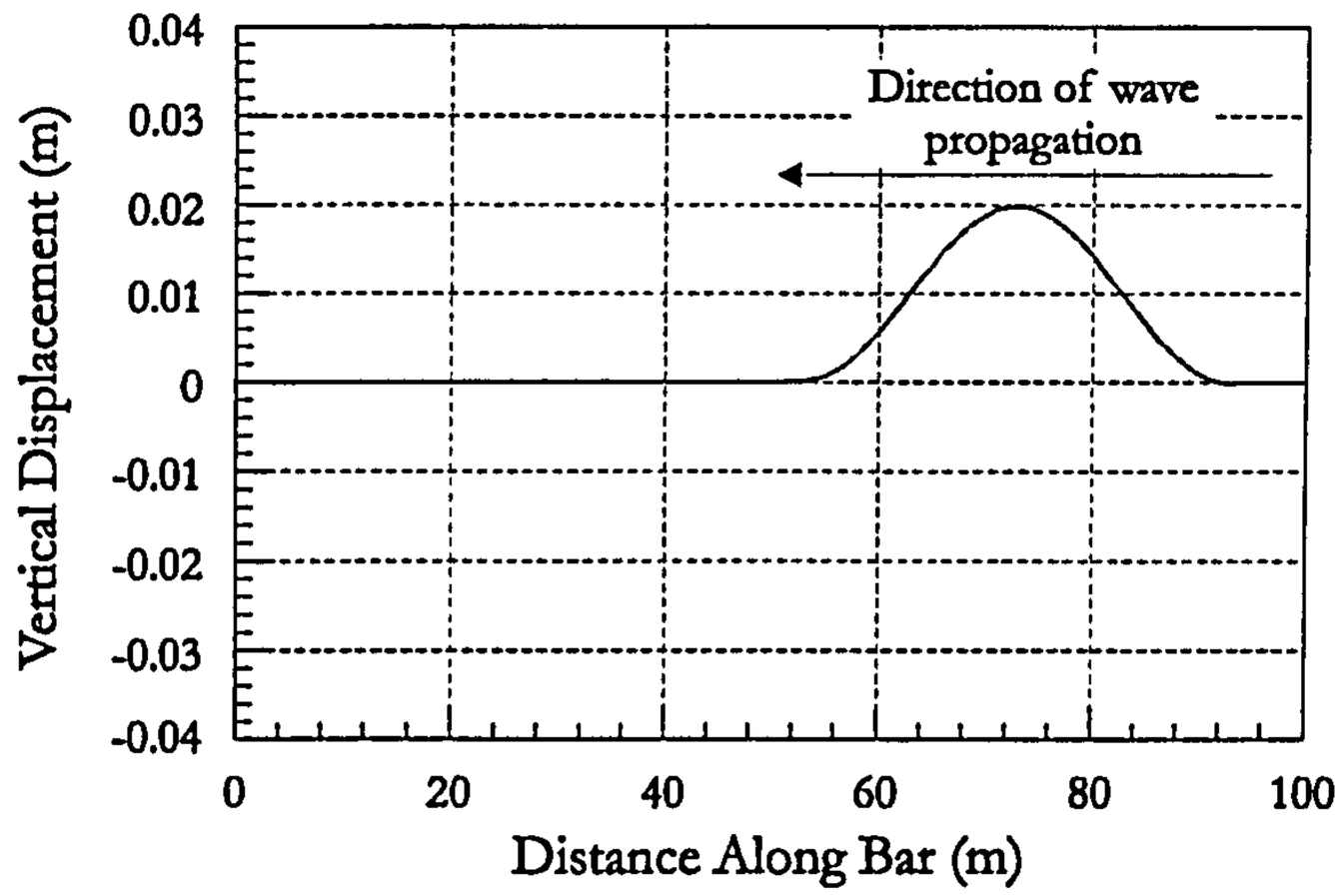

Figure 4.19: Analysis results at Increment: 60

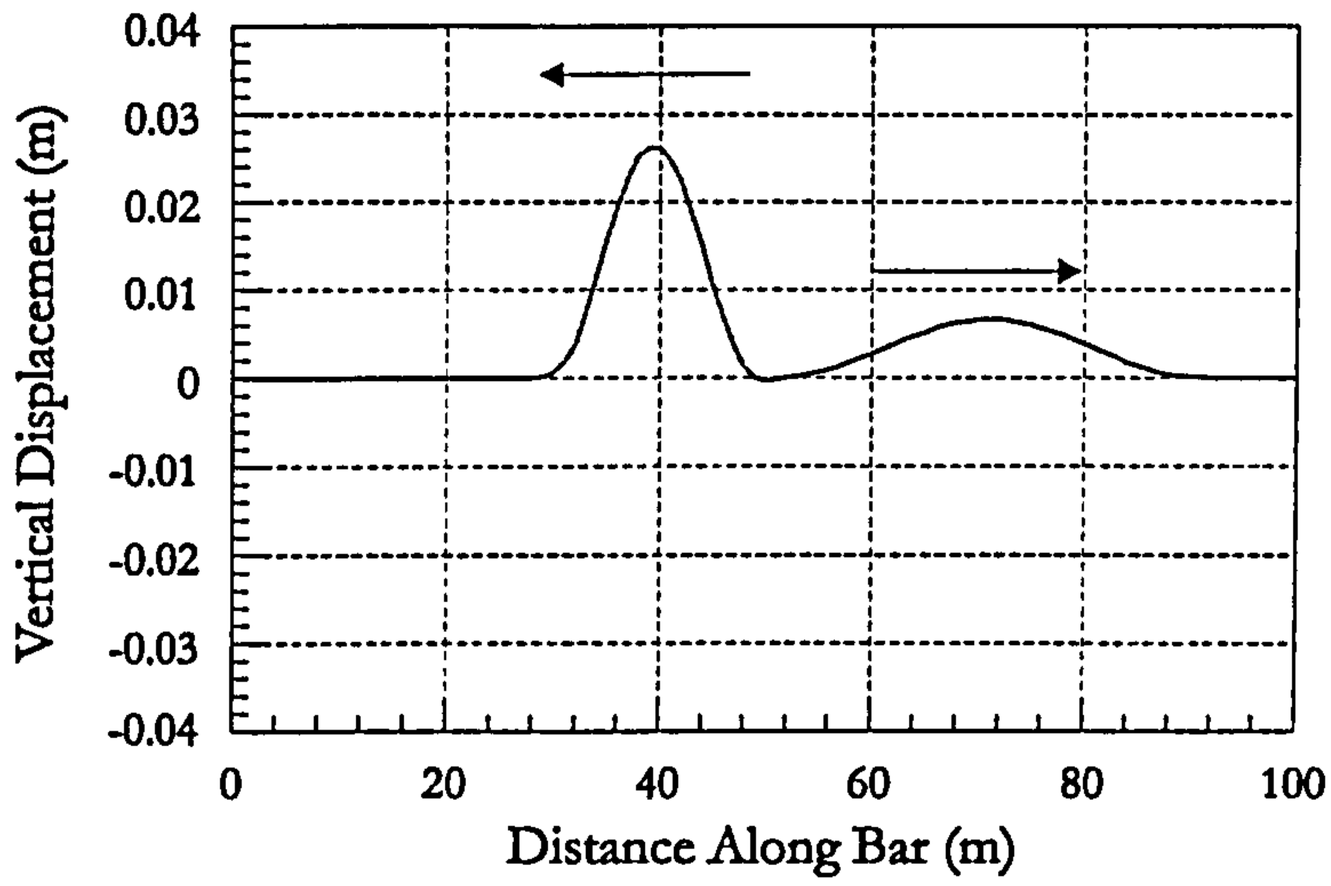

Figure 4.20: Analysis results at Increment: 115

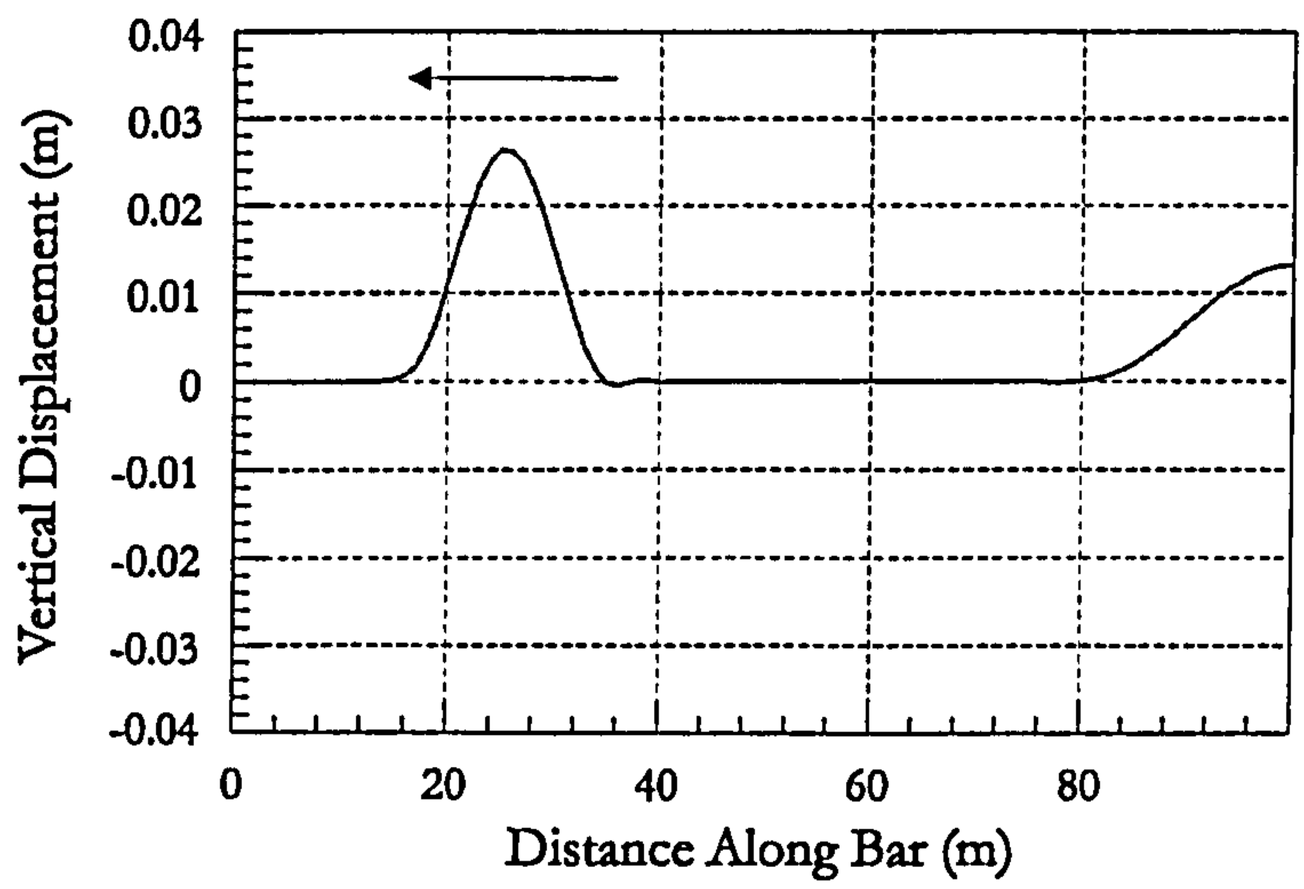

Figure 4.21: Analysis results at Increment: 150

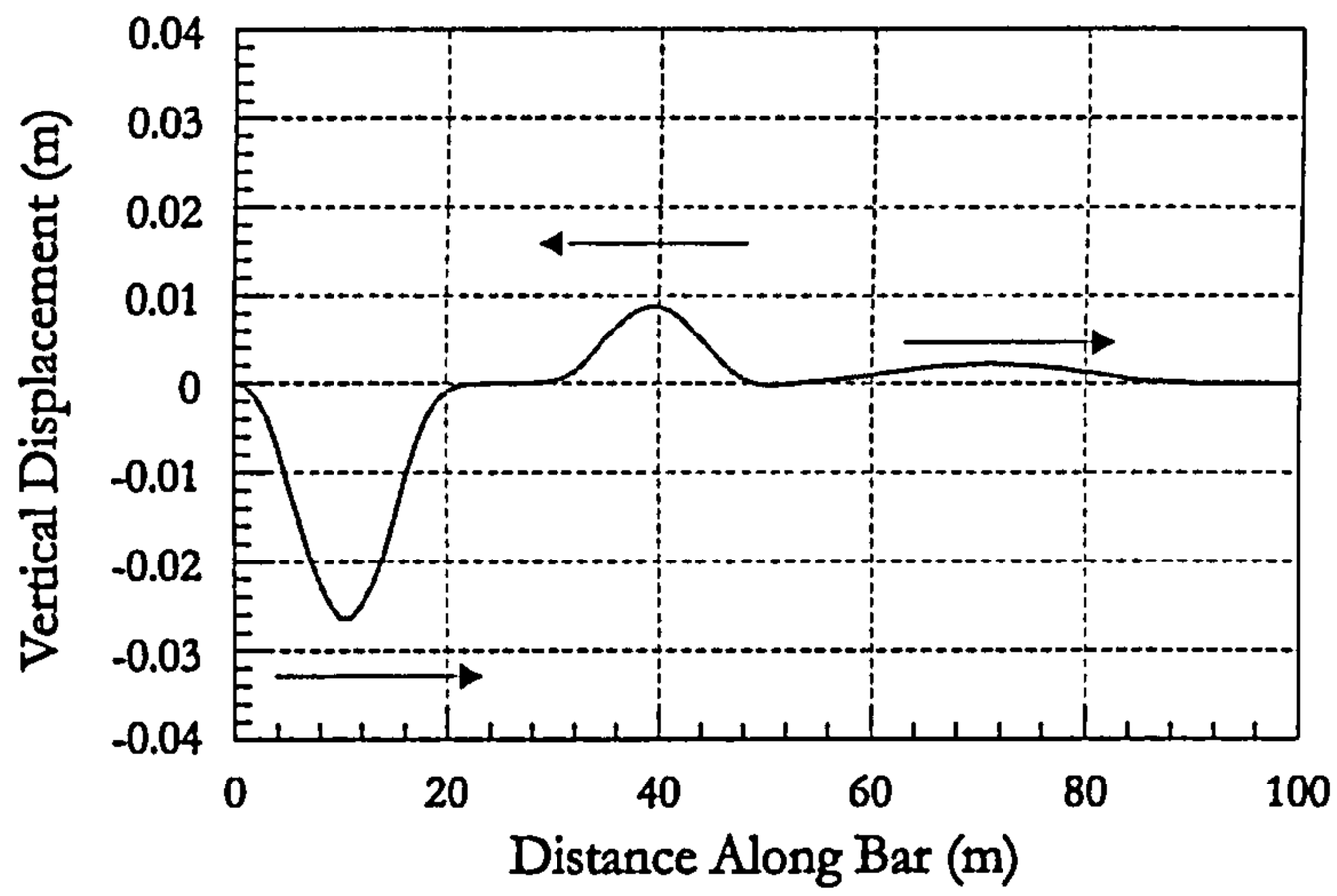

Figure 4.22: Analysis results at Increment: 240

After 60 increments the wave is completely contained within the first section of the bar and therefore the result is the same as that shown previously. When the wave passes the boundary between the two material types some of its energy is reflected back into the first part of the bar whilst the remainder is transmitted into the second half. This is consistent with wave propagation theory. The amplitude of each wave component can be calculated by considering displacement and stress compatibility at the interface. If A_i is the amplitude of the incident wave, the amplitudes of the reflected (A_r) and transmitted (A_t) waves are given by Equations 4.10 and 4.11 respectively (Kramer (1996)):

$$A_r = \frac{1-\alpha}{1+\alpha} A_i \tag{4.10}$$

$$A_t = \frac{2}{1+\alpha} A_i \tag{4.11}$$

where $\alpha = \frac{\rho_2 V_2}{\rho_1 V_1}$ = the impedance ratio

ρ_i is the density of material i and V_i is the velocity of propagation.

The amplitude of the incident wave shown in Figure 4.19 is 0.02 meters and the impedance ratio is 0.5. Equations 4.10 and 4.11 give the amplitude of the reflected and transmitted waves as 0.006667 meters and 0.026667 meters respectively. Closer

examination of the numerical values represented by the graph in Figure 4.20 confirms that this feature of wave propagation has been accurately modelled. Figure 4.21 shows the position of the waves at increment 150. The reflected wave has reached the free end of the bar with an amplitude twice its original value. This behaviour can be explained by closely examining Equation 4.11. The free end of the bar effectively has an impedance ratio of zero as ρ_2 and V_2 are also zero. Therefore A_t is equal to twice A_i. This can be explained physically by considereing the overlap of the incident and reflected wave at the free end of the bar. Figure 4.22 shows the position of the waves at increment 240. The initially transmitted wave has been reflected from the fixed end and is travelling back along the bar with the opposite sign. Due to the higher velocity in the top half of the bar, the reflected wave has now reached the material interface and again some of the energy has been reflected and the remainder transmitted into the lower half. Closer inspection of the numerical values confirms that the respective ratios of these waves are correct.

4.3.3 Analysis of a shear wave propagating through a one dimensional column

To ensure the velocity of a shear wave is also correctly replicated by the finite element model a similar exercise was performed by applying a shear force at the re end of the bar. However, applying a shear force to the surface of the bar used in the previous exercise is not suitable as the problem is three dimensional and the time taken to perform this type of analysis is prohibitive. To overcome this problem a plane strain mesh was used with a shear force applied at the surface. Assuming one dimensional behaviour, the shear wave velocity of an elastic material is given by Equation 4.12 (Kramer (1996)):

$$V_{shear} = \sqrt{\frac{E}{2(1+v)\rho}} \tag{4.12}$$

To ensure that the shear wave propagation is one dimensional the side boundaries of the mesh were prevented from moving vertically. The remainder of the boundary conditions are the same as those described previously. The mesh was divided into 200 equi-sized elements. The analysis arrangement is shown in Figure 4.23.

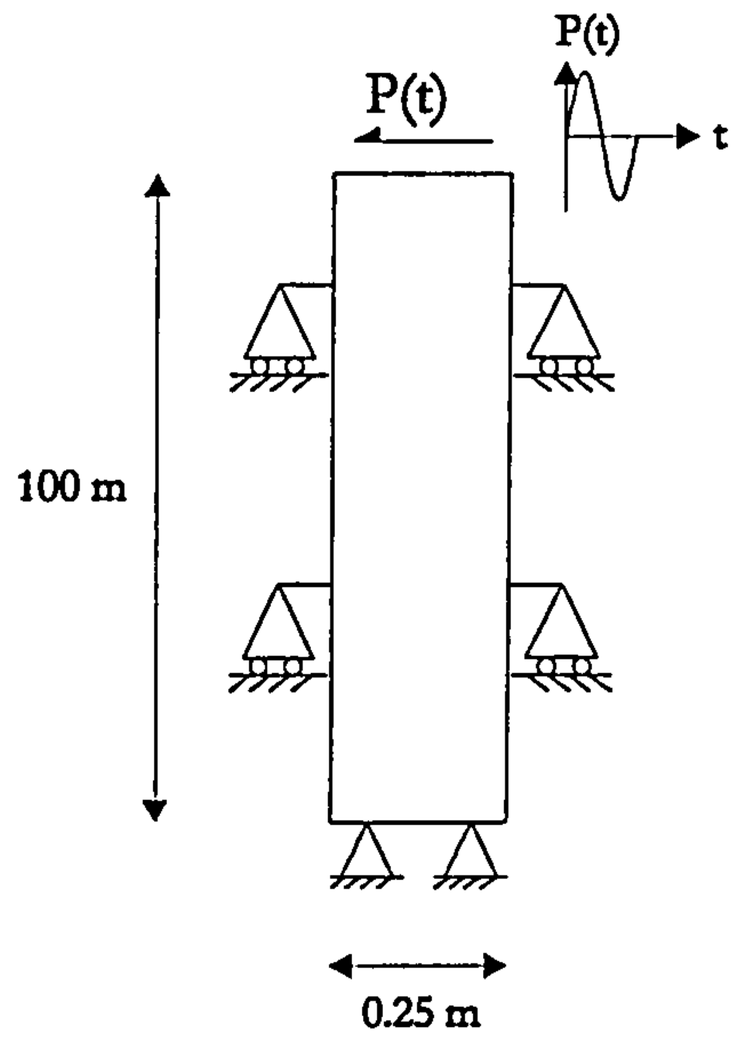

Figure 4.23: Analysis arrangement for the propagation of a shear wave

The material properties and time step chosen for this analysis are the same as those used in the compression wave analysis. This gives the material a shear wave velocity of 516 m/s.

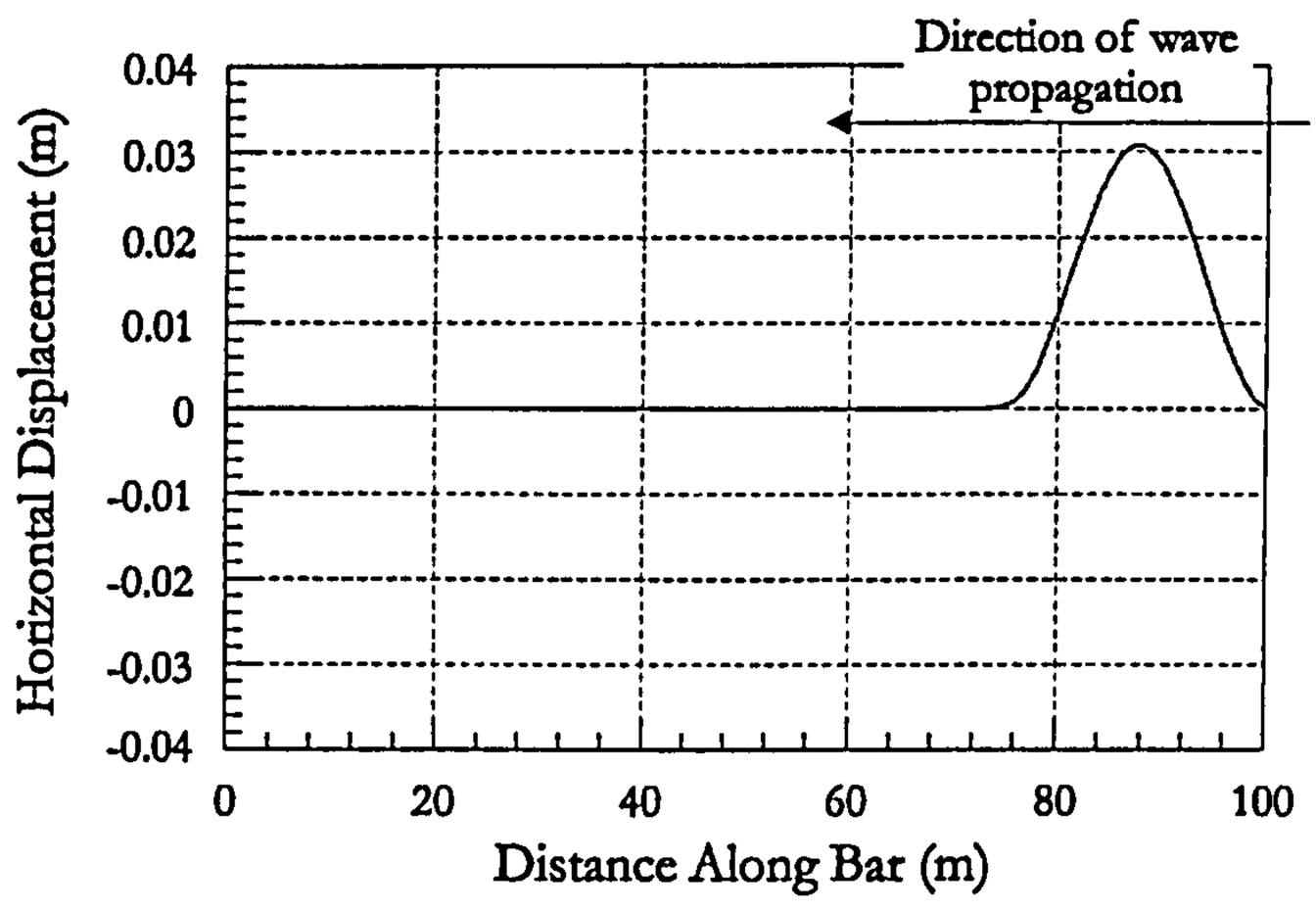

Figure 4.24: Shear wave analysis results Increment: 50

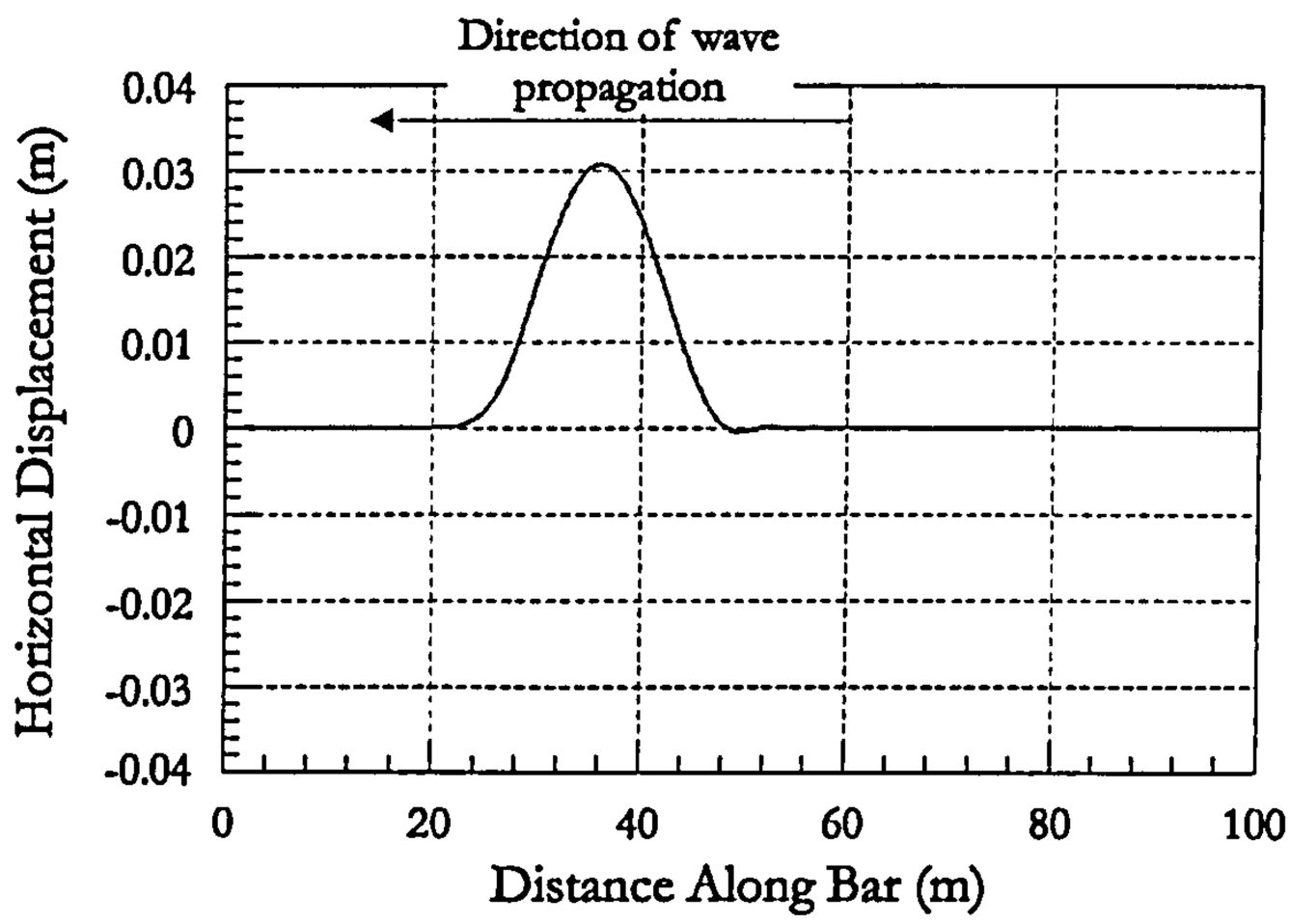

Figure 4.25: Shear wave analysis results Increment: 150

Figure 4.24 and Figure 4.25 show that the peak of the shear wave has moved from 89 meters along the bar to 37. The shear wave velocity can now be calculated:

$$Velocity = \frac{Distance}{Time} = \frac{(89.1-37.5)}{0.001\times(150-50)} = 516\,m/s$$

This is the same as that predicted from the elastic material parameters.

This exercise illustrates that the finite element formulation can model the correct velocity of propagation for compression and shear waves. In addition to these linear analyses the propagation of a compression wave through the cylindrical bar was also analysed using the Jardine *et al* (1986) small strain stiffness model. An isotropic confining stress of 200 kPa was applied to the bar to determine the initial stress conditions. The analyses were assumed to be elastic, but the stiffness, and hence the velocity of wave propagation, were dependent on the stress and strain level. The model tries to reproduce the characteristic reduction in stiffness with strain exhibited by real soils. This type of model is not well suited to dynamic problems because it cannot deal with stress reversals. When this type of model is used for static geotechnical finite element analyses, the strains in the mesh must arbitrarily be zeroed to reinvoke the high initial stiffness observed after stress reversals. Stress reversals may only occur a few times during the static analysis of say a tunnel excavation and therefore a realistic assessment can be made when to zero the strains. During an earthquake analysis stress reversals are occurring constantly at

different locations in the finite element mesh. If the strains are not zeroed the soil stiffness begins to travel back up the soil stiffness curve. Despite these problems an analysis was run using this type of model to ensure that non-linear elasticity could be dealt with by the finite element code. The stresses and strains at the centre of a wave are higher than those near the edge. This means the material stiffness is lower at the centre and therefore so is the propagation velocity (see Equation 4.9). This has the overall effect of flattening out the wave as the lower amplitude sections are travelling faster than those with higher amplitudes.

An elasto-plastic analysis was undertaken for the cylindrical bar assuming a Mohr-Coulomb failure criterion. While the cylindrical bar analysis is not a true geotechnical problem, and a Mohr-Coulomb failure criterion is not well suited to dynamic analysis, it did illustrate some important results. As the wave entered the bar, the strains induced were sufficient for the material behaviour to become plastic. As the wave travelled along the bar it left a permanent deformation. After some time, enough energy had been lost through plasticity and the analysis became elastic. From this point onwards the elastic wave travelled indefinitely along the bar. These results illustrate that energy is being lost due to plasticity and that the Mohr-Coulomb failure criterion is not well suited to soil dynamic analyses. The lack of plasticity upon unloading and the fact that the analyses becoming elastic after a certain point does not represent the true dynamic behaviour of soil satisfactorily. However, these results indicated that the program could deal with non-linear elasticity and plasticity.

4.3.4 Analysis of an impulse loading in a spherical cavity

The analyses of the cylindrical bar and one dimensional plane strain column illustrated some important aspects of dynamic analyses, however, further quantitative validation was sought. For this purpose further analyses were sought. The response of a spherical cavity to an impulse loading was solved by Sharpe (1942). A section of the mesh around the spherical cavity that was used to analyse the problem is shown in Figure 4.26 and the solution (Equation 4.13) is given in the form of the displacement normal to the boundary of the cavity. The mesh continues to a distance of 40 meters away from the centre of the cavity with equi-sized elements. The equation has three components. The first represents the static

displacement produced by the application of the load P, while the other two are dynamic components that die away as the wave passes.

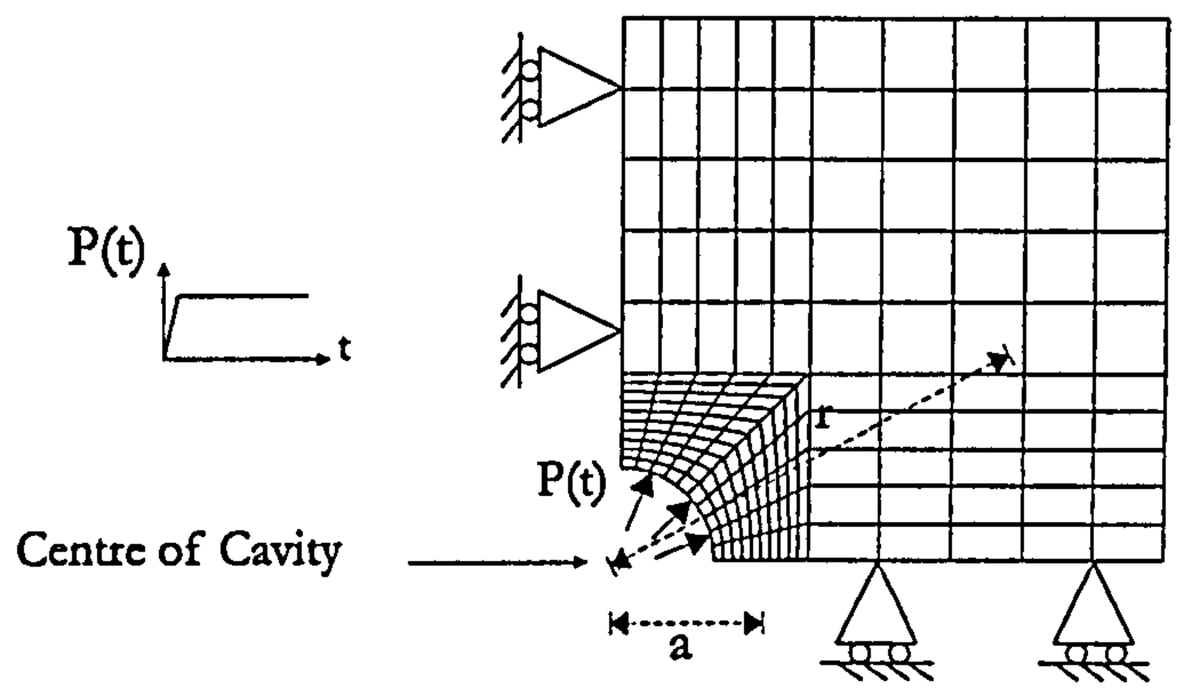

Figure 4.26:Analysis arrangement for cavity problem

$$u = \frac{aP_o}{4\mu}\left[\left(\frac{a}{r}\right)^2 - \sqrt{\frac{3}{2}}\left(\frac{a}{r}\right)^2 e^{\frac{-\omega\tau}{\sqrt{2}}}\sin\left(\omega\tau + \tan^{-1}\left(\sqrt{2}\right)\right) + \sqrt{2}\left(\frac{a}{r}\right)e^{\frac{-\omega\tau}{\sqrt{2}}}\sin(\omega\tau)\right] \quad (4.13)$$

where $\tau = t - \frac{r-a}{V}$, $V = \sqrt{\frac{\lambda + 2\mu}{\rho}}$, $\mu = \frac{E}{2(1+\nu)}$,

$$\lambda = \frac{E\nu}{(1+\nu)(1-2\nu)}, \quad \omega = \frac{2\sqrt{2}V}{3a}$$

The parameters chosen for the analysis are as follows:

E = Young's Modulus = 100.0 N/m^2, a = cavity radius = 1.0 m

ν = Poisons Ration = 0.25, r = current radius

P_0 = Impulse Loading = 1.0 N

The top half of the cavity was modelled by using axial symmetry, while the bottom half was included by utilising the horizontal plane of symmetry. This meant that only one quarter of the problem had to be meshed. The impulse load was applied over one increment of duration 0.01 seconds and then maintained for the rest of the analysis. The modified Newmark scheme was used with $\gamma = 0$, $\delta = 0.5$ and $\alpha = 0.25$ to give an unconditionally stable scheme with no added numerical damping.

The ICFEP results are compared against the closed form solution in Figure 4.27 to Figure 4.29. These figures compare predicted displacements normal to the cavity at different radii from the centre of the cavity with the closed form solution.

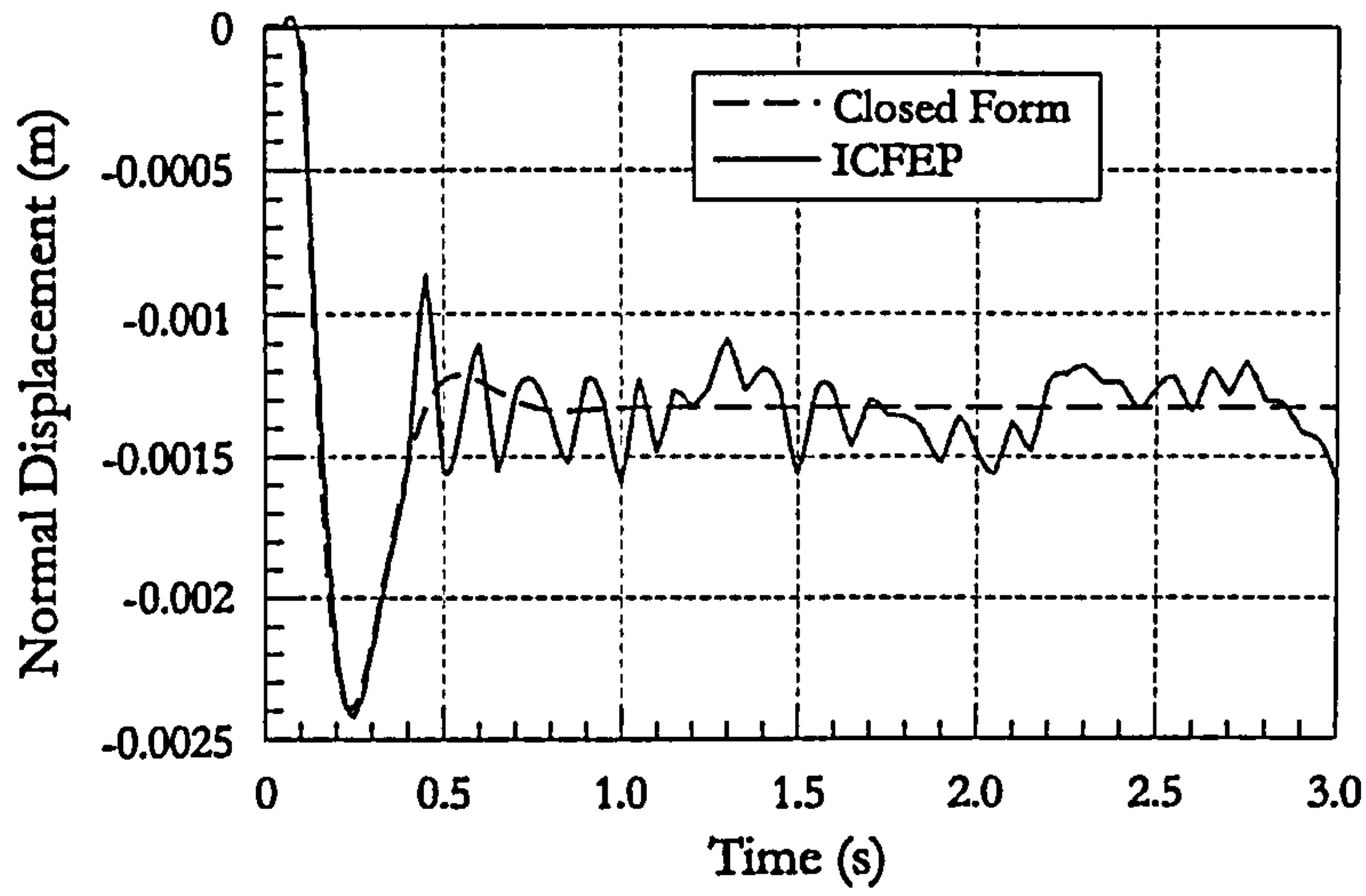

Figure 4.27: Displacement normal to cavity, $r = 2.17$ m

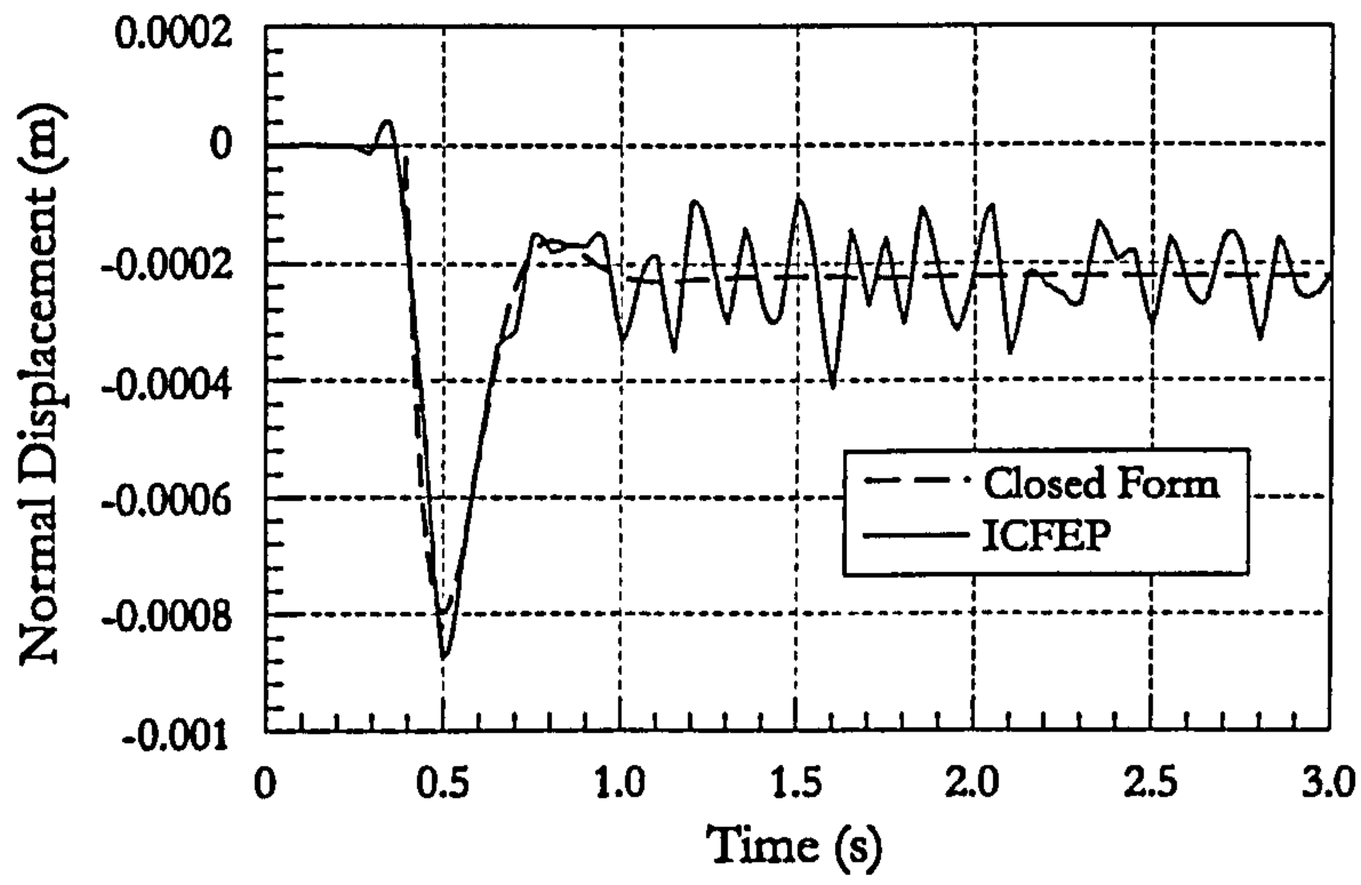

Figure 4.28: Displacement normal to cavity, $r = 5.29$ m

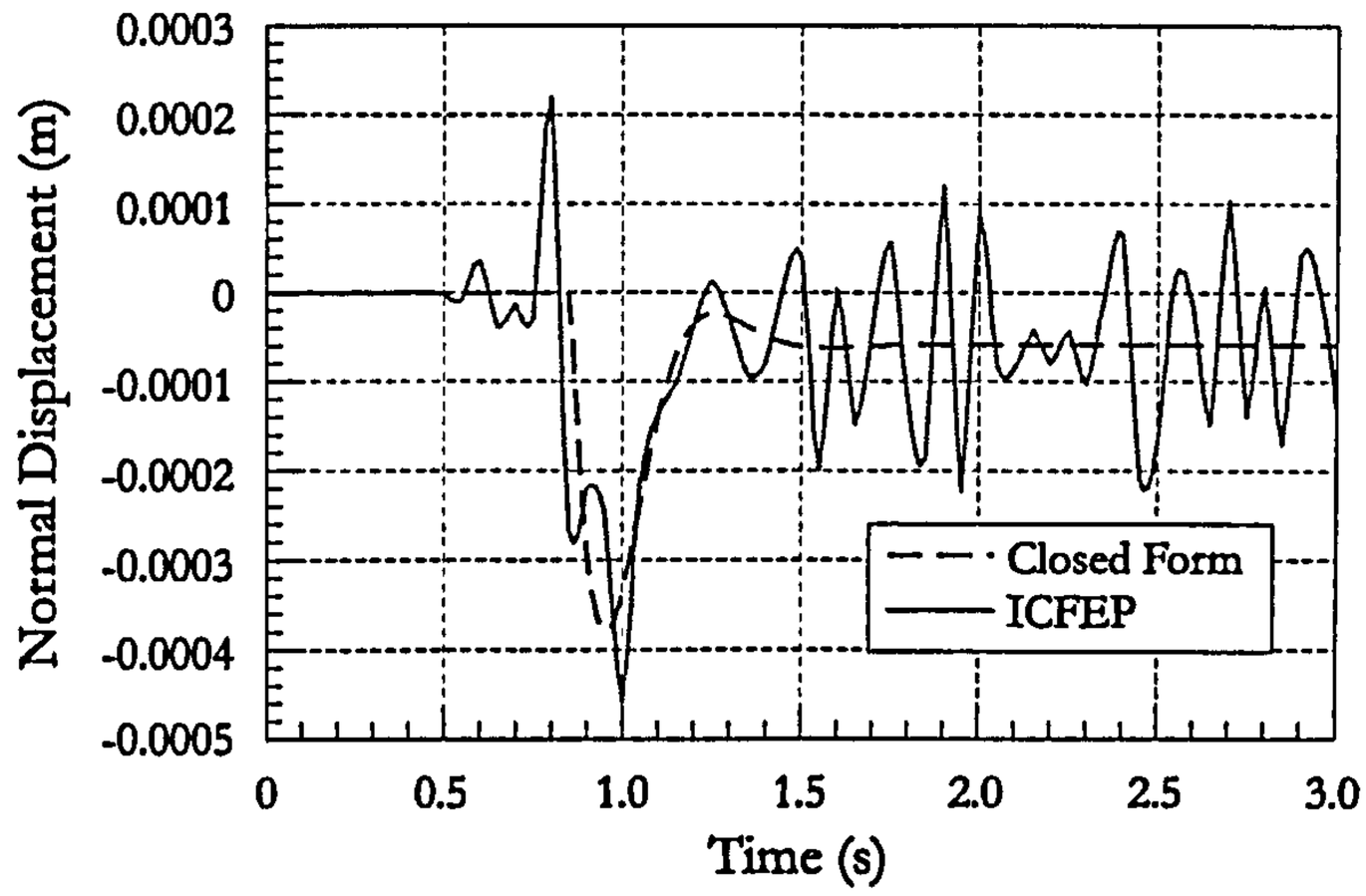

Figure 4.29: Displacement normal to cavity, $r = 10.36$ m

The results shown in Figure 4.27 and Figure 4.28 demonstrate that the finite element analysis accurately predicts the peak displacement experienced as the initial wave passes the respective radii and therefore validates quantitatively the finite element code. After the first wave has passed, the finite element results show considerable oscillations about the closed form solution. The results shown in Figure 4.29 for a radius of 10.36 meters show greater oscillations that are of a similar magnitude to those caused by the passing of the initial wave. These numerical inaccuracies make it difficult to identify the arrival of the compressive wave in this case. These kinds of numerical oscillations have been observed by other researchers and are due to the mesh discretisation not accurately modelling the response of the higher modes and the refraction and reflection of waves at the boundaries between elements with different size. To overcome this problem Zienkiewicz *et al* (1999) recommend introducing some numerical damping into the time discretisation scheme to remove these spurious oscillations. The influence of numerical damping on the cavity analysis will form one of the investigations to be presented in the next section.

4.3.5 Investigations using the Newmark method

One of the primary issues to be addressed before attempting a finite element analysis is the design of the finite element mesh. It has been found in practice that when analysing a static problem that is close to failure, the mesh must be refined around the area that will experience the most plasticity. Away from this region the

mesh can become coarser to reduce the overall number of degrees of freedom and hence reduce the analysis run time. This may not be possible for dynamic analyses, as the propagation of the wave must be accurately modelled at every point in the finite element mesh. To investigate how the propagation of a longitudinal wave is affected by mesh coarseness, the cylindrical bar analysis will be repeated with the mesh divided into a varying number of elements. All other aspects of the analysis are identical to those described in Section 4.3.2. The series of analyses are summarised in Table 4.2.

Number of Elements	Size of Elements d (m)	Wavelength of Input λ (m)	λ/d
200	0.5	40	80
100	1.0	40	40
50	2.0	40	20
25	4.0	40	10
20	5.0	40	8
10	10.0	40	4
5	20.0	40	2

Table 4.2: Summary of cylindrical bar analyses

The results of the cylindrical bar analyses at increments 85 and 210 for each mesh are shown in Figure 4.30 to Figure 4.31 respectively.

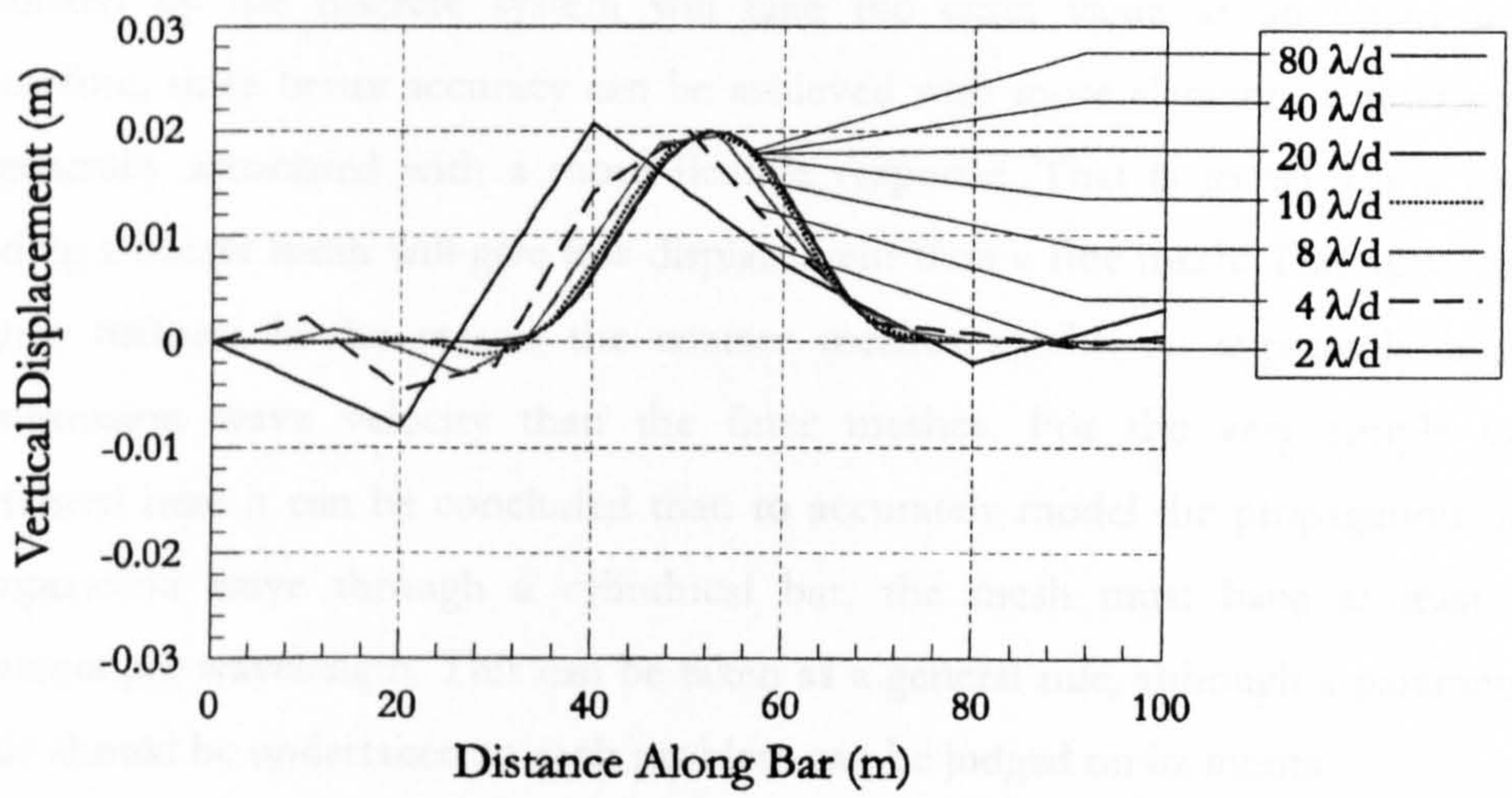

Figure 4.30: bar analysis with different meshes: Increment 85

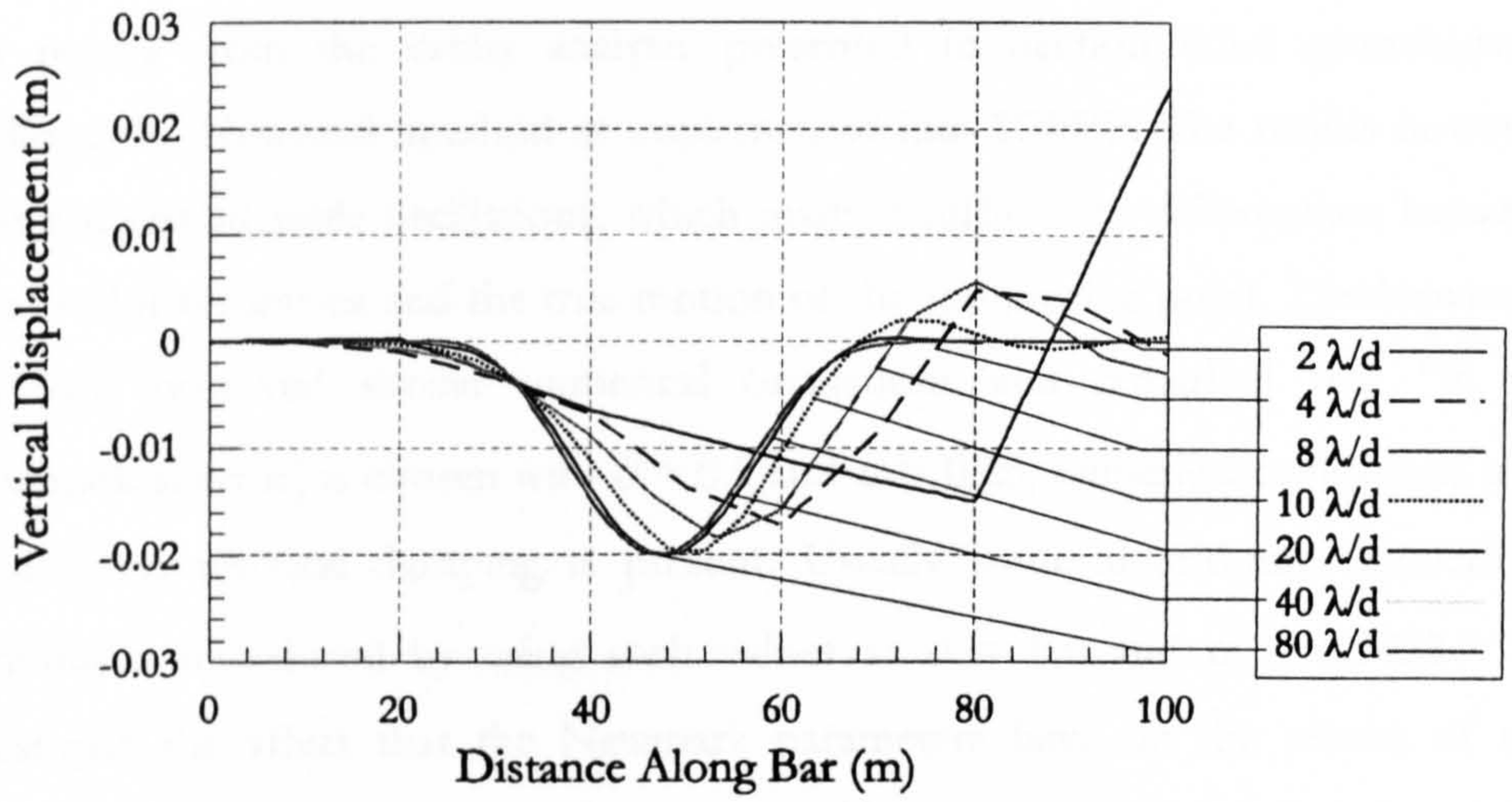

Figure 4.31: bar analysis with different meshes: Increment 210

As expected the number of elements per wavelength has a significant effect on the accuracy of the analysis. The results for increment 85 demonstrate that as the mesh becomes coarser the apparent compression wave velocity becomes greater and the shape of the propagated wave becomes more distorted. After the wave has reflected from the fixed end of the bar, shown in Figure 4.31, the wave shape in the analysis with the coarsest mesh has become more distorted and the difference in the apparent compression wave velocity has become greater.

In linear analyses, the use of variational finite elements (as used in ICFEP) guarantees that the work done by the loads is less than, or equal to that of the exact solution (Zienkiewicz and Taylor (1991)). This means that the displacements predicted by the discrete system will take the exact value as an upper limit. Therefore, since better accuracy can be achieved with more elements, a finer mesh is generally associated with a more flexible response. That is to say for a given loading a coarse mesh will give less displacement than a fine mesh. This apparently higher stiffness is the reason the coarser meshes exhibit an apparently higher compression wave velocity than the finer meshes. For the very simple case presented here it can be concluded that: to accurately model the propagation of a compression wave through a cylindrical bar, the mesh must have at least 10 elements per wavelength. This can be taken as a general rule, although a parametric study should be undertaken so each problem can be judged on its merits.

The results from the cavity analysis presented in Section 4.3.4 quantitatively validated the Newmark method as implemented into ICFEP. The results however exhibited considerable oscillations, which made it difficult to differentiate between numerical inaccuracies and the true motion of the monitoring point. Zienkiewicz *et al* (1999) observed similar numerical oscillations and remarked that "if the [Newmark scheme] is chosen with $\delta = 0.5$ and $\alpha = 0.25$, numerical oscillations may occur if no physical damping is present. Usually some algorithmic (numerical) damping is introduced by using such values as $\delta = 0.6$ and $\alpha = 0.3025$." To investigate the affect that the Newmark parameters have on the results of the dynamic finite element analyses, the cavity problem was rerun using the parameters suggested by Zienkiewicz *et al.* to introduce some numerical damping. The results for the same three monitoring points are shown in the following figures.

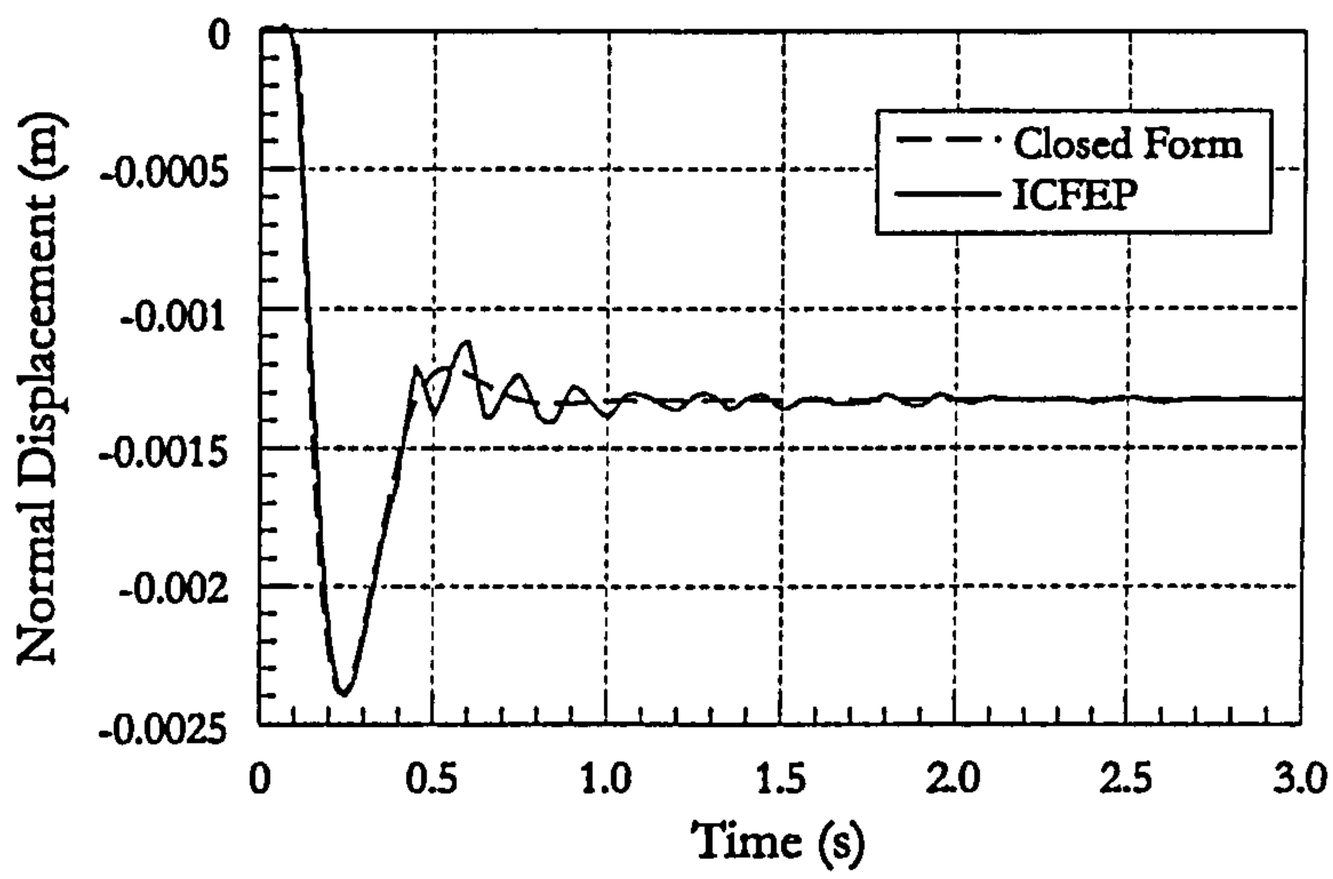

Figure 4.32: Displacement normal to cavity (damped analysis), $r = 2.17$ m

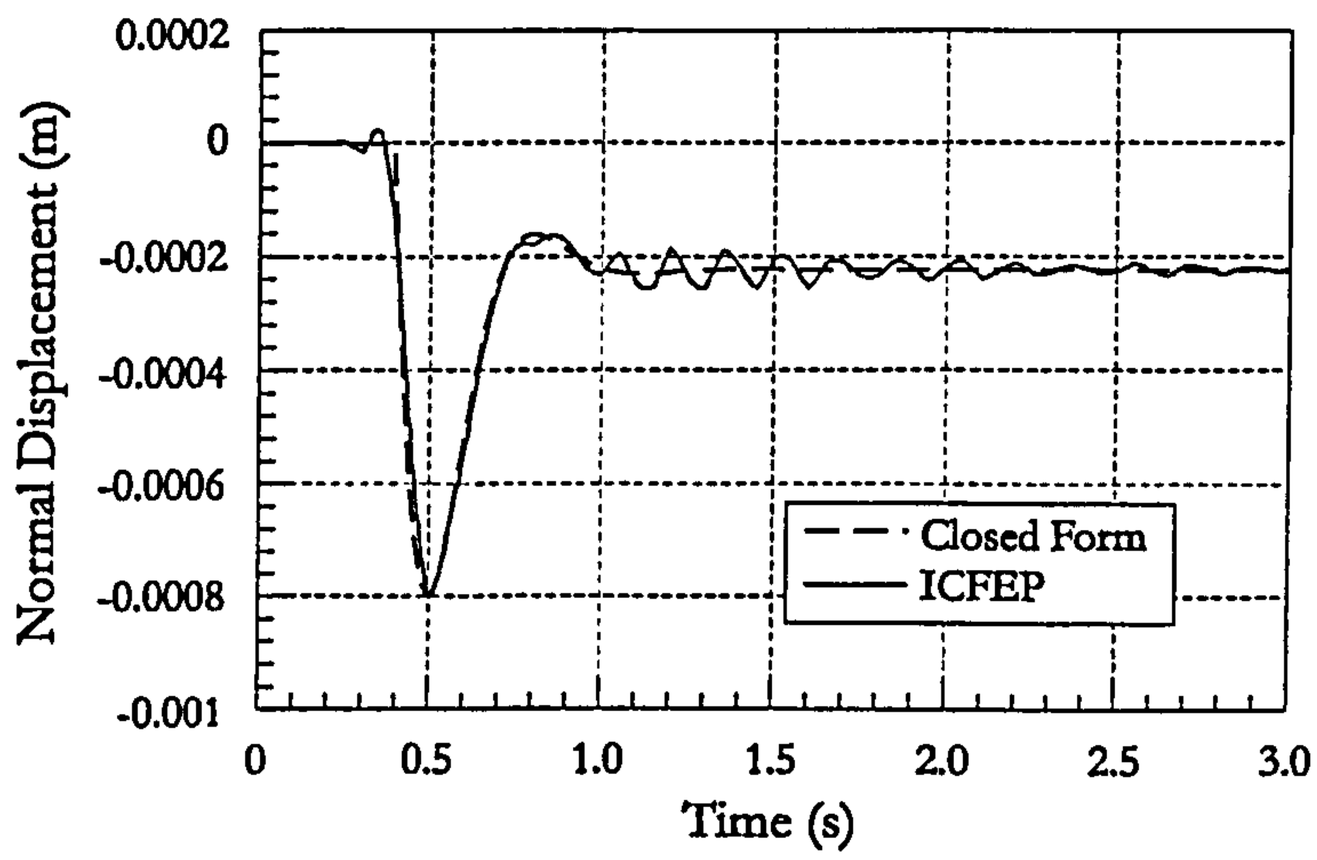

Figure 4.33: Displacement normal to cavity (damped analysis), $r = 5.29$ m

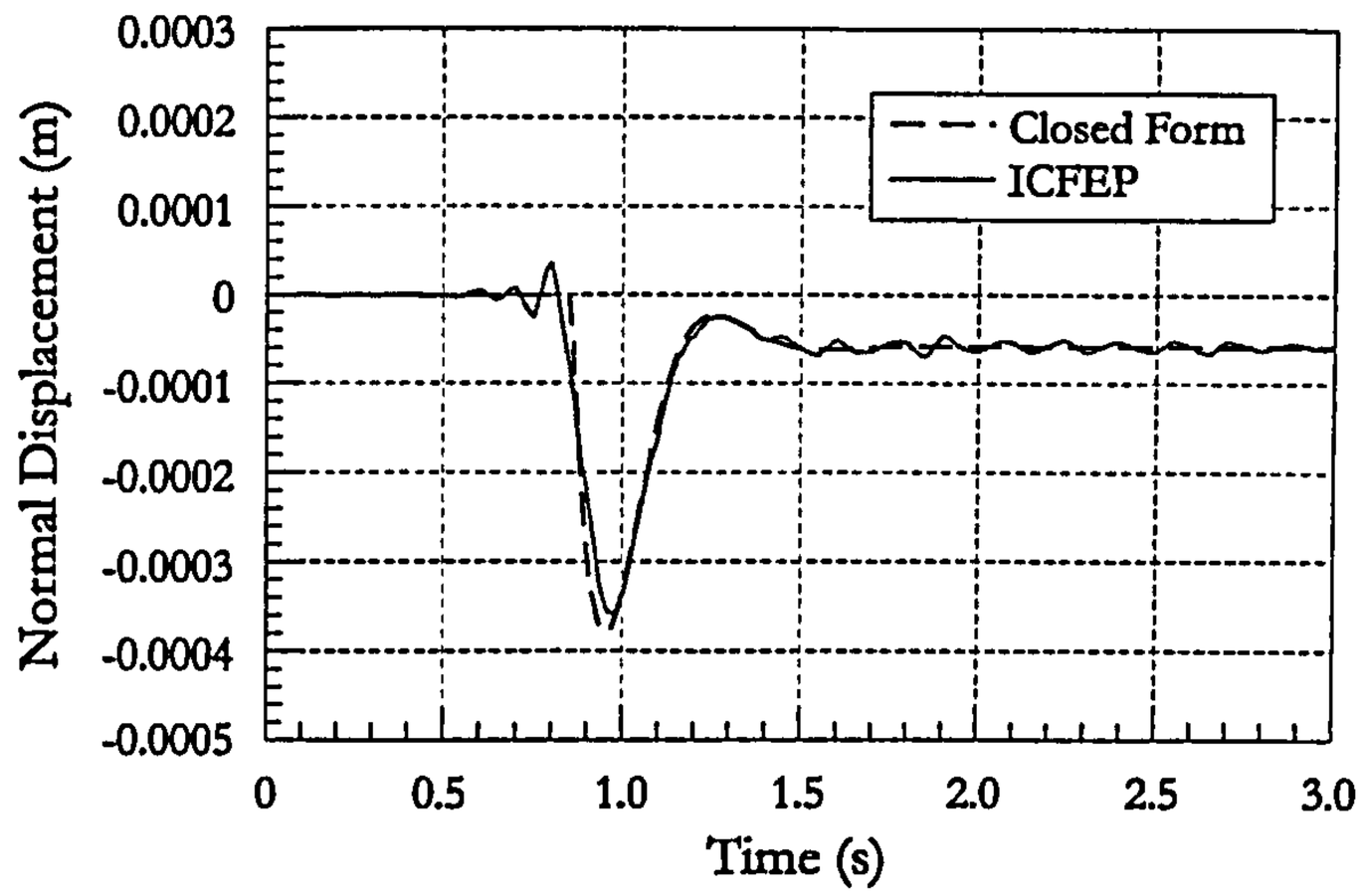

Figure 4.34: Displacement normal to cavity (damped analysis), $r = 10.36$ m

The numerical damping introduced by changing the Newmark parameters to $\delta = 0.6$ and $\alpha = 0.3025$ has not changed how well the passing of the wave front is modelled. There is no significant reduction in the amplitude of the first peak and the numerical oscillations have been reduced considerably. At all radii the long term displacement reduces to the static value and the arrival of the wave front at a radius of 10.36 meters is now clearly identifiable.

It was found while checking the evaluation of the element mass matrices, that using 2×2 or reduced Gaussian integration does not give the correct values for the terms in the element mass matrix. If 3×3 or full integration is used then the element mass matrices are correctly evaluated. It was found by Naylor (1974) that when full Gaussian integration is used for nearly incompressible solids, the predicted changes in mean stress can have large errors. To overcome this problem when analysing geotechnical problems in which the behaviour of the soil is assumed to be undrained (and therefore nearly incompressible), reduced integration is commonly used. It is therefore important to investigate how the use of reduced integration to evaluate the mass matrix influences the results from a dynamic finite element analysis. The difference between the mass matrices calculated using full and reduced integration for an isoparametric eight noded element is illustrated in Figure 4.35.

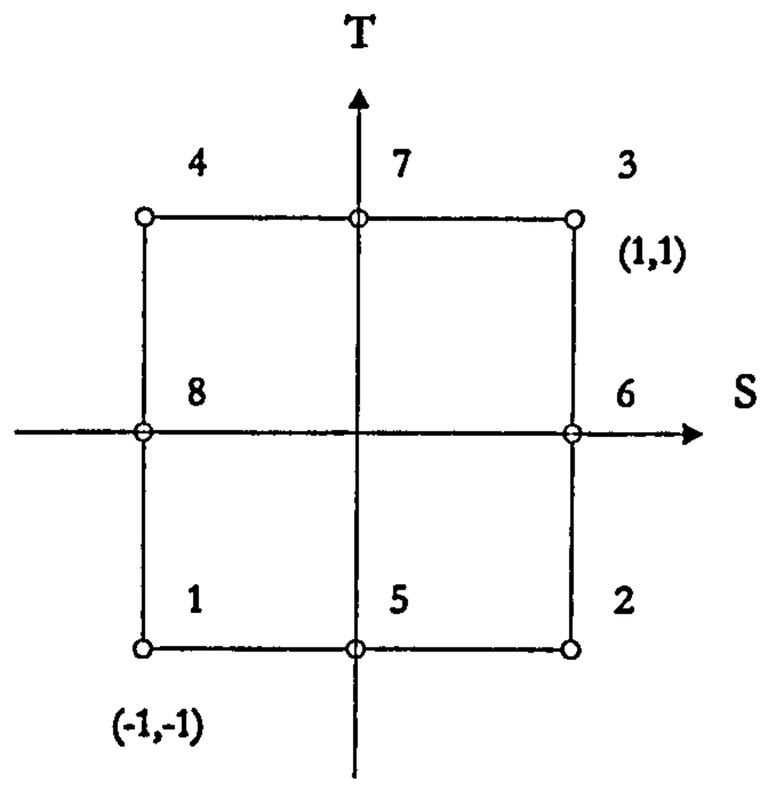

$$M = \frac{\rho}{135}\begin{bmatrix} 96 & 60 & 48 & 60 & -18 & -24 & -24 & -18 \\ 60 & 96 & 60 & 48 & -18 & -18 & -24 & -24 \\ 48 & 60 & 96 & 60 & -24 & -18 & -18 & -24 \\ 60 & 48 & 60 & 96 & -24 & -24 & -18 & -18 \\ -18 & -18 & -24 & -24 & 18 & 6 & 9 & 6 \\ -24 & -18 & -18 & -24 & 6 & 18 & 6 & 9 \\ -24 & -24 & -18 & -18 & 9 & 6 & 18 & 6 \\ -18 & -24 & -24 & -18 & 6 & 9 & 6 & 18 \end{bmatrix}$$

Mass Matrix Calculated Using Full Integration

$$M = \frac{\rho}{135}\begin{bmatrix} 80 & 60 & 40 & 60 & -10 & -20 & -20 & -10 \\ 60 & 80 & 60 & 40 & -10 & -10 & -20 & -20 \\ 40 & 60 & 80 & 60 & -20 & -10 & -10 & -20 \\ 60 & 40 & 60 & 80 & -20 & -20 & -10 & -10 \\ -10 & -10 & -20 & -20 & 10 & 0 & 5 & 0 \\ -20 & -10 & -10 & -20 & 0 & 10 & 0 & 5 \\ -20 & -20 & -10 & -10 & 5 & 0 & 10 & 0 \\ -10 & -20 & -20 & -10 & 0 & 5 & 0 & 10 \end{bmatrix}$$

Mass Matrix Calculated Using Reduced Integration

Figure 4.35: Mass matrices calculated using different orders of integration

The cause of the discrepancy between the two mass matrices is due to the accuracy of the Gaussian integration method. As the number of Gauss points used in the numerical integration procedure increases, the scheme can precisely integrate polynomials of a higher order. The expression that is integrated to obtain the mass matrix is of a higher order than the expression used to obtain the stiffness matrix.

To investigate how this discrepancy affects the results of dynamic finite element analyses, the cavity problem was rerun using reduced Gaussian integration. The analysis arrangement was identical to that described in Section 4.3.4 and to give a clear output the Newmark parameters $\delta = 0.6$ and $\alpha = 0.3025$ were used. The results for the three monitoring points are compared for the full and reduced integration methods with the closed form solution in Figure 4.36 to Figure 4.38.

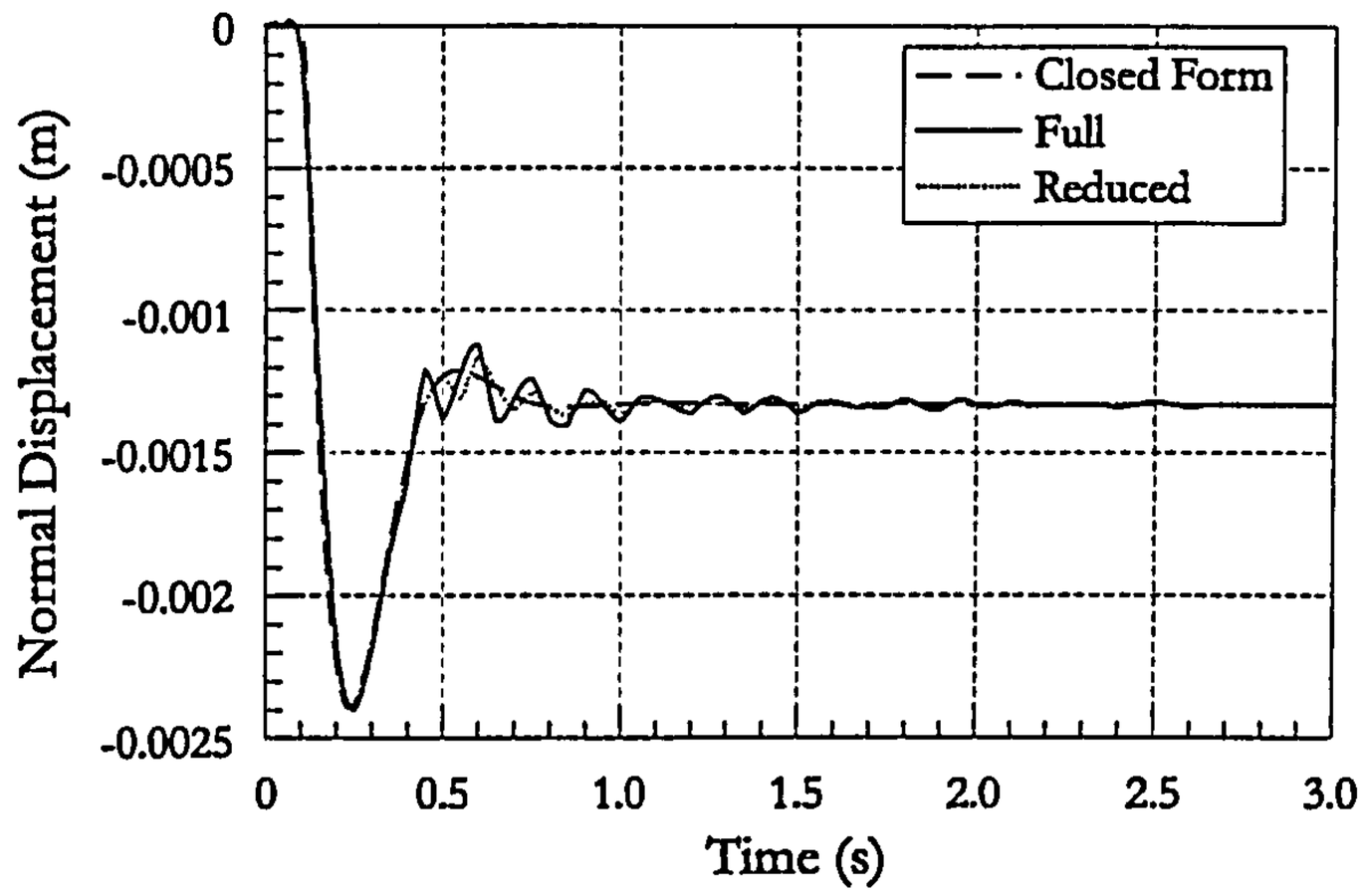

Figure 4.36: Displacement normal to cavity, $r = 2.17$ m

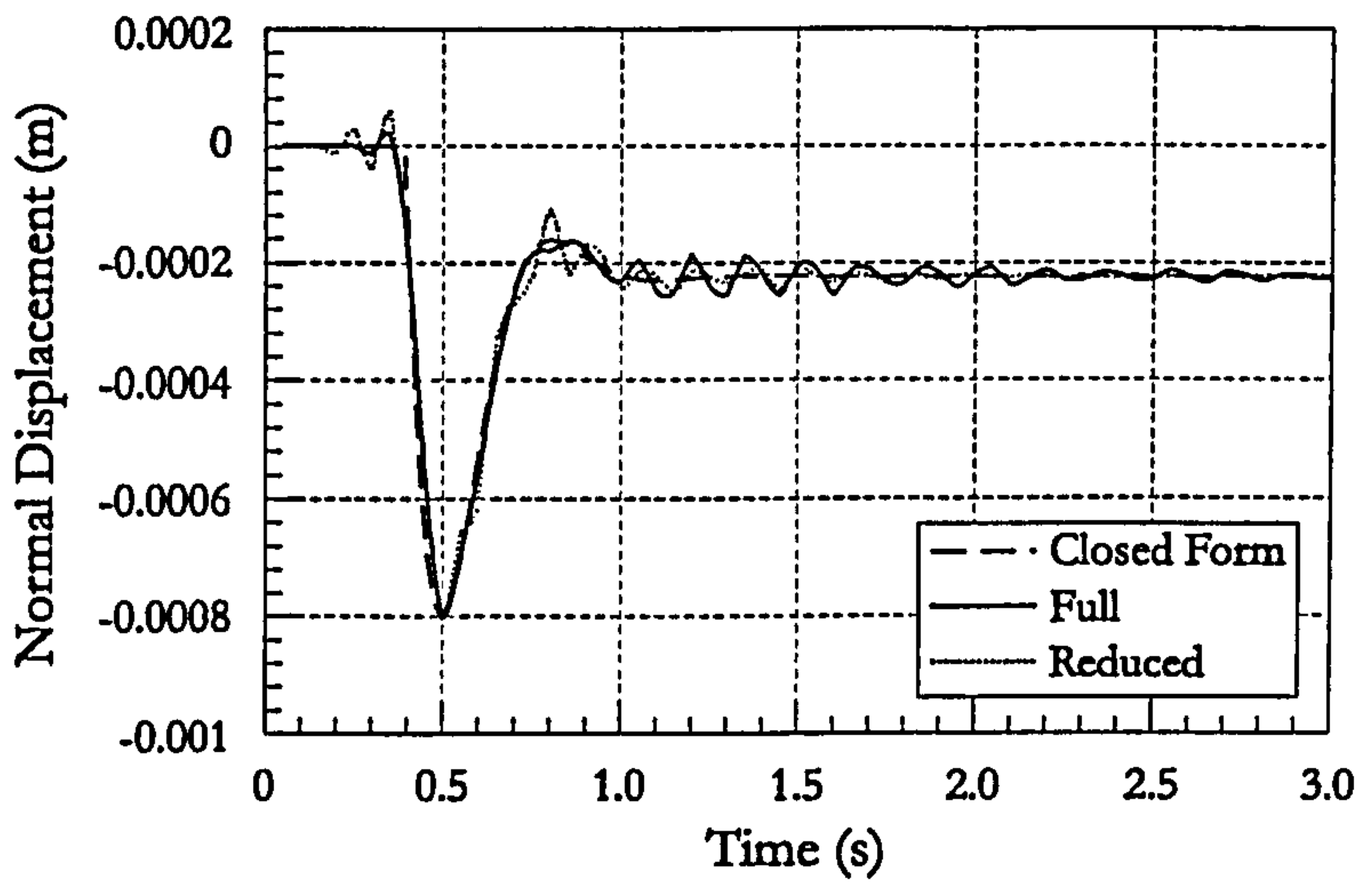

Figure 4.37: Displacement normal to cavity, $r = 5.29$ m

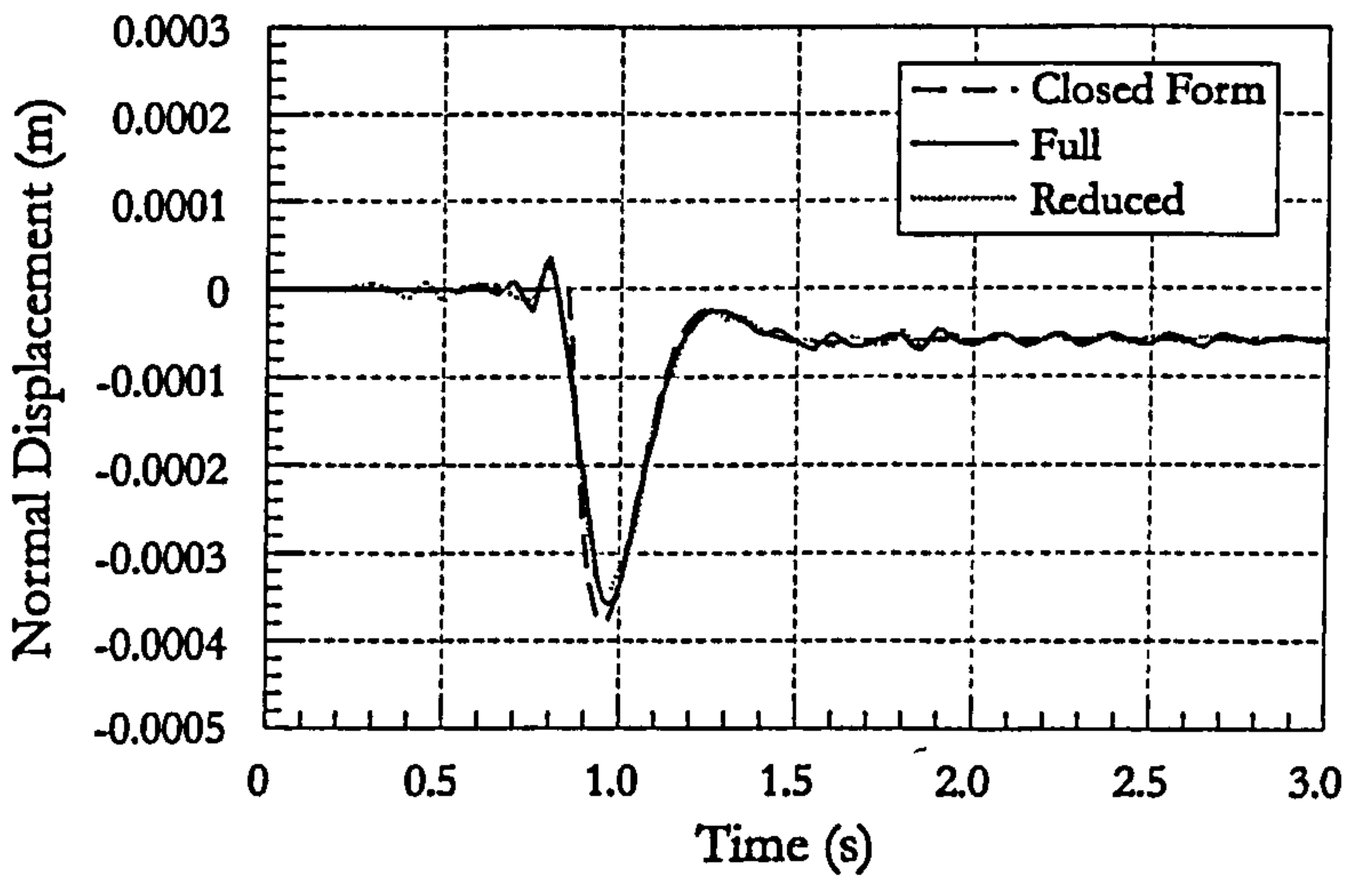

Figure 4.38: Displacement normal to cavity, $r = 10.36$ m

The results of the analysis at the three monitoring points show very little difference between using full and reduced Gaussian integration. The results of the analysis with reduced integration exhibit smaller numerical oscillations, implying that the inaccurate mass matrix introduces additional numerical damping to the analysis. Overall, it appears to make very little difference to the analysis although it is more consistent to use the full integration. If numerical locking does occur due to the use of the full integration scheme, the reduced method can be used, although it must be appreciated that there will be additional numerical damping in the analysis. It is also possible to use reduced integration for determining the stiffness matrix and full integration for calculating the mass matrix. In this way problems with numerical locking are avoided and the mass matrix is still accurately determined. This option is currently not possible in ICFEP.

4.4 Validation of the Finite Element Code: Quadratic Acceleration Method

4.4.1 Introduction

The work presented in the previous section validated the dynamic analyses that are undertaken using the original Newmark method. This technique does not involve calculating the third derivative of displacement with respect to time, or thrust, and therefore a further validation exercise must be performed using the quadratic acceleration method to ensure that the thrust is calculated correctly.

4.4.2 Analysis of an impulse loading in a spherical cavity

To validate the quadratic acceleration method, the analysis of an impulse loading on the interior of a spherical cavity will be used. The arrangement is the same as that described in Section 4.3.4, although it was found by trial and error that a smaller time step of 0.001 seconds was required to make the analysis stable. The results of the analysis using the quadratic acceleration method ($\gamma = 1.0$, $\delta = 1/3$ and $\alpha = 1/12$) are compared with the closed form solution for a radius of 2.17 meters in Figure 4.39.

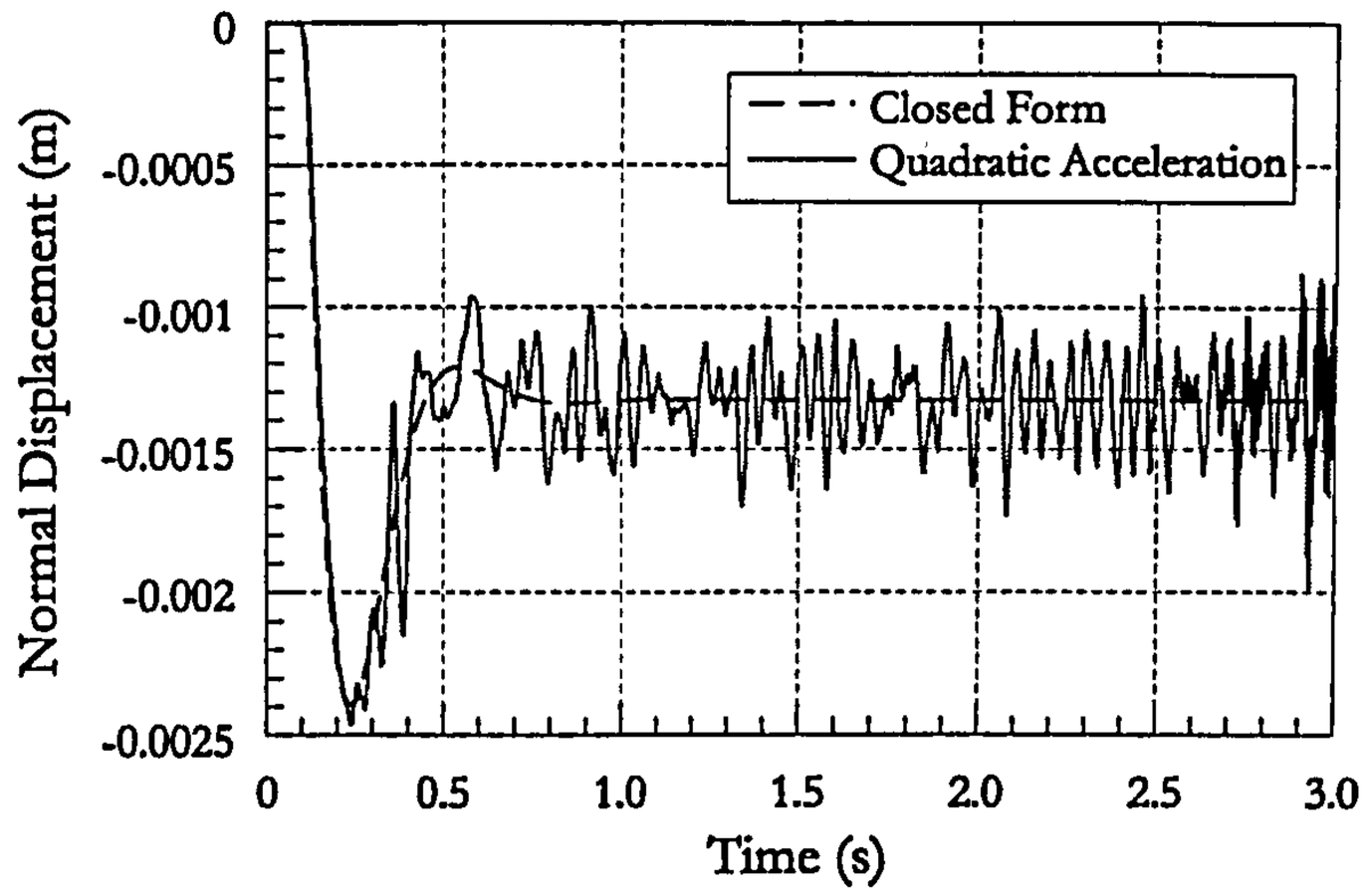

Figure 4.39: Results of analysis using the quadratic acceleration method with original parameters ($\gamma = 1.0$, $\delta = 1/3$ and $\alpha = 1/12$) $r = 2.17$ m

The initial rise as the wave passes the monitoring point is accurately modelled and then the solution exhibits considerable numerical oscillations around the permanent static displacement. After 2.5 seconds the analysis becomes unstable and the results after the 3 seconds are out of control. This is consistent with the analysis of the single degree of freedom problem presented in Section 4.2. In the absence of any material damping, the quadratic acceleration scheme is unconditionally unstable. It was however found that increasing the modified Newmark parameters could introduce sufficient numerical damping to ensure the time scheme remains stable. To investigate how these parameters affect the results of a boundary value problem, the spherical cavity problem was rerun with a range of values taken for the modified Newmark parameters. The results of the analysis that assumed $\alpha = 0.1$ and $\delta = 0.35$ are compared with the closed form solution in Figure 4.40.

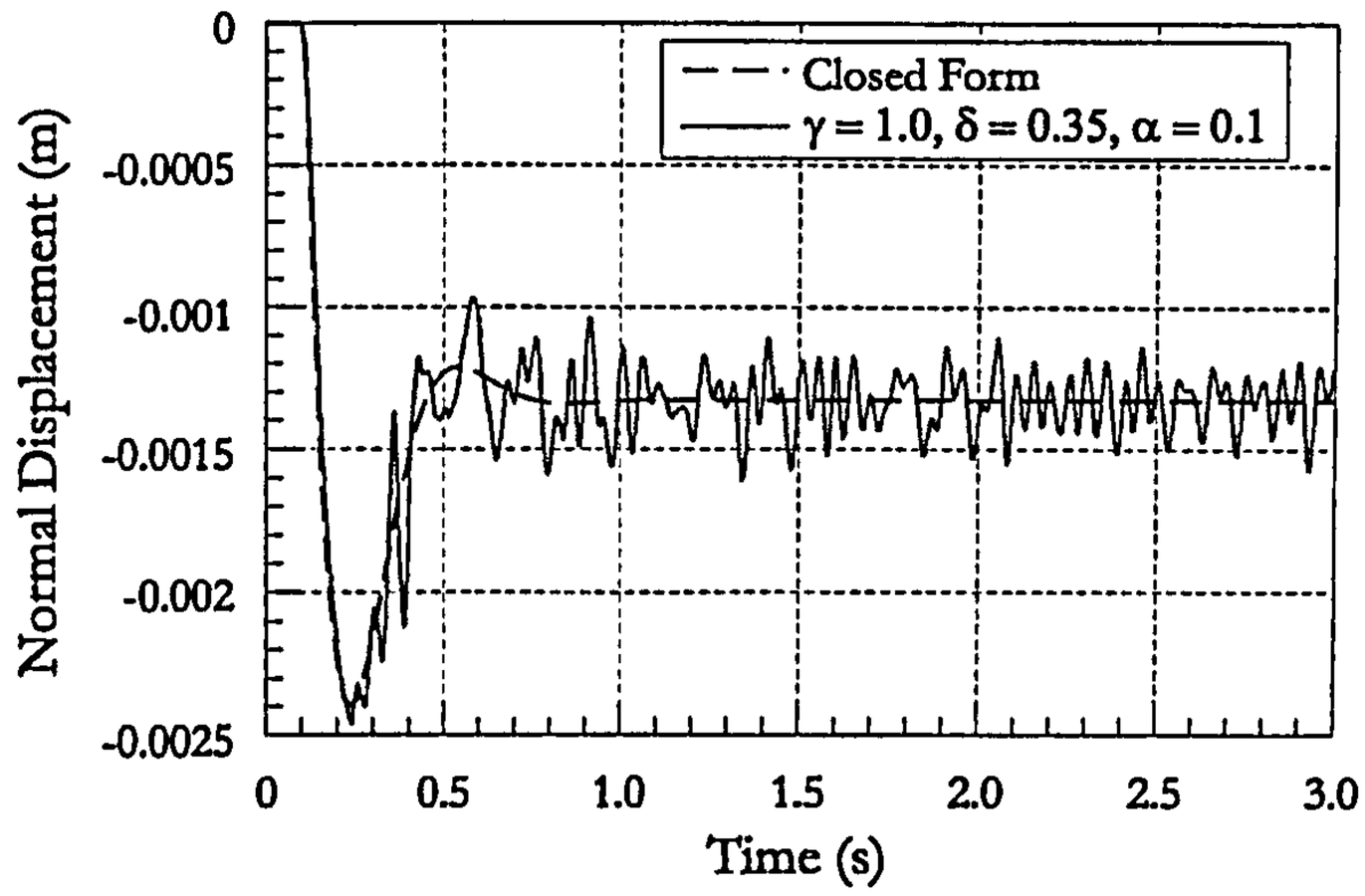

Figure 4.40: Results of analysis using the quadratic acceleration method with damped parameters ($\gamma = 1.0$, $\delta = 0.35$ and $\alpha = 0.1$) $r = 2.17$ m

Increasing the modified Newmark parameters has ensured that the time scheme has remained stable, although this small increase in the parameters has not reduced the level of the numerical oscillations that are present after the wave has passed the monitoring point. To investigate if the numerical oscillations can be controlled by the numerical damping introduced by varying the modified Newmark parameters, further analyses were run with increased values of γ, α and δ. The analyses with increased values of γ were found to be unstable and therefore the research was focused on the remaining parameters α and δ. To determine which of these two parameters most effectively controlled the numerical damping, the first analysis was run with only α increased and then for the second analysis only δ was increased. The results with α damping are shown in Figure 4.41 and the results with δ damping are shown in Figure 4.42.

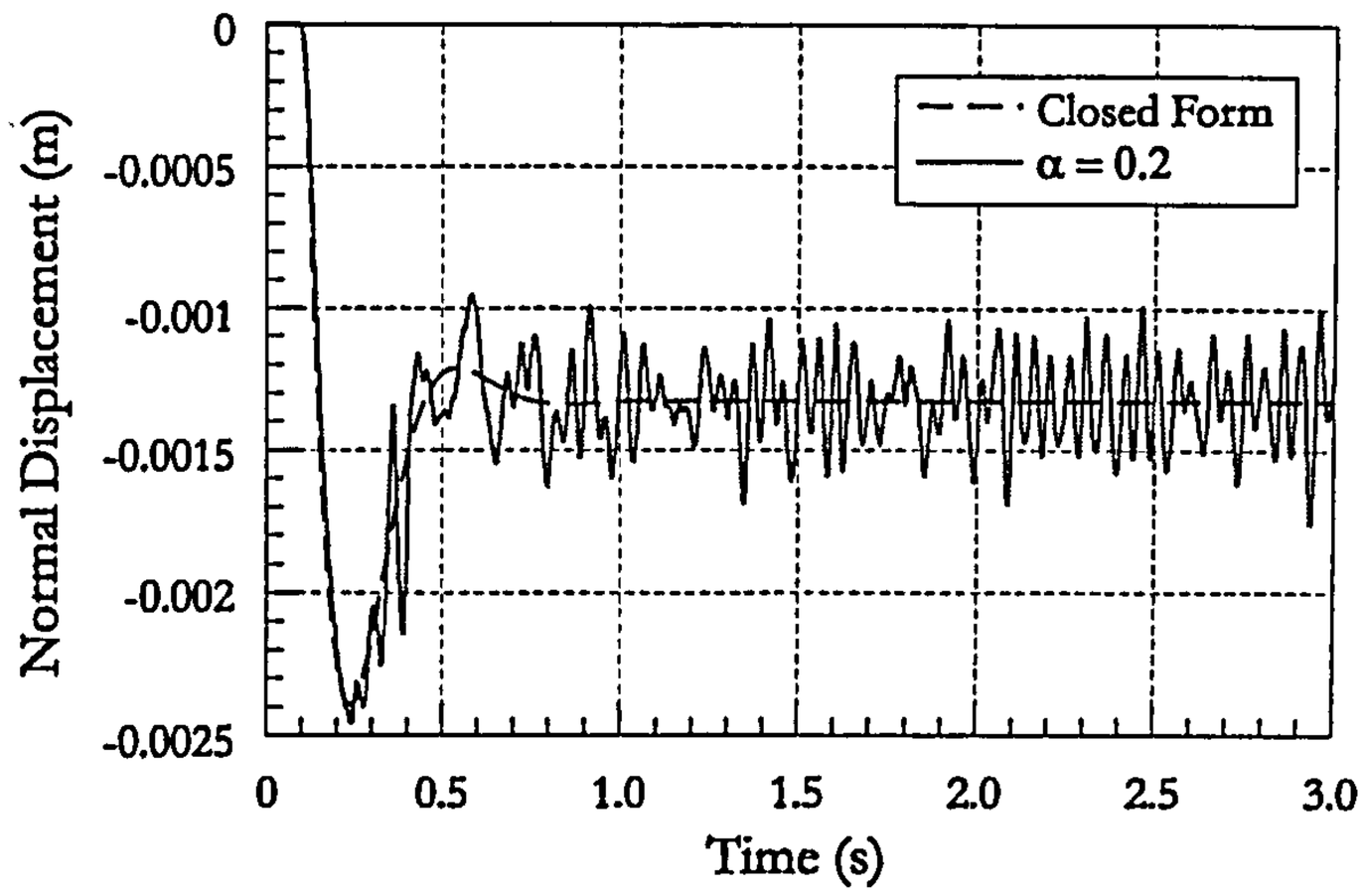

Figure 4.41: Results of analysis using the quadratic acceleration method with damped parameters ($\gamma = 1.0$, $\delta = 1/3$ and $\alpha = 0.2$) $r = 2.17$ m

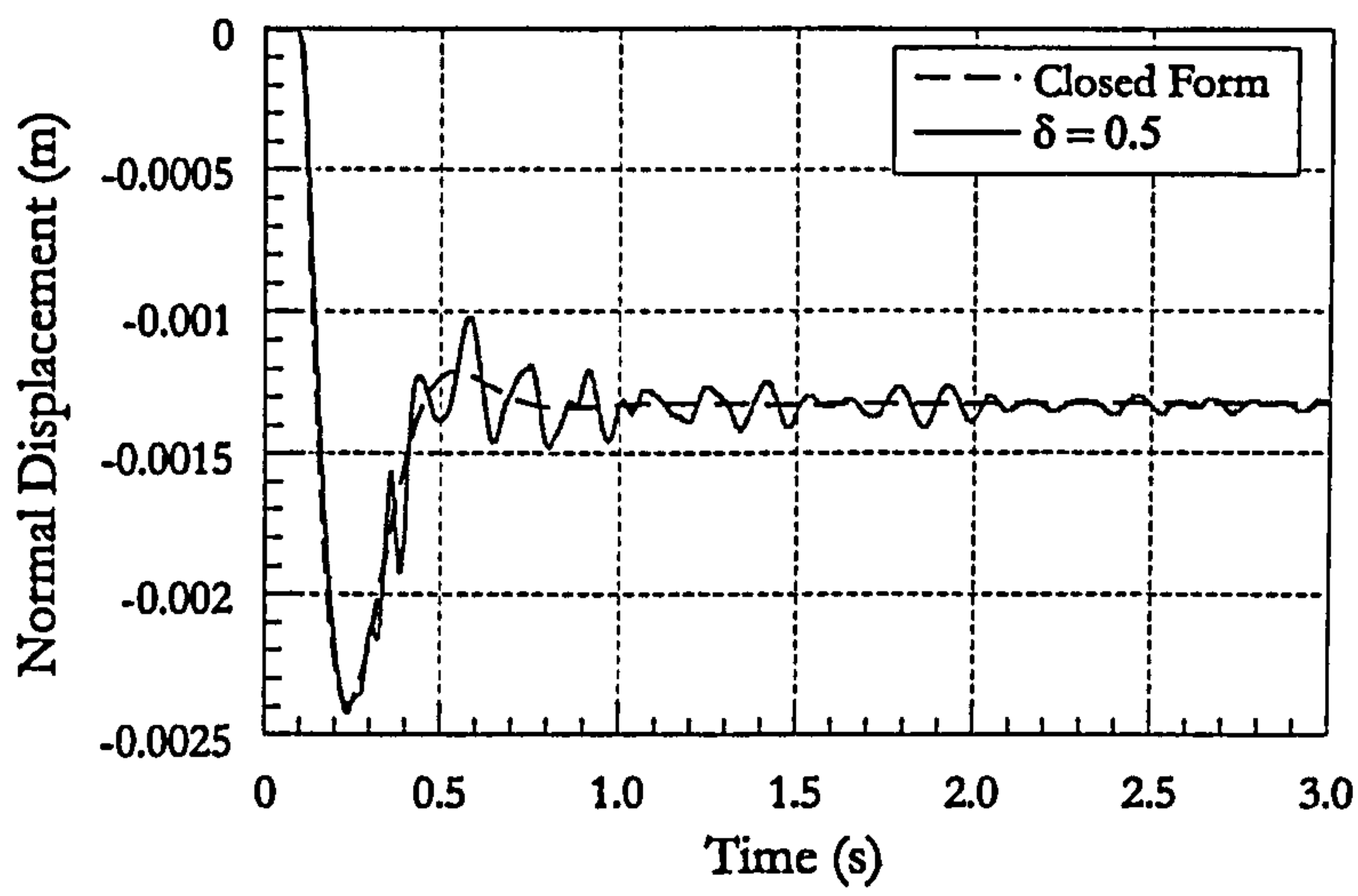

Figure 4.42: Results of analysis using the quadratic acceleration method with damped parameters ($\gamma = 1.0$, $\delta = 0.5$ and $\alpha = 1/12$) $r = 2.17$ m

Although increasing α to 0.2 ensures that the time scheme remains stable, the numerical damping introduced does not significantly reduce the level of the numerical oscillations present after the initial wave has passed the monitoring point. The numerical oscillations present in the analysis with a δ value of 0.5 have been significantly reduced and the solution appears to be tending towards the permanent static displacement. The results shown in Figure 4.42 are similar to those obtained using the original Newmark method with added numerical damping.

4.4.3 Discussion

Generally, the results of the analyses using the quadratic acceleration method have been disappointing. The main objective of implementing the higher order approximation was to achieve the same degree of accuracy that is possible when using the original Newmark method, but with larger time steps and hence less increments. This was demonstrated to be possible for the single degree of freedom problem analysed in Section 4.2. The opposite was found when the scheme was used to analyse boundary value problems. To ensure numerical stability it was found that a smaller time step had to be used, and therefore this perceived advantage was lost.

If no material damping was present, after some increments the analysis became unstable regardless of the size of the time step. This result was also found with the single degree of freedom problem and it was overcome by introducing numerical damping into the analysis by changing the modified Newmark parameters. A short parametric study demonstrated that increasing the δ parameter introduced the most controllable numerical damping. The results of the analysis with $\delta = 0.5$ were comparable to those obtained using the original Newmark method with $\delta = 0.6$ and $\alpha = 0.3025$, although it required ten times as many increments.

Overall the quadratic acceleration method performs inadequately when compared to the Newmark scheme for the following reasons:

- The perceived advantage associated with the increase in accuracy is lost due to the need for smaller time steps to ensure numerical stability.
- In the absence of material damping, irrespective of the size of the time, the scheme becomes unstable after some increments.
- The scheme can be made stable by increasing α and/or δ, although the numerical damping introduced is small.
- The scheme appears to suffer due to numerical oscillations introduced because of the poor representation of the higher order modes by the finite element mesh.

- The modified Newmark parameters needed to be increased significantly to damp out these numerical oscillations and for a more complicated problem it is unclear what effect this would have on the results.

For these reasons the quadratic acceleration method was not used for any of the investigations that are presented in the rest of this thesis. The original Newmark method was used and for each individual problem the influence of the time step was investigated and the influence of the numerical damping was accessed. It is felt that generally the Newmark method is accurate enough for the purposes of dynamic finite element analysis and its unconditional stability is beneficial, although it is important to investigate how the assumed time step influences the results of the analysis.

4.5 Validation of pore fluid compressibility and coupled dynamic analyses.

4.5.1 Introduction

In addition to the changes made to the solid equilibrium equations validated in the previous section, a change was also made to the equation of continuity for the pore fluid. The finite element theory developed in Chapter 2 for static coupled analyses assumed that the pore fluid is incompressible. This is a valid assumption when the compressibility of water is compared to that of the soil skeleton. However, in dynamic analyses it is not clear if the same assumption is still valid. The following section will concentrate on validating the inclusion of pore fluid compressibility in static analyses. An extended form of the same validation problem is then used to validate dynamic coupled analyses.

4.5.2 The validation problem

To validate the changes required to include the pore fluid compressibility in the equation of continuity, the validation exercise given by Zienkiewicz *et al.* (1980) is used. In this paper, the authors considered the steady state response of a soil column to cyclic loading. The problem is illustrated in Figure 4.43.

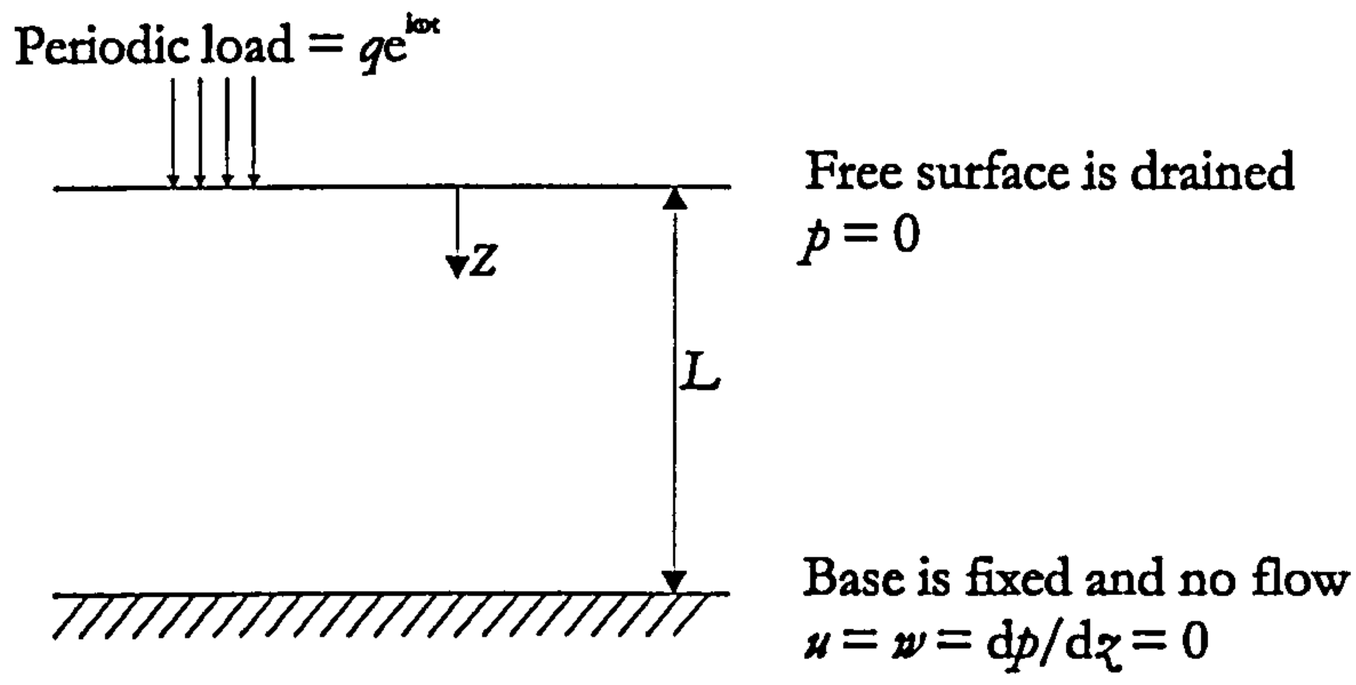

Figure 4.43: Soil layer subjected to periodic loading

The material behaviour is assumed to be coupled linear elastic and the initial pore pressure profile is hydrostatic. The full dynamic equilibrium condition for the soil column in terms of the soil and pore fluid displacements u and w is given by Equations 4.14 and 4.15. This represents the full Biot solution.

$$\frac{\partial^2 u}{\partial z^2} + \kappa \frac{\partial^2 w}{\partial z^2} = -\Pi_2 u - \beta \Pi_2 w \tag{4.14}$$

$$\kappa \frac{\partial^2 u}{\partial z^2} + \kappa \frac{\partial^2 w}{\partial z^2} = -\beta \Pi_2 u - \frac{\beta}{n} \Pi_2 w + \frac{i}{\Pi_1} w \tag{4.15}$$

where $\kappa = \dfrac{K_f/n}{D + K_f/n}$, $\quad D = \dfrac{E(1-\nu)}{(1+\nu)(1-2\nu)}$

$\Pi_1 = \left(\dfrac{2}{\beta\pi}\right)\dfrac{kT}{g\hat{T}^2}$, $\quad \Pi_2 = \pi^2 \left(\dfrac{\hat{T}}{T}\right)^2$

$\hat{T} = \dfrac{2L}{V_c}$, $\quad V_c = \dfrac{D + K_f/n}{\rho}$

And K_f = pore fluid compressibility

k = soil permeability

T = time period of loading

$\beta = \rho_f/\rho$ = fluid density / total density

n = porosity

V_c = velocity of compression wave in water

The solution of Equations 4.14 and 4.15 considers inertial forces and includes the effect of the acceleration of the pore fluid relative to the soil skeleton. This is equivalent to analysing the problem with the so called *u-w-p* theory discussed in Section 6 of Chapter 3. If these terms are ignored to be consistent with the *u-p* approximation implemented into ICFEP, the equations simplify to the following form.

$$\frac{\partial^2 u}{\partial z^2} + \kappa \frac{\partial^2 w}{\partial z^2} = -\Pi_2 u \tag{4.16}$$

$$\kappa \frac{\partial^2 u}{\partial z^2} + \kappa \frac{\partial^2 w}{\partial z^2} = -\beta \Pi_2 u + \frac{i}{\Pi_1} w \tag{4.17}$$

The solution to these equations will allow the dynamic coupled analyses to be validated. This problem will be returned to later. If all second-time derivatives are omitted from the derivation, the equations simplify further to:

$$\frac{\partial^2 u}{\partial z^2} + \kappa \frac{\partial^2 w}{\partial z^2} = 0 \tag{4.18}$$

$$\kappa \frac{\partial^2 u}{\partial z^2} + \kappa \frac{\partial^2 w}{\partial z^2} = \frac{i}{\Pi_1} w \tag{4.19}$$

These equations represent the quasi-static case equivalent to the simple consolidation problem and are independent of the parameter Π_2. With the application of the boundary conditions shown in Figure 4.43, the simultaneous partial differential equations can be solved to give expressions for *u* and *w*. The pore pressure response is then obtained from Equation 4.20.

$$p_f = \frac{K_f}{n}\left(\frac{\partial u}{\partial z} + \frac{\partial w}{\partial z}\right) \tag{4.20}$$

The following parameter values were chosen for the closed form solution:

κ	β	n	V_c
0.973	0.333	0.333	1000 m/s

Table 4.3: Parameters for the closed form solution of a soil column subjected to a periodic load

For the finite element analysis to be equivalent to the closed form solution the parameters given in Table 4.4 were used.

E (N/m^2)	ν	ρ (kg/m^3)	ρ_f (kg/m^3)	K_f/n	L (m)	Load q (Pa)	T (s)
67500	0.25	3.0	1.0	2919000	10	100	6.283

Table 4.4: Parameters for the finite element analysis of the soil column subjected to a periodic load.

Using these values, the permeability of the soil can be determined from Equation 4.21 for any desired value of Π_1.

$$k = \frac{(\Pi_1)\pi\beta g\hat{T}^2}{2T} = 3.27\times10^{-4}\Pi_1 \tag{4.21}$$

The results of the ICFEP analysis are compared with the closed form solution for a range of Π_1 values in Figure 4.44.

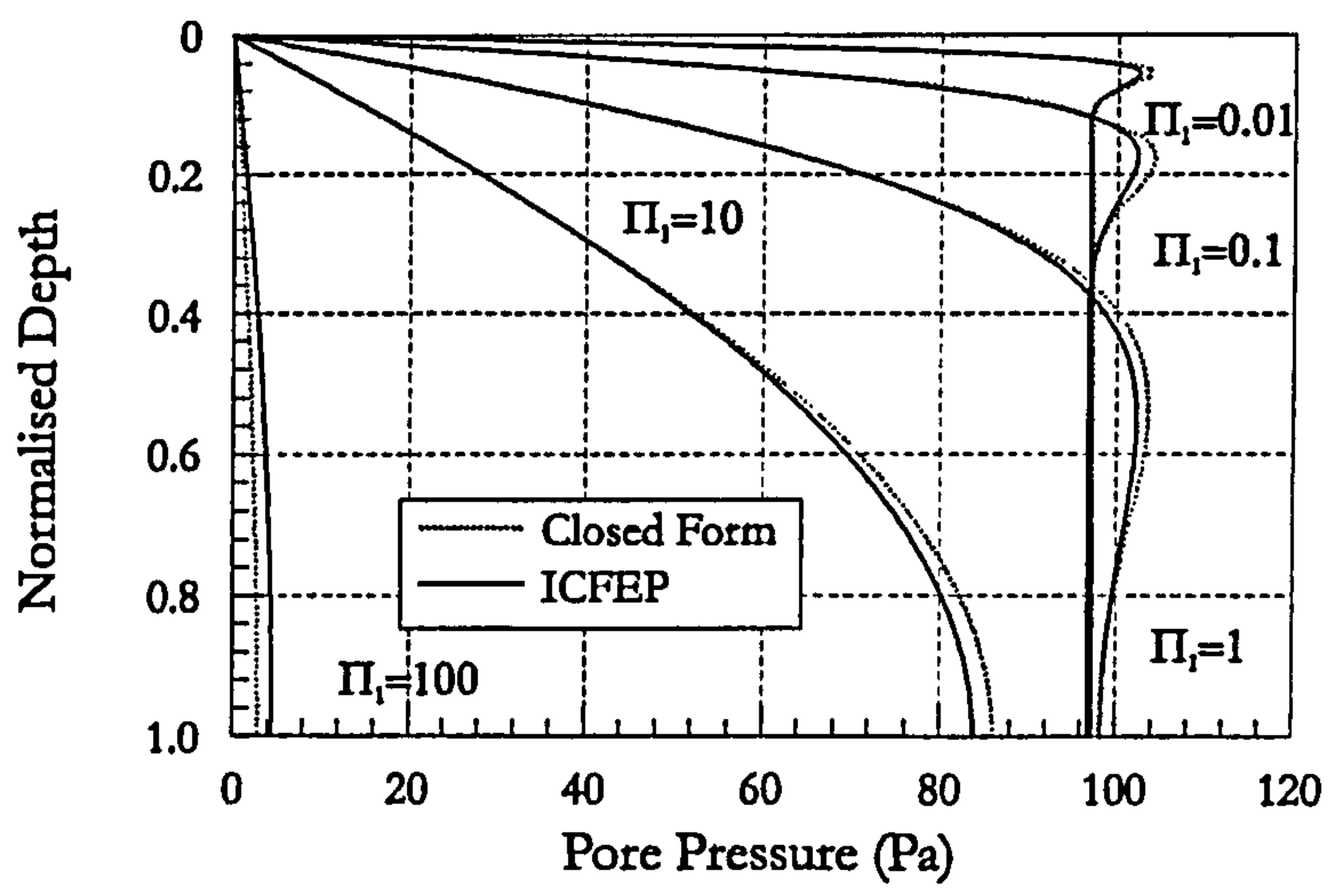

Figure 4.44: ICFEP results compared to closed form solution for different values of Π_1

The finite element results were taken after 20 cycles to ensure that a steady state condition was achieved. The pore pressures presented in Figure 4.44 are those present at the peak of the input wave. The finite element results are close enough to the closed form solution to consider the inclusion of the pore fluid compressibility validated. The small discrepancies can be attributed to the relatively course time step used in the analysis (equal to $1/20^{th}$ of the input frequency) and the assumption made in the closed form solution that the porosity of the soil remains constant during the cyclic loading. ICFEP recalculates the porosity at the end of each increment which is theoretically more sound.

The same problem can now be used to further validate the Newmark method and ensure that the dynamic coupled behaviour is correctly modelled. The closed form solution must now revert back to the form given by Equations 4.16 and 4.17 to include the inertia terms. The solution is now dependent on both the parameters Π_1 and Π_2. The analysis arrangement and material properties are the same as before, except the time period of the loading is now obtained from Equation 4.22 and the soil permeability is obtained by satisfying Equation 4.23.

$$T = \pi \frac{\hat{T}}{\sqrt{\Pi_2}} \tag{4.22}$$

$$k = \frac{(\Pi_1)\pi\beta g\hat{T}^2}{2T} = 2.053\times10^{-3}\frac{\Pi_1}{T} \tag{4.23}$$

The results from the dynamic ICFEP analyses are compared with the closed form solution for a constant Π_1 value of 0.1 in Figure 4.45 and 1.0 in Figure 4.46. For comparison, the static solution for the given value of Π_1 is also shown. The results are again taken at the peak of the input loading cycle and after steady state conditions had been achieved.

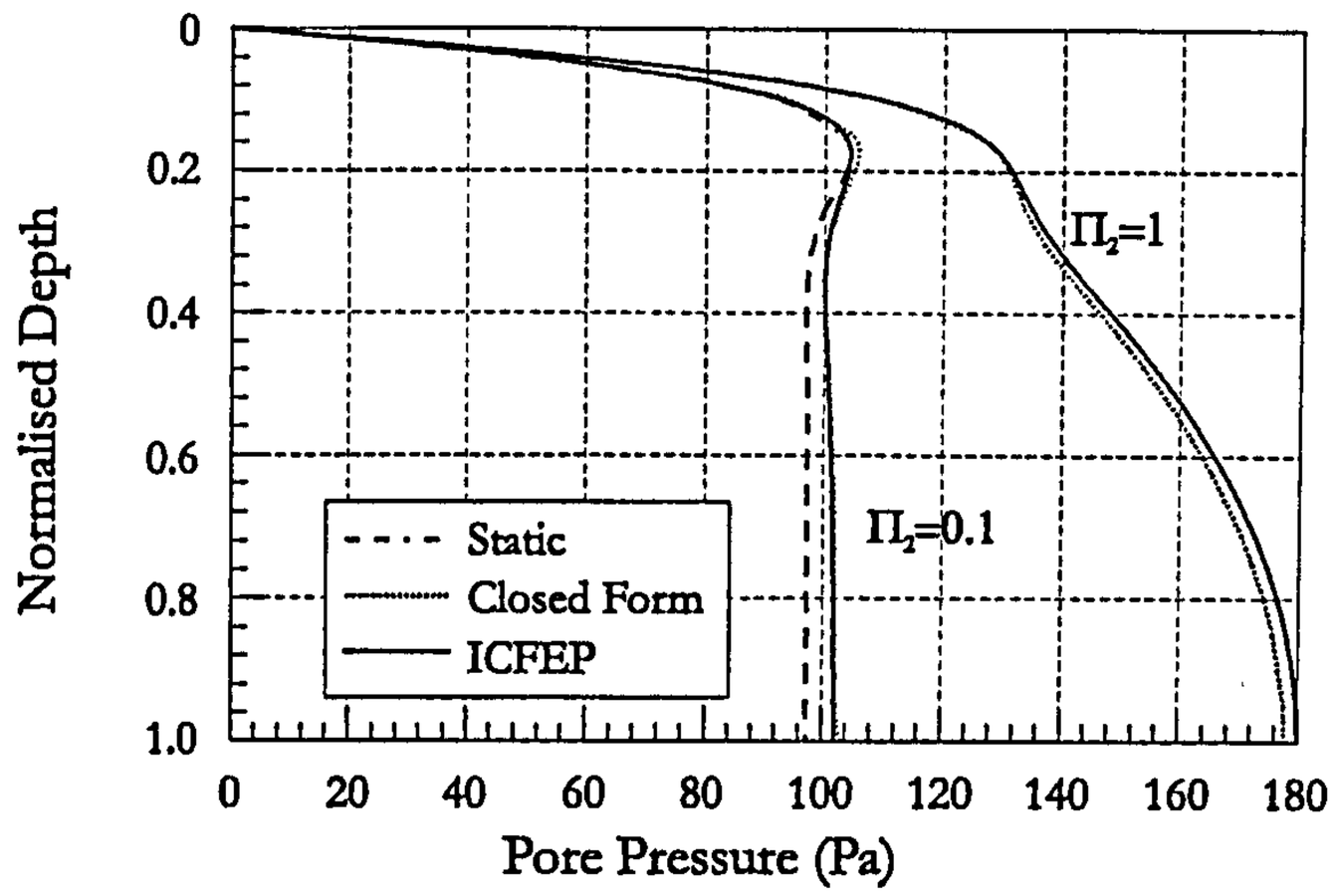

Figure 4.45: Validation of dynamic coupled analyses $\Pi_1 = 0.1$

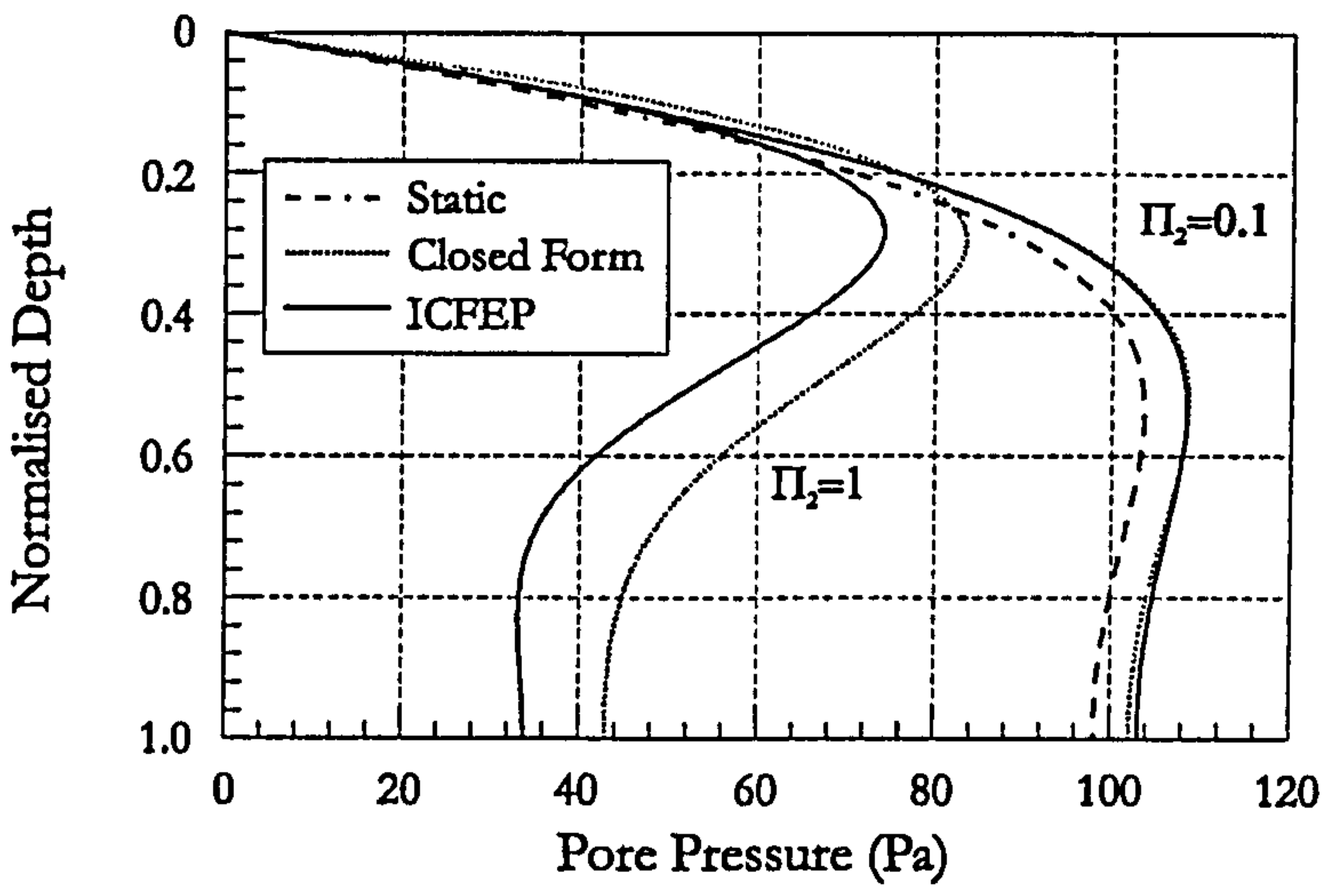

Figure 4.46: Validation of dynamic coupled analyses $\Pi_1 = 1.0$

The dynamic ICFEP analyses compare well with the closed form solution for all cases presented except for $\Pi_1 = \Pi_2 = 1.0$. This discrepancy can be attributed to the assumption made in the ICFEP implementation. As mentioned in Section 3.6 the inertia term that should be present in the equation of continuity for the pore fluid was not implemented as its inclusion renders the final system of equations non-symmetric. The decision was justified by the observation made by Chan (1988) that this term only becomes significant when the assumption of the *u-p* approximation was no longer applicable. Figure 4.47 is taken from Zienkiewicz *et al.* (1980) and shows the range of values of Π_1 and Π_2 over which the *u-p* approximation is valid.

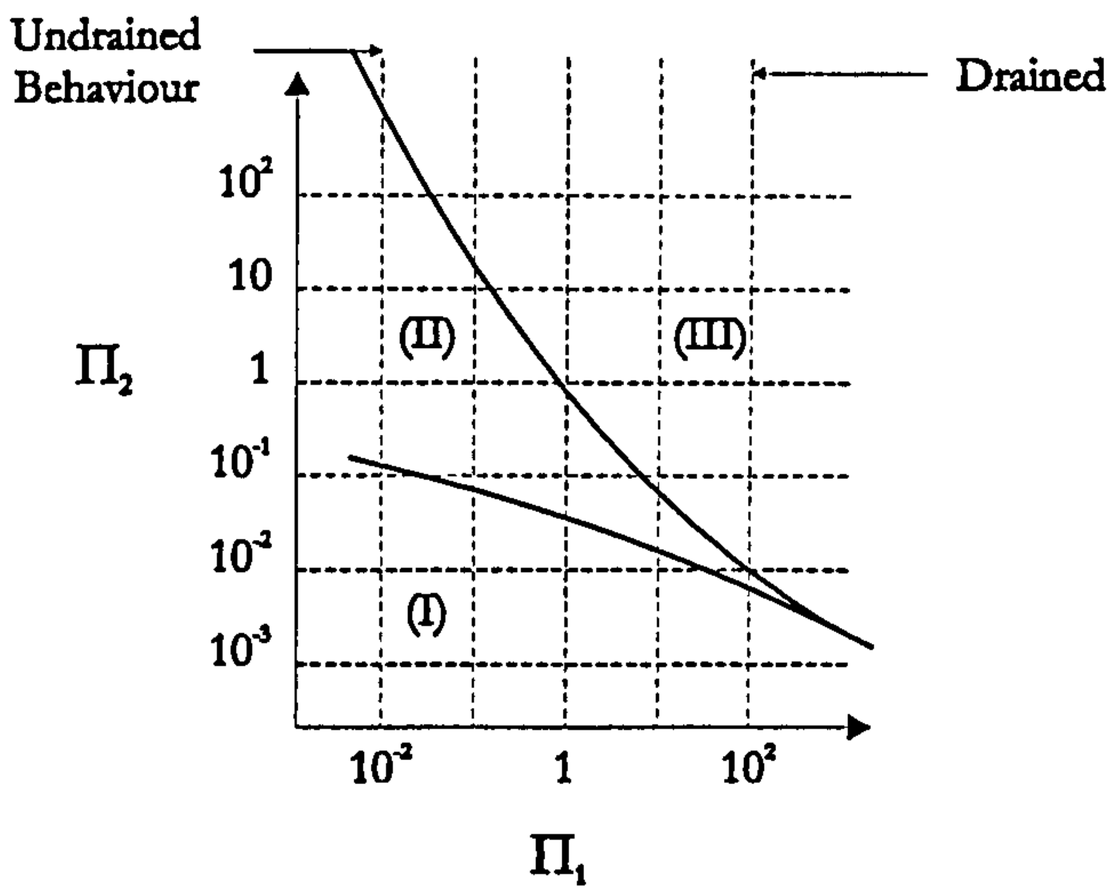

Figure 4.47: Zones of applicability of various assumptions (after Zienkiewicz *et al.* (1980))

Zone I represents very slow events in which a static consolidation analysis is valid. Zone III represents very fast events in which only the full *u-w-p* theory is applicable and zone II represents the intermediate region in which inertia forces are important but the *u-p* approximation is still valid. The case for which the ICFEP analysis did not match the closed form solution is on the boundary between zones II and III and therefore one would expect the inertia term in the equation of continuity for the pore fluid to be significant. This would explain why the results did not match. For the remaining cases that fall within zone II the results match well.

4.6 Conclusions

The changes that have been made to ICFEP to make dynamic analyses possible have been validated thoroughly both qualitatively and quantitatively. The simple cases of a compression wave travelling through a cylindrical bar and a shear wave through a one dimensional column have been used to check the velocity of propagation and to ensure the waves are transmitted and reflected in the correct ratios. Quantitative validation was achieved by analysing the problem of a spherical cavity subjected to an impulse loading, for which there is a known solution.

The results of the cavity analysis obtained by using the quadratic acceleration method led to the conclusion that the potential advantages to be made by using this scheme are lost due to its poor stability characteristics and its susceptibility to

numerical oscillations. Overall, the original Newmark scheme was considered the most robust option and will therefore be used for all future analyses.

A reduced static version of the closed form solution to a soil column subjected to a periodic loading given by Zienkiewicz *et al* (1980) was used to validate the inclusion of pore fluid compressibility in the equation of continuity. The *u-p* approximation form of the full dynamic closed form solution was used to validate dynamic coupled analyses. The findings of Chan (1988) regarding the non-inclusion of the inertia term in the pore fluid equation of continuity were confirmed.

In addition to validating the program some fundamental features of dynamic finite element analyses have been demonstrated. For example the importance of the ratio of element size to wavelength and how numerical damping can be used to eliminate spurious numerical oscillations.

Chapter 5:

LABORATORY MEASUREMENT OF SMALL STRAIN STIFFNESS

5.1. Introduction

The use of non-linear elastic soil models, incorporating stress and strain level dependent stiffness, in finite element analyses has increased considerably over recent years. Numerical investigations have shown that accurate modelling of the stiffness degradation of soils with stress and strain is vital in reproducing geotechnical features, such as the deformation of a retaining wall or the settlement trough above a tunnel excavation. The manner in which the stiffness of soil changes with stress and strain has been the subject of much research over the years. It is now recognised that the shear stiffness of a soil degrades with increasing strain level. At very small strains the soil is assumed to behave linear-elastically with a constant shear modulus (so called G_{max}). At a certain strain level, which depends on soil type, the shear modulus starts to reduce from its maximum value, and the behaviour becomes non-linear. The shape of the soil stiffness degradation curve is often assumed to be an *S* shape, which reduces to a small value at large strains, as shown in Figure 5.1.

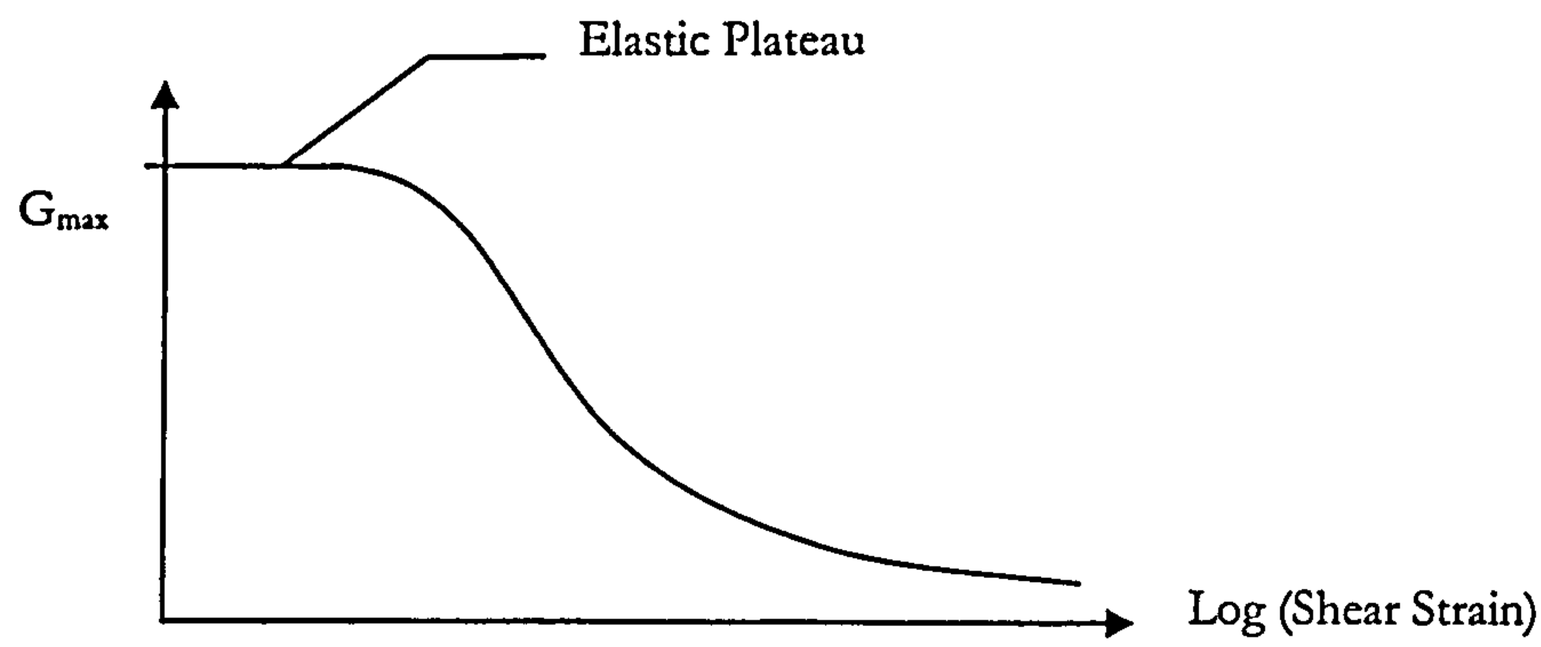

Figure 5.1: Schematic representation of stiffness against strain curve

Many soil models have been developed to try to capture this characteristic of soils. The small strain stiffness model of Jardine *et al.* (1986) is an example of an empirical model in which an equation is fitted to experimental data. The models of Al-Tabbaa and Wood (1989), Simpson (1992) and Stallebrass and Taylor (1997) are examples where a more theoretically sound elasto-plastic framework is adopted to try and incorporate the change in soil stiffness.

Whilst the development of local instrumentation in laboratory testing has allowed the stiffness degradation to be mapped, the measurement of G_{max}, the soil stiffness on the elastic plateau, is still beyond the resolution of most laboratory instrumentation. The first section of this chapter will discuss two options that are available for measuring the elastic stiffness of a soil, namely the resonant column device and piezoelectric transducers. The second part of the chapter will focus on the characteristics and main drawbacks associated with bender element tests which use the most common piezoelectric transducer. In the final part of the chapter the results from dynamic finite element analyses will be presented, along with some recommendations for the interpretation of bender element tests.

5.2. Laboratory Techniques

5.2.1 Resonant Column Test

The resonant column test is commonly used in the laboratory to measure the small strain elastic stiffness of soils. After a soil sample has been prepared and consolidated, a cyclic torsional or axial force is applied by means of an electromagnetic loading system. The frequency is initially set to a low value, and gradually increased. The frequency at which the strain amplitude reaches a maximum must correspond to the fundamental frequency of the sample. The shear modulus can be related to this fundamental frequency by considering the geometry of the sample. Consider a cylindrical sample of height h, with a polar moment of inertia J, subjected to a harmonic torsional loading. The torque (T) at the top of sample is given by Equation 5.1.

$$T = GJ\frac{\partial\theta}{\partial z} = G\frac{I}{\rho}\frac{\partial\theta}{\partial z} \tag{5.1}$$

where J is the polar moment of inertia, I is the mass polar moment of inertia, G is the shear modulus, θ is the angular rotation of the sample, z is the height above the base of the sample and ρ is the material density for the soil specimen. This must be equal to the inertial torque of the loading system. If the mass moment of inertia for the loading system is I_0, the inertial torque is given by Equation 5.2.

$$T = -I_0 h\frac{\partial^2\theta}{\partial t^2} \tag{5.2}$$

By assuming that the rotations of the specimen are harmonic, these equations can be solved to find the rotation of the sample, θ. Full details of the mathematical derivation can be found in many texts, for example Kramer (1996), and will not be repeated here. The result is Equation 5.3, relating the natural frequency of the sample, ω_n, to the shear wave velocity, v_s.

$$\frac{I}{I_0} = \frac{\omega_n h}{v_s}\tan\frac{\omega_n h}{v_s} \tag{5.3}$$

Assuming the soil sample to be an unbounded elastic medium, it is a simple matter to find the shear modulus from Equation 5.4.

$$G = \rho v_s^2 \tag{5.4}$$

The main disadvantage of the resonant column test is the relative high cost and complexity of the equipment. Considerable alterations need to be made to a standard piece of laboratory equipment before it can be used for resonant column testing, and thus the apparatus that are commonly used are dedicated solely to this purpose. However, they are particularly useful for obtaining dynamic soil properties that may be needed for basic earthquake engineering calculations. As the strain level is directly controlled during a test, the dynamic stiffness degradation curve can be mapped by obtaining the natural frequency of the sample at different strain levels. The damping ratio can also be found by allowing the sample to vibrate freely and then measuring the logarithmic decrement of strain amplitude. Whilst damping in soils is often approximated as being viscous, that is proportional the bodies velocity,

the damping measured in a resonant column test would relate to hysteretic damping and would therefore be strain level dependant. This implies that the level of damping present in the freely vibrating resonant column test would change as the amplitude of the vibration reduced, hence resulting in a non-unique value for damping if the logarithmic decrement method where used.

5.2.2 Bender Element Tests

The use of bender elements to measure the elastic small strain stiffness of soils was first described by Shirley and Hampton (1977). Each bender element is made up of two oppositely polarised pieces of piezoelectric material bonded together back to back. The reason for the choice of this material is that when a voltage is applied to it, depending on the materials polarity, it will either contract or expand, and similarly when it expands or contracts it produces a voltage. Therefore if a voltage is applied to both sides of the bender element, one side will lengthen while the other will shorten. This in turn will cause the bender element to flex in one direction, and then in the opposite direction when the voltage is reversed as shown in Figure 5.2

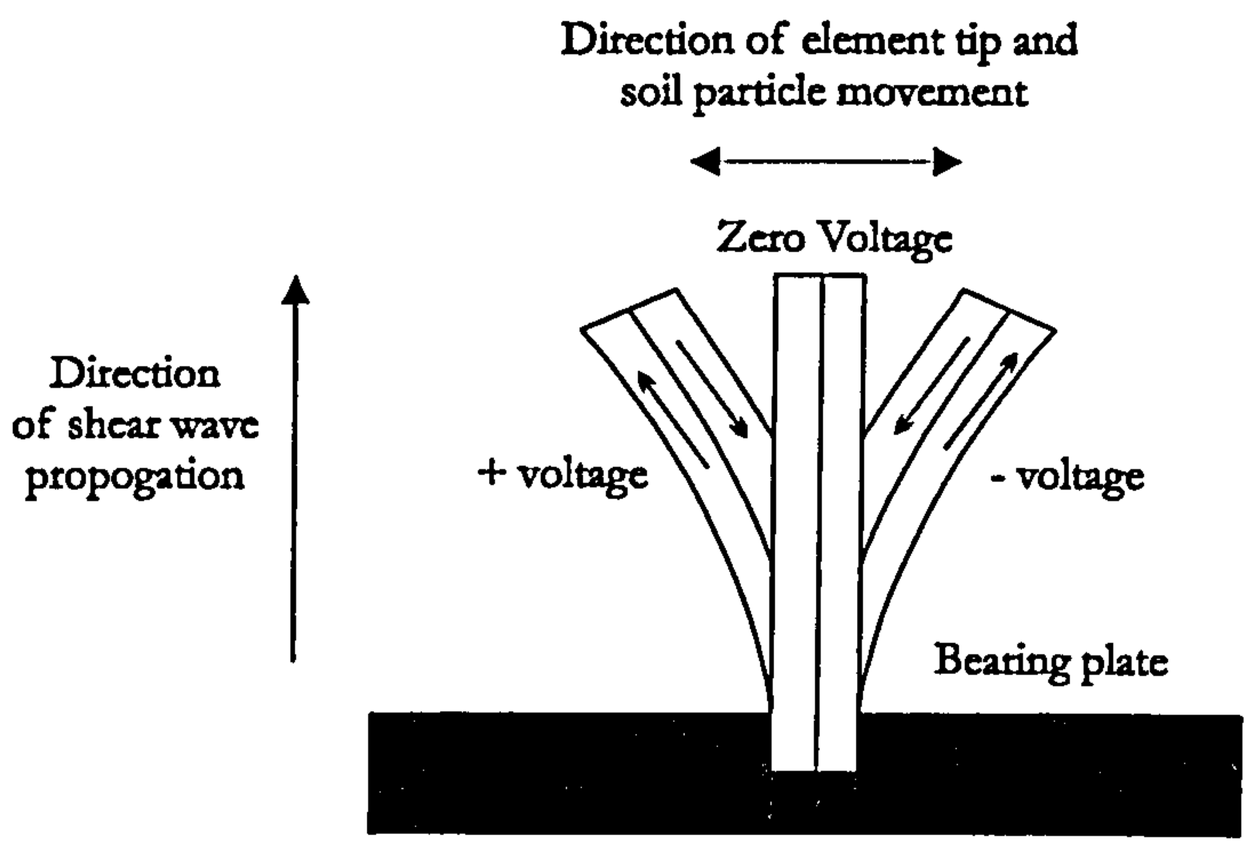

Figure 5.2: Piezoelectric bender element (after Kramer (1996))

The motion of the bender element initiates a shear wave to propagate through the soil sample. When the shear wave reaches another bender element some distance away, it causes it to flex and thus producing a voltage. This output signal can be captured on an oscilloscope and the travel time determined by measuring the time difference between the input and the output signals. From this the shear wave

velocity can be found by dividing the travel distance by the travel time and then G_{max} can be calculated using Equation 5.4. The principal advantage that bender elements have over a resonant column test is that they can be incorporated into a variety of testing devices, and hence the shear modulus can be measured during different soil tests. They are most commonly incorporated into triaxial samples, with a bender element placed in the top and the bottom platens, although they have been used in oedometers as well (Thomann and Hryciw 1990). Another advantage of bender elements over a resonant column test is that the anisotropy of soil stiffness can be investigated, by locating bender elements on two vertical and opposite sides of a sample as well, and initiating a shear wave laterally.

5.2.3 Other Dynamic Soil Tests

Bender elements are not the only piezoelectric devices used to measure the small strain stiffness of soils. Brignoli *et al.* (1996) compared the performance of three different ceramic transducers, namely a compression transducer, a bender transducer (or bender element) and a shear plate transducer.

The first of these is designed to initiate a compression wave to propagate through the soil sample. A schematic representation of the layout is shown in Figure 5.3.

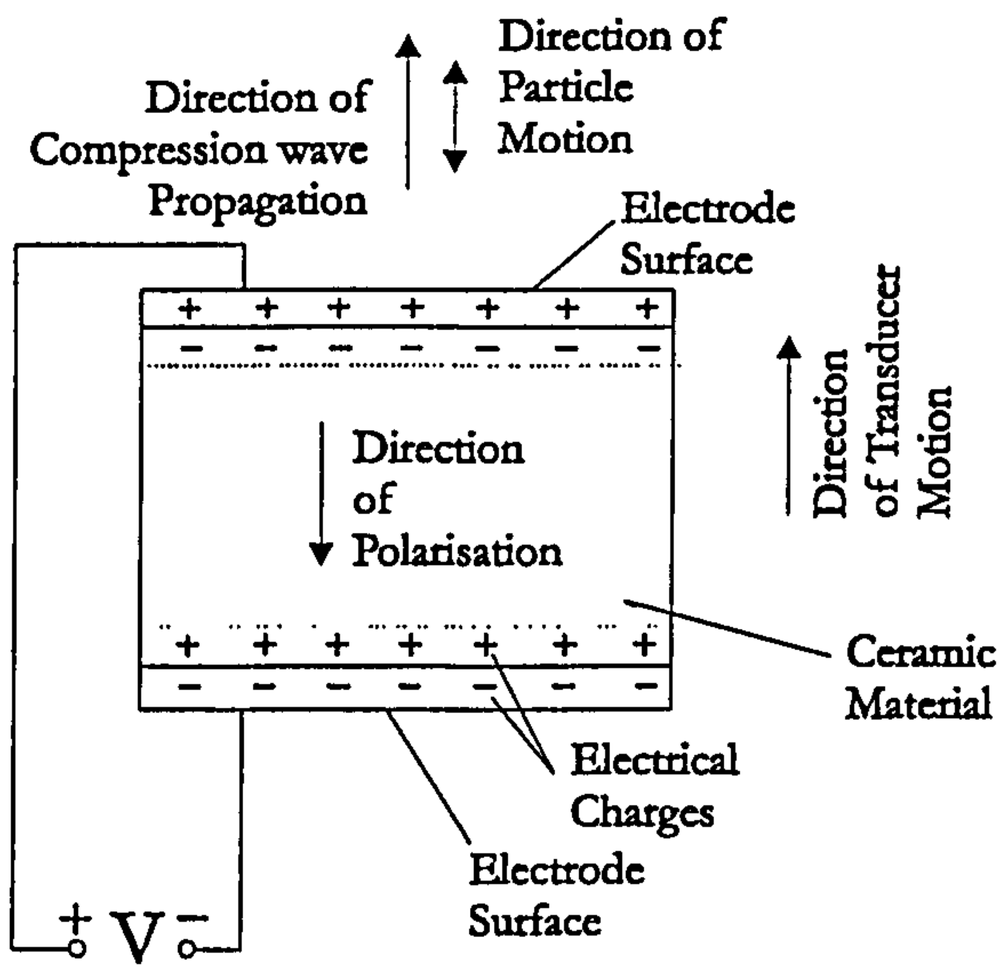

Figure 5.3: Compression Transducer (after Brignoli *et al.* (1996))

In a similar fashion to the bender elements, a compression transducer is placed in the top and bottom platens of a triaxial cell. A voltage is applied to the transmitting

transducer to initiate a compression wave to travel through the sample. The arrival of the compression wave is then taken from the output signal of the receiving transducer. The velocity of the compression wave can then be calculated from the travel time and the travel distance. The calculation is complicated as two compression wave velocities exist for all materials. The first is associated with constrained compression, were no lateral deformation perpendicular to the direction of the wave propagation can occur. The compression wave velocity, is related to the elastic material properties by Equation 5.5.

$$V = \sqrt{\rho \frac{E(1-\nu)}{(1+\nu)(1-2\nu)}} \tag{5.5}$$

where E is the Young's modulus

ν is the Poisson's ratio

If unconstrained conditions apply then the compression wave velocity is given by Equation 5.6.

$$V = \sqrt{\frac{E}{\rho}} \tag{5.6}$$

Brignoli *et al.* (1996) reported that Vaghela and Stokoe (1995) had shown that with compression transducers located at the centre of the platens of a triaxial cell, the results typically related to the generation of constrained compression waves. However, the main reason compression transducers have not achieved the same level of popularity as bender elements is that most soil specimens are tested in saturated conditions and compression waves travel faster through the pore water than through the soil skeleton.

The shear plate was one of the first piezoelectric transducers used to measure the shear wave velocity of soil samples in the laboratory. It was first described for this purpose by Lawrence (1963, 1965), although since then it has received little attention. A typical arrangement is shown in Figure 5.4.

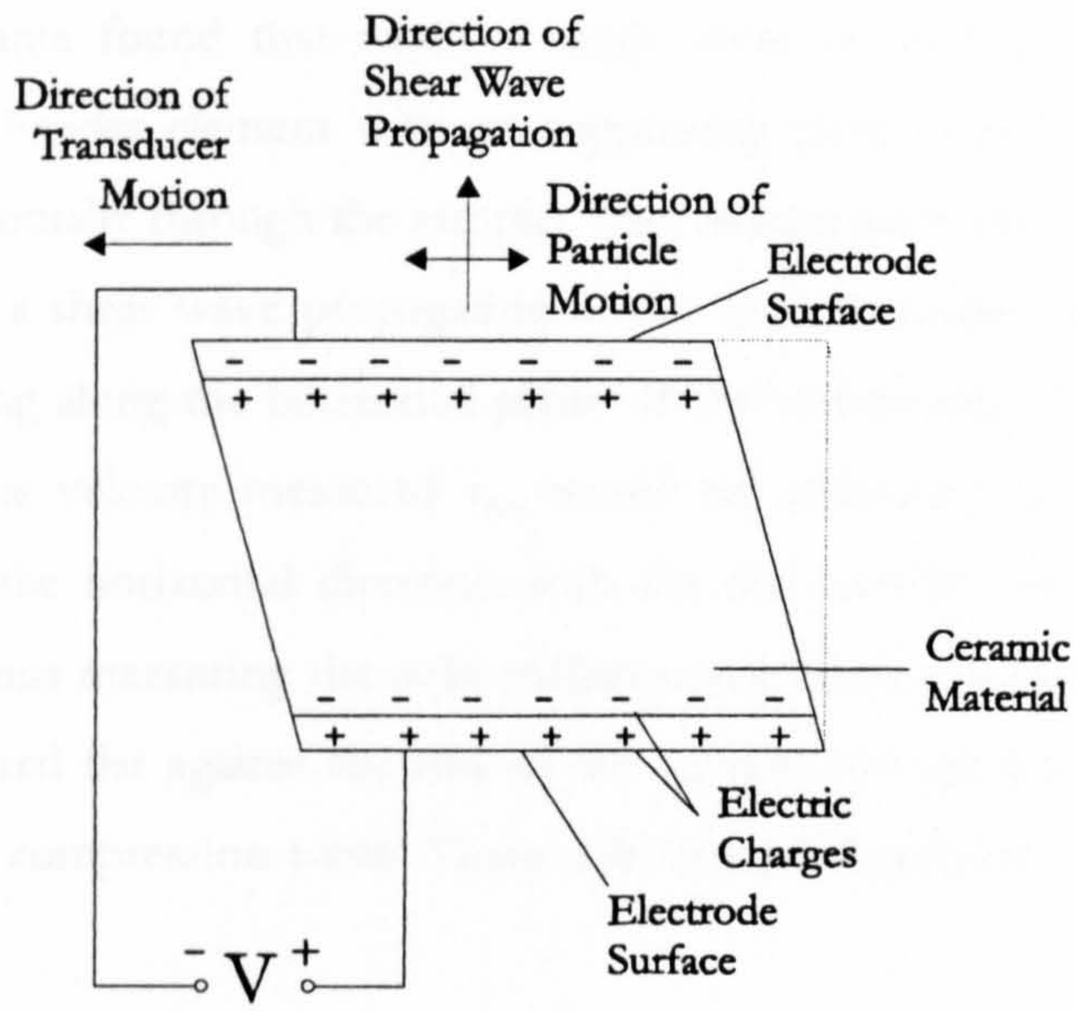

Figure 5.4: Shear Plate Transducer (after Brignoli *et al.* (1996))

The principles are similar to the bender element and compression transducers techniques described previously. One transducer is placed in the top platen and one in the bottom platen of a triaxial cell, although neither of them protrude into the sample. The application of a sinusoidal voltage to the transmitting transducer initiates a shear wave to propagate through the sample. The arrival of this shear wave then excites the receiving transducer and an output voltage is recorded. The shear modulus, G_{max} can then be calculated in the same manner as described in the bender element section using the shear wave velocity. The principal advantage of shear plates over bender element transducers is that they are totally non-invasive. This is an important consideration when testing undisturbed samples or soils with large aggregates.

5.2.4 Measuring Anisotropy with Piezoelectric Devices

By using a combination of bender elements and compression transducers Fioravante (2000) measured the five constants required to completely model a cross anisotropic elastic material. As well as installing bender elements and compression transducers in their traditional location in the top and bottom platens, Fioravante developed a novel method of transmitting shear and compression waves across a sample. By simply adhering the bender element to the side of the sample, with the transducer pointing outwards in the same plane as the sample's horizontal cross

section, Fioravante found that when a single cycle of voltage was applied, the rocking of the bender element with its supporting plate caused a shear wave to propagate horizontally through the sample. This arrangement gives the velocity, v_{hh}, associated with a shear wave propagating in the horizontal direction with the soil particles vibrating along the horizontal plane. If the bender element is then rotated through 90°, the velocity measured v_{hv}, would be associated with a shear wave propagating in the horizontal direction with the soil particles vibrating along the vertical plane, thus measuring the soils stiffness anisotropy. Similarly, if the bender element is adhered flat against the side of the sample, the application of a voltage would initiate a compression wave. These different configurations are illustrated in Figure 5.5.

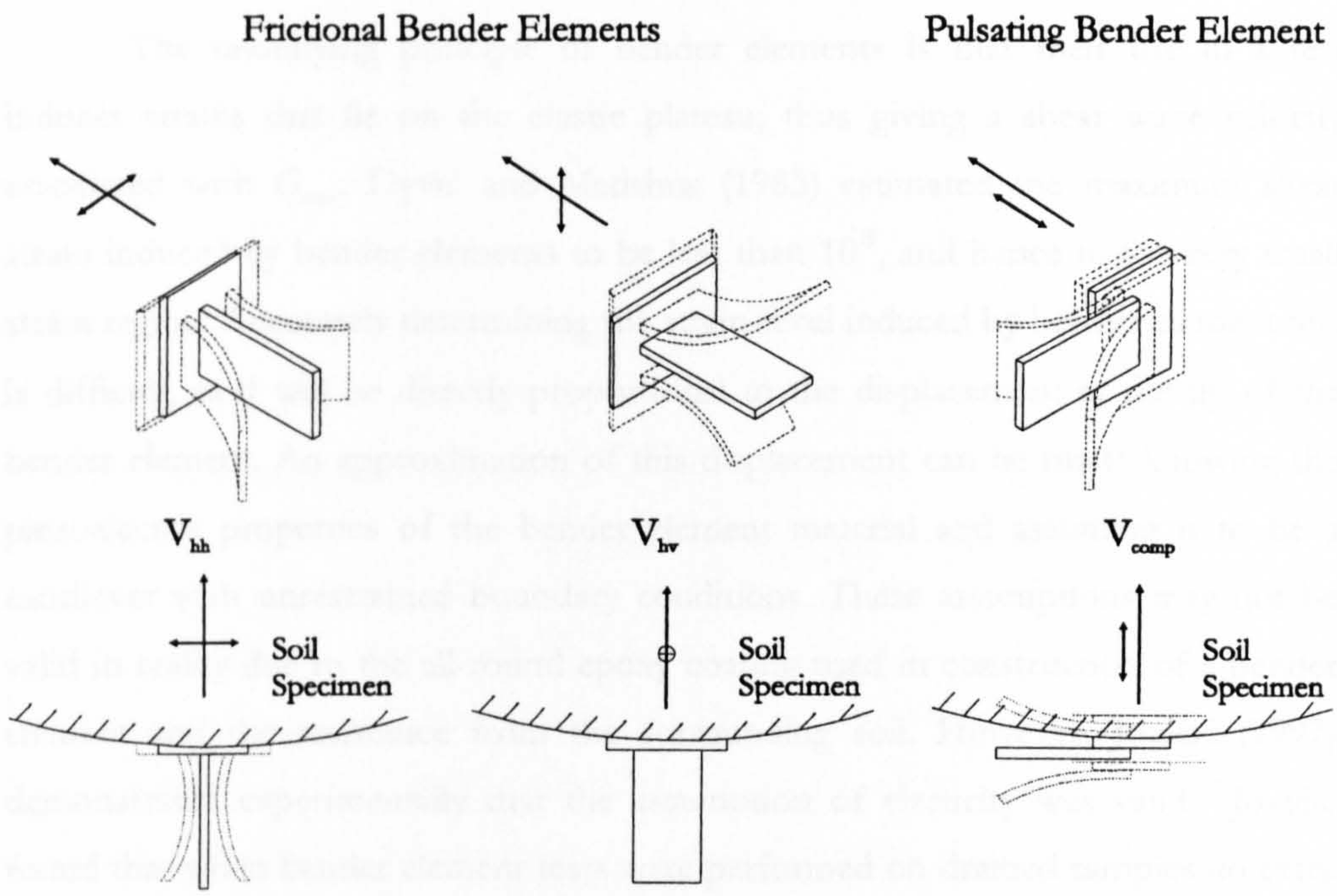

Figure 5.5: Arrangement of External Piezoelectric Transducers to Measure Soil Anisotropy (after Fioravante (2000))

The principal advantage that these so called frictional and pulsating bender elements have over embedded traditional bender elements in the sides of soil samples is that they are non-intrusive and, as mentioned previously, this is an important consideration when testing undisturbed samples.

5.3 Analysis of Bender Element Tests

5.3.1 Introduction

Although in principle the use of bender elements appears to be straight forward, in practice their use can lead to ambiguous and uncertain results. This has led to a great deal of research focused on the principles and assumptions underlying their use. The next section of this chapter will summarise the most important work published on the use of bender elements.

5.3.2 Strain Level

The underlying principle of bender elements is that their use in a test induces strains that lie on the elastic plateau, thus giving a shear wave velocity associated with G_{max}. Dyvic and Madshus (1985) estimated the maximum shear strain induced by bender elements to be less than 10^{-5}, and hence in the very small strain region. Accurately determining the strain-level induced by bender element test is difficult, as it will be directly proportional to the displacement at the tip of the bender element. An approximation of this displacement can be made knowing the piezoelectric properties of the bender element material and assuming it to be a cantilever with unrestrained boundary conditions. These assumptions may not be valid in reality due to the all-round epoxy coating used in construction of a bender element and the resistance from the surrounding soil. However, Jovičić (1997) demonstrated experimentally that the assumption of elasticity was valid. Jovičić found that when bender element tests were performed on drained samples no extra volume change was observed or when they were performed on undrained samples no build up of excess pore pressures was found. Further numerical analysis of this assumption is required.

5.3.3 Wave Travel Distance

The main task when using bender elements is to calculate the shear wave velocity. Once the travel time between the transmitting and receiving bender element has been measured, it should be a simple matter to calculate the shear wave velocity, by diving the travel distance by the travel time. However, when bender

elements were first used to measure the small strain stiffness of soils, there was some doubt as to what should be taken as the true travel distance. Intuitively one would take the distance between the bender element tips, although some practitioners thought it may be the full height of the sample. Laboratory tests on samples of reconstituted Speswhite kaolin of different heights were conducted by Viggiani and Atkinson (1995) to investigate what should be taken as the travel distance. For different confining pressures the sample length was plotted against the travel time. Their results are shown in Figure 5.6.

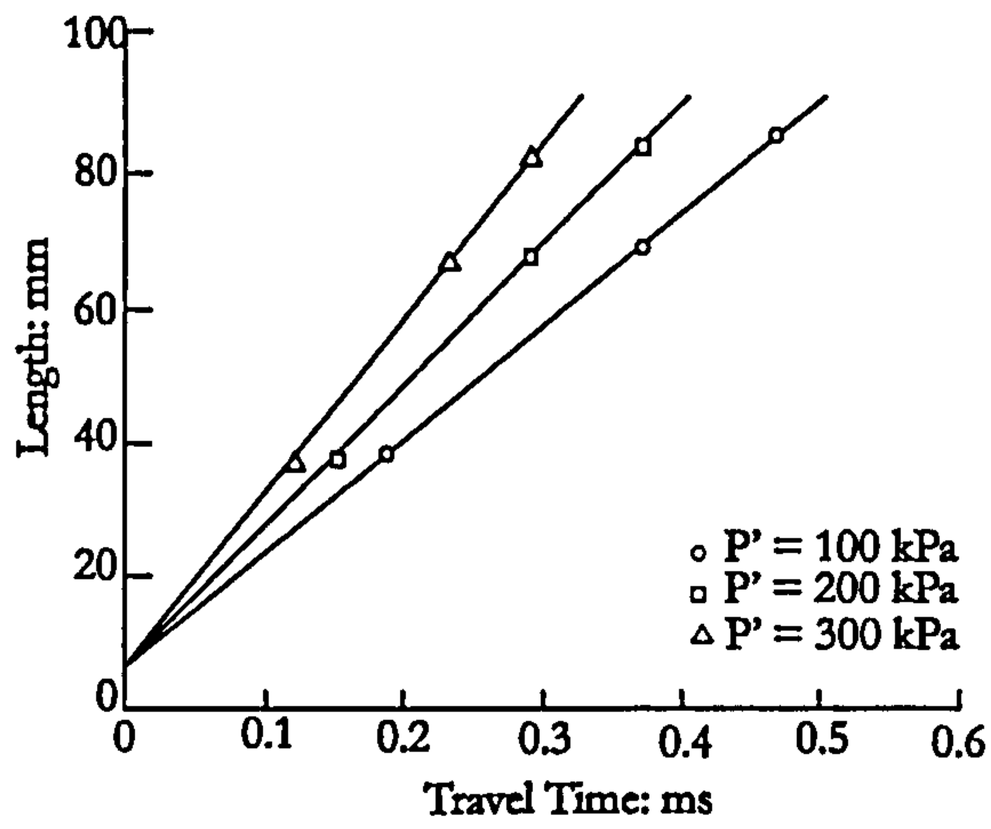

Figure 5.6: Relationship between travel time and sample length (after Viggiani and Atkinson (1995))

The bender elements used for these laboratory tests were 3 mm long. The intercept on the sample length axis is at 6 mm (i.e. twice the bender element length), implying that the travel distance should be taken as the tip to tip distance, not the total sample height. This conclusion was also reached by Dyvic and Madshus (1985) and Brignoli *et al.* (1996).

5.3.4 Wave Travel Time

The next parameter that needs to be ascertained is the travel time of the shear wave from the transmitting to the receiving bender element. In practice, the clarity of the arrival signal is greatly influenced by the shape of the transmitted signal. In early bender element tests the most popular input signals were either a step function or a square pulse. Tests performed by Viggiani and Atkinson (1995) demonstrated that using a square wave causes considerable distortion to the output

signal. They concluded that this was caused by the square wave being composed of a wide spectrum of frequencies and each component therefore having different dispersive qualities. The effect of the dispersion of the input wave is that each frequency will travel with a different velocity and hence the output signal will become blurred. The solution suggested by Viggiani and Atkinson to overcome this problem was to use a sine wave input which is made up of predominantly one frequency. The results using this signal type were considered superior, as the output signal more closely resembled the input signal.

Although using a sine wave does clarify the first wave arrival, commonly the output signal still differs in form from the input signal. The result from a typical bender element test is shown in Figure 5.7.

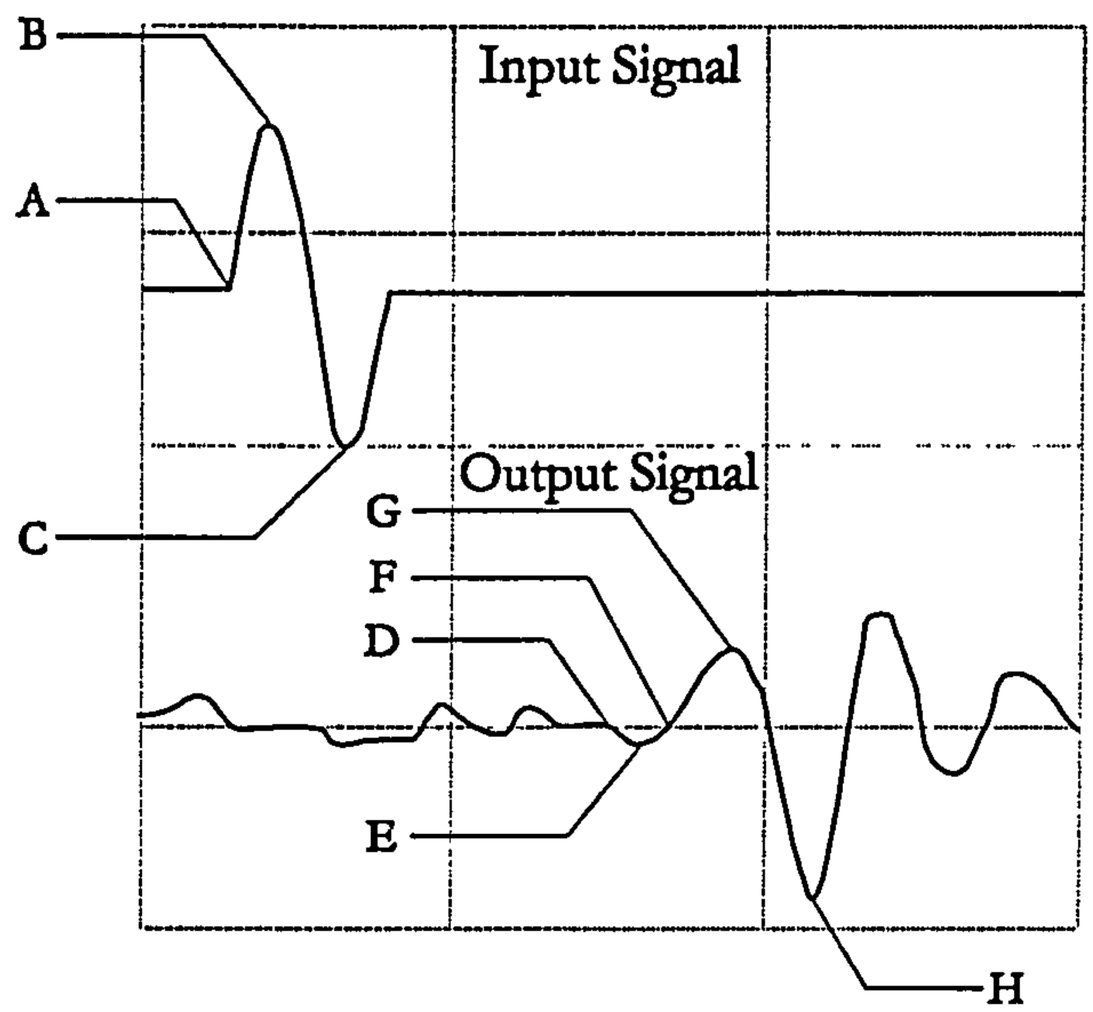

Figure 5.7: Typical input and output waves from bender element test

Identifying at which point the shear wave arrives is open to user interpretation. Several options for the travel time have been suggested in the literature. They include A-D, A-E, A-F, B-G or C-H. The problem arises due to a phenomenon called the near field effect. This is characterised by an initial deflection of the output signal before the significant motion of the receiving bender element, seen in the output wave in Figure 5.7 between points D and F. This has the effect of masking the true arrival of the first shear wave. The presence of a near field effect in bender element tests was first identified by Brignoli and Gotti (1992), and further investigated by Jovičić *et al.* (1996). In their paper, Jovičić *et al.* used the analytical

solution for a point source subjected to a transverse sine pulse in an infinite isotropic elastic medium, found by Sanches-Salinero *et al.* (1986), to demonstrate that even for this simplified case, the near field effect exists. The solution uses the Cartesian coordinate system shown in Figure 5.8. The input motion is described in an exponential form of a complex number $e^{i\omega t}$ where t is the time and ω the angular velocity. The point source is located at the origin and the input motion is prescribed in the X direction.

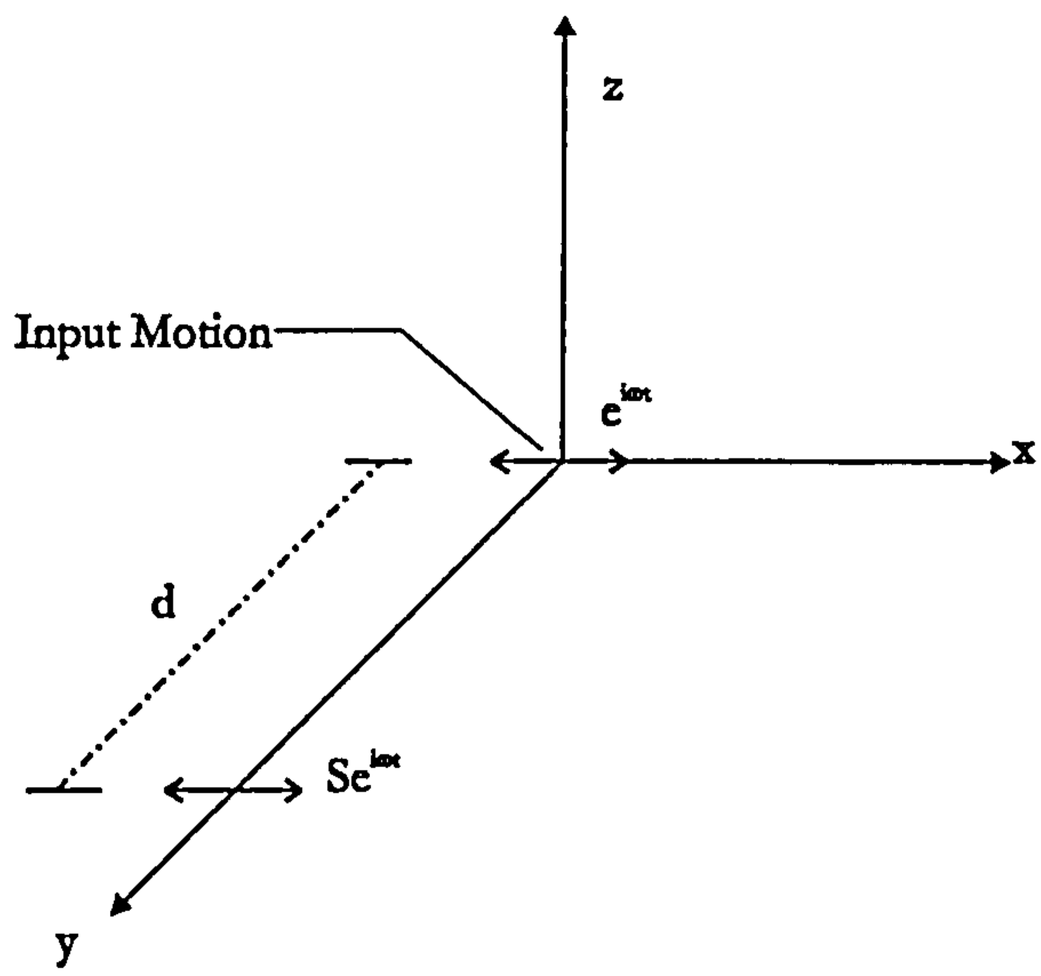

Figure 5.8: Notation for three-dimensional motion of points (after Jovičić *et al.* (1996))

The solution for the transverse motion S is given by Equation 5.7.

$$S = \frac{1}{4\pi\rho v_s^2}\Gamma \tag{5.7}$$

where v_s is the shear wave velocity, ρ is the material density and Γ is a function given by Equation 5.8 representing the geometric radiation of the wave.

$$\Gamma = \frac{1}{d}e^{-i(\omega d/v_s)} + \left(\frac{1}{i\frac{\omega d^2}{v_p}} - \frac{1}{\frac{\omega^2 d^3}{v_p^2}}\right)e^{-i(\omega d/v_s)} - \left(\frac{v_s}{v_p}\right)^2\left(\frac{1}{i\frac{\omega d^2}{v_p}} - \frac{1}{\frac{\omega^2 d^3}{v_p^2}}\right)e^{-i(\omega d/v_p)} \tag{5.8}$$

Equation 5.8 illustrates that the wave propagation is made up of three components. The first two travel with the velocity of a shear wave, v_s, whilst the third travels with

the velocity of a compression wave v_p. The salient features of the solution are the coefficients that appear before the exponential terms. For the first term this coefficient is proportional to $1/d$, however for the second and third terms the coefficients are proportional to a linear sum of $1/d^2$ and $1/d^3$. This means that they are only significant at small distances and are therefore termed the near field components, whilst the first term, because it is more significant at larger distances, is termed the far field component. Sanches-Salinero *et al.* expressed their results in terms of a ratio d/λ where d is the distance between the bender element tips and λ is the wavelength of the input signal, which Jovičić *et al.* (1996) later renamed R_d. The value of R_d gives the number of wavelengths that exist between the bender element tips and was found to control the degree of attenuation for each component of Equation 5.8. For low values of R_d the near field components were found to be significant at the monitoring point, while for high value their influence was minimal. This is illustrated by Figure 5.9 where the analytical solution is plotted against normalised time for R_d values of 1.0 and 8.0. T_a is the theoretical arrival time.

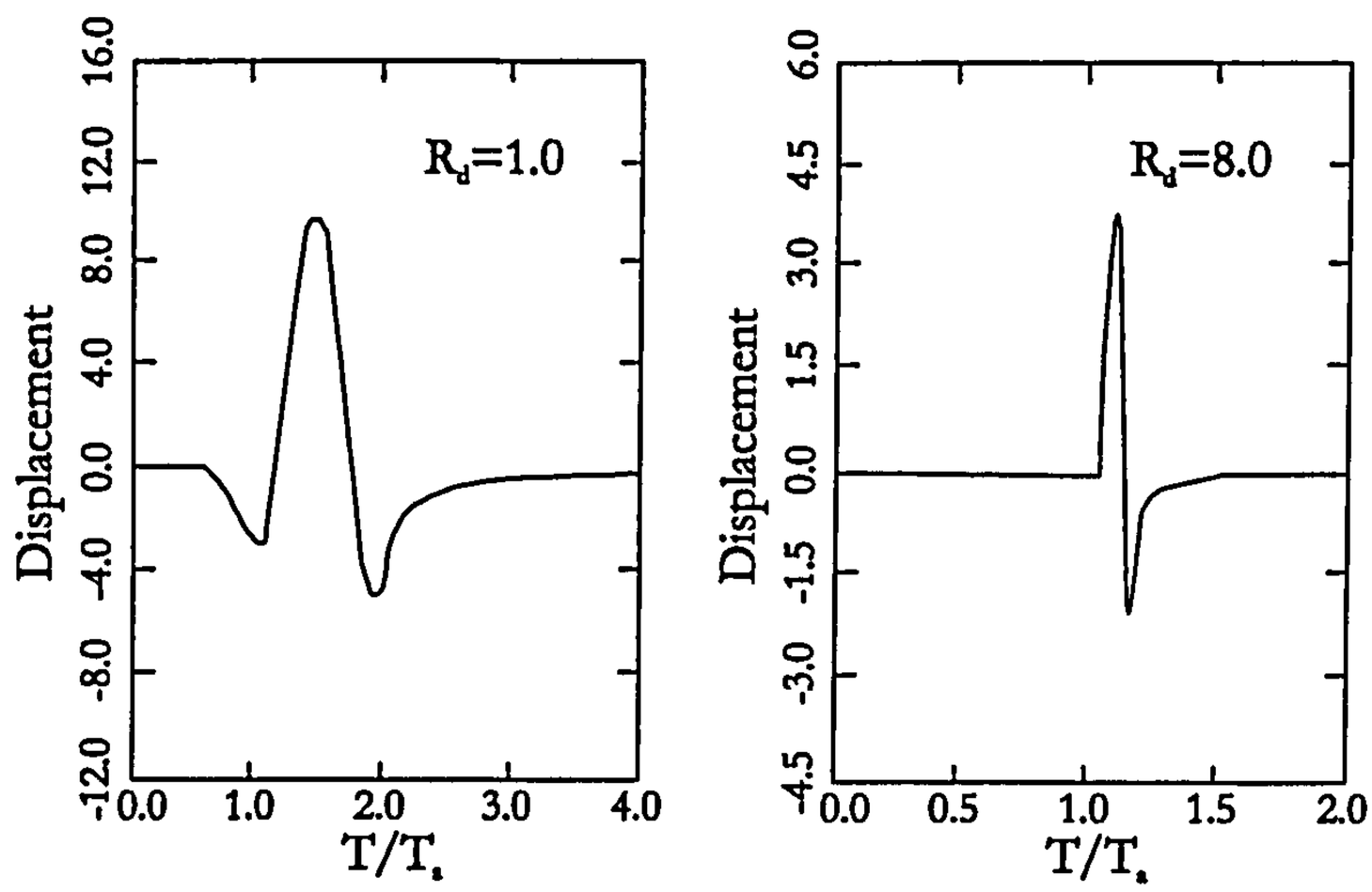

Figure 5.9: Analytical solution of the motion at the monitoring point (after Sanches-Salinero *et al.* (1986))

To validate the analytical solution with regard to the geometry of bender element tests, Jovičić *et al.* (1996) performed a series of experiments on Speswhite kaolin with a range of input frequencies chosen to give R_d values similar to those shown in Figure 5.9. The results clearly demonstrated that for the higher input frequency and hence the higher value of R_d, the near field effect is negligible and the shear wave

arrival clearer. Therefore to observe an obvious shear wave arrival from bender element tests and hence an accurate estimation of G_{max}, Jovičić *et al.* recommended that an input frequency should be chosen so as to give a high R_d ratio. In practice however this may not be possible when measurements are to be made in a relatively stiff material. When a high input frequency is used (as would be required in a stiff material), the transmitting bender element can pass through its original resting position and continue oscillating after the first cycle. This phenomenon is known as over-shooting. By using self monitoring bender elements Jovičić *et al.* (1996) were able to capture the phenomenon of overshooting in their experiments. By wiring part of the transmitting bender element as a receiver, the response of the transmitter to the input voltage can be measured. The experiments were carried out on a cemented granular soft rock, with a G_{max} of 2.5 GPa, at an effective confining stress of 200 kPa. At an input frequency of 2.96 kHz the output from the self monitoring bender element follows the input voltage. However, as the input frequency was increased to 29.6 kHz, the transmitting bender element was seen to overshoot its resting position. To overcome the apparent dichotomy of needing to use a high input frequency to eliminate the near field effect, whilst requiring a low enough input frequency to avoid the problem of overshooting, Jovičić *et al.* (1996) recommended using a distorted sine wave where the first peak is reduced in magnitude so as to cancel out the near field effect. By many experimentalists this solution is deemed unacceptable as it treats the symptoms of the problem rather than the cause.

5.3.5 Finite Element Analysis of Bender Element Tests

Whilst the Sanches-Salinero solution demonstrates the complexity of the wave forms that are generated from a point source, it still neglects the true geometry of a bender element test. No closed form solution exists for the propagation of a wave generated by a plate in a cylindrical sample and therefore researchers have used numerical methods to investigate the accuracy of the bender element technique. Jovičić *et al.* (1996) used the finite element package SOLVIA 90 to check the influence of the boundary conditions when compared to the Sanches-Salinero solution. The soil was modelled as isotropic and undrained, with linear elastic material properties chosen to represent a normally consolidated Speswhite kaolin at an effective confining stress of 200 kPa. The analyses presented by Jovičić *et al.*

assumed plane strain conditions and used a mesh with 200 elements, although some mention is made of a full three dimensional simulation which qualitatively gave similar results. The input motion of the bender element was prescribed as a transverse sinusoidal displacement at a point representing the tip of the transmitting bender element. The output signal was then taken as the transverse displacement of the receiving bender element. Two analyses were performed to compare with the Sanches-Salinero solution, one with a low R_d ratio of 1.1 and another with a high ratio of 8.1. The displacements of the monitoring points are plotted against the normalised time in Figure 5.10. For the case when R_d = 1.1 the near field effect is clearly present as a significant downwards deflection before the arrival of the true shear wave at a T/T_a value of 1.0. When R_d = 8.1 the trace from the receiving bender element is smooth with no evidence of an initial downwards deflection.

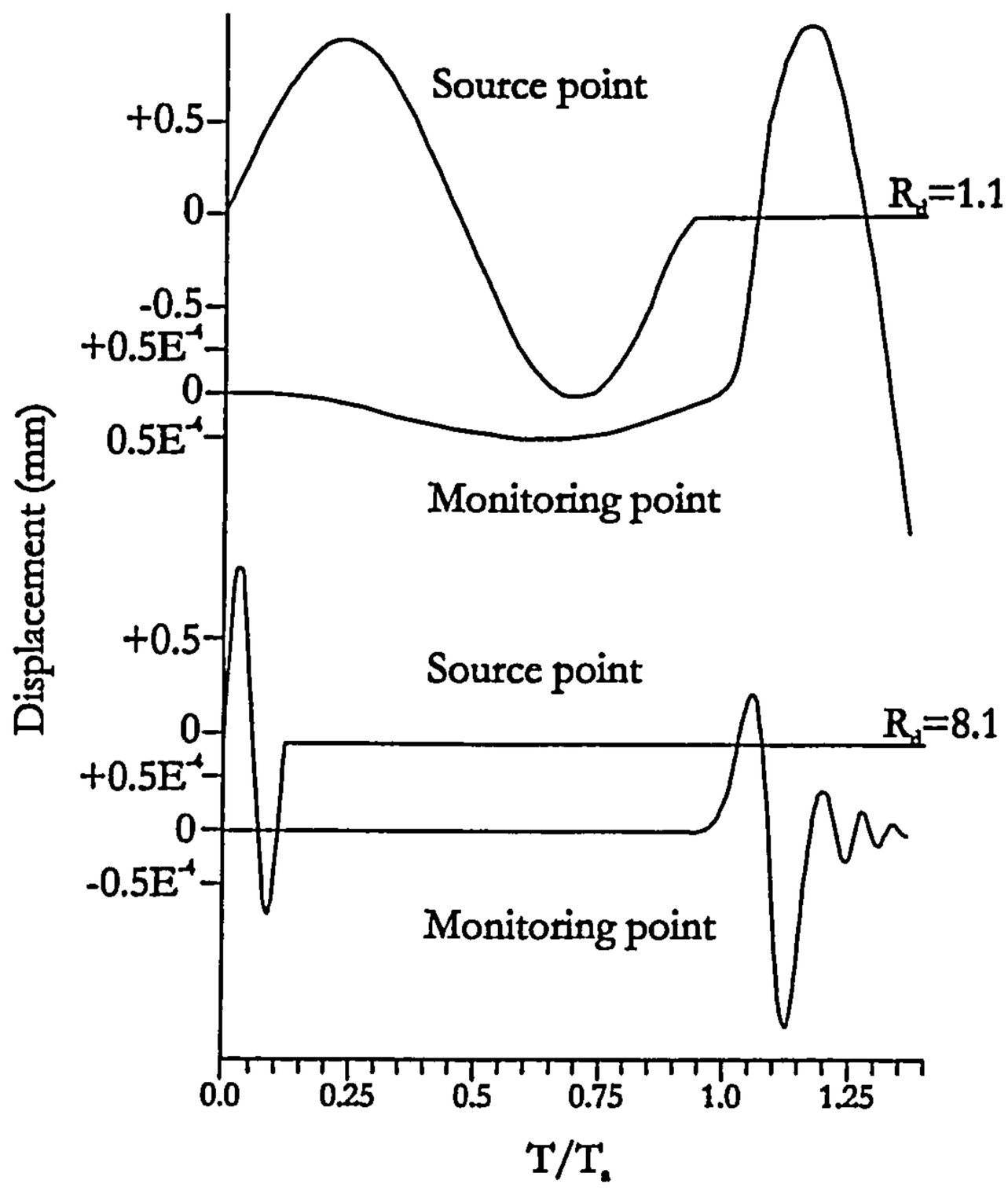

Figure 5.10: Finite element analysis of bender element test (after Jovičić *et al.* (1996))

From their studies Jovičić *et al.* concluded that the near field components of the wave propagation were responsible for the initial downwards deflection of the monitoring point as identified in the Sanches-Salinero solution, and it is this that is

responsible for the uncertainty surrounding the identification of the shear wave arrival.

Further numerical studies were undertaken by Arulnathan *et al.* (1998) to quantify the potential errors associated with some of the techniques proposed in the literature to calculate G_{max}. Two dimensional plane strain, linear elastic undrained finite element analyses using GeoFEAP (Bray *et al.* (1995)) were used to estimate the combined errors resulting from wave interference at the caps, the relationship between the input signal and the transmitted wave, the non-one-dimensional wave travel and near field effects. One significant difference between these analyses and those of Jovičić *et al.* (1996) is that the input motion was prescribed as a single sine wave bending moment uniformly distributed along the length of the transmitting bender element. It was felt that whilst the complex interaction between the input voltage and the displacement of the bender element was difficult to model, the application of a bending moment was more realistic than prescribing a displacement at the tip of the bender element. The geometry was assumed to be that of a triaxial sample, 72 mm high and 36 mm wide. On the top and bottom boundaries of the mesh the displacement was fixed in both horizontal and vertical directions, whilst the sides were considered stress free. The mesh was relatively fine with 1818 four noded elements, with the benders represented by beam elements. A parametric study was then carried out for a range of bender element lengths and input frequencies. The shear wave velocities were calculated using some of the techniques proposed in the literature. These are summarised as follows:

1. Measuring the time difference between the first peak of the input wave and the first peak of the output wave.
2. Measuring the time difference between the first trough of the input wave and the first trough of the output wave.
3. Measuring the time difference between the first shear wave arrival and its second arrival after reflecting from the top cap.
4. Measuring the time lag at which the cross correlation coefficient of the input and output waves is a maximum.
5. Measuring the time difference between the first and second maximums in the cross correlation plot.

Points 4 and 5 derive from a method first suggested by Viggiani and Atkinson (1995) to remove the ambiguity surrounding the identification of the shear wave arrival. In this method the input signal is shifted by a series of time steps, and the cross correlation coefficient calculated for each. These are then plotted against the time lag, and the point at which the maximum correlation is found corresponds to the shear wave travel time (details of the cross correlation calculation can be found in section 5.5.3.8).

The results of the analysis showed a considerable scatter. The example given by Arulnathan *et al.* was for a bender element length of 4.0 mm and an excitation frequency of 2.5 kHz. The travel time determined using option 2 overestimated the shear wave velocity by 6%, whilst option 5 underestimated it by 3.1%. The rest of the results lied within this range. The reasons for these discrepancies were given as follows by Arulnathan *et al.*:

1. The output signal from the receiving bender element is measuring a complex interaction of incident and reflected waves.
2. The transfer function relating the physical wave forms to the measured electrical signals introduces significant phase or time lags that are different at the transmitting and receiving benders.
3. Non-one-dimensional wave travel and near field effects are not accounted for.

The recommendation made by Arulnathan *et al.* was to use a range of excitation frequencies and interpretation methods for the first set of tests carried out on a new soil. This should help the user gain insights into which of these were most appropriate for the given soil.

5.3.6 Further Studies of the Sanches-Salinero Solution

Clear guidance therefore is still required for the use and interpretation of laboratory based dynamic soil tests. The question of what input frequency should be used and what should be taken as the point of shear wave arrival still remains unanswered. The result of the cross borehole work by Sanches-Salinero *et al.* (1986) was a proposed frequency limit when using field based seismic soil testing. The limits proposed where as follows.

$$2 < r\frac{f}{v_s} = R_d < 4 \tag{5.9}$$

Where r is the distance between the measurement points, f is the input frequency and v_s is the shear wave velocity of the soil. The lower limit is proposed to avoid measurements in the near field of the source and the upper limit is introduced to ensure that the signal will be strong enough to be measured. The fact that these limits were proposed for use in large scale field measurements has not deterred experimentalists from applying them to laboratory based seismic soil testing. Arroyo *et al.* (2002) reported that while some researchers found the proposed limits to be satisfactory for avoiding near field effects (Jovičić *et al.* (1996) and Brignoli *et al.* (1996)), others have found it difficult to ever obtain a clear shear wave arrival (Gajo *et al.* (1997), Pennington (1999) and Kuwano (1999)). These apparent problems and the need for a definitive, objective criterion for determining shear wave travel time from any type of input signal led Arroyo *et al.* (2002) to look in more detail at the often quoted Sanches-Salinero solution. The work is based on Stokes' fundamental solution describing the movements generated by a unit impulse force isolated in an infinite elastic medium. By breaking the solution down into its constituent parts, Arroyo *et al.* could analyse the behaviour of each component for different values of the ratio R_d. The mathematics involved is complicated and will not be repeated here, although the results are of interest. The fundamental property of a soil that bender element tests are designed to measure is the bulk shear wave velocity. As previously mentioned this can then be used to calculate the shear modulus of the soil. What one actually measures in the laboratory is the group shear wave velocity of the soil and this is only equal to the bulk shear wave velocity for true one-dimensional boundary and loading conditions. The influence of the near field effect and hence the non-one-dimensionality of the loading condition on the group velocity is illustrated by Figure 5.11.

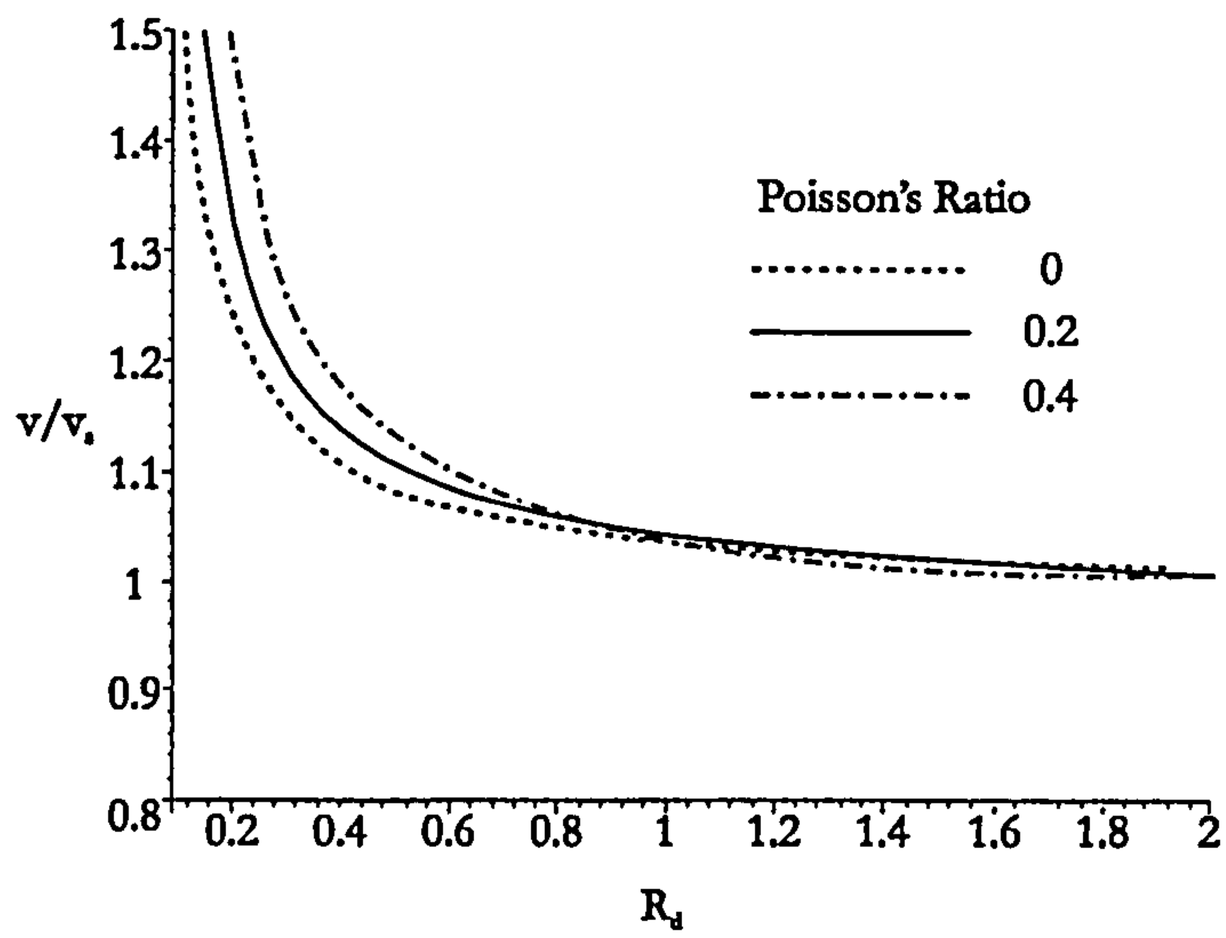

Figure 5.11: Ratio of Group Velocity and Bulk Velocity Against R_d (after Arroyo *et al.* (2002))

It is clear that as the ratio R_d increases the group wave velocity tends to the bulk shear wave velocity (that is the ratio v/v_s tends to unity). Acceptable results are found if R_d is greater than 1.6, the difference between the measured group velocity and the bulk velocity of the soil will remain below 5%.

In practise this criterion for avoiding the near field effect may not be sufficient. As mentioned previously, the input frequency required to satisfy this criterion for stiff soils may cause the bender element to overshoot its resting position. Arroyo *et al.* (2002) suggested that to overcome this problem, a criterion is needed that can be used to identify the arrival of the far field component for any input type at any input frequency. Figure 5.12 shows the near and far field components calculated separately using the Stokes solution. The input motion used in this analysis is not the standard single sine wave but the distorted sine wave recommended by Jovičić *et al.* (1996) with an R_d ratio of 2.0. The scale for the near field component has been exaggerated to make it clearer.

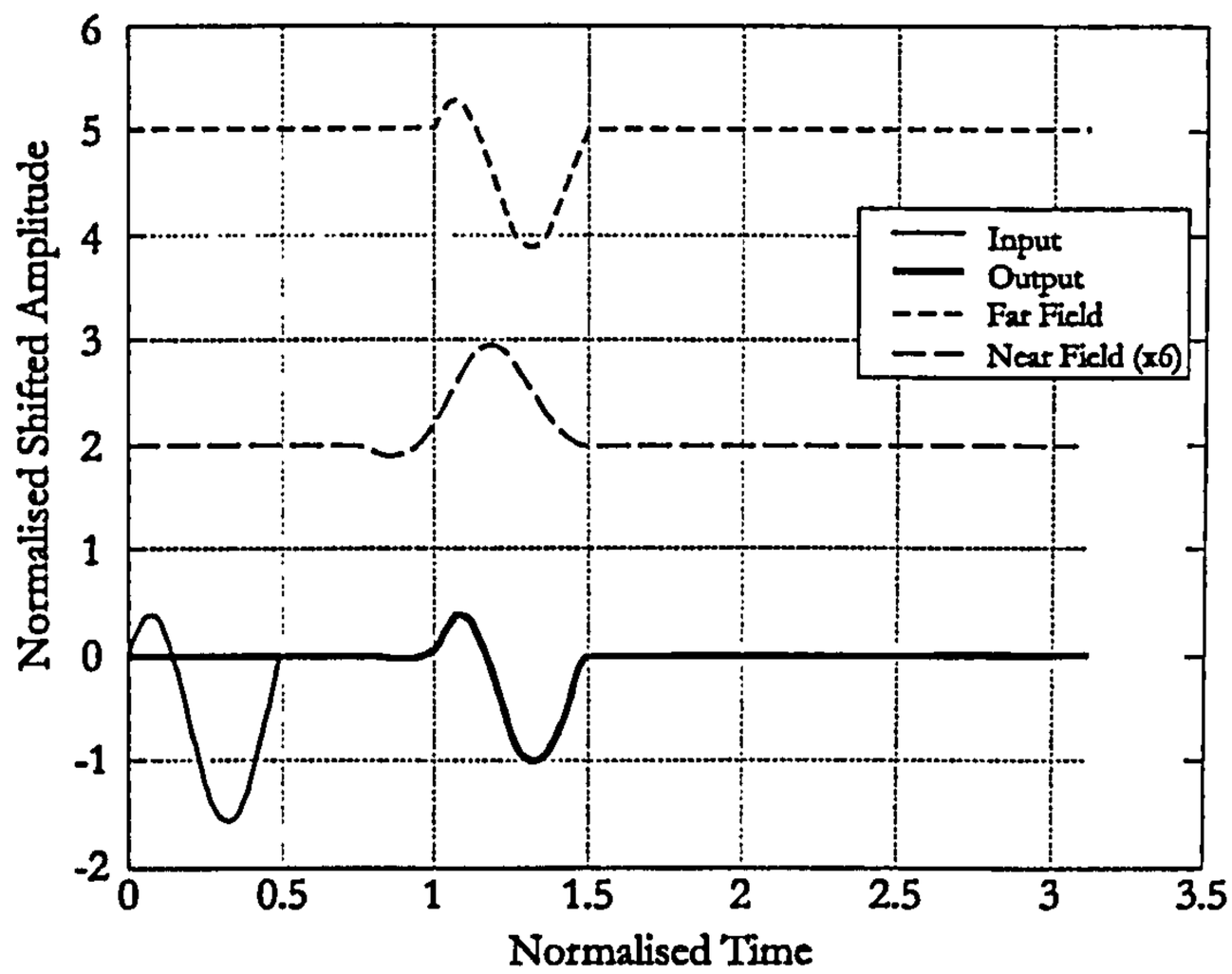

Figure 5.12: Stokes Propagation of a distorted Sine Wave (after Arroyo *et al.* (2002))

Figure 5.12 shows that the far field component is a time shifted version of the original, arriving at the monitoring point at a time that corresponds to the bulk shear wave velocity (i.e. a normalised time of 1.0). The near field component is a time shifted and distorted version of the input wave, arriving before the far field component. The results when combined are similar to those shown if Figure 5.9 calculated by Jovičić *et al.* (1996). Arroyo *et al.* suggested that an objective criterion for identifying the arrival of the far field wave could be to ignore deviations in the output wave below some fraction of the maximum amplitude. For example in Figure 5.12, ignoring peaks below 10% of the maximum would be successful, giving the first arrival corresponding to the bulk shear velocity (at a normalised time of 1.0). Arroyo *et al.* went on to determine the height of the near field component as a percentage of the maximum signal height for a range of input shapes and R_d ratios. The results are shown in Figure 5.13.

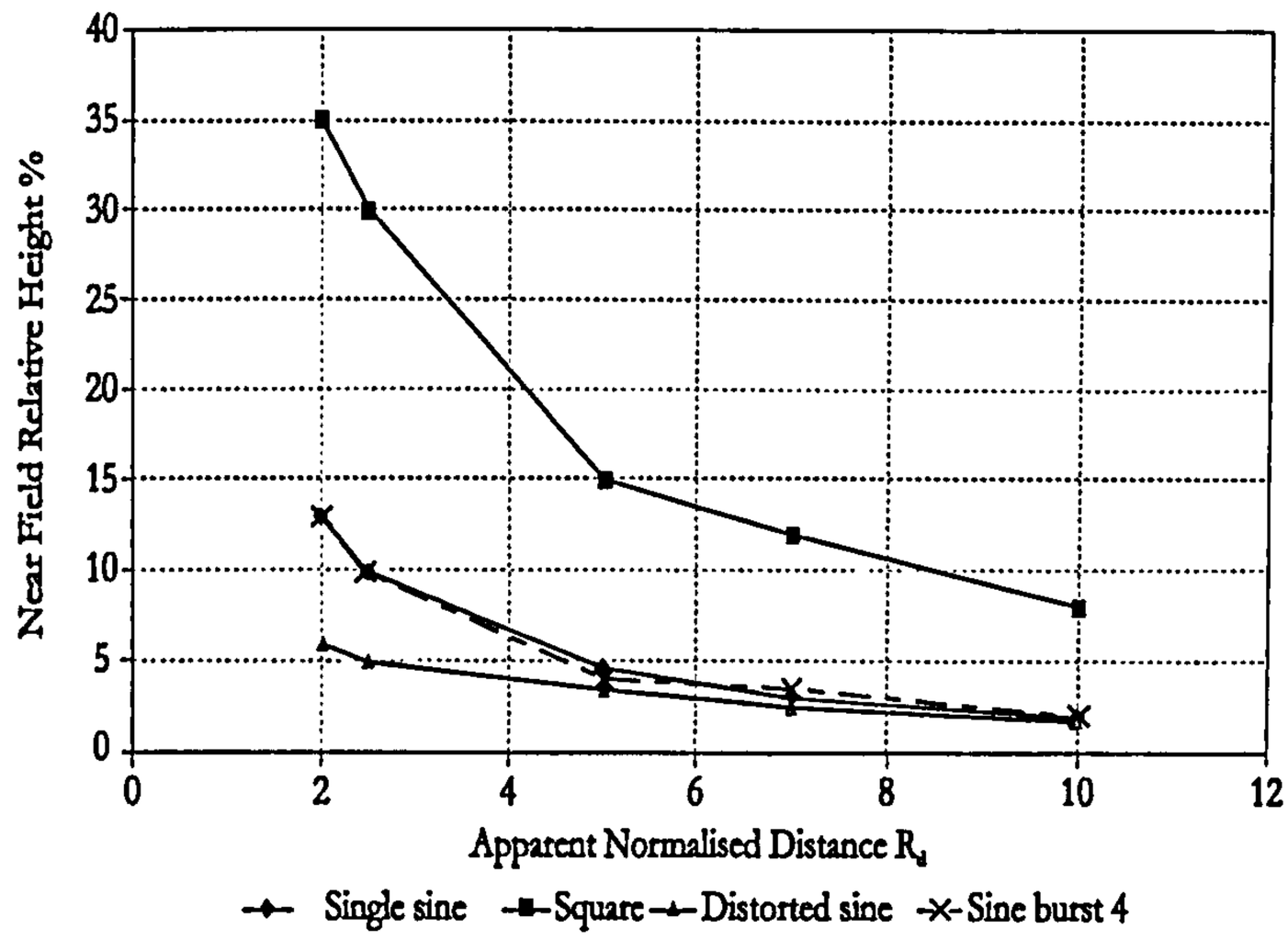

Figure 5.13: Near Field Effect for Different Signal Types (after Arroyo *et al.* (2002))

It is clear that only the analyses using a burst of four sine waves gave a similar near field component to the single sine wave analysis. The square wave as expected gave a larger near field component whilst the distorted sine wave (or Jovičić shape) gave less. Although this implies that no unique observation criteria can be applied to all input shapes to distinguish the near and far field components, Arroyo *et al.* went on to apply those shown in Figure 5.13 to a series of bender element tests performed in Gault clay. The results are shown in Figure 5.14.

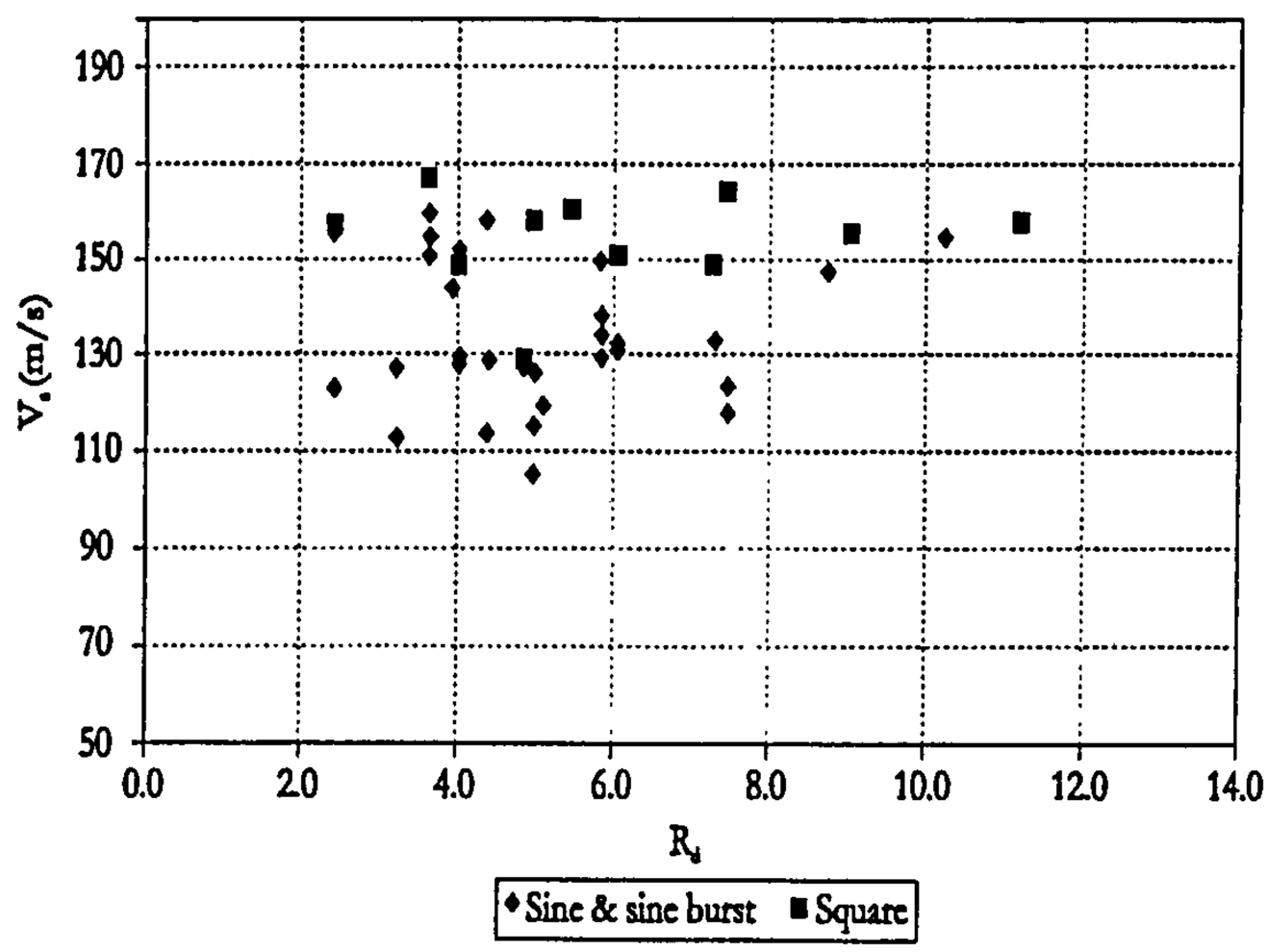

Figure 5.14: Influence of Near Field on First Arrival Estimate of V_s (after Arroyo *et al.* (2002))

The large scatter in the results illustrate that applying the criteria suggested by Arroyo *et al.* (2002) and shown in Figure 5.13 for identifying the far field component does not reduce the uncertainty in measuring the shear wave velocity. This led Arroyo *et al.* to conclude that the near field component is not wholly responsible for the ambiguity surrounding the use of bender element tests.

5.3.7 Inertial Coupling

There is clearly some feature of the laboratory tests that the numerical models have so far failed to capture. One possibility is the effect of inertial coupling. Gajo (1996) first illustrated this phenomenon by considering Biot's solution for a harmonic wave propagating in a fluid saturated linear elastic porous media (Biot (1941), (1956a), (1956b), (1962)). In Biot's theory, the soil skeleton and pore fluid are idealised as two continuous and superimposed phases which are coupled at three different levels: viscous, mechanical and inertial. Whilst the first two coupling terms are familiar to geotechnical engineers, the last is often ignored. It can be visualised by considering a rigid body accelerating through a fluid. A force must be applied to accelerate the mass of the body and an additional force must be applied to accelerate the mass of fluid set in motion by the body. The magnitude of the force generated by inertial coupling is small and only becomes significant when the level of viscous coupling is low. For example, for a soil that has a low permeability the viscous coupling will be high and relative movement between the soil skeleton and the pore fluid will practically be prevented. This will result in a low level of inertial coupling. If however the permeability is high, the relative movement between the pore fluid and the soil skeleton will be higher and hence so will the effects of inertial coupling. To examine the influence that inertial coupling has on the velocity of a wave propagating in a saturated media, Gajo used the analytical solution of a semi infinite layer of saturated sand subjected to a step load. The results demonstrated that inertial coupling reduces the velocity of both longitudinal and rotational waves. Gajo went on to conclude that accurate evaluation of inertial coupling is essential for a reliable interpretation of dynamic tests and that this subject requires further study for recommendations to be made. Modelling of inertial coupling is not possible with ICFEP at present. As described in Chapter 3, ICFEP utilises the simplified u-p approximation for modelling soil and pore fluid interaction. This does not include any inertial effects in the equilibrium equation for the pore fluid

and therefore inertial coupling is not included. To include inertial coupling would involve using the so called *u-w-p* formulation described by Zienkiewicz *et al.* (1999). The reasons for not choosing this option were discussed in Chapter 3, although any development in this direction in the future may allow the phenomenon of inertial coupling to be investigated fully.

5.4 Continuously Cycled Bender Element Tests

5.4.1 Introduction

An alternative method of using bender elements to measure the small strain stiffness of soils was proposed by Blewett *et al.* (1999). They argued that while using a single sine wave may reduce the distortion of the output signal when compared with a square wave, the non-repetition of the sine wave still introduces an infinite series of frequency components. In their original paper Blewett *et al.* proposed using a continuously cycled input voltage to overcome this problem.

5.4.2 Description of the Method

The technique no longer relies on the user identifying the arrival time of the shear wave and then calculating the velocity, but instead uses a dual-phase lock-in amplifier to determine the phase shift between the input and output waves. The testing procedure must begin with a traditional time of flight (single cycle test described in Section 5.3) test to gain an estimate of the shear wave velocity. The input is then changed to a continuously cycled voltage and the phase difference between the input and output waves measured using the dual-phase lock-in amplifier. An example of this technique is shown in Figure 5.15 and Figure 5.16. Figure 5.15 shows the results from a single square wave test carried out on a sample of loose Leverseat sand at 100 kPa confining pressure. Figure 5.16 shows the results from a continuously cycled test, which is also known as the phase sensitive detection method.

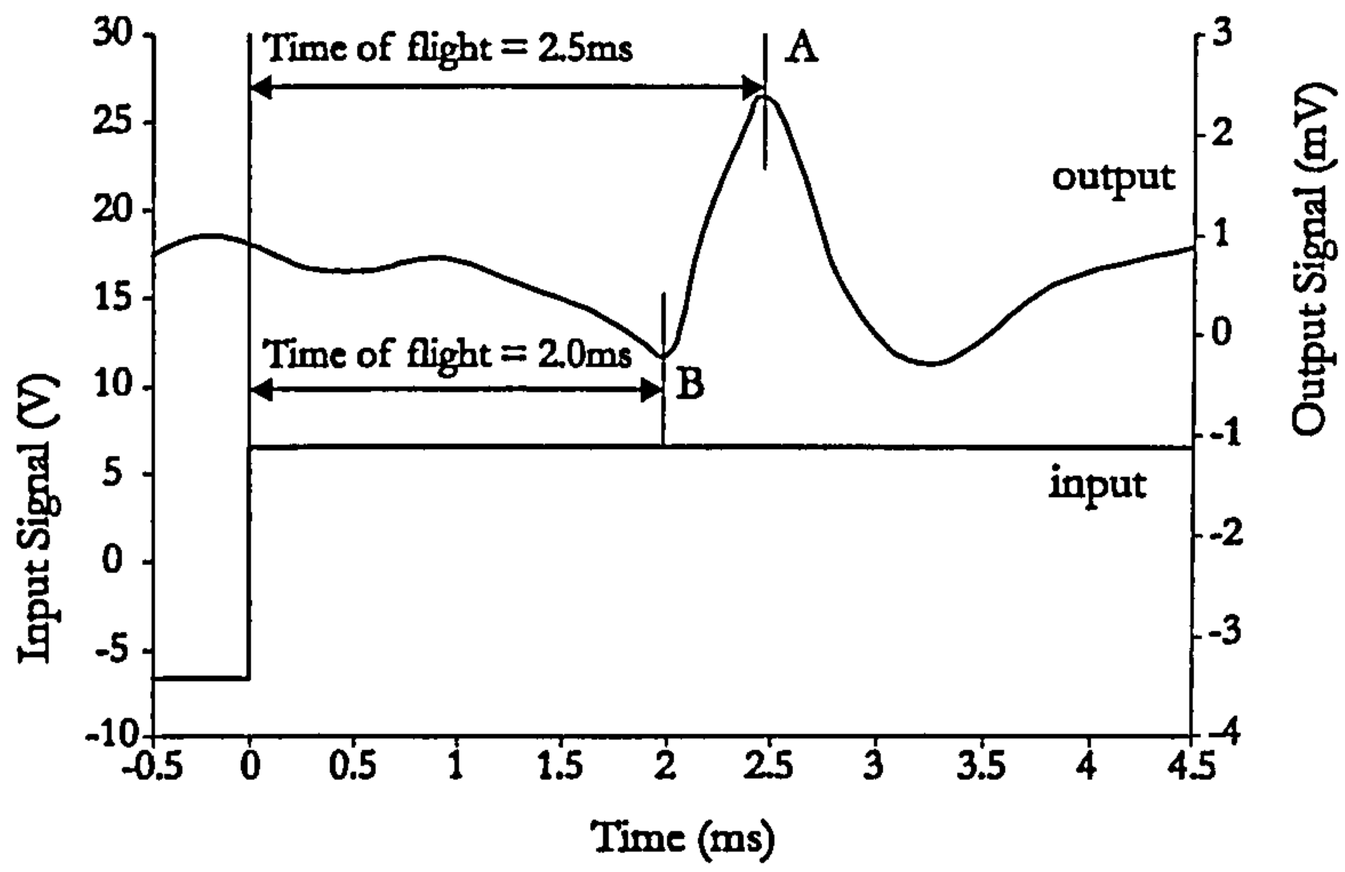

Figure 5.15: Traditional time of flight method, using a square wave input (after Blewett *et al.* (1999))

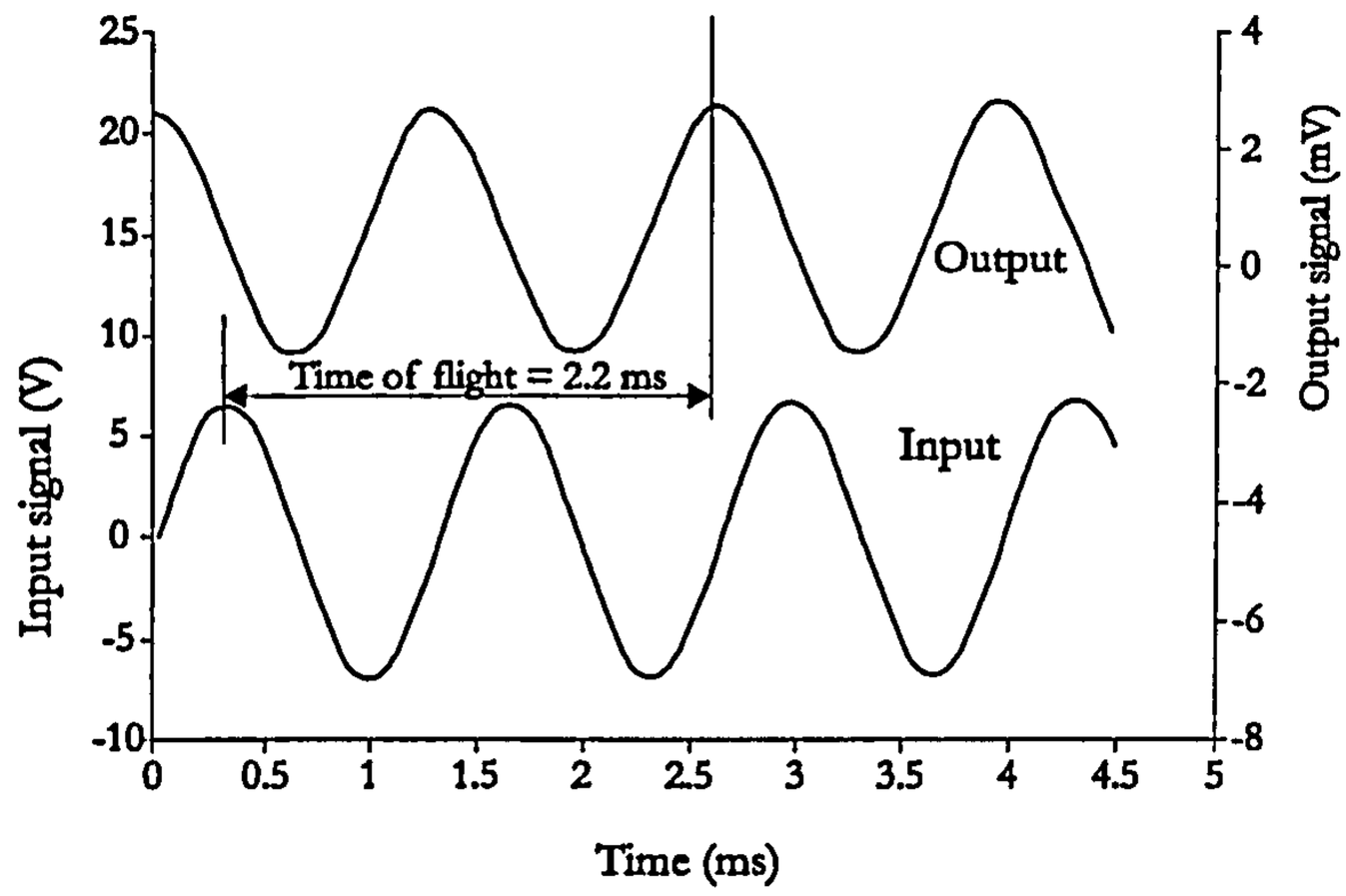

Figure 5.16: Results from phase sensitive detection method (after Blewett *et al.* (1999))

It is important to note that the results from the time of flight method must be used to determine which peak corresponds to the shear wave travel time. If the wrong peak is chosen the shear wave travel time will be wrong by multiples of the input frequency.

An alternative to using the dual-phase lock-in amplifier is to increase the input frequency until the input and output waves come into phase. This should be a simple matter on a modern oscilloscope. If the starting frequency is low enough, there must be at least one complete wavelength between the bender element tips. The frequency can then be increased further until the desired number of wave

lengths has been achieved. It is then a simple matter to calculate the shear wave velocity using Equation 5.10.

$$V = \frac{d}{N} f \tag{5.10}$$

where V is the shear wave velocity, d is the distance between the tips of the bender elements, N is the number of complete wavelengths and f is the input frequency. The principal advantage of the phase sensitive detection method is that determining the travel time has a more objective criteria than the traditional time of flight method. It is interesting to note that in Figure 5.16 the travel time determined using the phase sensitive detection method does not correspond to the first peak (marked point A, recommended by Brignoli *et al.* (1996)) or the first downwards deflection (marked point B, recommended by Viggiani and Atkinson (1995)) of the time of flight method shown in Figure 5.15. This suggests that the arrival of the shear wave in the traditional time of flight method does not correspond to any definite wave reversal observed in the oscilloscope trace. The remainder of this chapter will concentrate on the numerical modelling of this method to determine if the assumption of one dimensional wave propagation is correct and investigate the influence of the geometry of the triaxial sample.

5.5 Numerical Analyses Undertaken

5.5.1. Introduction

Despite the concentrated efforts of many researchers, no clear guidance has been proposed for the effective use of bender elements using the traditional time of flight method. Whilst many experimentalists believe that the near field effect is responsible for the ambiguity surrounding the identification of the shear wave arrival, the work by Arroyo *et al.* (2002) has shown that eliminating the near field components does not reduce the scatter associated with the measured shear wave velocity.

The technique of using a continuously cycled input (or phase sensitive detection method) described by Blewett *et al.* (1999) purports to overcome the problems of

shear wave identification by utilising an objective measurement criterion. Measuring the excitation frequency at which the input and output waves come into phase does not rely on the user interpretation of the output signal, and thus is more objective. The remainder of this chapter is dedicated to a series of dynamic finite element analyses that were undertaken to investigate the accuracy of the phase sensitive detection method. First the results from a traditional time of flight method will be presented. The purpose of these is to compare qualitatively with experimental data to validate the analysis set up and to confirm the findings of previous researchers. The results from these analyses will then be used to back calculate the material properties of the soil. These can then be compared with the known input parameters and some estimate of the error associated with the time of flight method made. A series of analyses will then be presented for the phase sensitive detection method. The technique described in section 5.4.2 will be used to back calculate the material properties which will then be compared to the known input parameters. The results from both methods will then be compared and some recommendations made regarding their use.

5.5.2 Geometry Assumed in the Analyses

All the analyses presented in the literature to date have assumed the bender elements to be placed in the top and bottom platens of a triaxial sample. This is the most common arrangement in the laboratory and the same assumption will be made for this study. Since a triaxial sample has a cylindrical geometry, a simple axi-symmetric finite element analysis could be performed. However, the shear wave propagation and the bender element motion are not axi-symmetric boundary conditions and therefore this type of analysis is not appropriate. To overcome this problem, other researchers have assumed plane strain conditions (Jovičić *et al.* (1996) and Arulnathan *et al.* (1998)). This implies that the triaxial sample modelled in the analysis has a rectangular section and is infinitely long in the out of plane direction, with infinitely long bender elements embedded in the top and bottom platens. In reality the problem is truly three dimensional, and hence a three dimensional analysis should be employed. A conventional three dimensional analysis, which involves generating a full three dimensional mesh, imposes large requirements on computer memory and analysis run times. Another option for performing three dimensional analyses is the Fourier Series Aided Finite Element

Method (FSAFEM), which is applicable to problems with axi-symmetric geometry, but where boundary conditions and/or material properties are not axi-symmetric (see Genendra (1993)). The finite element mesh is still two dimensional, but the displacements and loads are varied in the out of plane direction as a Fourier series. This type of analysis makes considerable savings in both time and memory demands. In this chapter both two dimensional plane strain analyses and Fourier Series Aided three dimensional analyses will be presented for the time of flight method and the phase sensitive detection method.

5.5.3 Plane Strain Analyses

There are several user defined parameters that, whilst often chosen by user preferences, can significantly affect the accuracy of the analysis. A series of parametric studies were carried out to determine what values should be taken for these parameters and how their choice affects the accuracy of the results. Each one shall now be investigated in turn.

5.5.3.1 Material Properties

To ensure the correct shear wave velocity is reproduced by the finite element analysis, a simple shear wave propagation problem will be analysed using the two dimensional plane strain mesh. To be consistent with the assumption that bender element tests measure the small strain stiffness on the elastic plateau, all analyses will assume linear elastic material properties. The bulk shear wave velocity is related to the elastic material properties by Equation 5.11.

$$V_{shear} = \sqrt{\frac{E}{2(1+\nu)\rho}} \tag{5.11}$$

where E is the Young's modulus, ν the Poisson's ratio and ρ is the material density. For the purpose of this study the following values where chosen for these parameters:

$$E = 201528900 \text{ N/m}^2$$

$$\nu = 0.4999$$

$$\rho = 2200 \text{ kg/m}^3$$

This gives the soil a shear wave velocity of 174.8 m/s. The Poisson's ratio was assumed to be as close to 0.5 as possible to give undrained conditions without causing numerical instability (see Potts and Zdravković (1999)). The assumption of undrained conditions is thought to be realistic considering the frequency range at which bender element tests are performed. This assumption will however be investigated later, as it has a significant influence on the behaviour of a dynamic finite element analysis. The group shear wave velocity observed in the analysis will only be equal to the bulk shear wave velocity of the soil given by Equation 5.11 when the wave propagation is truly one dimensional. The two dimensional plane strain mesh for the 36×76 mm triaxial sample is shown in Figure 5.17. The geometry is divided into 5000 equally sized eight noded isoparametric solid elements.

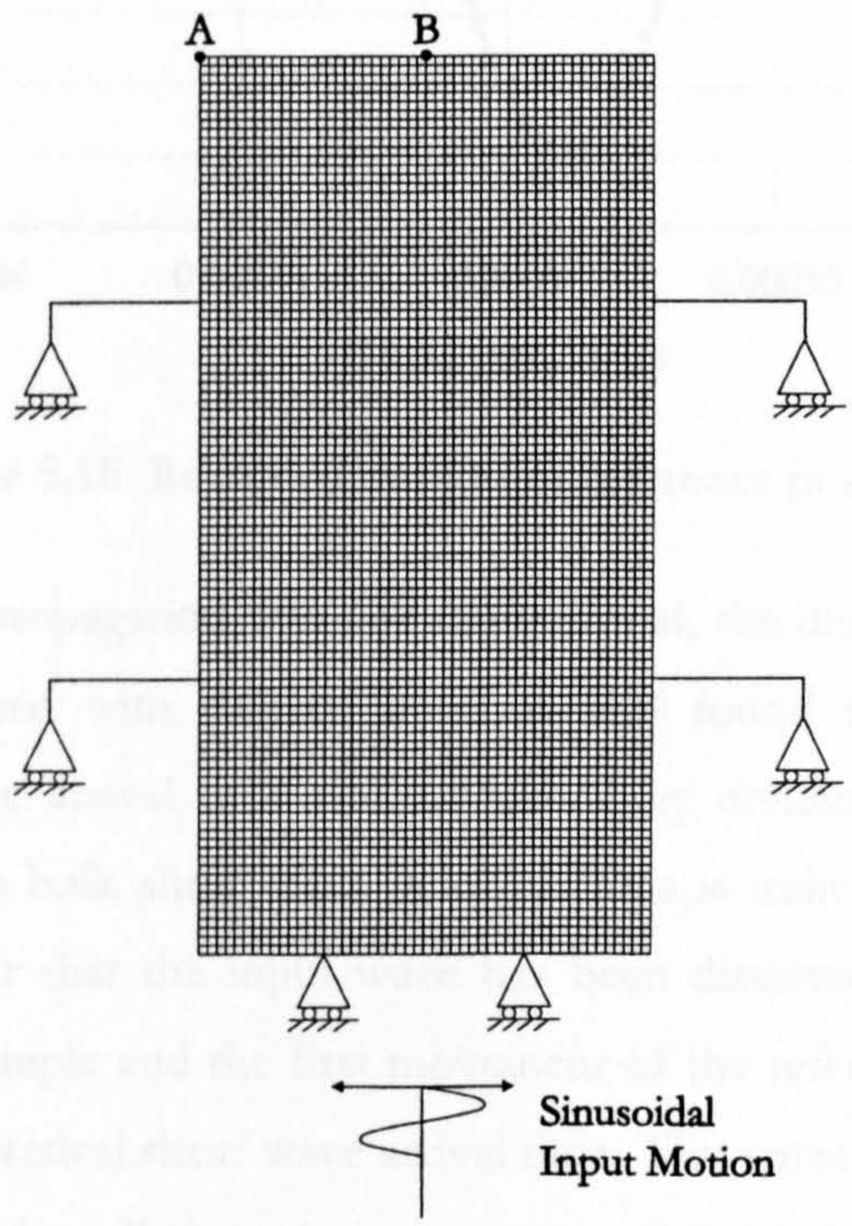

Figure 5.17: Mesh used to investigate one dimensional wave propagation

The shear wave is initiated by applying a sinusoidal horizontal displacement with an amplitude of 1 mm at the base of the mesh. Horizontal displacements were allowed for all the boundaries whilst vertical displacements were restricted on the base of the mesh and on both sides. By not allowing vertical motion on the side boundaries,

the shear wave is prevented from converting to a surface wave, and hence the wave propagation is one dimensional. No initial stresses are set for any of the single phase analyses. This will not affect the results as all analyses are linear elastic. The frequency of the input motion was chosen to be 10 kHz, with each cycle divided into 50 increments. This gives a time step of 2×10^{-6} seconds and a wavelength of 17.48 mm. The horizontal displacement history for point A is shown in Figure 5.18. The input signal has been multiplied by two and shifted to the theoretical arrival time to allow comparison with the motion of point A.

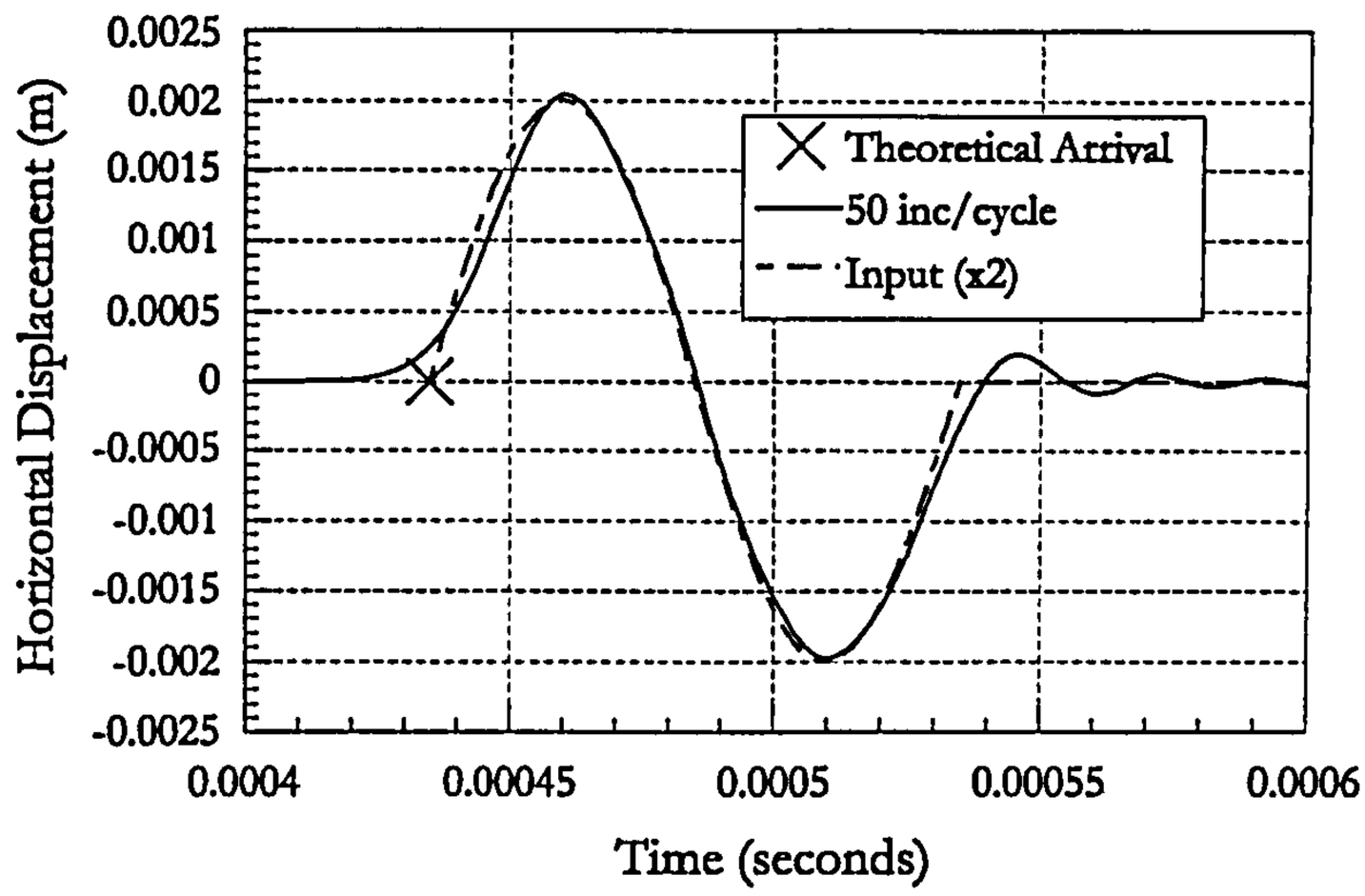

Figure 5.18: Recorded motion of reference point A

To ensure the wave propagation was one dimensional, the displacement history of point B was compared with that of point A and found to be identical. The theoretical shear wave arrival time was calculated by dividing the height of the triaxial sample by the bulk shear wave velocity. This is indicated by the cross in Figure 5.18. It is clear that the input wave has been distorted by its propagation through the triaxial sample and the first movement of the reference point does not coincide with the theoretical shear wave arrival time. This spreading out of the wave form and the numerical oscillations that are present after the shear wave has passed, are common features of dynamic finite element analyses that employ the Newmark method for time discretisation. Further analyses were undertaken with the input wave divided into 50, 100, 150, 200, 300 and 500 increments to investigate how this phenomenon is affected by the size of the time step. The results of this parametric study are shown in Figure 5.19.

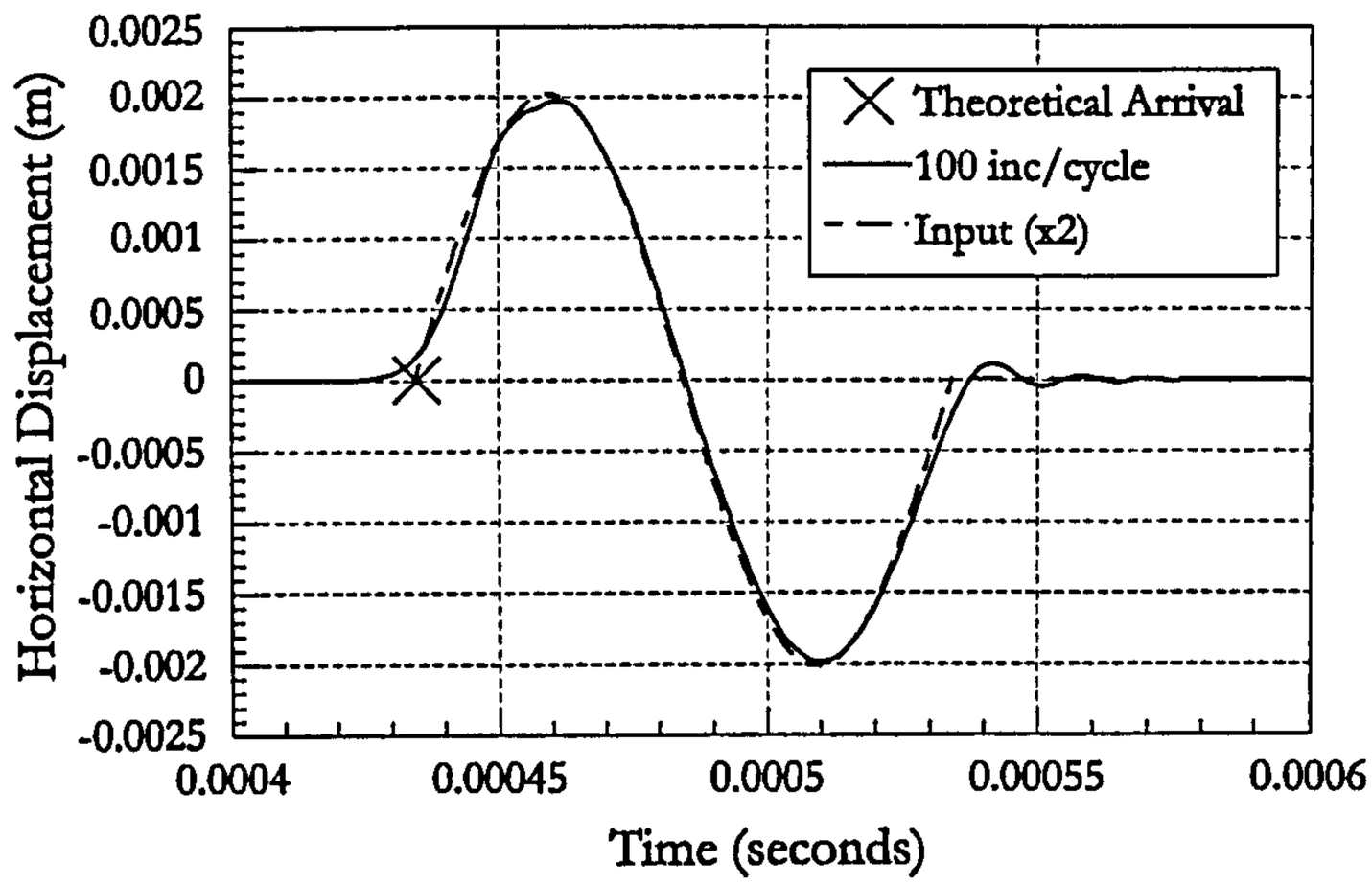
Theoretical Arrival
100 inc/cycle
Input (x2)
Horizontal Displacement (m)
0.0025
0.002
0.0015
0.001
0.0005
0
-0.0005
-0.001
-0.0015
-0.002
-0.0025
0.0004
0.00045
0.0005
0.00055
0.0006
Time (seconds)

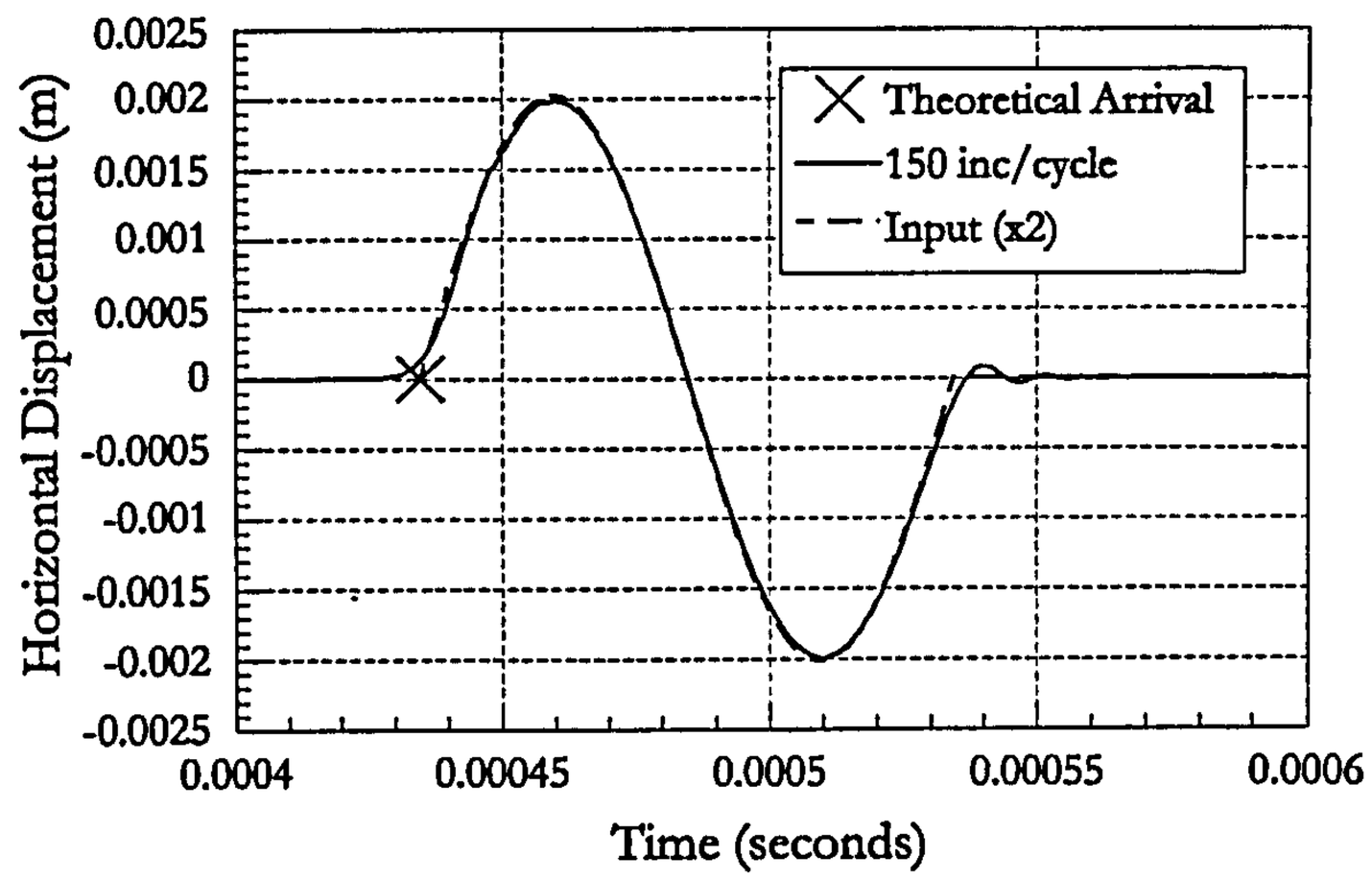
Theoretical Arrival
150 inc/cycle
Input (x2)
Horizontal Displacement (m)
0.0025
0.002
0.0015
0.001
0.0005
0
-0.0005
-0.001
-0.0015
-0.002
-0.0025
0.0004
0.00045
0.0005
0.00055
0.0006
Time (seconds)

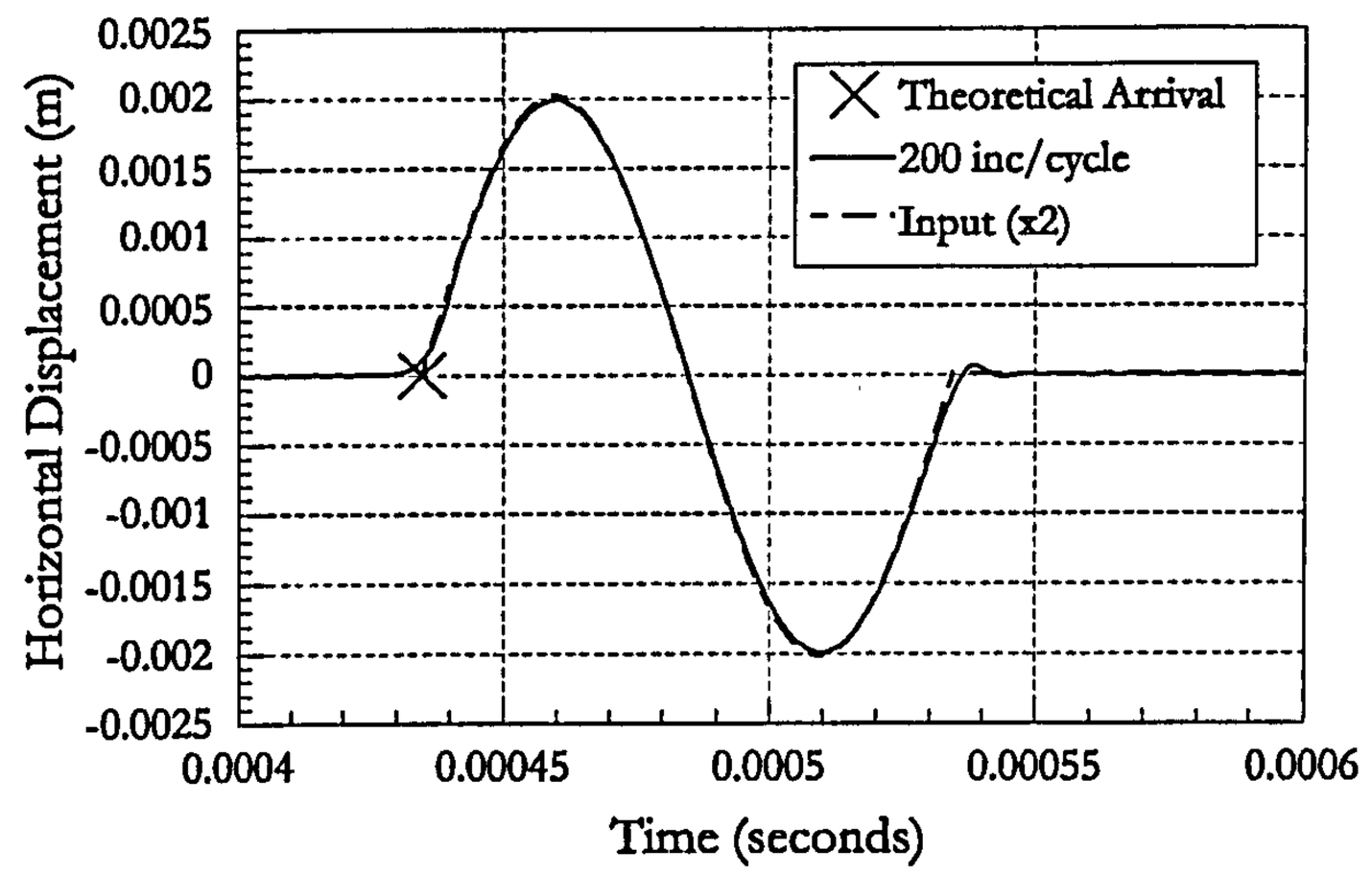
Theoretical Arrival
200 inc/cycle
Input (x2)
Horizontal Displacement (m)
0.0025
0.002
0.0015
0.001
0.0005
0
-0.0005
-0.001
-0.0015
-0.002
-0.0025
0.0004
0.00045
0.0005
0.00055
0.0006
Time (seconds)

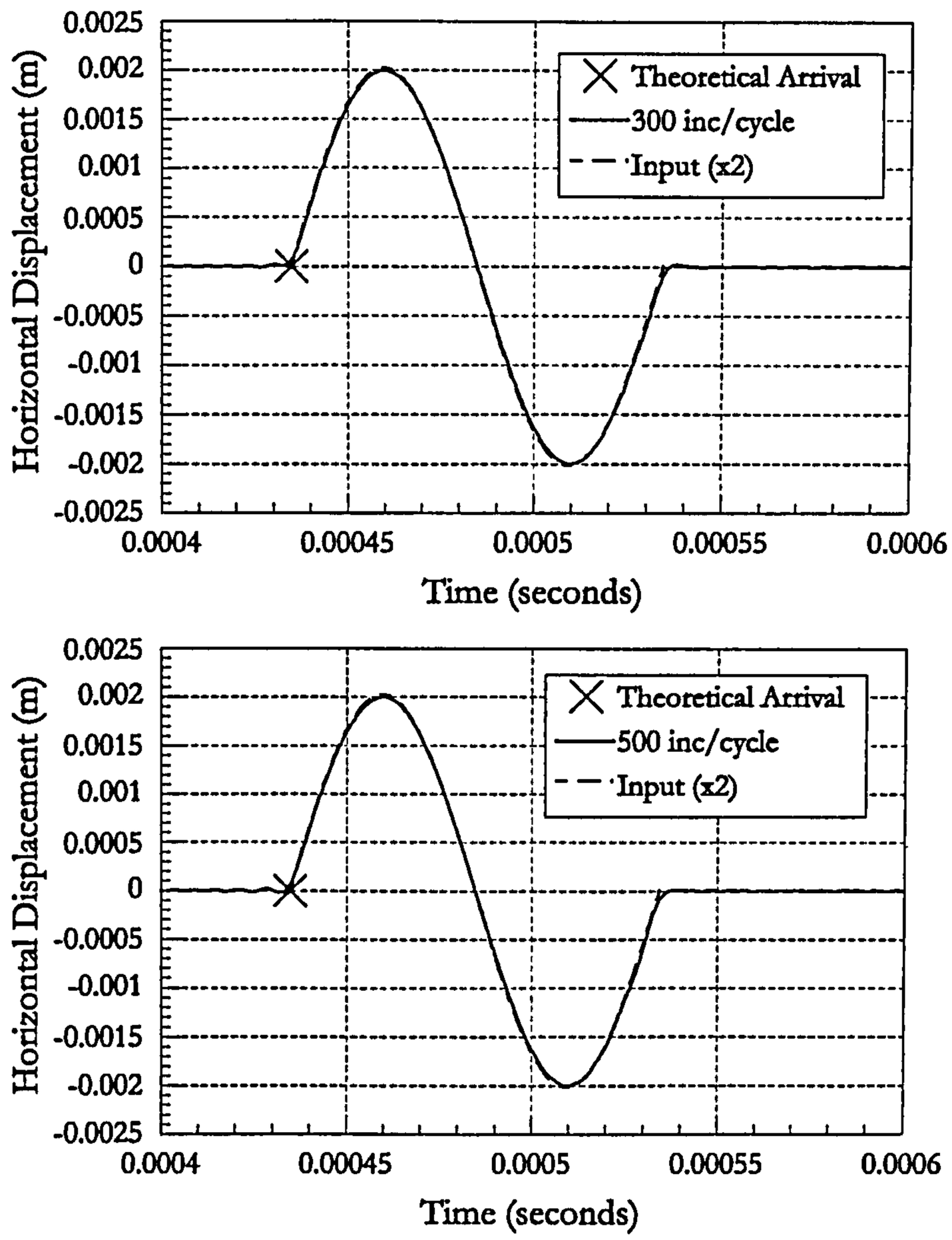

Figure 5.19: Result of analyses with different increment size

As the time step becomes smaller, the shear wave arrival becomes sharper and tends to the theoretical arrival time. The numerical oscillations at the tail of the wave reduce in magnitude and the motion of the reference point more closely resembles the shape of the input wave. Therefore one can conclude that the finite element analysis is capable of reproducing the shear wave velocity characteristics of the soil, however, the size of the time step employed is an important consideration and will have to be investigated further for realistic bender element analysis.

5.5.3.2 Details of the Bender Element Analyses

For the purpose of the parametric study a standard analysis will be described. The mesh is the same as that shown in Figure 5.17, with the addition of beam elements, located at the midpoint of the top and bottom boundaries,

protruding into the sample to model the bender elements. Each bender element was assumed to be perfectly connected to the surrounding soil. Each was assumed to be 3.04 mm long, consisting of four 3 noded beam elements (see Day and Potts (1990)). The input motion can either be prescribed as a bending moment (Arulnathan *et al.* (1998)) or as a displacement (Jovičić *et al.* (1996)). The reason Arulnathan *et al.* (1998) chose to use bending moments was to investigate the potential error from the transfer function relating the physical wave forms to the measured electrical signal. In reality this relationship is a very complicated interaction problem and studying its effect is not the purpose of this work. Therefore to eliminate its influence, the excitation of the bender element was input as a sinusoidal horizontal displacement, with a maximum value of 1 μm prescribed at its tip. In turn, the output signal was taken as the displacement recorded at the tip of the receiving bender element. The mesh and the boundary conditions used in the following analyses are shown in Figure 5.20.

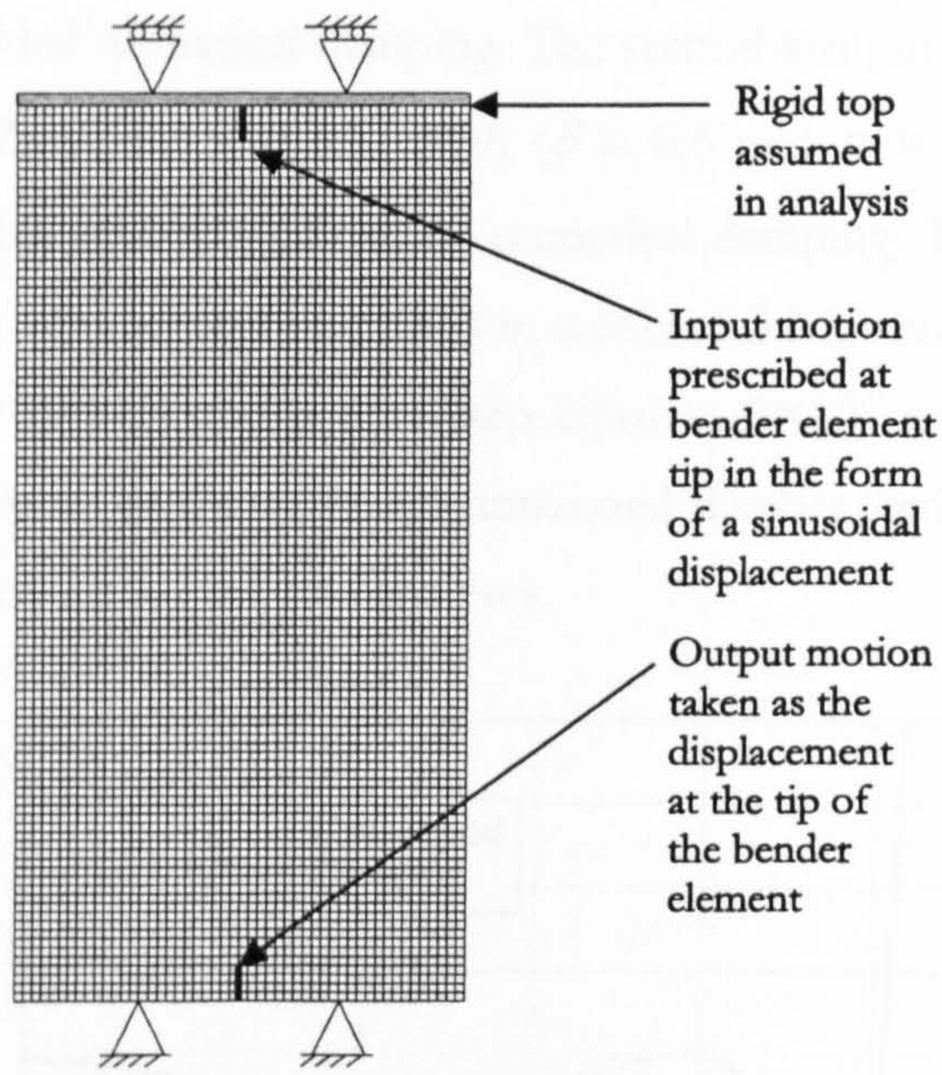

Figure 5.20: Finite element mesh and boundary conditions used in bender element analyses

The boundary conditions were chosen to replicate those of a triaxial test condition. The movements of the bottom of the mesh were fixed both horizontally and vertically, while only horizontal movement was restrained along the top of the mesh. To model the presence of an infinitely stiff top cap, the vertical displacements

for the top boundary were tied together thus making sure that a uniform vertical deformation of the top boundary is achieved. The side boundaries were assumed stress free. No initial stresses were set for any of the single phase material analyses. This will not affect the results as analyses performed assumed linear elastic material behaviour.

5.5.3.3 Newmark Parameters

The analysis of the dynamic cavity problem presented in Chapter 4 illustrated the importance of the numerical damping that can be introduced to an analysis by increasing the Newmark parameter δ. The second parameter α also has to be changed according to Equation 3.66 to ensure the time scheme remains unconditionally stable. Two analyses will be presented here to determine how the choice of these parameters affects the results of the bender element analysis. The first assumes values of $\delta = 0.5$ and $\alpha = 0.25$ to give an unconditionally stable scheme, with no added numerical damping. The second analysis assumes the values recommended by Zienkiewicz *et al.* (1999) ($\delta = 0.6$ and $\alpha = 0.3025$) to give an unconditionally stable scheme, with some numerical damping. The mesh shown in Figure 5.17 and the arrangement described in section 5.5.3.2 were employed with an input frequency of 10 kHz and a time step equal to 5×10^{-7} seconds. Figure 5.21 shows an enlarged view of the recorded horizontal displacements at the tip of the receiving bender element for the two analyses.

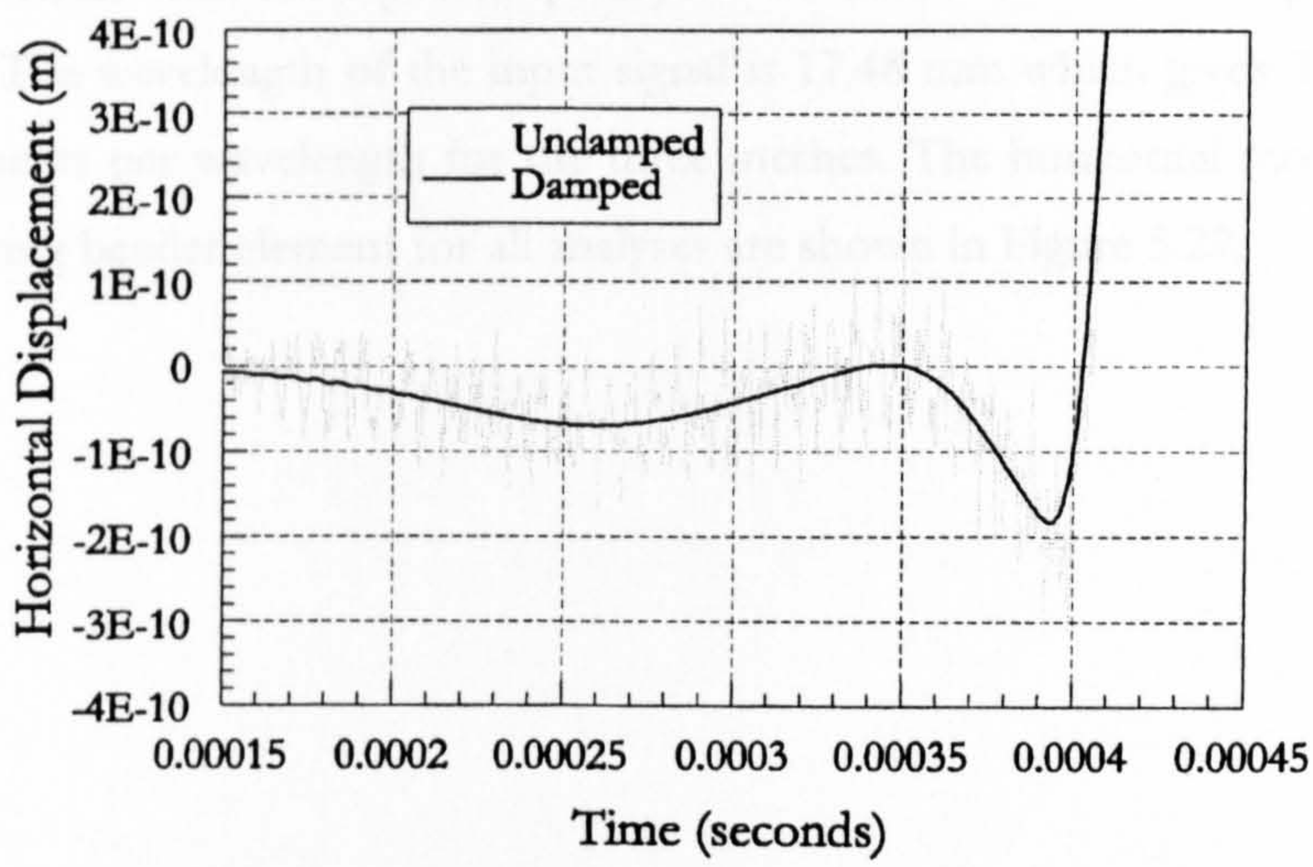

Figure 5.21: Analysis to investigate the influence of the Newmark parameters

The recorded displacement at the receiving bender element for the analysis with no additional numerical damping exhibits considerable numerical oscillations. The effect of adding numerical damping is to smoothen the response, without altering the general motion of the bender element. The damped analysis follows the mean position of the undamped case with slightly reduced amplitude. The times at which peak oscillations occur are identical for both analyses, suggesting that the shear wave velocity is unaffected by numerical damping. For this reason, and to give a smooth response, the remainder of the analyses presented in this chapter will assume the Newmark parameters $\delta = 0.6$ and $\alpha = 0.3025$.

5.5.3.4 Finite Element Mesh

The importance of mesh density for dynamic finite element analyses has been illustrated in Chapter 4. The parametric study for the propagation of a compression wave along a bar showed that a minimum number of elements per wavelength are required to accurately model the wave propagation. For this example 10 elements per wavelength was found to be the minimum requirement to prevent significant distortion of the input wave. Whilst this may be taken as a rough guidance, the influence of mesh density will be investigated for the bender element analysis. Three meshes will be used, the first is shown in Figure 5.17 with 5000 elements, the second and the third have the same dimensions but 1300 and 11400 elements respectively. The analysis arrangements are the same as those described in section 5.5.3.2, with an input frequency of 10 kHz and a time step of 5×10^{-7} seconds. The wavelength of the input signal is 17.48 mm which gives 34.5, 23 and 11.5 elements per wavelength for the three meshes. The horizontal movements of the receiving bender element for all analyses are shown in Figure 5.22.

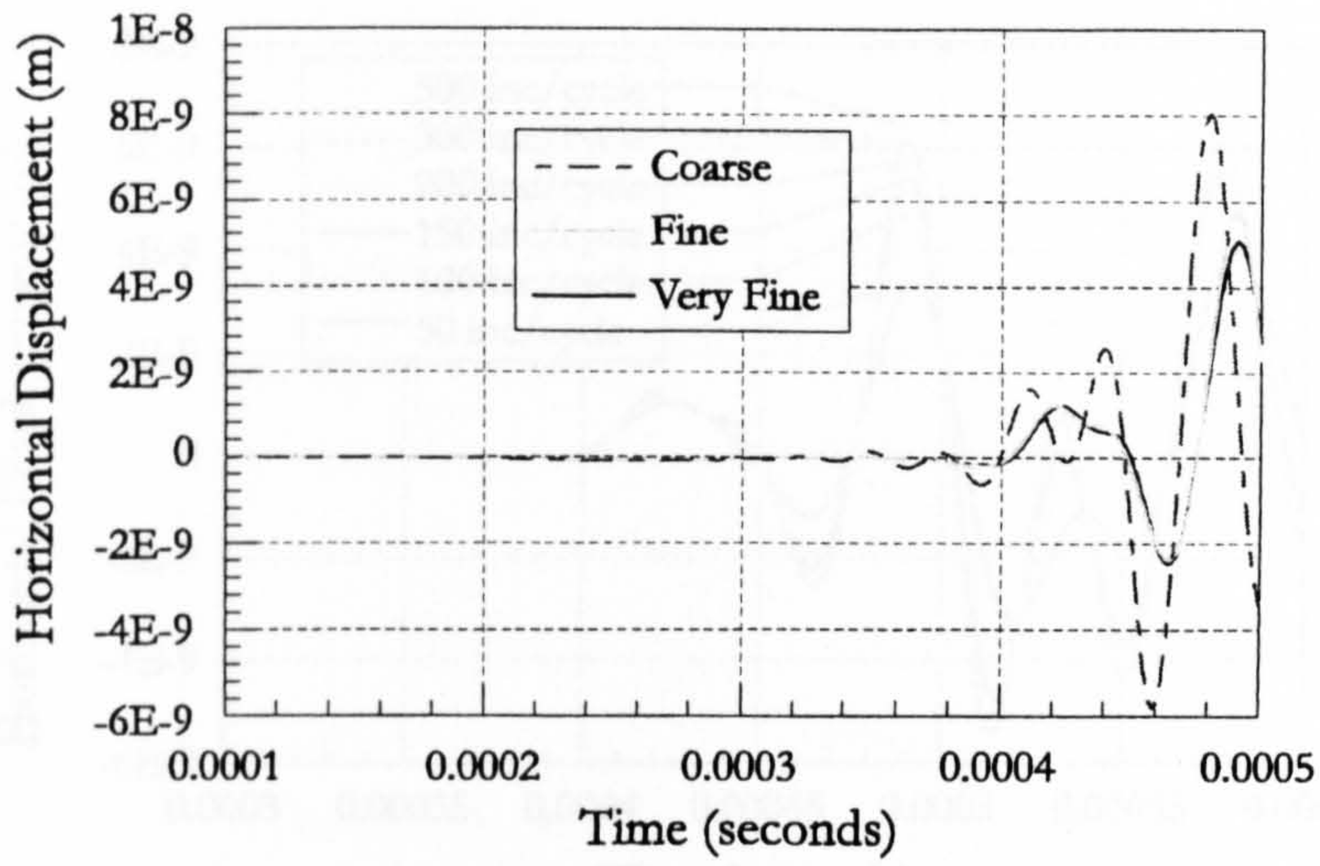

Figure 5.22: Analyses comparing different mesh densities

The results for the very coarse mesh show considerable oscillations, but follow the same trend as the results using the finer meshes. This is unacceptable as it is difficult to tell which oscillations are true wave arrivals and which are numerical inaccuracies. However, the results from the two fine meshes are very similar and give the same shear wave arrival. It can therefore be concluded that the mesh with 5000 elements is sufficiently fine to represent the shear wave propagation accurately and offers considerable savings in run time compared to the very fine mesh, and will therefore be used for the remaining numerical analyses.

5.5.3.5 Time Step

The one dimensional shear wave propagation presented in Section 5.5.3.1 illustrated how the time step employed controls the accuracy of an analysis. A series of analyses were performed with a range of time steps to find the most appropriate value for the following study. The input frequency was chosen to be 10 kHz and analyses performed with each sine wave divided into 50, 100, 150, 200, 300 and 500 increments. An overall view of the motion of the receiving bender element is shown if Figure 5.23 and an enlarged view of the shear wave arrival is shown in Figure 5.24.

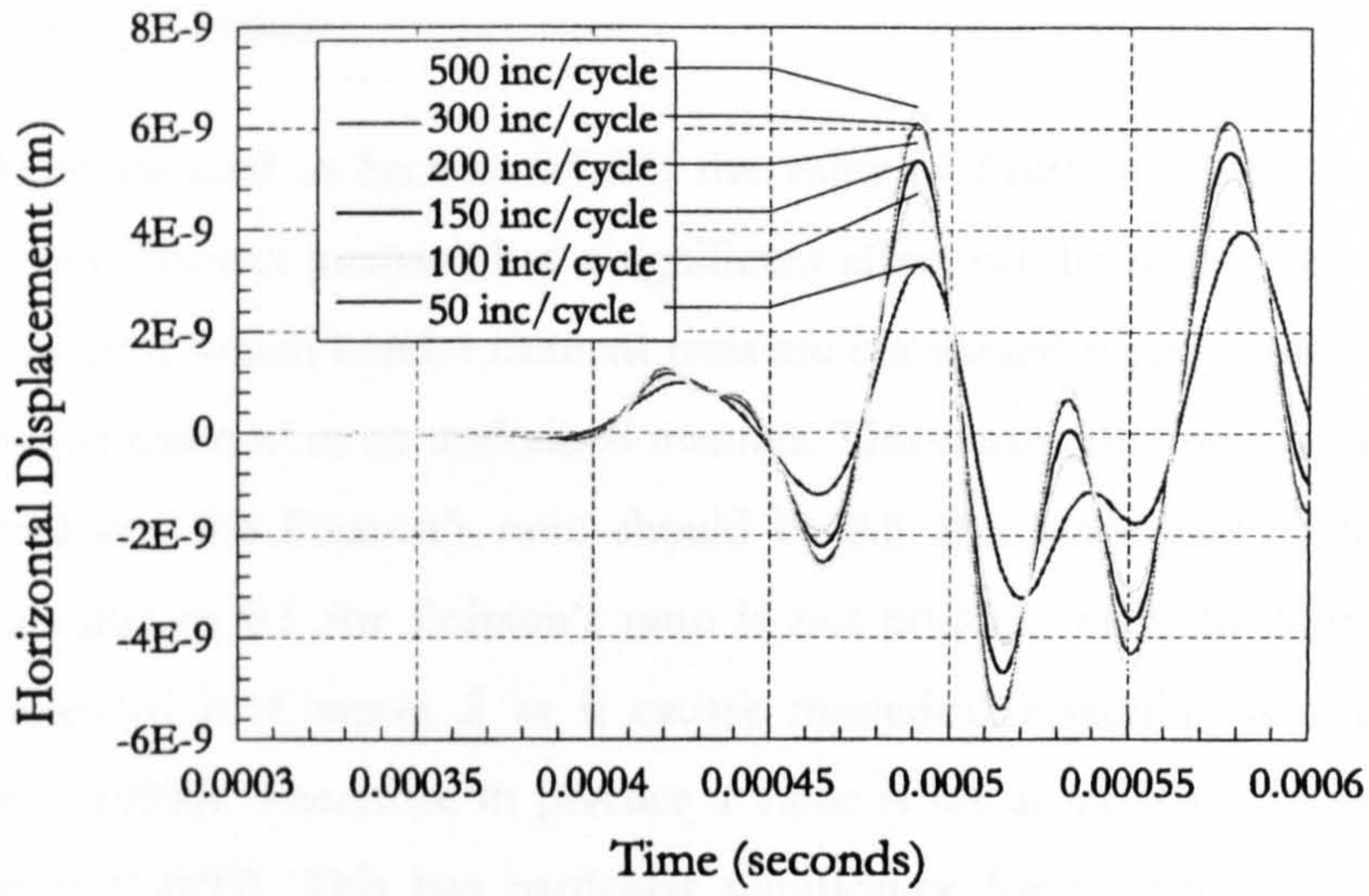

Figure 5.23: Motion of receiving bender element for different size time steps

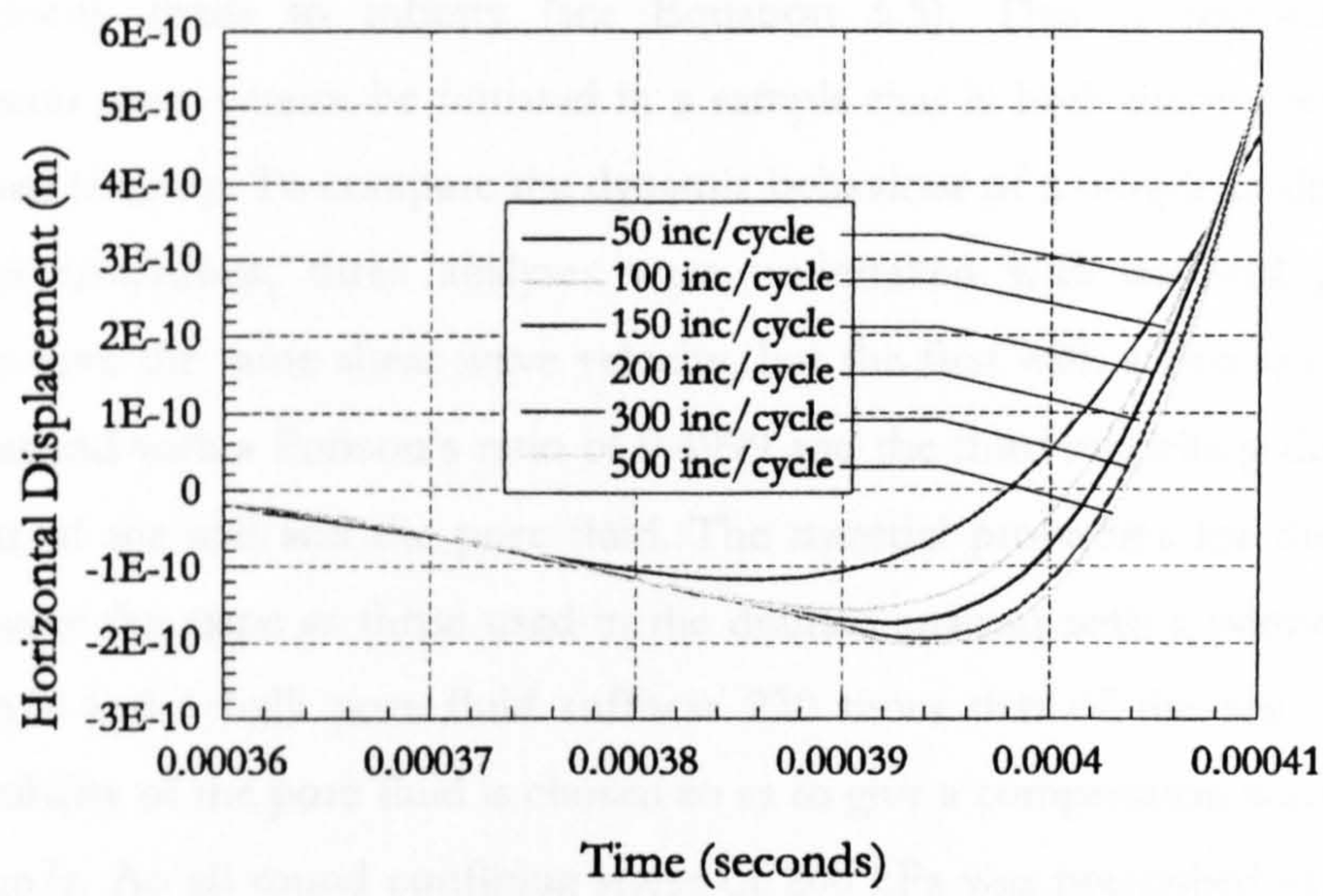

Figure 5.24: Enlarged view of shear wave arrival for analyses with different time steps

Again the importance of the time step used in an analysis is illustrated. The motion of the receiving bender element for the 50 increments per cycle analysis is significantly different from the others, whilst the remaining analyses converge to give a similar result. When choosing the time step for the remaining analyses, a balance had to be found between obtaining accurate results and minimising the time an analysis takes to run. The improvement between using 50 increments per cycle and 150 is very large, but after this the improvements are small. Therefore, for the remaining analyses 200 increments per cycle will be used, as this strikes the best balance between accuracy and efficiency.

5.5.3.6 Drainage Conditions

As mentioned in Section 5.5.3.1, the value of Poisson's ratio assumed for dynamic finite element analyses has a significant effect on the results obtained. The high frequency at which bender element tests are conducted suggests intuitively that the soil would respond in an undrained manner. This means that no volume change is permitted and the Poisson's ratio should be 0.5. For undrained finite element analyses a value of 0.5 for Poisson's ratio is not possible with the finite element theory presented in Chapter 2 as it causes numerical instability (see Potts and Zdravković (1999)). Therefore in practice a value is set as close to 0.5 as possible (for example 0.4999). This has particular significance for dynamic finite element analyses because, as the Poisson's ratio tends to 0.5, the constrained compression wave velocity tends to infinity (see Equation 5.5). This is reasonable as a compression wave cannot be initiated in a sample that is both incompressible and constrained laterally. To compare the dynamic behaviour of a sample in drained and undrained conditions, three analyses were undertaken with material properties chosen to give the same shear wave velocity, but the first with a Poisson's ratio of 0.3 the second with a Poisson's ratio of 0.4999 and the third modelling the coupled behaviour of the soil and the pore fluid. The material properties for the coupled analysis were the same as those used in the drained analysis with a permeability of 1×10^{-6} m/s and a bulk pore fluid stiffness 230 times that of the soil. The bulk compressibility of the pore fluid is chosen so as to give a compression wave velocity of 1000 m/s. An all round confining stress of 200 kPa was prescribed as an initial stress condition with a constant pore water pressure of 50 kPa. The analysis arrangements were as described in Section 5.5.3.2, with an input frequency of 10 kHz and a time step of 5×10^{-7} seconds. The horizontal displacements of the receiving bender element for all analyses are shown in Figure 5.25.

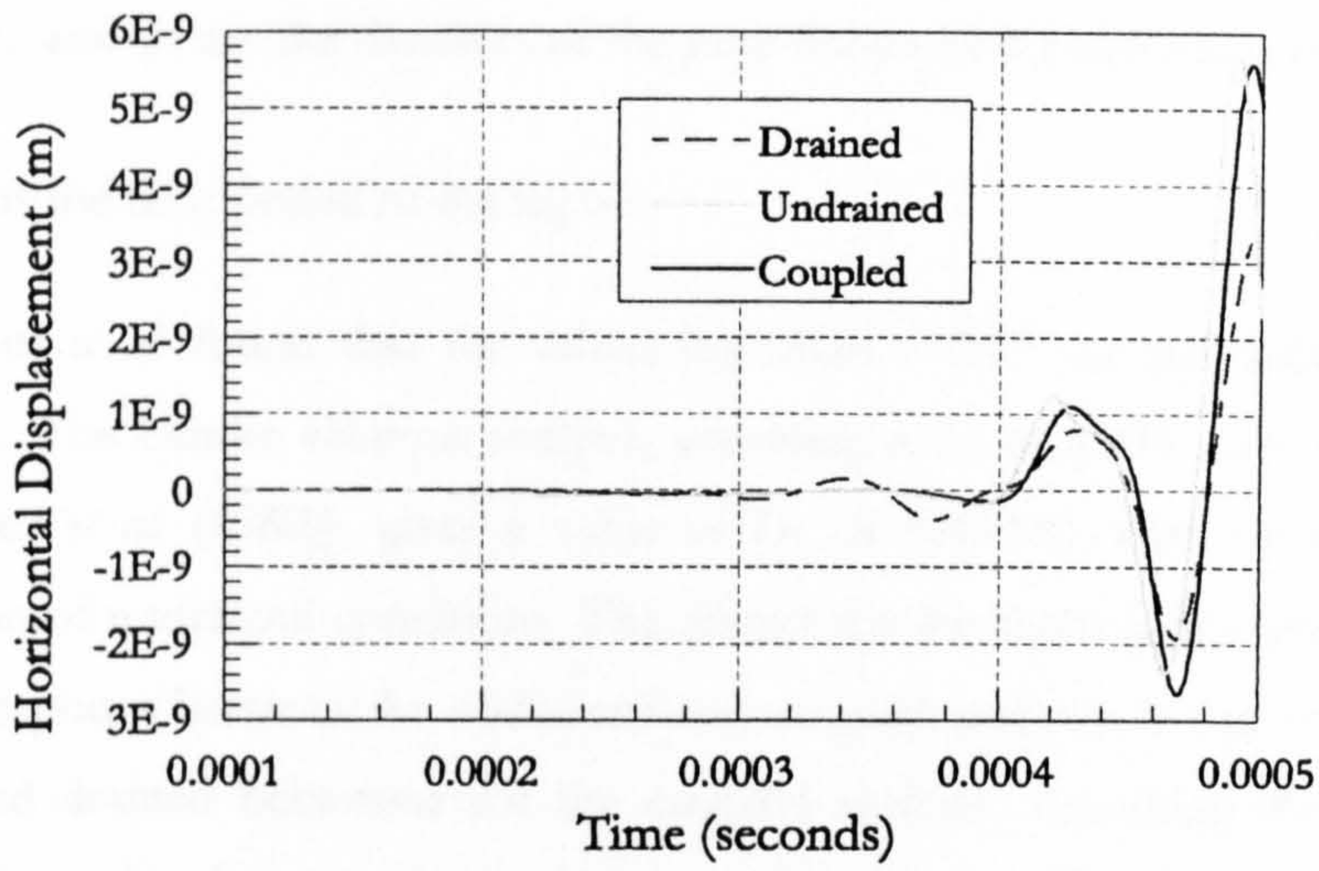

Figure 5.25: Comparing first shear wave arrival assuming drained, undrained and coupled behaviour.

The results for the drained analysis do not resemble those obtained in real bender element tests and no distinct shear wave arrival is evident. The results of the undrained and the coupled analyses are similar, implying that the assumption of undrained conditions is reasonable for this combination of input frequency and permeability. This finding is supported by the work of Zienkiewicz *et al.* (1980). To determine if a drained, undrained or fully coupled analysis should be performed for a dynamic problem, Zienkiewicz *et al.* proposed the use of a dimensionless parameters Π_1, given by Equation 5.12.

$$\Pi_1 = \frac{2kT}{\beta \pi g \hat{T}^2} \tag{5.12}$$

Where: $\hat{T} = \dfrac{2L}{V_c}$

V_c is the speed of sound in water

L is the distance travelled by the wave

k is the permeability in m/s

$\beta = \dfrac{\rho_f}{\rho}$

ρ_f and ρ are the densities of the pore fluid and the soil respectively.

T is the time period of the input.

Zienkiewicz *et al.* found that for values less than 1×10^{-2} the soil behaviour was undrained. The bender element analysis, assuming a V_t of 1000 m/s (taken from Zienkiewicz *et al.* (1980)), gives a value of Π_1 of 8.4×10^{-4}, thus confirming the assumption of undrained conditions. The reason for the slight difference in bender element response between the undrained and coupled analyses is due to the effect of localised drained behaviour for the coupled analysis. Assuming the Poisson's ratio is 0.5 ensures that no volume change occurs for any element within the mesh. Modelling the soil as virtually impermeable with a realistic drained Poisson's ratio ensures that overall no volume change is allowed, however locally it may occur.

5.5.3.7 Estimate of G_{max} by First Shear Wave Arrival

The results from the preceding parametric investigations have led to the following assumptions being made for all the plane strain analyses that will be presented hereafter:

1. The behaviour of the soil is undrained, with the following linear elastic properties:

   E = 201528900 N/m^2 (Young's modulus)

   ν = 0.4999 (Poisson's ratio)

   ρ = 2200 kg/m^3 (Material density)

   V_s = 174.8 m/s (Bulk shear wave velocity)

2. The mesh used is the same as that shown in Figure 5.17 with 5000 eight noded isoparametric elements.
3. Each bender element is modelled by four three noded beam elements.
4. The input and output signals are taken as the displacements at the tip of the transmitting and receiving bender elements respectively.
5. The boundary conditions are chosen to replicate triaxial test conditions as described in section 5.5.3.2.

6. The time step is chosen to correspond to the input period divided by 200.

The first results to be presented are for an input frequency of 10 kHz. Figure 5.26 shows the horizontal displacement of the receiving bender element against time.

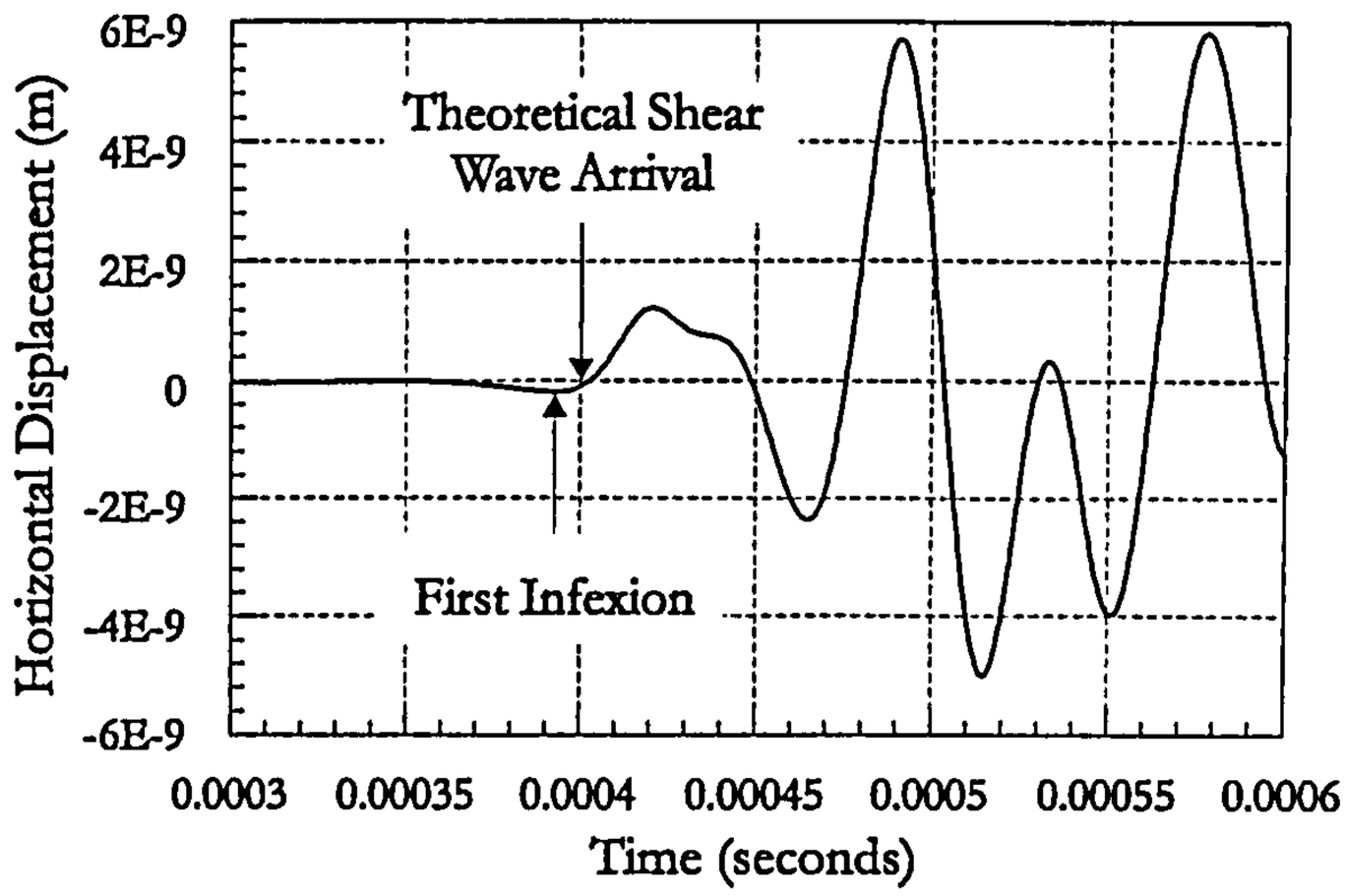

Figure 5.26: Recorded motion of receiving bender element for $R_d = 4$ (2D analysis)

The initial downwards deflection of the receiving bender element signifies the arrival of the near field component as identified by Sanches-Salinero *et al.* (1986). Given the distance between the tips of the bender elements of 69.92 mm and the bulk shear wave velocity of 174.8 m/s, the shear wave arrival time should be 0.0004 seconds. No obvious reversal of the bender element motion is present at this time and therefore the conclusion made by Jovičić *et al.* (1996) that the near field component masks the arrival of the first shear wave appears to be confirmed. Viggiani and Atkinson (1995) recommended that the shear wave arrival should be taken as the first inflexion of the output signal as illustrated by the arrow in Figure 5.26. For this example the first inflexion occurs at 0.000393 seconds. This gives a shear wave velocity of 177.9 m/s, which is 1.77% higher than theoretical shear wave velocity and results in a 3.6% error when used to calculate G_{max}.

To investigate the influence of input frequency on the recorded displacement of the receiving bender element, a series of analyses were performed for R_d ratios between 1 and 8 which gave a frequency range of 2.5 kHz to 20 kHz. Figure 5.27 to Figure 5.33 show the horizontal displacement of the receiving bender element for each analysis and Table 5.1 summarises the interpreted shear wave velocities.

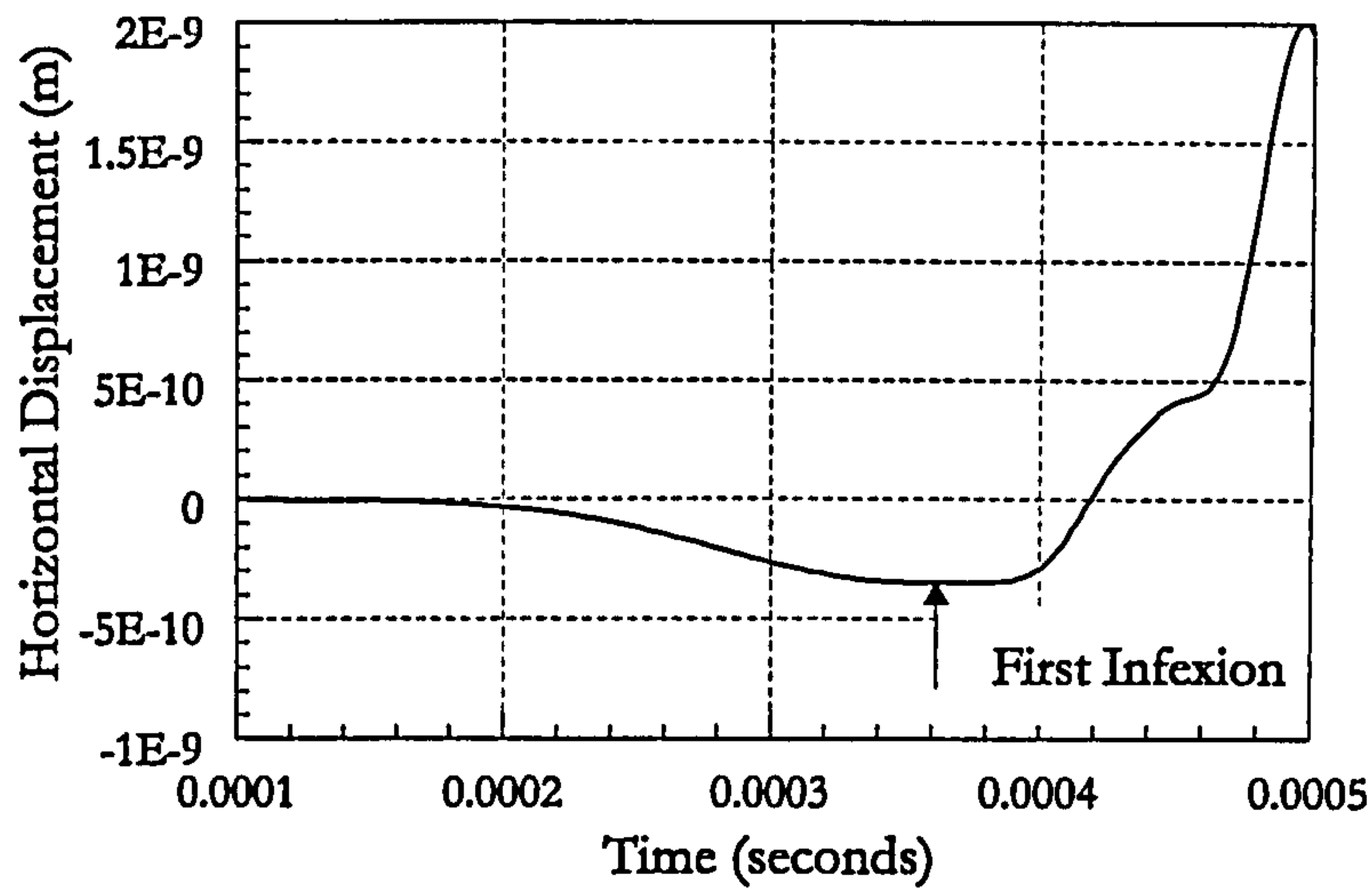

Figure 5.27: Recorded motion of receiving bender element for $R_d = 1$ (2D analysis)

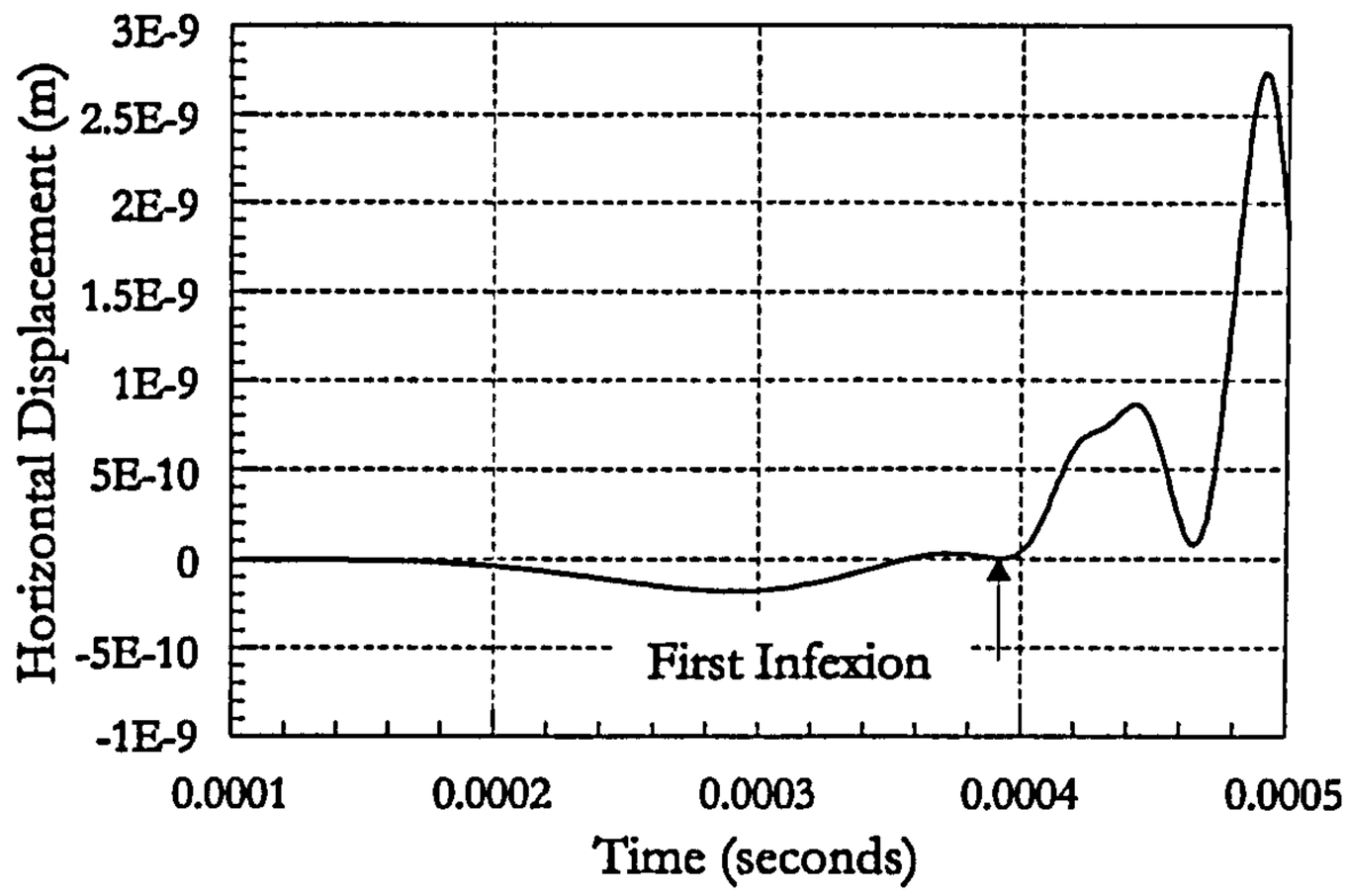

Figure 5.28: Recorded motion of receiving bender element for $R_d = 2$ (2D analysis)

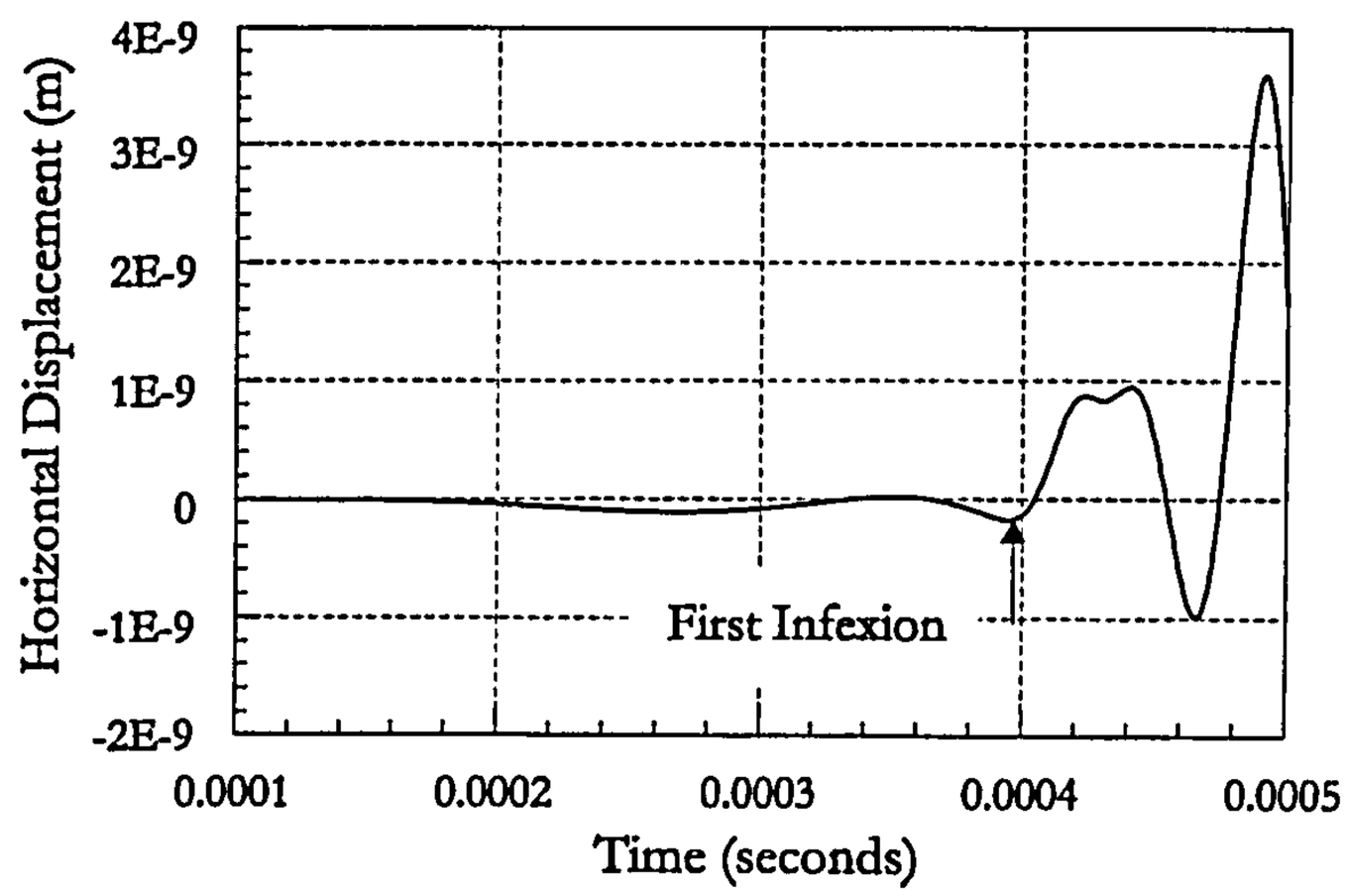

Figure 5.29: Recorded motion of receiving bender element for $R_d = 3$ (2D analysis)

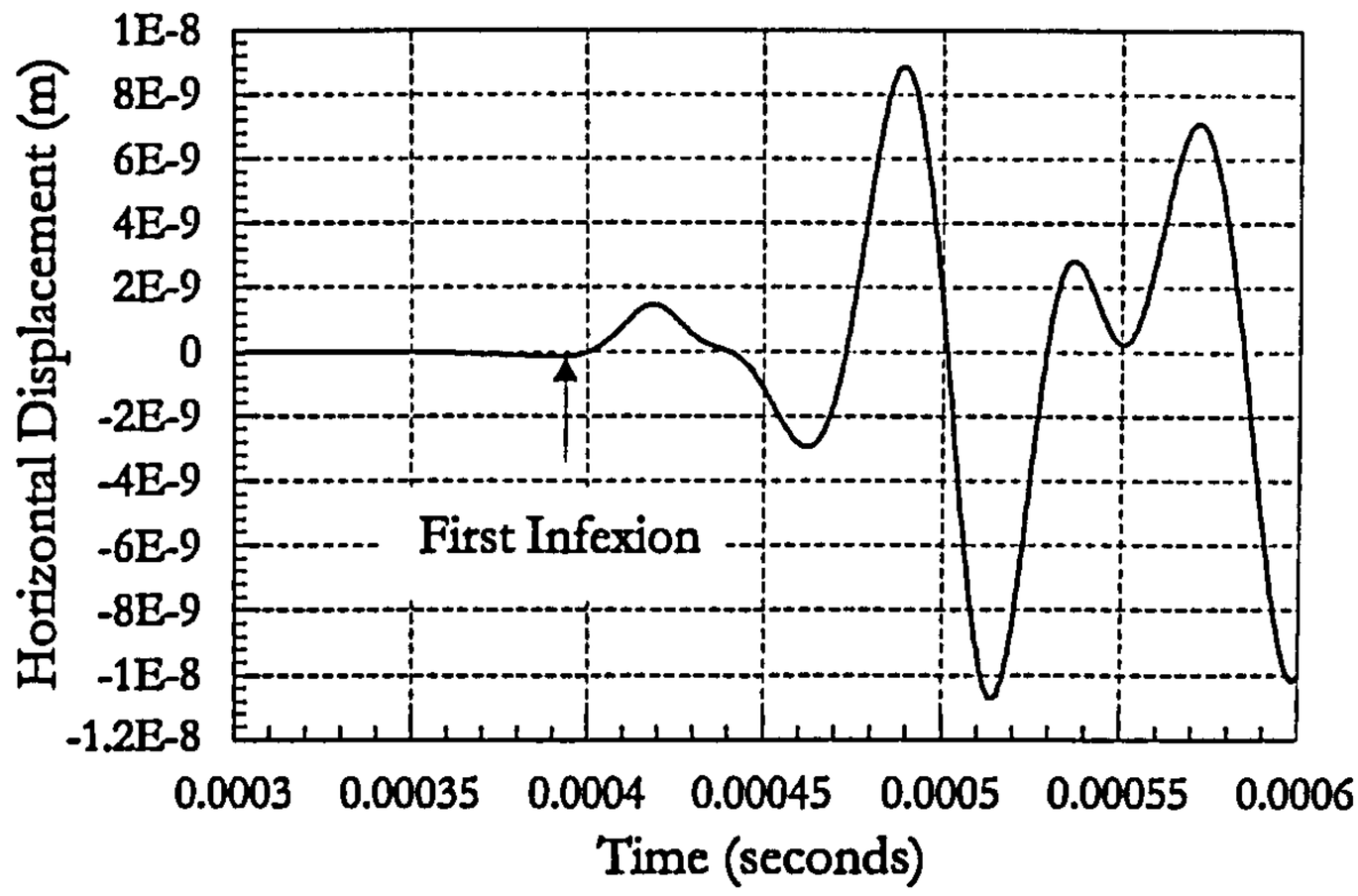

Figure 5.30: Recorded motion of receiving bender element for $R_d = 5$ (2D analysis)

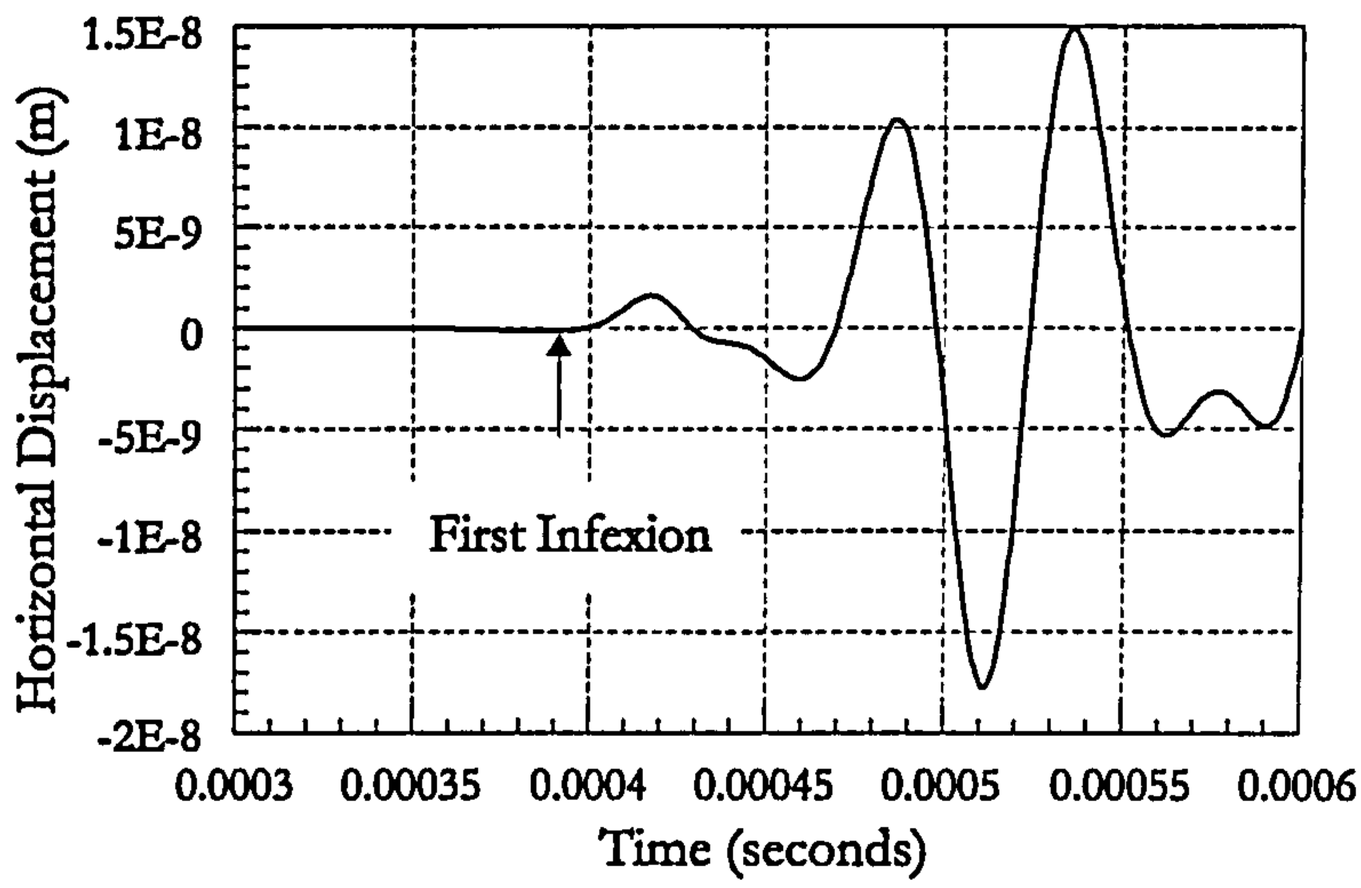

Figure 5.31: Recorded motion of receiving bender element for $R_d = 6$ (2D analysis)

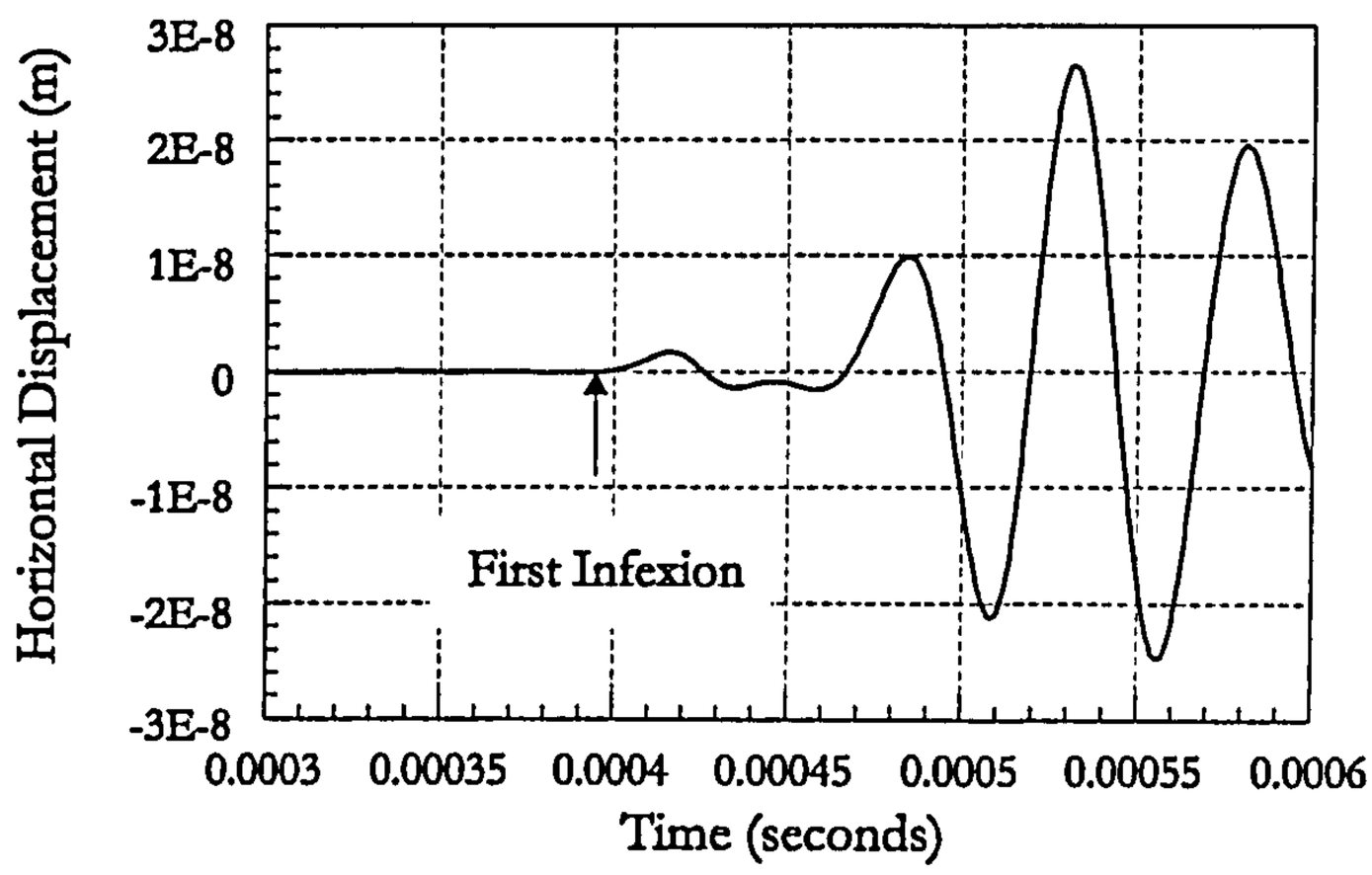

Figure 5.32: Recorded motion of receiving bender element for $R_d = 7$ (2D analysis)

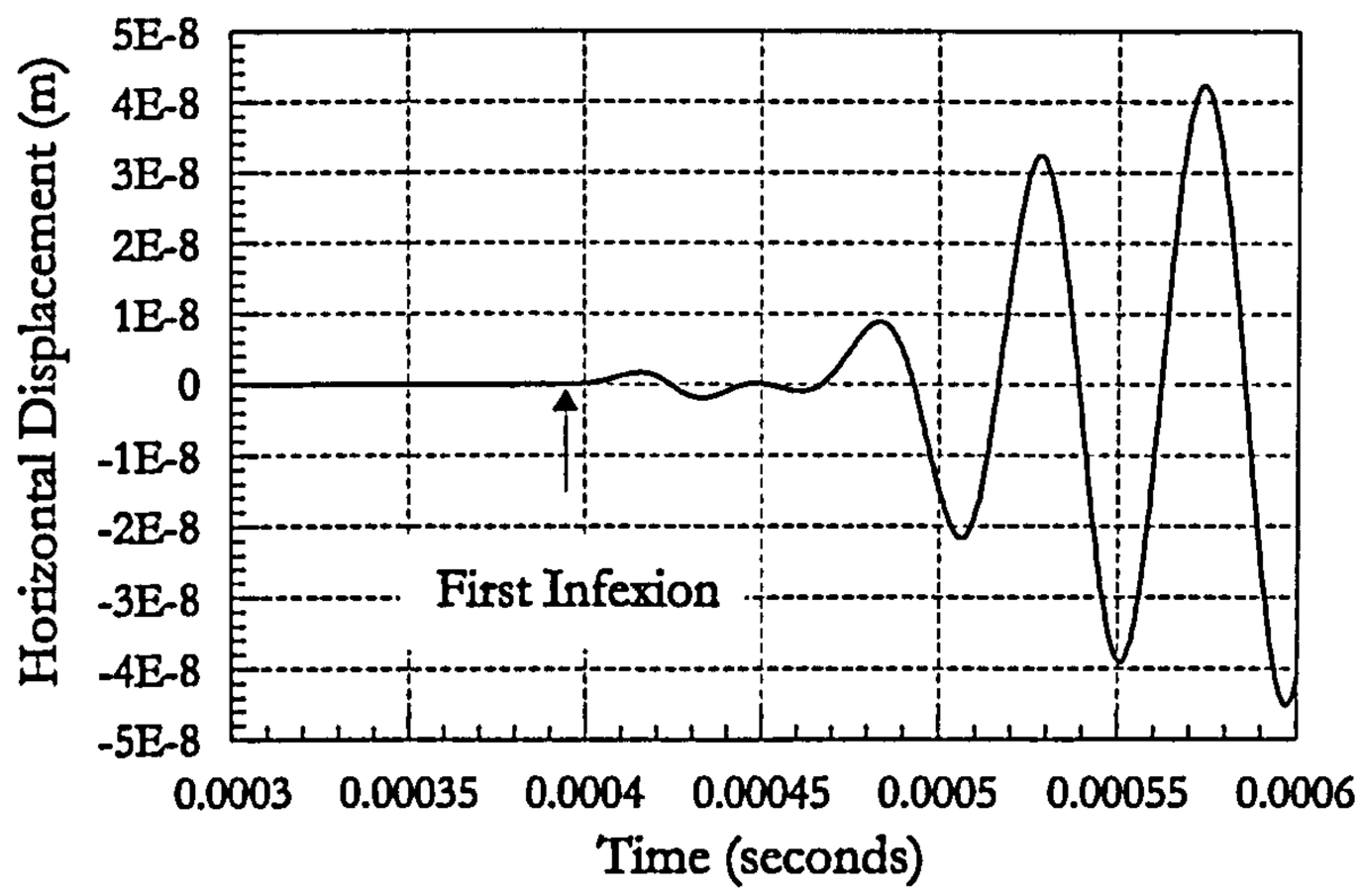

Figure 5.33: Recorded motion of receiving bender element for $R_d = 8$ (2D analysis)

Input Frequency (kHz)	R_d	Time of First Inflexion (s)	Calculated V_s (m/s)	% Error in V_s	% Error in G_{max}
2.5	1	0.000363	192.62	10.19	21.42
5	2	0.000393	177.91	1.78	3.59
7.5	3	0.00039467	177.16	1.35	2.72
10	4	0.000393	177.91	1.78	3.59
12.5	5	0.000392	178.37	2.04	4.12
15	6	0.000391	178.82	2.30	4.66
17.5	7	0.0003914	178.64	2.20	4.44
20	8	0.000392	178.37	2.04	4.12

Table 5.1: Input wave parameters and interpreted shear wave velocities from first shear wave arrival plane strain bender element analyses

The results of the finite element analyses show that as the input frequency and the number of wavelengths between the bender elements increase the near field effect becomes less prominent. This is consistent with the findings of Sanches-Salinero *et al.* (1986) and Jovičić *et al.* (1996). Interpreting what should be taken as the shear wave arrival time for the analyses with low R_d ratios is difficult. For example, the analysis with an R_d ratio of 2 has a significant downwards motion in the time interval 0.0002 – 0.00036 seconds. Its magnitude is larger than the traditionally identified near field component and if the theoretical arrival time were not known,

this perturbation could be mistaken for the shear wave arrival. The result would be a significantly higher shear wave velocity and a large error in the calculated G_{max}. The same early downward motion is also present for the analyses with R_d ratios of 3, 4 and 5 but could not be mistaken for the shear wave arrival in these cases, as its magnitude is smaller than the near field component. These results demonstrate the need for conducting a series of tests with a wide range of input frequencies to ensure that any anomalous shear wave velocity, that for example may have been calculated using the results from the analysis with an R_d ratio of 2, can be identified and ignored.

Except for the analysis with an R_d ratio of 1, the remaining results give a reasonably consistent error of between 2.7 and 4.7 percent for the calculated G_{max}. This suggests that using the first inflexion of the output signal to identify the arrival of the shear wave is not theoretically sound. However, no other feature of the output waves can consistently be correlated with the theoretical shear wave arrival time, suggesting that either the near field effect totally masks the true shear wave arrival, or the wave propagation is not one dimensional and therefore the group shear wave velocity measured does not correspond to the bulk shear wave velocity. Both of these potential sources of error reduce as the input frequency increases. This is apparent in Figure 5.33 where the significant motion starts at precisely the theoretical shear wave arrival time. An error of 4.12% is given in Table 5.1, as the arrival time was taken as the first inflexion of the output signal which still corresponded to the near field component. However, the near field component in this case is only detectable from looking closely at the exact values obtained from the numerical analyses. In practice the arrival time would have be taken as the correct one since to the naked eye the near field component is not visible.

5.5.3.8 Measurement of G_{max} by the Phase Sensitive Detection Method

The results of the traditional time of flight method presented in the previous section highlight the difficulty surrounding the identification of the first shear wave arrival. The phase sensitive detection (PSD) method purports to overcome this problem by employing an objective measurement criterion. In the following section finite element analyses will be used to investigate the accuracy of the PSD method. In practice the arrangement for a PSD test are the same as for a traditional time of

flight method. The bender elements are placed in the top and bottom platens of a triaxial cell and the transmitting element is excited by applying a signal voltage. The only modification is that the signal is a continuously cycled sine wave instead of a single sine wave pulse. This is reflected in the arrangement of the following finite element analyses. The mesh, boundary conditions, time step and material properties are the same as those used for the time of flight study. The input motion is now a continuously cycled sine wave displacement prescribed at the tip of the transmitting bender element. The input is cycled 50 times to ensure steady state conditions. Each analysis of 10000 increments took approximately seven days to run. The first results to be presented are for an R_d ratio of 2. Figure 5.34 shows a section of the horizontal displacement recorded at the tip of the receiving bender element. Plotted on the same time axis is the input displacement of the transmitting bender element.

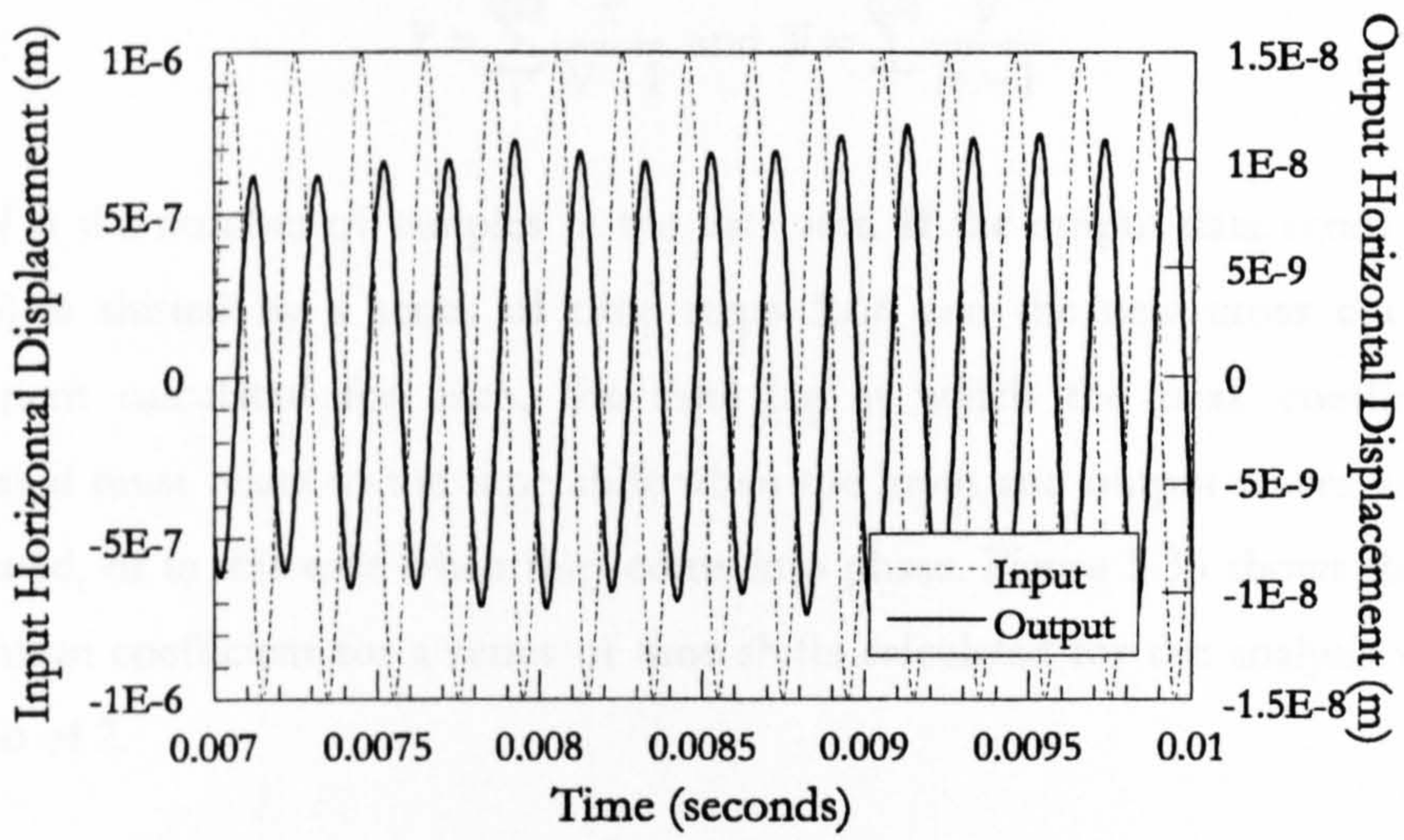

Figure 5.34: Input and output waves for continuously cycled test, $R_d = 2$ (2D)

An input frequency of 5 kHz was chosen to give an R_d ratio of 2. This means that if the group shear wave velocity was equal to the bulk shear wave velocity, there should be two complete wavelengths between the bender element tips. Therefore, the motions of the two bender elements should be in phase, although clearly they are not. It is at this point where the analysis of the finite element results differ from the procedure observed in the laboratory. In practice the frequency of the input wave would be increased or decreased until the input and the output waves came into phase. This is not possible for the finite element analyses, as each one takes several days to run. To overcome this problem a statistical analysis is performed on the results to determine the phase shift between the input and output waves. This

procedure determines the time necessary to shift the output signal so that it comes into true phase with the input signal. The results can then be used to calculate the actual number of wavelengths that exist between the bender element tips and hence the shear wave velocity can be back calculated using Equation 5.10. The cross correlation coefficient (r) given by Equation 5.13 is useful for this purpose as it gives a numerical indication of how strongly two series of data (x and y) are correlated to each other.

$$r = \frac{\sum_{1}^{N-1}(x-\bar{x})(y-\bar{y})}{\sqrt{\left[\sum_{1}^{N-1}(x-\bar{x})^2 \sum_{1}^{N-1}(y-\bar{y})^2\right]}} \tag{5.13}$$

where:

$$\bar{x} = \sum_{1}^{N-1}\frac{x}{N-1} \text{ and } \bar{y} = \sum_{1}^{N-1}\frac{y}{N-1} \tag{5.14}$$

and N is the number of samples in the data sets. If the output data series (in this case y) is shifted by a series of time steps $\pm\Delta t$, and the new cross correlation coefficient calculated for each, the time lag at which the peak coefficient is calculated must relate to the time shift when the input and output waves are most correlated, or in this case when they come into phase. Figure 5.35 shows the cross correlation coefficient for a series of time shifts calculated for the analysis with an R_d ratio of 2.

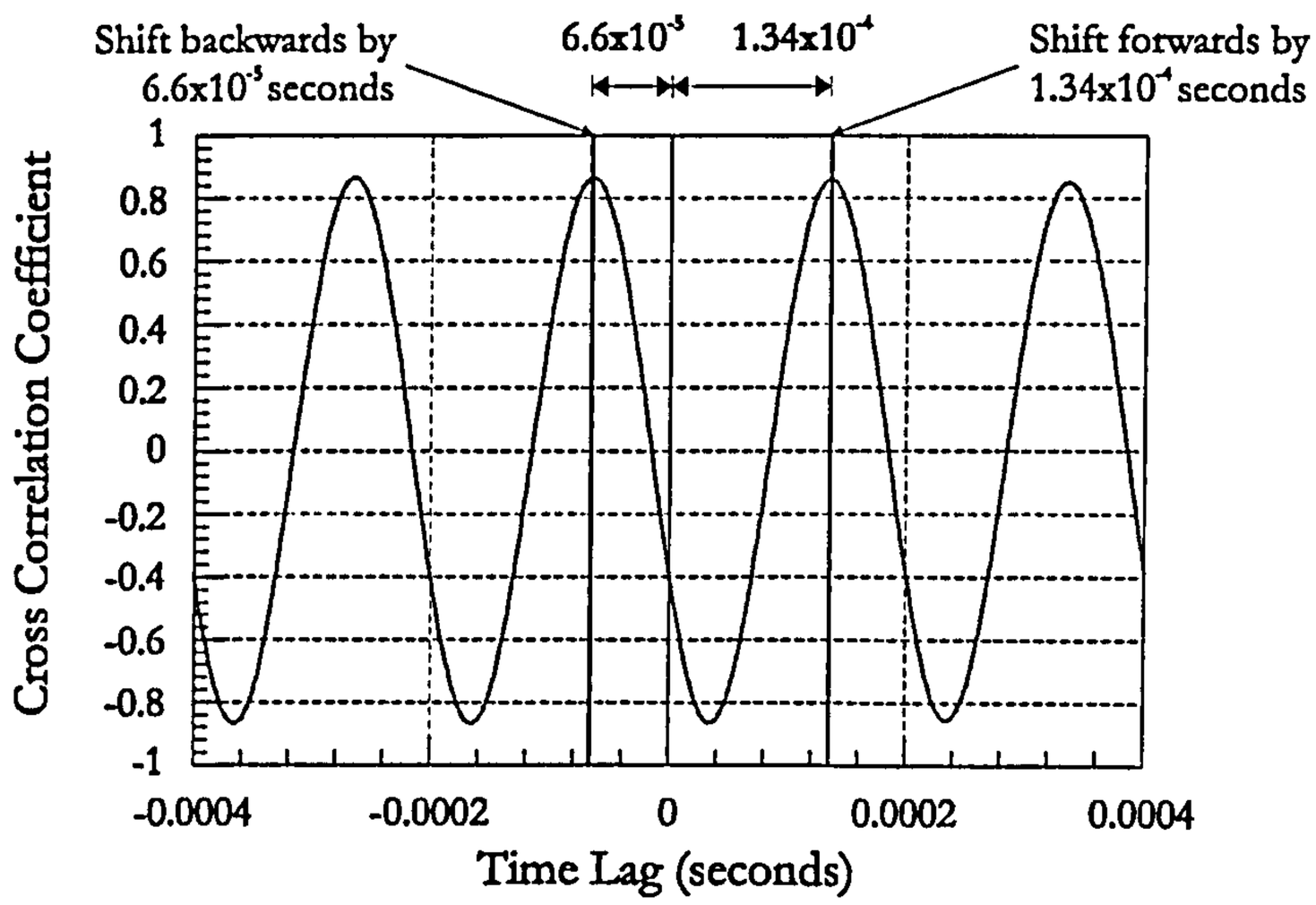

Figure 5.35: Cross correlation coefficient for $R_d = 2$, 2D analysis

If the input and output waves were in phase, the first peak in the cross correlation plot would occur at a time shift of zero seconds. Each subsequent peak would then occur at 0.0002 seconds intervals (equal to the time period of the 5 kHz input). The results shown in Figure 5.34 clearly demonstrated that the input and output waves were not in phase and this is confirmed by the cross correlation plot. There are two choices as to the correct time shift that would bring the input and output waves into phase. The output wave could either be shifted forwards by 1.34×10^{-4} seconds or shifted backwards by 6.6×10^{-5} seconds. The first option implies that in practice more than two wavelengths are present between the bender element tips and the second implies that there are less than two. To decide which is correct, a plot of the horizontal displacement along the centre line of the mesh was made and the number of waves counted. If the wave was shifted backwards, the reduced travel time would give a higher velocity and according to Equation 5.10, a lower number of wavelengths between the bender element tips. If however the wave was shifted forwards, the result would be a reduced velocity and an increased number of wavelengths. It was found to be less than two and hence the output wave should be shifted backwards by 6.6×10^{-5} seconds. To illustrate that this is the correct time shift, Figure 5.36 shows the same section of the input wave as Figure 5.34, with the output wave plotted on the same time axis, but shifted by -6.6×10^{-5} seconds.

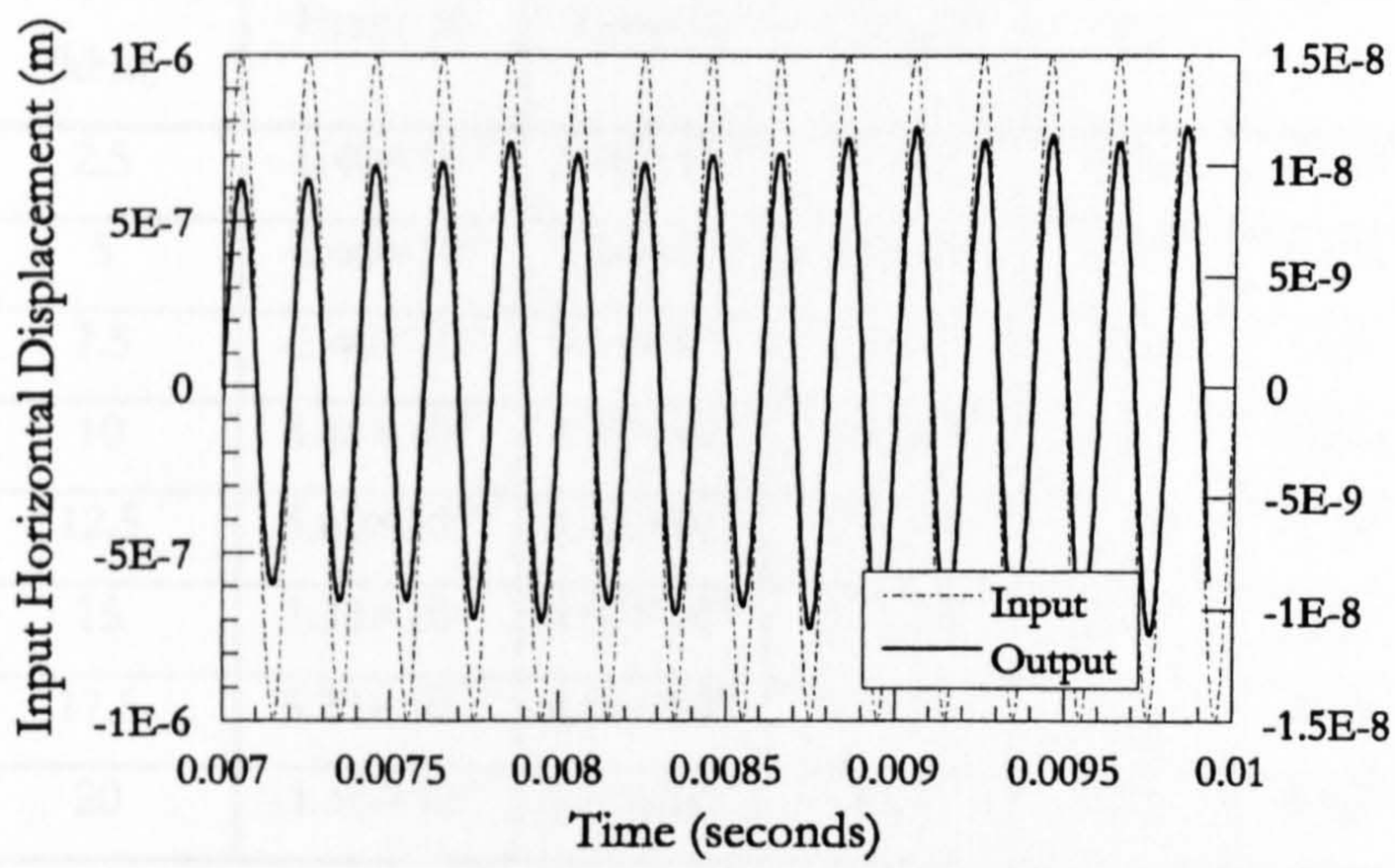

Figure 5.36: Input and time shifted output waves $R_d = 2$

Clearly all the peaks of the two wave forms coincide and the waves are now in phase. The phase difference determined by this technique can now be used to

calculate the shear wave velocity. The actual shear wave travel time is given by the theoretical value, plus or minus the error found from the cross correlation plot:

Theoretical Travel Time = 4.0×10^{-4} seconds

Error found = -6.6×10^{-5} seconds

Actual Travel Time = $4.0\times10^{-4} - 6.6\times10^{-5} = 3.34\times10^{-4}$ seconds

Theoretical Shear Wave Velocity = $0.06992 / 3.34\times10^{-4} = 209.34$ m/s

Actual R_d ratio = df/V = $(0.06992\times5000) / 209.34 = 1.67$

This is 19.76% higher than the correct shear wave velocity and gives a 43.43% error in the calculated shear modulus. The analysis was repeated for R_d ratios of 1, 3, 4, 5, 6, 7 and 8. The results of these analyses and the cross correlation plots are shown in Figure 5.58 to Figure 5.71 at the end of this chapter. The results are summarised in Table 5.2.

R_d	Input Frequency (kHz)	Time Shift Error (s)	Travel Time (s)	Measured V_s (m/s)	Actual R_d	% Error in V_s	% Error in G_{max}
1	2.5	-8.40×10^{-5}	3.16×10^{-4}	221.27	0.79	26.58	60.23
2	5	-6.60×10^{-5}	3.34×10^{-4}	209.34	1.67	19.76	43.43
3	7.5	-2.40×10^{-5}	3.76×10^{-4}	185.97	2.82	6.39	13.19
4	10	4.65×10^{-5}	4.47×10^{-4}	156.60	4.47	-10.41	-19.74
5	12.5	5.60×10^{-6}	4.06×10^{-4}	172.39	5.07	-1.38	-2.74
6	15	7.33×10^{-6}	4.07×10^{-4}	171.65	6.11	-1.80	-3.57
7	17.5	5.71×10^{-7}	4.01×10^{-4}	174.55	7.01	-0.14	-0.29
8	20	-1.30×10^{-5}	3.87×10^{-4}	180.67	7.74	3.36	6.83

Table 5.2: Input wave parameters and interpreted shear wave velocities from continuously cycled plane strain bender element analyses

Figure 5.37 shows the input frequency plotted against the measured R_d ratio and the theoretical relationship given by Equation 5.10.

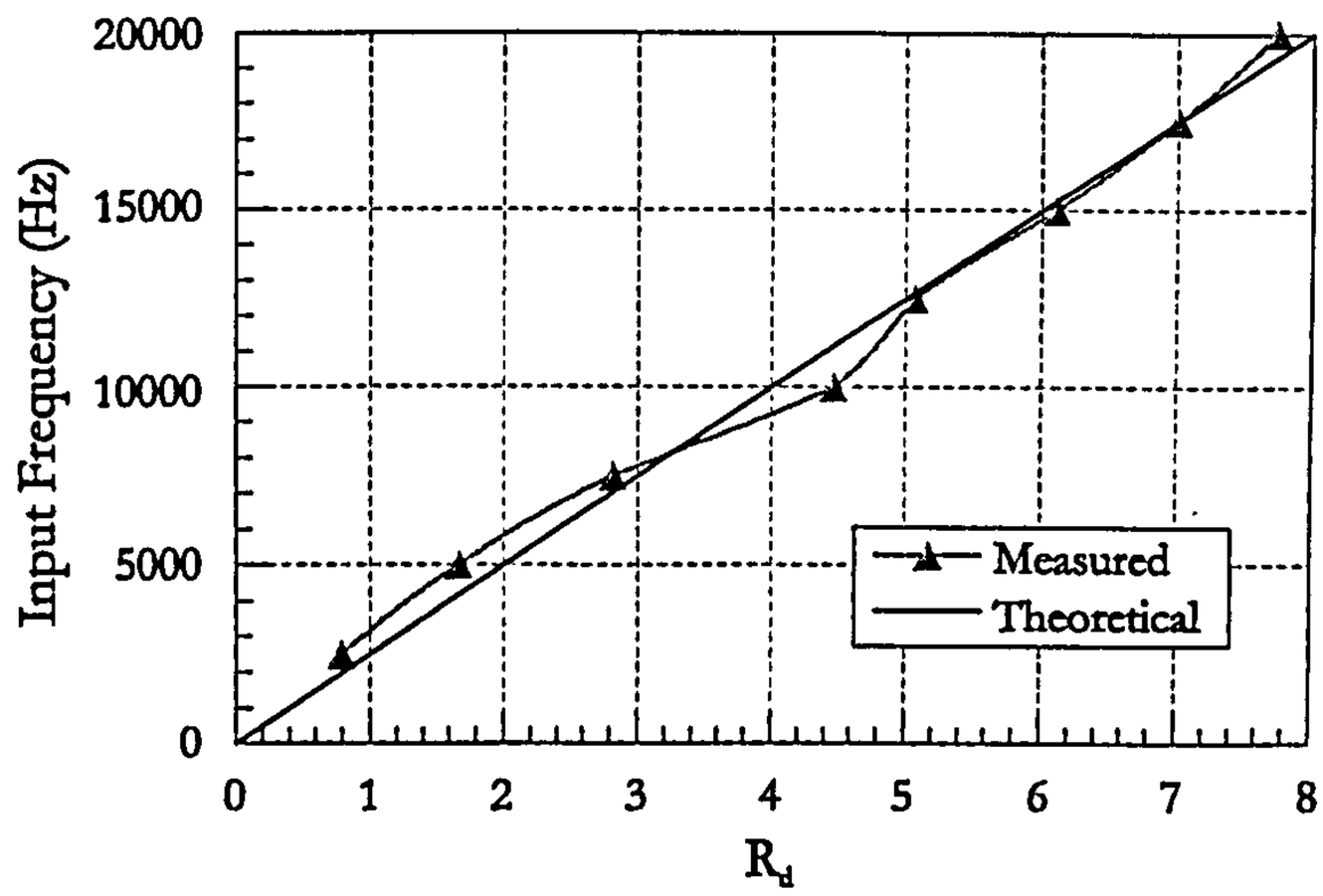

Figure 5.37: Measured and theoretical relationship between input frequency and R_d (2D analysis)

It is clear that the measured values deviate considerably from the theoretical relationship, particularly at low R_d ratios. The differences between the measured and the actual shear wave velocities do not follow any pattern and appear to be frequency dependent.

5.5.4 Fourier Series Aided Finite Element Analyses

The results presented in the previous section assumed that the geometry of a triaxial sample can be idealised by a plane strain analysis. In reality the problem is truly three dimensional and to assess the accuracy of the bender element technique it is it important to be able to model its true geometry. As mentioned previously, the computational demands of full three dimensional analyses are prohibitive. However, considerable savings can be made in analysis run time and memory storage requirements by using Fourier series aided finite element analysis to model three dimensional geometries. This technique allows problems to be analysed that have an axi-symmetric geometry but non-axi-symmetric boundary conditions and/or material properties. Bender elements are suitable for this type of analysis because the geometry of a triaxial sample is axi-symmetric but the input motion is not. The only restriction is that the geometry of the bender elements is not axi-symmetric and therefore in the analysis they will be modelled as cylindrical rods rather than as plates. This is illustrated in Figure 5.38. The finite element mesh has 950 equal 8 noded solid isoparametric elements and is also shown in Figure 5.38. Although the

Fourier series aided finite element method offers considerable time savings, it was still necessary to use a coarser mesh than in the two dimensional analysis, in order to reduce the analysis time. Each analysis of 10000 increments took approximately ten days to run.

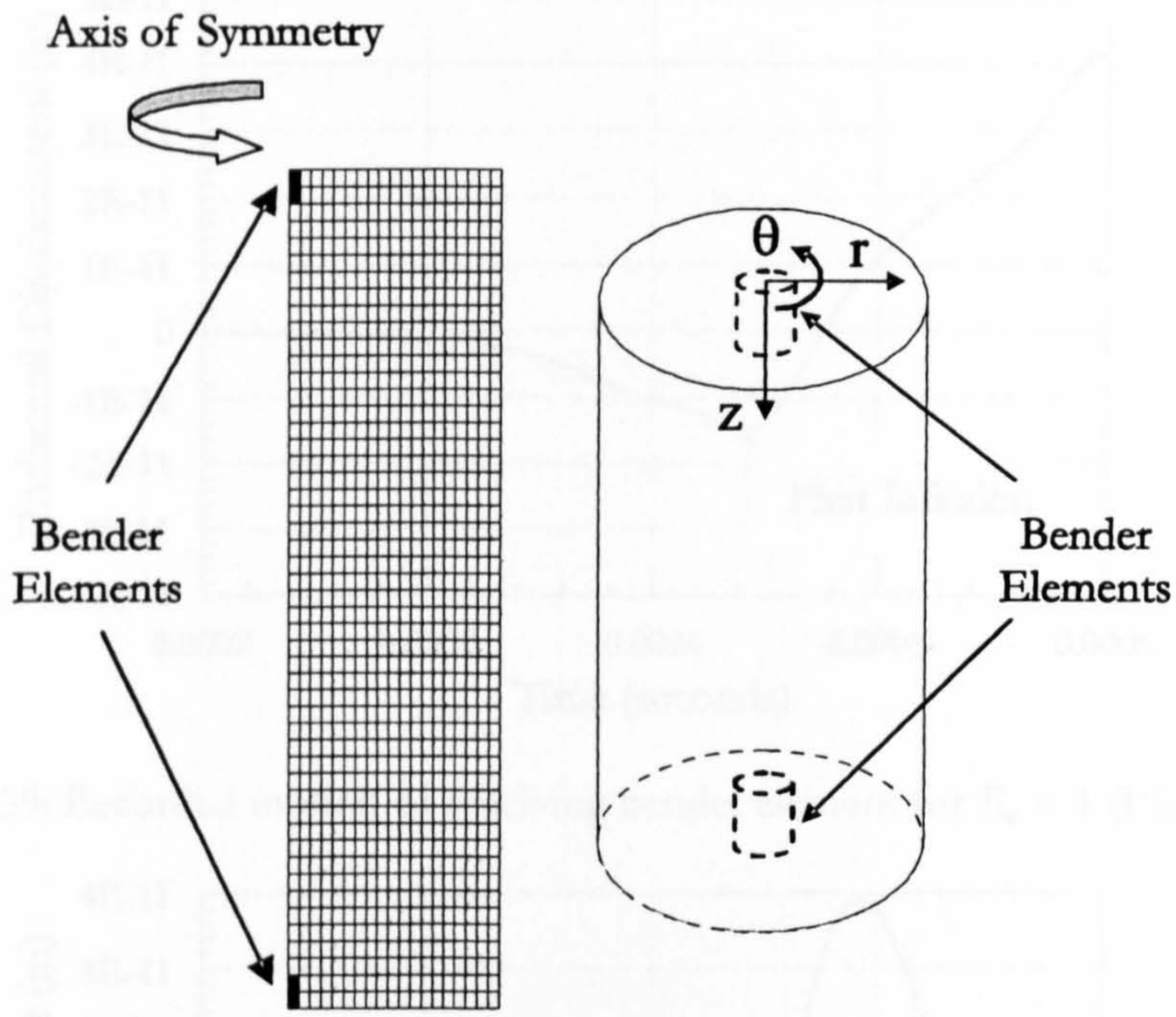

Figure 5.38: Finite element mesh and equivalent model for Fourier series aided three dimensional analysis

It is important to note that the benders are modelled by solid elements rather than beam elements, as they were modelled in the plane strain analysis. In reality the bender elements are not cylindrical and therefore the diameter chosen for the analysis is arbitrary. Several diameters were tested and it was not found to influence their dynamic behaviour significantly. For the analyses presented in the following sections a diameter of 2 mm was chosen. The boundary conditions, material properties and increment size were the same as those used in the plane strain analysis. No boundary condition should be prescribed on the axes of symmetry as movement in all three coordinate directions must be permitted. To obtain an accurate three dimensional representation, ten Fourier harmonics were used.

5.5.4.1 Estimate of G_{max} by First Shear Wave Arrival

Figure 5.39 to Figure 5.46 show enlarged views of the first shear wave arrivals for R_d ratios of 1 to 8 for the three dimensional analysis.

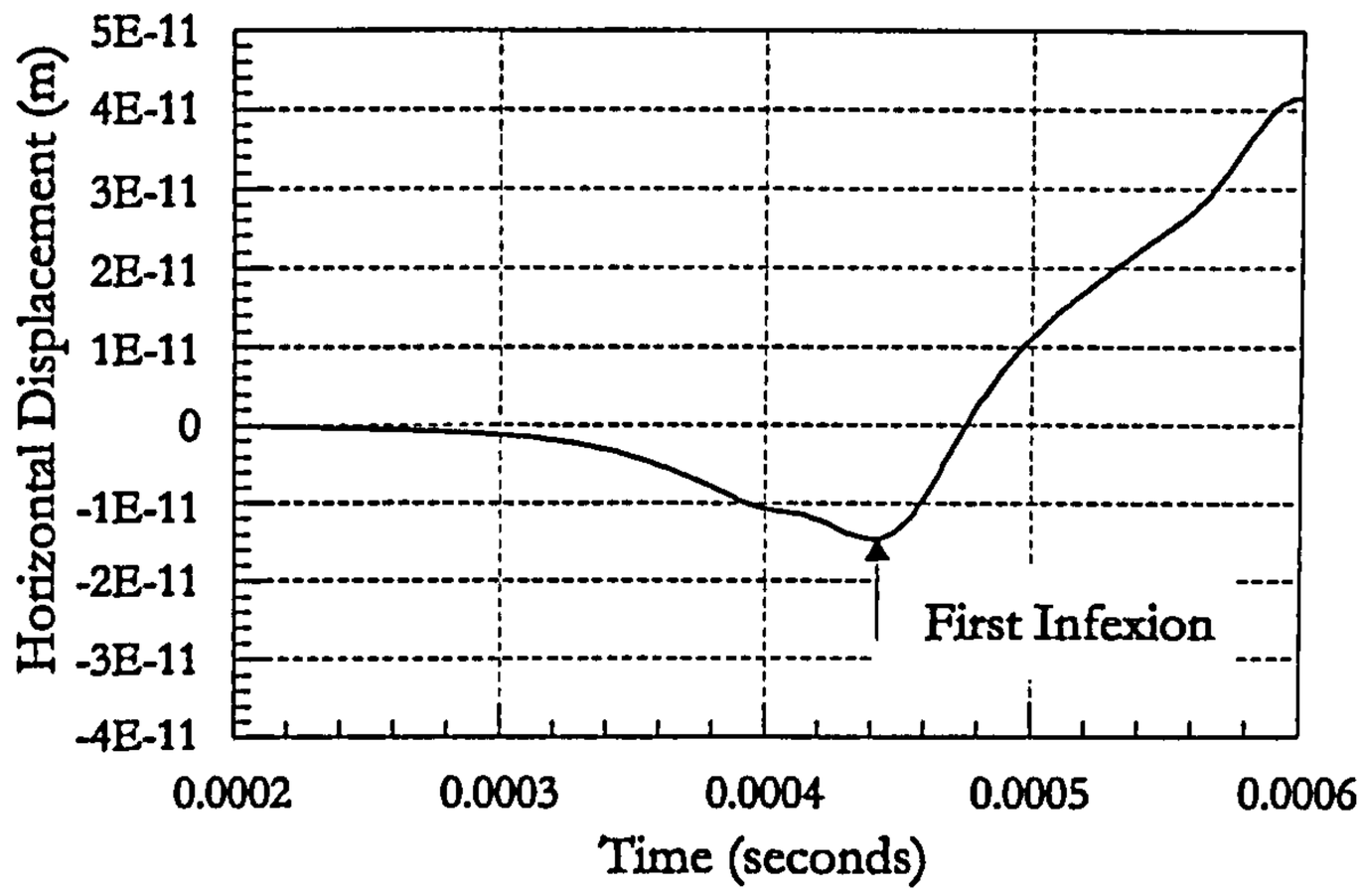

Figure 5.39: Recorded motion of receiving bender element for $R_d = 1$ (FS analysis)

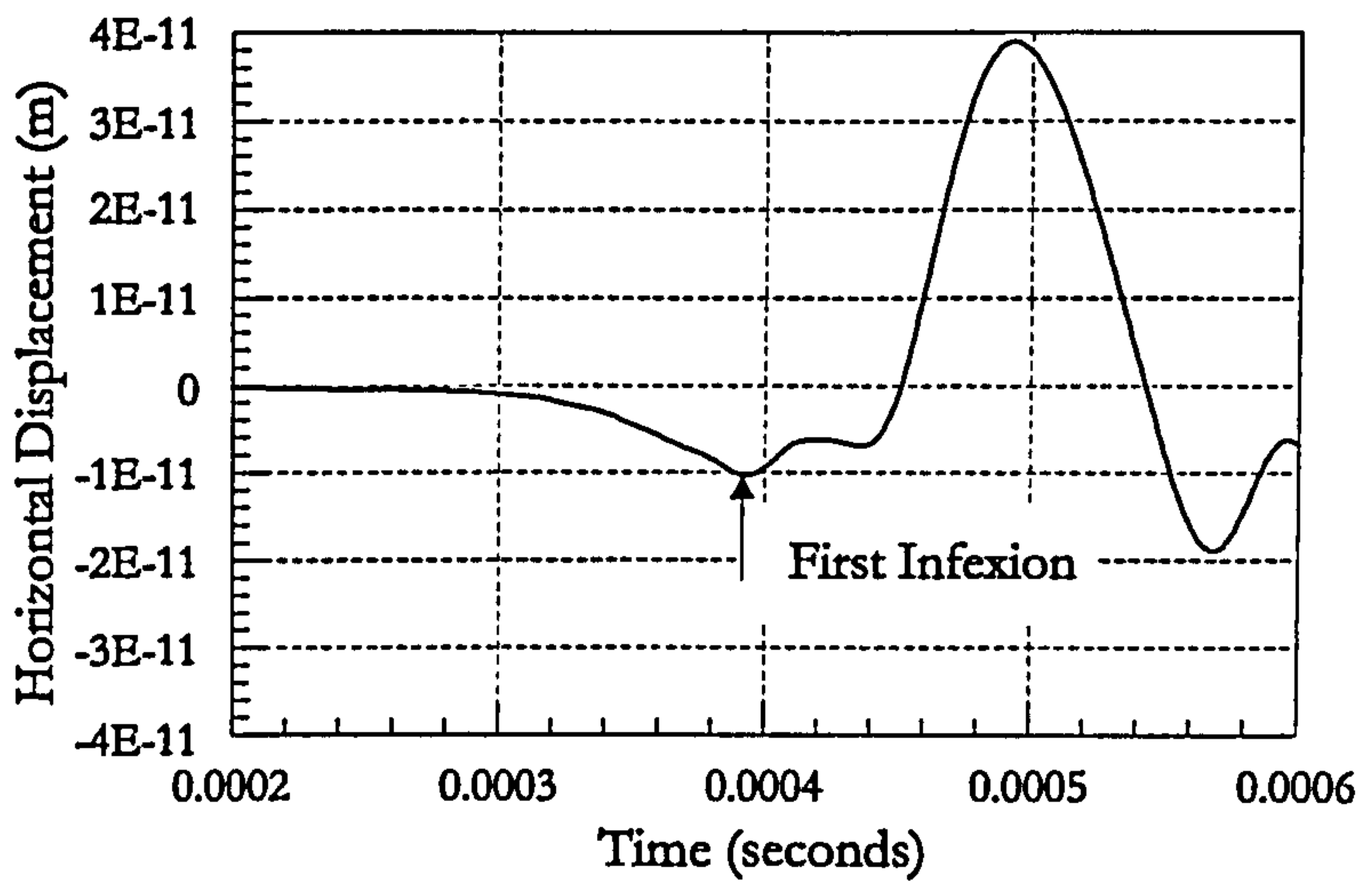

Figure 5.40: Recorded motion of receiving bender element for $R_d = 2$ (FS analysis)

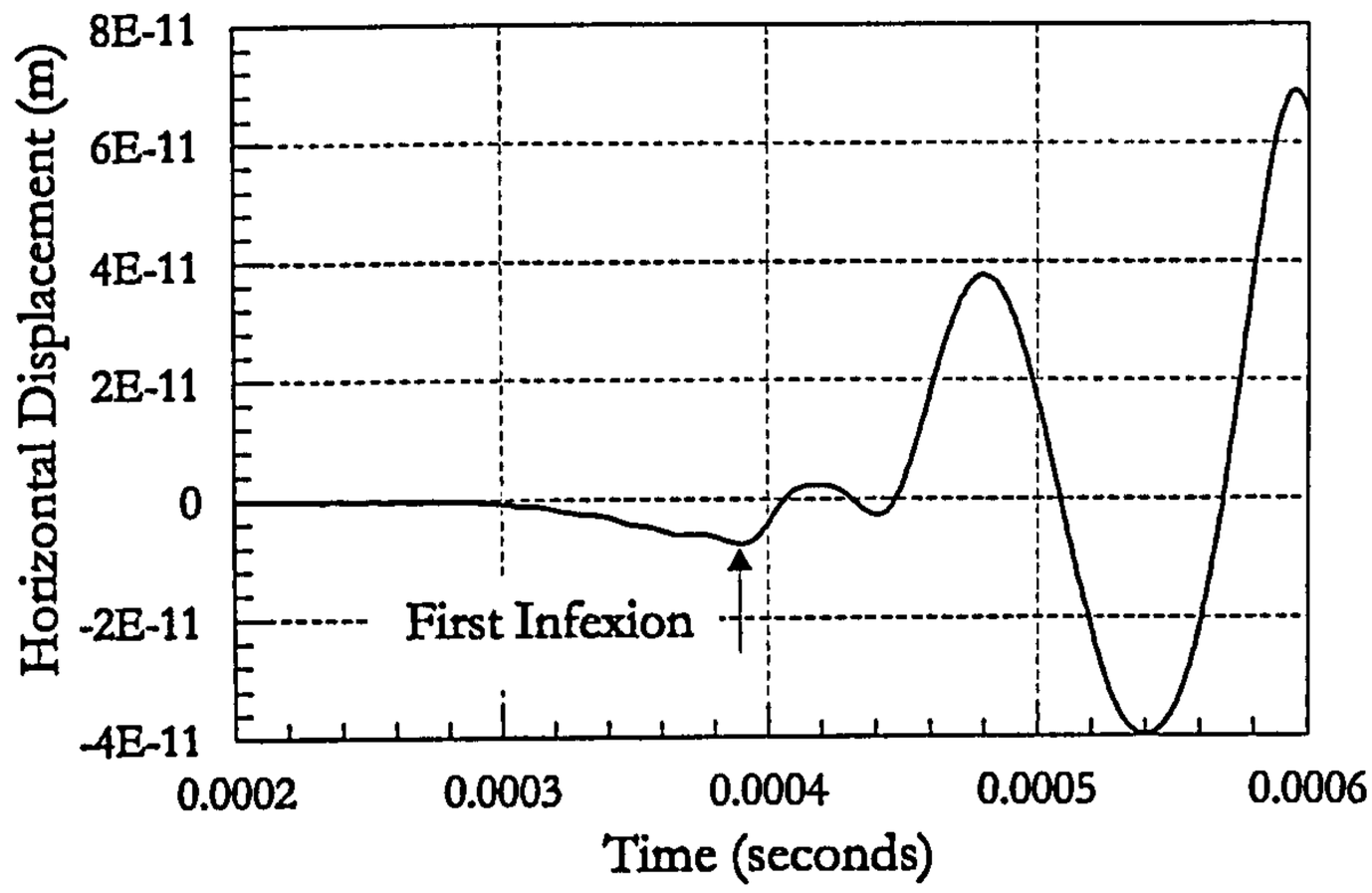

Figure 5.41: Recorded motion of receiving bender element for $R_d = 3$ (FS analysis)

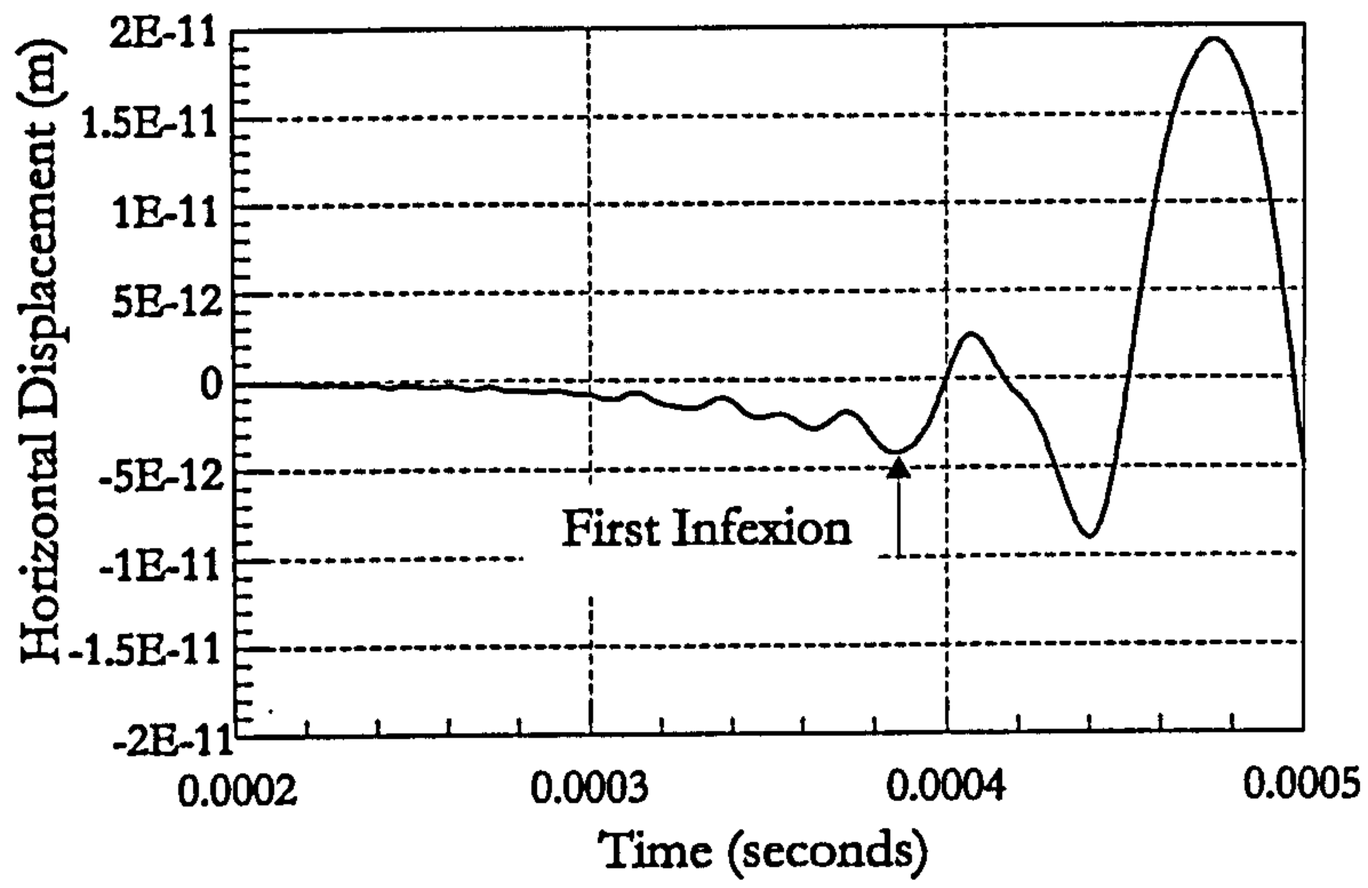

Figure 5.42: Recorded motion of receiving bender element for $R_d = 4$ (FS analysis)

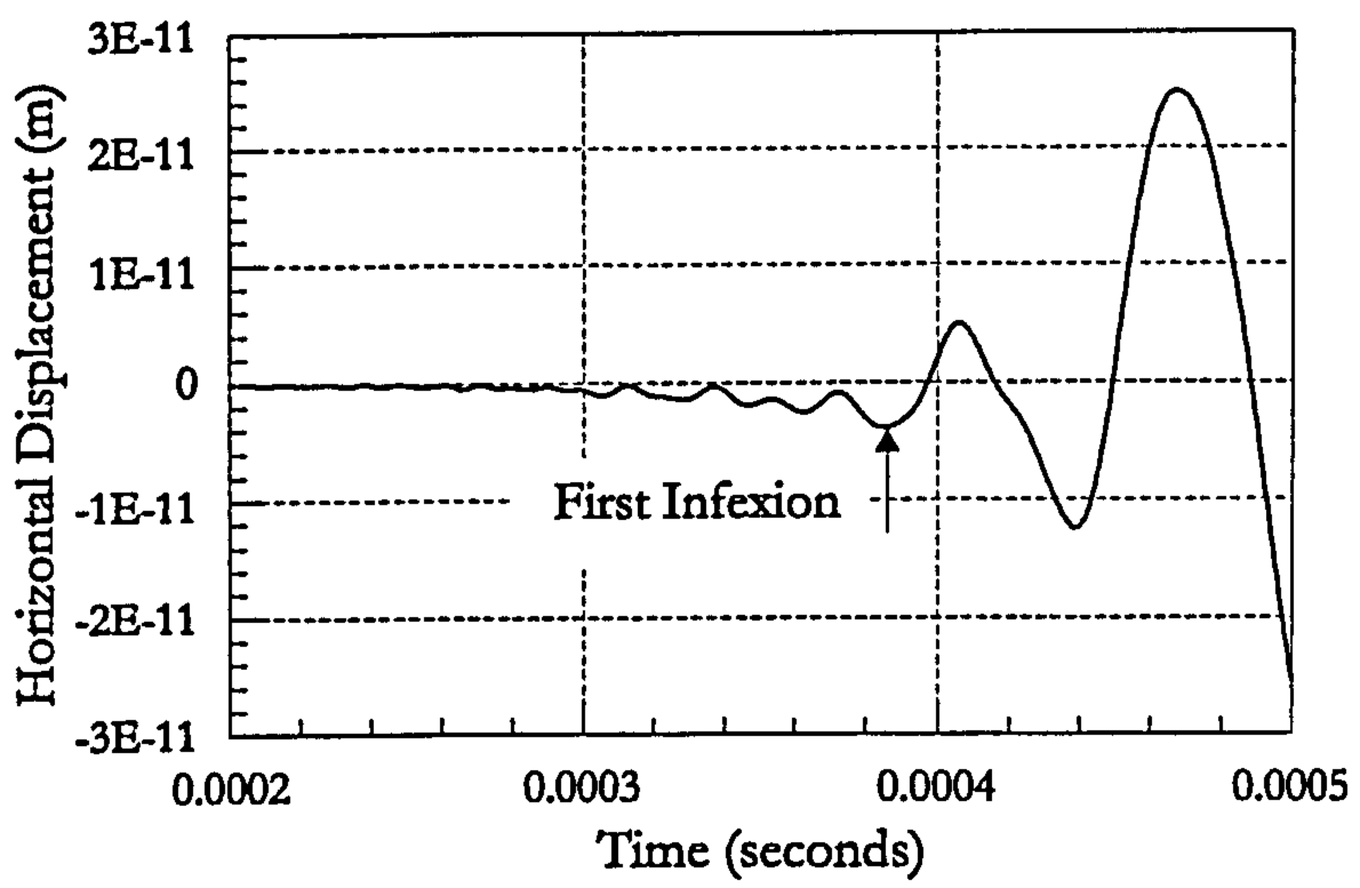

Figure 5.43: Recorded motion of receiving bender element for $R_d = 5$ (FS analysis)

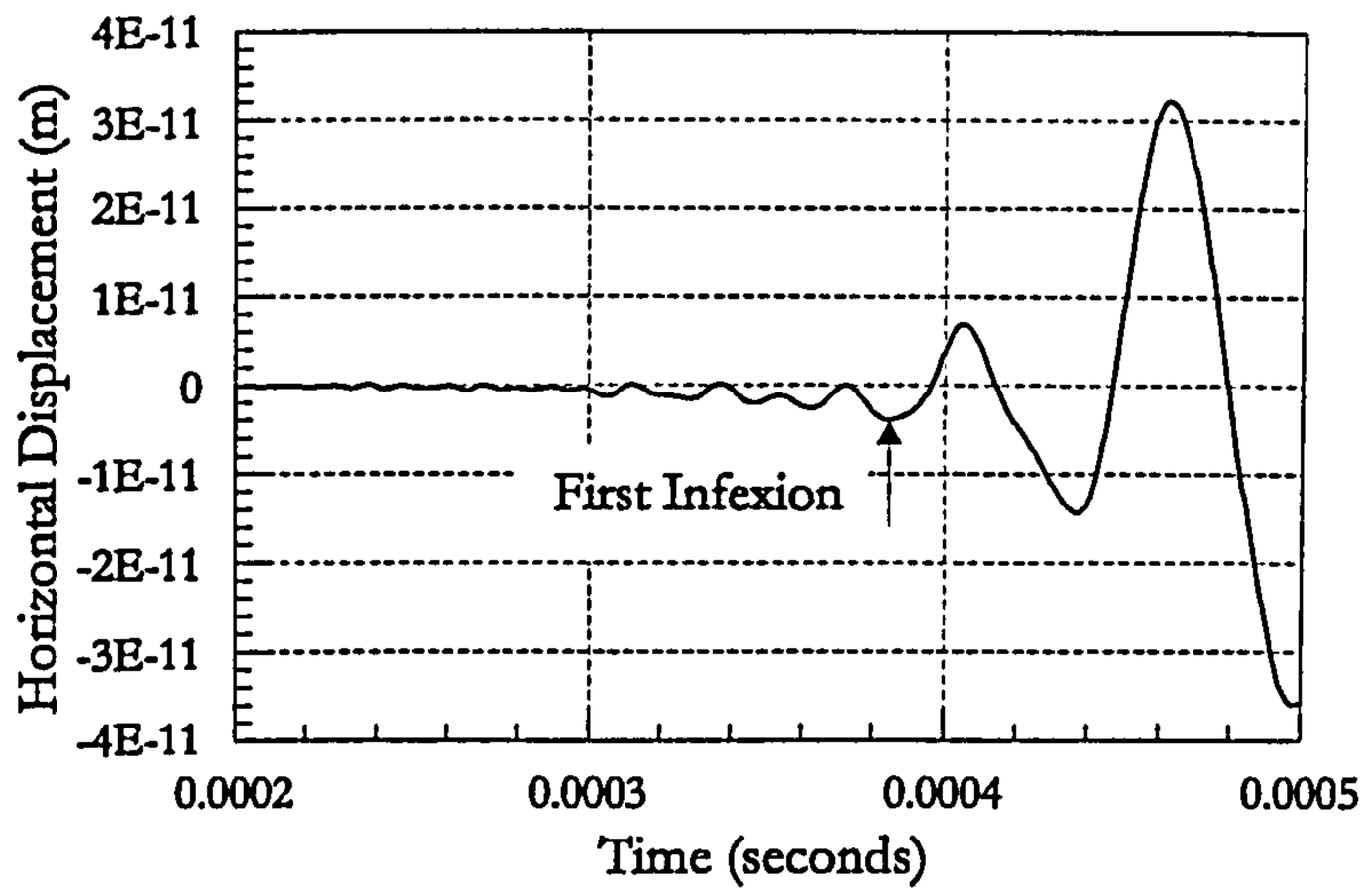

Figure 5.44: Recorded motion of receiving bender element for $R_d = 6$ (FS analysis)

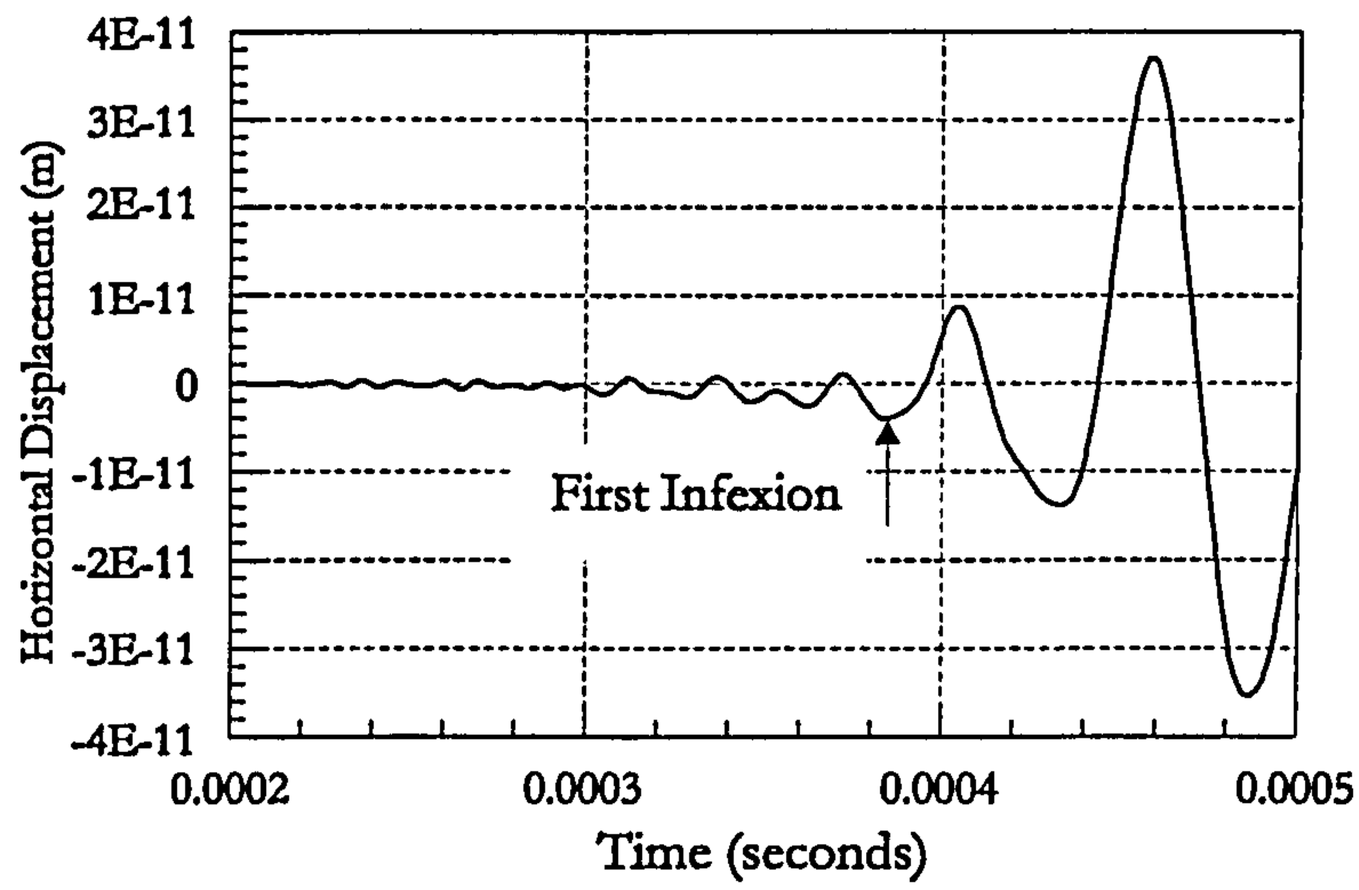

Figure 5.45: Recorded motion of receiving bender element for $R_d = 7$ (FS analysis)

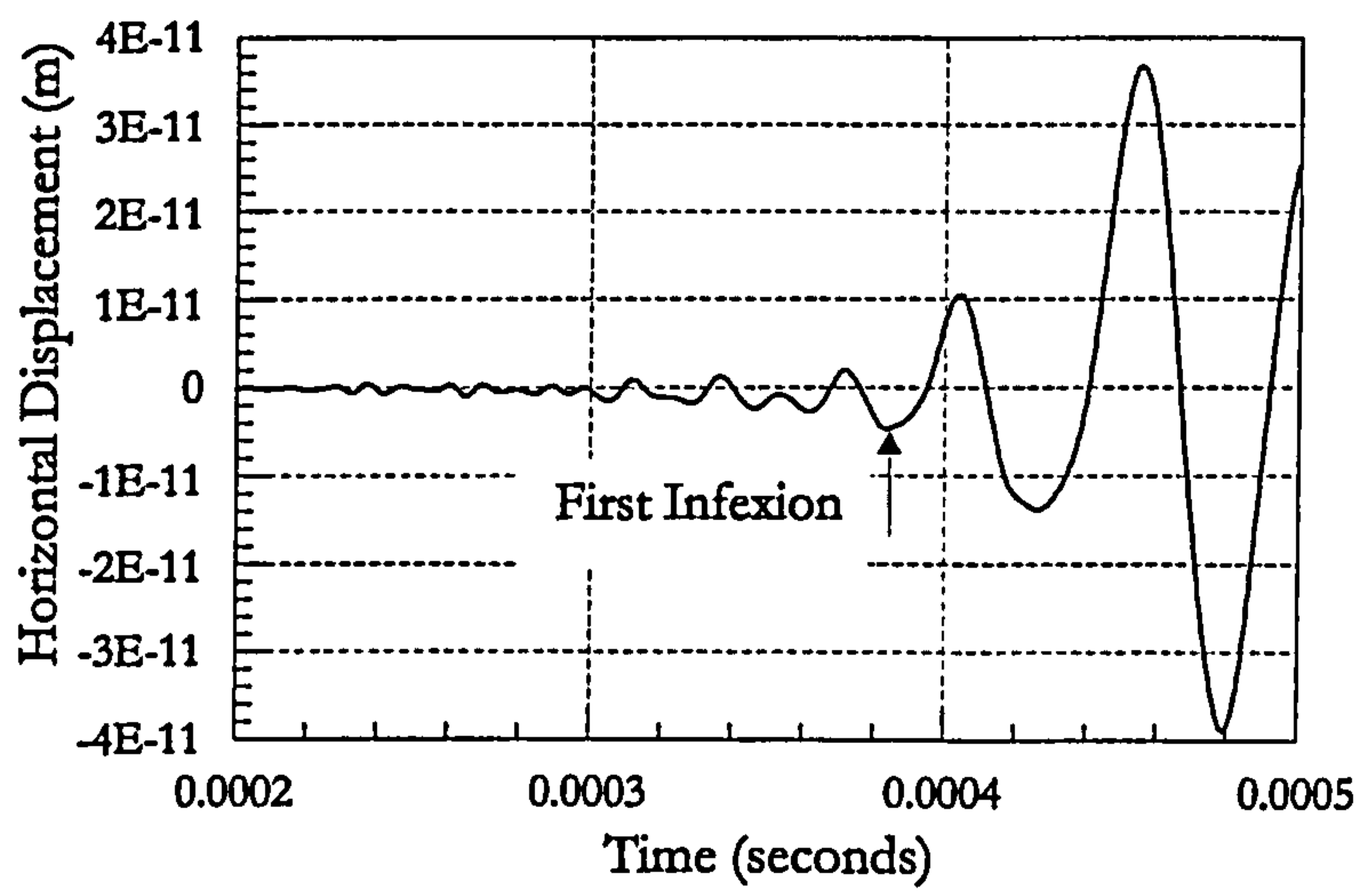

Figure 5.46: Recorded motion of receiving bender element for $R_d = 8$ (FS analysis)

The necessity of using a coarser mesh has caused the response of the receiving bender element to be less smooth than in the plane strain analyses. The parametric study of the two dimensional analyses showed that if a coarse mesh was used the results were less smooth, but they followed the same trend as the analyses that used a finer mesh. The measured shear wave arrival times and the associated shear wave velocities for the Fourier series aided finite element analysis results are summarised in Table 5.3.

Input Frequency (kHz)	R_d	Time of First Inflexion (s)	Calculated V_s (m/s)	% Error in V_s	% Error in G_{max}
2.5	1	0.000440	158.91	-9.09	-17.36
5	2	0.000393	177.91	1.78	3.59
7.5	3	0.000390	179.28	2.56	5.19
10	4	0.000386	181.14	3.63	7.39
12.5	5	0.000385	181.70	3.95	8.06
15	6	0.000384	181.93	4.08	8.32
17.5	7	0.000384	182.08	4.17	8.51
20	8	0.000384	182.32	4.30	8.79

Table 5.3: Input wave parameters and interpreted shear wave velocities from first shear wave arrival plane strain bender element analyses (FS analysis)

Generally the results follow a similar trend to the two dimensional plane strain analyses. Although distinguishing between numerical oscillations and genuine wave motion is made difficult by the use of a coarser mesh, the near field component (approximated by the dotted lines in Figure 5.42 to Figure 5.46) can be seen to reduce as the ratio, R_d increases. Again no consistent point can be associated with the theoretical shear wave arrival time and therefore the three dimensional analyses confirm the conclusion of the two dimensional study that the assumption of one dimensional wave propagation for bender element tests has an inherent error associated with it.

5.5.4.2 Estimate of G_{max} by the Phase sensitive Detection Method

To investigate if representing the three dimensional geometry has an effect on the accuracy of the phase sensitive detection method, the same procedure as

described in Section 5.5.3.8 was used for the Fourier series aided analyses. The input was cycled a total of 50 times and the phase shift between the input and output waves calculated by means of the cross correlation plot. The results of the analyses and the cross correlation calculations are shown in Figure 5.72 to Figure 5.87 at the end of this chapter. A summary of the result are shown in Table 5.4.

R_d	Input Frequency (kHz)	Time Shift Error (s)	Travel Time (s)	Measured V_s (m/s)	Actual R_d	% Error in V_s	% Error in G_{max}
1	2.5	-1.24×10^{-4}	2.76×10^{-4}	253.33	0.69	44.93	110.04
2	5	-1.44×10^{-4}	2.56×10^{-4}	273.13	1.28	56.25	144.14
3	7.5	-1.33×10^{-5}	3.87×10^{-4}	180.83	2.90	3.45	7.02
4	10	5.10×10^{-5}	4.51×10^{-4}	155.03	4.51	-11.31	-21.34
5	12.5	2.64×10^{-5}	4.26×10^{-4}	163.98	5.33	-6.19	-12.00
6	15	4.47×10^{-5}	4.45×10^{-4}	157.24	6.67	-10.05	-19.08
7	17.5	1.09×10^{-5}	4.11×10^{-4}	170.18	7.19	-2.64	-5.22
8	20	0.00	4.00×10^{-4}	174.80	8.00	0.00	0.00

Table 5.4: Input wave parameters and interpreted shear wave velocities from continuously cycled Fourier series aided bender element analyses

The input frequency is plotted against the measured ratio R_d in Figure 5.47.

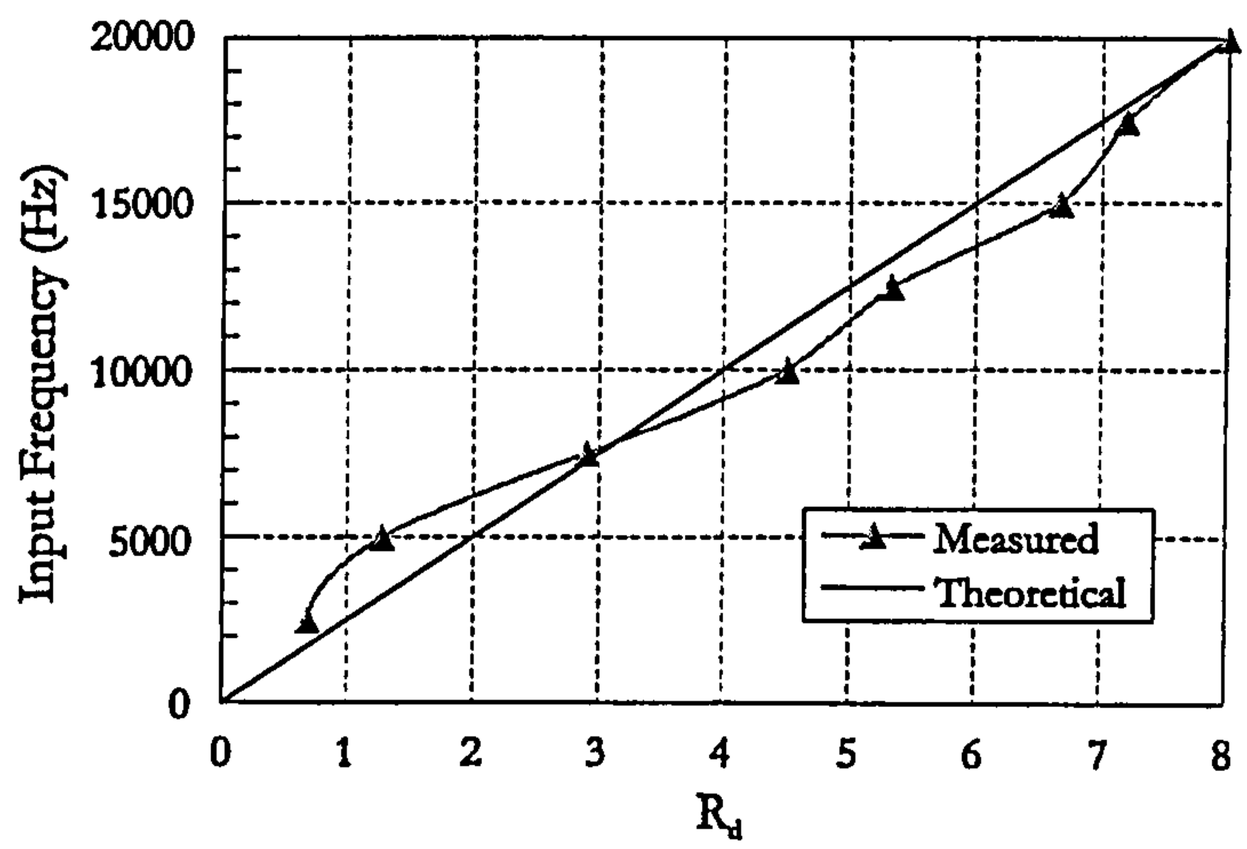

Figure 5.47: Measured and theoretical relationship between input frequency and R_d (FS analysis)

The general trend of the results is similar to that observed for the plane strain analyses. There is a large discrepancy between the measured values and the theoretical relationship which does not appear to follow any clear pattern. For R_d ratios below 3 the method over estimates the shear wave velocity. For R_d ratios above 3 the shear wave velocity is underestimated, although the results appear to tend towards the theoretical relationship at high R_d ratios.

5.6 Discussion

5.6.1 First Shear Wave Arrival Technique

To restrict the difference between the group and bulk shear wave velocities to less than 5%, Arroyo *et al.* (2002) proposed the following frequency limit.

$$f_{\min} = \frac{v_s}{\lambda} \geq \frac{v_s}{1.6d} \tag{5.15}$$

where λ is the wavelength, v_s is the shear wave velocity and d the distance between the bender element tips. The frequency limit implies that the value of the ratio R_d should be above 1.6. The results from both the two and three dimensional analyses presented in this study suggest that if the ratio R_d is two or above, the near field effect does not significantly affect the measured shear wave velocity. This is consistent with the findings of Arroyo *et al.* who also proposed a rigorous criterion for identifying the first shear wave arrival by ignoring peaks below a certain limit, depending on the type of input wave. When this criterion was applied to real test data it did not reduce the scatter in the measured shear wave velocity. This must therefore be due to some phenomenon that cannot be modelled by the finite element analysis. Gajo (1996) suggested that the inertial coupling between the soil matrix and the pore fluid causes a reduction in the velocity of all types of waves. The importance of inertial coupling is dependent on the combination of the input frequency and the permeability of the soil. For example, soils of high permeability will have low levels of viscous coupling and therefore the inertial coupling will become more significant. Whilst this may explain the input frequency dependent nature of the shear wave velocity that has been observed by some experimentalists

in the laboratory (Moncaster (1997)), it cannot explain the scatter in the data for a given soil, which for a certain input frequency should exhibit the same degree of inertial coupling. There must be some mechanical feature that cannot be reproduced by the finite element analysis that causes the scatter in the experimental data. This maybe the lack of connectivity between the bender elements and the surrounding soil, which may cause the delay in the initiation of the shear wave or create unintended local perturbations. At this point these ideas are pure speculation and their influence cannot be investigated numerically.

Despite the problems still encountered in the laboratory, some conclusions can be drawn from this study.

- The results confirm the frequency limit proposed by Arroyo *et al.* (2002) to avoid the significant influence of the near field effect.
- No characteristic feature of the output waves could be associated with the theoretical shear wave arrival time.
- The first inflexion of the output signal does not correspond to the first shear wave arrival, as this is masked by the near field effect. However, it is probably as good as any other measurement criterion for use with low input frequencies as it appears to have a reasonably consistent error associated with it (see Figure 5.26 to Figure 5.30).
- For higher input frequencies the first significant motion of the output signal should be taken as the first shear wave arrival (see Figure 5.31 to Figure 5.33).
- A series of tests should be performed for a range of input frequencies to eliminate any anomalous measurements.

Theoretically the method appears to be sound. Working with an input frequency that creates more than two wavelengths between the bender element tips and then assuming the shear wave arrival to be signified by the first inflexion of the output wave results in a small, but well understood error. Working with an R_d ratio of over 6 whenever possible and taking the shear wave arrival to be the first significant motion of the bender element results in virtually no error at all. In practice the results are not as ideal as those modelled by the finite element analysis and these simple criteria can only be applied if the output motion is clear and consistent.

Therefore the scatter in the experimental results demonstrated by Arroyo *et al.* (2002) must be due to erroneous interpretation of the output signal due to anomalous oscillations in the output signal. This may be due to poor installation of the bender elements or electrical interference from neighbouring wires and reducing these interferences is where the research effort now must be concentrated.

5.6.2 Phase Sensitive Detection Method

It appears that the time of flight method for determining the shear wave velocity of a soil, although theoretically sound when operated outside the near field, does suffer from erroneous user interpretations. The phase sensitive detection method is designed to overcome this problem by using an objective measurement criterion. The purpose of this numerical study was to investigate whether the group shear wave velocity of a standing wave produced by a continuously cycled input corresponded to the bulk shear wave velocity of the soil. Figure 5.48 shows the results of the two and three dimensional analyses compared to the theoretical relationship.

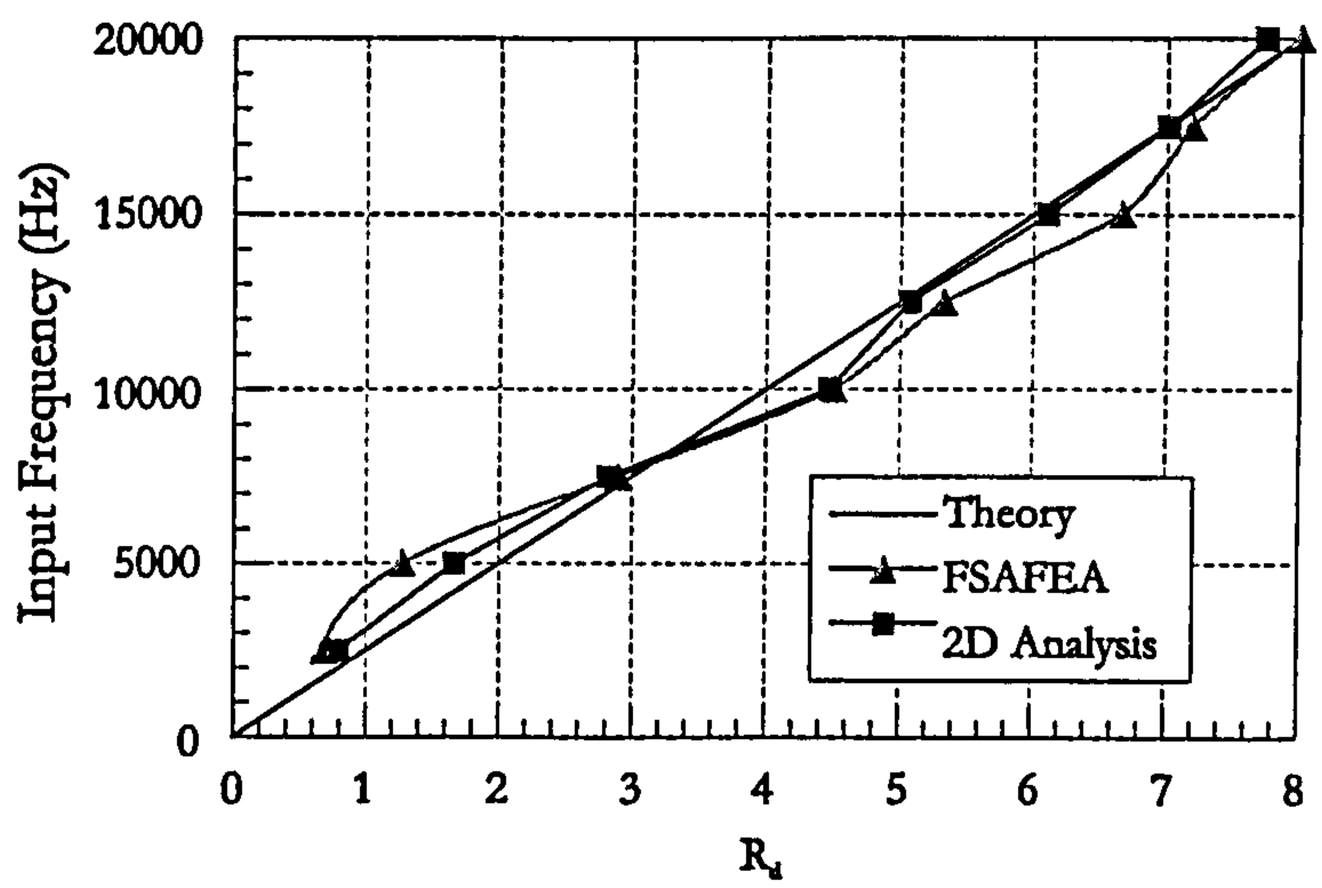

Figure 5.48: Results of phase sensitive detection method for two and three dimensional analyses

Both sets of analyses give an *S* shape for the relationship between the input frequency and the ratio R_d. Figure 5.49 shows the results of a series of continuously cycled bender element tests conducted by Rolo (2003). The tests were performed on a silty material at a confining pressure of 50 kPa in a triaxial sample.

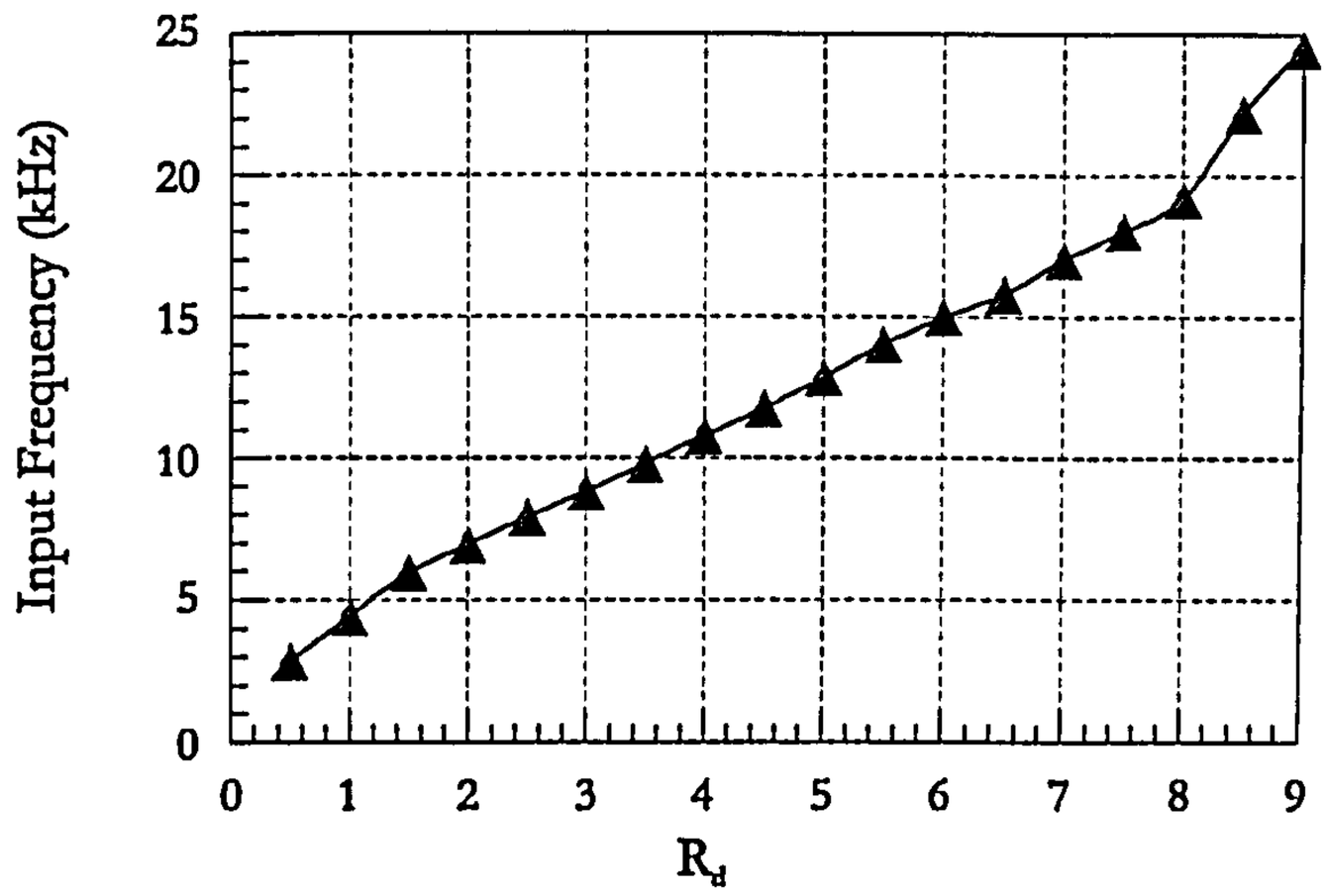

Figure 5.49: Experimental results of continuously cycled tests

The experimental results exhibit the same *S* shape as the finite element results and confirm that the shear wave velocity of the standing wave created by a continuously cycled bender element is frequency dependent. Determining what should be taken as the true bulk shear wave velocity in practice from the kind of results shown in Figure 5.49 is extremely difficult. The advantage of the finite element analyses is that the bulk shear wave velocity is known from the input parameters and hence the results can be correlated to the theoretical relationship. For both the two and three dimensional analyses the shear wave velocity appears to be considerably over estimated at lower R_d ratios. There is a suggestion, especially for the three dimensional analysis, that at higher R_d ratios the results tend to the theoretical relationship. Therefore, in practice the line representing the bulk shear wave velocity is best estimated by fitting a line through the mean position of the test results but tending to the results at higher R_d ratios.

To investigate why the numerical results do not follow the theoretical relationship exactly, a fast Fourier transform analysis was performed on the results of the two dimensional plane strain analyses using the Matlab computer package to determine the frequency components of the output wave. The results for each R_d ratio are shown in Figure 5.50 to Figure 5.57.

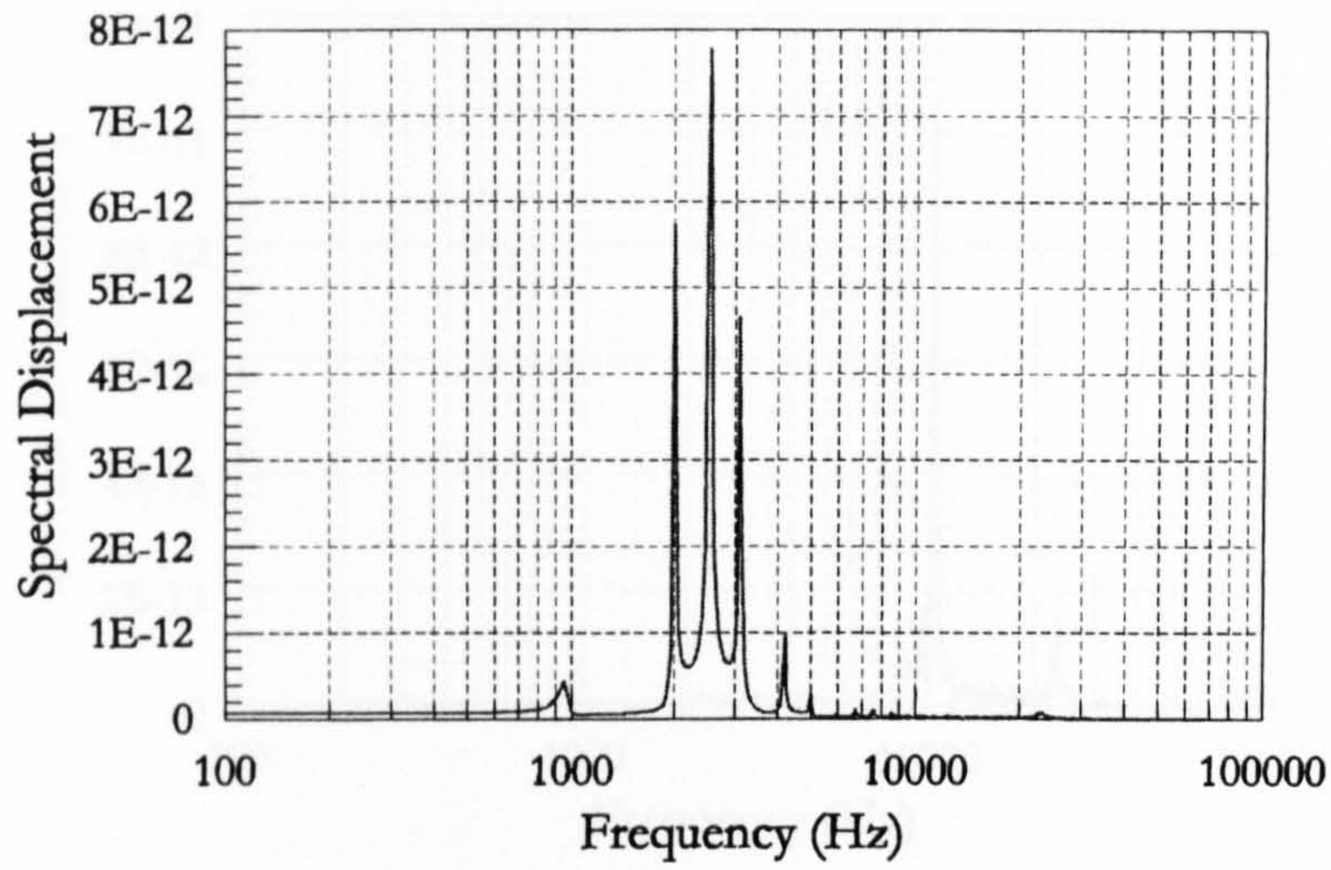

Figure 5.50: Fast Fourier transform for two dimensional analysis with $R_d = 1$

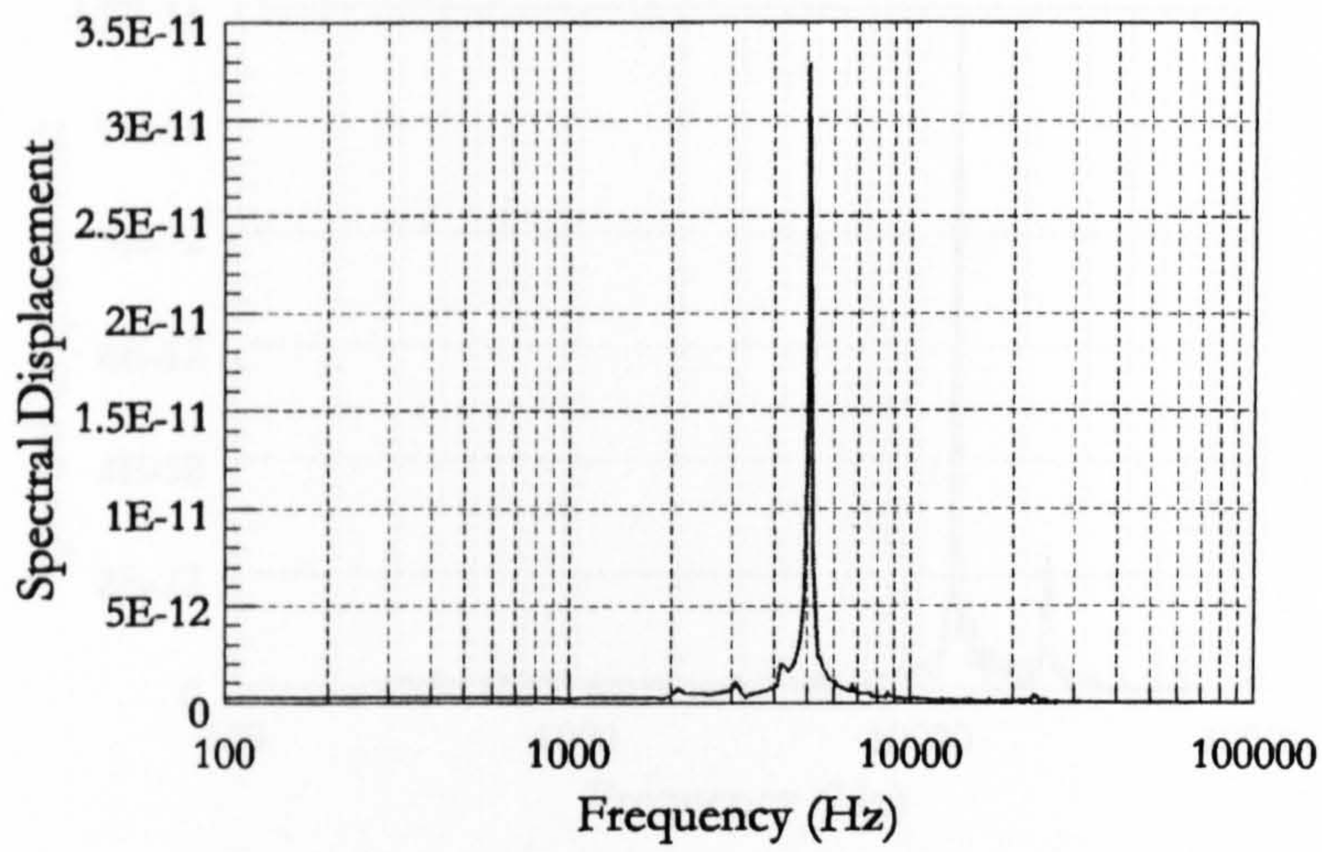

Figure 5.51: Fast Fourier transform for two dimensional analysis with $R_d = 2$

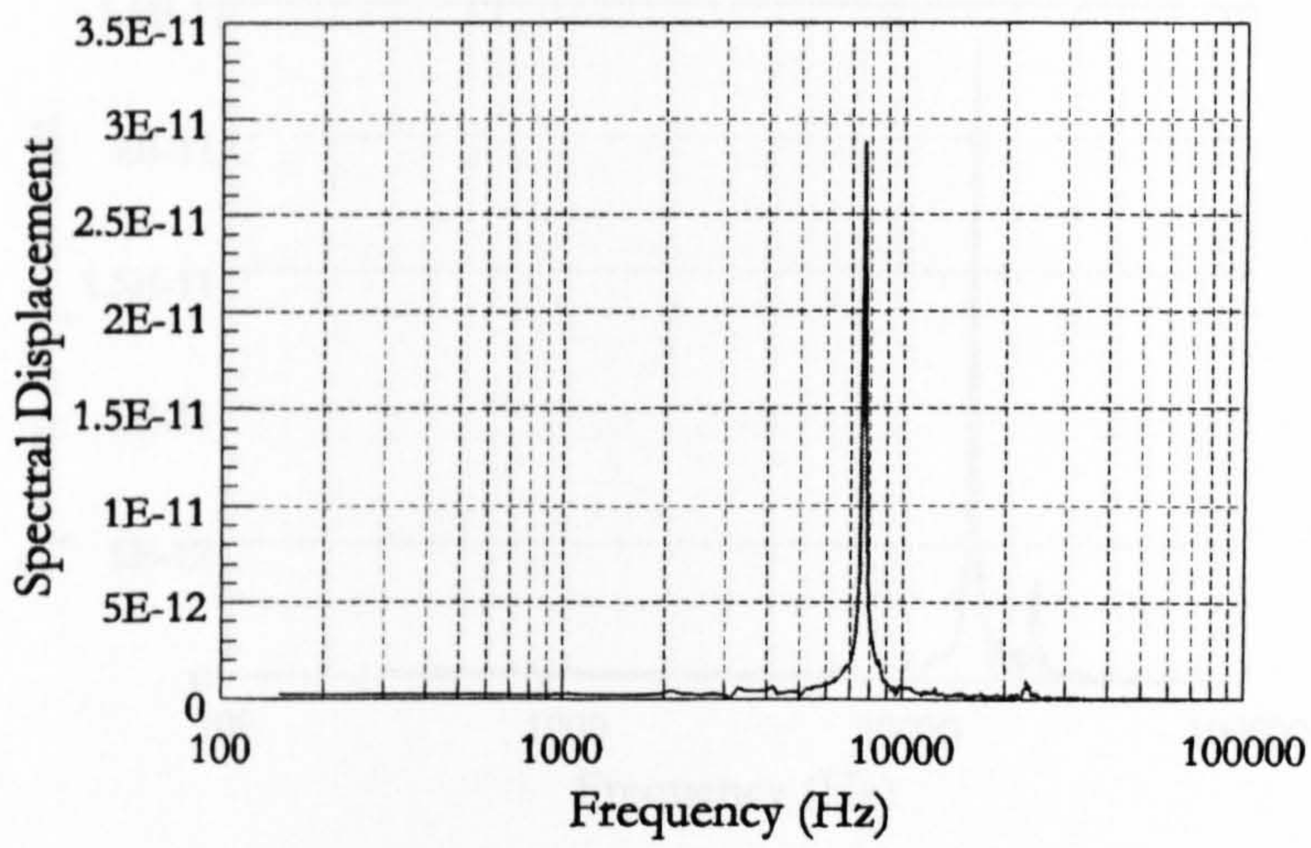

Figure 5.52: Fast Fourier transform for two dimensional analysis with $R_d = 3$

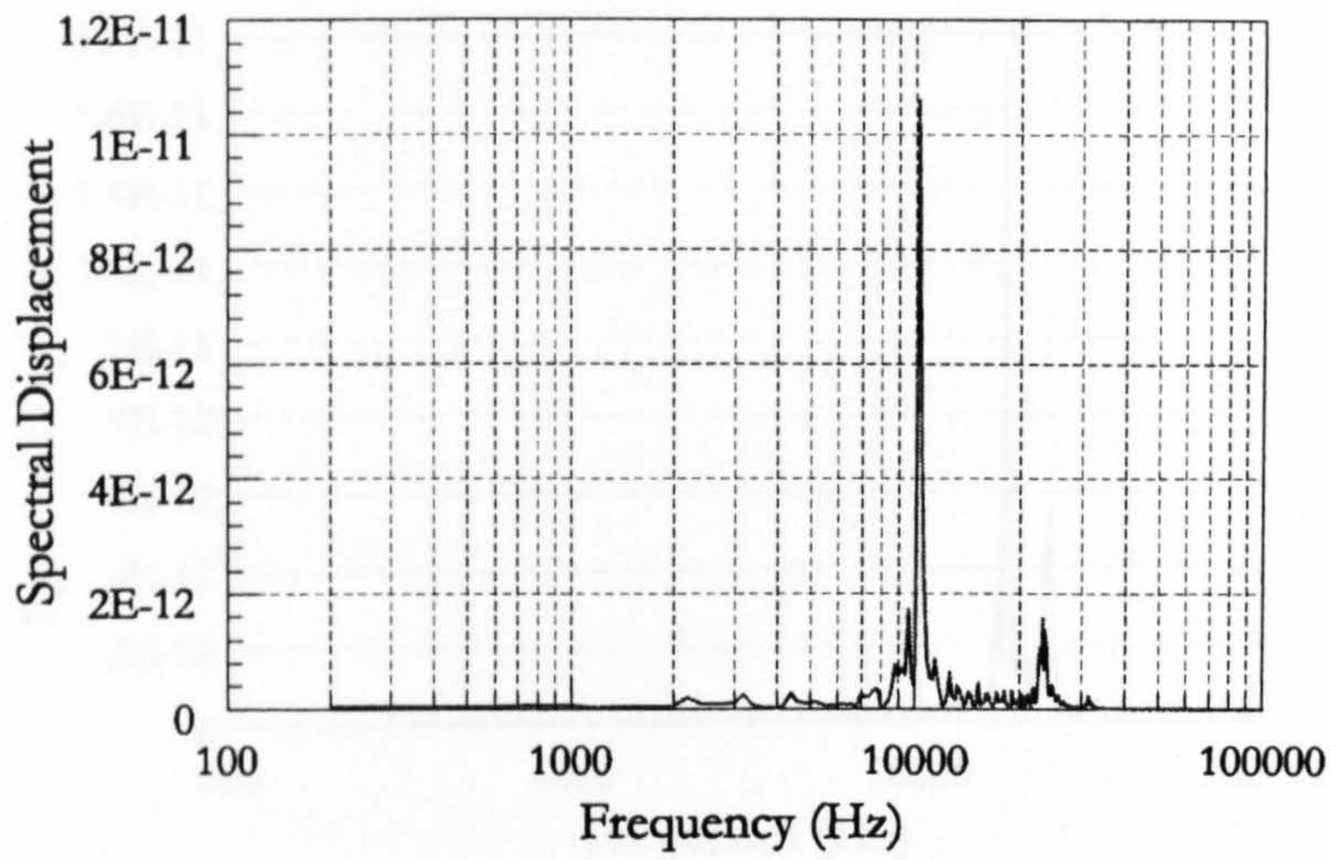

Figure 5.53: Fast Fourier transform for two dimensional analysis with $R_d = 4$

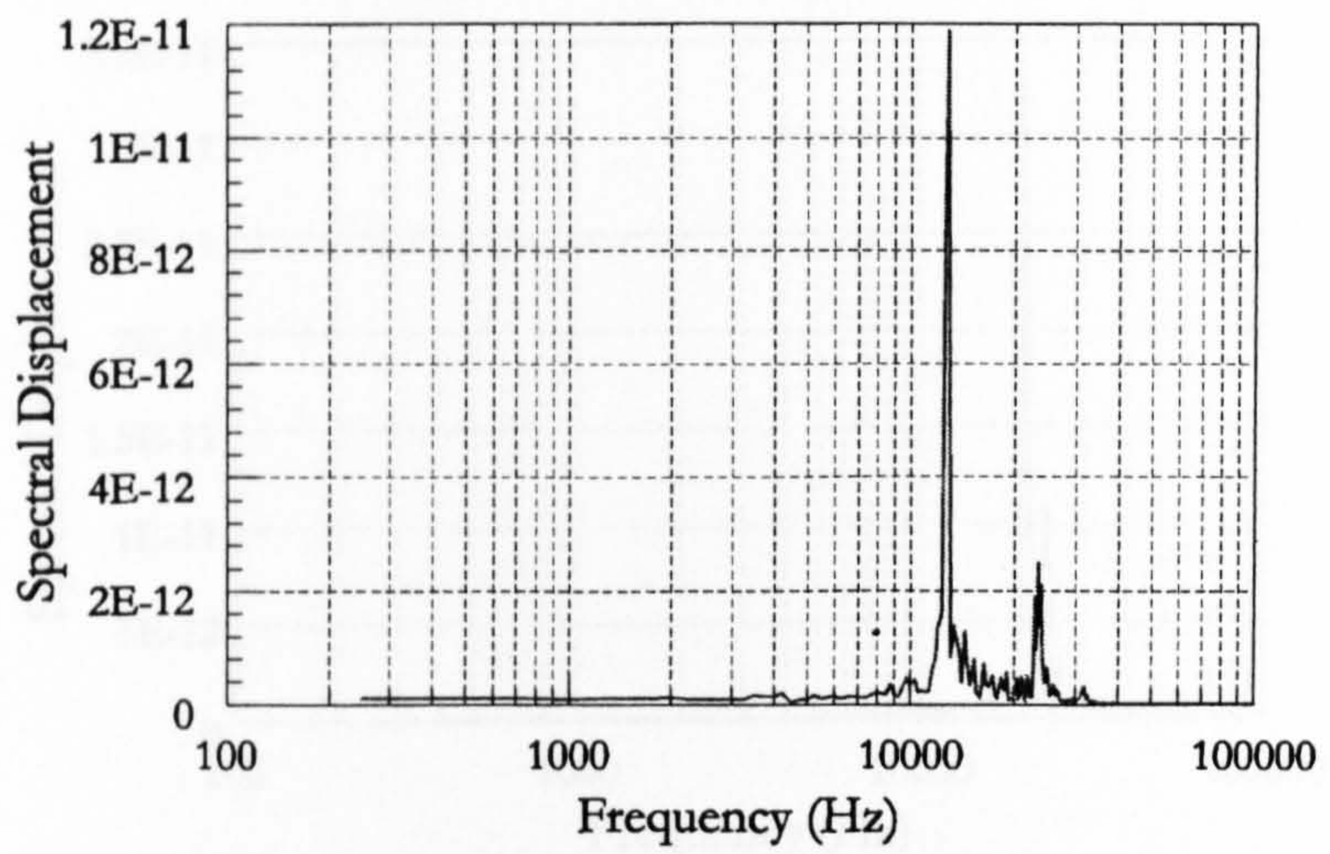

Figure 5.54: Fast Fourier transform for two dimensional analysis with $R_d = 5$

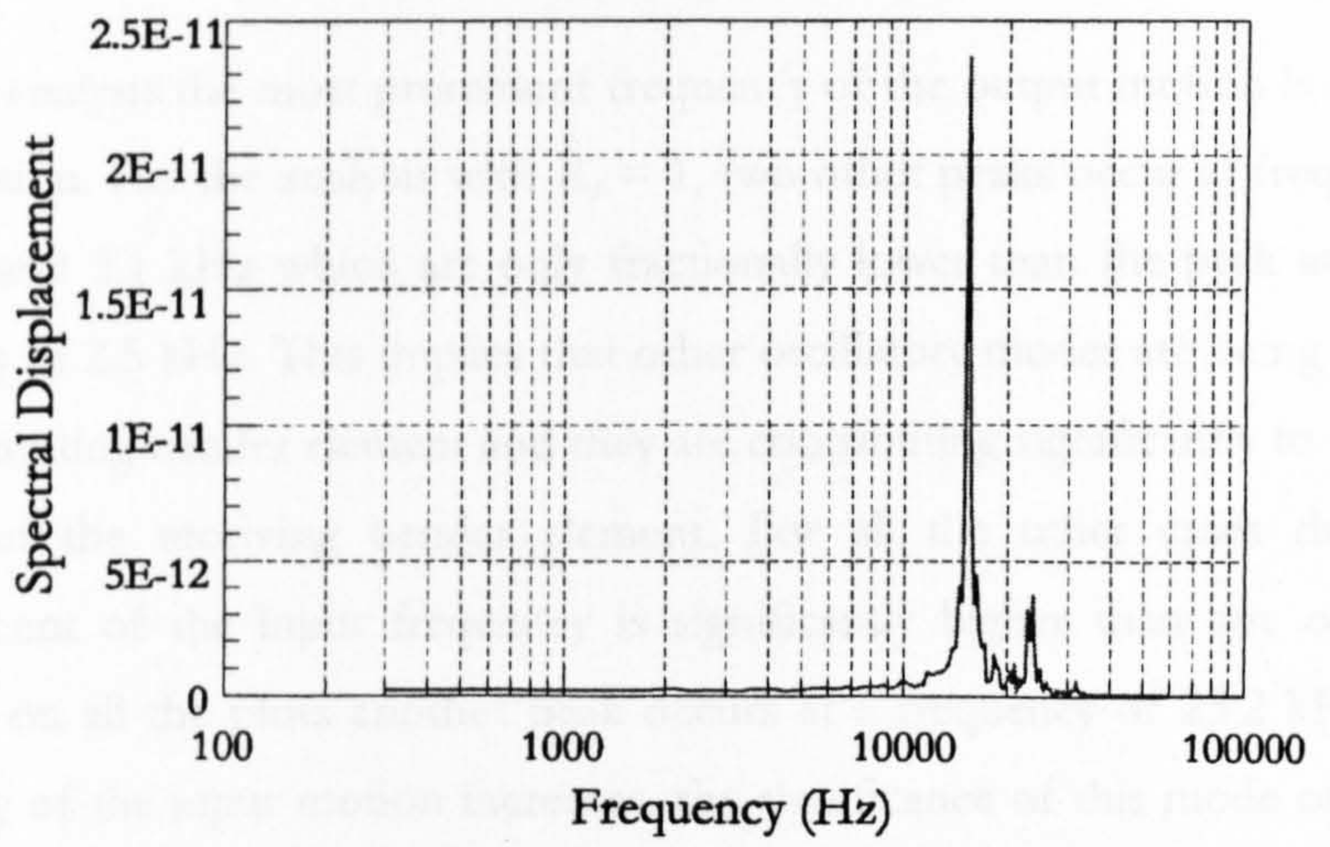

Figure 5.55: Fast Fourier transform for two dimensional analysis with $R_d = 6$

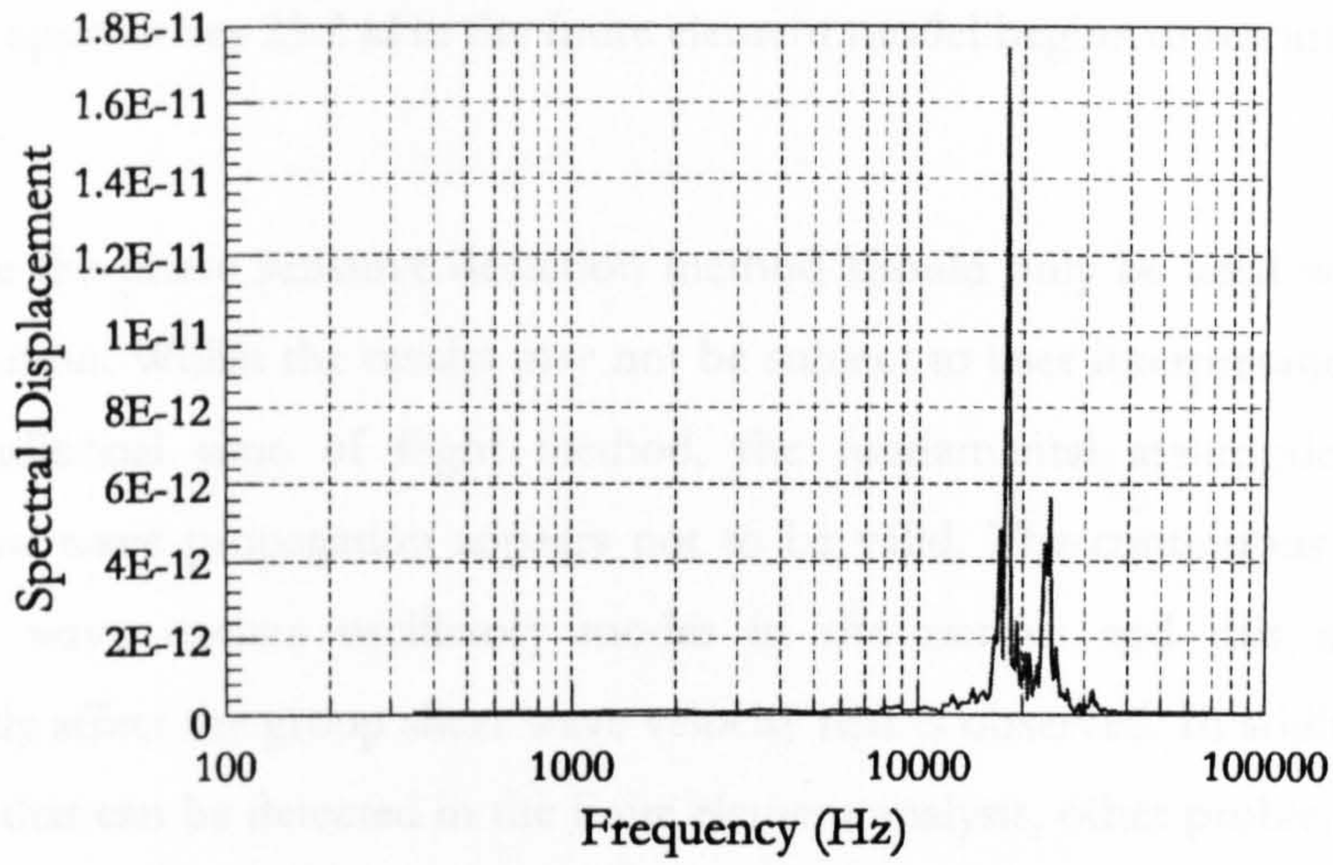

Figure 5.56: Fast Fourier transform for two dimensional analysis with $R_d = 7$

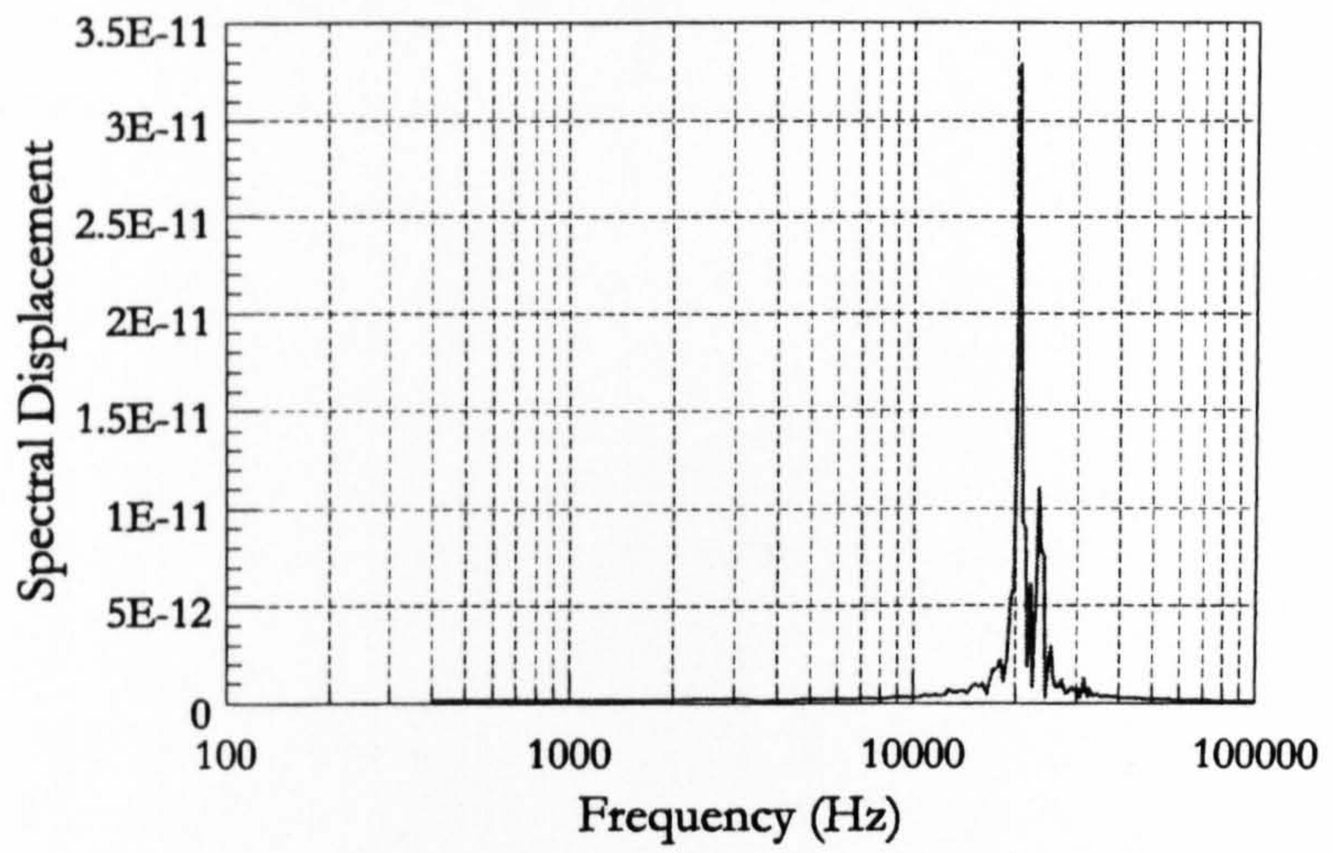

Figure 5.57: Fast Fourier transform for two dimensional analysis with $R_d = 8$

For each analysis the most prominent frequency of the output motion is that of the input motion. For the analysis with $R_d = 1$, two other peaks occur at frequencies of 2.0 kHz and 3.1 kHz which are only fractionally lower than the peak at the input frequency of 2.5 kHz. This implies that other oscillatory modes are being excited by the transmitting bender element and they are contributing significantly to the overall motion of the receiving bender element. For all the other cases the spectral displacement of the input frequency is significantly higher than any other peak, although on all the plots another peak occurs at a frequency of 23.2 kHz. As the frequency of the input motion increases, the significance of this mode of vibration increases. This represents a natural frequency of the system, and as the input

frequency approaches 23.2 kHz the finite element model begins to resonate more in this mode.

In practice the phase sensitive detection method should only be used with a good deal of caution. Whilst the results may not be subject to user interpretation error as in the traditional time of flight method, the fundamental assumption of one dimensional wave propagation appears not to be valid. The continuous cycling of the input wave excites oscillatory modes in the sample and this appears to significantly affect the group shear wave velocity that is observed. In addition to the problems that can be detected in the finite element analysis, other problems such as inertial coupling that could not be modelled in this study may cause greater unseen inaccuracies in the method.

5.7 Results of Continuously Cycled Tests

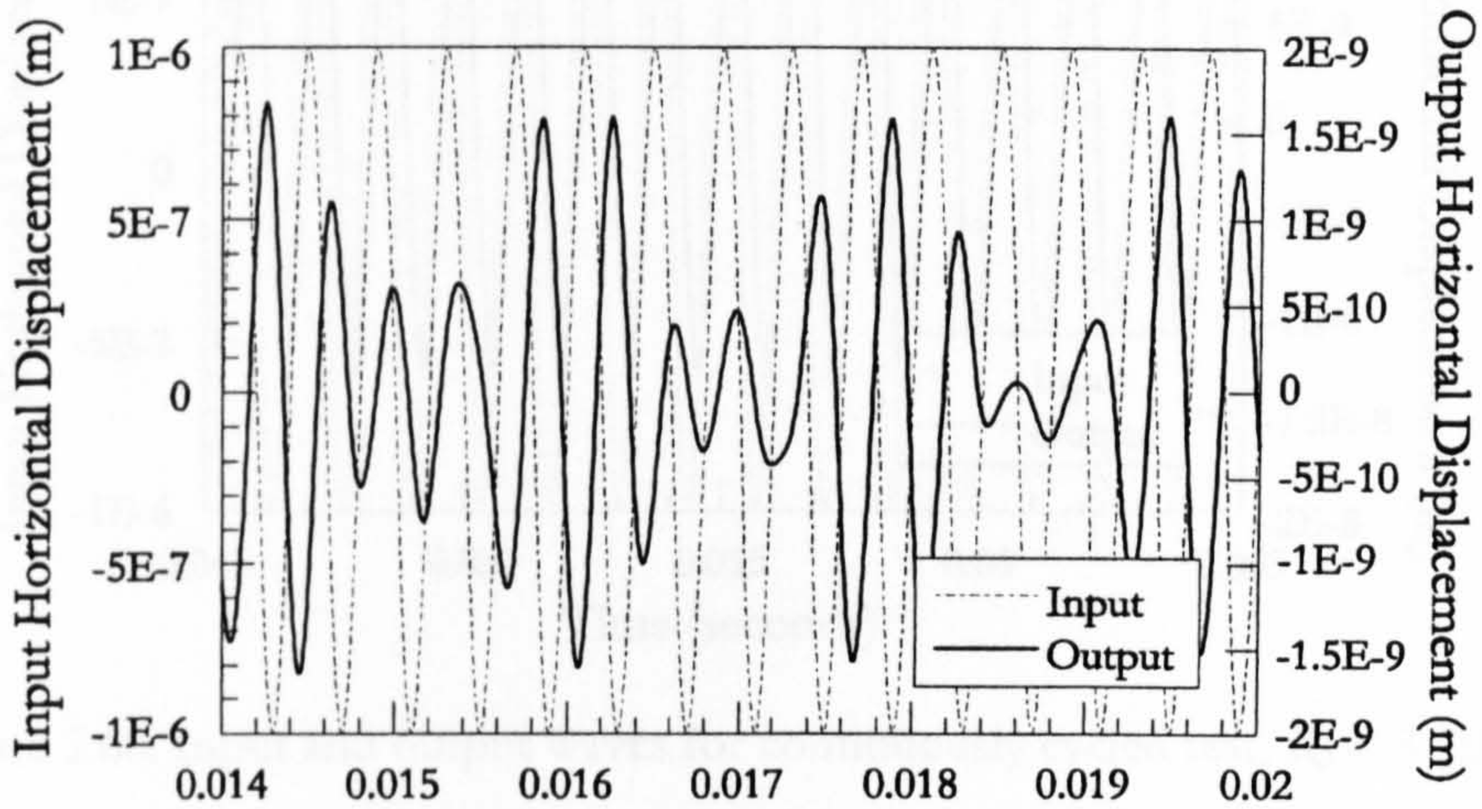

Figure 5.58: Input and output waves for continuously cycled test, $R_d = 1$ (2D)

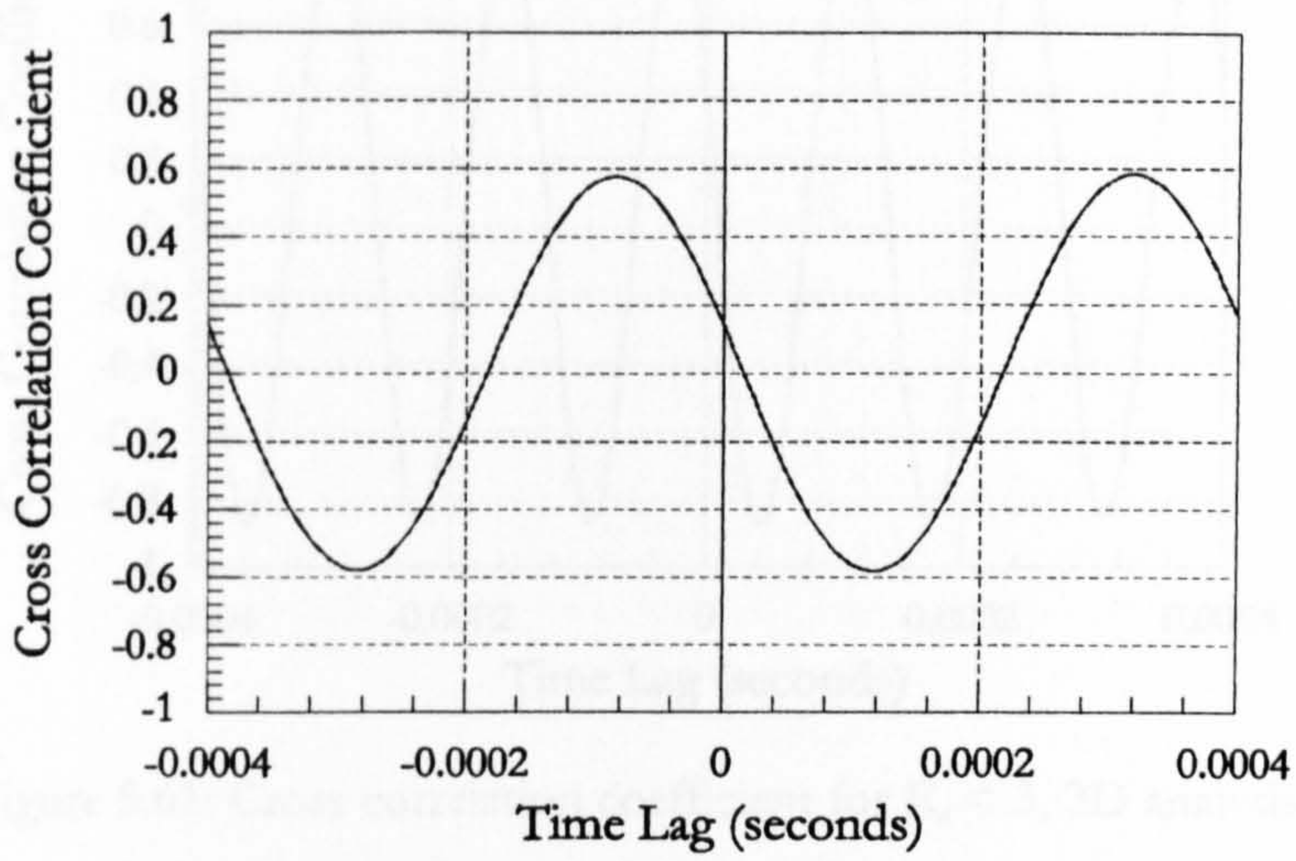

Figure 5.59: Cross correlation coefficient for $R_d = 1$, 2D analysis

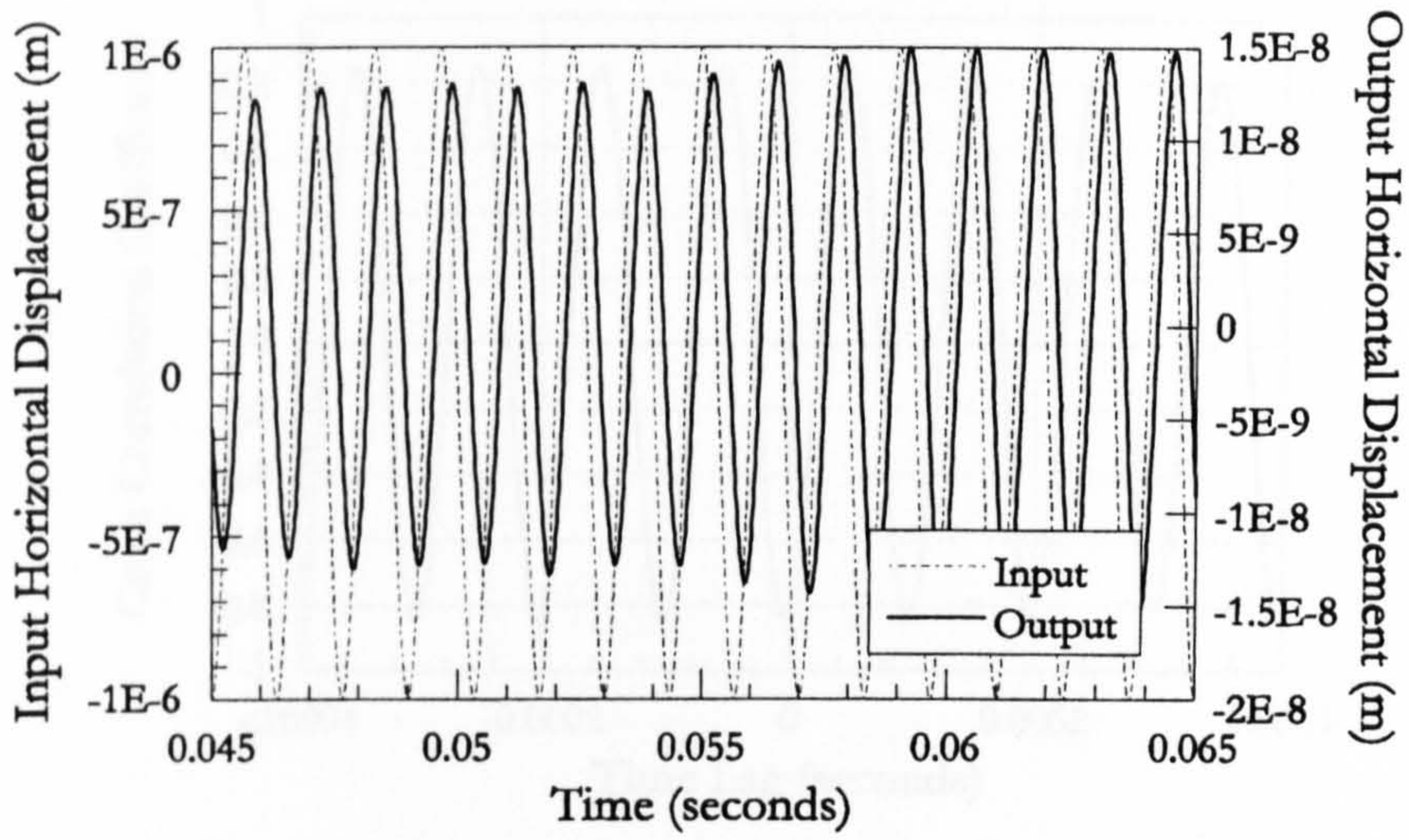

Figure 5.60: Input and output waves for continuously cycled test, $R_d = 3$ (2D)

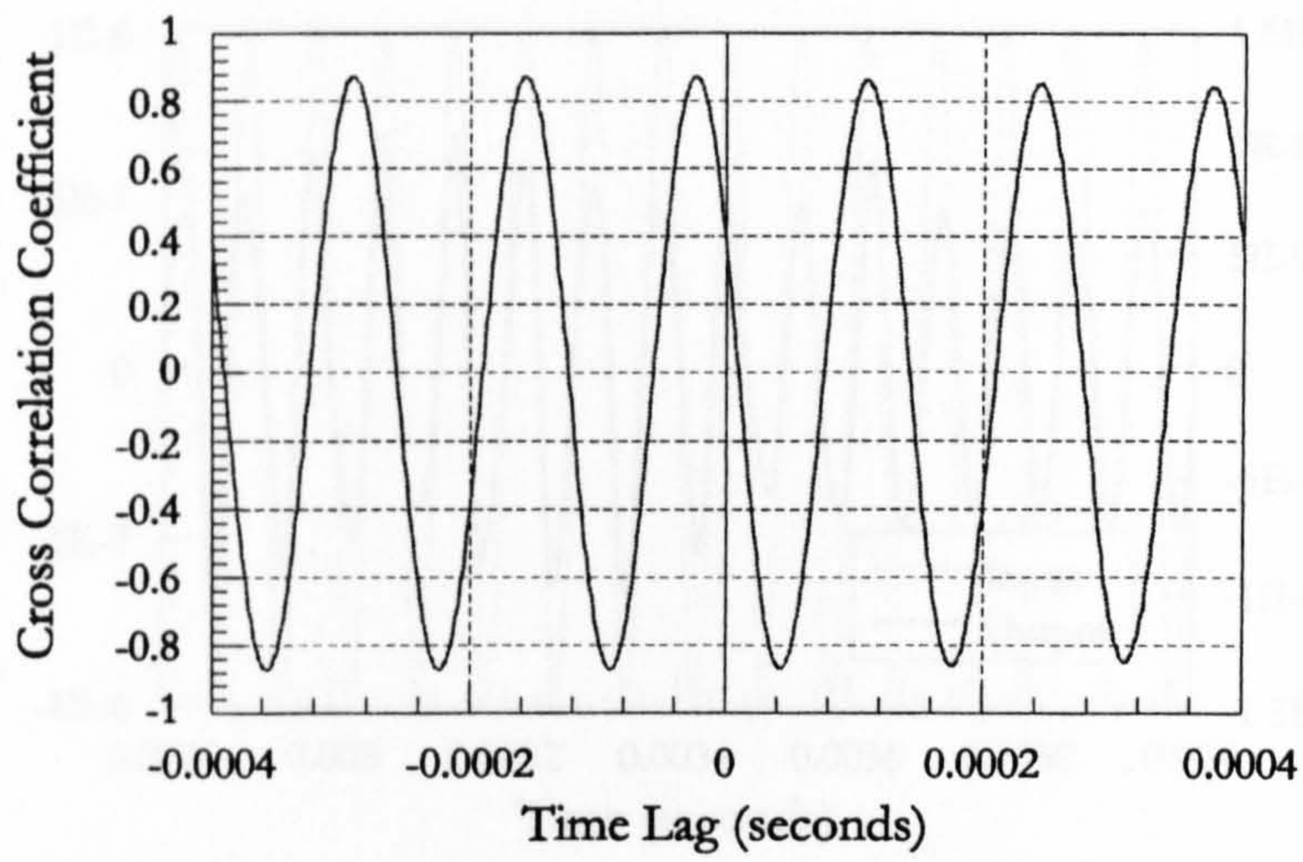

Figure 5.61: Cross correlation coefficient for $R_d = 3$, 2D analysis

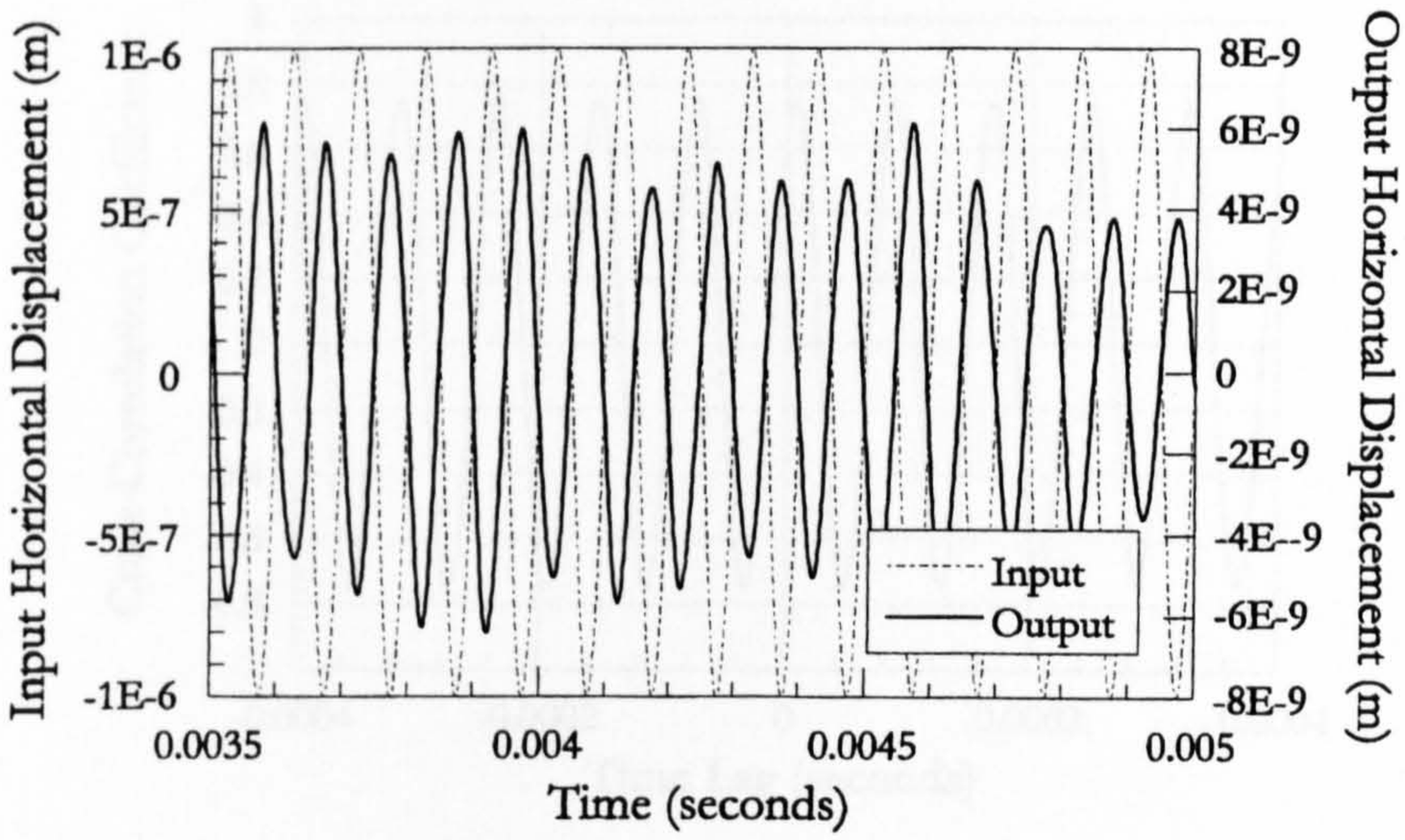

Figure 5.62: Input and output waves for continuously cycled test, $R_d = 4$ (2D)

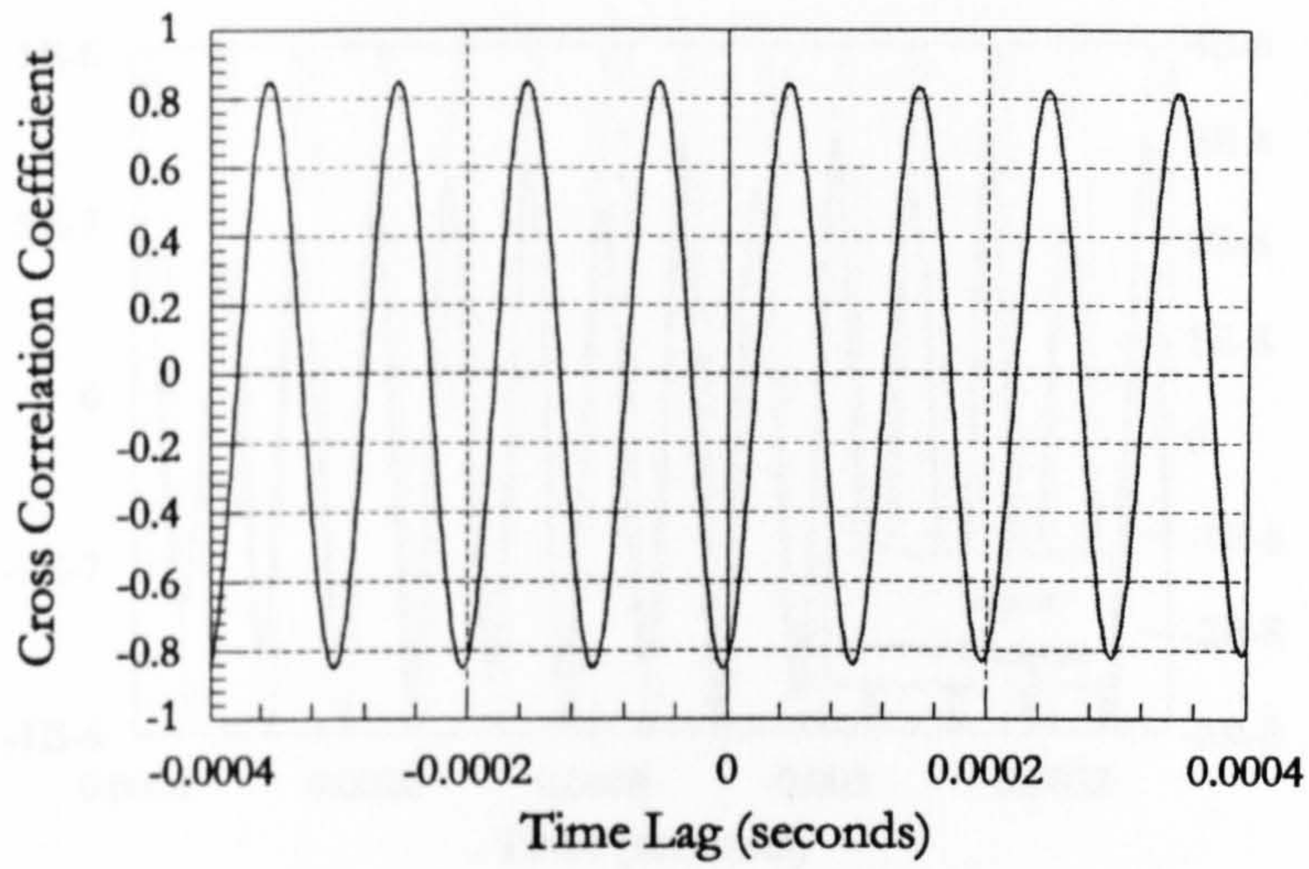

Figure 5.63: Cross correlation coefficient for R_d = 4, 2D analysis

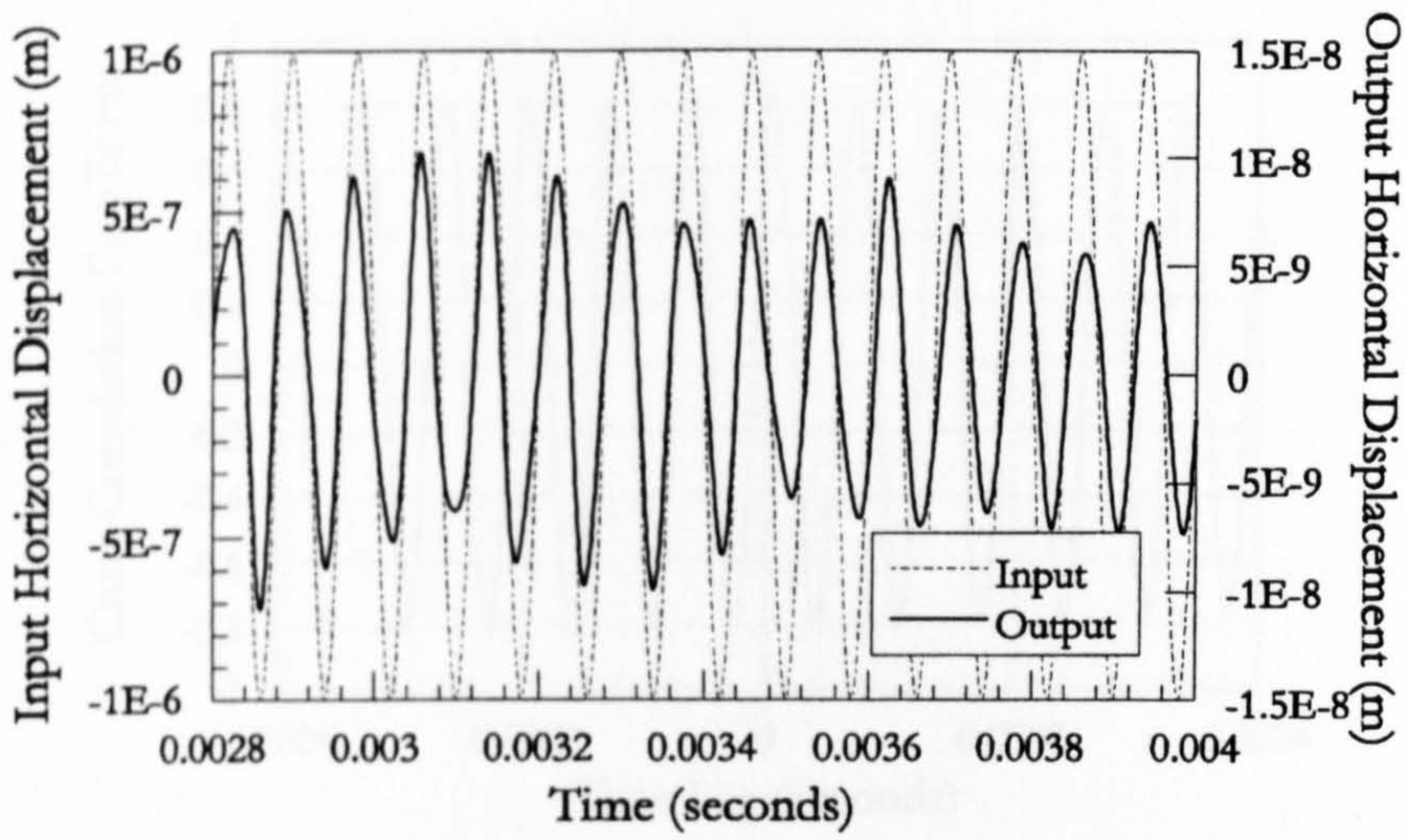

Figure 5.64: Input and output waves for continuously cycled test, R_d = 5 (2D)

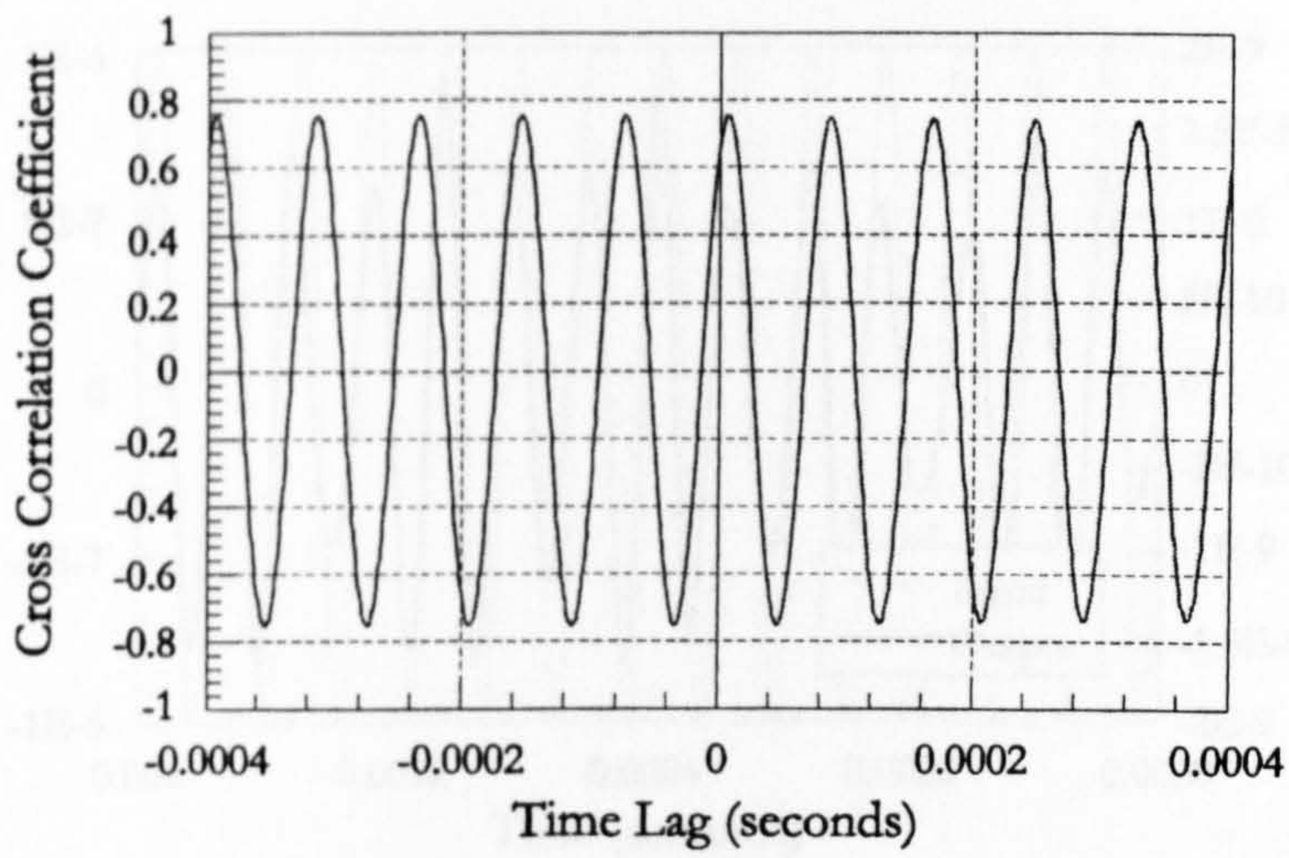

Figure 5.65: Cross correlation coefficient for R_d = 5, 2D analysis

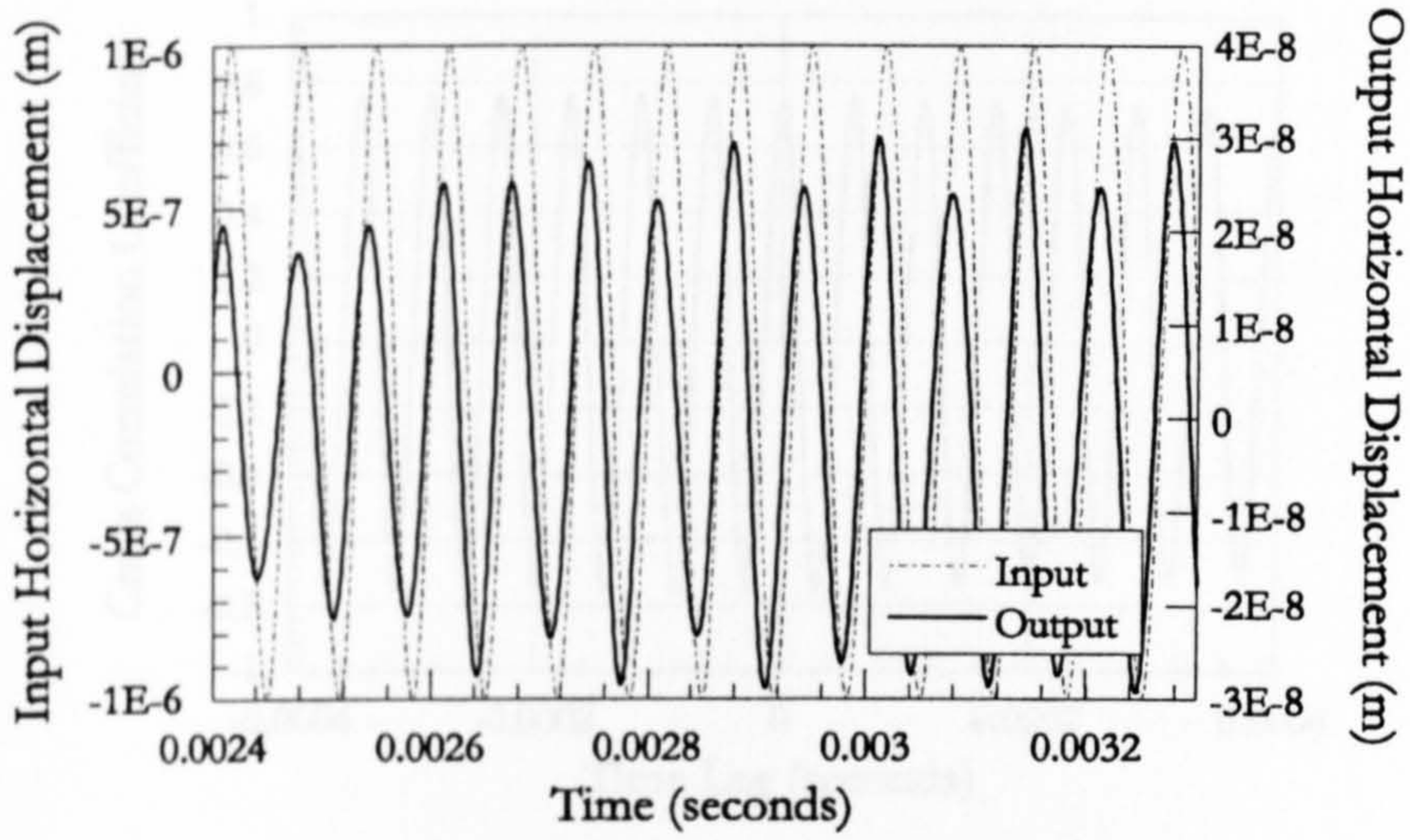

Figure 5.66: Input and output waves for continuously cycled test, $R_d = 6$ (2D)

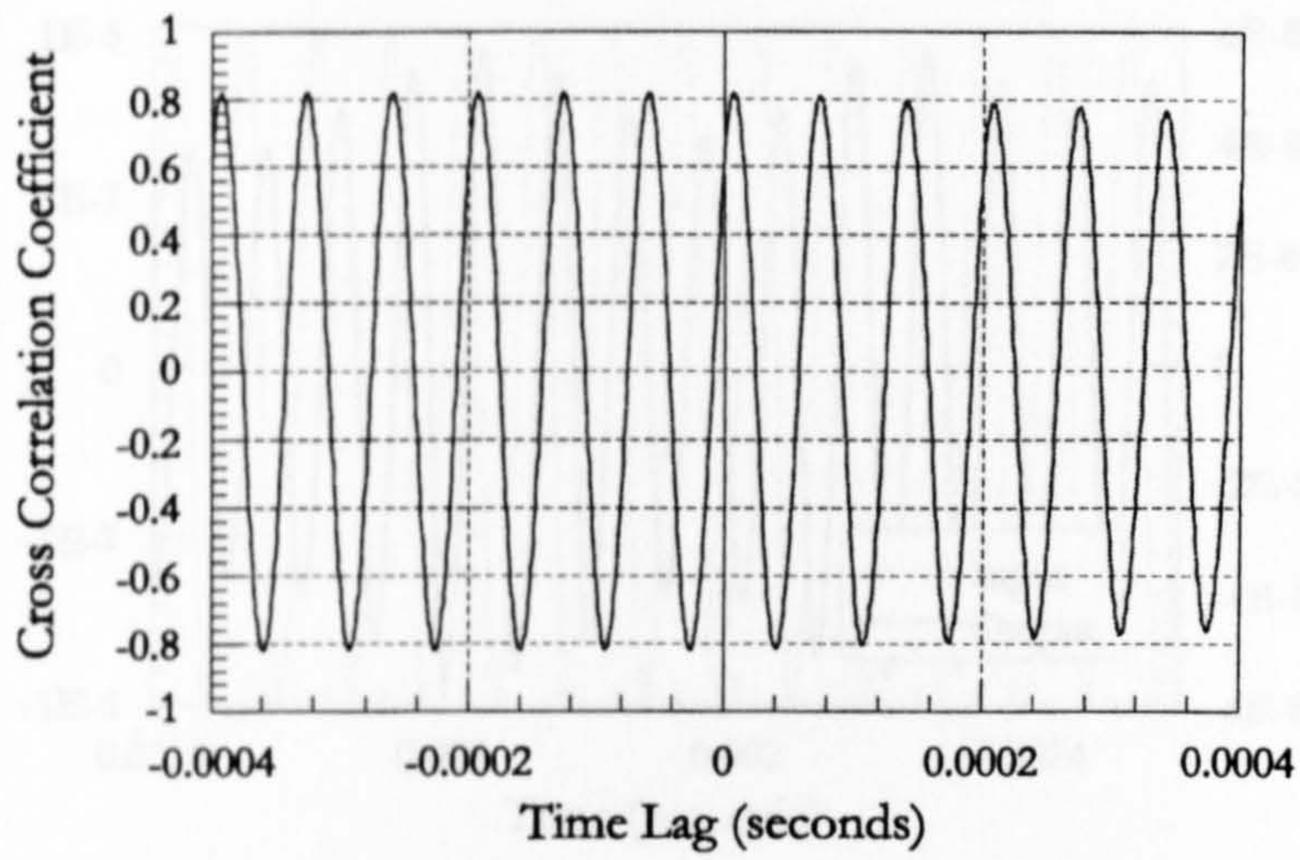

Figure 5.67: Cross correlation coefficient for $R_d = 6$, 2D analysis

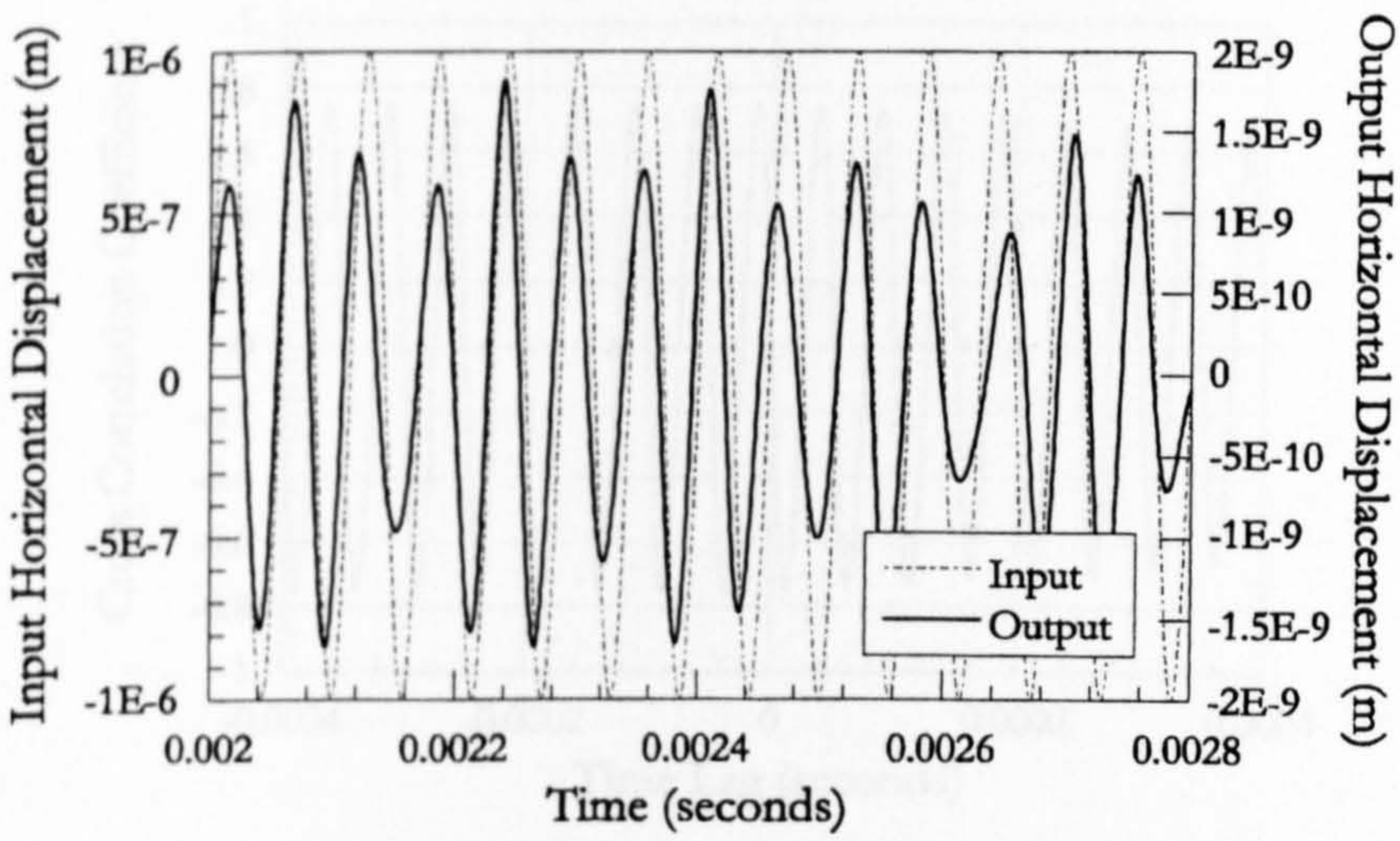

Figure 5.68: Input and output waves for continuously cycled test, $R_d = 7$ (2D)

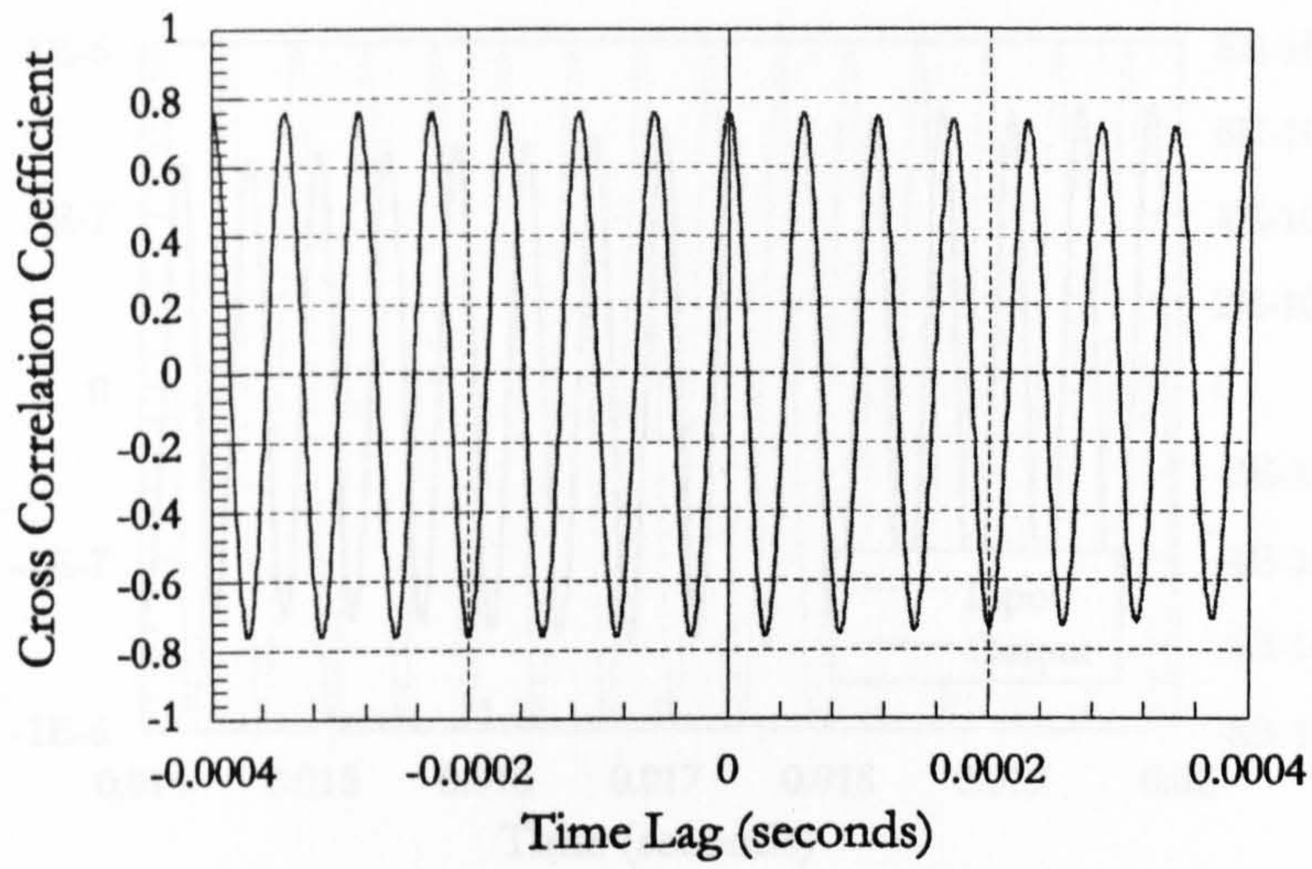

Figure 5.69: Cross correlation coefficient for $R_d = 7$, 2D analysis

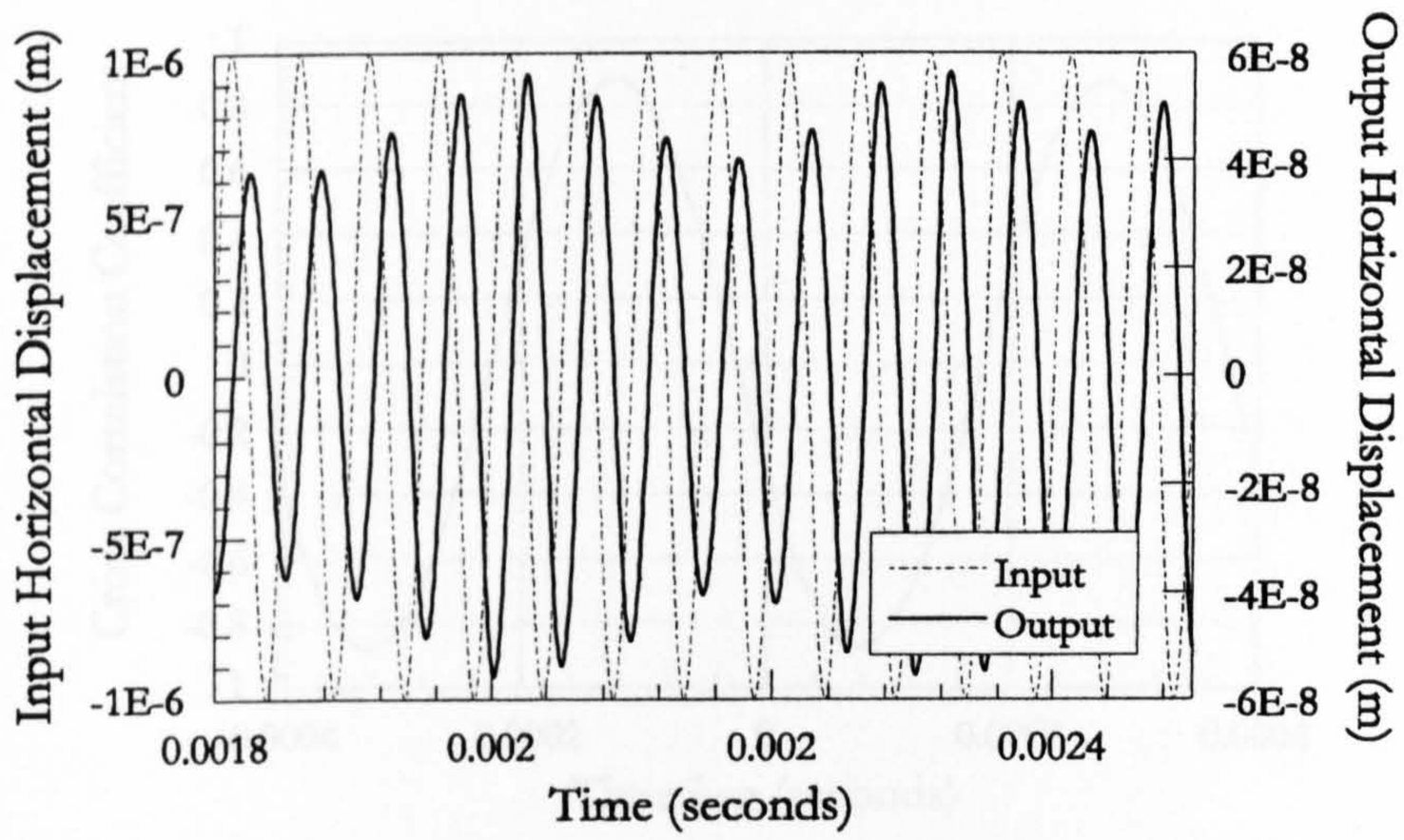

Figure 5.70: Input and output waves for continuously cycled test, $R_d = 8$ (2D)

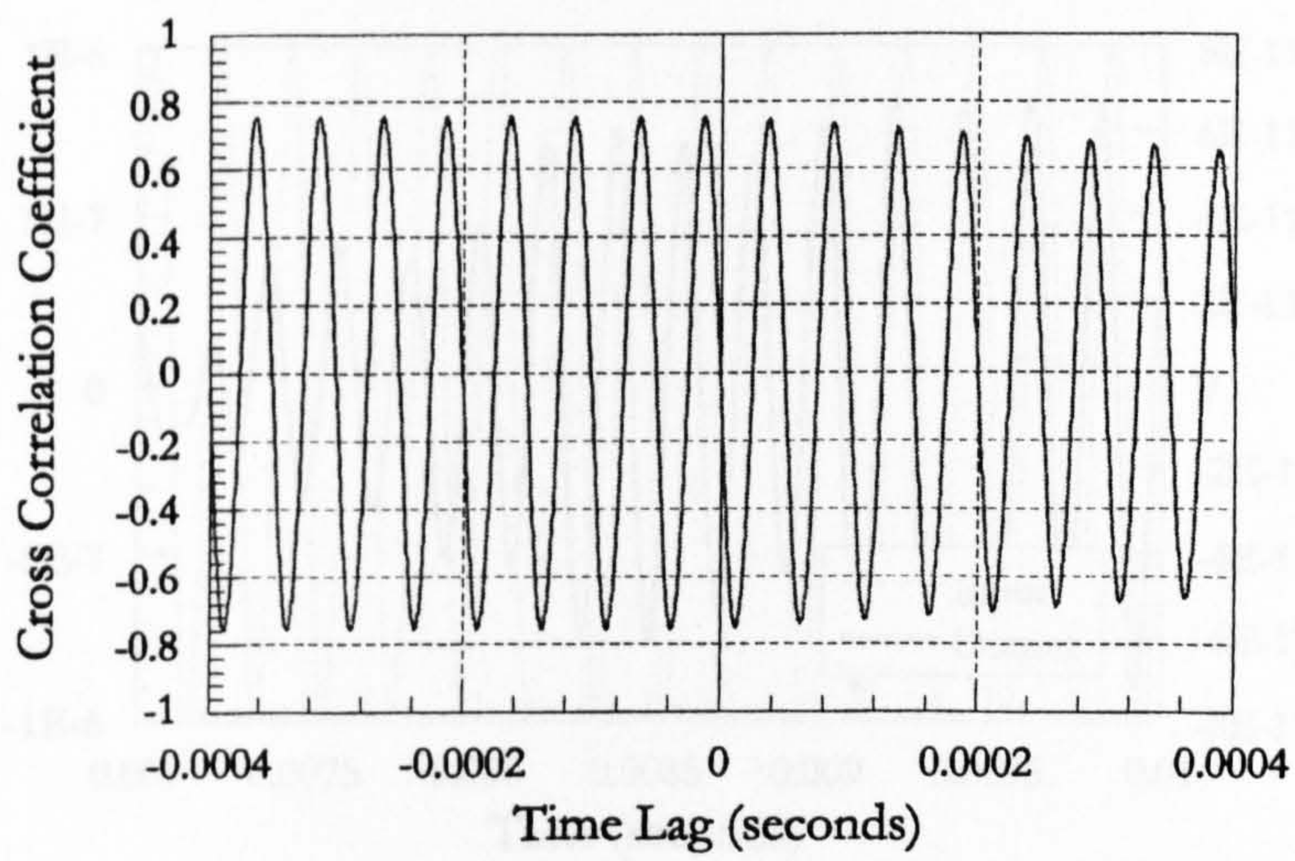

Figure 5.71: Cross correlation coefficient for $R_d = 8$, 2D analysis

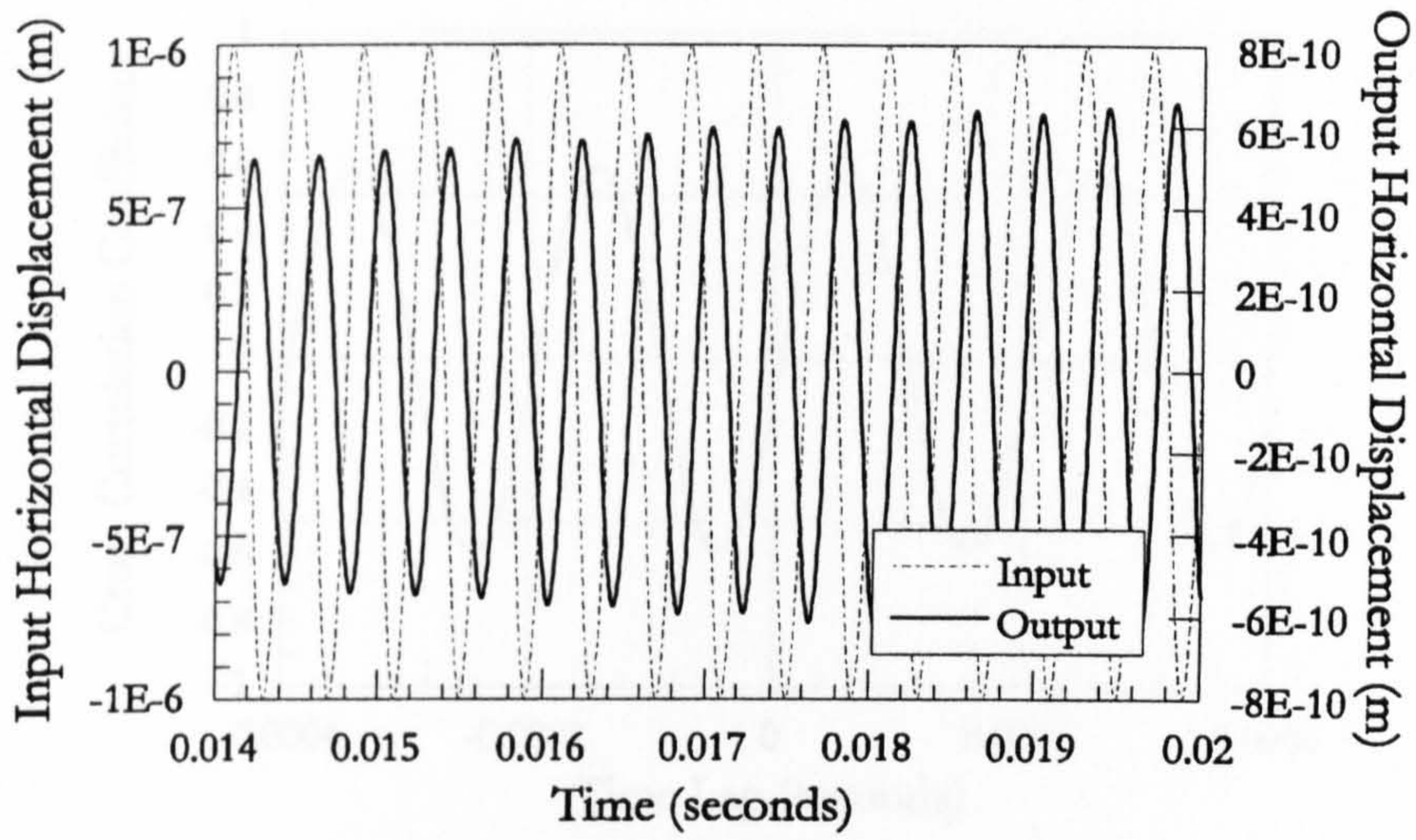

Figure 5.72: Input and output waves for continuously cycled test, $R_d = 1$ (FS)

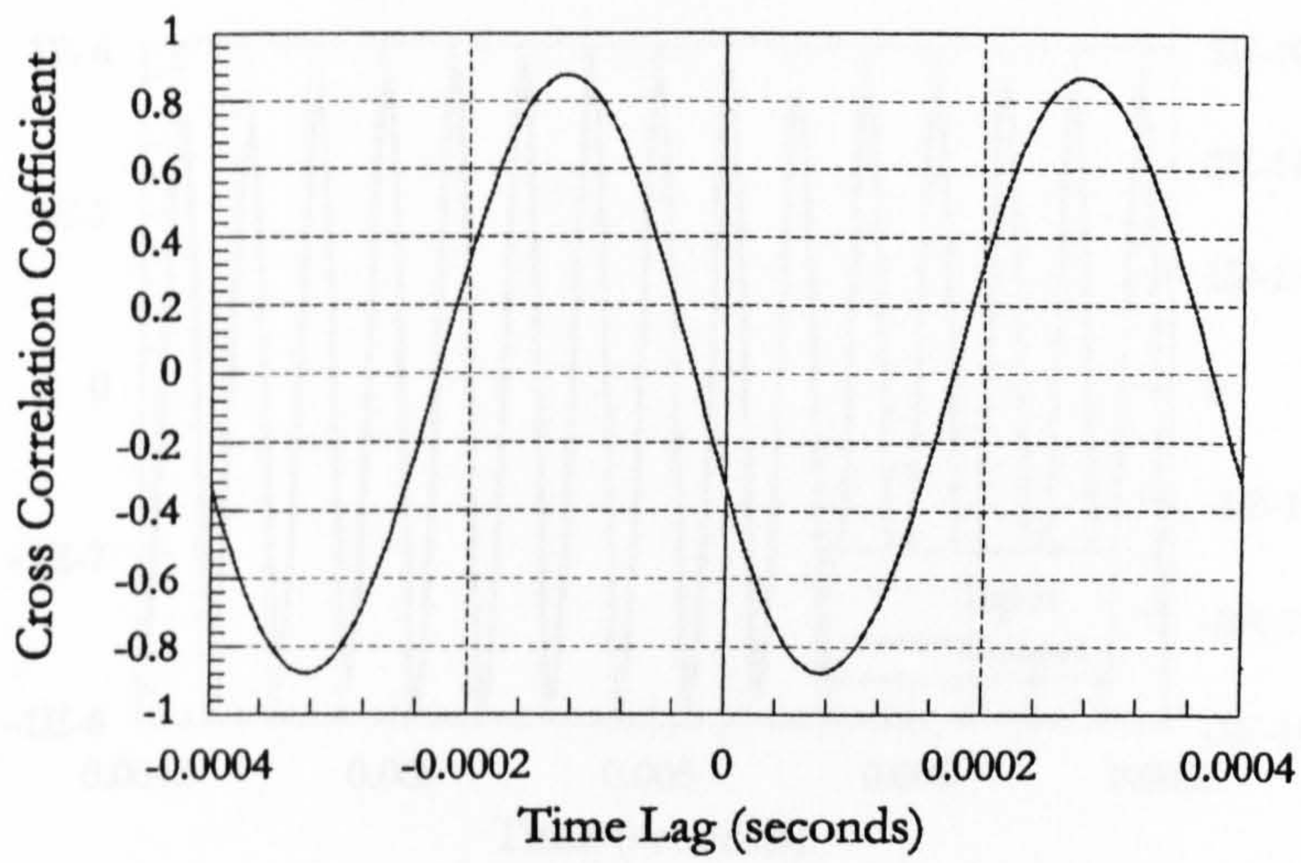

Figure 5.73: Cross correlation coefficient for $R_d = 1$, FS analysis

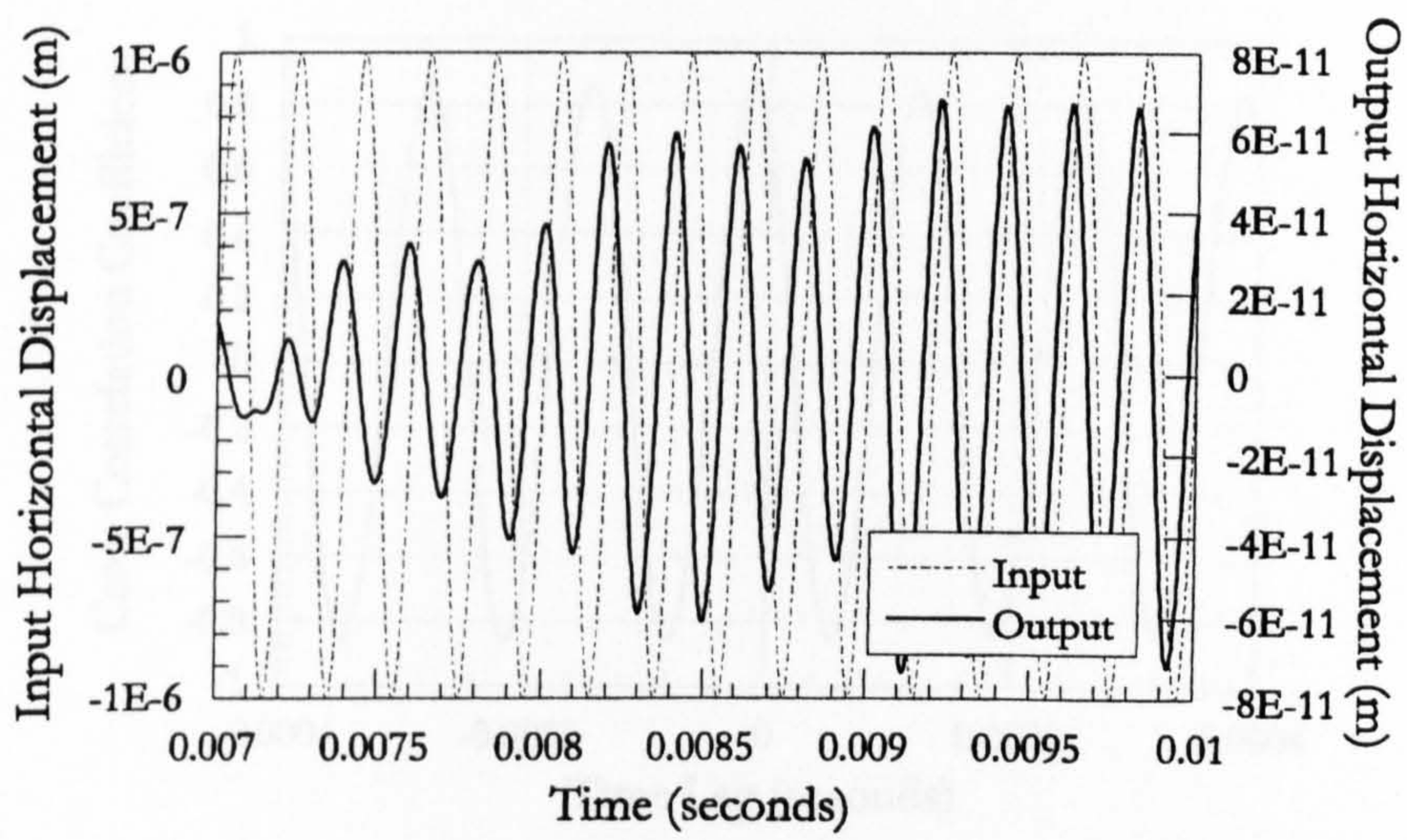

Figure 5.74: Input and output waves for continuously cycled test, $R_d = 2$ (FS)

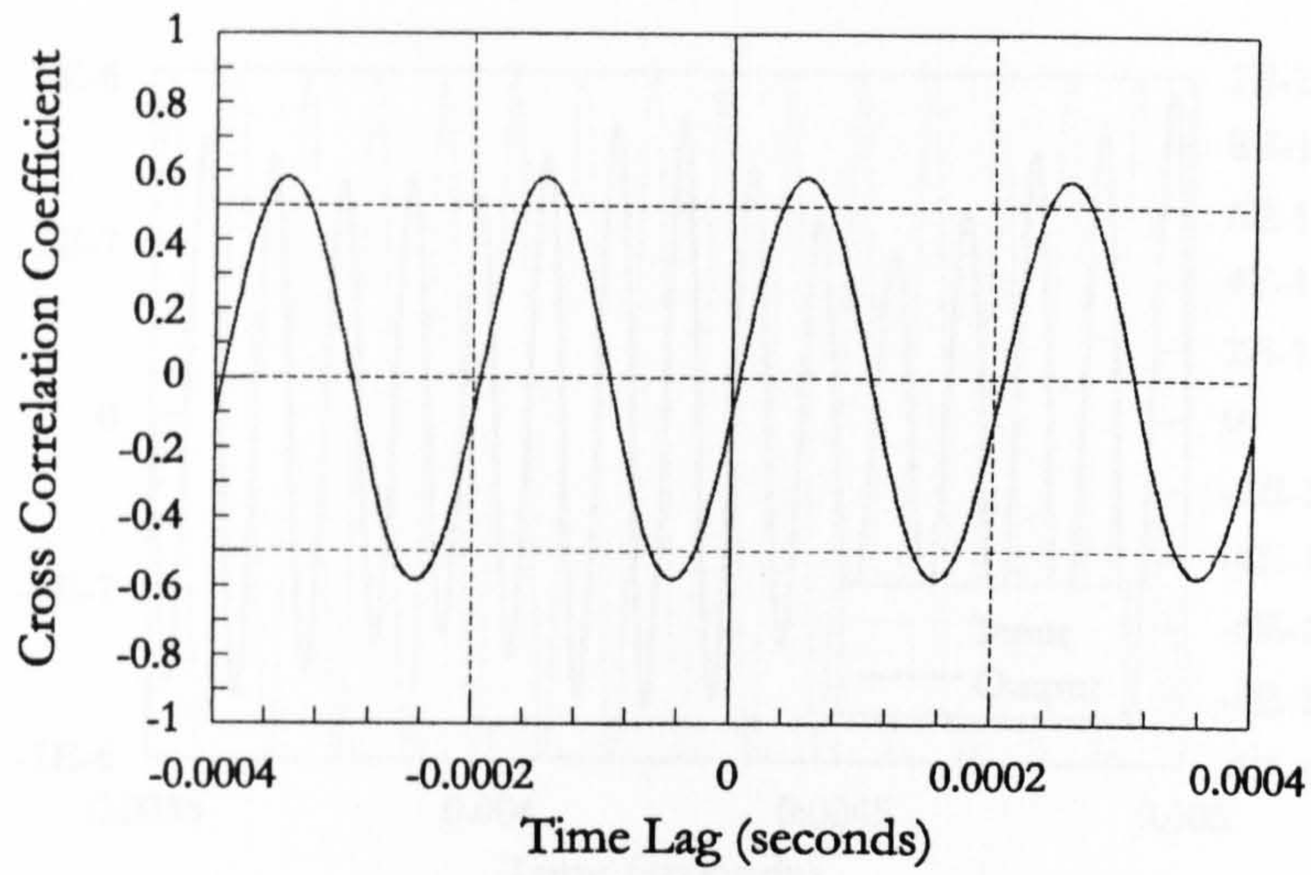

Figure 5.75: Cross correlation coefficient for $R_d = 2$, FS analysis

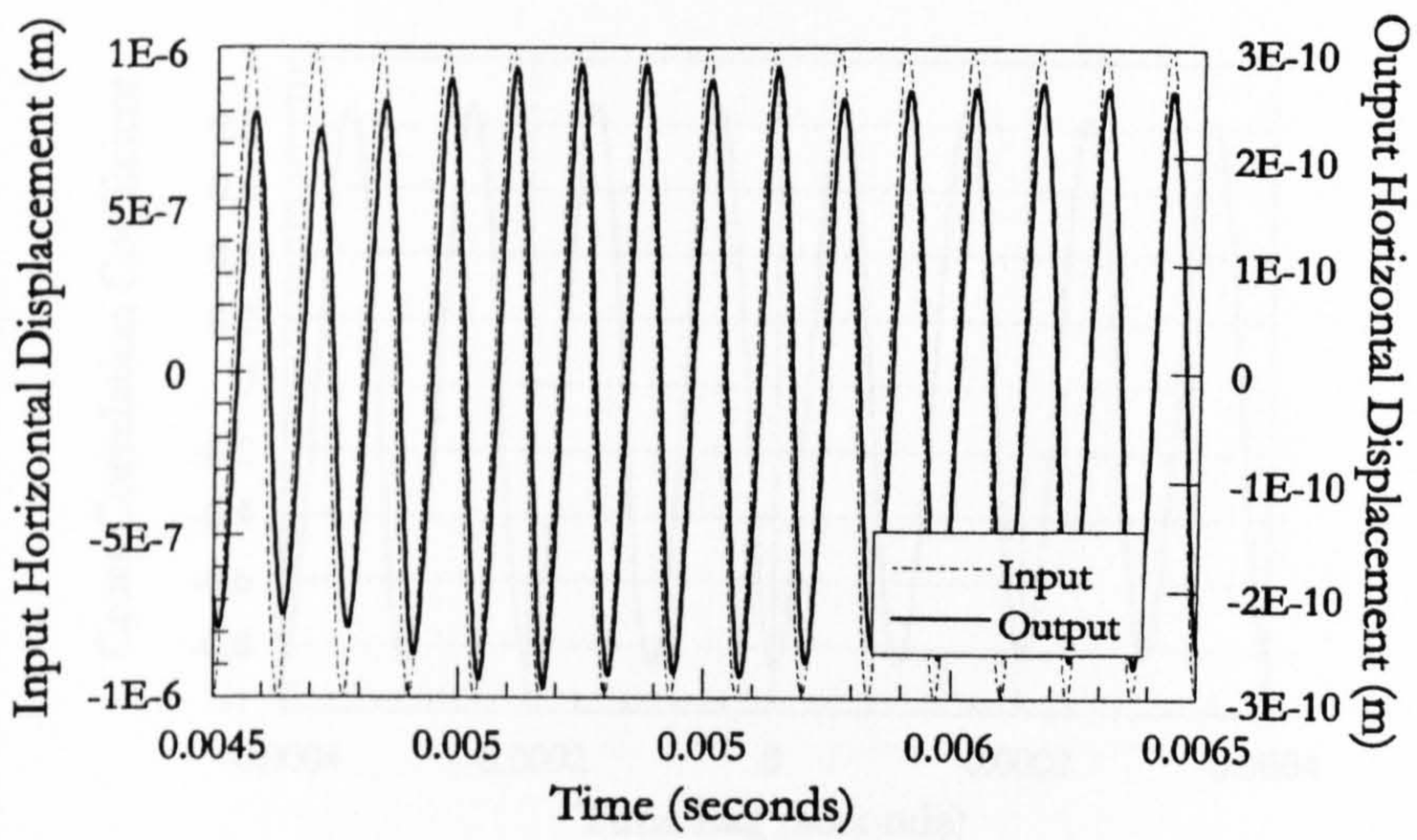

Figure 5.76: Input and output waves for continuously cycled test, $R_d = 3$ (FS)

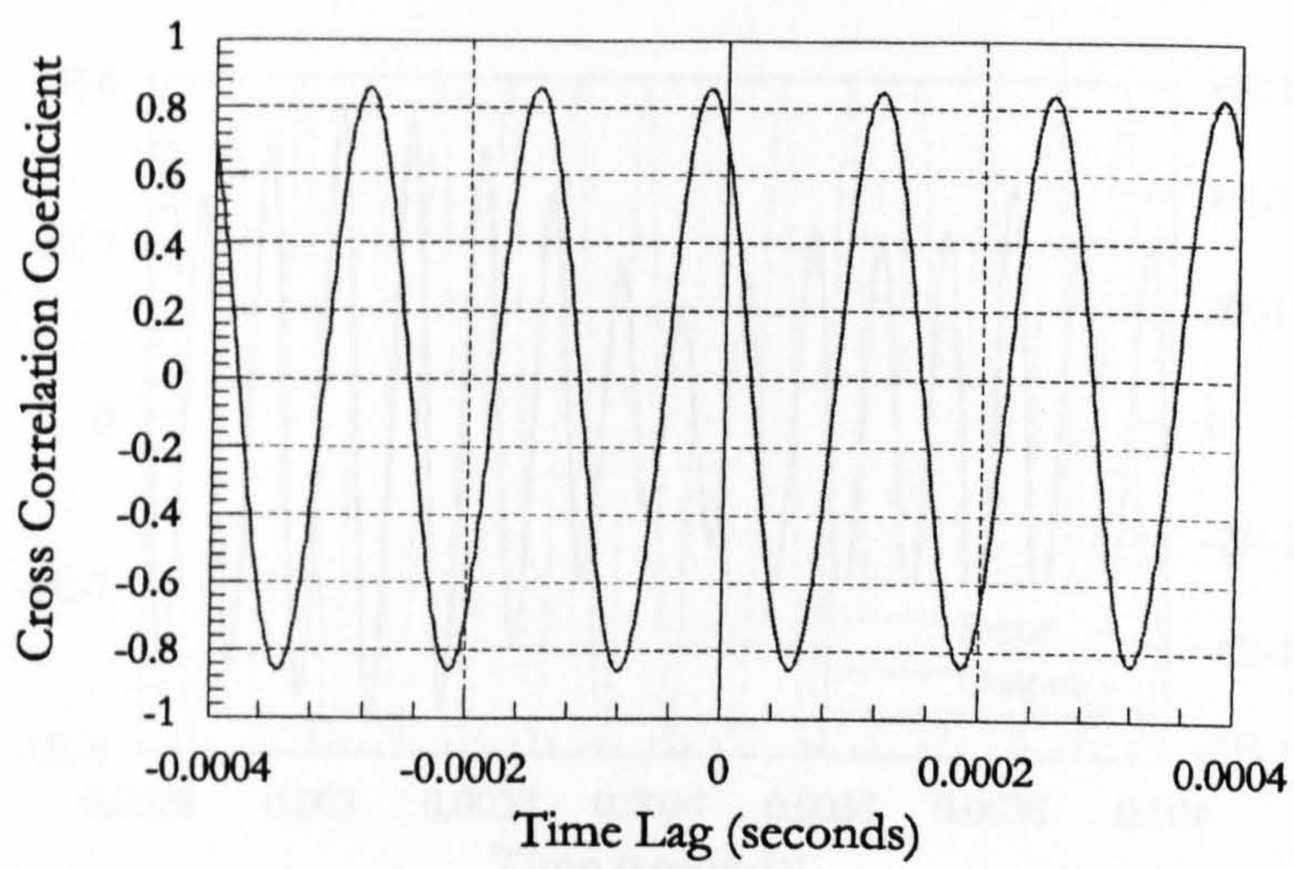

Figure 5.77: Cross correlation coefficient for $R_d = 3$, FS analysis

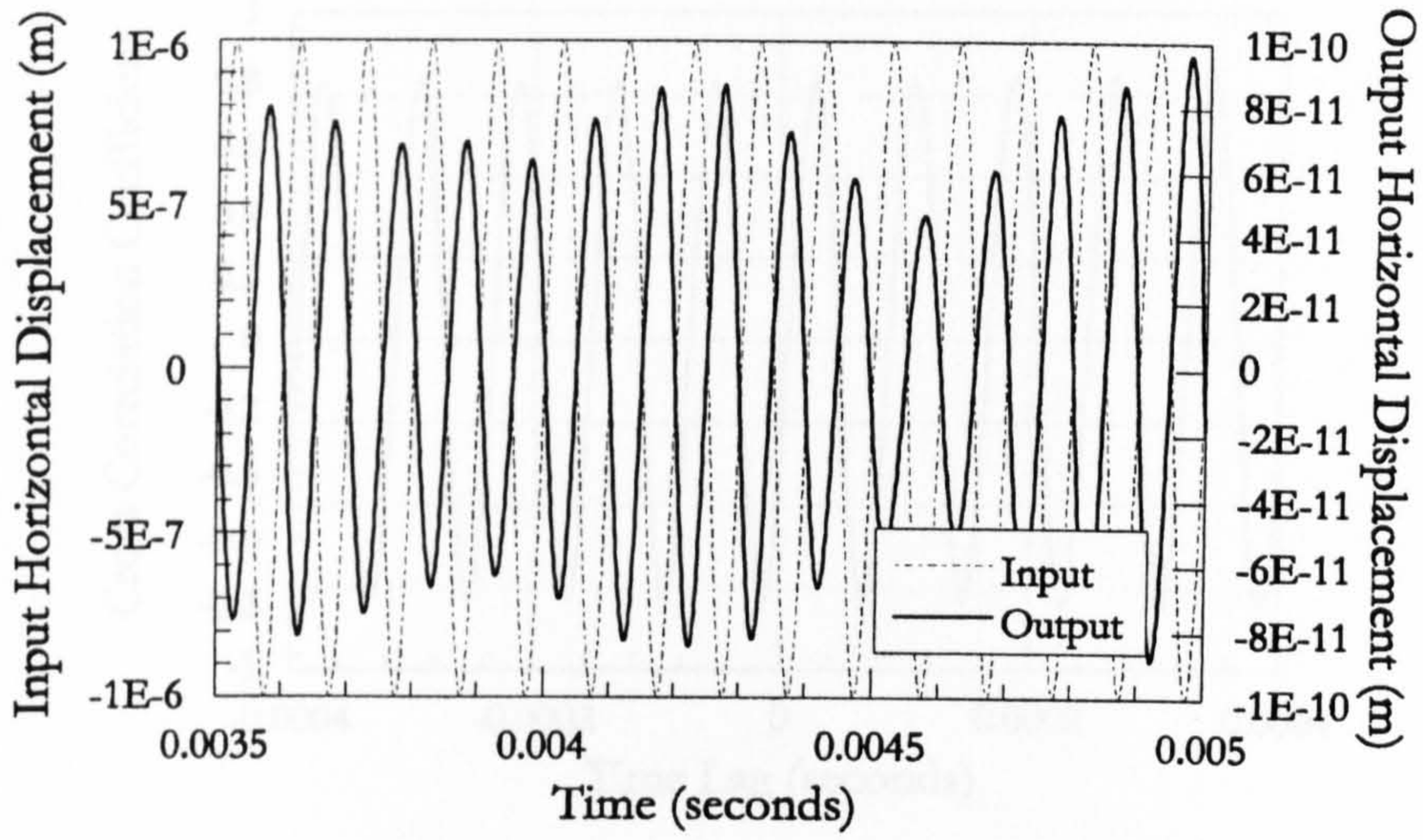

Figure 5.78: Input and output waves for continuously cycled test, $R_d = 4$ (FS)

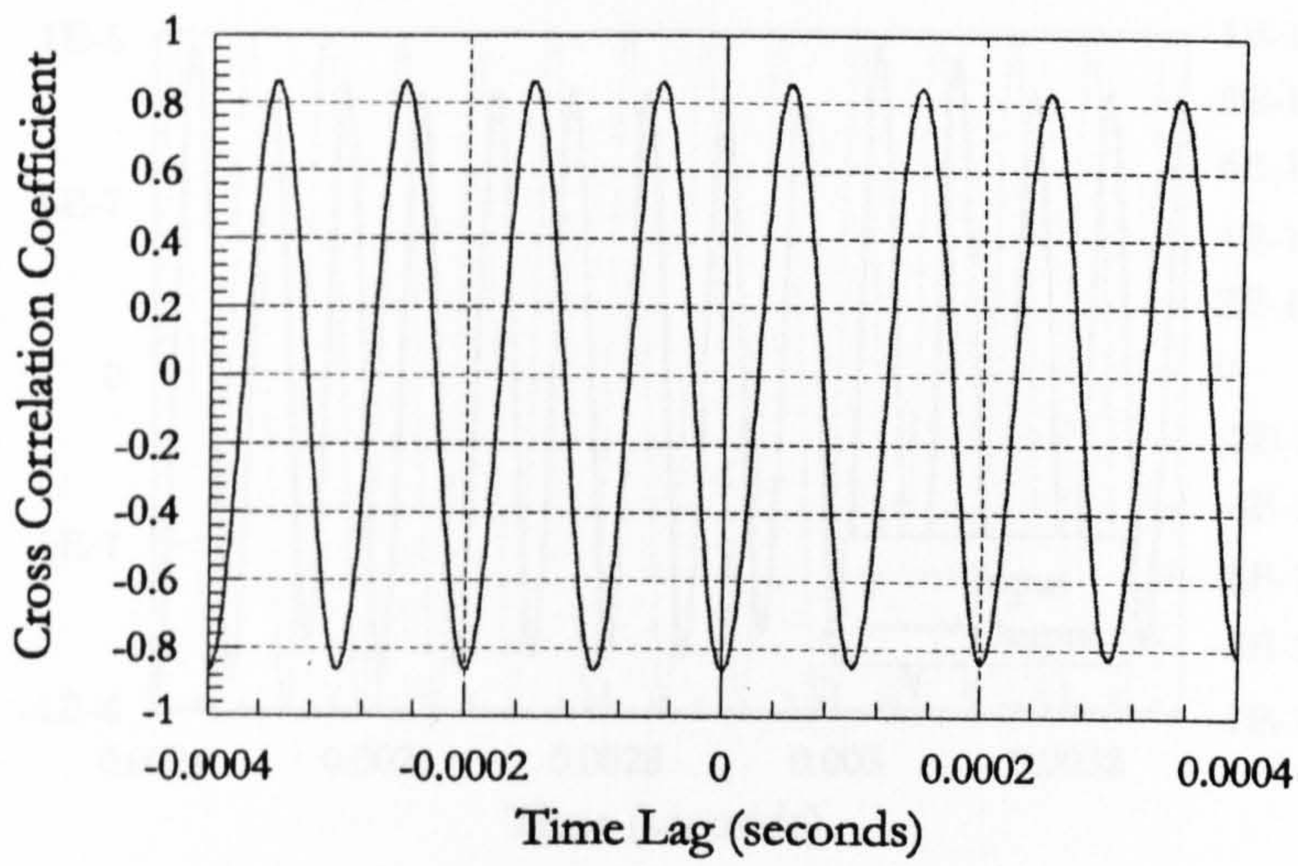

Figure 5.79: Cross correlation coefficient for $R_d = 4$, FS analysis

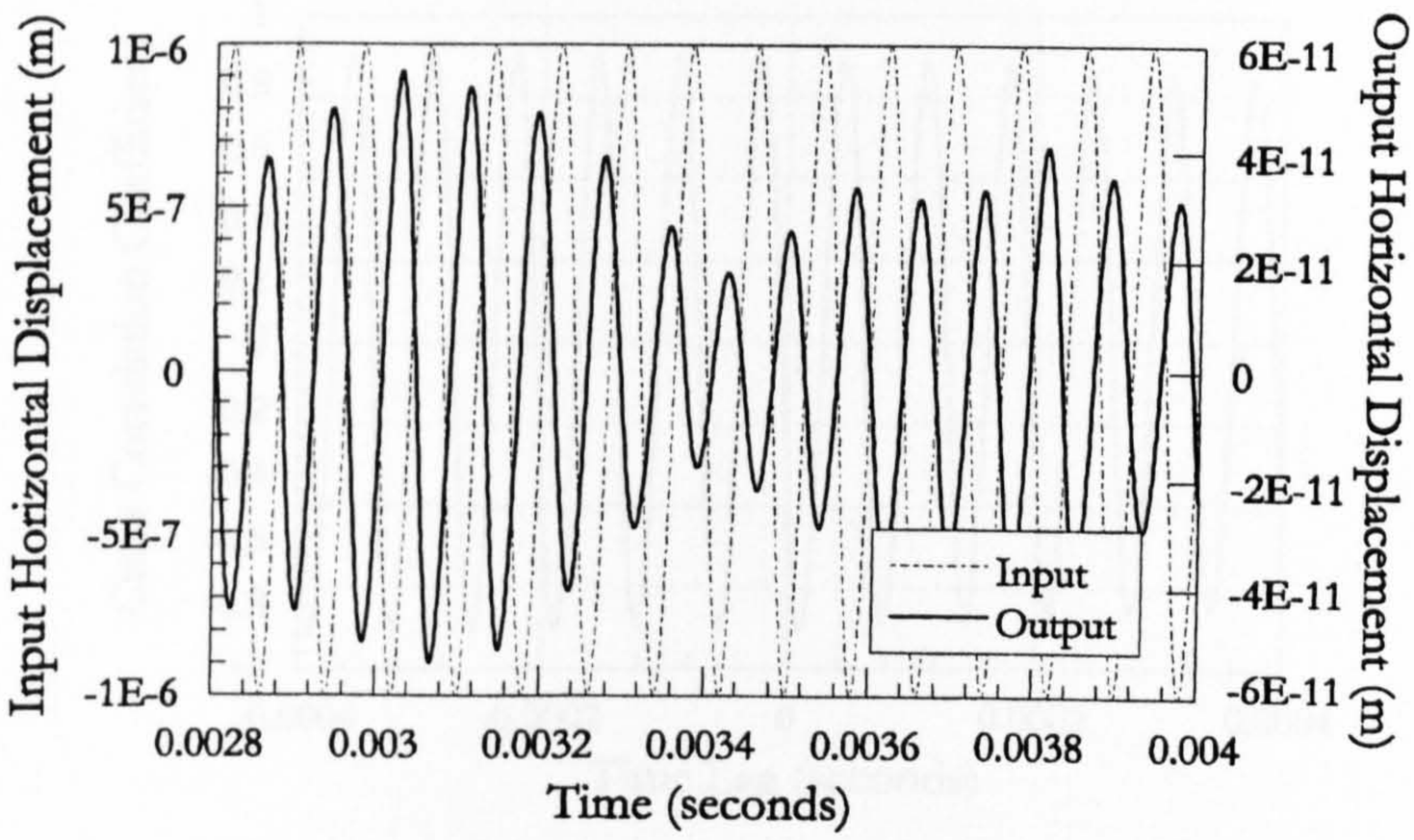

Figure 5.80: Input and output waves for continuously cycled test, $R_d = 5$ (FS)

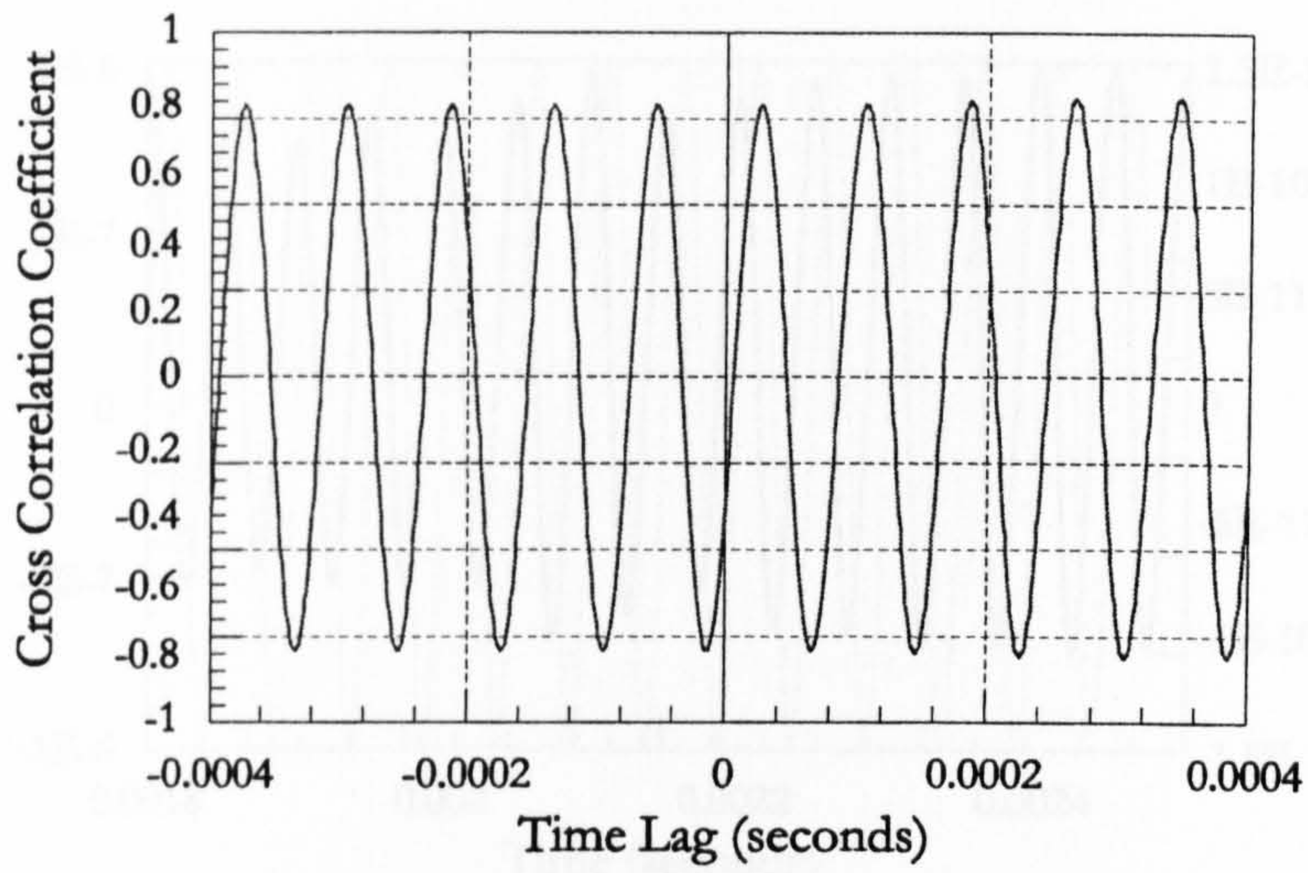

Figure 5.81: Cross correlation coefficient for R_d = 5, FS analysis

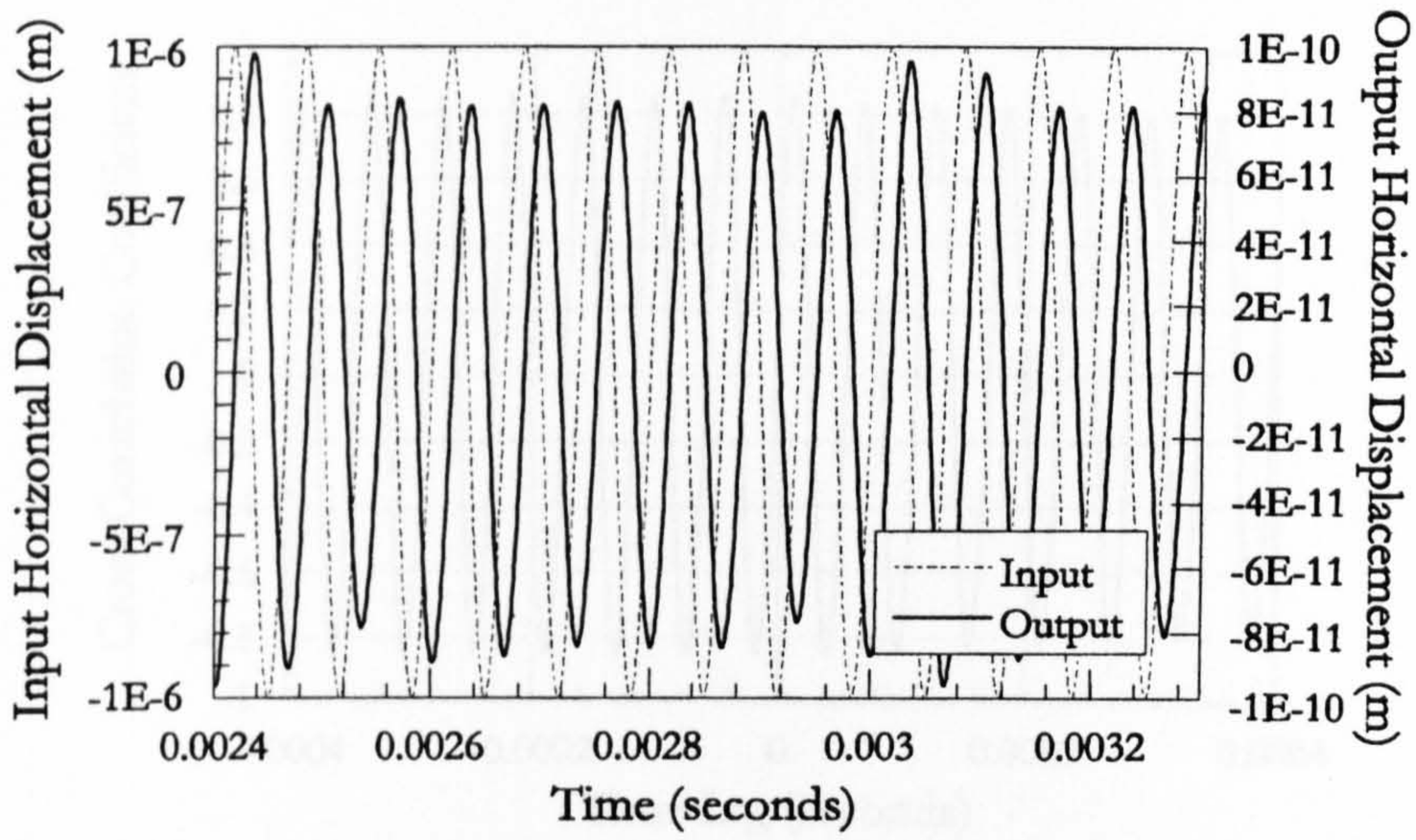

Figure 5.82: Input and output waves for continuously cycled test, R_d = 6 (FS)

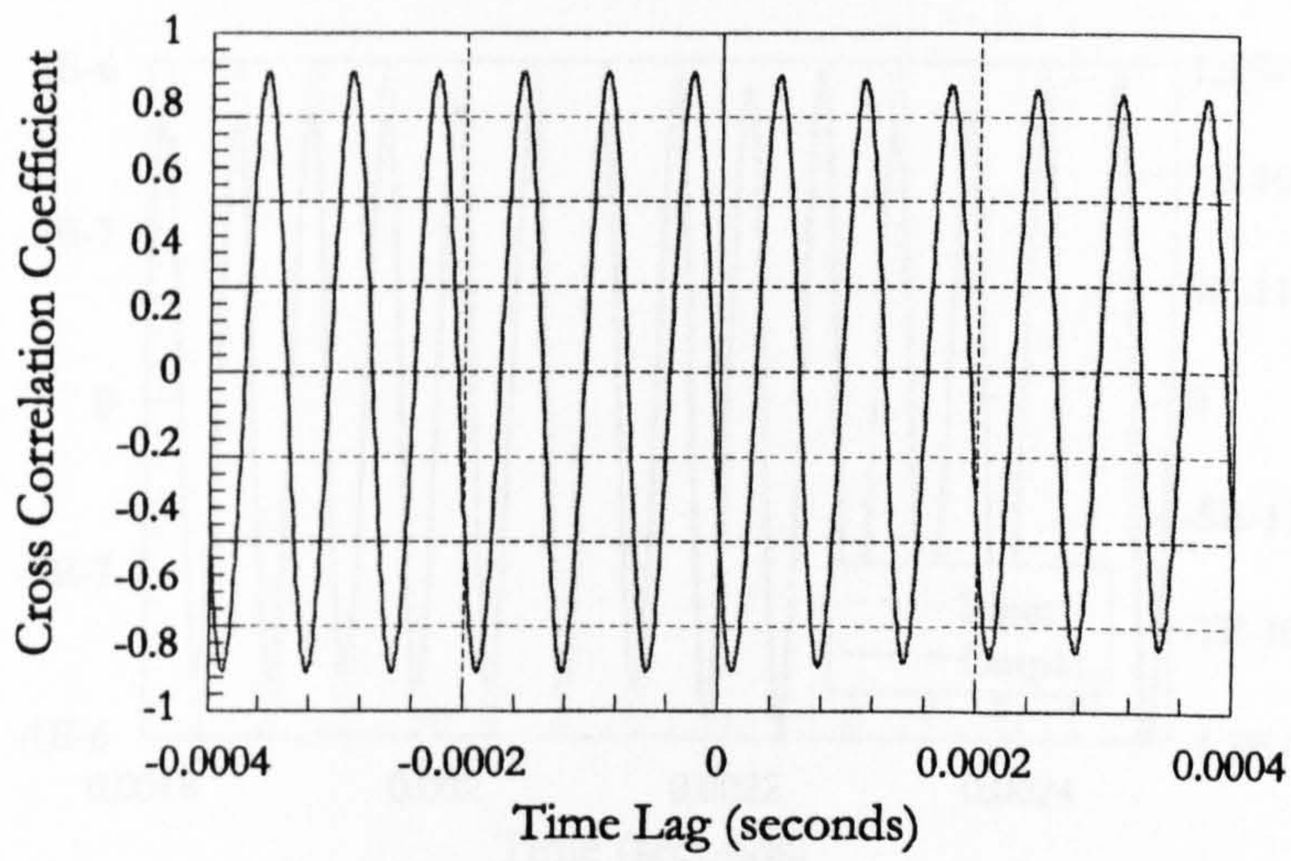

Figure 5.83: Cross correlation coefficient for R_d = 6, FS analysis

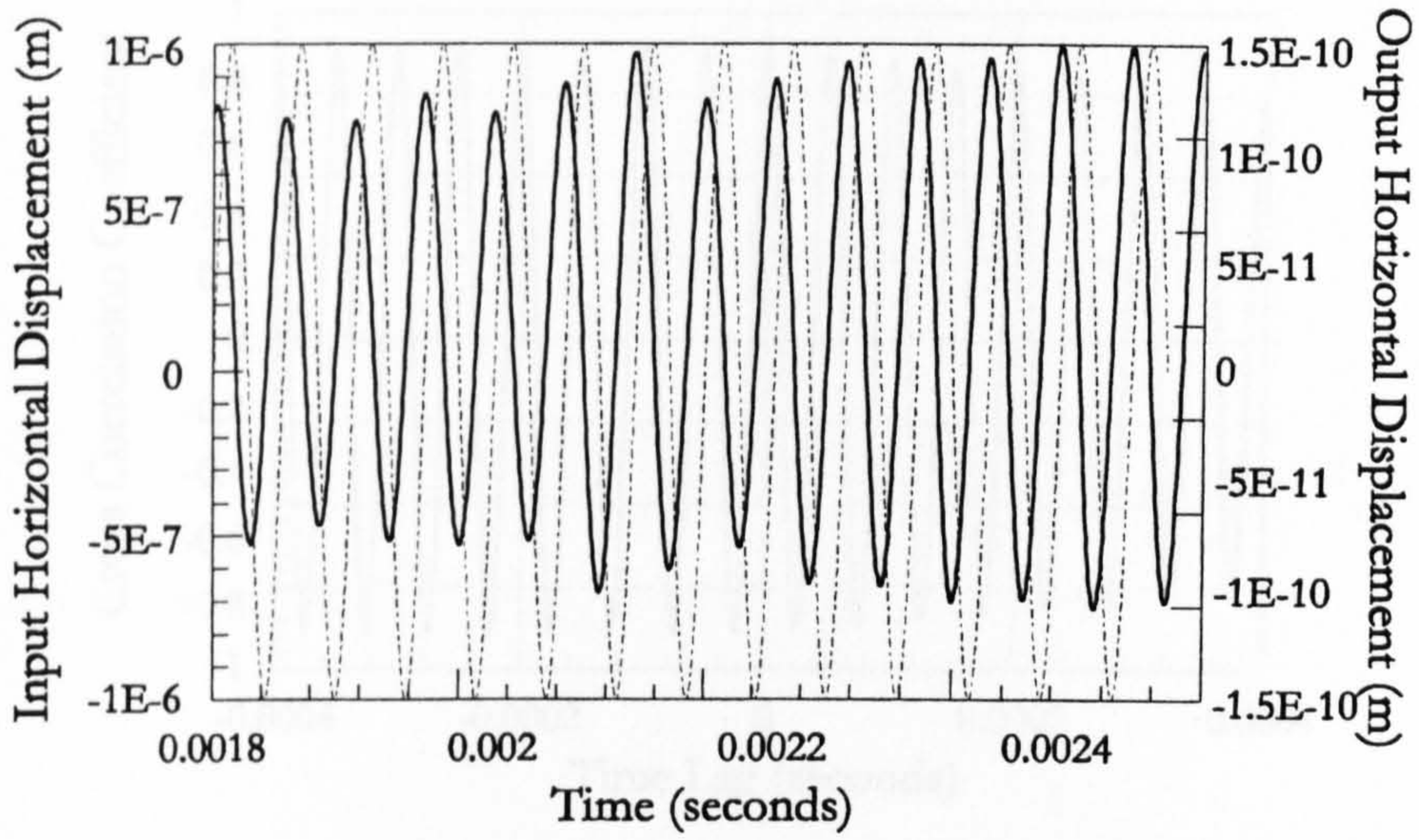

Figure 5.84: Input and output waves for continuously cycled test, R_d = 7 (FS)

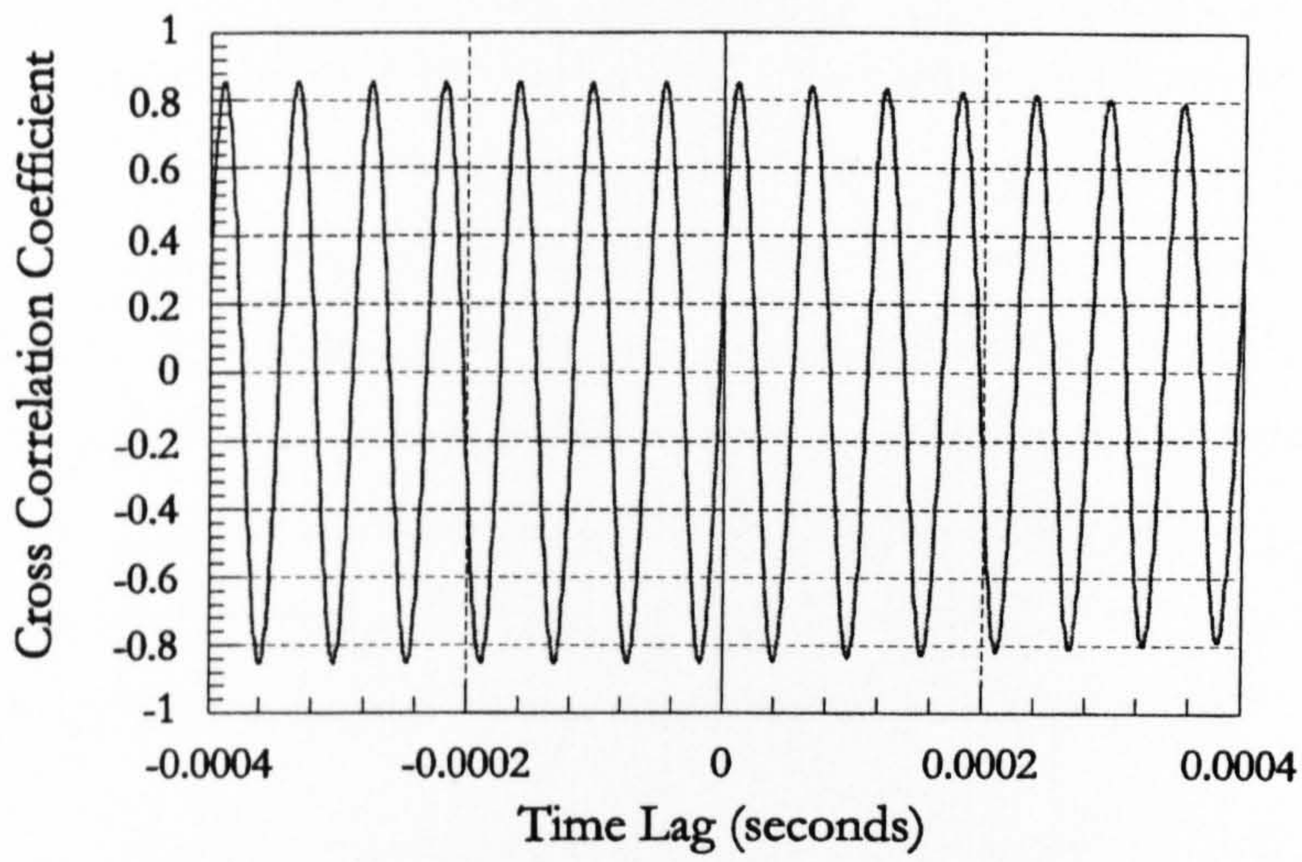

Figure 5.85: Cross correlation coefficient for R_d = 7, FS analysis

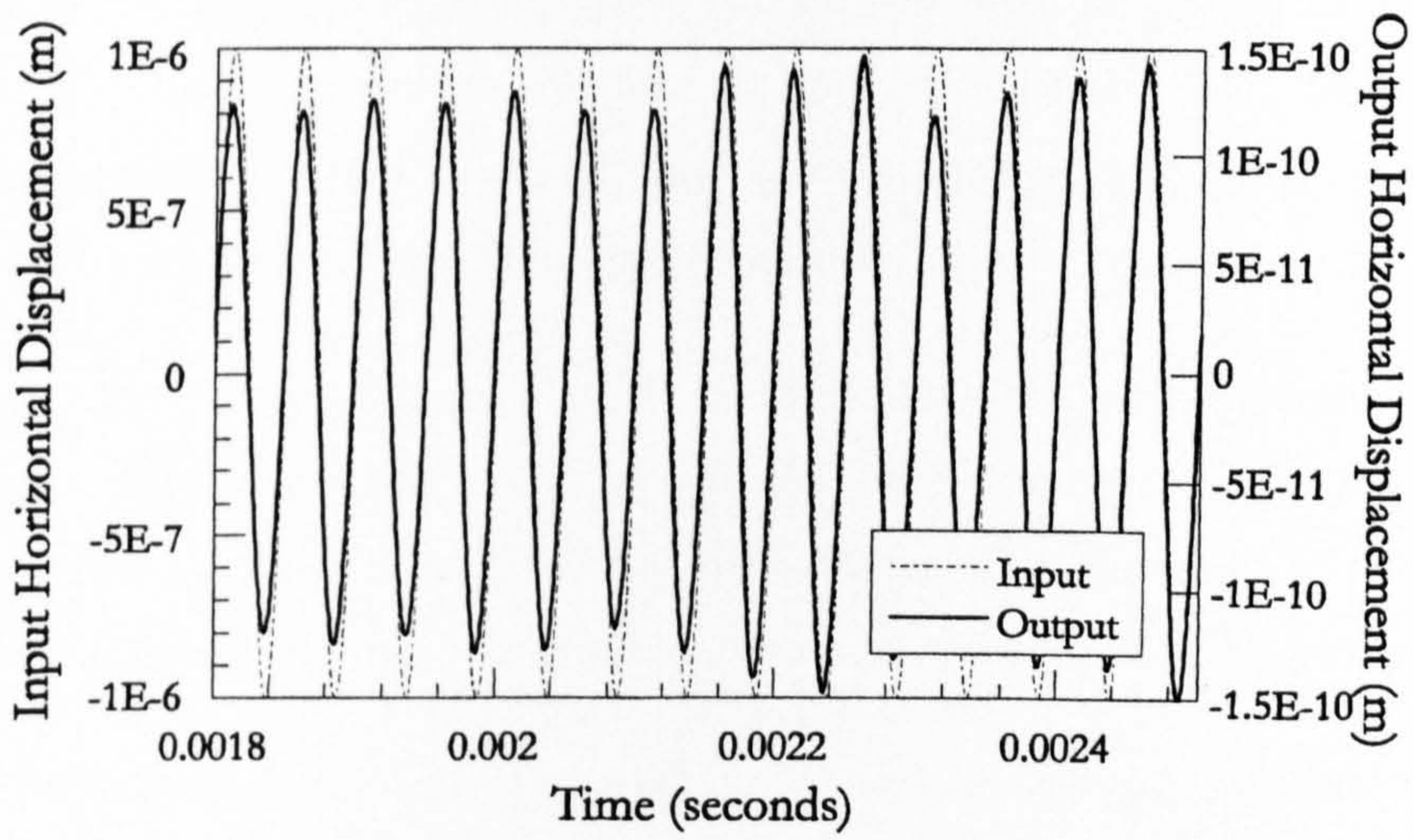

Figure 5.86: Input and output waves for continuously cycled test, R_d = 8 (FS)

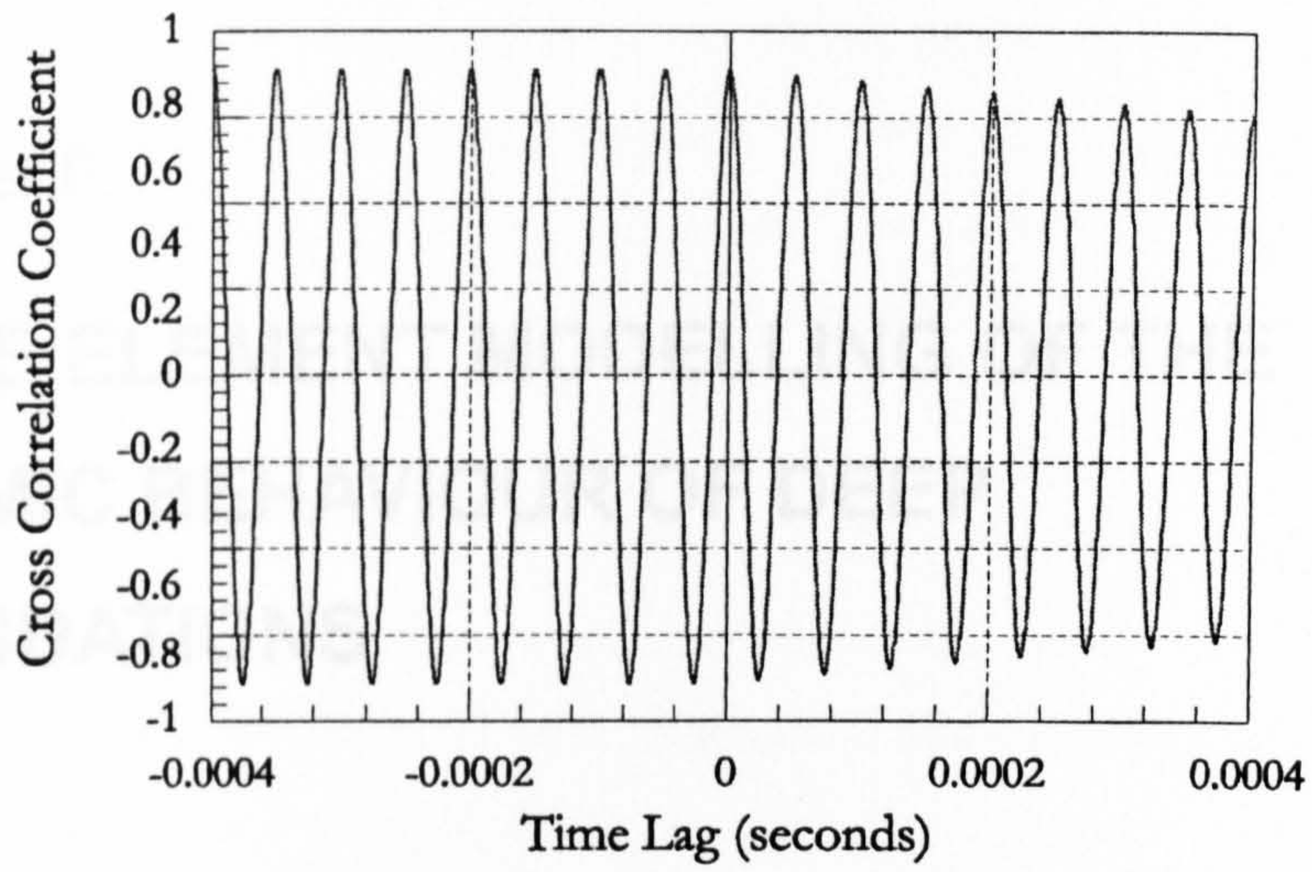

Figure 5.87: Cross correlation coefficient for R_d = 8, FS analysis

Chapter 6:

FINITE ELEMENT MODELLING OF THE SEISMIC BEHAVIOUR OF DEEP FOUNDATIONS

6.1 Introduction

For foundations built in seismic areas, the demands made to sustain load and deformation during an earthquake will probably be the most severe in their design life. It is therefore surprising that the reported number of foundation failures during destructive earthquakes is so few. There are two main hypotheses that attempt to explain the successful performance of foundations during seismic events. The first is the positive rate effects associated with rapid cyclic loading which may lead to a foundation having a higher capacity under dynamic loads than under static loads. The second is the general over design of foundations to reduce settlement.

Due to the encouraging performance of foundations during seismic events, research efforts have now moved away from trying to avoid foundation failures and towards attempting to make financial savings with regard to their design. The aim of this chapter is to use dynamic finite element analyses to investigate the behaviour of a deep foundation subjected to seismic loading and to compare the results with those predicted by the currently available design methods.

The first part of this chapter summarises the current understanding of the behaviour of foundations during seismic events. The performance of foundations in two seismic zones is presented, the first from Mexico City where the soil is mainly clay and the second in Kobe, Japan where the soil is mainly loosely compacted fill.

The second part of the chapter looks at the current methods available for the seismic design of foundations. The theory and assumptions that form the basis of these methods are also presented and their limitations discussed.

The third part of the chapter presents the results of pseudo static finite element analyses of a deep foundation first presented by Potts (2000) and in part reanalysed for this thesis. The aim of this study is to check the underlying assumptions of the limit equilibrium method that is used in the design of deep foundations subjected to seismic loading.

The fourth part of the chapter presents the results of dynamic finite element analyses of a deep foundation that use actual earthquake records for their input. The results of this study are then compared qualitatively and quantitatively with the limit equilibrium and pseudo static analyses.

6.2 The Behaviour of Foundations Subjected to Seismic Loads

6.2.1 Foundations in Clay

The lack of understanding of the fundamental seismic behaviour of deep foundations led to a number of failures during the Mexico City earthquake of 1985. The city is particularly vulnerable to damaging earthquakes due to it being built on a thick clayey deposit with low shear strength and high compressibility. On September 19th 1985 a magnitude 8.1 M_g earthquake struck Mexico City, in which between 330 and 757 (depending on the source) buildings were seriously damaged (Mendoza and Auvinet (1988)).

The buildings that were worst affected during the earthquake were those founded on frictional piles and raft foundations. Several buildings on raft foundations exhibited very large non-uniform settlements, which ultimately led to tilting of the structures (Mendoza and Auvinet (1988)). One six storey building was reported to have experienced 0.92 meters of earthquake induced settlement, despite having a static factor of safety of 2.0. The cause of the excessive earthquake induced settlement in this case was thought to be the over stressing of the ground beneath the raft foundation under static loads. The stresses already present in the ground due to the static loading caused large permanent deformations to develop when the earthquake occurred. The passage of the seismic waves through the soil induced large shear stresses which resulted in large permanent displacements. Buildings

founded on frictional piles performed worst of all. Mendoza and Auvinet (1988) reported that 13.5% of all 9 to 12 story buildings, most of them founded on friction piles, were severely damaged. Sudden differential settlements were reported, with consequential tilting.

The study by Mendoza & Auvinet (1988) highlighted how significant the static factor of safety is during dynamic loading. They reported that most of the instances of ill behaviour of building foundations in Mexico City during the September 19, 1985 earthquake were close to yielding under static loads, which promoted the generation of permanent deformations under the earthquake induced high cyclic shear stress increments. End bearing piles and footing type foundations (i.e. strip and raft footings) were reported to have been the most successful during the Mexico City earthquake.

To better understand the seismic behaviour of frictional pile foundations during seismic events, the foundations of a bridge pier in Mexico City were fully instrumented (Mendoza *et al.* (2000a)). The foundations consisted of 77 square reinforced concrete driven piles which were capped by a concrete raft. The instrumentation consisted of thirteen pile load cells, eight soil-slab-contact pressure cells, six piezometers, three sets of triaxial accelerometers and three vertical arrays of magnetic extensometers extending down to a depth of 60 meters. The aim of the exercise was to evaluate how the pile and raft system shared the static load during and after construction and how this distribution was affected by an earthquake.

When long term conditions were reached, it was found that 85% of the static load was taken by the piles and the remaining 15% by the slab. After the bridge was opened to traffic the effects of two earthquakes were recorded at the bridge foundation. The first hit on the 11th of January 1997 and had a magnitude $M_e = 7.3$ and the second struck on the 19th July 1997 and had a magnitude $M_a = 6.3$. Whilst they came from different sources and had quite different magnitudes, their effects were very similar and are summarised below. Due to their similarity only the larger event is discussed:

Effect on pile loads:

- The Fourier response spectra of the pile-box system variables (acceleration and pore pressures) were very similar to that of the free field response, implying that there is negligible dynamic pile-soil interaction for these events.
- The measured load on the piles initially dropped due to some load, caused by a small vertical settlement being temporarily transferred to the slab.
- The initial static load for the example pile given by Mendoza *et al.* (2000a) was 530 kN. The maximum cyclic amplitude caused by the earthquake was 24.5 kN.
- The load on the pile after the seismic event was unchanged, implying there was no degradation of the soil-pile interface.

Effect on contact pressure:

- At first the contact pressure went up due to the vertical displacement of the foundation mentioned previously.
- During the event the contact pressure increased, implying that the piles and the slab were sharing the additional cyclic loading.
- After some point the pile load stopped increasing, but the slab pressure continued to rise. Mendoza *et al* (2000a) attributed this to some yielding of the pile and any further increase in load being taken by the slab.
- As mentioned previously, the pore pressure response oscillated in phase with the foundation-soil system, but no residual pore pressure remained.

No settlement data was available for the two earthquakes reported by Mendoza *et al.* (2000a) although measurements were presented by Mendoza *et al.* (2000b) for another earthquake that occurred in June 1999 at the same site. The settlement along one axis of the foundation is shown in Figure 6.1.

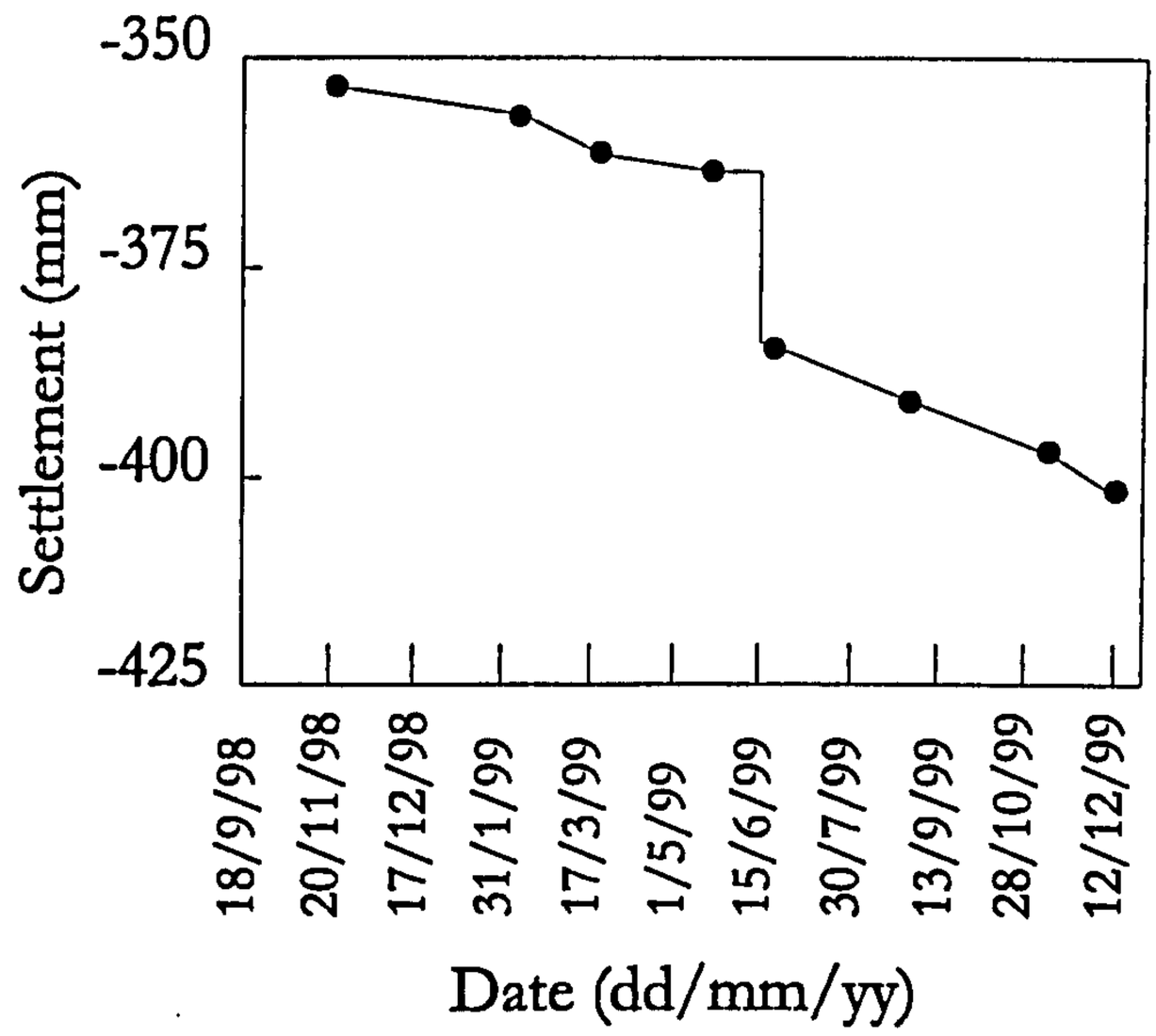

Figure 6.1: Settlements on the Impulsora Bridge foundation (after Mendoza et al. (2000b))

The data indicates that the foundations were still settling under static loads, although the earthquake clearly caused an accelerated movement of some 20 millimetres.

To over come the lack of instrumented piles subjected to earthquake loading some research has focused on recreating the effect of earthquake loading on deep foundations by using scale models in centrifuge machines (for example Maheetheran (1990)). This work has concentrated on the frequency response of the foundation and not the fundamental behaviour of the foundation during the earthquake and is therefore not relevant to the work presented in this thesis.

Due to the lack of instrumented piles of the type mentioned previously, most investigations into the seismic capacity of deep foundations have concentrated on full scale tests subjected to cyclic loads. However, it is only possible to apply relatively low frequency axial loading and this type of artificial scenario cannot recreate the complex in-situ stress state induced during seismic events.

Despite the number of tests performed of this type, the effect of cyclic loading on the capacity of a deep foundation is still not fully understood. Briaud and Felio (1986) found that below some threshold load, continued cycling has no significant influence on pile capacity. The value of this threshold loading was given as between

70 and 80% of the ultimate pile capacity for one way loading and 40% for two way loading. It is generally accepted that for loads above the threshold value the action of cyclic loading has two contradictory effects. The first is the beneficial increase in undrained strength and soil stiffness due to the rapid application of the loading. Increases in the ultimate capacity of a deep foundation of between 5% and 20% of the static capacity have been reported for each order of magnitude increase in the loading rate (Dunnavant *et al.* (1990)). Kraft *et al.* (1981) and Jaime *et al.* (1991) reported an increase in pile-soil stiffness of between 10 and 25% per ten fold increase of loading rate. This feature of soil behaviour could be captured by a soil model in which the stiffness and/or strength parameters are related to strain rate, although no such soil model is available in ICFEP at present. The second effect is the degradation of the pile-load transfer mechanism due to a reduction of radial stresses, the destruction of the soil particle bonds, or the generation of residual failure surfaces (Saldivar (2002)).

It appears from full scale experience, mainly from off-shore piles, that of these two effects, the beneficial gain in undrained strength and increase in stiffness induced by the rapid application of the load is the most significant. Therefore generally the design of piles to sustain cyclic loading in clays is not explicitly considered, provided the piles possess adequate factors of safety for static loading (Jardine (1991), Focht and O'Neill (1985) and Grosh & Reese (1980)).

6.2.2 Foundations in Residual Soils and Sands

Extra considerations must be made when designing foundations to sustain cyclic loading in sands. Generally, friction piles are avoided in this situation and end bearing piles that extend down to a stiffer stratum at depth are used in preference. In the case of sand, the strain rate effect mentioned previously for clay has very little effect and there is the added danger of liquefaction. As mentioned previously, during the seismic events recorded at the instrumented bridge pier in Mexico City clay no pore pressures accumulated. The same result has been found for other piles subjected to cyclic loading in clays (Chow (1997), McAnoy *et al.* (1982) and Puech & Jezequel (1980)). Conversely, laboratory tests on clay have shown the accumulation of pore pressures when subjected to cyclic loading (Van Eekelen and Potts (1978)).

The accumulation of pore pressures in clay is, however, not an issue when designing foundation for seismic loading in clays because the rate of increase of pore pressures in clay is very slow and is therefore not an issue in the time scale of an earthquake. For foundations built in drained material, for example sand, the accumulation of pore water pressures reduces the effective stress and may cause the soil to liquefy. In this state the soil has zero shear strength and any foundation built in the material will fail catastrophically. The most famous example of this type of failure occurred during the Niigata earthquake in 1964. Figure 6.2 shows a photograph of a residential building for which the foundations have failed due to the liquefaction of the surrounding ground.

Figure 6.2: Failure of building foundations due to liquefaction during Niigata earthquake, Japan 1964 (after Zienkiewicz *et al.* (1999))

Further evidence of this kind of failure was apparent during the devastating earthquake that struck Kobe, Japan on the 17th of January 1995. The areas that suffered most damaged were those around the coastline that were reclaimed after World War II. The material used to reclaim these areas was either decomposed Granite or crushed sandstone from the Rokko mountains. Many of the buildings in this area, built since the revisions to the Japanese buildings codes in 1974 and 1988, did not exhibit any significant foundation damage. However, in some cases the ground settlement caused by widespread liquefaction induced a large gap to form between the new height of the street and the base of many engineered buildings constructed on end bearing piles, which otherwise suffered no damage. Evidence of this type of failure is shown in Figure 6.3.

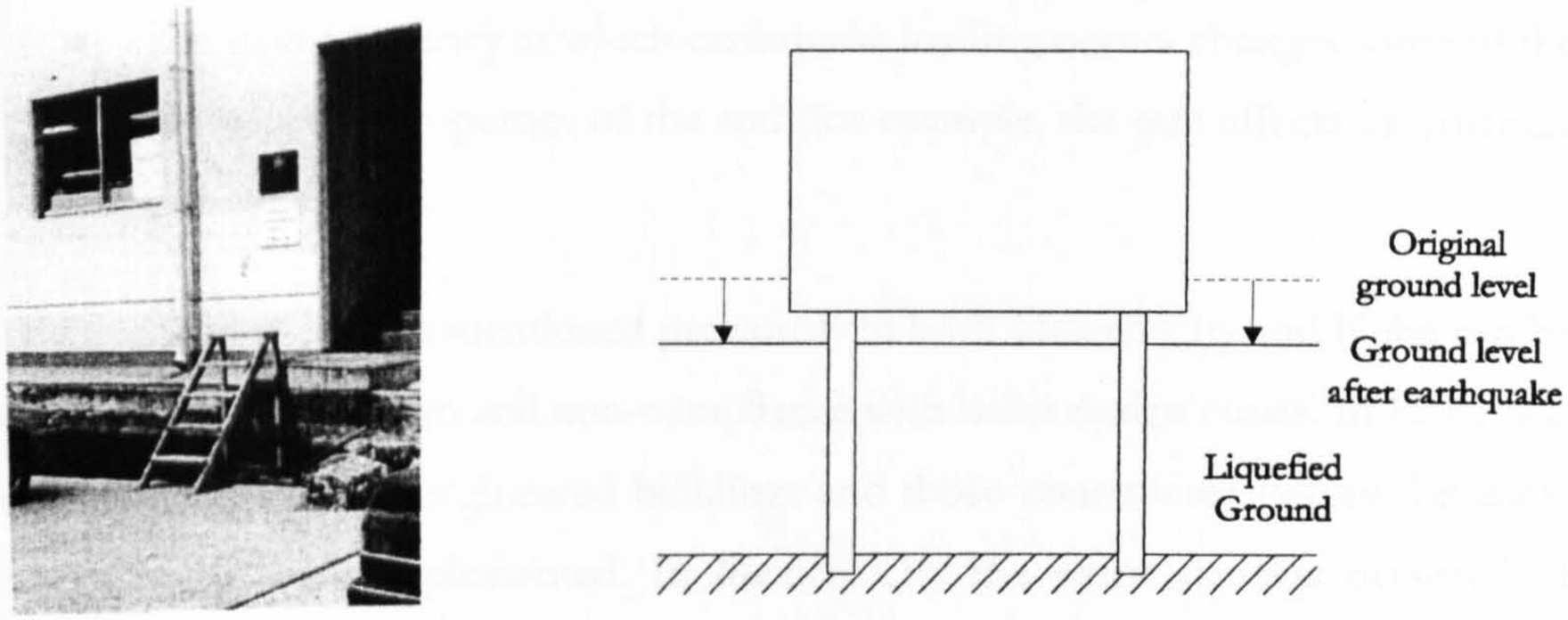

Figure 6.3: Large gap induced by liquefaction-induced ground settlement in Port Island, Kobe (after Tokimatsu *et al.* (1996))

Buildings founded on frictional piles or spread foundations experienced large settlements, often accompanied by severe tilt, due to bearing capacity failure of their foundations induced by soil liquefaction. Tokimatsu *et al.* (1996) gave several examples of the magnitude of settlement that was induced by liquefaction around piled foundations. These included a three storey building in Wadamiya-dori, Hyogo-ku, which settled about 1.1 meters and tilted considerably; and a two story building in Uosakihama that subsided more than 1.5 meters. However, not all foundation damage was attributable to liquefaction. Some buildings which were founded in material that did not liquefy still experienced significant amounts of settlement and tilting. Examples of this include a building in Tamon-dori, Chuo-ku and the Uosaki Junior High School in Uosaki that settled and tilted by 3° (Tokimatsu *et al* (1996)).

6.2.3 Summary

The effects of earthquake loading on deep foundations can be summarised as follows.

- The passage of the seismic wave through the soil surrounding the foundation induces inertial forces that change the stress conditions in the ground.
- The shaking of the ground upon which the structure is built causes it to rock back and forth on its foundations. This motion causes a cyclic loading on the foundation which oscillates around the permanent static load.

- The high frequency at which earthquake loading occurs changes some of the fundamental properties of the soil (for example, the rate effects on stiffness and strength).

The foundation failures mentioned previously in both Mexico City and Kobe can be attributed to poor design and non-compliance with latest design codes. In Kobe this was restricted to non-engineered buildings and those constructed before the latest design codes were implemented. In Mexico City the worst damage occurred in those buildings that were poorly designed for static loads. Due to the foundations being overstressed, the cyclic shear stresses induced by the earthquake created large permanent strains. In both events the most severely affected buildings were those founded on frictional piles and, except for a few extreme cases, most did not fail by creating a one sided slip surface, but rather settled, in some cases by more than 1 meter. Due to the heterogeneous nature of the building design and/or underlying soil, the buildings that settled considerably also tended to tilt.

The generation of excess pore water pressures during cyclic loading does not appear to be a problem for clays and dense sands. For loose fill material of the type used in the reclamation of the land around the port of Kobe, liquefaction can pose massive problems for foundations. The complete loss of bearing capacity as the soil losses its shear strength can cause large settlements and in the most extreme cases the foundation may fail catastrophically.

6.3 Current Design Practice for Foundations Subjected to Seismic and Cyclic Loads

As mentioned previously, the two principal effects that an earthquake has on a foundation are (i) the stress changes in the ground caused by the passage of the seismic wave through the ground, and (ii) the second is the cyclic loading above the permanent static loading caused by the shaking of the structure above. Generally, the interaction between these two features is ignored and each is dealt with separately.

6.3.1 *The Design of Foundations for Cyclic Loading*

The additional cyclic loading caused by the inertial forces from the structure is generally only taken into account if either: (i) the transient component of the load (Q_{cyclic}) is equal to or higher than 30% of the permanent static load (Q_{av}) or (ii) if the permanent load (Q_{av}) plus the cyclic load (Q_{cyclic}) is greater than 90% of the static capacity ($Q_{max.static}$) for one way loading, or 75% in the case of two way loading (Focht and O'Neill (1985)). This is due to the widely held belief that the dynamic capacity of a foundation is higher than the static capacity, for the reasons outlined in Section 6.2. For large projects, like off-shore foundations, so called interaction diagrams of the type shown in Figure 6.4 have been developed.

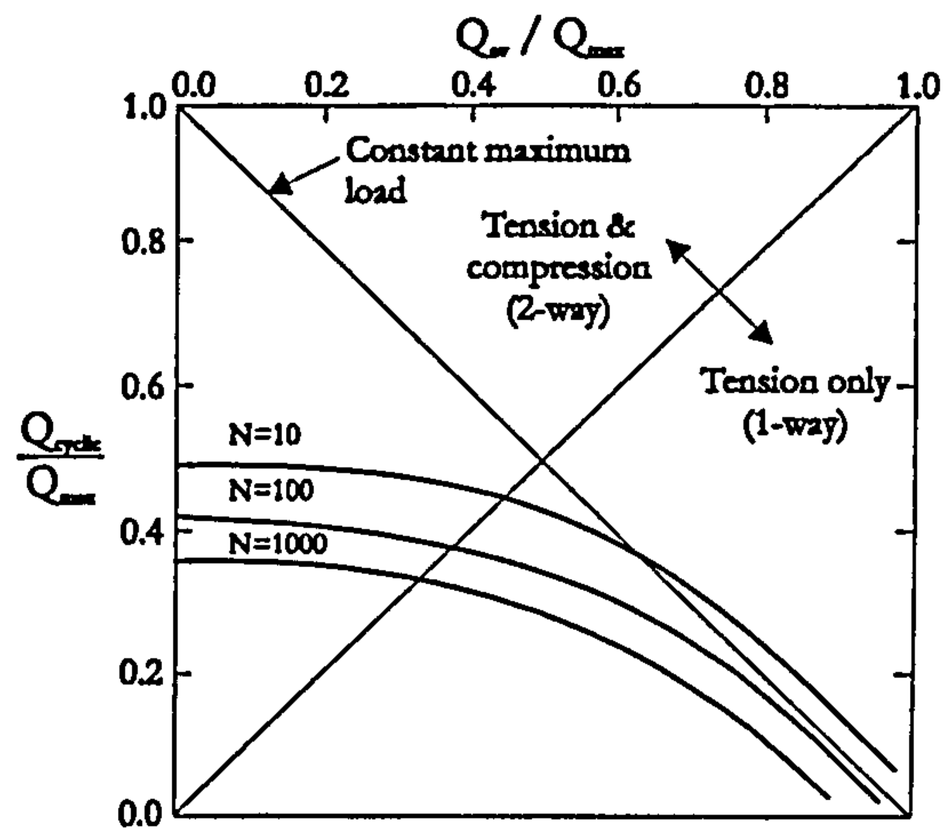

Figure 6.4: Cyclic interaction diagram from Haga tension pile tests (after Jardine, (1991)).

These diagrams are based on full scale field tests (Karlsrud and Haugen (1985)) or cyclic response analyses (Jardine (1991)) and are only applicable to the situation for which they were developed. They can be used to determine how many cycles (*N*) would cause failure for a given loading scenario or what level of cyclic loading would be acceptable for a given number of cycles. An example of how such a diagram was derived for piles in Mexico City clay can be found in Saldivar (2002).

6.3.2 *The Seismic Design of Foundations*

The static load bearing capacity of a foundation constructed in a frictional material, with an angle of shearing resistance φ' and cohesion intercept c', cannot be

found exactly. Over the years many analyses of the problem have been presented in the literature and as early as 1973 Vesić listed 15 different solutions (Bowles (1988)). It is therefore no surprise that an exact solution has not been found for the bearing capacity of a foundation under seismic loading.

The first notable solution for a shallow foundation was proposed by Terzaghi in 1943. Following the classic work on plasticity by Prandtl, Terzaghi calculated the capacity of a shallow foundation by assuming the failure mechanism shown on the left hand side of Figure 6.5 and applying a modified version of the bearing capacity theory developed by Prandtl (ca. 1920).

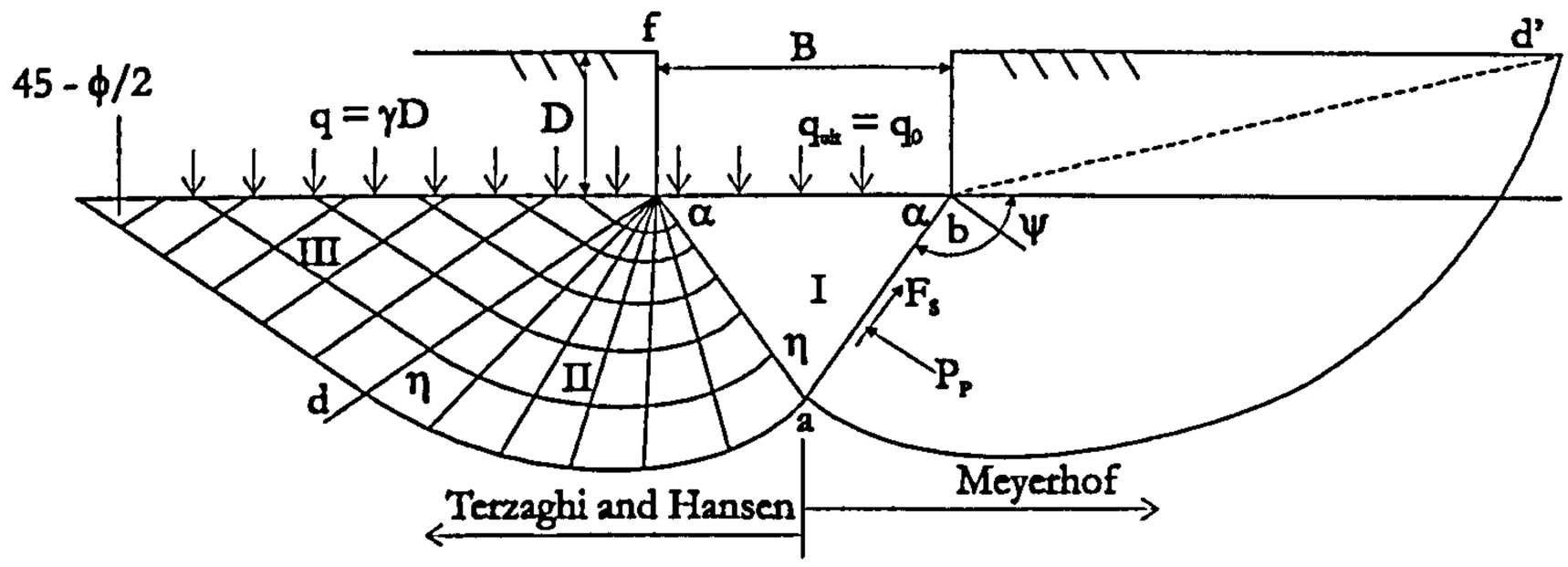

Figure 6.5: General footing-soil interaction for bearing capacity equations for strip footings (after Bowles (1988))

The resultant capacity is given by Equation 6.1.

$$q_{ult} = c'N_c + q'N_q + 0.5\gamma BN_\gamma \tag{6.1}$$

where N_γ is the bearing capacity factor for self weight

N_q is the bearing capacity factor for surcharge

N_c is the bearing capacity factor for cohesion

γ is the effective unit weight of the soil

q' is the effective surcharge

B is the width of the foundation

The bearing capacity factors for cohesion and surcharge are given by Equations 6.2 and 6.3 respectively. The values for N_γ were given in graphical form although Terzaghi never made it clear how they were calculated.

$$N_q = \frac{\left(e^{(0.75\pi-\varphi/2)\tan\varphi}\right)^2}{2\cos^2(45+\varphi/2)} \tag{6.2}$$

$$N_c = \left(N_q - 1\right)\cot\varphi \tag{6.3}$$

The framework proposed by Terzaghi was adopted by Meyerhof (1951, 1963) to include the effects of foundation shape, foundation depth and load inclination. The failure surface assumed by Meyerhof is shown on the right hand side of Figure 6.5. The bearing capacity of the foundation is given by Equation 6.4, which is of the same form as Equation 6.1 but includes the correction factors for load inclination (i_c, i_q and i_γ) and depth (d_i, d_q and d_γ).

$$q_{ult} = cN_c d_c i_c + q' N_q d_q i_q + 0.5\gamma B N_\gamma d_\gamma i_\gamma \tag{6.4}$$

Where $N_q = e^{\pi\tan\varphi} K_p$

$$N_c = \left(N_q - 1\right)\cot\varphi$$

$$N_\gamma = \left(N_q - 1\right)\tan(1.4\varphi)$$

$$d_c = 1 + 0.2\sqrt{K_p}\,\frac{D}{B}$$

$$d_q = d_\gamma = 1 + 0.1\sqrt{K_p}\,\frac{D}{B}$$

$$i_c = i_q = \left(1 - \frac{\theta^\circ}{90^\circ}\right)$$

$$i_\gamma = \left(1 - \frac{\theta^\circ}{\varphi^\circ}\right)^2$$

$$K_p = \tan^2(45+\varphi/2)$$

θ = angle of resultant loading without a sign.

The approach used by Meyerhof was utilised by Hansen (1970) and Vesić (1973, 1974) to reanalyse the bearing capacity calculation. For both studies, the resulting values of the bearing capacity factors for cohesion and overburden where found to

be the same as Meyerhof's. The N_γ terms differed and are given by Equations 6.5 and 6.6 by Hansen and Vesić respectively.

$$N_\gamma = 1.5\left(N_q - 1\right)\tan\varphi \tag{6.5}$$

$$N_\gamma = 2\left(N_q + 1\right)\tan\varphi \tag{6.6}$$

The correction factors (i_c, i_q and i_γ) for inclined loading differed from those found by Meyerhof and are given by Equations 6.7, 6.8 and 6.9 in the study by Hansen and Equations 6.7, 6.10 and 6.11 in that of Vesić.

$$i_c = i_q - \frac{1 - i_q}{N_q - 1} \tag{6.7}$$

$$i_q = \left(1 - 0.5 m_b \tan\varphi\right)^5 \tag{6.8}$$

$$i_\gamma = \left(1 - 0.7 m_b \tan\varphi\right)^5 \tag{6.9}$$

$$i_q = \left(1 - m_b \tan\varphi\right)^m \tag{6.10}$$

$$i_\gamma = \left(1 - m_b \tan\varphi\right)^{m+1} \tag{6.11}$$

where $m_b = \left(Q_b \tan\theta\right)/\left(Q_b \tan\varphi + c\right)$

$m = \left(2 + B/L\right)/\left(1 + B/L\right)$

Q_b = vertical load

B and L are the dimensions of the foundation

θ is the angle of the resultant load to the vertical

The early work by Terzaghi, Meyerhof, Hansen and Vesić did not explicitly include the effects of seismic loading, although its effects can be included indirectly by using some of the correction factors. Consider the forces applied to a foundation under seismic conditions shown in Figure 6.6.

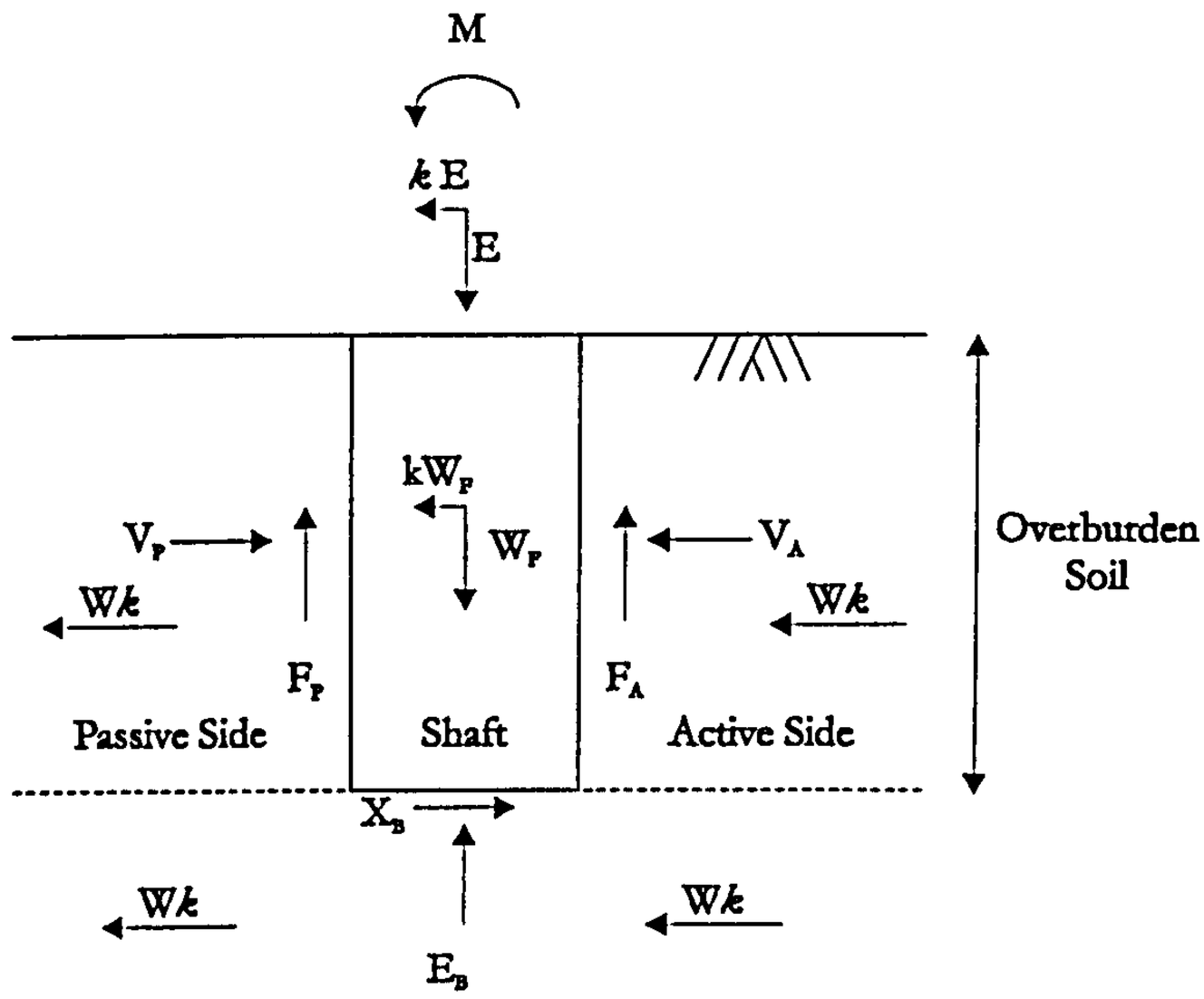

Figure 6.6: A deep strip foundation subjected to a horizontal acceleration *k.g* (after Potts (2000))

Where E is the vertical component of loading at ground level

E_H and X_H are the normal and shear forces on the shaft base

V_P, F_P and V_A, F_A are the normal and shear forces on the active and passive sides of the shaft, respectively

W_F is the self weight of the shaft

W is the self weight of the soil

A_H is the area of the shaft base

F_S is the skin resistance of the shaft, $F_S = F_P + F_A$

M is the seismically induced moment

g is the acceleration due to gravity

k is the applied horizontal acceleration as a fraction of gravitational acceleration

The moment applied to the foundation due to the inertia forces in the structure can be included into the foundation analysis by reducing it to an equivalent eccentric load. If the applied vertical load is *E*, then the moment can be represented by an eccentric force with an offset of e=M/E. Meyerhof (1953) recommended that in the case of eccentric loading the effective width of the foundation *B'* should be reduced according to Equation 6.12.

$$B' = B - 2e \tag{6.12}$$

If the inertia forces in the ground (W.*k*) are ignored (as they often are in foundation design (Chen (1997))) then the problem shown in Figure 6.6 reduces to that of a foundation on sloping ground. The ground surface and the foundation load are now inclined at an angle given by $i = \tan^{-1}(k)$, where *k* is the horizontal acceleration as a fraction of gravity. This is illustrated in Figure 6.7.

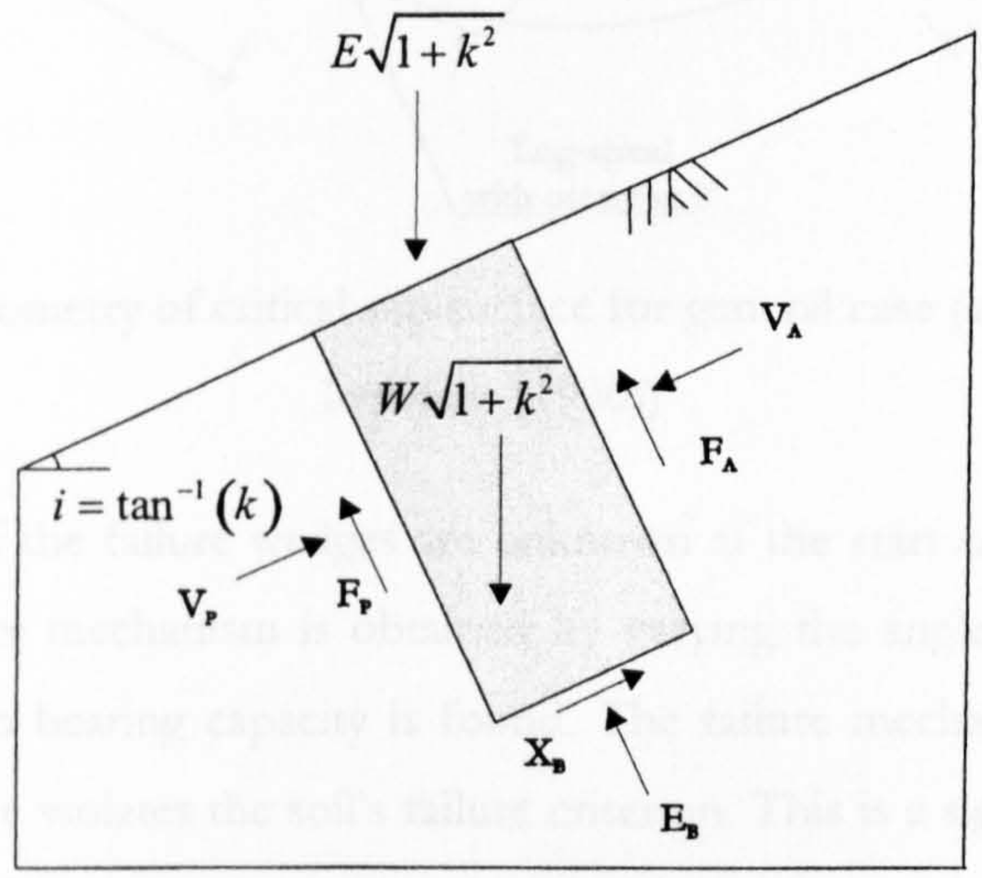

Figure 6.7: The inclined loading condition (after Potts (2000))

The foundation bearing capacity can now be calculated by using the solutions of Hansen or Vesić with the appropriate correction factors for load inclination.

The importance of the inertial forces in the soil on the bearing capacity was investigated by Sarma and Iossifelis (1990) for the case of a surface foundation. The earthquake acceleration was represented by a constant horizontal force which is the same for the structure and the surrounding soil. As indicated in Figure 6.8, the lateral inertial force from the structure is represented by a shear force acting at foundation level. The bearing capacity factors are obtained using the method of inclined slices (Sarma (1979)) which is commonly applied to slope stability problems. The asymmetrical failure mechanism assumed is shown in Figure 6.8.

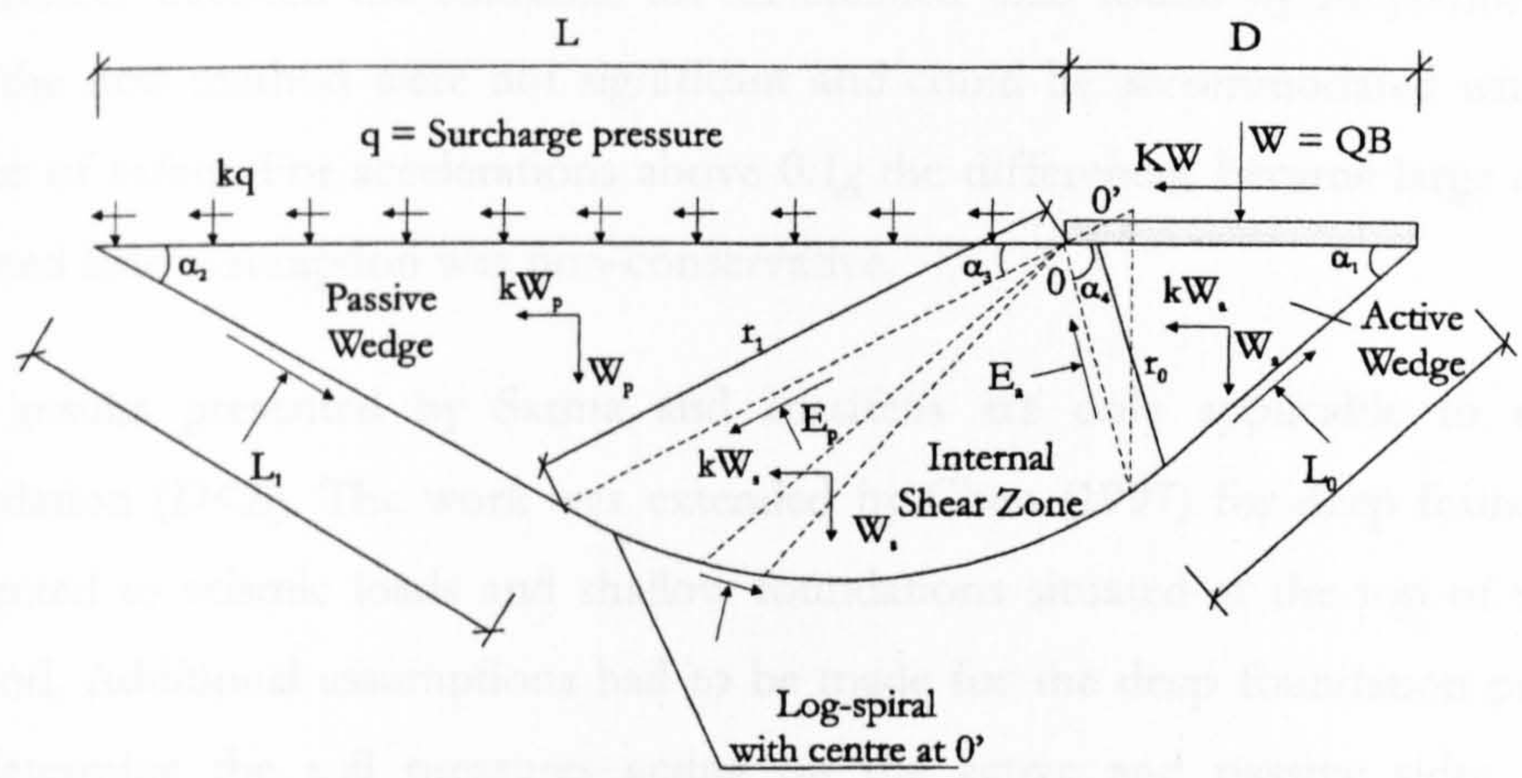

Figure 6.8: Geometry of critical slip surface for general case (after Sarma and Iossifelis (1990))

The geometries of the failure wedges are unknown at the start of the analysis. The most critical failure mechanism is obtained by varying the angles α_1, α_2, α_3 and α_4 until the minimum bearing capacity is found. The failure mechanism is rejected if any inter-slice force violates the soil's failure criterion. This is a significant and more theoretically sound assumption than that of previous researchers. Although the blocks are assumed to behave rigidly, the material they are composed of must satisfy the same failure criterion as the forces between the blocks. The resultant bearing capacity factors for a range of horizontal accelerations and angles of internal friction are shown in Figure 6.9.

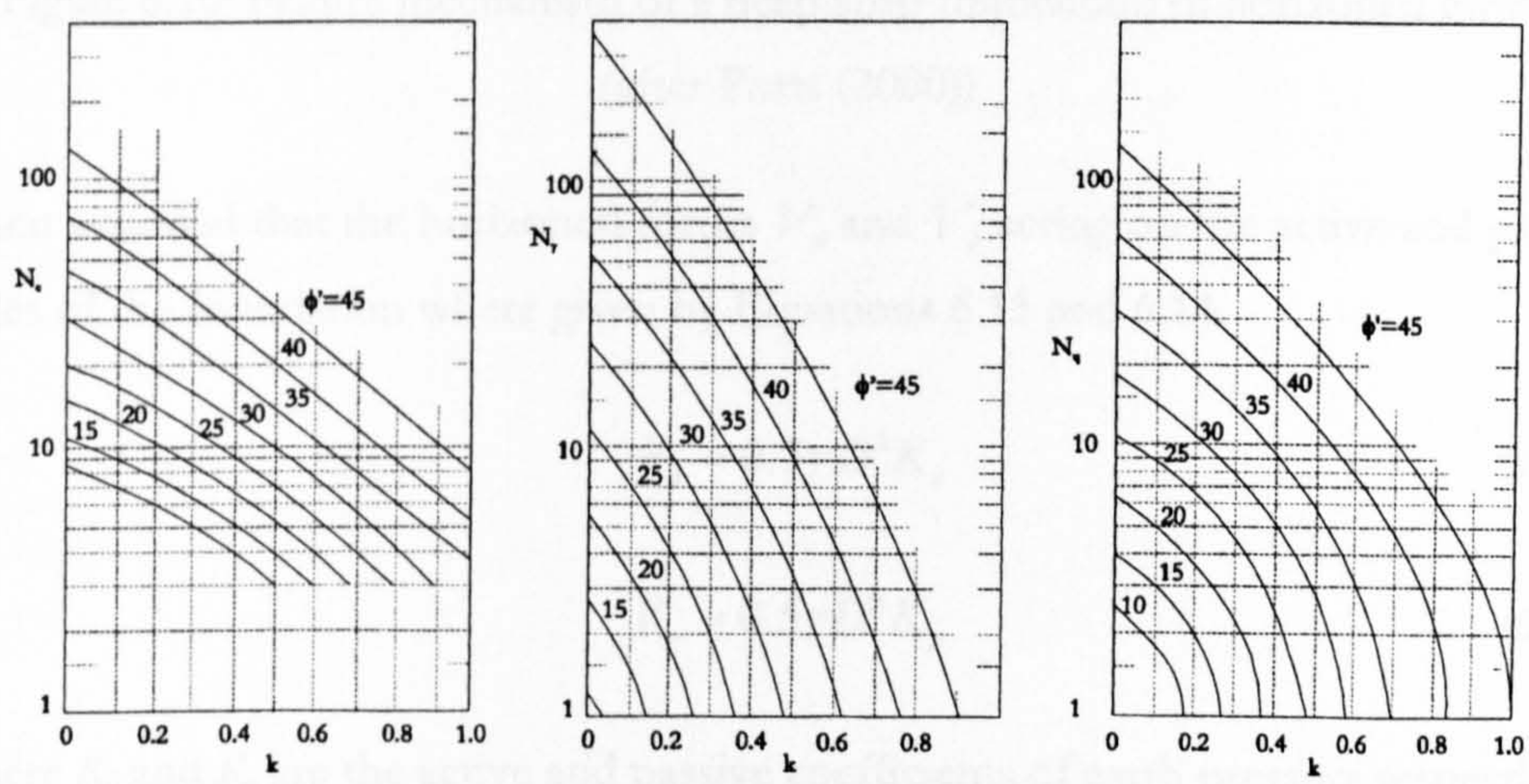

Figure 6.9: Bearing capacity factors as a function of horizontal acceleration and angle of internal friction (after Sarma and Iossifelis (1990))

Sarma and Iossifelis found that for horizontal accelerations below 0.1g the differences between the solutions for an inclined load found by Meyerhof (1953) and the new method were not significant and could be accommodated within the factor of safety. For accelerations above 0.1g the differences became large and the inclined load assumption was non-conservative.

The results presented by Sarma and Iossifelis are only applicable to shallow foundation ($D<B$). The work was extended by Chen (1997) for deep foundations subjected to seismic loads and shallow foundations situated at the top of sloping ground. Additional assumptions had to be made for the deep foundation problem to determine the soil pressures acting on the active and passive sides of the foundation. The assumed failure mechanism and applied forces are shown in Figure 6.10.

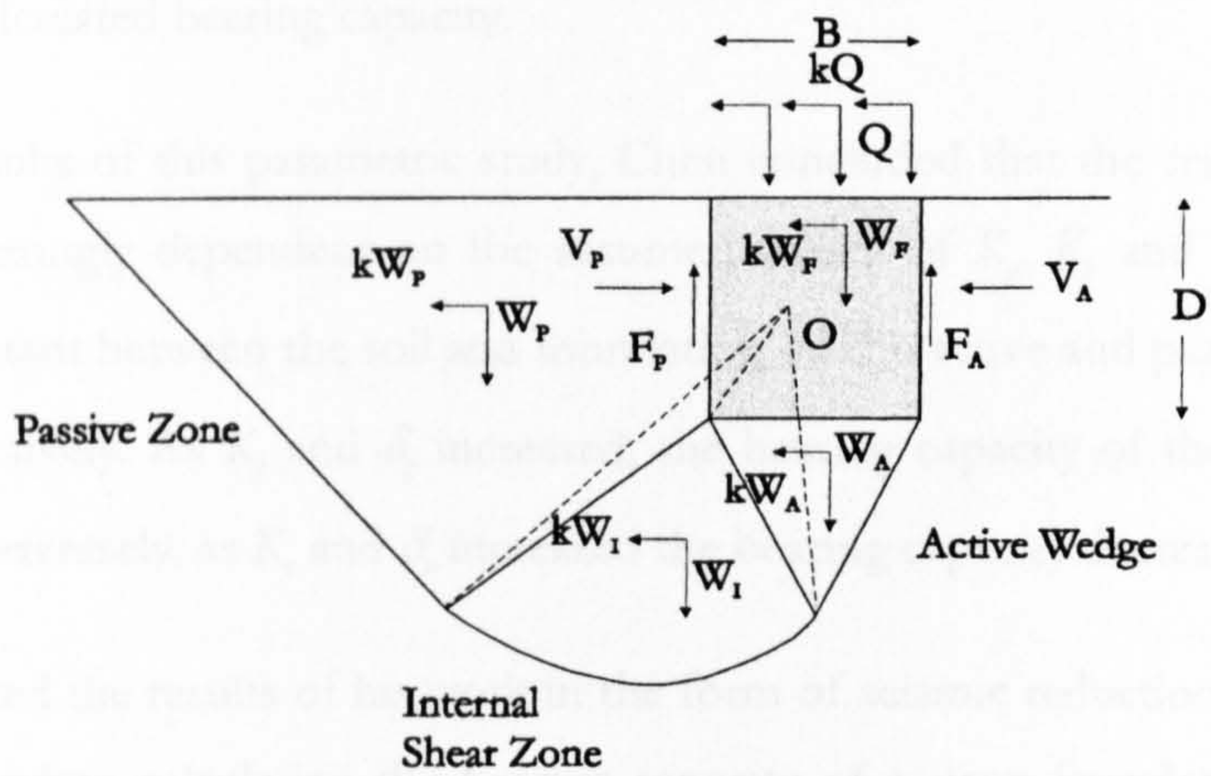

Figure 6.10: Failure mechanism of a deep strip foundation in horizontal ground (after Potts (2000))

Chen assumed that the horizontal forces V_a and V_p acting on the active and passive sides of the foundation where given by Equations 6.13 and 6.14.

$$V_a = 0.5\gamma D^2 K_a \tag{6.13}$$

$$V_p = 0.5\gamma D^2 K_p \tag{6.14}$$

where K_a and K_p are the active and passive coefficients of earth pressure respectively. The actual values of these parameters cannot be calculated beforehand and therefore maximum and minimum values were derived using the work by Okabe

(1924) and Mononobe and Matsuo (1929) on the seismic analysis of retaining walls. The minimum value for K_a is given by Equation 6.15 and the maximum value for K_p is given by Equation 6.16.

$$K_a = \frac{\cos\delta\cos^2(\varphi+i)}{\cos i\cos(\delta+i)\left[1+\sqrt{\frac{\sin(\varphi+i)\sin(\varphi+\delta)}{\cos(\delta+i)}}\right]^2} \tag{6.15}$$

$$K_p = \frac{\cos\delta\cos^2(\varphi-i)}{\cos i\cos(\delta+i)\left[1-\sqrt{\frac{\sin(\varphi-i)\sin(\varphi+\delta)}{\cos(\delta+i)}}\right]^2} \tag{6.16}$$

A parametric study was then undertaken to determine the influence this assumption has on the calculated bearing capacity.

From the results of this parametric study, Chen concluded that the seismic bearing capacity is strongly dependent on the assumed values of K_a, K_p and the angle of shearing resistant between the soil and foundation on the active and passive sides, δ_a and δ_p respectively. As K_p and δ_p increased, the bearing capacity of the foundation increased. Conversely, as K_a and δ_a increased the bearing capacity decreased.

Chen presented the results of his work in the form of seismic reduction factors that can be used when calculating the bearing capacity of a deep foundation on level ground subjected to an earthquake acceleration of *k.g*. An example of the reduction factor for the N_γ term ($i_{\gamma e}$) is shown in Figure 6.11 for a foundation with a D/B ratio of 5. For comparison, the reduction factors for a surface foundation are also shown in the figure.

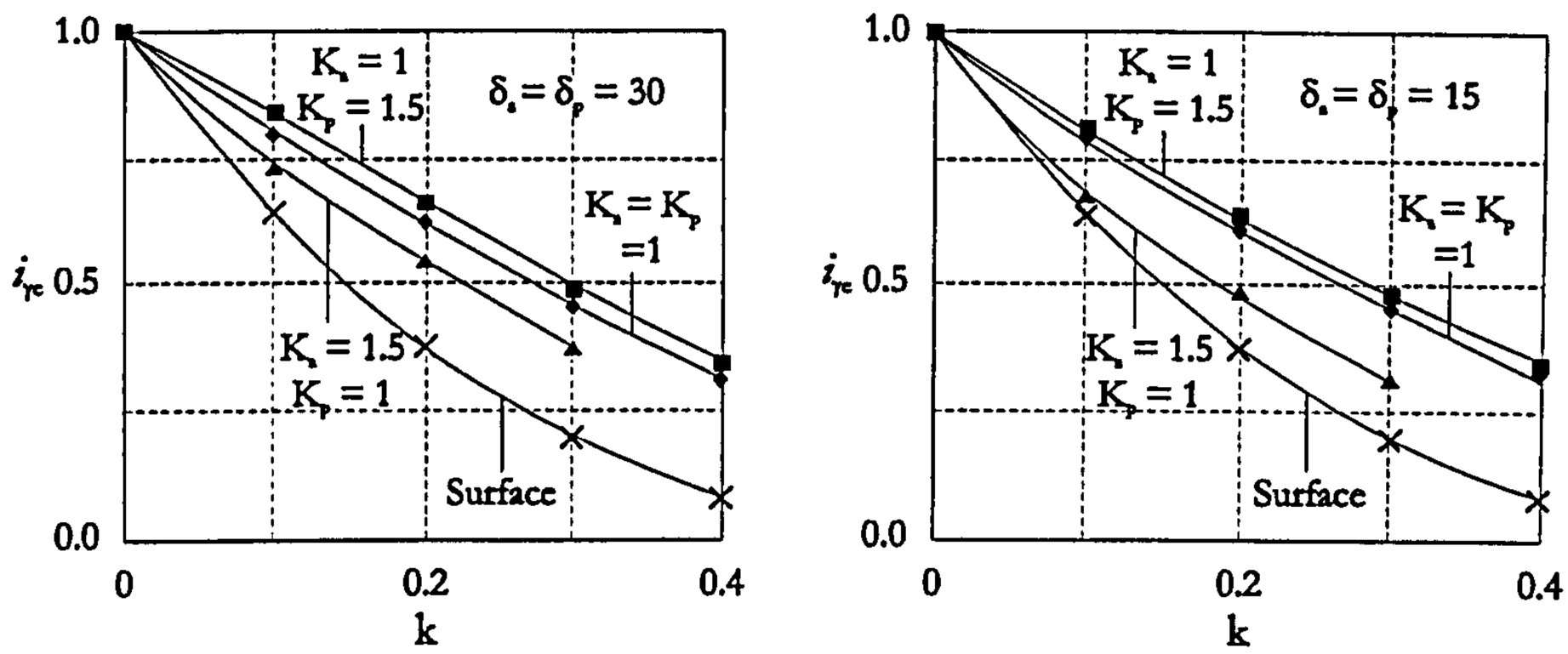

Figure 6.11: Seismic reduction factor $i_{\gamma c}$ for a deep foundation for $\varphi = 30°$, c = 0, D = 5B (after Chen (1997))

As mentioned previously, it is clear that the results are heavily dependant on the assumed values of K_a and K_p.

Potts (2000) used pseudo static finite element analysis to investigate the applicability of the earth pressures assumed in Chen's analysis. The term pseudo static applies to static analyses that account for the earthquake induced inertia forces in the soil mass by applying a body force horizontally. This arrangement is analogous to that assumed in the limit equilibrium problem analysed by Chen. To give comparable results, Potts analysed a 5 meter deep and 1 meter wide strip foundation in plane strain assuming a Mohr-Coulomb failure criterion with the following material properties.

E = Young's modulus = 60000 kPa

ν = Poisson's ratio = 0.25

K_0 = earth pressure coefficient at rest = 1.0

γ = unit weight of soil = 19 kN/m^3

c' = cohesion = 0 kPa

ψ = angle of dilation = 0

The mesh used is shown in Figure 6.12.

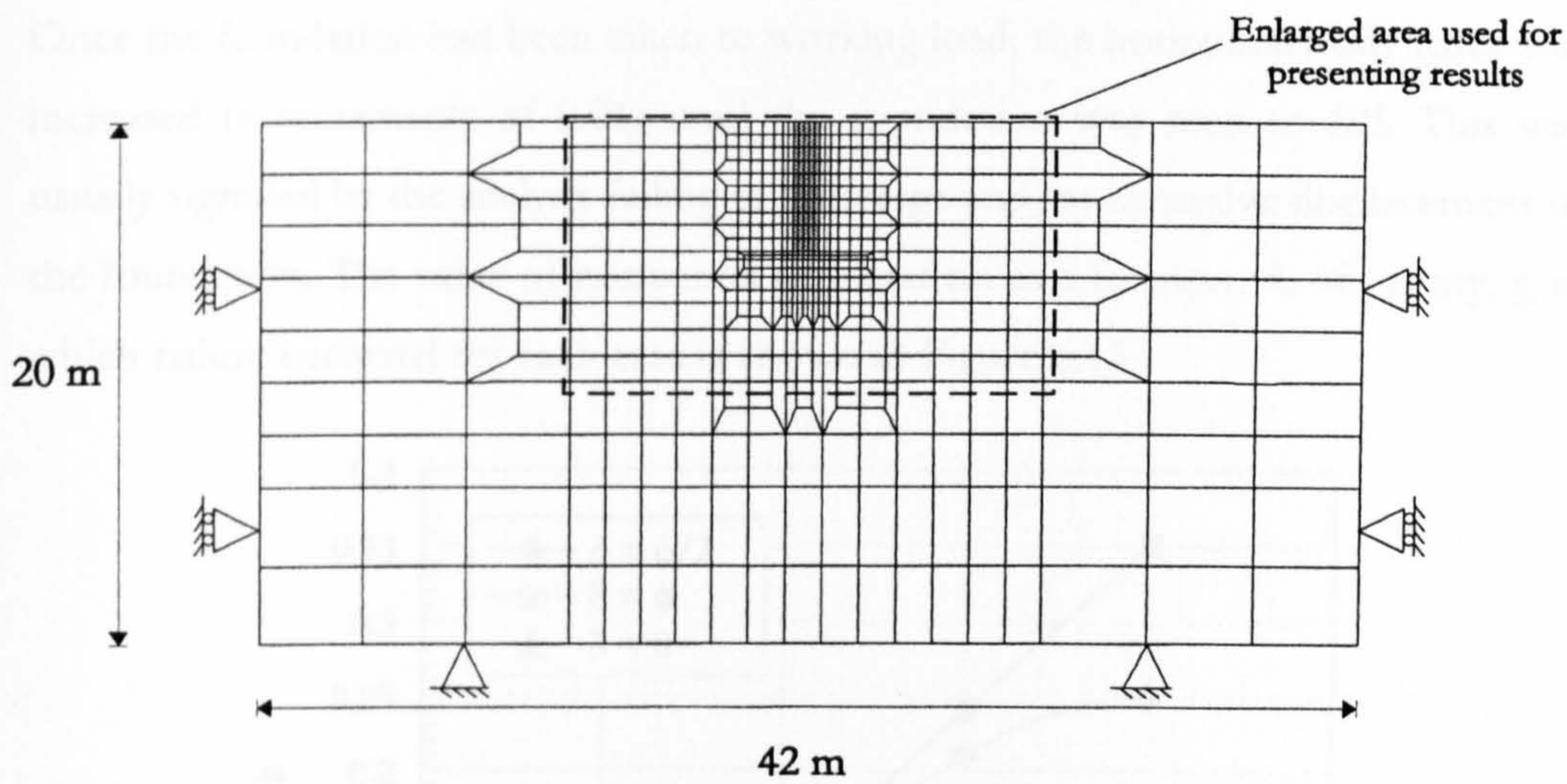

Figure 6.12: Finite element mesh used in pseudo static analyses

To investigate the effect that φ' (the angle of shearing resistance) and δ (the angle of soil-shaft interface friction) have on the behaviour of the foundation, the problem was analysed for 3 values of φ' (20°, 30° and 40°) and for each φ', two values of δ were chosen: $\delta=\varphi'$ and $\delta=\varphi'/2$. One analysis was run for $\delta=0$, however since this is an unrealistic case no further such analyses were performed. For each combination of φ' and δ, the foundation was taken to a constant working load of 1000 kN. The static capacity (found from displacement controlled analyses) and factors of safety at working load for each foundation are given in Table 6.1.

φ'°	δ°	Collapse Load (kN)	Factor of Safety at Working Load
20	20	1200	1.20
20	10	1100	1.10
30	30	3250	3.25
30	15	3000	3.00
30	0	2850	2.85
40	40	8250	8.25
40	20	7500	7.5

Table 6.1: Summary of bearing capacities and factors of safety for each combination of φ and δ

Once the foundation had been taken to working load, the horizontal body force was increased in increments of 0.01*g* until the foundation was seen to fail. This was usually signified by the analysis failing to converge and/or excessive displacement of the foundation. The value of horizontal acceleration as a fraction, *k*, of gravity, *g*, at which failure occurred for each case is shown in Figure 6.13.

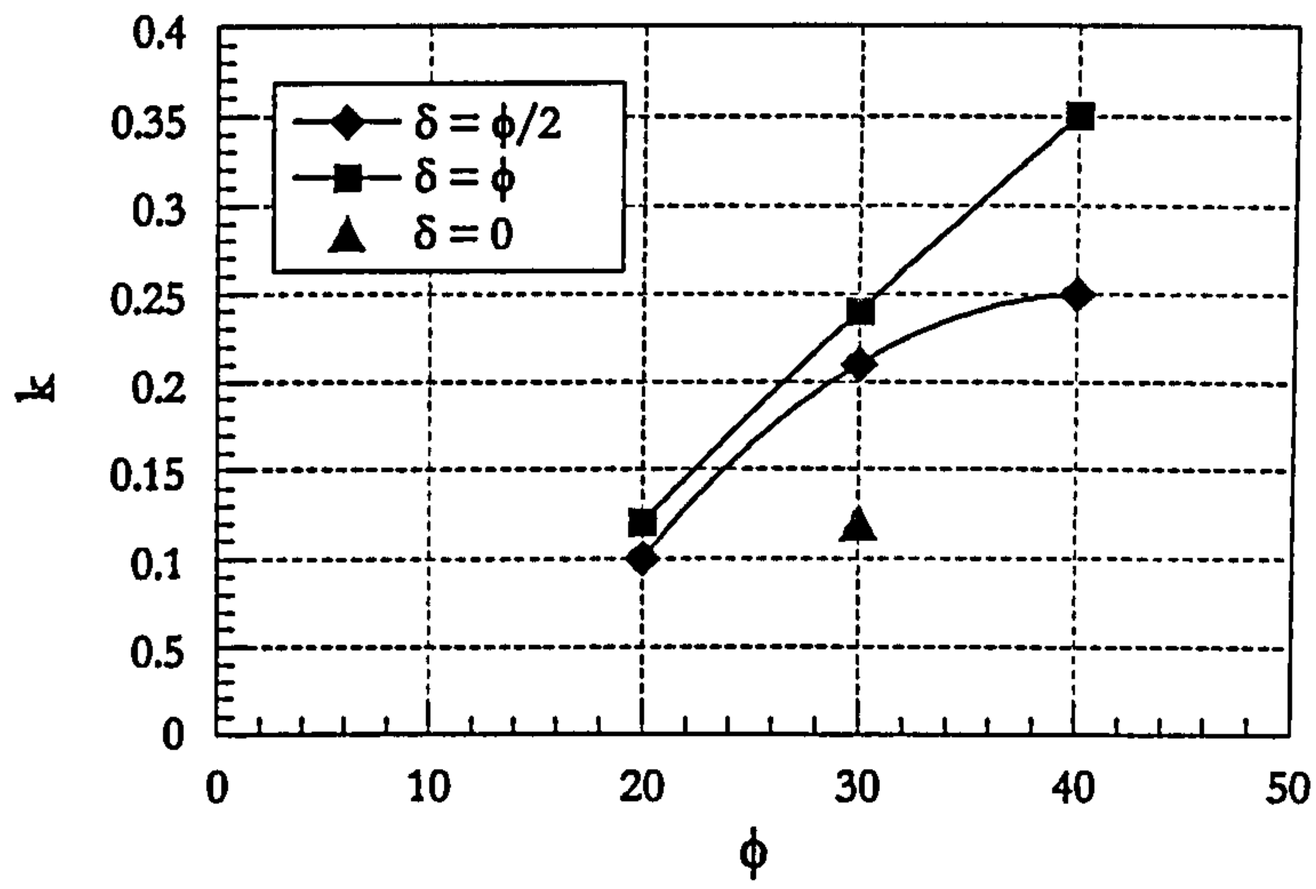

Figure 6.13: The effects of φ and δ on the limiting value of the seismic coefficient (*k*) (after Potts (2000))

For the purpose of this thesis the case with $\varphi = 30°$ and $\delta = 15°$ was reanalysed and will form the basis of the discussion that follows. However, any conclusions that are drawn from this analysis also apply to the other cases analysed by Potts (2000). Figure 6.14 shows the vectors of incremental displacement at the last stable increment of the analysis prior to failure and Figure 6.15 shows the degree of strength mobilisation at failure for this case. The results are presented for the area highlighted in Figure 6.12.

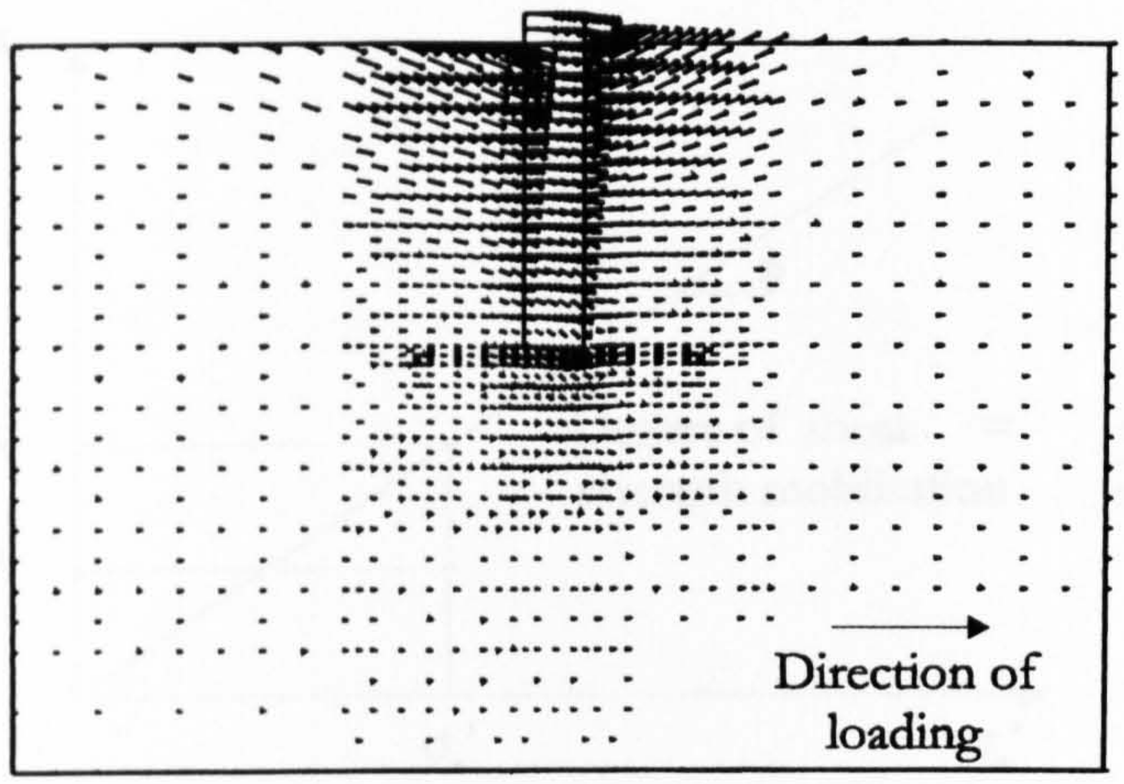

Figure 6.14: Vectors of incremental displacement at failure for φ =30° and δ = 15°

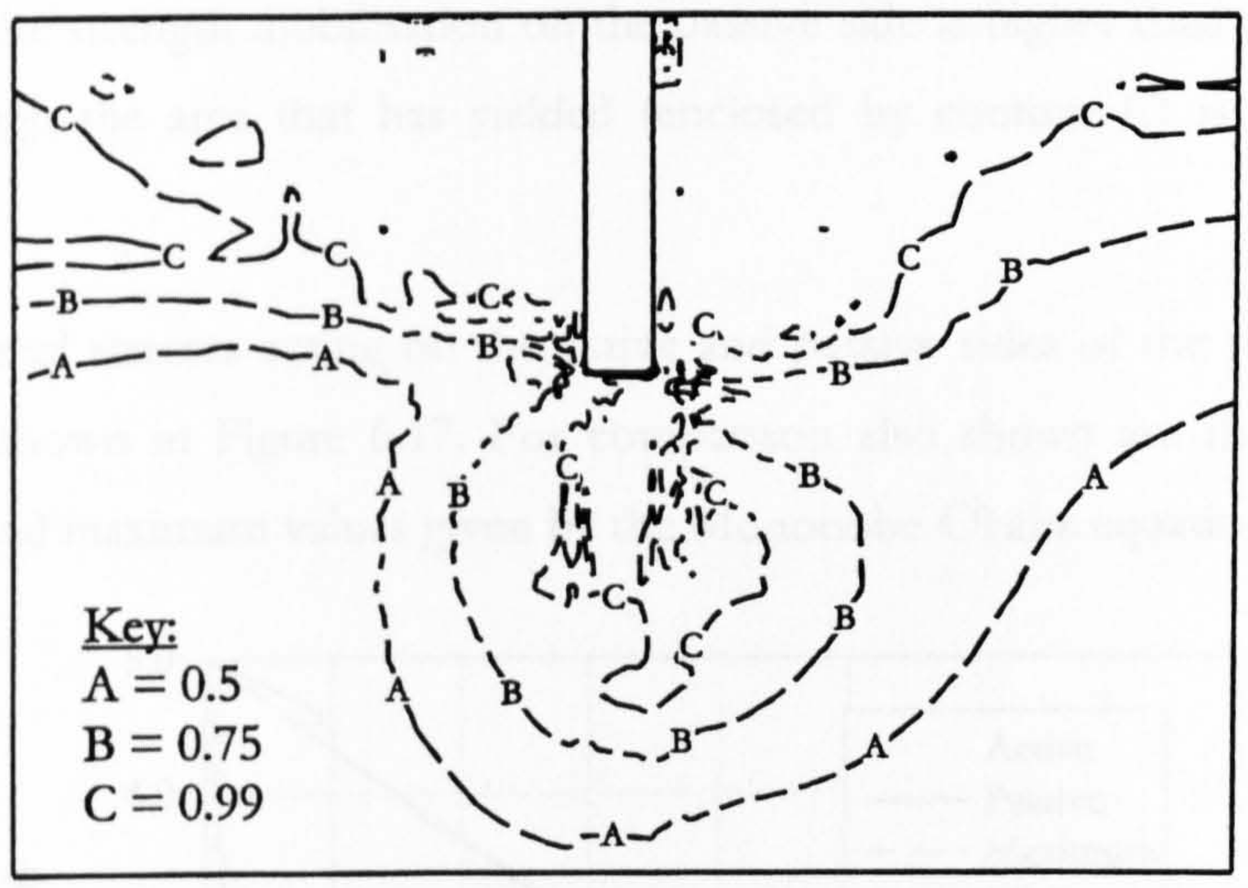

Figure 6.15: Degree of strength mobilisation at failure for pseudo static analysis

The movement of the foundation shown in Figure 6.14 for the pseudo static analysis is similar to that observed when a retaining wall rotates due to excessive passive pressure. It is clear that the movement of the foundation is concentrated near the surface and that no failure mechanism of the type assumed in the bearing capacity analysis is present.

The plot shown in Figure 6.15 shows contours of stress level as a ratio of the shear strength of the soil, making it possible to identify where failure has occurred (that is the area enclosed by a contour with a value of 0.99). The way this ratio is calculated is illustrated in Figure 6.16.

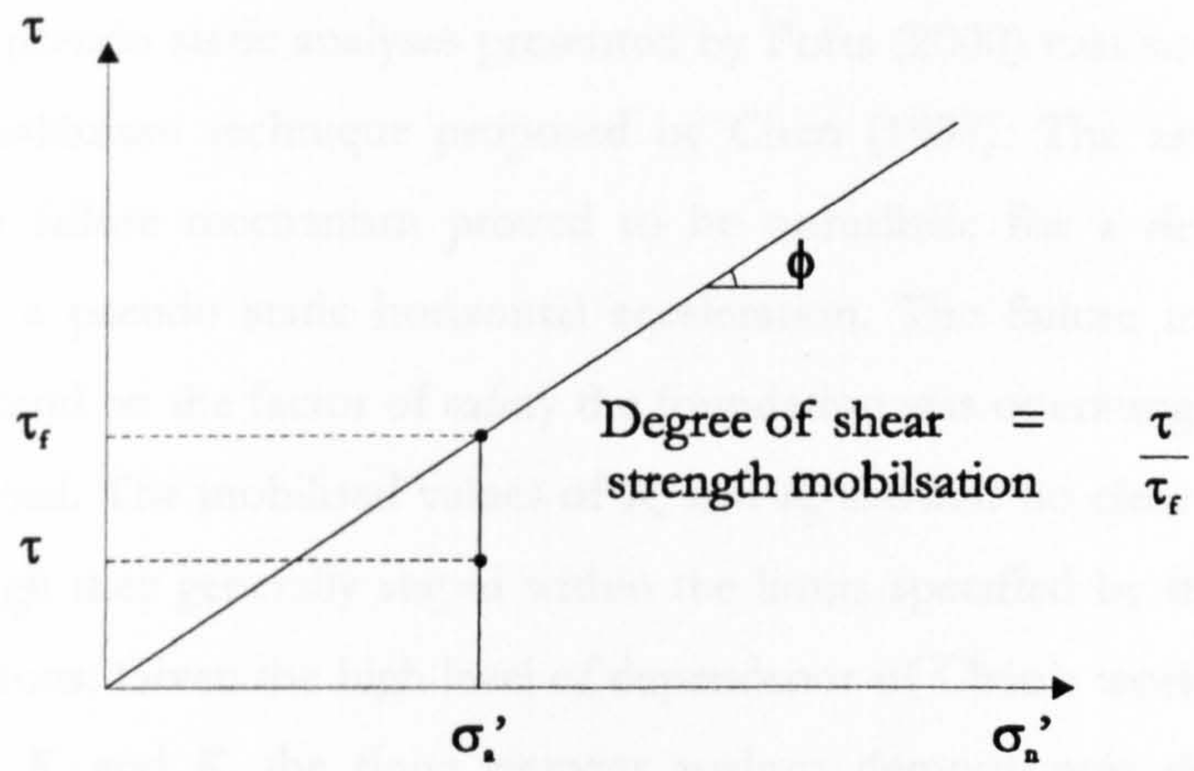

Figure 6.16: Calculation of degree of shear strength mobilisation (after Potts (2000))

Generally, the strength mobilisation on the passive side is higher than on the active side, although the area that has yielded (enclosed by contour C) is only slightly larger.

The horizontal stresses acting on the active and passive sides of the foundation at failure are shown in Figure 6.17. For comparison also shown are the theoretical minimum and maximum values given by the Mononobe-Okabe equations.

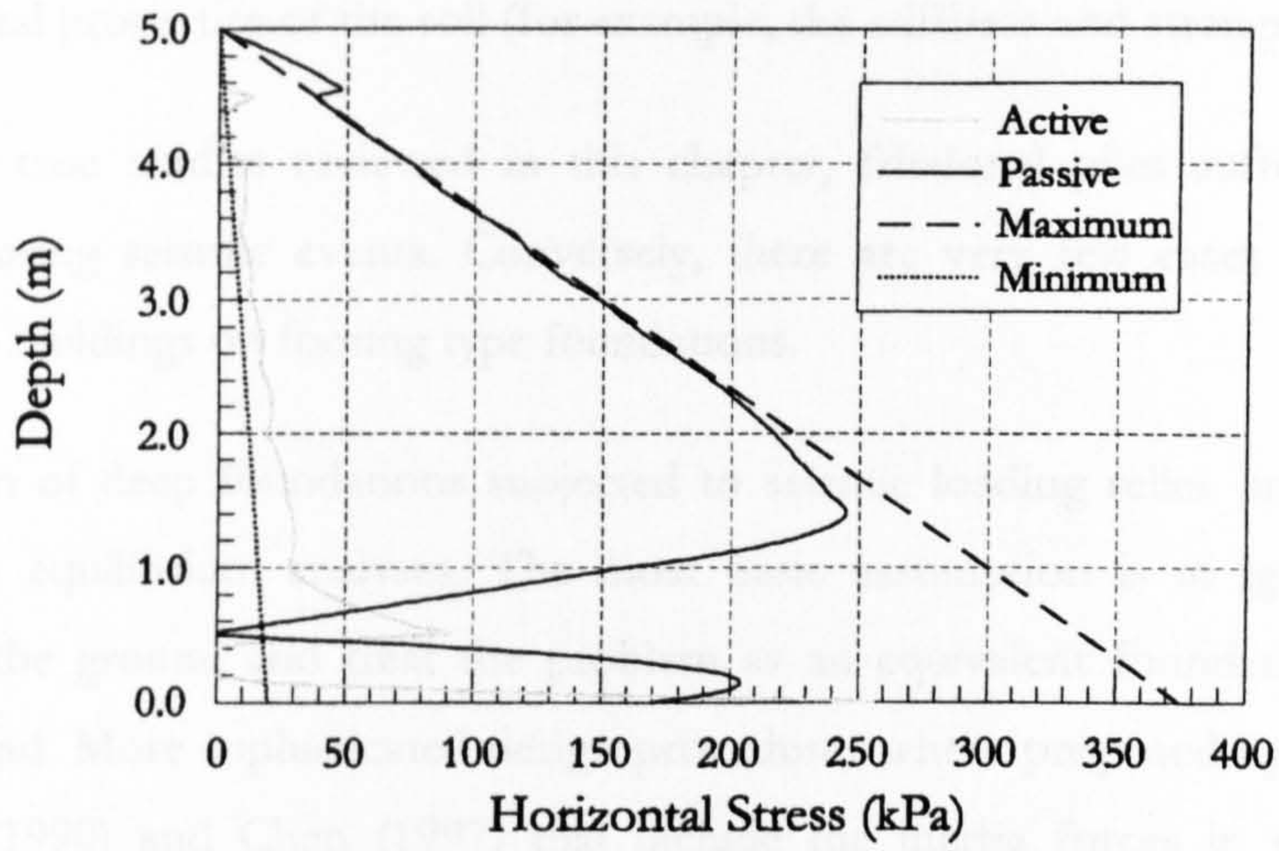

Figure 6.17: Active and passive pressures on foundation at failure (φ = 30°, δ = 15°)

The pressures closely follow the limits given by the Mononobe-Okabe equations and at no point exceed these limits. The same trend was also found in the remaining cases presented by Potts (2000). Generally, the passive pressure was mobilised in all cases, whilst the full active stress was not always reached.

Overall, the pseudo static analyses presented by Potts (2000) cast some doubt over the limit equilibrium technique proposed by Chen (1997). The assumption of a Prandtl type failure mechanism proved to be unrealistic for a deep foundation subjected to a pseudo static horizontal acceleration. The failure mechanism was found to depend on the factor of safety the foundation was operating at when taken to working load. The mobilised values of K_a and K_p showed no clear pattern for all cases, although they generally stayed within the limits specified by the Mononobe-Okabe equations. Given the high level of dependence of Chen's work on the values assumed for K_a and K_p the finite element analysis demonstrates that the results obtained using this method must be used with caution.

6.4 Summary

The behaviour of deep foundation under seismic loading is not yet fully understood. The problem involves interaction between the seismic waves travelling through the ground and the cyclic loading applied to the foundation from the structure above. The rate at which these forces are applied can change some of the fundamental properties of the soil (for example, the stiffness and strength of a soil).

From the case studies reviewed in this chapter, frictional piles suffer the most damage during seismic events. Conversely, there are very few cases of reported damage to buildings on footing type foundations.

The design of deep foundations subjected to seismic loading relies on the results from limit equilibrium analyses. The most basic assumption is to ignore inertia forces in the ground and treat the problem as an equivalent foundation with an inclined load. More sophisticated design procedures where proposed by Sarma and Iossifelis (1990) and Chen (1997) that include the inertia forces in the ground. However, pseudo static finite element analysis by Potts (2000) demonstrated that the failure mechanism assumed in these two studies may not be correct.

The pseudo static analysis approximates the earthquake induced inertia forces as a constant horizontal body force applied throughout the mesh. This loading condition then initiates a one sided failure mechanism. The number of one sided failure mechanisms observed in the field is very few and can usually be explained by

building eccentricities. The most common form of damage sustained by foundations during earthquakes is large amounts of settlement and in some cases, tilting.

6.5 Finite Element Analyses

6.5.1 Introduction

The design procedures presented in the previous section for deep foundations subjected to seismic loading are inconsistent with the behaviour observed in the field. The assumption of a one sided failure mechanism appears to be incorrect in the majority of cases and the limited number of recorded failures implies that the majority of foundations may generally be over designed. Dynamic finite element analyses will be used in this section to investigate the behaviour of deep foundations under seismic conditions. The results obtained will then be used to make an appraisal of the design methods presented in the previous section. To make the analysis as realistic as possible the acceleration records from actual earthquakes will be used and the elasto-plastic behaviour of the soil will be modelled.

6.5.2 Description of analysis

To allow comparison to be made with the work by Chen (1997) and Potts (2000), a foundation five meters deep and one meter wide will be analysed in plane strain, using the same finite element mesh and material properties as in the pseudo static analysis. As mentioned in Chapter 3, the choice of location for the romote boundaries of the mesh poses extra problems for dynamic analyses. In addition to making them far enough away so as not to affect the results in the areas of interest, any boundary will also cause the reflection of waves back into the finite element mesh. Placing the bottom boundary 20 meters from the ground surface implies the presence of a very stiff stratum at this depth. Due to ICFEP not having any type of absorbing boundary conditions this was the assumption made for this study. If the mesh is not wide enough the stress bulb created by the loading of the foundation will begin to be affected. For this study a 42 meter wide mesh was used and its

influence on the results investigated by performing an analysis with a wider mesh. Vertical displacements were restricted on the bottom and side boundaries and the earthquake record was applied to all nodes on the bottom and side boundaries of the finite element mesh. This is illustrated in Figure 6.18.

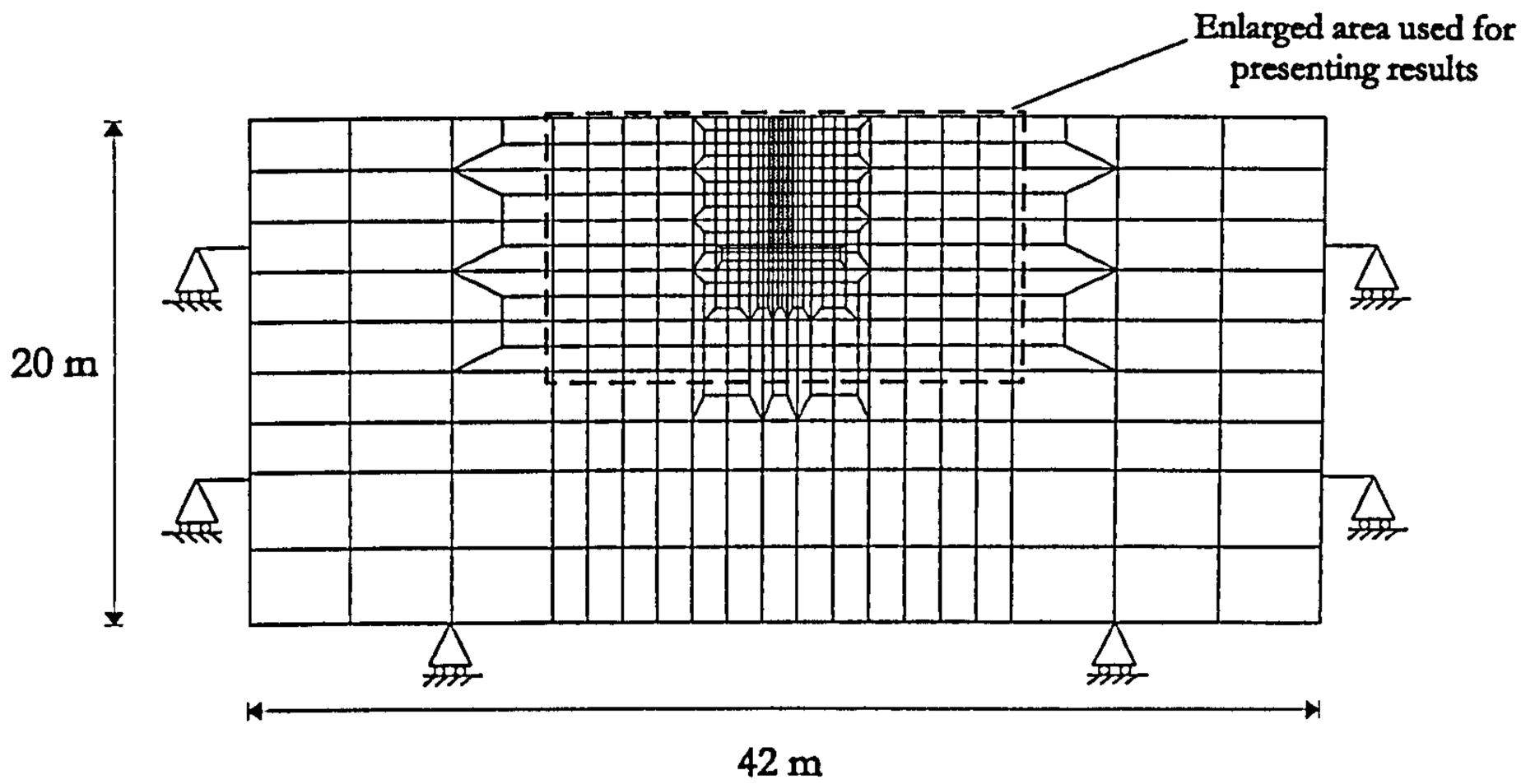

Figure 6.18: Figure showing mesh and boundary conditions assumed in dynamic analyses

Applying the acceleration to all nodes on the side and bottom boundaries of the mesh is equivalent to the foundation and the surrounding material being contained in a rigid box. Crewe *et al.* (1995) suggested that this assumption may affect the overall response of the system by altering the shear stresses present at the boundary. This was not felt to be an issue for this study as the remote lateral boundaries were sufficiently far away so as not to affect the behaviour around the foundation. The effect of the location of the lateral boundaries was investigated and is presented later in the chapter. The material properties of the soil are the same as those used in the pseudo static finite element analysis and are repeated below for completeness:

E = Young's modulus = 60000 kPa

ν = Poisson's ratio = 0.25

K_0 = earth pressure coefficient at rest = 1.0

γ = unit weight of soil = 19 kN/m^3

c' = cohesion = 0 kPa

ψ = angle of dilation = 0

The foundation is modelled as linear elastic with the following material properties:

E = Young's modulus = 30×10^6 kPa

ν = Poisson's ratio = 0.2

γ = unit weight = 24 kN/m^3

To allow relative movement between the foundation and the surrounding soil, interface elements were placed around this boundary. The material properties assigned to these elements can have a large effect on the overall behaviour of the analysis (see Potts and Zdravkovic (2001)). To determine the appropriate material properties for the interface elements, a parametric study was undertaken. An angle of shearing resistance of 30° was given to both the interface elements and the surrounding soil for a range of interface element stiffness. The resultant load displacement curves were then compared with that obtained from an analysis with no interface elements. The results showed that for this arrangement the load-displacement curves were not sensitive to the values given to the normal (K_n) and shear (K_s) stiffness' attributed to the interface elements provided their order of magnitude was above 1×10^3. For the remaining analyses the following values were used.

$$K_s = K_n = 1\times10^5 \text{ kN/m}^3$$

The standard analysis used in the following discussion assumes the soil has an angle of shearing resistance of 30° and an angle of interface friction between the foundation and soil of 15° with a Mohr-Coulomb failure criterion. Although not realistic, to allow direct comparison with the work of Chen (1997) and Potts (2000) the presence of a pore fluid is not modelled.

6.6 Calculation of Foundation Capacity

To allow appraisal to be made of the currently available design methods, the most popular will now be used to calculate the static and seismic capacity of the standard foundation chosen for the finite element analysis.

6.6.1 *Static Capacity*

The solutions of Meyerhof, Hansen and Vesić presented earlier are now used to determine the ultimate bearing capacity of the deep foundation described in Section 6.5.2. The geometry and material properties of this foundation are illustrated in Figure 6.19.

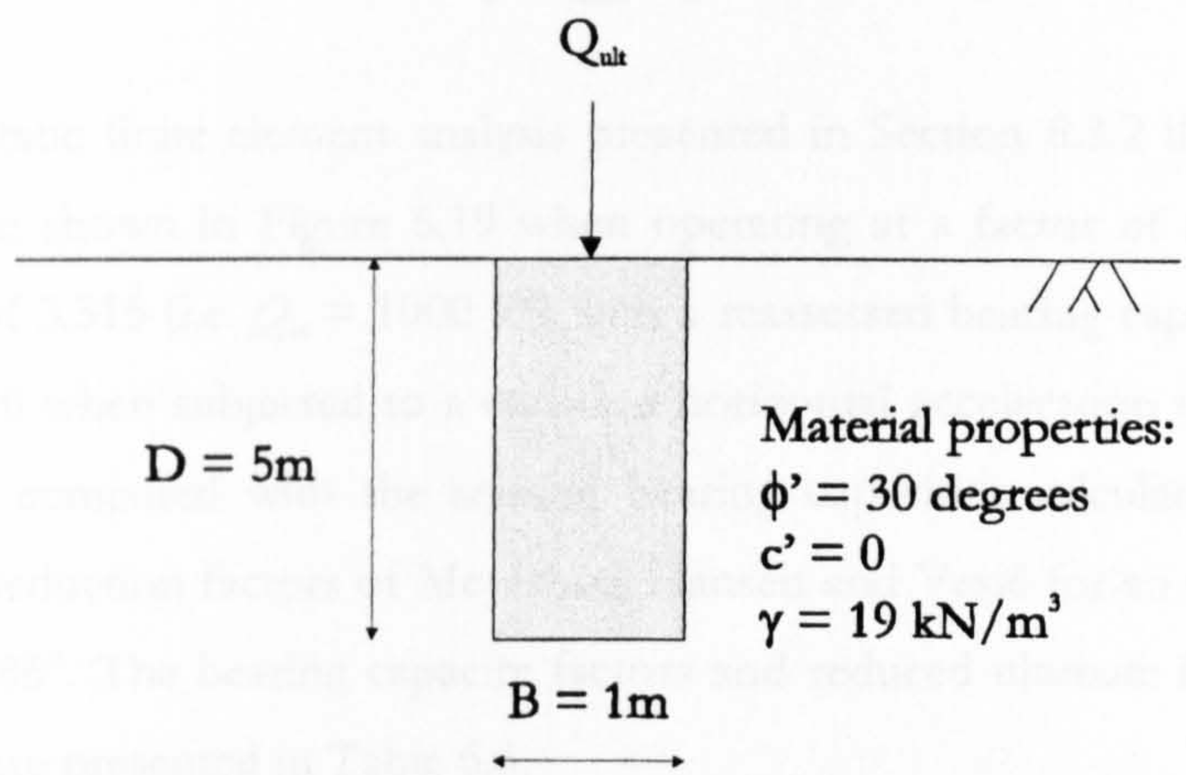

Figure 6.19: Arrangement of standard deep foundation

The bearing capacity factors calculated for each method and the resultant limit load are summarised in Table 6.2. Due to there being no cohesion in the soil, no N_c bearing capacity factors have been calculated.

Method	N_q	N_γ	d_q	d_γ	Q_{ult}
Meyerhof	18.401	15.668	1.866	1.866	3540 kN
Hansen	18.401	15.070	1.793	1.0	3277 kN
Vesić	18.401	22.402	1.793	1.0	3347 kN

Table 6.2: Bearing capacity of standard foundation by different methods

Potts (2000) found the capacity of the same foundation using a displacement controlled finite element analysis to be 3000 kN. However, when the problem was re-analysed for this thesis with smaller displacement increments and a tighter convergence criteria, the capacity was reassessed to be 3315 kN. Details of this analysis will be given later in this chapter. The capacities found by the Hansen and Vesić method agree remarkably well with the finite element analysis, whilst the bearing capacity obtained using Meyerhof's method is higher.

6.6.2 *Seismic Capacity*

The simplest way to account for seismically induced forces is to reduce the problem to that of a foundation subjected to an inclined load. The equivalent load is inclined from the vertical by an angle (θ) given by Equation 6.18.

$$\theta = \tan^{-1} k \tag{6.18}$$

The pseudo static finite element analysis presented in Section 6.3.2 illustrated that the foundation shown in Figure 6.19 when operating at a factor of safety against static failure of 3.315 (i.e. Q_w = 1000 kN with a reassessed bearing capacity of 3315 kN), would fail when subjected to a constant horizontal acceleration of 0.21g. This result can be compared with the seismic bearing capacities calculated using the inclined load reduction factors of Meyerhof, Hansen and Vesić for an angle of (θ = $\tan^{-1}$ 0.21) 11.86°. The bearing capacity factors and reduced ultimate limit load for each method are presented in Table 6.3.

Method	N_q	N_γ	i_q	i_γ	d_q	d_γ	Q_{ult}
Meyerhof	18.401	15.668	0.754	0.366	1.866	1.866	2561 kN
Hansen	18.401	15.070	0.574	0.452	1.793	1.0	1865 kN
Vesić	18.401	22.402	0.624	0.493	1.793	1.0	2061 kN

Table 6.3: Seismic bearing capacity of standard foundation by different methods

The reduced bearing capacities, calculated assuming the earthquake loading condition can be replaced by an equivalent inclined load, are much higher than the working load used in the pseudo static finite element analysis (1000 kN), for which the foundation failed at a horizontal acceleration of 0.21g.

Replacing the seismically induced inertial forces in a foundation by an inclined loading does not include the effect of inertia forces in the ground on the bearing capacity. As discussed previously, the work by Chen (1997) extended that of Sarma and Iossifelis (1990) to include this additional force. Chen only presented his results for a limited range of K_a and K_p values, and as these are not known quantities for the limit equilibrium analysis, the values that most closely resemble those found from the pseudo static analysis will be assumed. The finite element results showed that the values of K_a and K_p at failure were close to the minimum and maximum values

given by the Mononobe-Okabe equations. For the soil parameters in this case, the minimum and maximum values of K_a and K_p are 0.206 and 3.945 respectively. Chen presented no result for values of this order and therefore the closest will have to be assumed (K_a = 1.0 and K_p = 1.5). The bearing capacity is given by Equation 6.19.

$$q_{ult} = 0.5\gamma B i_{\gamma e} N_\gamma \tag{6.19}$$

where $i_{\gamma e}$ is the seismic reduction factor and the value of N_γ includes the effect of surcharge and skin friction on the bearing capacity. Chen's results give the value of N_γ as 342.67 and $i_{\gamma e}$ as 0.6344, resulting in a seismic bearing capacity of 2065 kN.

The results from Chen's work are very similar to those obtained from the inclined load analysis. One would intuitively think that including the inertia forces in the ground would result in a lower bearing capacity than that obtained by analysing the inclined loading case. These results suggest the opposite, although Chen's results include the contribution to the overall capacity from the shaft which is not considered in the other cases. The calculation of this contribution is very difficult as it relies on the assumed values of K_a and K_p which are not known at failure.

The large difference between the seismic bearing capacities calculated using an equivalent inclined load and those obtained from pseudo static finite element analysis, implies that the seismically induced inertia forces in the ground significantly reduce the bearing capacity of a foundation. However, the method proposed by Chen (1997) which includes these effects in a limit equilibrium approach predicts a virtually identical seismic bearing capacity to that obtained from the inclined load analysis. This may be due to the unrealistic values assumed for K_a and K_p in the analyses. As noted by Potts (2000), although the software was developed at Imperial College, it has not been possible to locate the program and re-analyse the problem with realistic values for K_a and K_p.

There is clearly a discrepancy between the pseudo static finite element analysis and the results of the limit equilibrium approach. However, both techniques assume that seismically induced forces can be represented by a constant horizontal body force equal to the mass multiplied by the maximum horizontal acceleration in the earthquake record. This is unrealistic as the maximum acceleration only occurs once during the earthquake and has much lower values for the rest of the record. The

only way to account for the time dependant behaviour is to model the problem with dynamic finite element analysis and to use a real earthquake record as the input.

6.6.3 Finite Element Analysis of the Static Bearing Capacity

As mentioned previously, Potts (2000) carried out a displacement controlled analysis of the foundation shown in Figure 6.19 to determine its ultimate bearing capacity. The problem was re-analysed for this thesis to gain a better understanding of the foundations behaviour under static loading. The displacement controlled analysis was conducted by applying an incremental displacement of 0.01 meters at the top of the foundation and then summing the reaction forces at the nodes with this prescribed displacement. Horizontal displacements were allowed for nodes directly under the foundation, and therefore the foundation was assumed to be smooth and rigid. The test was continued until the reaction forces had plateaued and the foundation had failed. The division of the applied load between the shaft and the base was determined by summing the nodal forces along these boundaries and then subtracting the nodal forces due to the initial stress conditions. The total capacity and individual components for the standard foundation are shown in Figure 6.20.

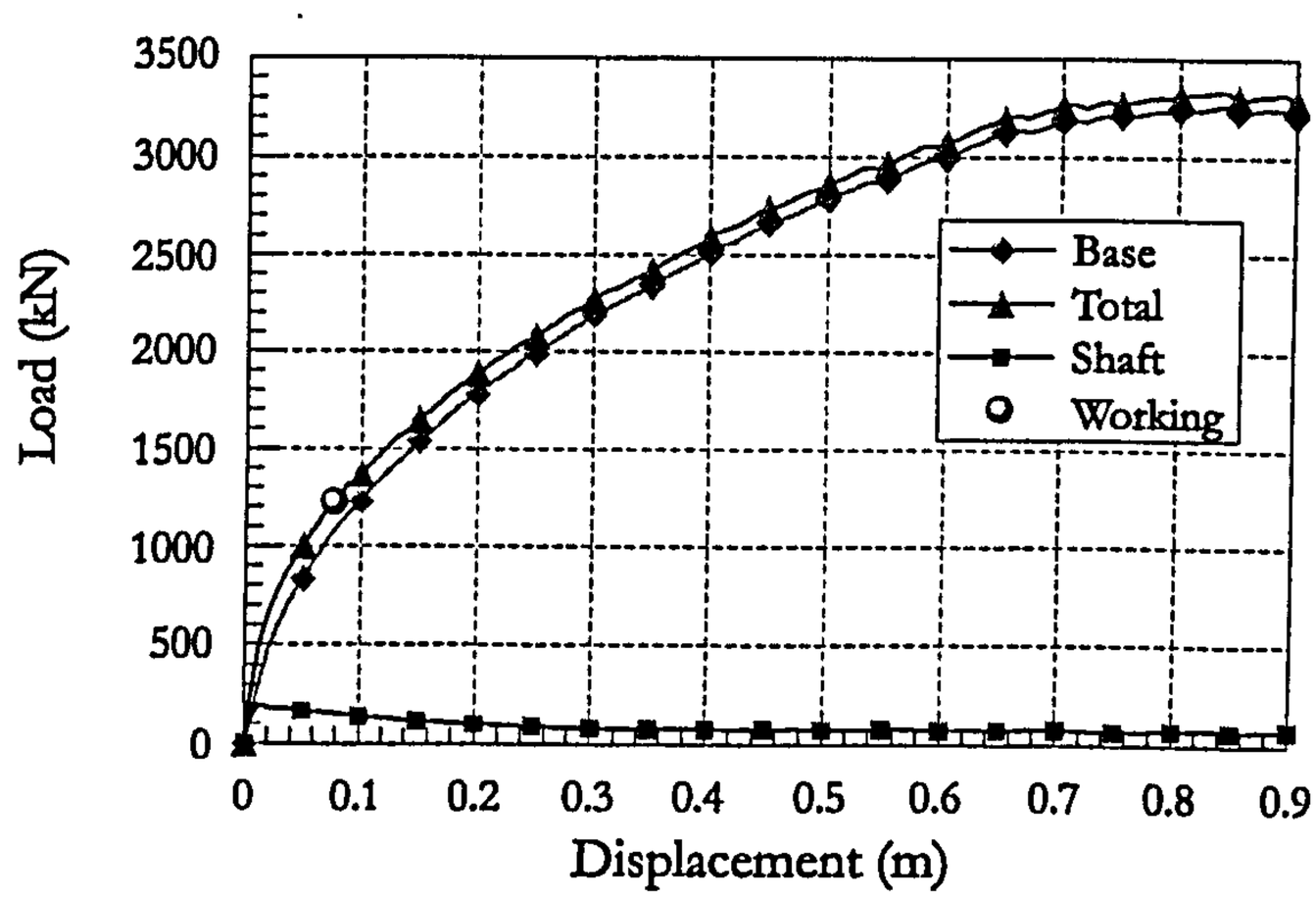

Figure 6.20: Load-displacement curve for standard foundation

The ultimate bearing capacity is 3315 kN which agrees well with the bearing capacity found by the limit equilibrium techniques presented in Section 6.6.1 and is slightly higher than that found by Potts (2000). This difference is probably due to

the smaller displacement increments and tighter convergence criteria used in the analysis presented here.

6.6.4 *Working Load*

A factor of safety of 2.7 against static bearing capacity failure has been chosen for the foundation. This gives a working load of 1228 kN which is similar to that used by Potts (2000) for the equivalent pseudo static analysis. The working load was applied to the foundation statically over 100 relatively small load increments to ensure that no residual errors were carried over to the dynamic part of the analysis. The displacement of the foundation at working load is illustrated on Figure 6.20. The point lies on the load displacement curve and confirms that the load controlled and displacement controlled analyses are equivalent. The degree of strength mobilisation for the area around the foundation highlighted in Figure 6.18 at working load is illustrated in Figure 6.21.

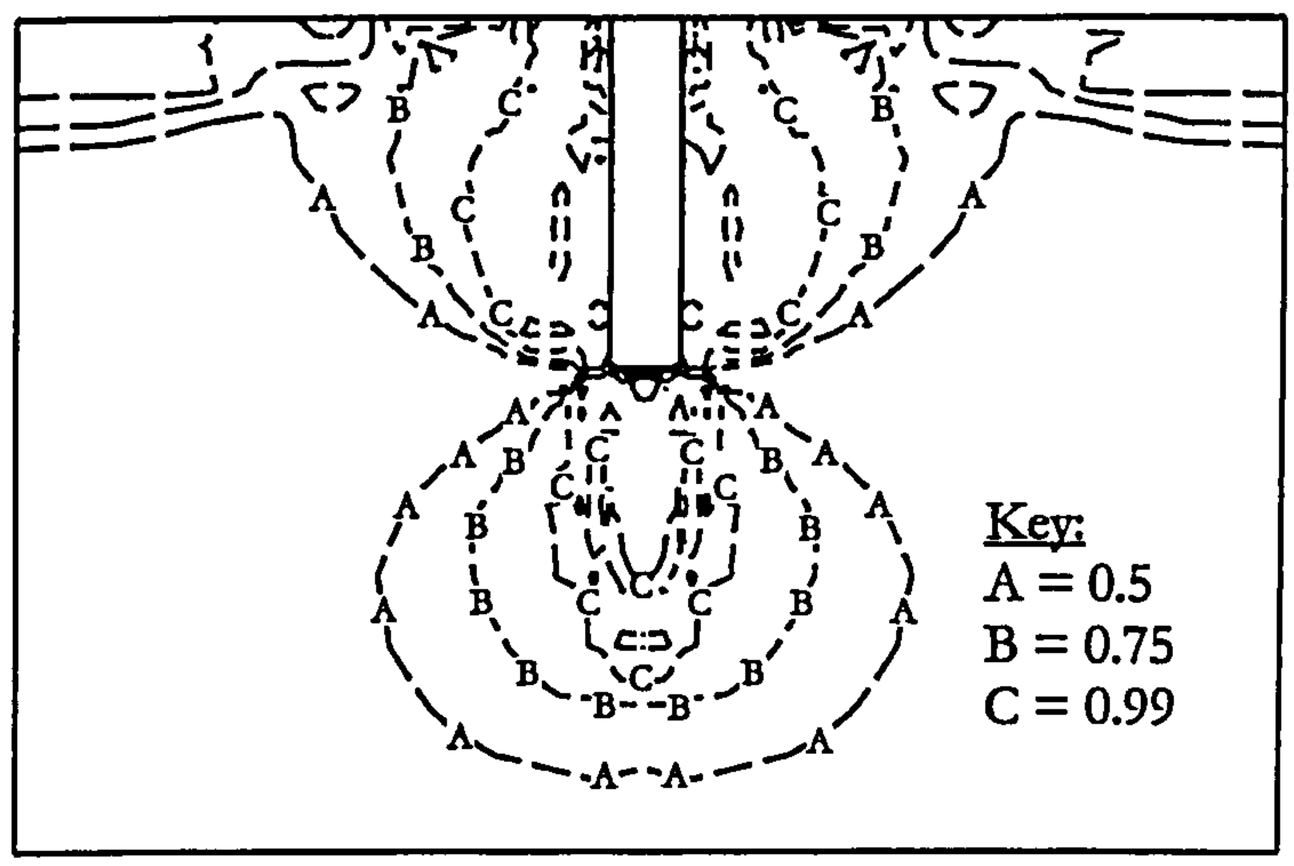

Figure 6.21: Degree of strength mobilisation around foundation at working load

There is a small bulb of soil under the foundation in which the strength has been fully mobilised. In the area around the shaft of the foundation all the adjacent soil has yielded. This is due to the shaft resistance being fully mobilised at working load which is also illustrated in Figure 6.20 where the shaft component has plateaued and begins to decrease slightly. This reduction is due to a small decrease in horizontal stress around the foundation which in turn reduces the available shaft resistance.

6.7 Description Input Earthquake (Athens 7/9/1999)

The record chosen for the dynamic finite element analysis of the standard foundation was the Athens earthquake of 1999. The earthquake was of magnitude 5.6 M_s and struck at 11.56 on the 7th of September 1999, with its epicentre located 20 km North-West of Athens. The East-West record from station Athens3, which is located in the basement of a building founded on rock, with a shear wave velocity of 1530 m/s in the Kallithea district of Athens (Ambraseys *et al.* (2000)) was chosen from the many available. The original acceleration record and Fourier spectrum are shown in Figure 6.22 and Figure 6.23 respectively.

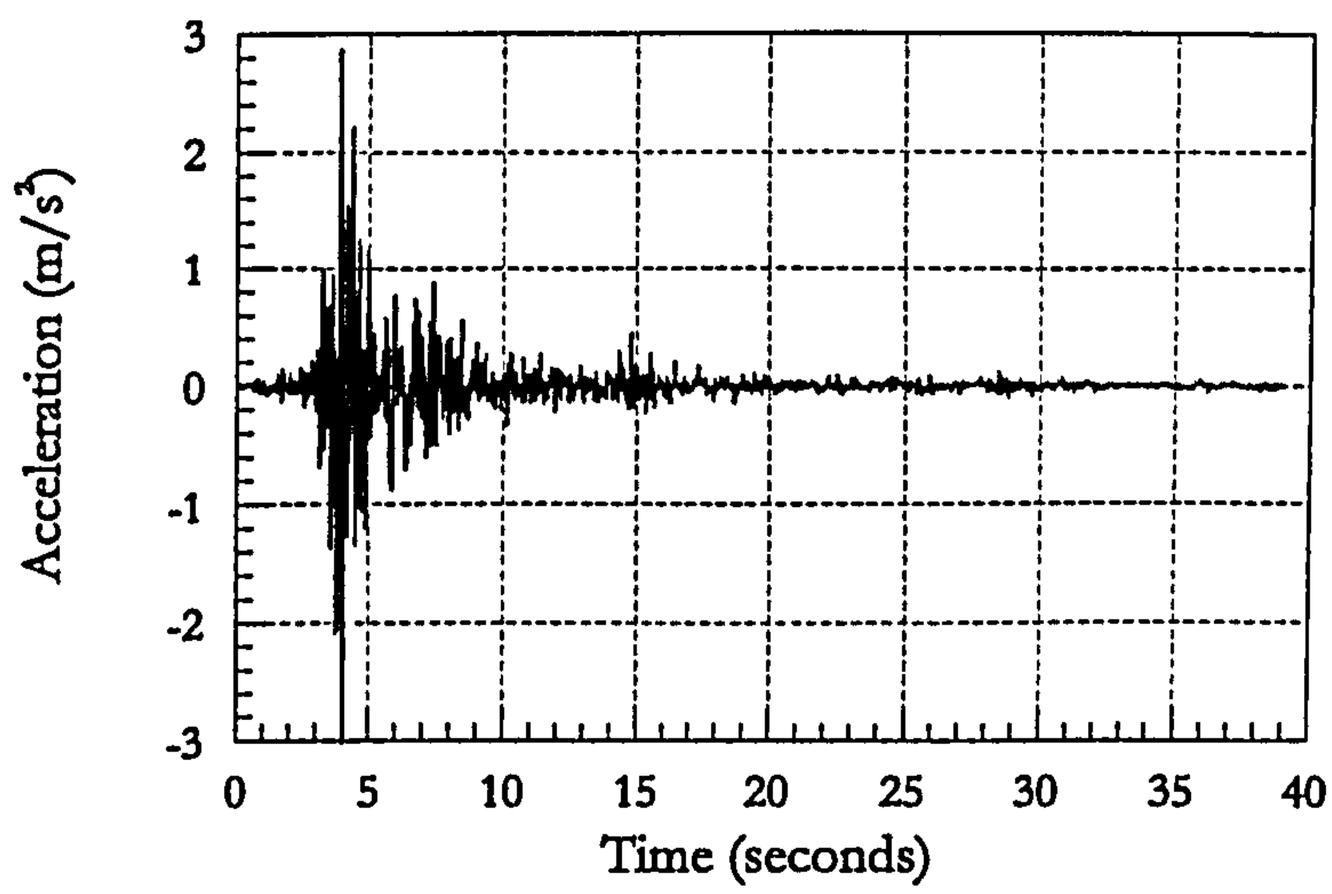

Figure 6.22: Original East-West component of Athens earthquake (7/9/1999)

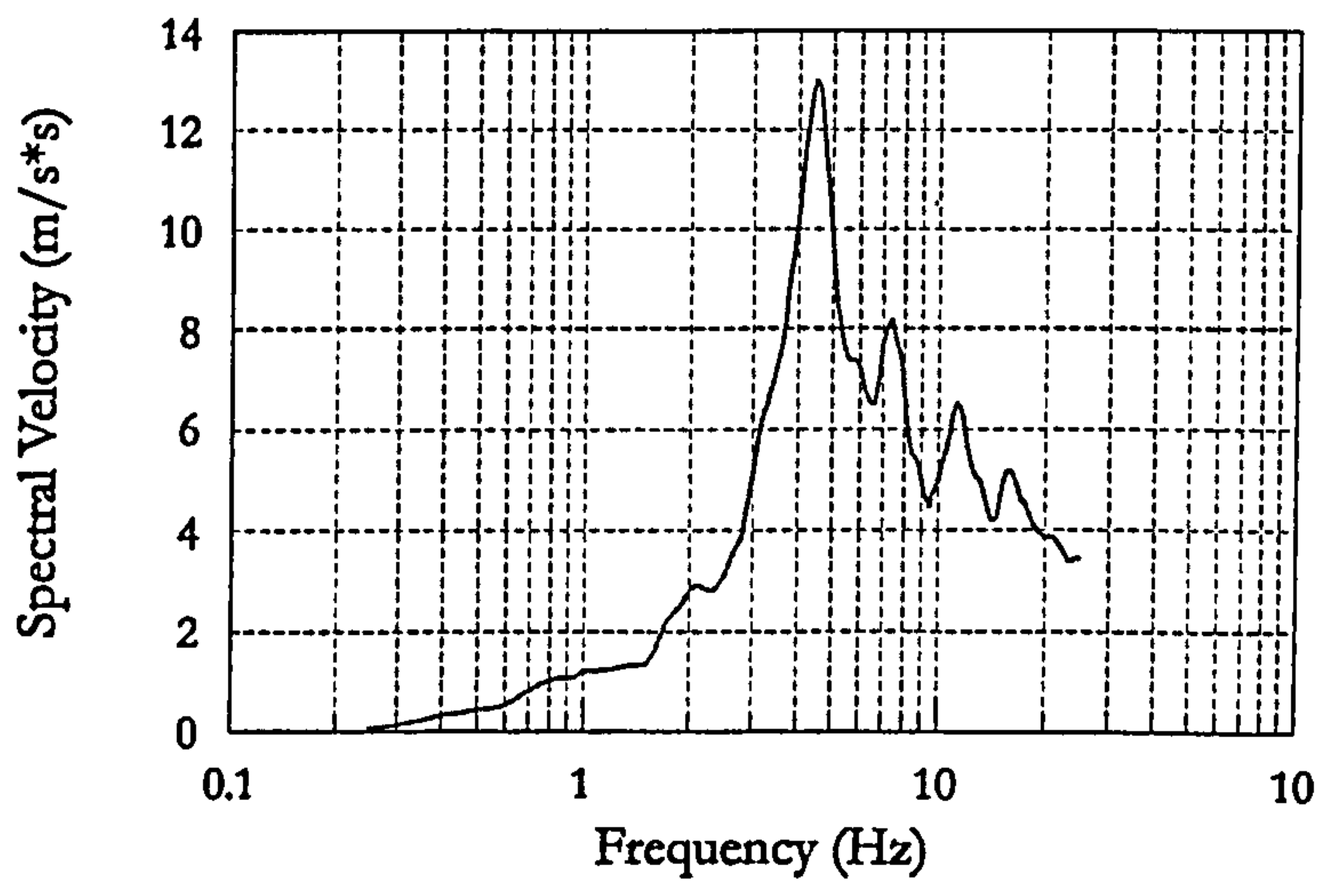

Figure 6.23: Fourier spectra of original East-West component of Athens earthquake (7/9/1999)

The original record has a dominant frequency component at 4.5 Hz, a maximum acceleration amplitude of 3.01 m/s^2 and a time step of 1/100th of a second. It is important at this point to compare the predominant frequency component of the earthquake record with the natural frequency of the finite element mesh. Assuming the presence of the foundation will not alter the overall dynamic behaviour of the finite element mesh, the fundamental natural frequency (T_1) of a soil column is given by Equation 6.20 (Kramer (1996)).

$$T_1 = \frac{4H}{V} \tag{6.20}$$

where H is the height of the soil column and V is the shear wave velocity of the soil. The height of the soil column in this case is 20m and the shear wave velocity is 111.3 m/s giving a fundamental period of 0.7187 seconds and a fundamental frequency of 1.391 Hz.

The pseudo static finite element analysis by Potts (2000) predicted a limiting horizontal acceleration of 0.21g (2.06 m/s^2) for the standard foundation chosen for this study. To compare the dynamic analysis with the pseudo static finite element analysis, the Athens record will be scaled to a maximum acceleration of 0.2g.

The earthquake record shown in Figure 6.22 is in its raw form and therefore has not been filtered. The recording, digitisation and processing of the acceleration record introduces noise into the signal, particularly in the low and high frequency ranges (Shyam Sunder and Connor (1982)). The noise measured in the intermediate range is relatively less noticeable (Menu (1986)). The problem associated with using non-filtered input data is illustrated in Figure 6.24. The graph shows the unfiltered acceleration record integrated twice using the Newmark time scheme ($\delta = 0.6025$ and $\alpha = 0.3025$) to give the equivalent displacement time history.

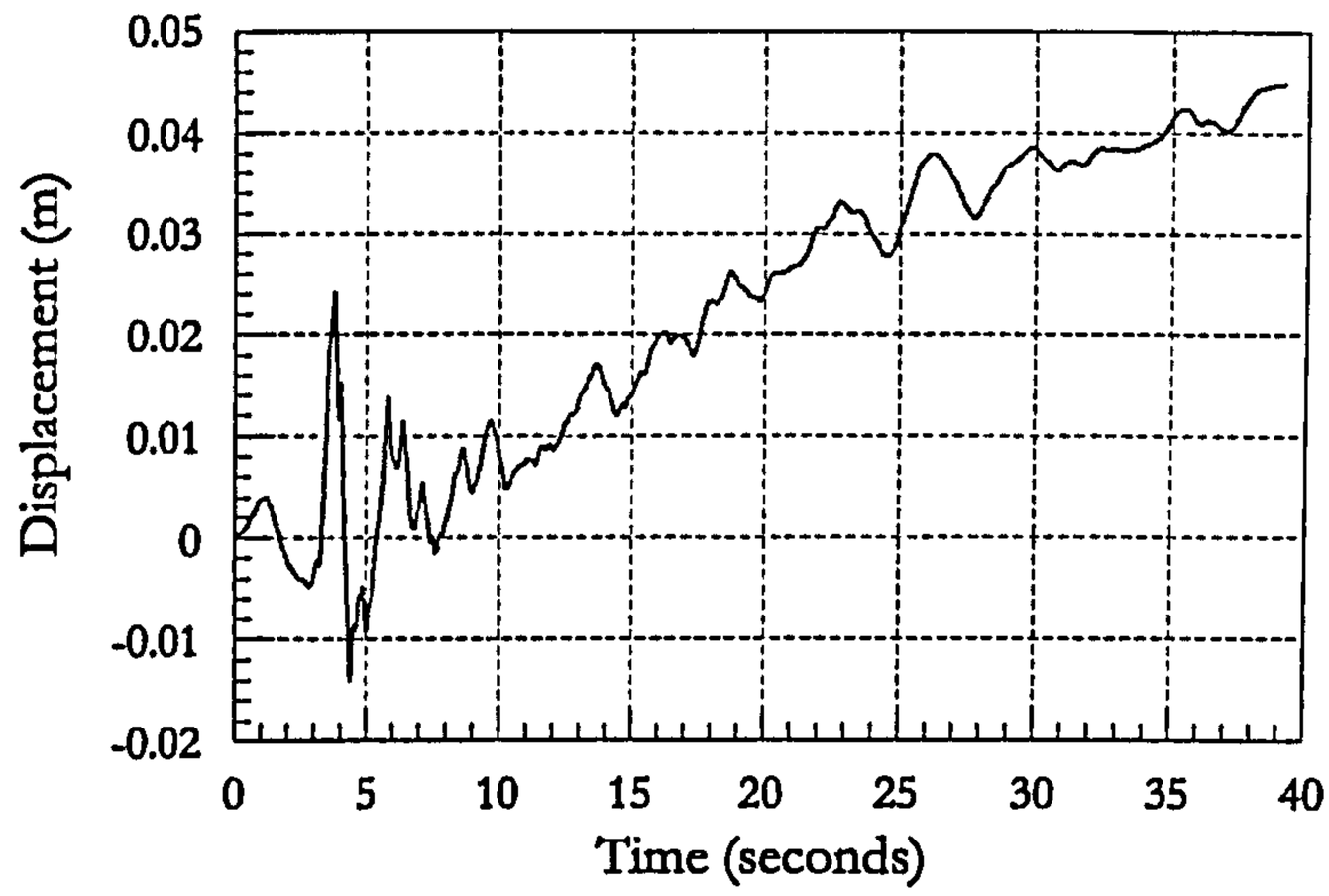

Figure 6.24: Equivalent displacement history from original East-West component of Athens earthquake (7/9/1999)

The noise in the low frequency range causes the displacement time history, which is dominated by the low frequency components, to drift away from the zero displacement axis. This is unrealistic as it is known the accelerometer does not experience any permanent displacement after the earthquake event.

To overcome this problem a filter is used to remove the extreme low and high frequency components without affecting the important intermediate range. The most accurate form of filter is an elliptic band-pass filter of the type developed at Imperial College by Menu (1986). The filter works by completely removing frequency components above and below maximum and minimum frequency limits specified by the user. For a particular range below the minimum and above the maximum frequencies the components are removed according to a linear variation. This is illustrated in Figure 6.25.

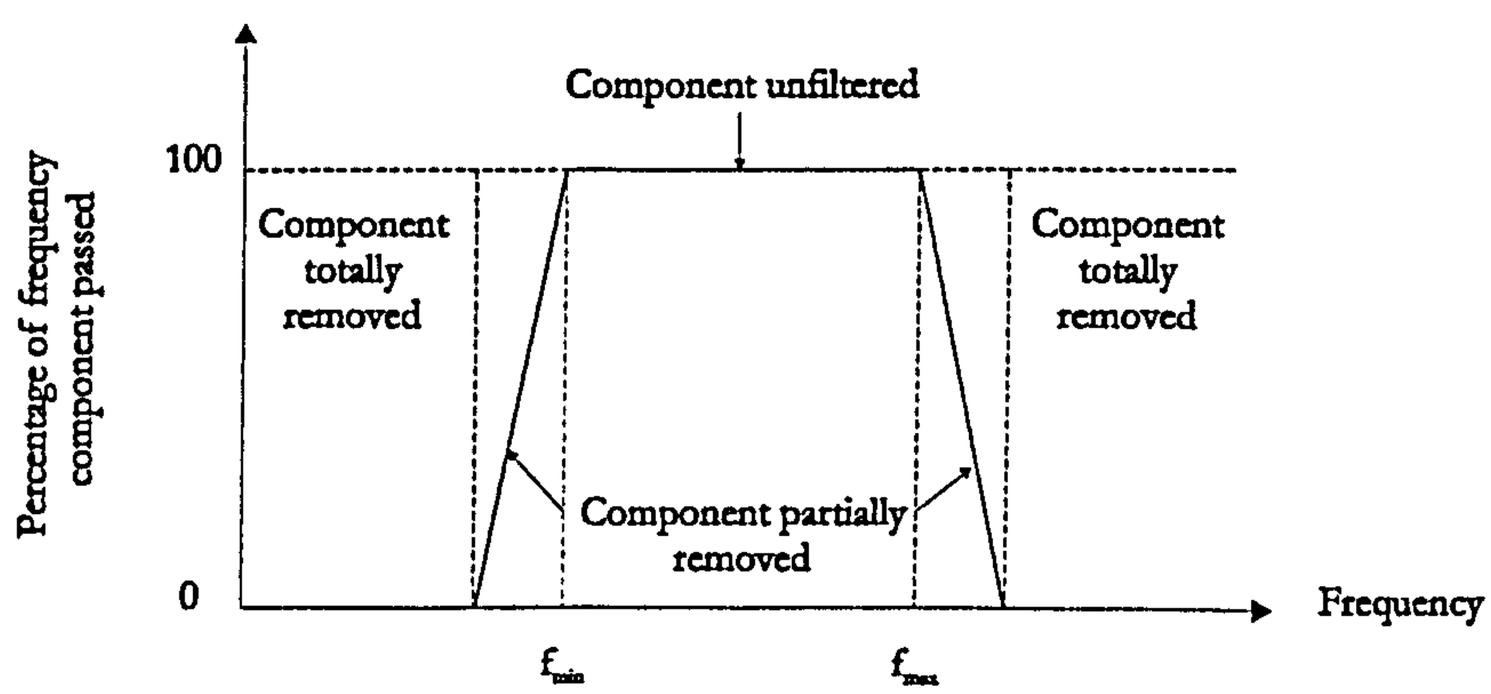

Figure 6.25: Frequency components passed by filter

An initial guess is made from the users previous experience regarding what lower frequency limit should be imposed. The earthquake record is passed through the filter and the resultant acceleration is integrated twice to give the equivalent displacement time record. If this record drifts away from the zero displacement axis, the lower limit is increased and the process repeated. If, however, the displacement remains on the zero displacement axis, the lower limit can be reduced until the point is reached where the lowest possible frequency limit is used whilst ensuring the displacement record remains on the zero displacement axis. The lower frequency limit for the Athens record which had been scaled to a maximum acceleration of 0.2*g*, was found to be 0.25 Hz. A standard maximum frequency of 25 Hz is used for all earthquake records. The resultant acceleration record and equivalent displacement time history are shown in Figure 6.26 and Figure 6.27 respectively.

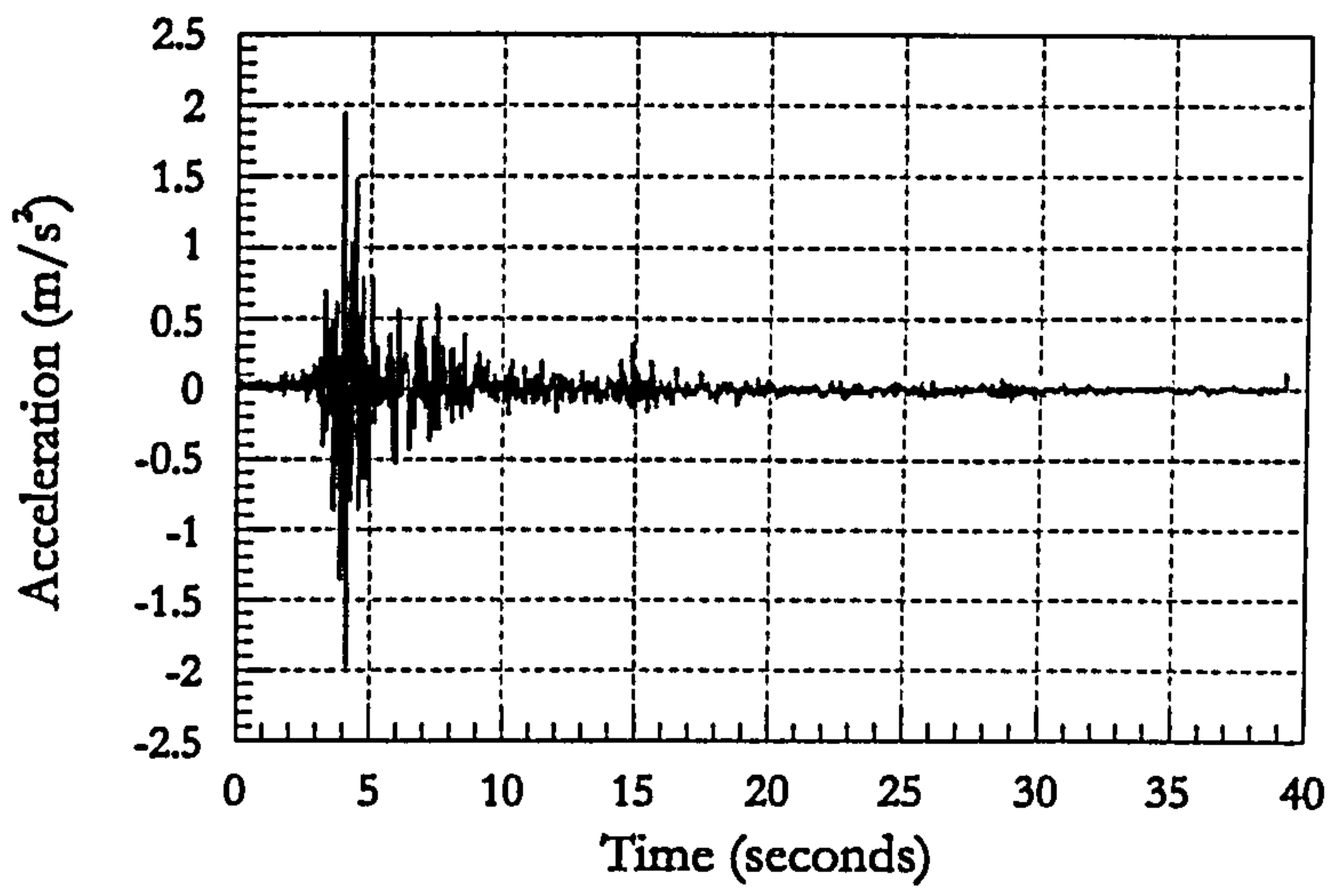

Figure 6.26: Athens earthquake record scaled to 0.2*g* maximum acceleration and filtered

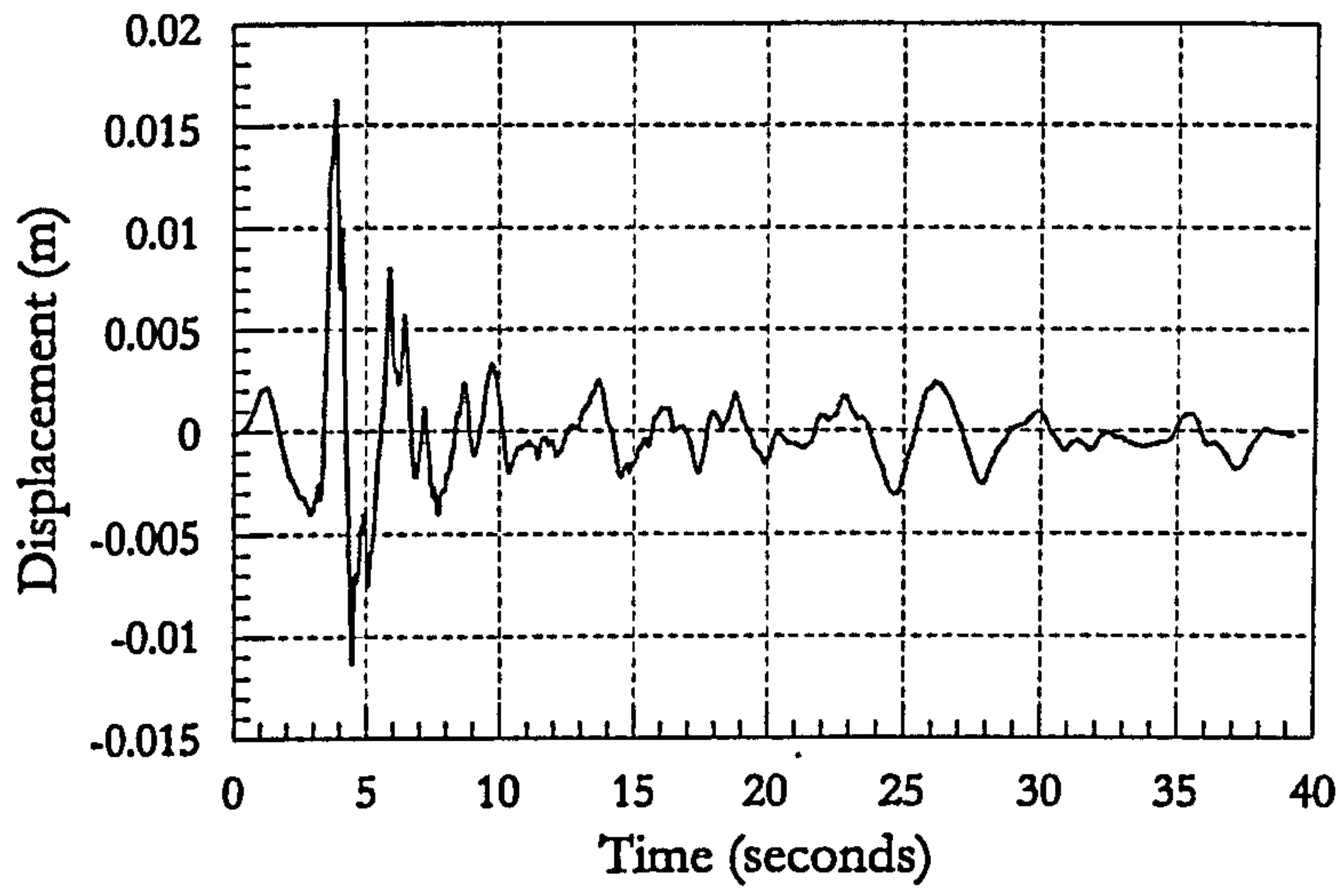

Figure 6.27: Equivalent displacement time history from Athens earthquakes after filtering

It is clear that the important characteristics of the acceleration record have not been changed whilst the displacement record now behaves in a much more realistic manner.

6.8 Results of Dynamic Finite Element Analysis

6.8.1 Introduction

The static analysis of the working load presented in Section 6.6 represents the initial conditions for the dynamic finite element analysis and the filtered earthquake record presented in Section 6.7 represents the analysis input. The earthquake is applied to the foundation by specifying a horizontal acceleration at all nodes along the base of the finite element mesh. Using the specified time step of 0.01 seconds and the Newmark scheme, this acceleration is converted into an equivalent incremental displacement which is specified in the list of nodal displacements. The inclusion of inertia forces in the overall equilibrium equations allows the shear wave induced by this displacement to propagate through the finite element mesh. This section of the chapter will give details of the effects that this shear wave has on the foundation. The Newmark parameters $\delta = 0.6$ and $\alpha = 0.3025$ have been chosen for this analysis to give an unconditionally stable time

discretisation scheme with some added numerical damping. The analysis which contained almost 4000 increments took approximately five days to run.

6.8.2 Results

The effects of the earthquake upon the foundation will be divided into the effects during the earthquake and the permanent changes that remain after the earthquake has finished. All results plotted for the mesh are for the area around the foundation highlighted in Figure 6.18.

6.8.2.1 During the Earthquake

The most obvious difference between the pseudo static and dynamic finite element analyses is the manner in which inertia forces are included. The pseudo static analysis assumed the inertia forces could be included by applying a constant horizontal body force which is equal to the acceleration multiplied by the soils mass. This assumes the inertia force is constant and affects all parts of the soil equally at all times. The dynamic finite element analysis on the other hand takes into account the transient nature of the seismic wave. This is demonstrated in the following strength mobilisation plots from various times during the earthquake analysis.

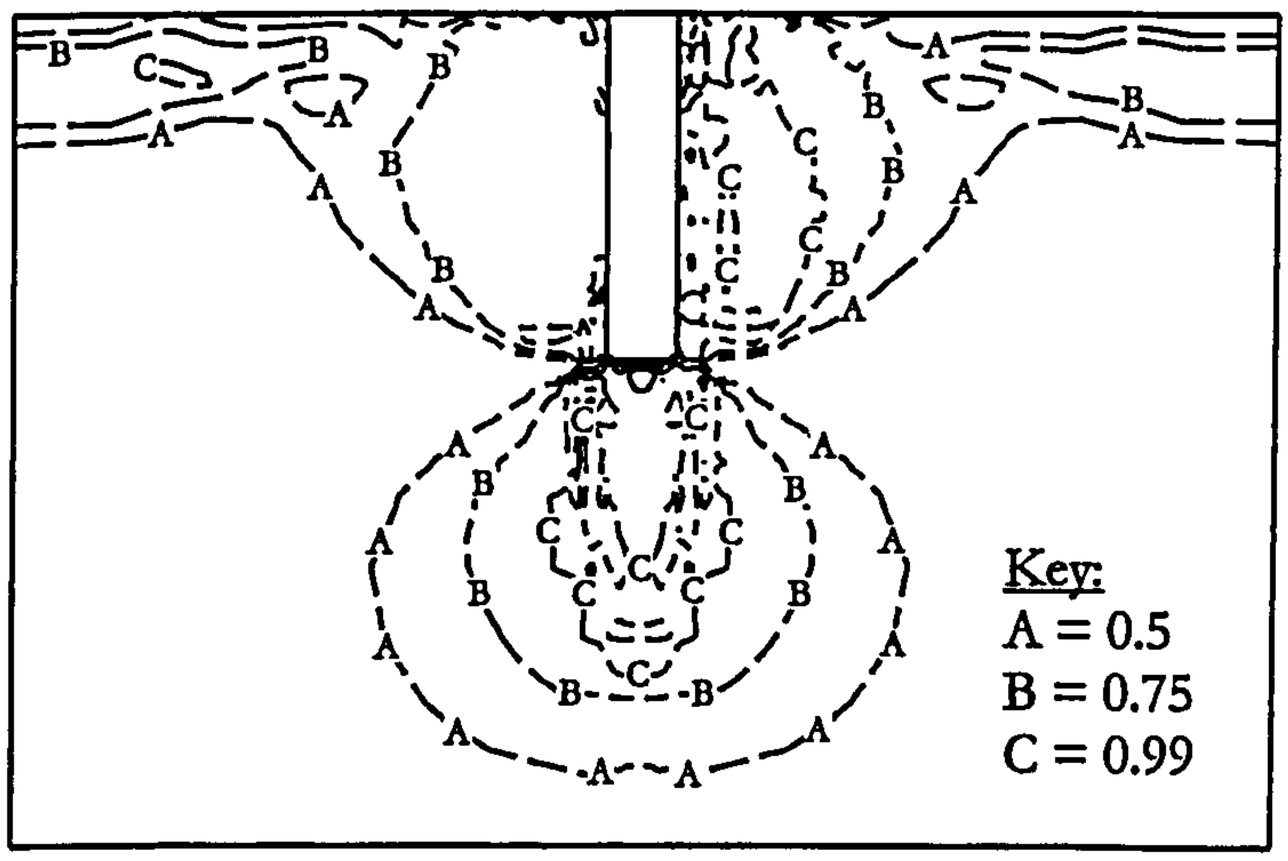

Figure 6.28: Degree of strength mobilisation around foundation after 2.0 seconds

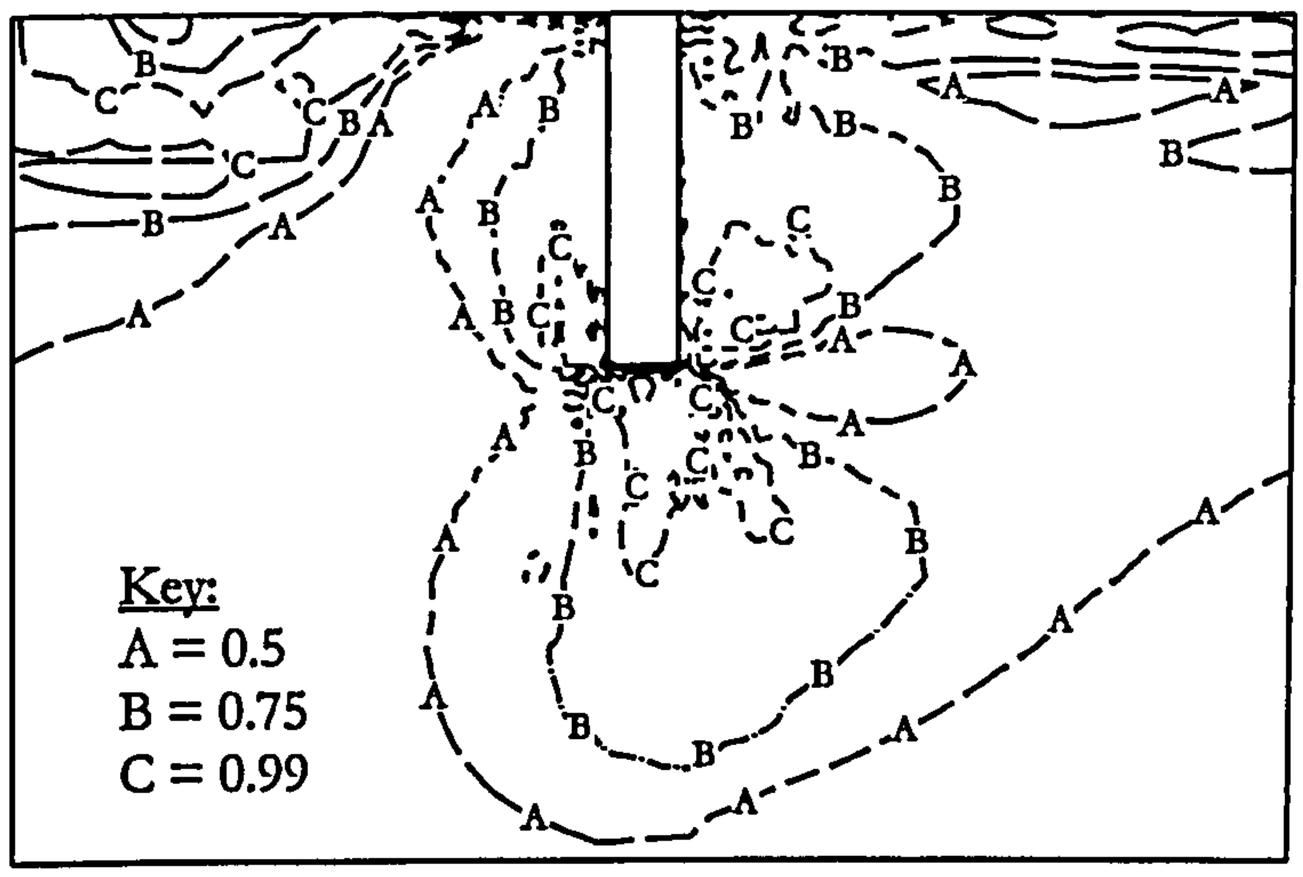

Figure 6.29: Degree of strength mobilisation around foundation after 4.1 seconds

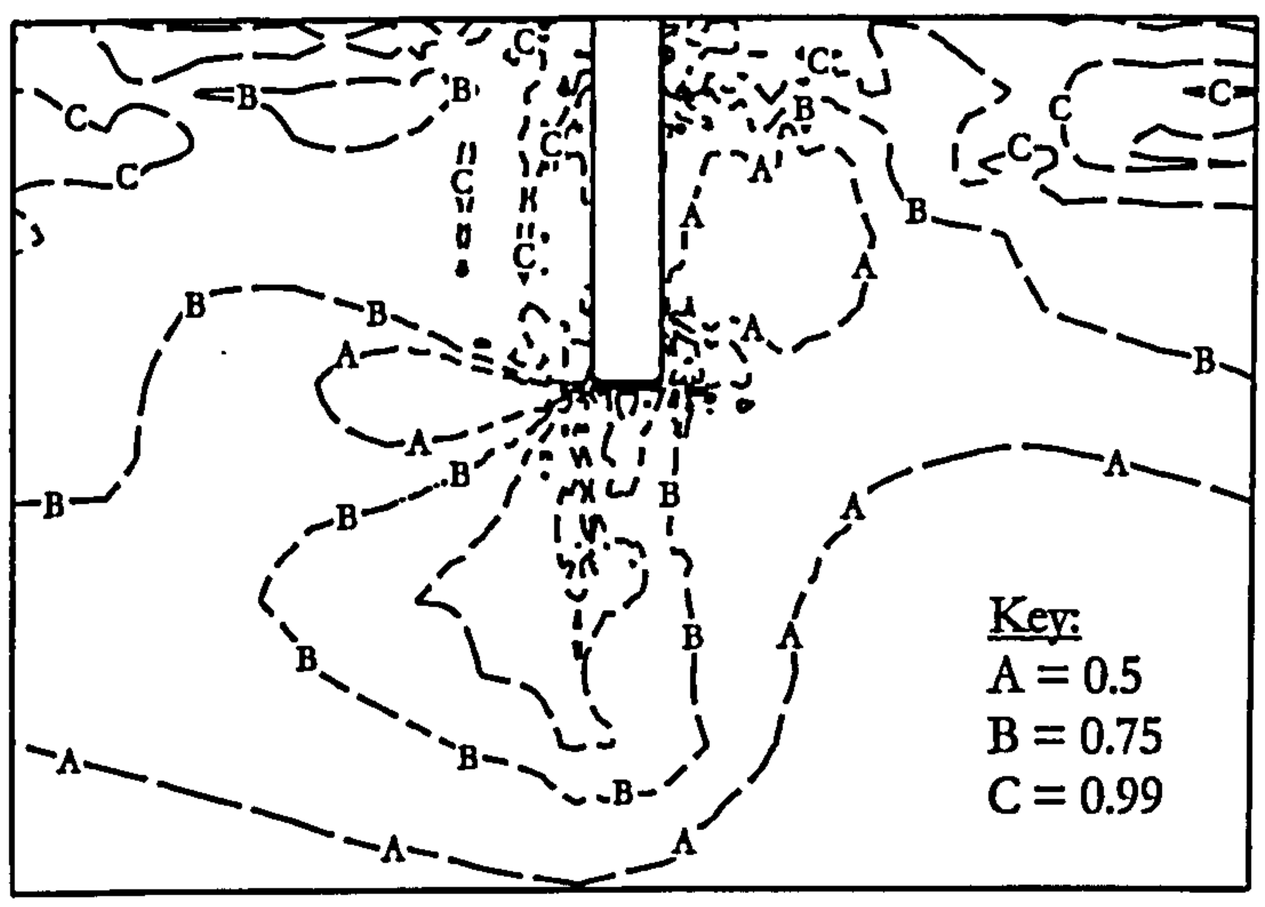

Figure 6.30: Degree of strength mobilisation around foundation after 4.2 seconds

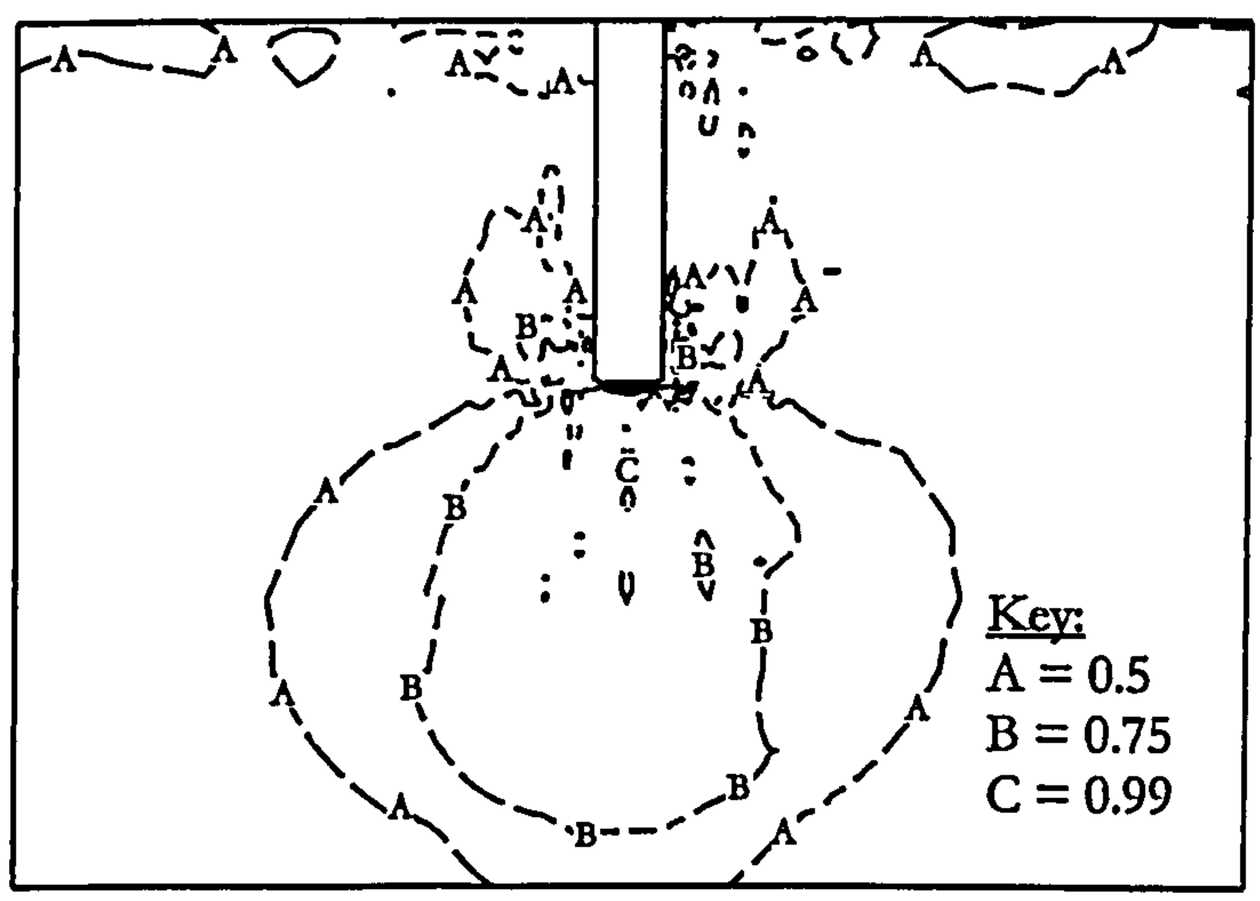

Figure 6.31: Degree of strength mobilisation around foundation after 35.0 seconds

The first plot shows the strength mobilisation around the foundation after 2.0 seconds of the earthquake. The area of soil that has yielded has not changed significantly from the condition at working load shown in Figure 6.21. This is due to the earthquake motion not being significant enough at this point to induce additional plastic behaviour in the ground around the foundation.

Figure 6.29 shows the strength mobilisation after 4.1 seconds of the earthquake. The area of ground that has yielded has clearly increased on the right hand side of the foundation and decreased on the left hand side. One increment later (shown in Figure 6.30) the large area of yielded ground has switched to the left hand side and the right hand side now has less plasticity. The cause of this significant amount of yielding is the greater intensity of the earthquake shaking which is illustrated by Figure 6.26. The acceleration record reveals that the most intense period of the earthquake shaking occurs around 4 seconds into the earthquake. The shape of the contours during the most intense period of the earthquake is similar to that shown in Figure 6.15 for the pseudo static analysis, although clearly during the dynamic analysis the active and passive sides of the foundation change continuously during the earthquake. The final figure shows the degree of strength mobilisation after 35 seconds of the earthquake. The total area of soil that has yielded is now less than before the earthquake was applied and from this point onwards does not change from increment to increment. The total earthquake record is almost forty seconds long, although significant amounts of plasticity are only induced during the most intense periods between 3 and 5 seconds into the earthquake. This behaviour and the switching of plasticity from one side of the foundation to the other cannot be recreated in pseudo static analyses and indicates that applying a constant and homogenous horizontal body force to represent the earthquake induced inertia forces may be over conservative.

Figure 6.32 shows an expanded view of the displacement time history during the most intense period of shaking from the Athens 0.2*g* earthquake used in this analysis.

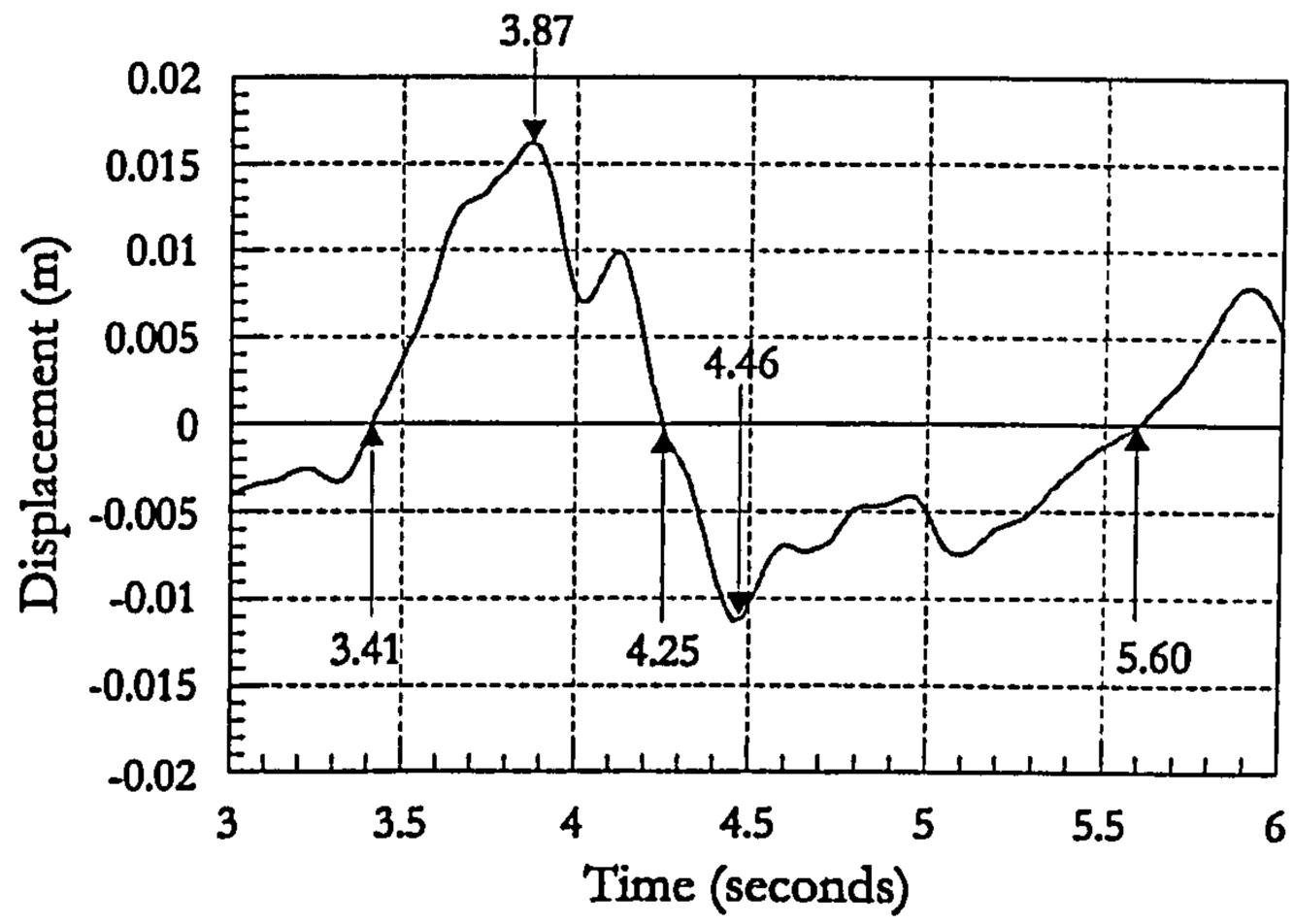

Figure 6.32: Expanded view of the total displacement time history for Athens 0.2*g* record, highlighting important analysis increments

Figure 6.33 to Figure 6.37 show the vectors of incremental displacement at the increments highlighted in Figure 6.32. These time steps have been chosen to represent snap shots of the foundations behaviour during the complete analysis. They include increments where the input record is passing through the zero displacement axis, as well as increments where the displacement is a maximum, both in the positive and negative directions.

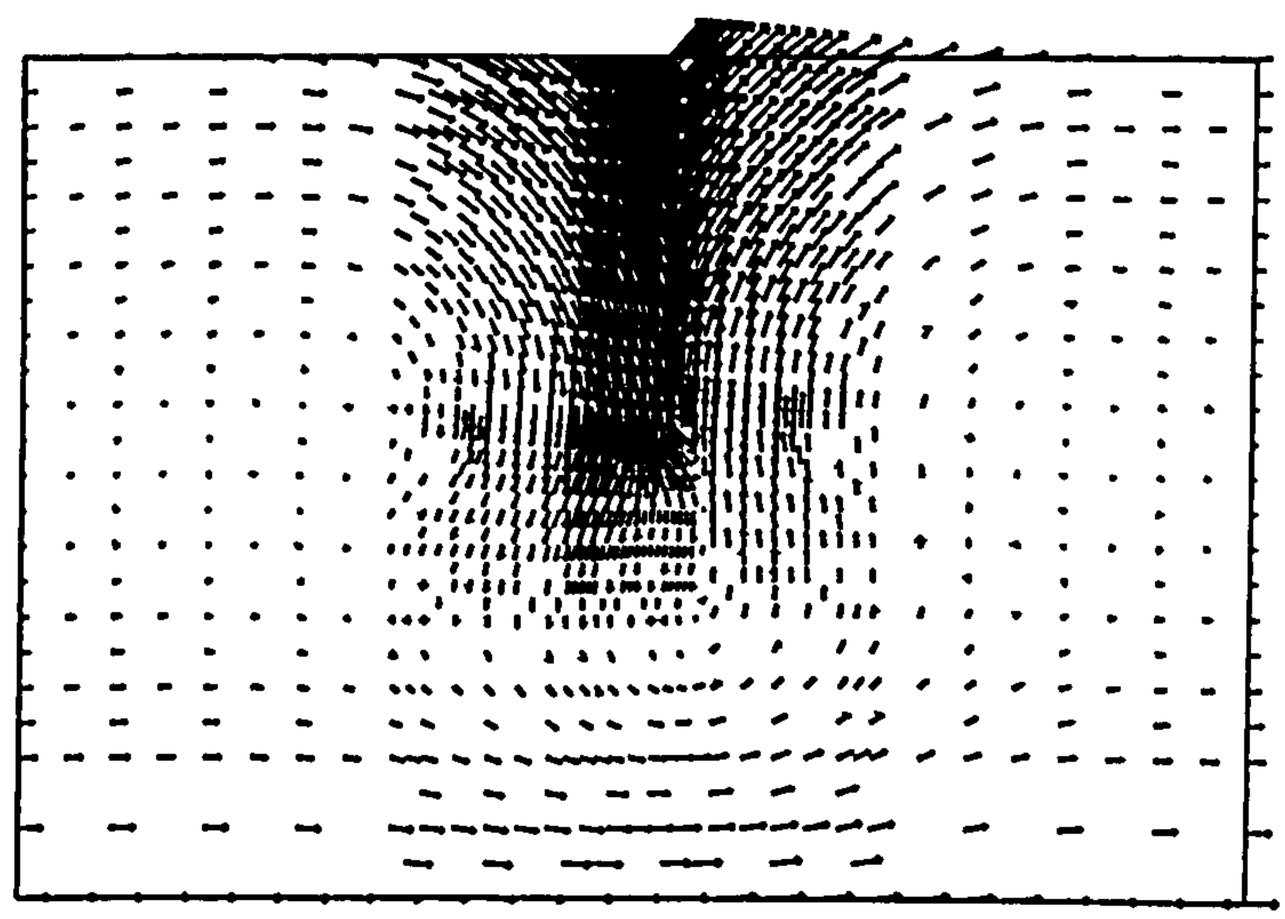

Figure 6.33: Vectors of incremental displacement at time 3.41 seconds

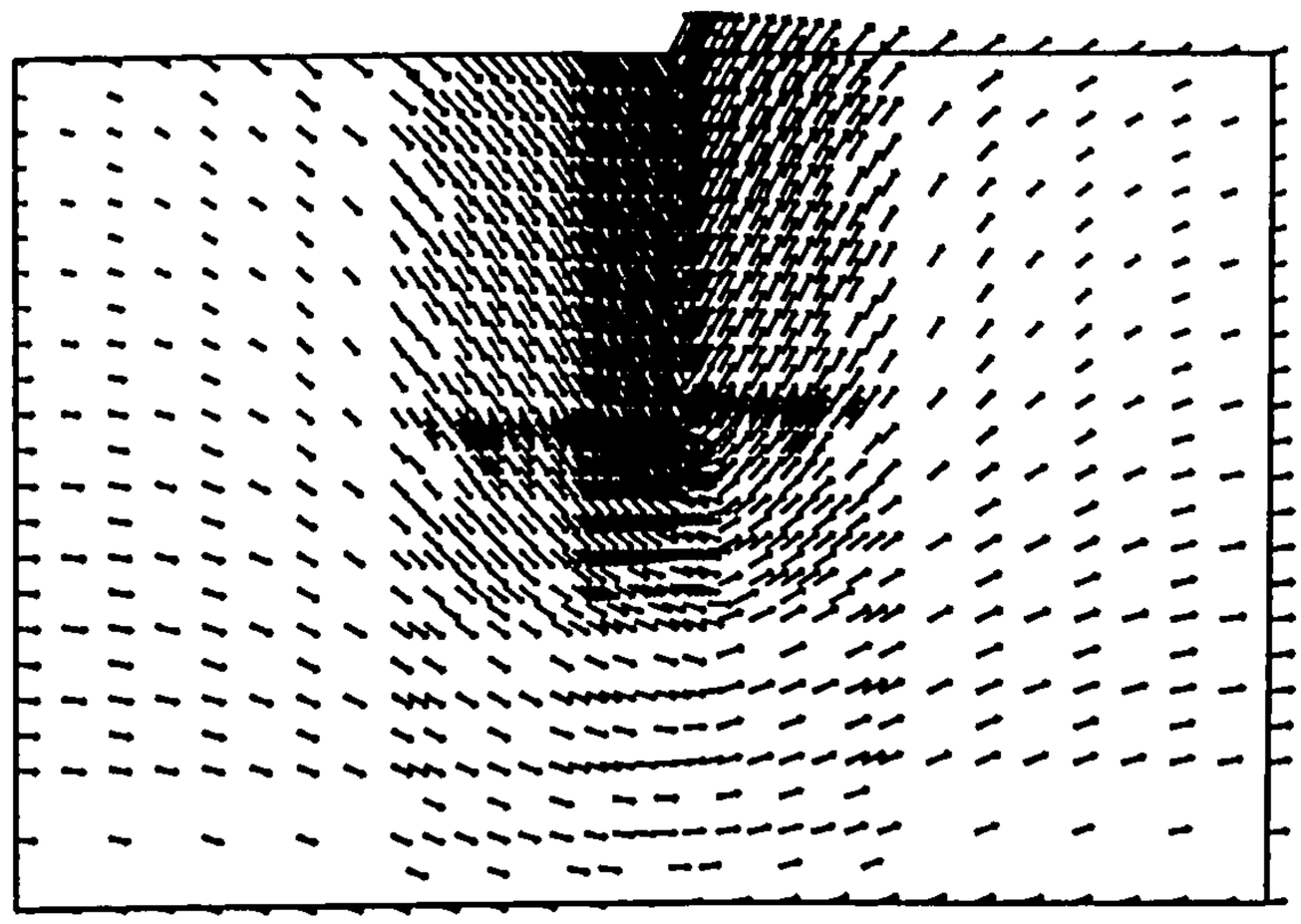

Figure 6.34: Vectors of incremental displacement at time 3.87 seconds

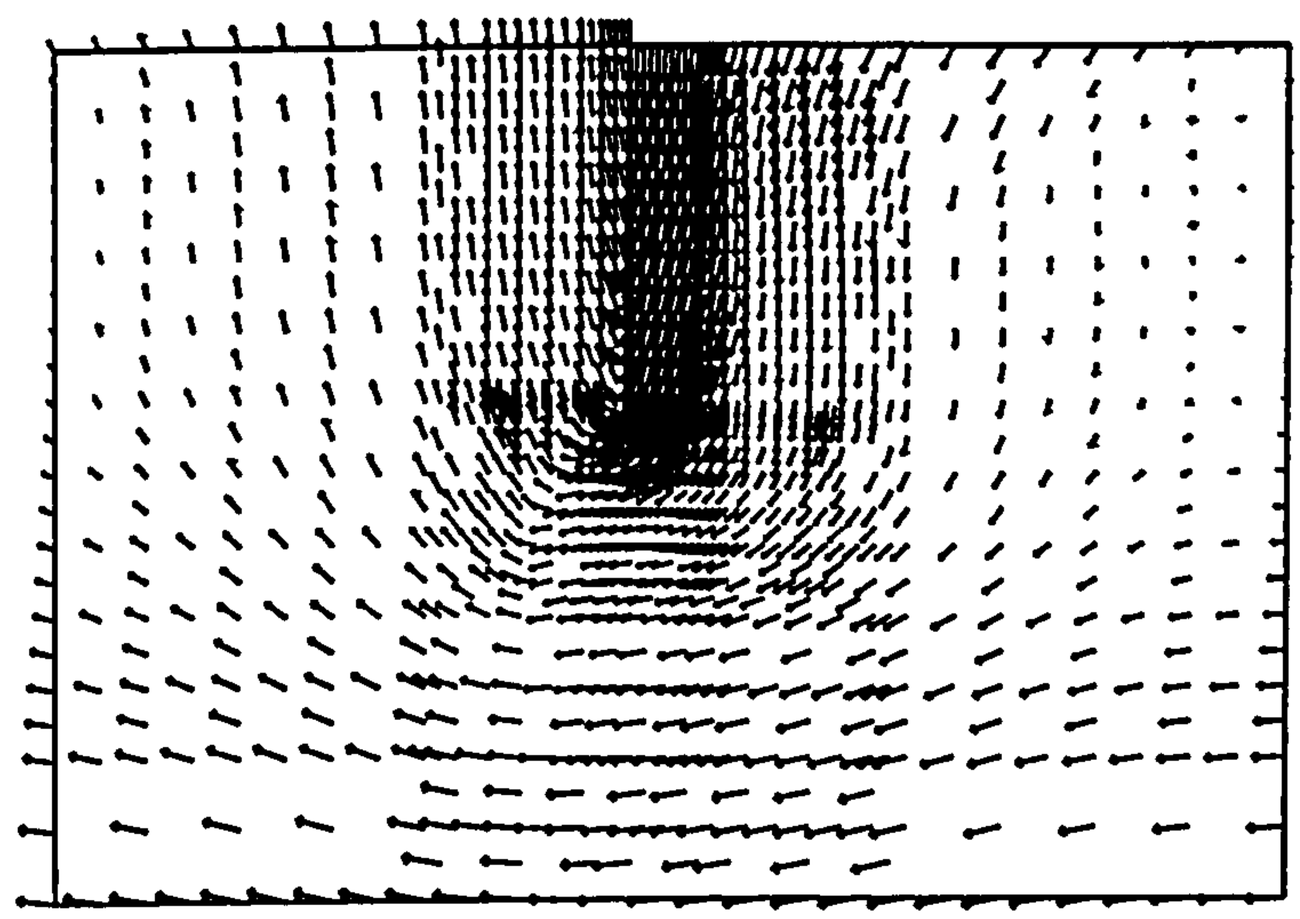

Figure 6.35: Vectors of incremental displacement at time 4.25 seconds

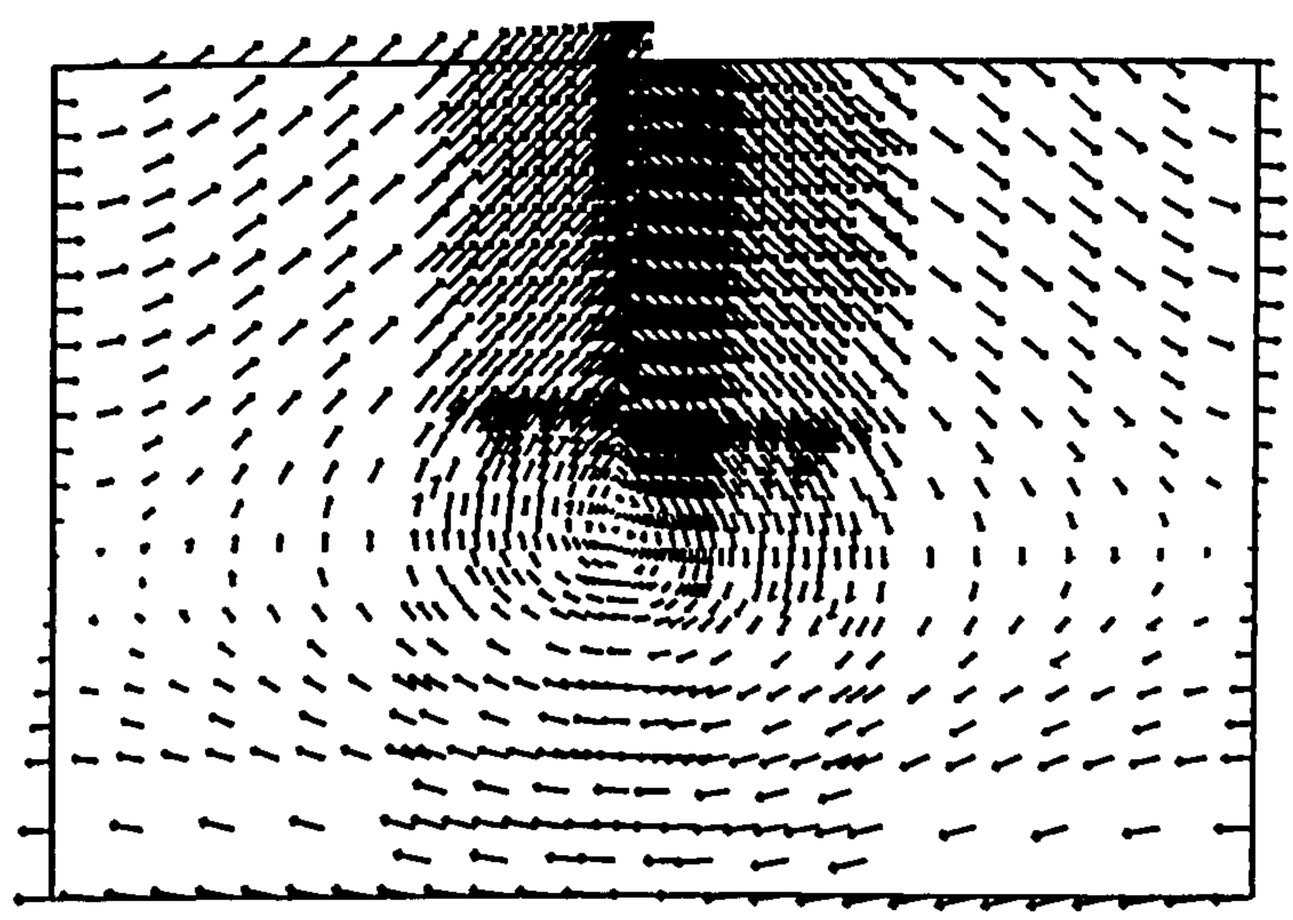

Figure 6.36: Vectors of incremental displacement at time 4.46 seconds

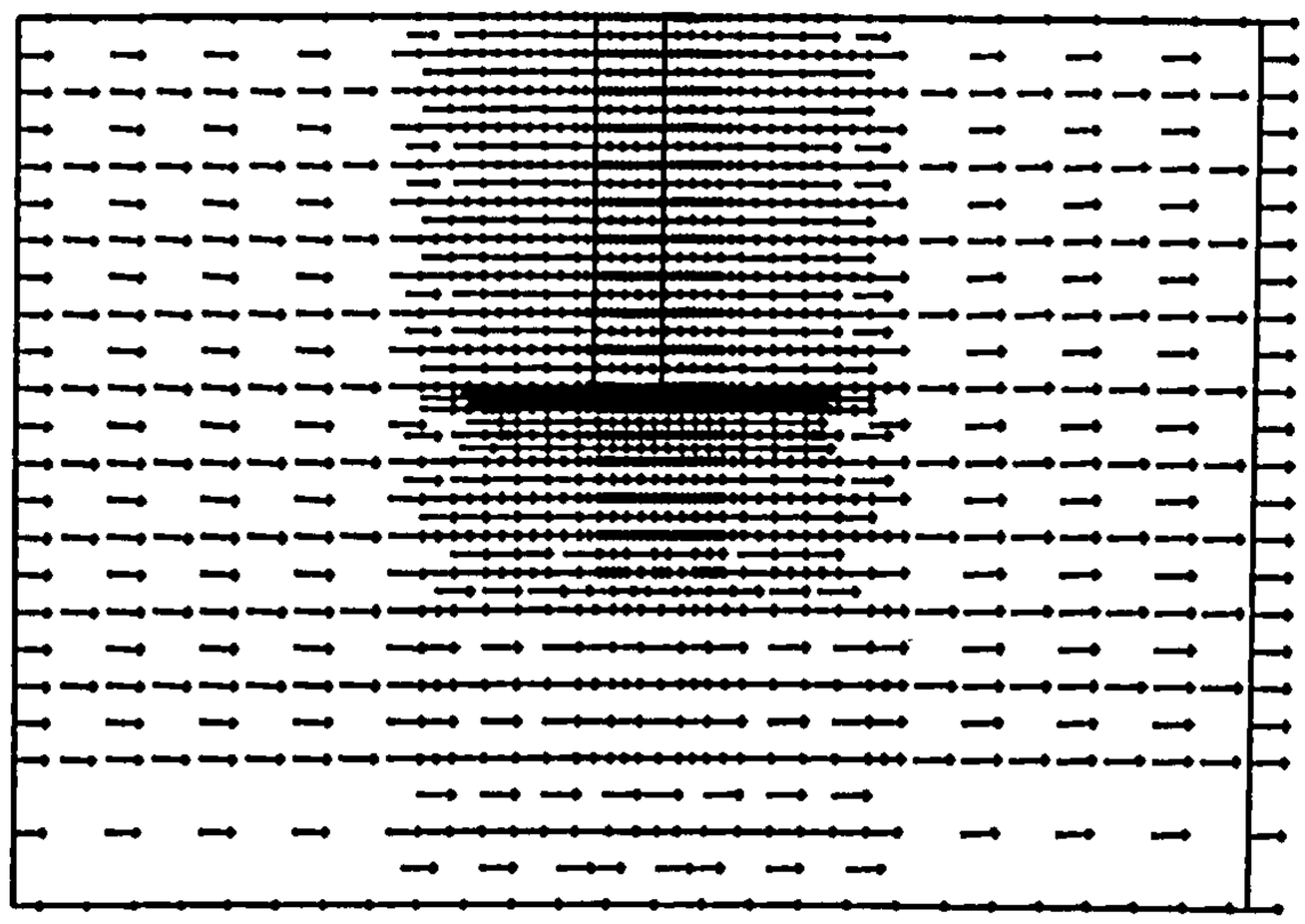

Figure 6.37: Vectors of incremental displacement at time 5.60 seconds

As the direction of the displacement time history changes, the predominant direction of the displacement vectors change accordingly. This is noticeable between Figure 6.34 and Figure 6.35, where the displacement time history, shown in Figure 6.32, changes from a positive to a negative gradient. The vectors of incremental displacement correspondingly change from pointing predominantly to the right hand side to pointing predominantly to the left. Figure 6.33 to Figure 6.36 demonstrate the complex interaction that exists between the foundation and the surrounding soil during an earthquake event, although at no point does a failure mechanism develop that could justify using a Prandtl type failure mechanism to determine the bearing capacity of a deep foundation subjected to seismic loading.

To understand the overall behaviour, the stress paths experienced by two soil elements located at different positions around the foundation will be investigated. Figure 6.38 shows the stress path for a Gauss point located at a depth of 2.75 meters and 0.1 meters to the left of the foundation. Also shown are the failure envelopes for the interface and solid elements. The stress paths are plotted in terms of s' and t' which are given by the following relationships:

$$s' = \frac{\sigma_1 + \sigma_2}{2} \text{ and } t' = \frac{\sigma_1 - \sigma_2}{2}$$

where σ_1 and σ_2 are the major and minor principle stresses respectively.

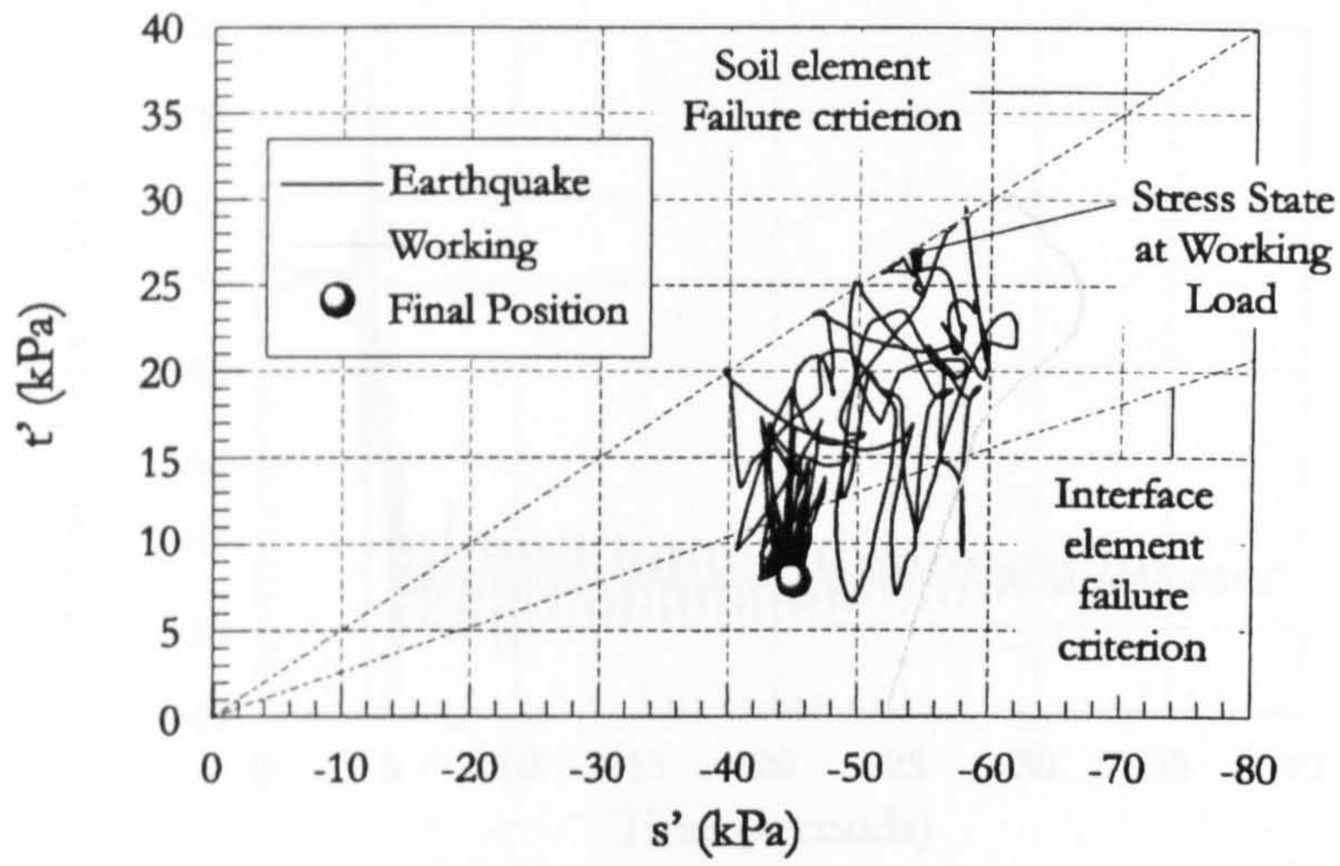

Figure 6.38: Stress path for element adjacent to foundation

The initial part of the line represents the stress path associated with the application of the working load. The stress path is for a solid element, however its close proximity to the interface elements means that its behaviour will be heavily influenced by their failure criterion, which is different to the rest of the soil. The first part of the stress path is linear, moving towards the soils failure criterion as the foundation load increases. After the interface elements have yielded, the stress regime changes and the stress path alters its direction and begins to hook backwards until it reaches the soil failure criteria. From this point onwards the stress path moves down the failure envelope until the working load is reached. For the first two to three seconds of the earthquake the stress point does not move significantly from its position at the end of the working load. During the most intense period of shaking both the values of *s'* and *t'* reduce until the shaking intensity reduces and both stabilise. The horizontal and vertical stresses during the earthquake are plotted for the same Gauss point in Figure 6.39 and Figure 6.40 respectively.

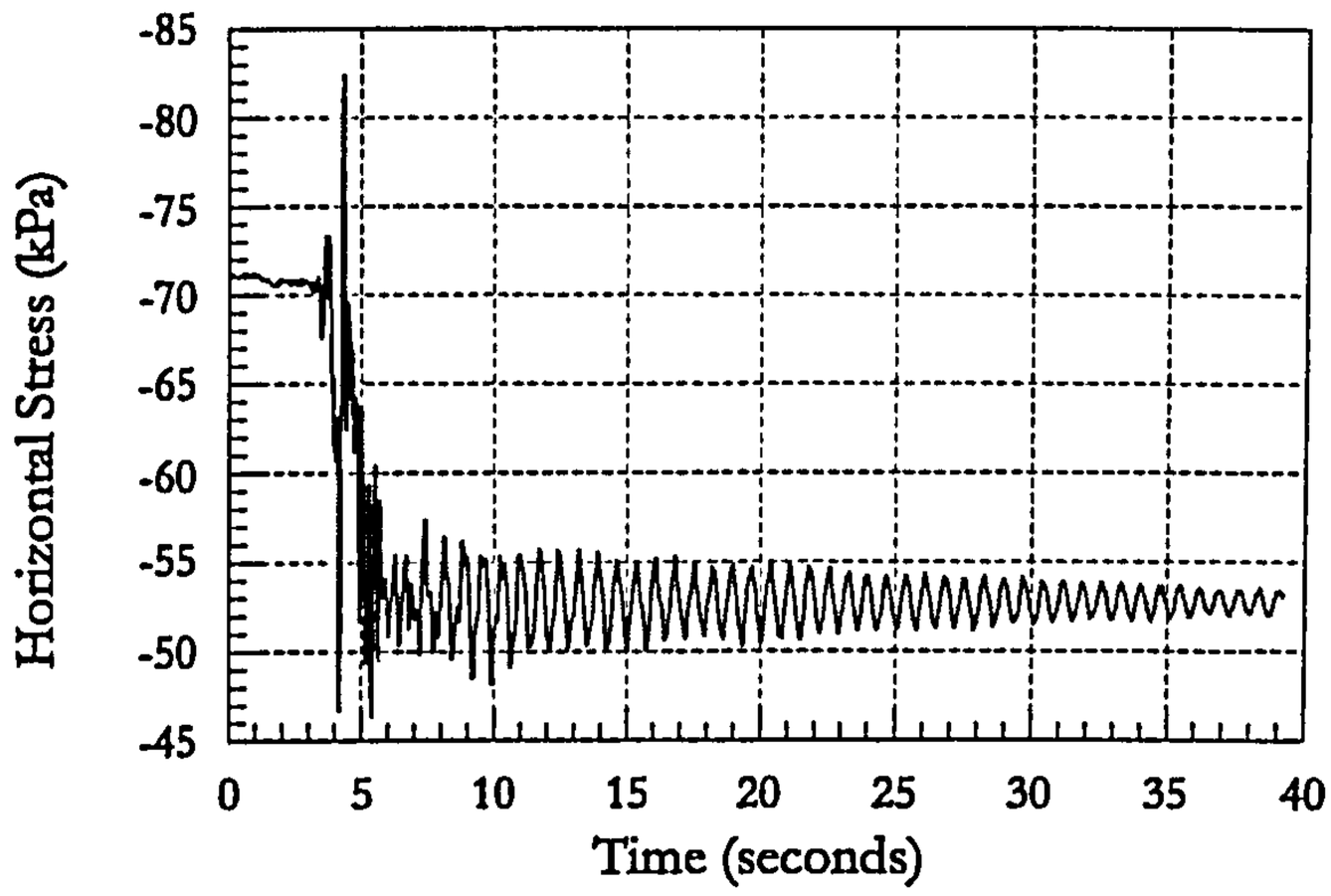

Figure 6.39: Horizontal stress history for Gauss point adjacent to foundation

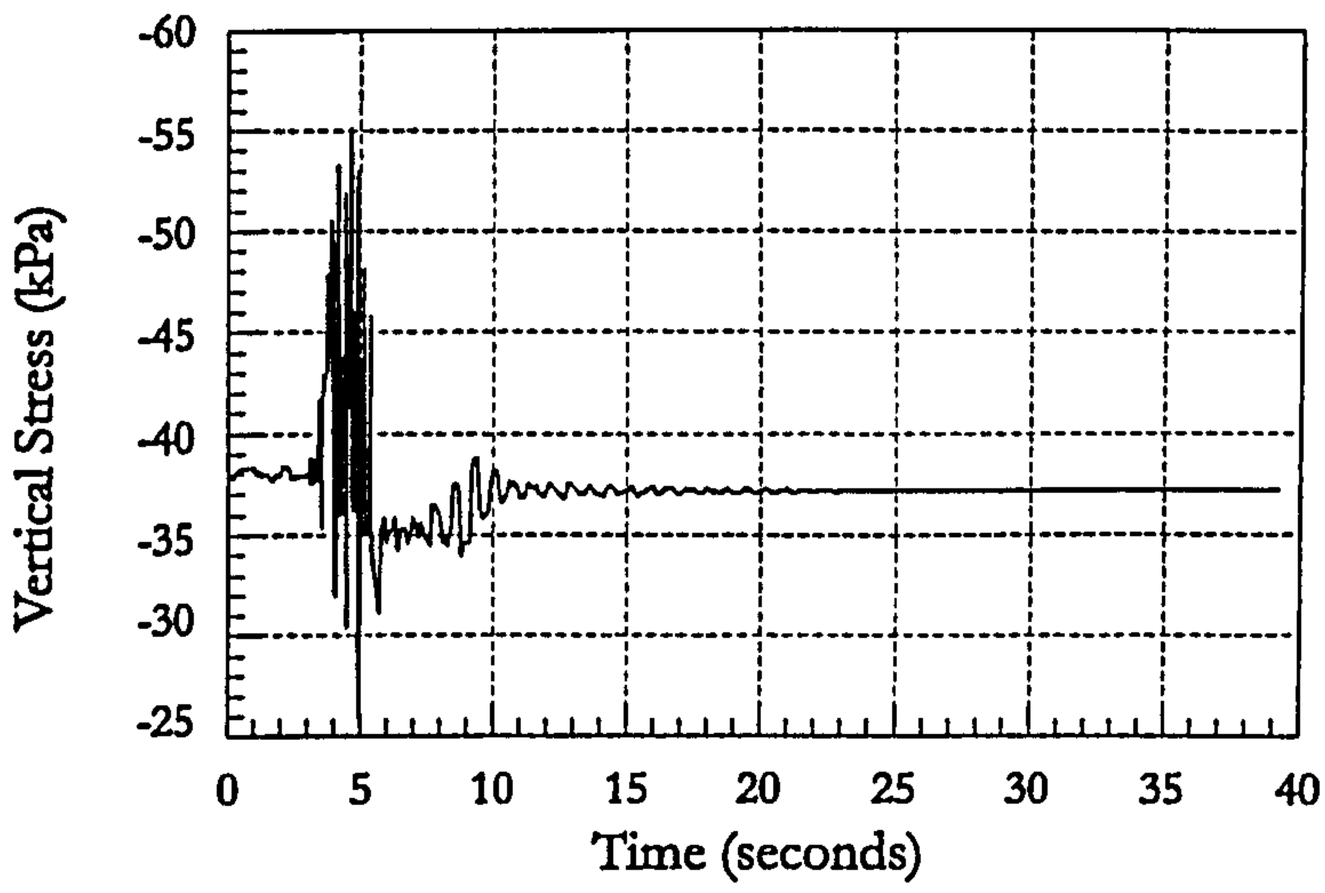

Figure 6.40: Vertical stress history for Gauss point adjacent to foundation

During the most intense period of shaking the horizontal stress reduces significantly whilst for the vertical stress, which experiences a similar transient component, the permanent reduction is only slight. When the shaking intensity has reduced both stresses stabilise to a residual value.

Figure 6.41 shows the stress path of a Gauss point 0.07 meters below the centre line of the foundation and the failure criteria for the solid elements.

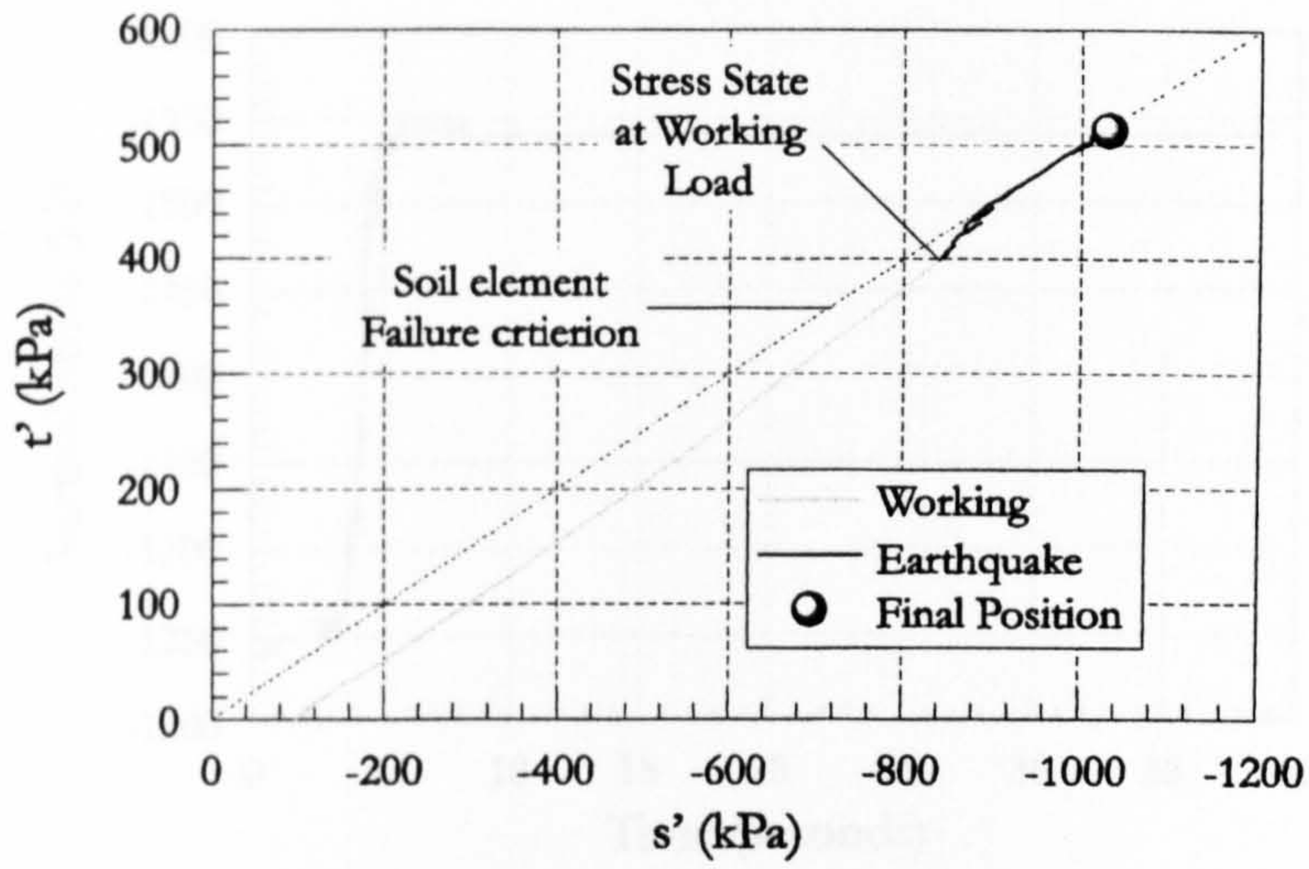

Figure 6.41: Stress path for element below foundation

The first part of the stress path, which represent the foundation being taken to working load, is linear and shows the element tending towards the failure envelope as the load increases. When the working load is reached the stress path for this particular Gauss point had not quite reached the failure envelope, although Figure 6.21 shows that most elements at the base of the foundation had yielded at working load. As the earthquake was applied, in a similar fashion to the element adjacent to the foundation, the stress state did not change significantly. During the most intense period of the earthquake record both the stress invariants *s'* and *t'* increased and the stress path moved towards and up the failure envelope. The horizontal and vertical stresses for the same Gauss point are shown in Figure 6.42 and Figure 6.43 respectively.

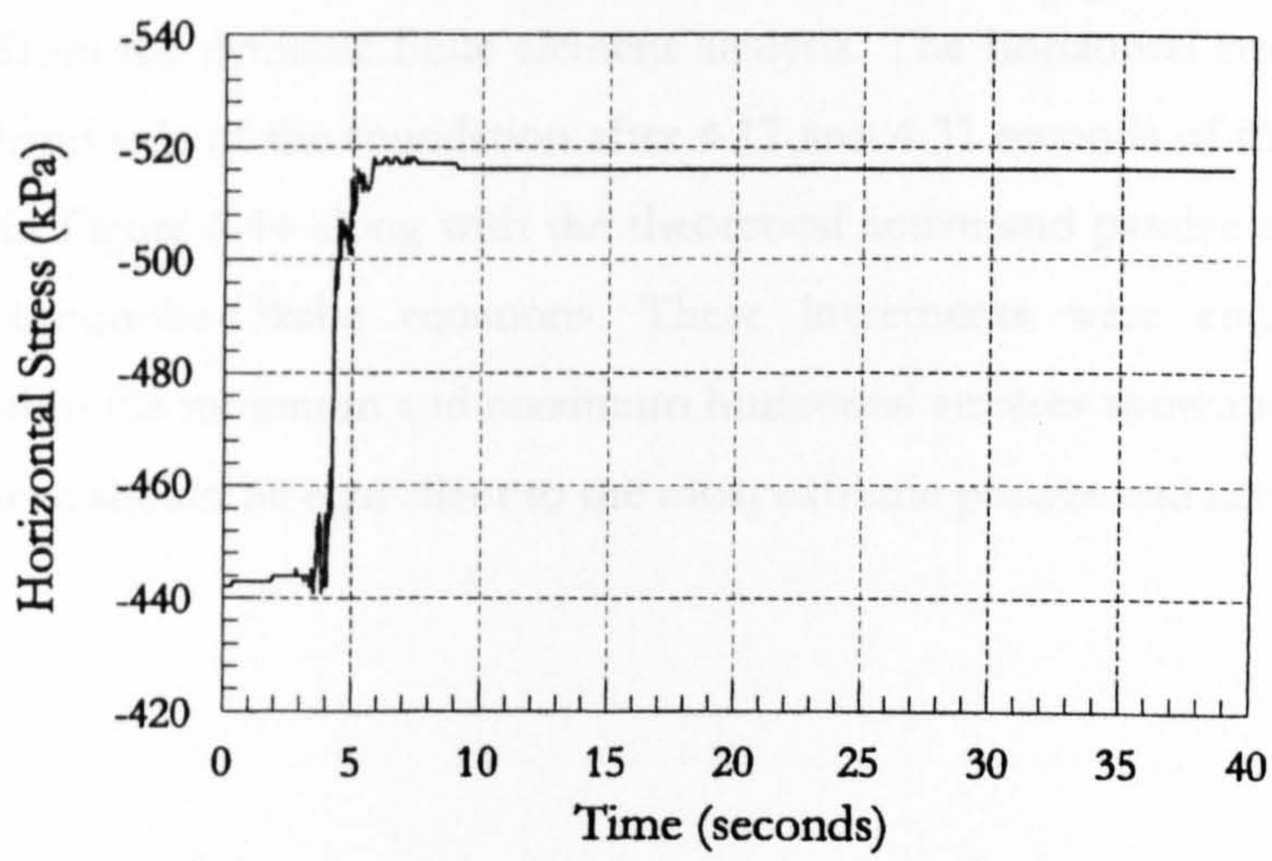

Figure 6.42: Horizontal stress below foundation during earthquake

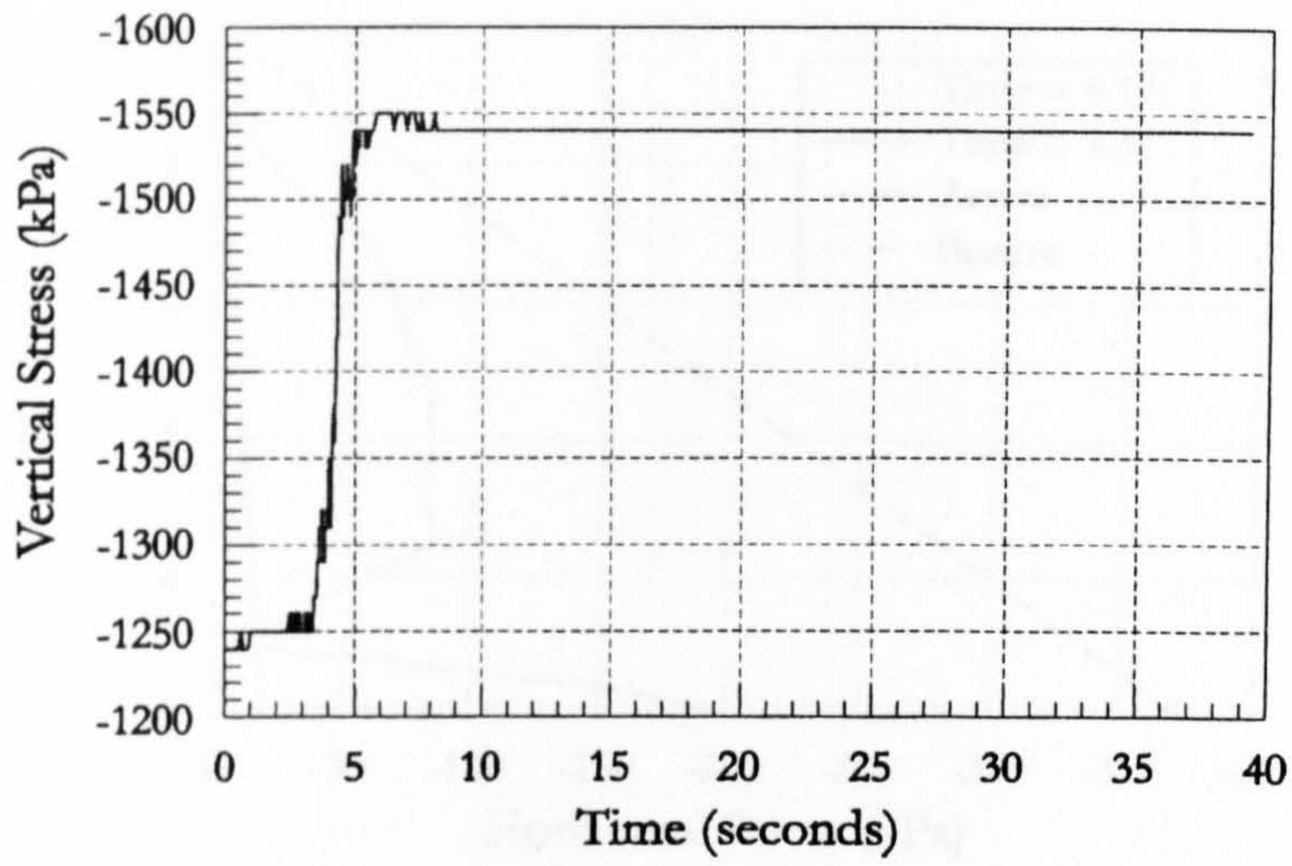

Figure 6.43: Vertical stress below foundation during earthquake

The horizontal and vertical stresses below the foundation follow a very similar pattern of behaviour during the analysis. At the start of the analysis neither changes significantly until the most intense part of the earthquake motion. Between 3 and 5 seconds into the earthquake record the horizontal and vertical stresses increase by 15 and 25% respectively, causing the element to yield as shown Figure 6.41. After the intense period of the earthquake both stresses stabilise to residual values.

One of the most significant observations made from the pseudo static analyses presented by Potts (2000) was the active and passive pressures acting on the foundation at failure. The results showed that the passive pressure is fully mobilised whilst the active stress is not. All of the results presented lied within the limits given by the Mononobe-Okabe equations. These results can now be compared with those obtained from the dynamic finite element analysis. The horizontal stress acting on the right hand side of the foundation after 4.17 and 4.31 seconds of the earthquake is shown in Figure 6.44 along with the theoretical active and passive stresses given by the Mononobe-Okabe equations. These increments were chosen as they correspond to the minimum and maximum horizontal stresses shown in Figure 6.39 and therefore should be equivalent to the most extreme passive and active cases.

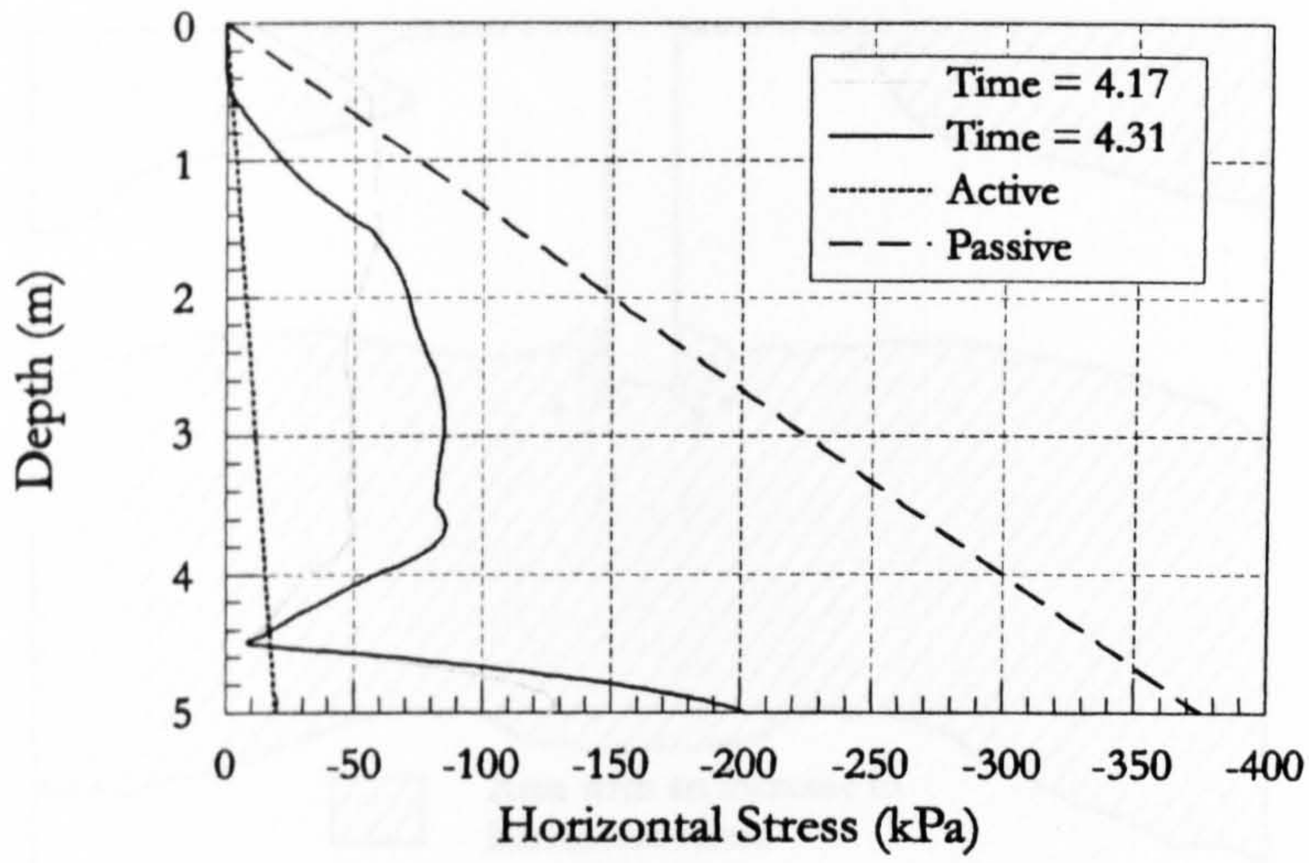

Figure 6.44: Horizontal stress on side of foundation during earthquake

The minimum and maximum stresses given by the Mononobe-Okabe equations depend upon the acceleration applied to the soil around the foundation. In the pseudo static analysis the horizontal acceleration applied to the mesh could be used to calculate the available active and passive stresses. For the dynamic analysis the earthquake record that was applied to the base of the mesh was scaled to have an equivalent maximum acceleration value. However, the peak acceleration experienced during the analysis will be different throughout the mesh due to the complex interaction of the seismic wave. It is therefore difficult to determine what should be taken as the available active and passive stresses. Despite this, Figure 6.44 illustrates that the stresses acting on the foundation during the earthquake do not change significantly and whilst they generally remain within the limits given by the Mononobe-Okabe equations, they are very different to those shown in Figure 6.17 for the pseudo static analysis.

6.8.2.2 After the Earthquake

The stress paths presented in the previous section show a decrease in horizontal stress adjacent to the foundation and an increase in horizontal and vertical stress below the foundation due to the earthquake motion. To confirm this trend for the whole mesh Figure 6.45 and Figure 6.46 show the sub-accumulated horizontal and vertical stresses from the beginning to the end of the earthquake analysis.

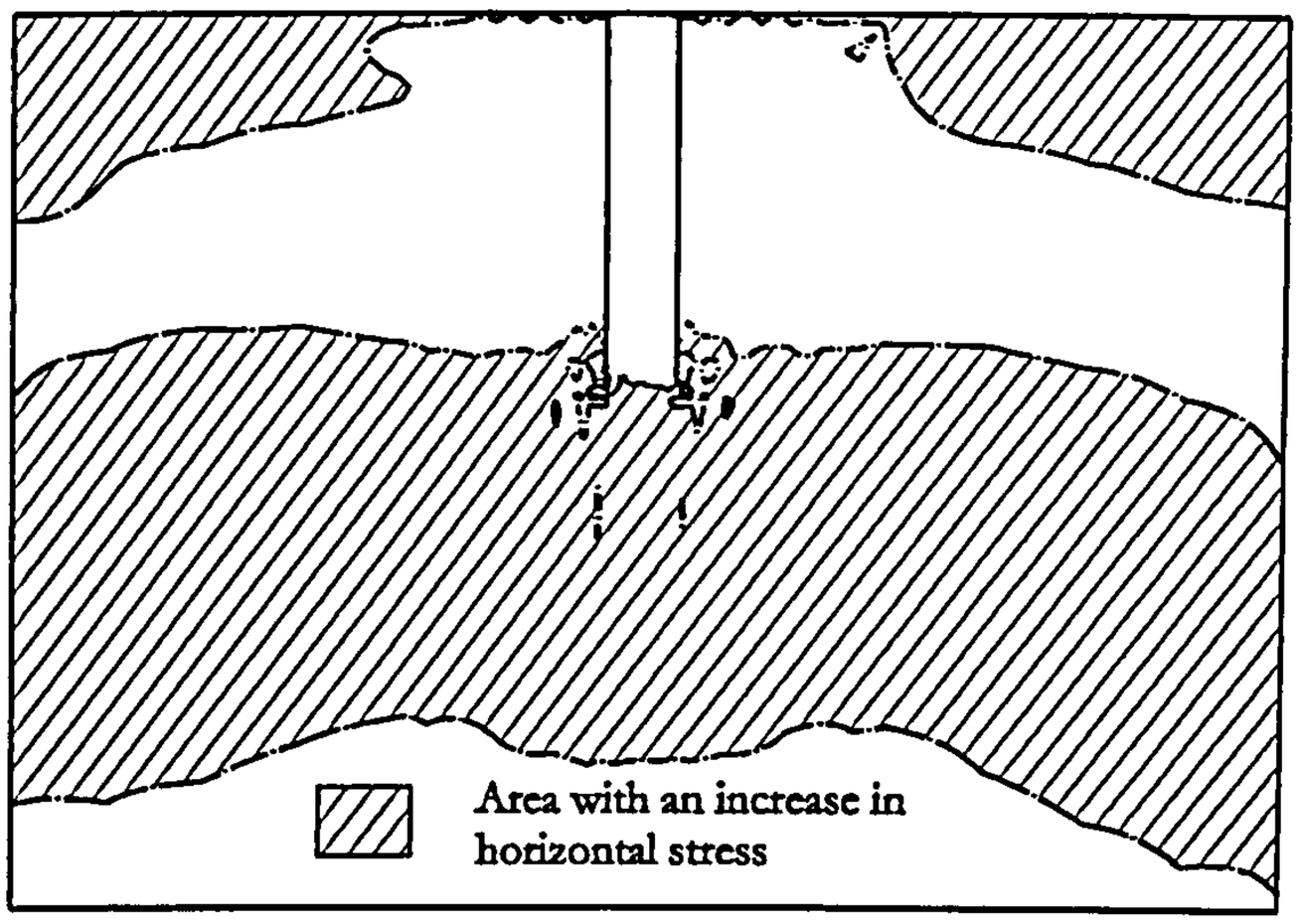

Figure 6.45: Areas of mesh showing an increase in horizontal stress

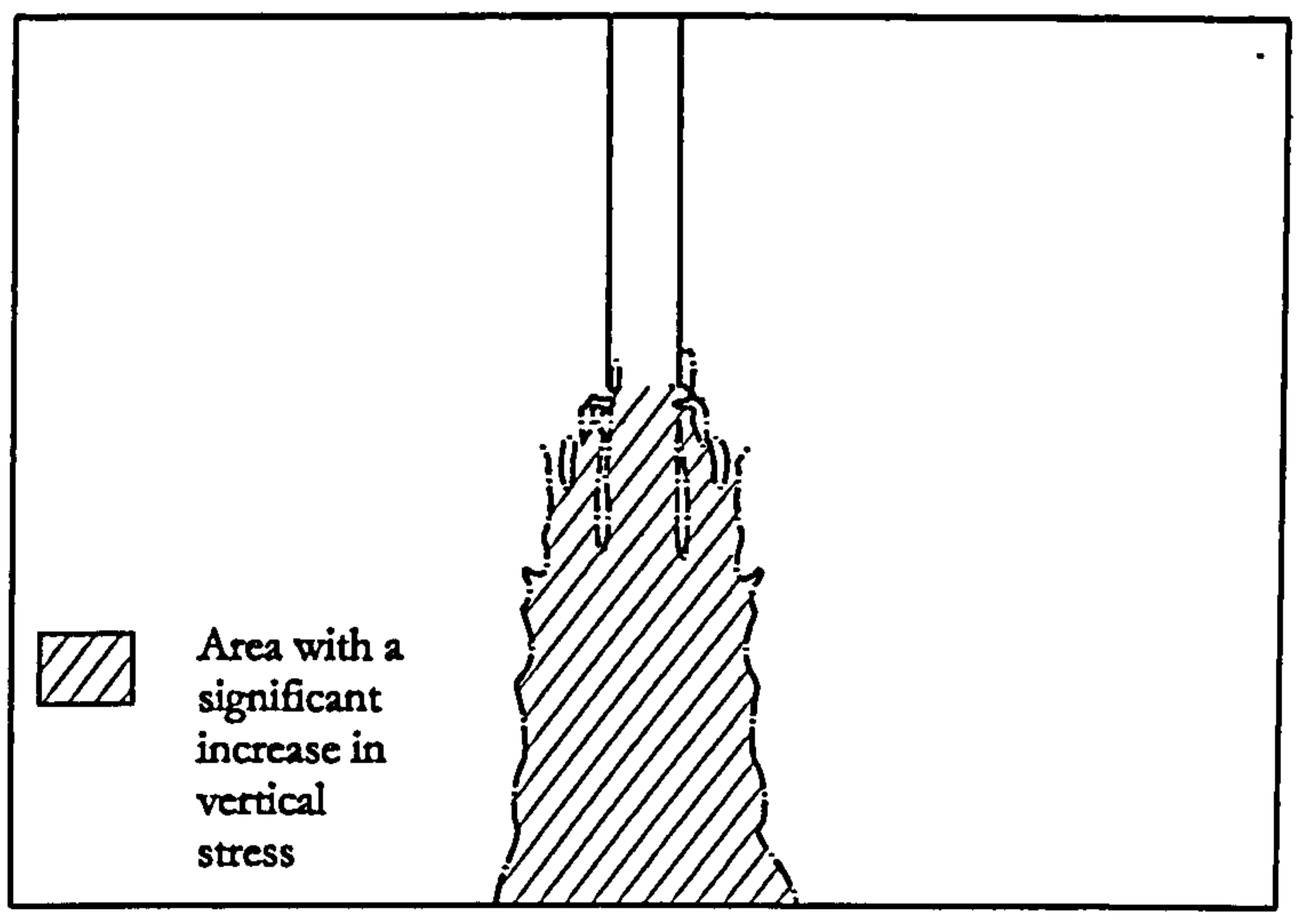

Figure 6.46: Areas of mesh showing a significant increase in vertical stress

Figure 6.45 shows a band of soil adjacent to the foundation in which the horizontal stress has reduced due to the earthquake analysis. The strip of soil below the foundation shows an increase in horizontal stress. Figure 6.46 shows a narrow strip of soil directly below the foundation in which the vertical stress has increased. The soil surrounding the foundation has not experienced a significant change in vertical stress. These results confirm that the trends observed in the stress paths shown in Section 6.8.2.1 are representative for the whole mesh. Whilst the previous two figures demonstrate the areas in which permanent stress changes had occurred, they do not give an indication by what amount they had changed. A quantitative assessment can be made by comparing the horizontal stresses acting on the side of the foundation and the vertical stresses acting on the base of the foundation at the

end of the earthquake, with those present at working load. The results are shown in Figure 6.47 and Figure 6.48.

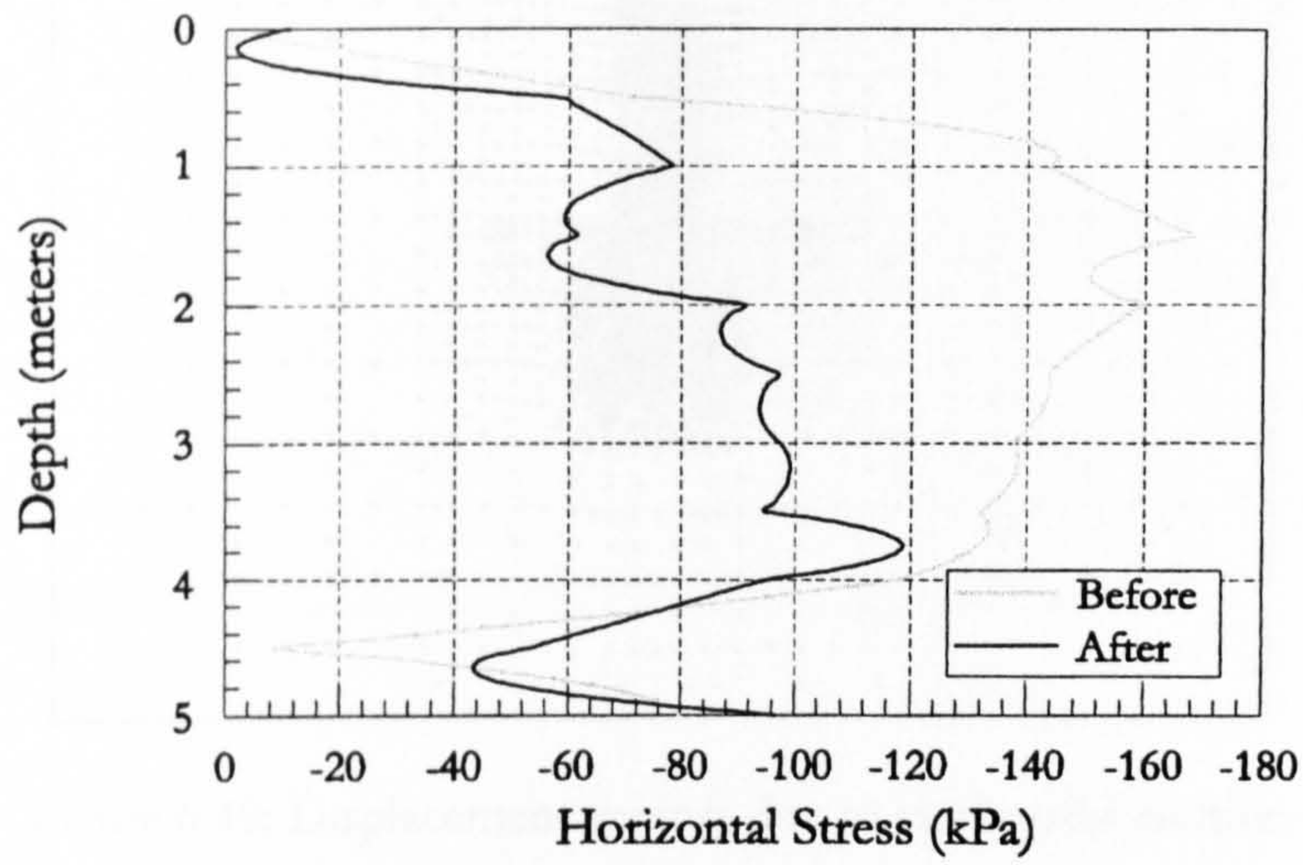

Figure 6.47: Horizontal stress distribution before and after earthquake

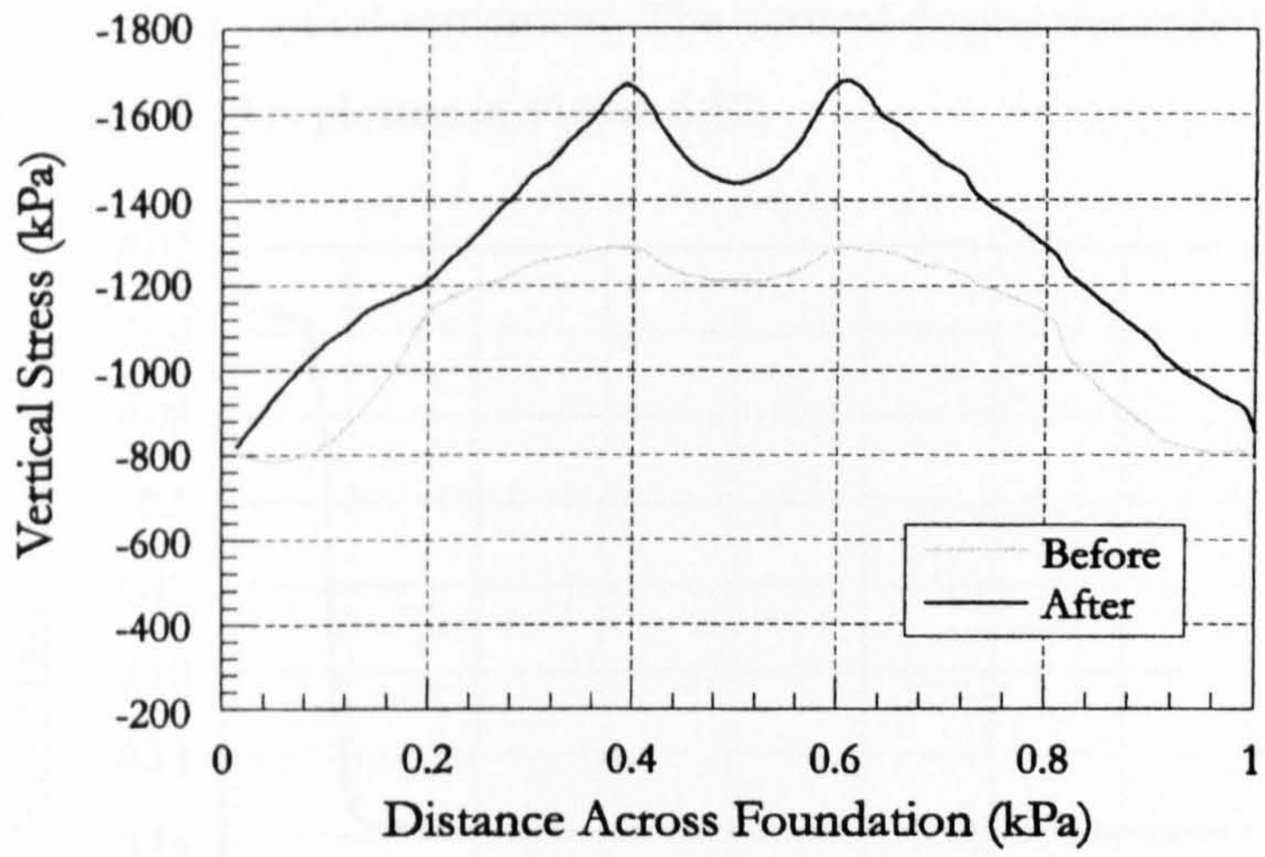

Figure 6.48: Vertical stress distribution before and after earthquake

Figure 6.47 shows a maximum reduction of 50.8 kPa at a depth 1.6 m which represents 64% of the horizontal stress at working load. The largest increase shown in Figure 6.48 occurs 0.6 meters across the foundation and represents an increase of 30% over the vertical stress present at working load.

To allow comparison with the pseudo static analysis presented in Section 6.3.2, the displacement vectors accumulated due to the earthquake motion are shown in Figure 6.49 for the dynamic analysis.

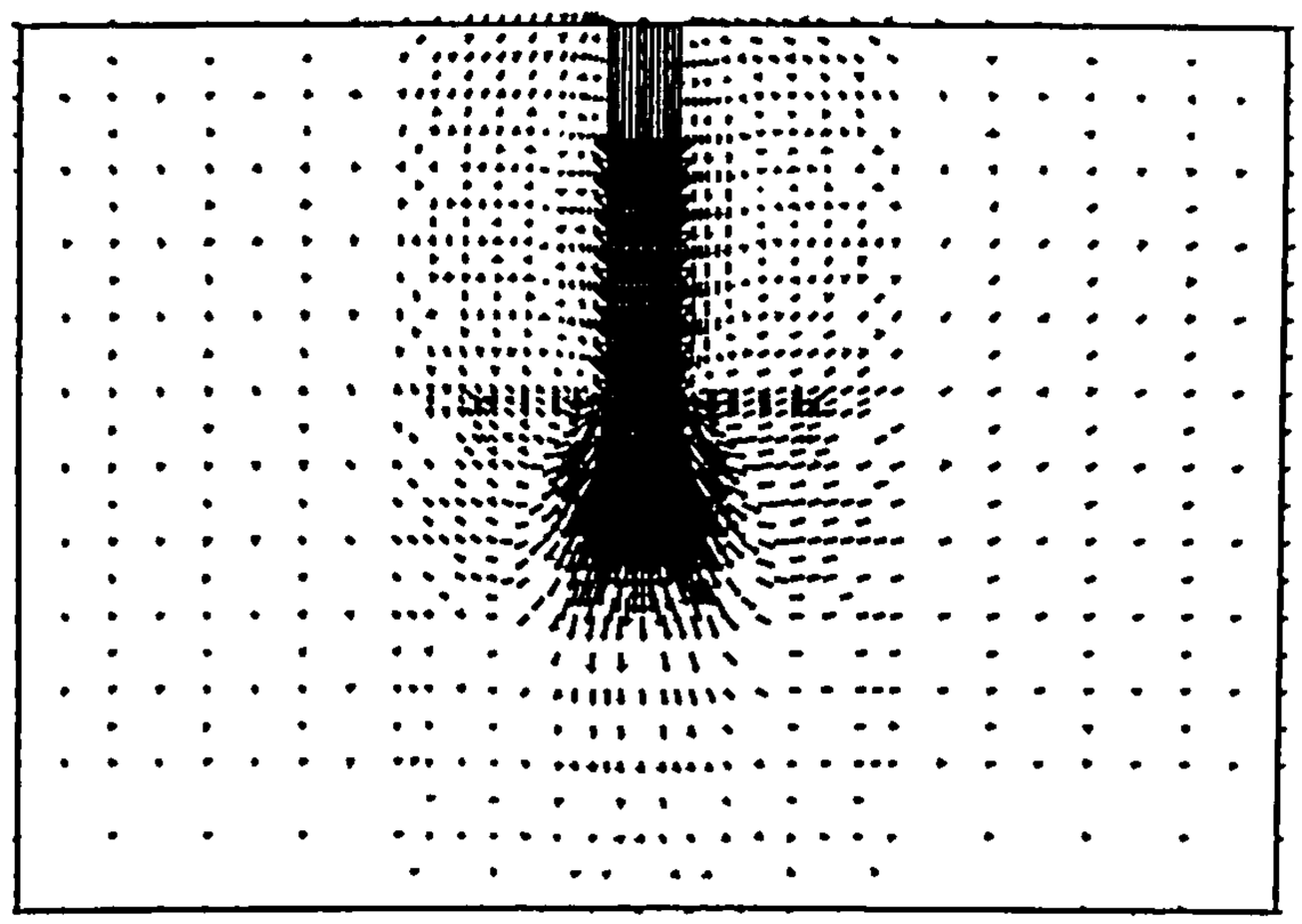

Figure 6.49: Displacement vectors due to earthquake motion

It is clear that no failure mechanism has developed and the predominant movement of the foundation is a vertical settlement. The vertical displacement history of point A shown in Figure 6.49 is plotted in Figure 6.50.

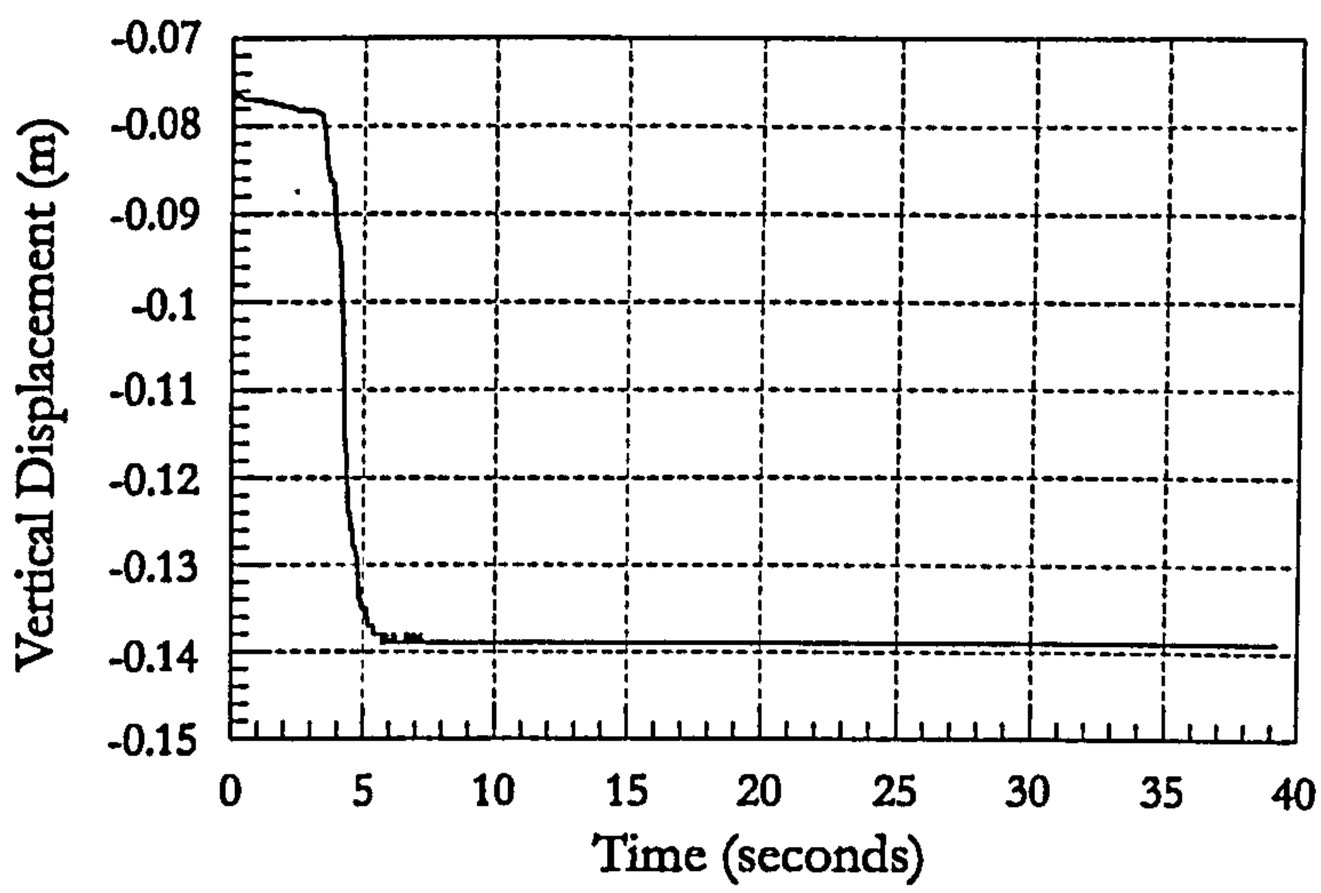

Figure 6.50: Vertical displacement history of point A

The initial displacement of 7.7 cm represents the vertical displacement of the foundation at working load, which corresponds with the value shown in Figure 6.20. The vertical displacement plot follows a similar pattern to the stress plots presented in the previous section. The foundation only settles during the most intense period of the earthquake, which is between the period of 3 and 5 seconds into the earthquake record. The settlement stabilises very quickly after the most intense part

of the earthquake to a value of 13.9cm, which represents an 80% increase above the displacement at working load.

6.8.3 Discussion

The principal effects of the earthquake on the behaviour of the foundation can be summarised as follows:

- The seismic wave has caused a reduction in horizontal stress around the foundation and an increase in both horizontal and vertical stress below the foundation.
- The reduction in horizontal stress around the foundation has reduced the load carrying capacity of the foundation shaft and consequently the base capacity has been further mobilised to maintain equilibrium.
- The vectors of incremental displacement during the earthquake show no failure mechanism forming, however, they do illustrate the complex interaction that occurs between the foundation and surrounding soil.
- The displacement vectors accumulated during the period of the earthquake around the foundation indicate large vertical displacements, but give no indication of a failure mechanism.
- The seismically induced shear stresses around the base of the foundation have caused large plastic deformations to accumulate, resulting in considerable foundation settlement.

The overall behaviour of the dynamic analysis is considerably different to that found with the pseudo static analysis. The principal difference is the absence of a failure mechanism in the dynamic analysis. The results of the pseudo static analysis demonstrated that the assumption of a Prandtl type failure mechanism for limit equilibrium calculations may not be realistic. The results presented by Potts (2000) demonstrated that no consistent failure mechanism could be identified for all cases. The results of the dynamic finite element analysis presented in Section 6.8.2.2 showed that the Athens earthquake of 1999 scaled to a maximum acceleration of 0.2*g* does not initiate any type of failure mechanism, but does however, cause the foundation to settle a significant amount. This type of behaviour is more consistent with that described for real events in Section 6.2. It was noted that the number of

bearing capacity type failures observed in the field are very few, whilst the most common form of damage sustained during earthquakes is significant amounts of settlement.

The reduction in horizontal stress caused by the earthquake, and the subsequent reduction in shaft capacity illustrates why friction piles should be avoided in seismic areas. The foundation used in this study is predominantly end bearing and therefore did not fail when the load carried by the foundation shaft was transferred to the base. If, however, a larger proportion of the working load where distributed to the shaft, the results presented here demonstrate that a significant earthquake would cause the load to transfer to the base and may cause catastrophic failure.

6.8.4 Analyses Using Wider Mesh

As mentioned in Chapter 3, the boundary conditions assumed in dynamic finite element analyses introduce complications that are additional to those that already exist with static analysis. At present ICFEP cannot model absorbing boundary conditions and therefore all the analyses presented in this thesis assume reflecting boundaries. With regard to the foundation analysis, the reflecting boundary along the base of the mesh is equivalent to having a stiff rock at this depth. This is a common scenario in reality and will be assumed for the foundation analyses presented in this thesis. The boundary conditions on the side of the mesh imply that an identical foundation is present on both sides of the original foundation at a spacing of 42 meters. Therefore, because we are only interested in the behaviour of a single foundation it is important to determine what effect the location of the side boundaries has on the foundation analysis. For this purpose the analysis using the Athens earthquake record scaled to a maximum acceleration of 0.2*g* was repeated using a wider mesh. The mesh shown in Figure 6.12 was used with extra elements placed on both sides to make the total width of 82 meters. The displacement history for point A is compared with the results from the standard mesh in Figure 6.51.

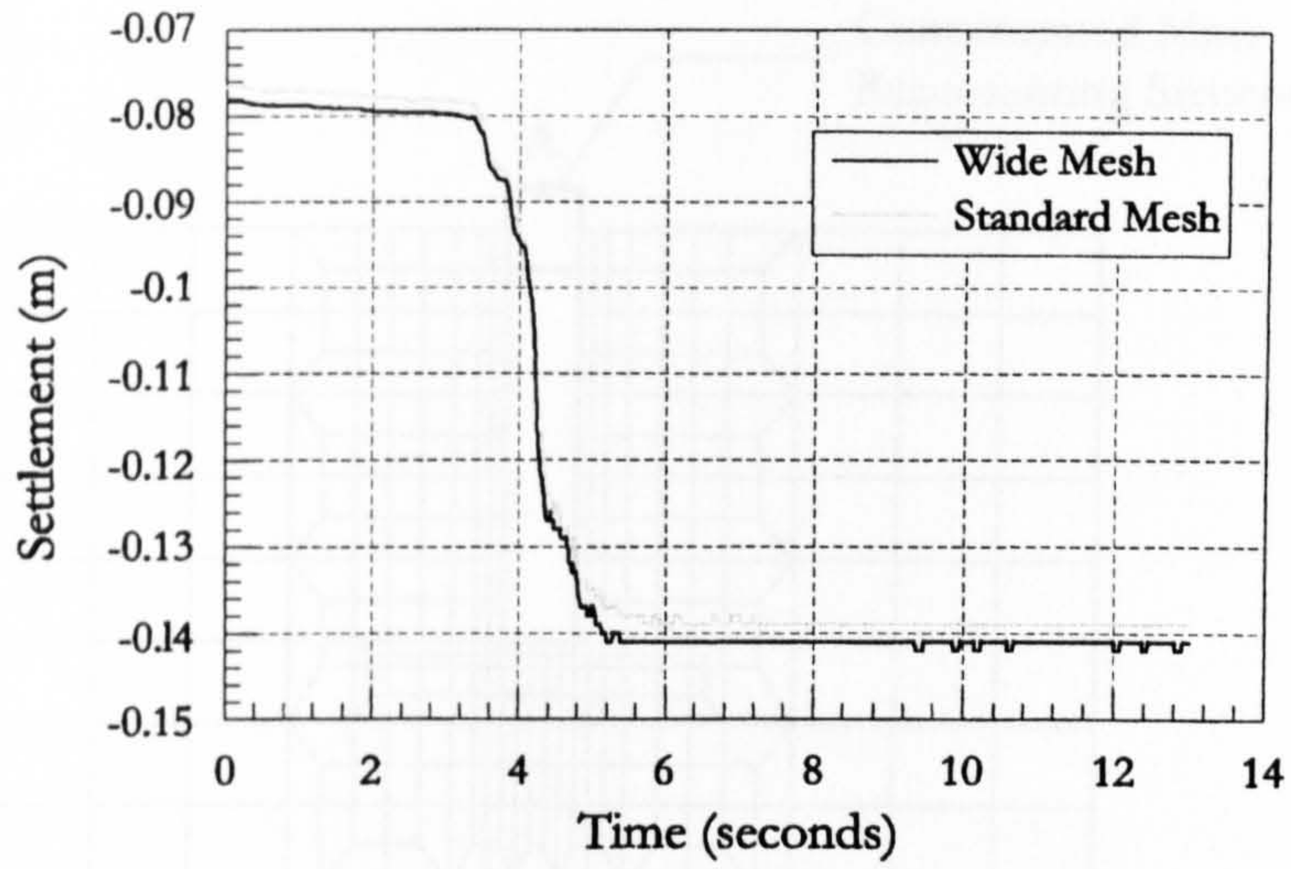

Figure 6.51: Settlement history for point A subjected to 0.2*g* Athens earthquake

The settlement of the foundation at working load is slightly different, however for the duration of the earthquake the difference between the two analyses did not change. This implies that the side boundaries of the mesh are sufficiently far away so that they do not influence the behaviour of the foundation significantly.

6.8.5 Analysis Including Structural Mass

The working load in the preceding analyses was reached by applying a boundary stress on the top of the foundation. This was to isolate the effect of inertia forces in the ground from the inertia forces in the building. This is of course an unrealistic situation as the working load would in reality be applied by the structure above the foundation, which would generate its own inertia forces when an earthquake occurred. To investigate the influence that these inertia forces may have on the behaviour of the foundation, the analysis was repeated with the working load being applied by placing a concentrated mass on top of the foundation and then gradually increasing the vertical body force in it until the correct working load was achieved. This set up is illustrated in Figure 6.52.

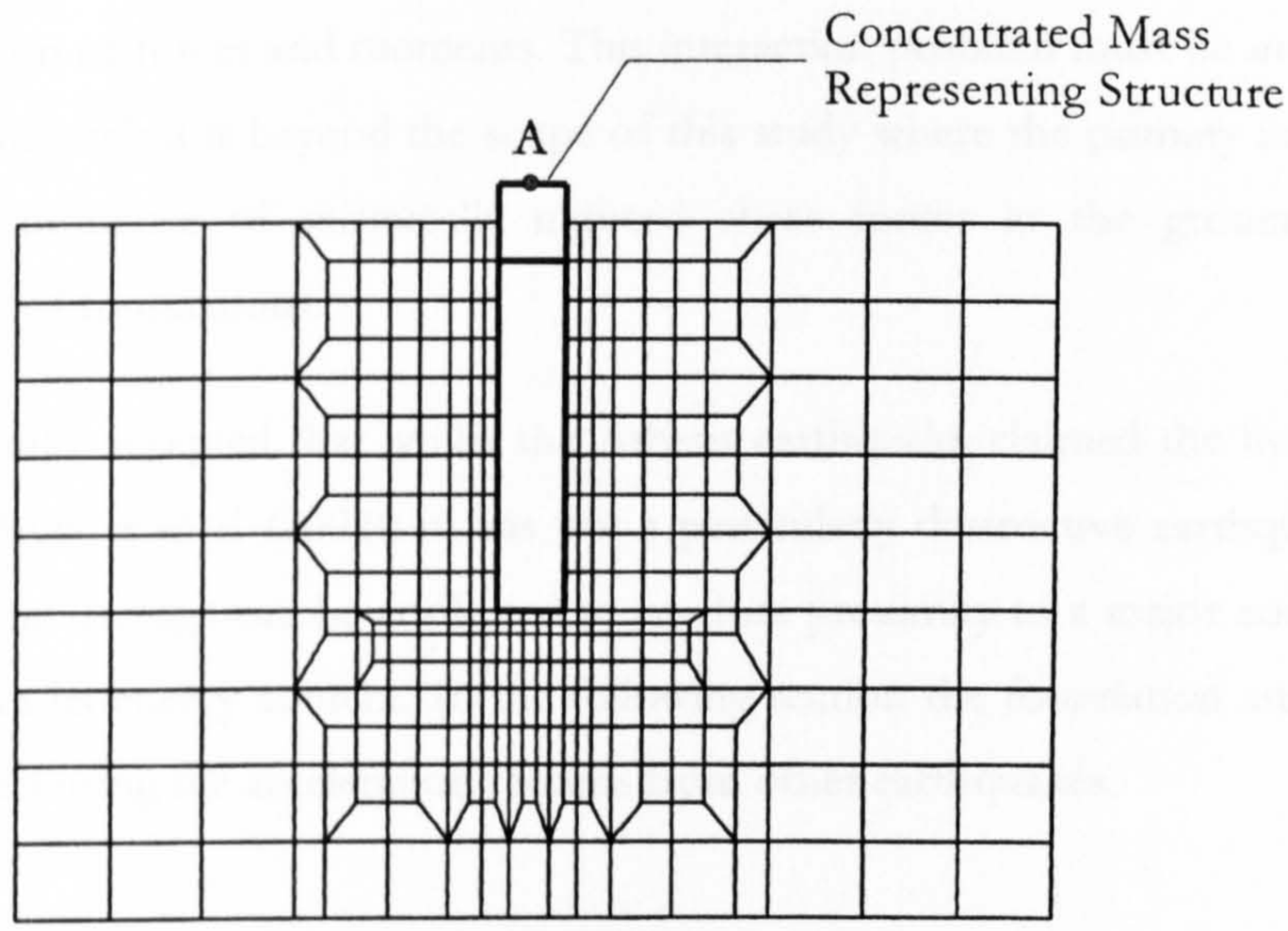

Figure 6.52: Detail of mesh used in analysis including structural mass

The elements at the top of the foundation used to represent the concentrated mass are extended above the ground surface to ensure that no moment is induced about the top of the foundation. The displacement history of point A is compared with the results from the analysis that did not include the structural mass in Figure 6.53.

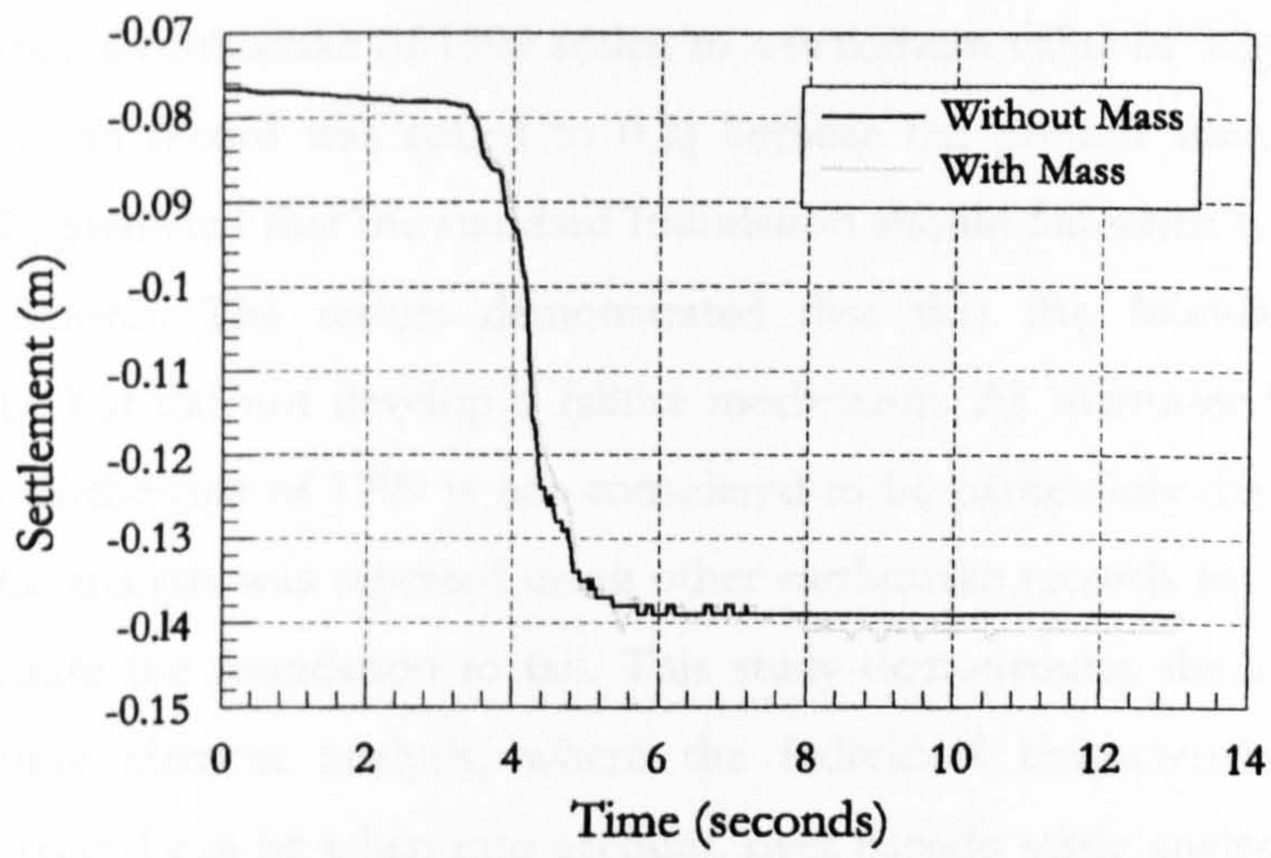

Figure 6.53: Settlement history of point A subjected to Athens 0.2*g* earthquake with and without structural mass

The result of including the structural mass in the analysis is a slightly higher settlement at point A, although the difference is very small. Of course in reality the structure will be much more complicated than the lumped mass used in this analysis. The structure will vibrate in different modes and apply a complex

combination of forces and moments. This interaction problem must be investigated further, although it is beyond the scope of this study where the primary interest lies with the influence of seismically induced shear forces in the ground on the behaviour of foundations.

It is generally accepted that whilst the Athens earthquake claimed the lives of 455 people (Pavlides *et al.* (2002)) it was not a particularly destructive earthquake. The cause of the damage can be attributed to its close proximity to a major conurbation rather than its energy content. In the following section the foundation analysis will be repeated using the acceleration records from other earthquakes.

6.9 Dynamic Finite Element Analysis Results using Different Input Earthquakes

6.9.1 Introduction

The analysis presented in the previous section used the acceleration record from the Athens earthquake of 1999 scaled to a maximum value of 0.2*g* as its input. The acceleration record was scaled to 0.2*g* because the pseudo static analysis of Potts (2000), predicted that the standard foundation should fail when subjected to a 0.21*g* acceleration. The results demonstrated that that the foundation settled considerably, but did not develop a failure mechanism. As mentioned previously, the Athens earthquake of 1999 is not considered to be particularly destructive and therefore the analysis was repeated using other earthquake records to investigate if these can cause the foundation to fail. This study demonstrates the advantage of dynamic finite element analysis, where the individual characteristics of each earthquake record can be taken into account, over pseudo static analysis, in which only a constant acceleration can be applied.

6.9.2 Description of Earthquake Records

The three additional earthquake records chosen for this study are described in Table 6.4.

Name	Country	Station	Component	Date	Magnitude	$\ddot{u}_{max}$ (m/s2)	f_{min} (Hz)
Kocaeli	Turkey	Izmit	E-W	17/8/99	Ms=7.8	2.193	0.5
Tabas	Iran	Dayhook	E-W	16/9/78	Ms=7.33	3.317	0.475
Spitak	Armenia	Gukasian	N-S	7/12/88	Ms=6.76	1.794	0.3

Table 6.4: Details of earthquake records used in study

Each record was scaled to a maximum acceleration of 0.2*g* and filtered in the same fashion as described in Section 6.7 to eliminate the drift of the displacement time history away from the zero displacement axis. The minimum frequency used in this process for each record is given in the final column of Table 6.4. The filtered acceleration and displacement records and the Fourier spectra of each earthquake record are shown in the following figures.

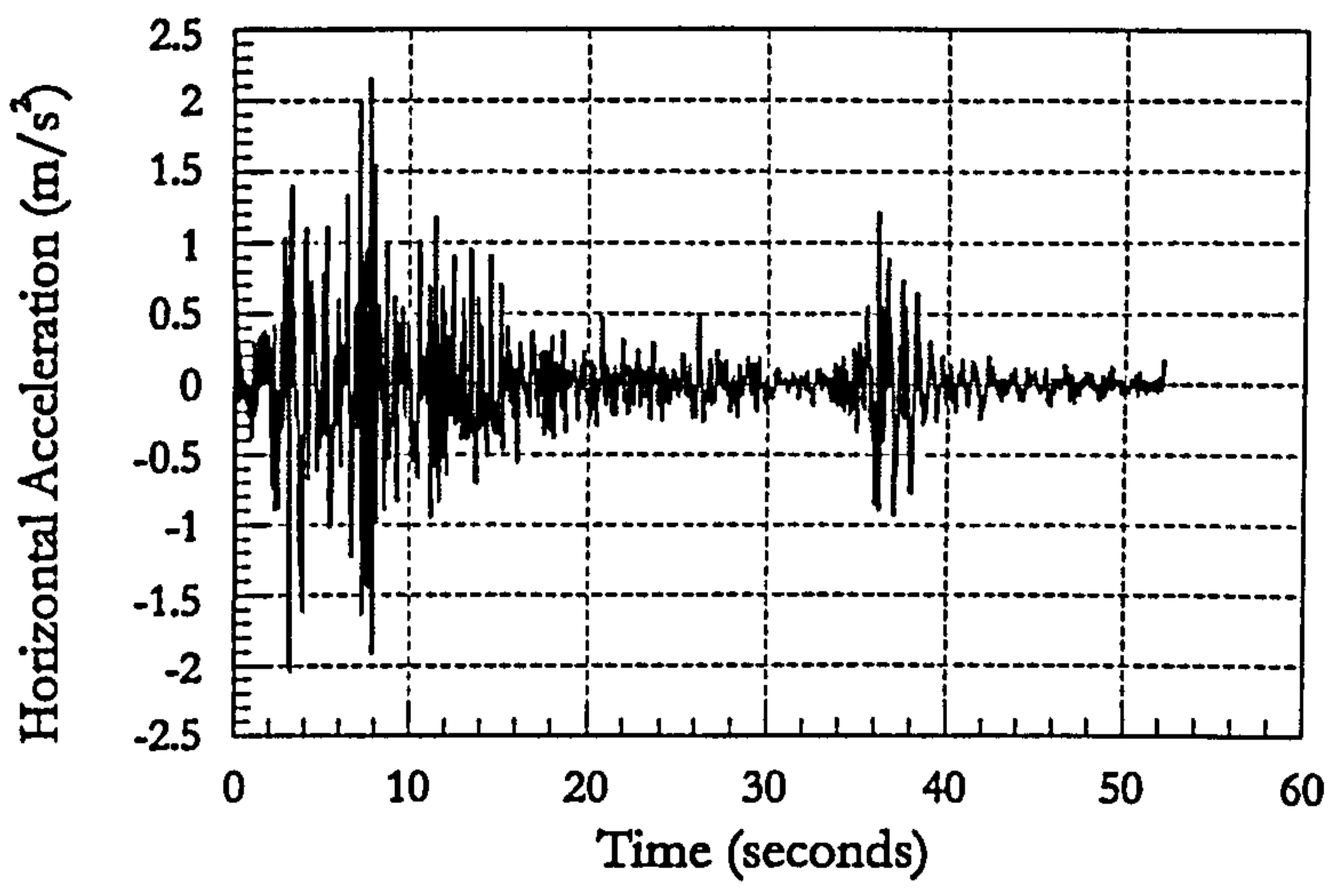

Figure 6.54: Kocaeli earthquake acceleration record scaled to 0.2*g*

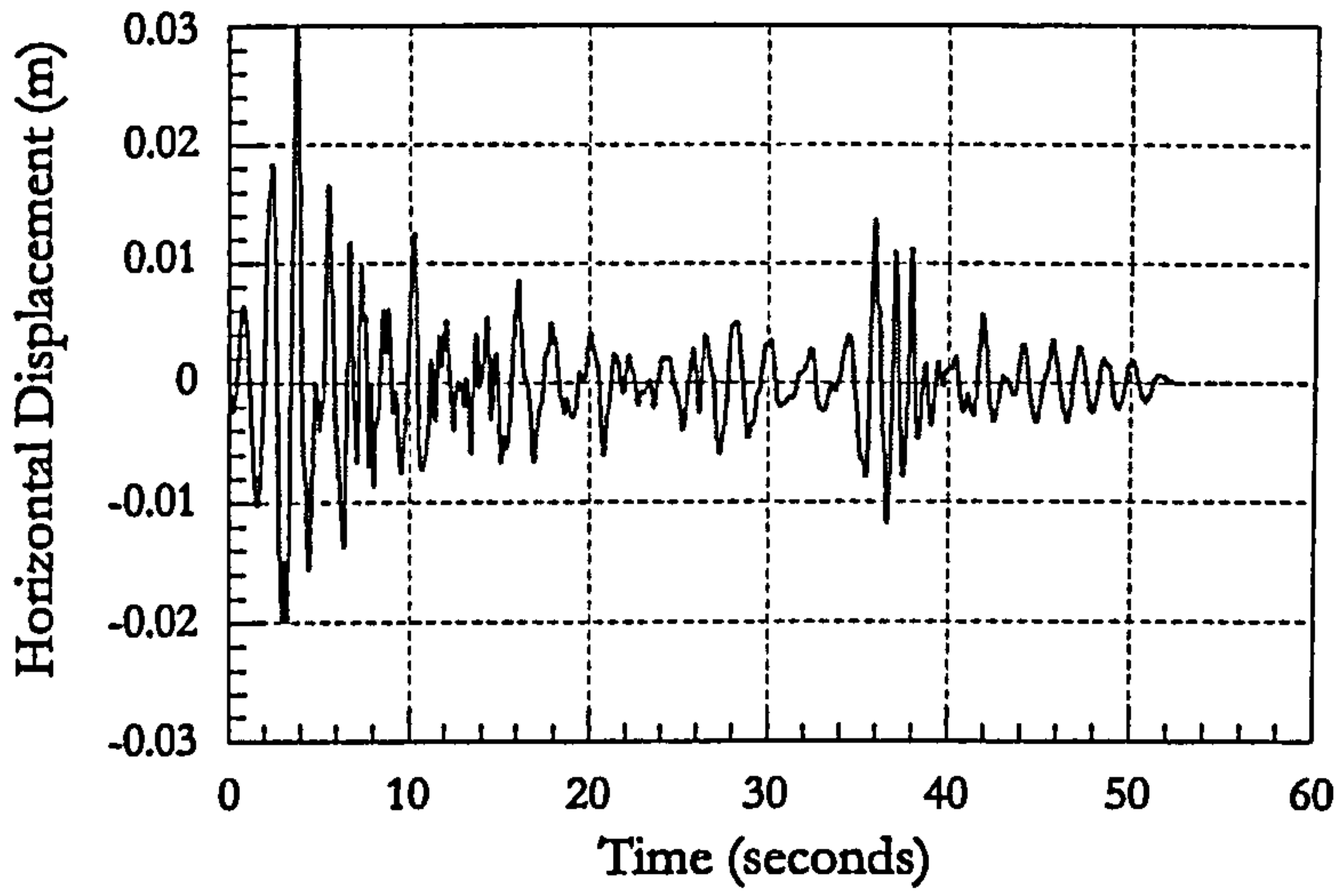

Figure 6.55: Kocaeli earthquake displacement record

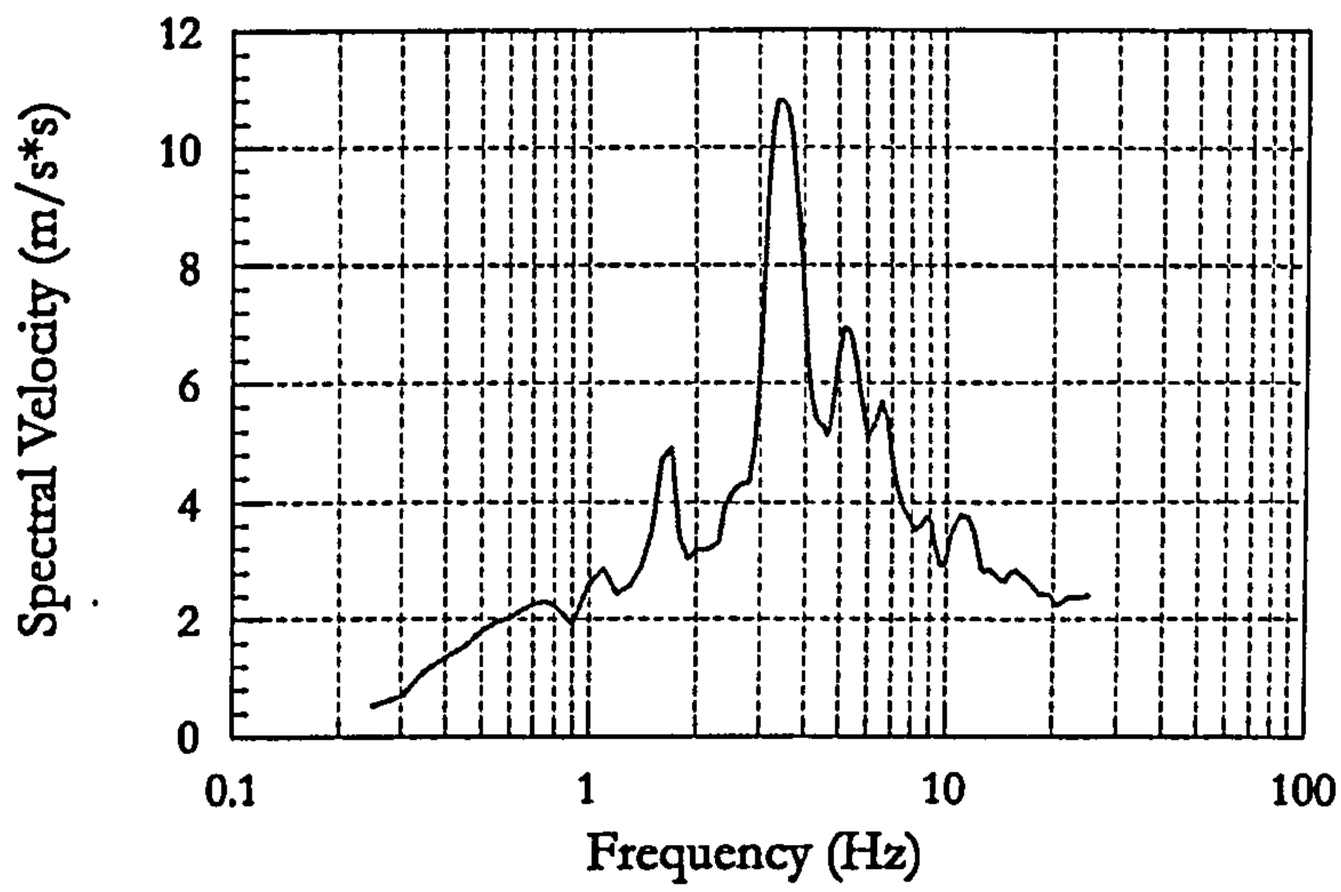

Figure 6.56: Kocaeli earthquake Fourier spectrum

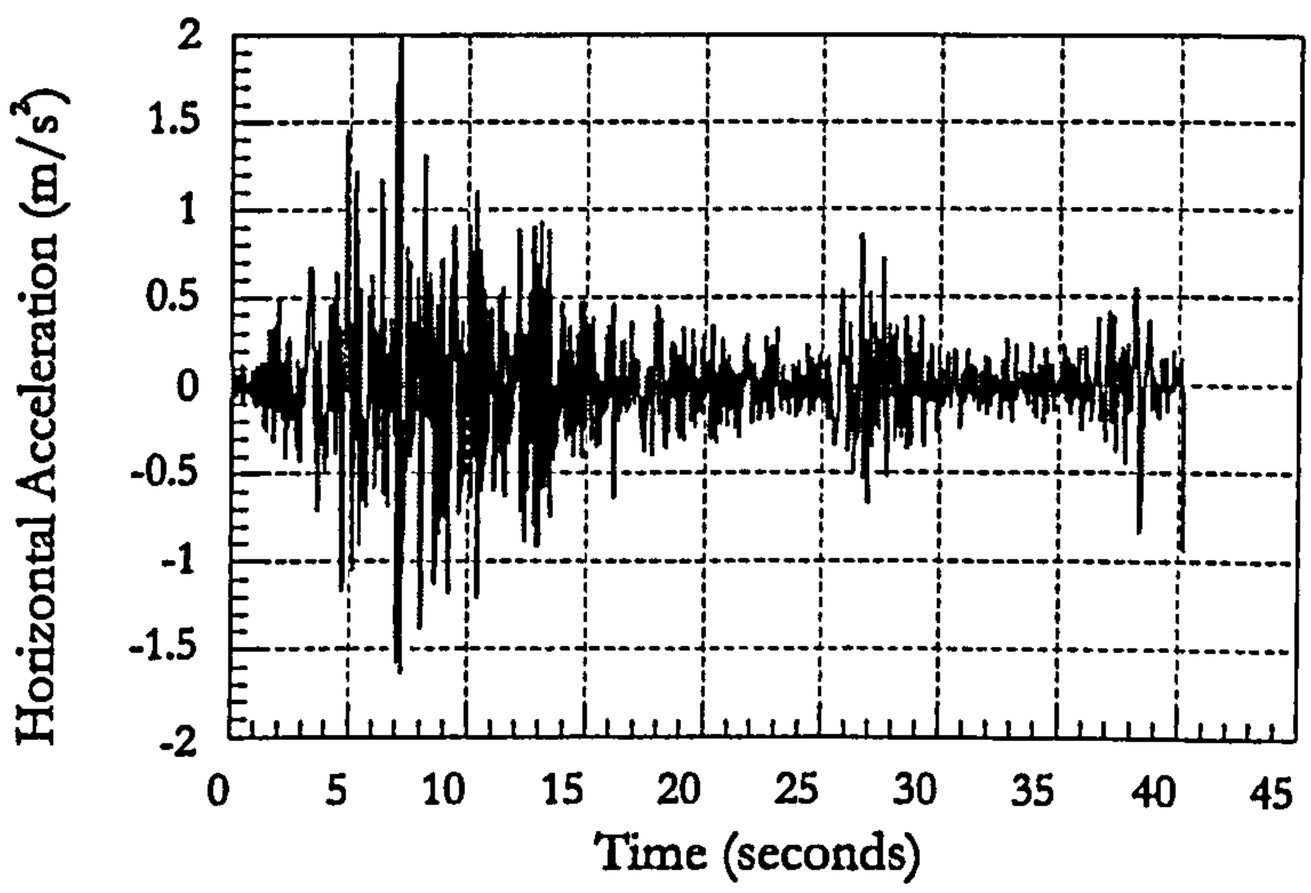

Figure 6.57: Tabas earthquake acceleration record scaled to 0.2*g*

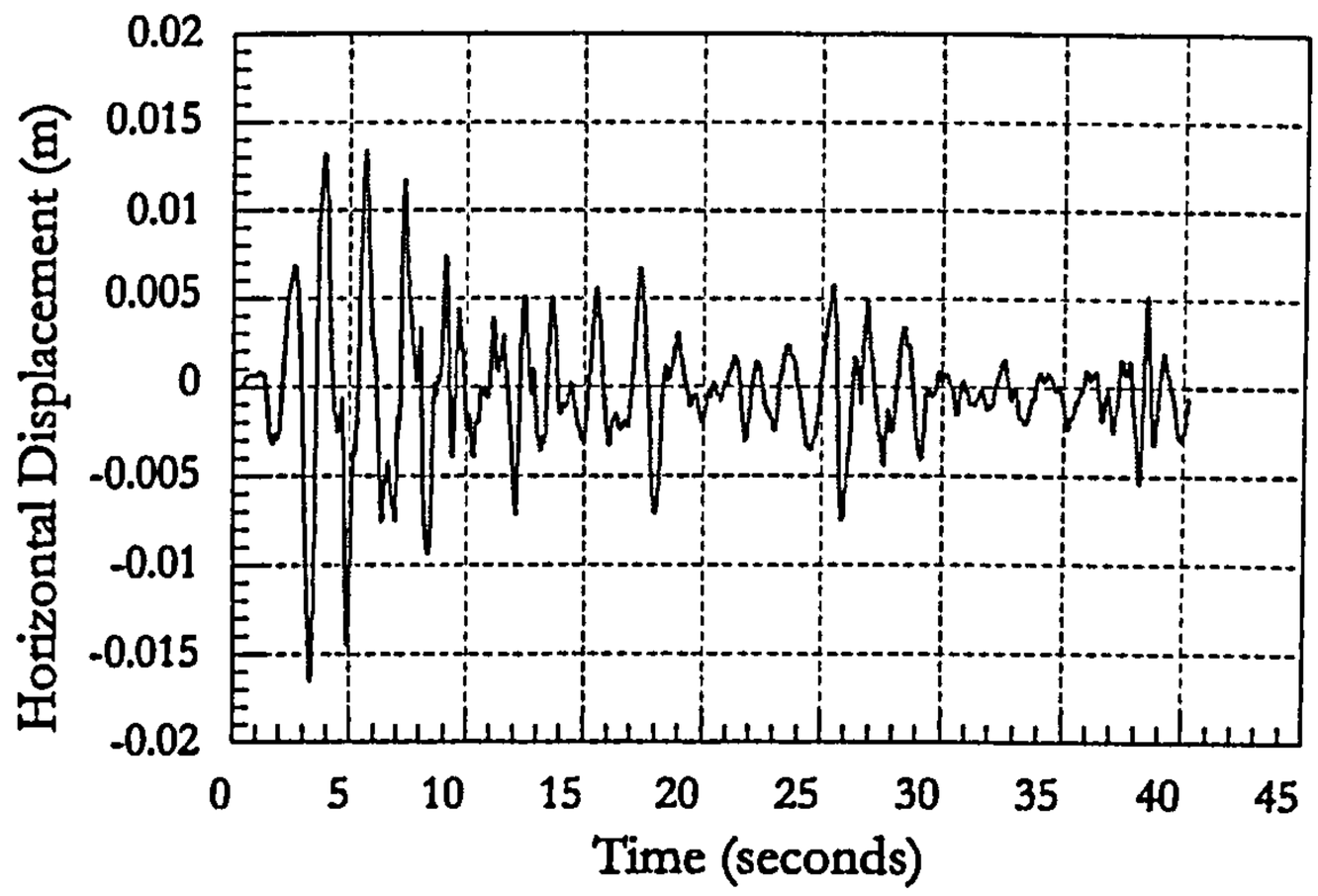

Figure 6.58: Tabas earthquake displacement record

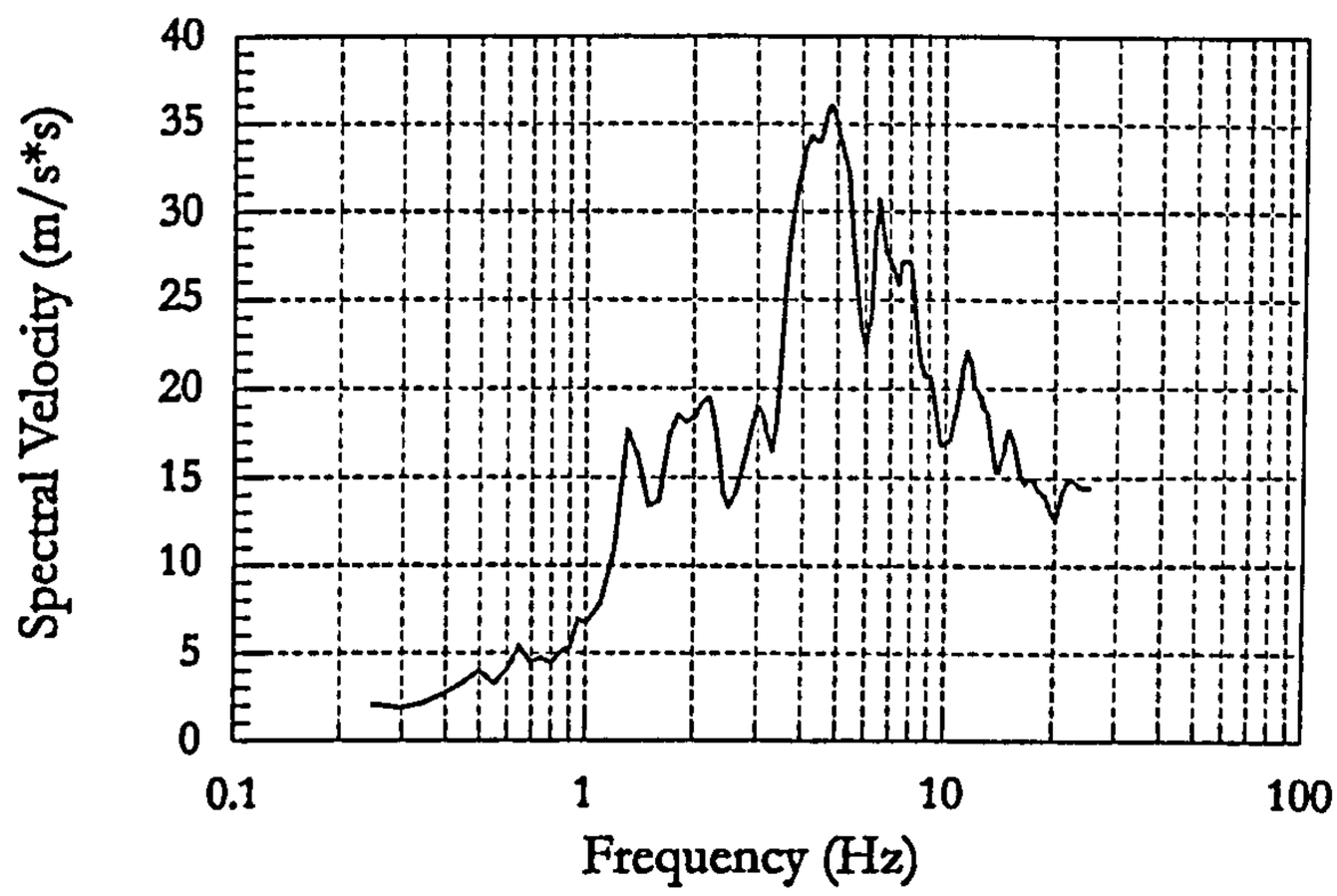

Figure 6.59: Tabas earthquake Fourier spectrum

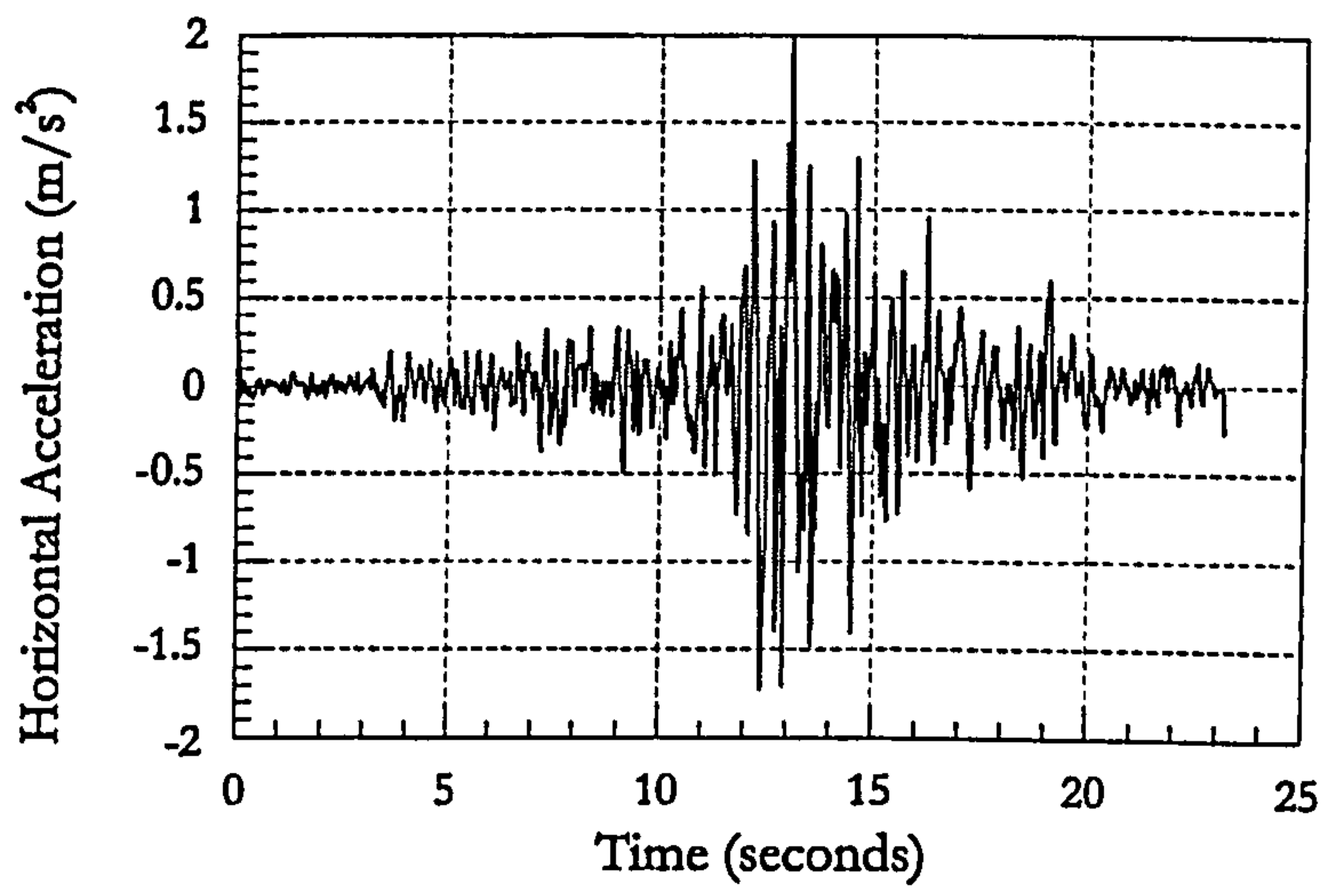

Figure 6.60: Spitak earthquake record scaled to 0.2*g*

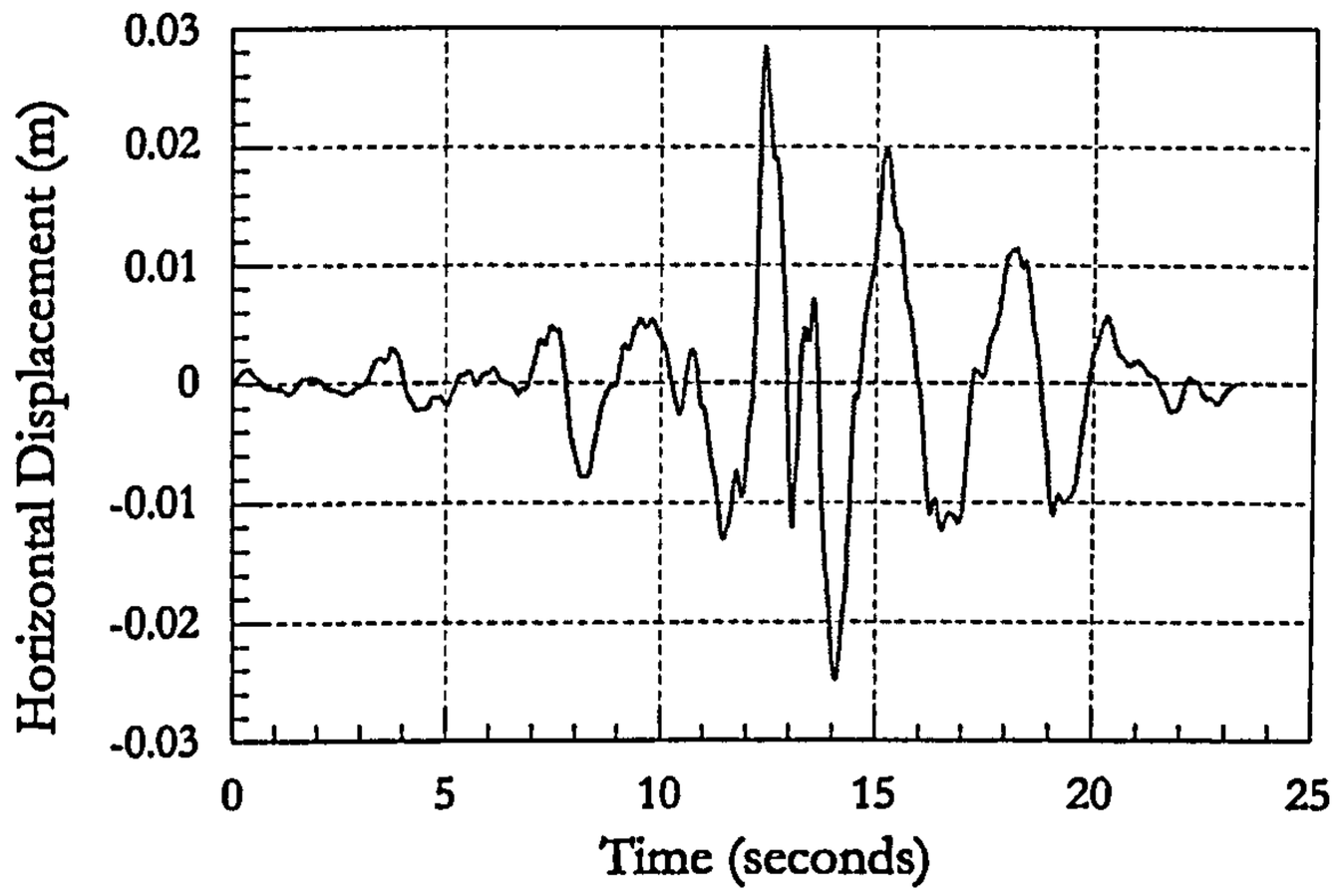

Figure 6.61: Spitak earthquake displacement record

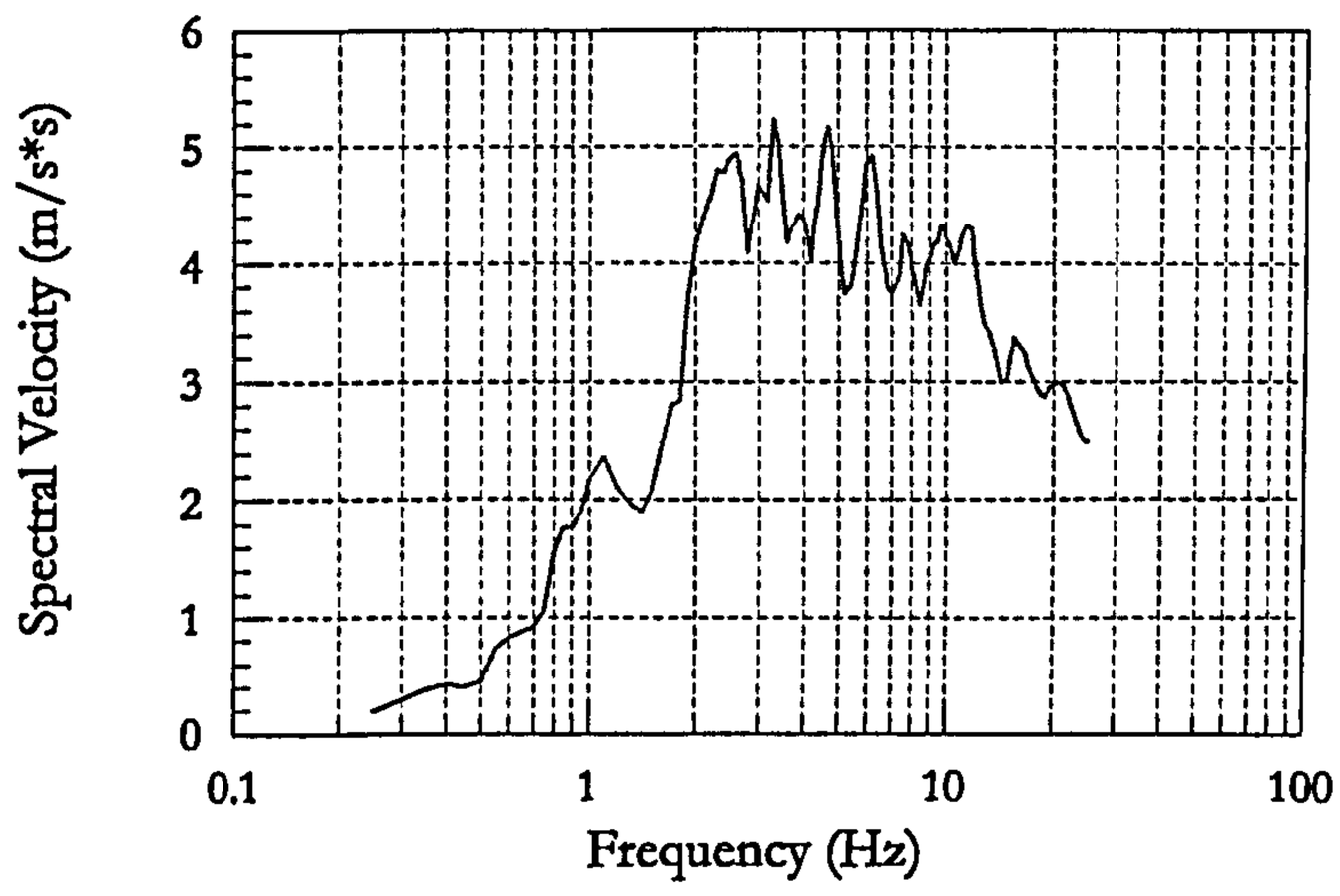

Figure 6.62: Spitak earthquake Fourier spectrum

6.9.3 Results

Each analysis behaved in a similar fashion to the Athens earthquake. All exhibited a reduction in horizontal stress around the foundation and an increase in horizontal and vertical stress at the base of the foundation. However, the earthquake induced settlement of the foundation varied considerably between each earthquake. The settlement of point A shown in Figure 6.49 for each analysis is shown in Figure 6.63.

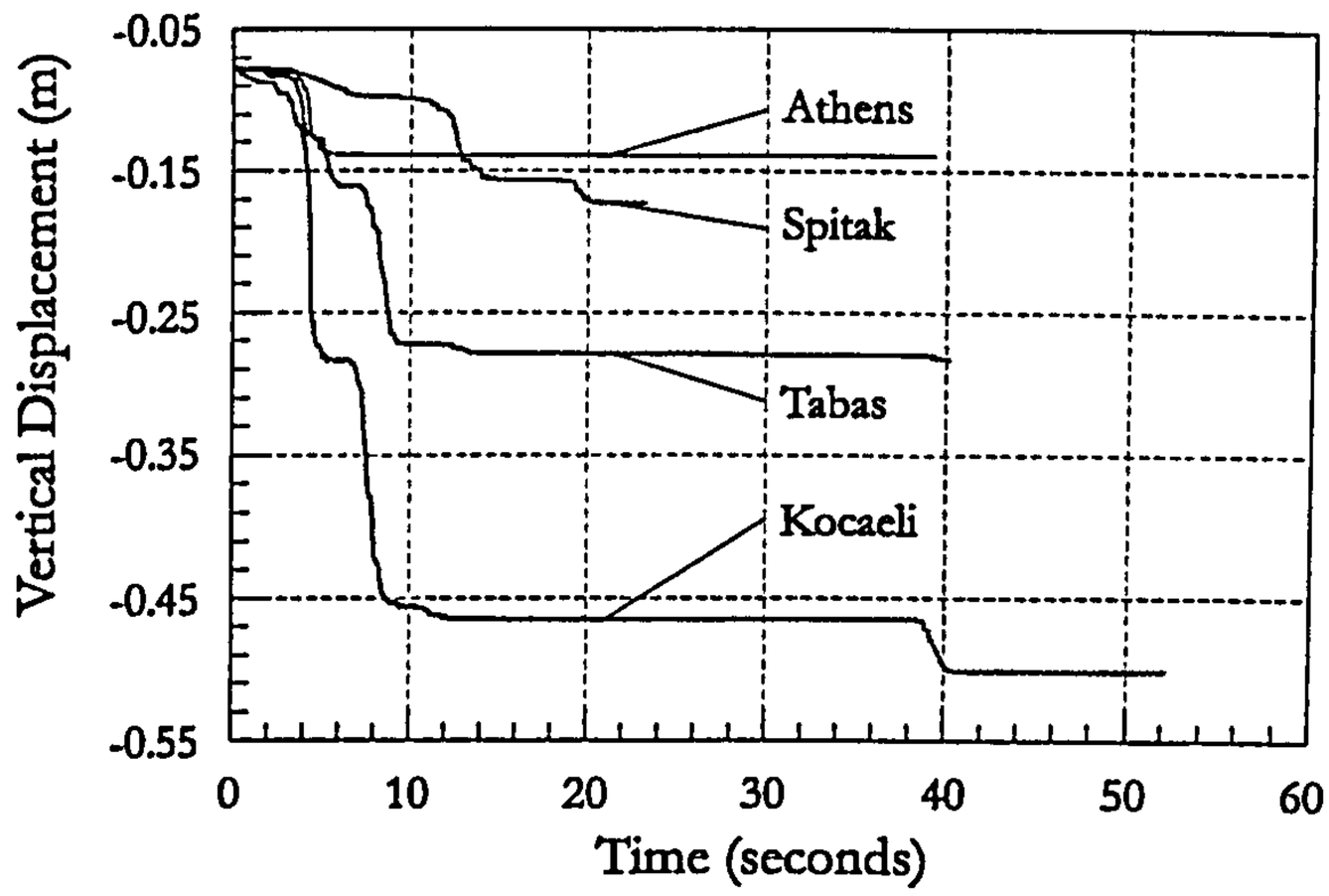

Figure 6.63: Settlement of point A for different earthquakes scaled to 0.2*g*

All analyses started from the same displacement at working load (7.7cm), however clearly the Kocaeli earthquake was the most damaging of all the records. The earthquake induced settlement was 42.5cm which represents a 550% increase over the displacement at working load. The rapid settlements observed in each plot coincide with intense periods of shaking observed in their respective acceleration records. For example, consider the settlement plot for the Kocaeli earthquake. The graph shows three periods of rapid settlement. The first is between 3.0 and 5.0 seconds into the earthquake record and the second and third occur in the intervals 7.0 to 9.0 seconds and 38.0 to 41.0 seconds respectively. These periods of rapid settlement can be correlated with periods of intense shaking identified in the acceleration record shown in Figure 6.54. In between these periods the foundation does not settle, implying that the foundation begins to settle when some threshold acceleration is exceeded. The results for each analysis are summarised in Table 6.5.

Earthquake	Earthquake Induced Settlement (cm)	Percentage Increase
Athens	6.2	80.5%
Spitak	9.6	124.7%
Tabas	20.6	267.5%
Kocaeli	42.5	551.9%

Table 6.5: Summary of results for 0.2*g* earthquakes

The results of this study clearly demonstrate that the peak ground acceleration, which is commonly used in design codes, does not give an indication of the destructive potential of an earthquake. The Athens earthquake of 1999 is clearly the least destructive of all the records and produces 85% less settlement than the Kocaeli earthquake, although they have the same peak ground acceleration.

To further investigate the behaviour of the foundation when subjected to earthquakes with different energy content, the analysis was repeated with the four earthquake records described previously scaled to different peak acceleration values. The analyses performed are as follows:

Athens earthquake (7/9/1999):	0.1*g*, 0.2*g*, 0.3*g*, 0.4*g*, 0.5*g*
Kocaeli earthquake (17/8/1999):	0.05*g*, 0.1*g*, 0.125*g*, 0.175*g*, 0.2*g*, 0.3*g*
Tabas earthquake (16/9/1978):	0.1*g*, 0.166*g*, 0.2*g*, 0.25*g*, 0.3*g*, 0.4*g*
Spitak earthquake (7/12/1988):	0.1*g*, 0.2*g*, 0.3*g*, 0.4*g*, 0.5*g*

To ensure that the displacement record does not drift from the zero displacement axis, each record was filtered using the same procedure as described in Section 6.7 and the same frequency limits described in Table 6.4. The earthquake induced settlement for each analysis is plotted against their respective peak ground accelerations in Figure 6.64.

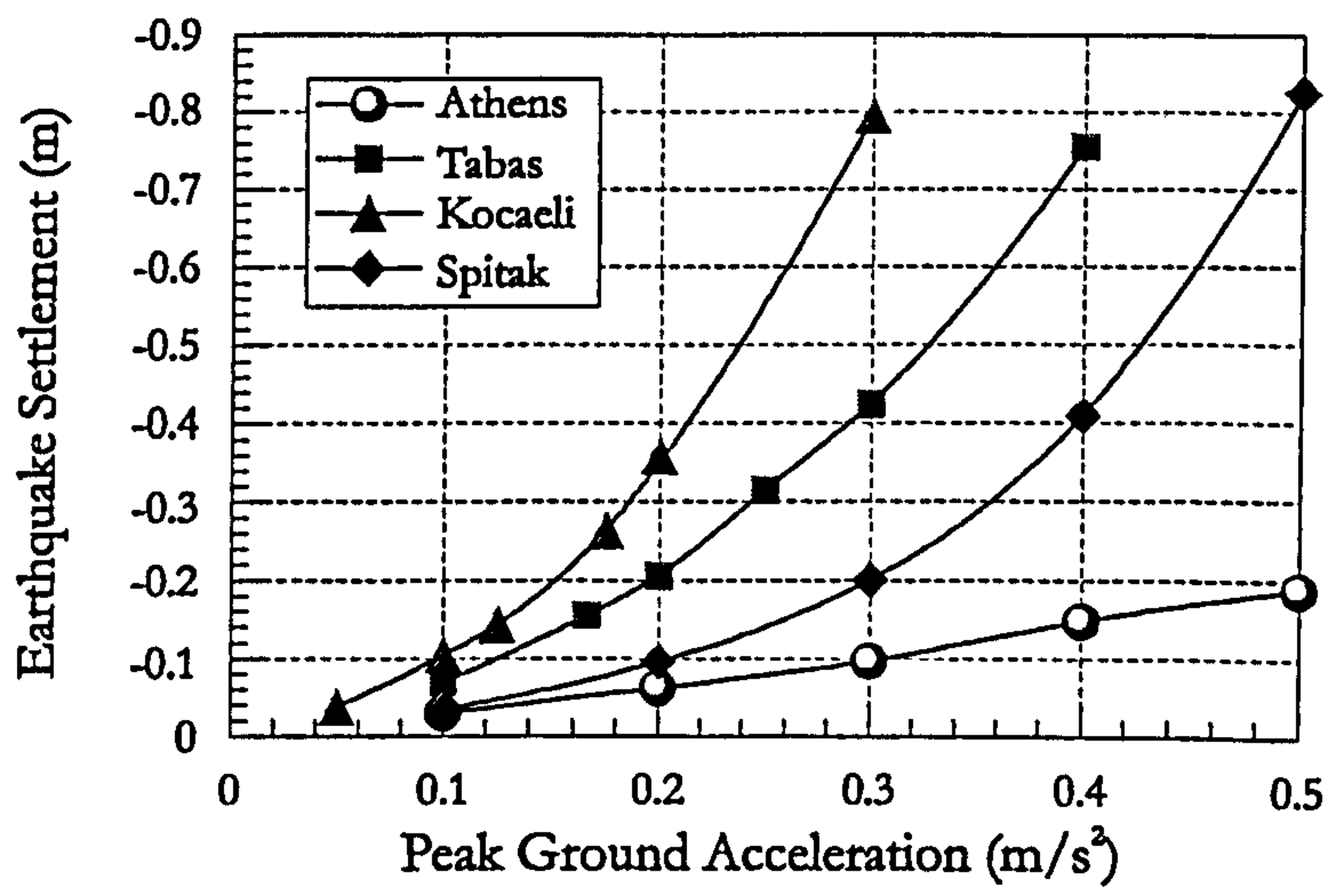

Figure 6.64: Earthquake induced settlement for the four earthquakes scaled to different peak ground accelerations

Of the 22 earthquakes analysed the most destructive of all was the Spitak record scaled to a maximum acceleration of 0.5*g*. This earthquake caused 82.5cm of settlement, however the Kocaeli earthquake scaled to 0.3*g* gave only slightly less settlement (79.5 cm) and is therefore overall the most destructive record. The results demonstrate that for each record the peak ground acceleration is related to the settlement of the foundation, however, between records there is a large discrepancy between records with similar peak acceleration values. The problem of finding a single parameter that can characterise an earthquake record has been the focus of attention for many seismologists since earthquakes have been studied. Many parameters have been proposed that characterise the amplitude, frequency content and duration of strong ground motion, although it is regarded as impossible to combine all three in a single parameter (Jennings (1985) and Joyner and Boore (1988)). The results of the study presented in this chapter demonstrate that the maximum acceleration values from an earthquake record cannot be used to assess the destructive potential of an earthquake. The strong motion parameter proposed by Arias (1970) attempts to include the total duration of the earthquake motion and a measure of the prolonged intensity of shaking by integrating the acceleration squared over the entire earthquake motion. The Arias intensity (I_a) is defined by Equation 6.21.

$$I_a = \frac{\pi}{2g}\int_0^{T_d}\left[a(t)\right]^2 dt \tag{6.21}$$

Where g is the acceleration due to gravity and $a(t)$ is the earthquake acceleration record. The cumulative absolute velocity, given by Equation 6.22, has also been proposed as a ground motion parameter and has been found to correlate well with structural damage potential (Kramer (1996)):

$$CAV = \int_0^{T_d}\left|a(t)\right|dt \tag{6.22}$$

where T_d is the duration of the strong motion. The main difficulty in assessing different strong motion parameters is the lack of earthquake records close to recorded damage. The results of the finite element analyses presented in this chapter will now be used to try and correlate structural damage (in this case foundation settlement) with strong motion parameters calculated from the input earthquake

records. The following parameters will be used in this investigation; *acceleration squared (AS), velocity squared (VS), displacement squared (DS), absolute acceleration (AA), absolute velocity (AV)* and *absolute displacement (AD),* which are defined by the following equations:

$$AS = \int_0^{T_d} \left[a(t)\right]^2 dt \tag{6.23}$$

$$VS = \int_0^{T_d} \left[v(t)\right]^2 dt \tag{6.24}$$

$$DS = \int_0^{T_d} \left[d(t)\right]^2 dt \tag{6.25}$$

$$AA = \int_0^{T_d} \left|a(t)\right| dt \tag{6.26}$$

$$AV = \int_0^{T_d} \left|v(t)\right| dt \tag{6.27}$$

$$AD = \int_0^{T_d} \left|d(t)\right| dt \tag{6.28}$$

where $v(t)$ and $d(t)$ are the velocity and displacement time histories of the earthquake record respectively found by integrating the filtered acceleration records using the Newmark scheme (δ = 0.6, α = 0.3025). The earthquake induced settlement is plotted against each parameter for each earthquake record in the following figures.

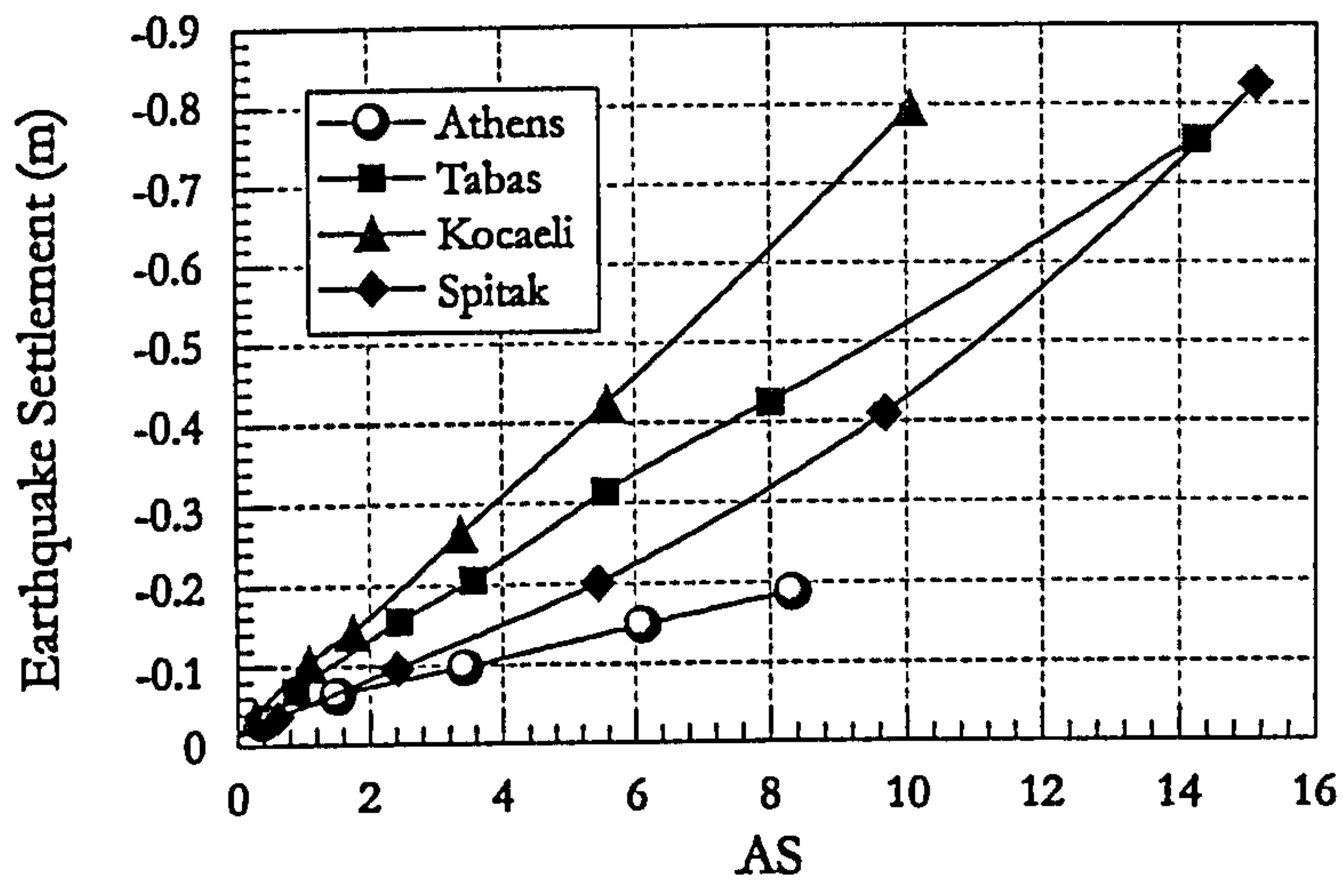

Figure 6.65: AS parameter against earthquake induced settlement

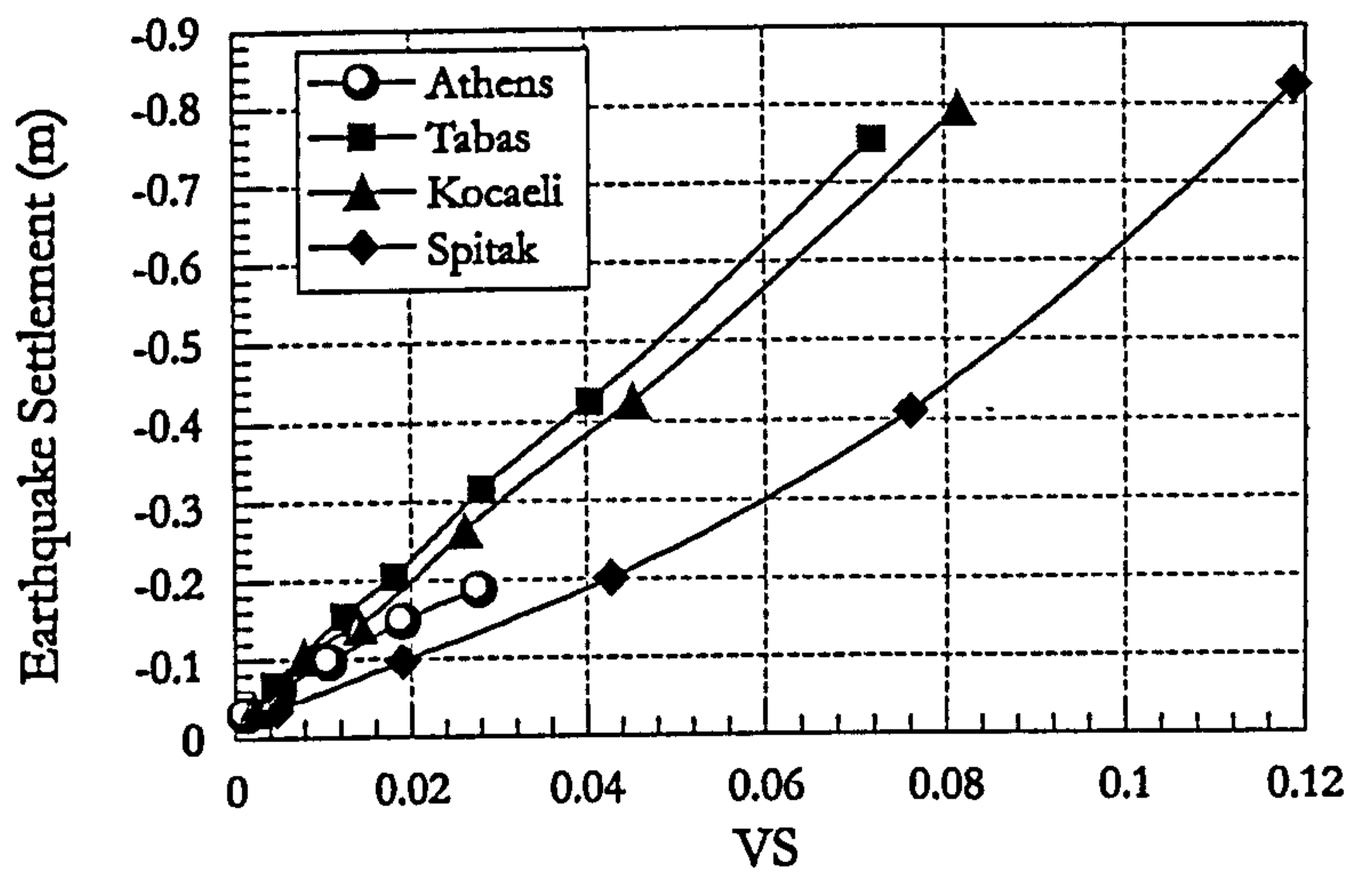

Figure 6.66: VS parameter against earthquake induced settlement

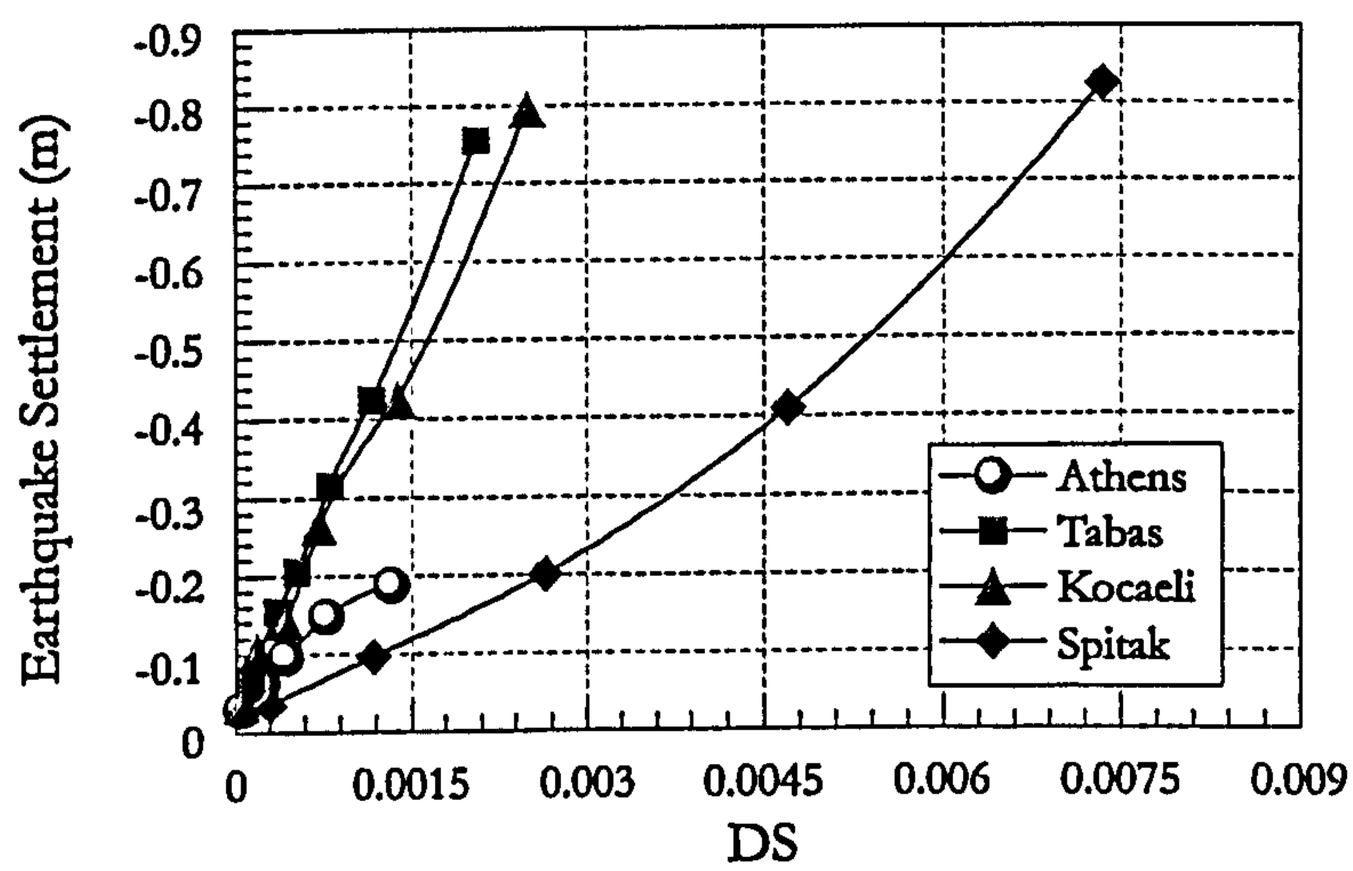

Figure 6.67: DS parameter against earthquake induced settlement

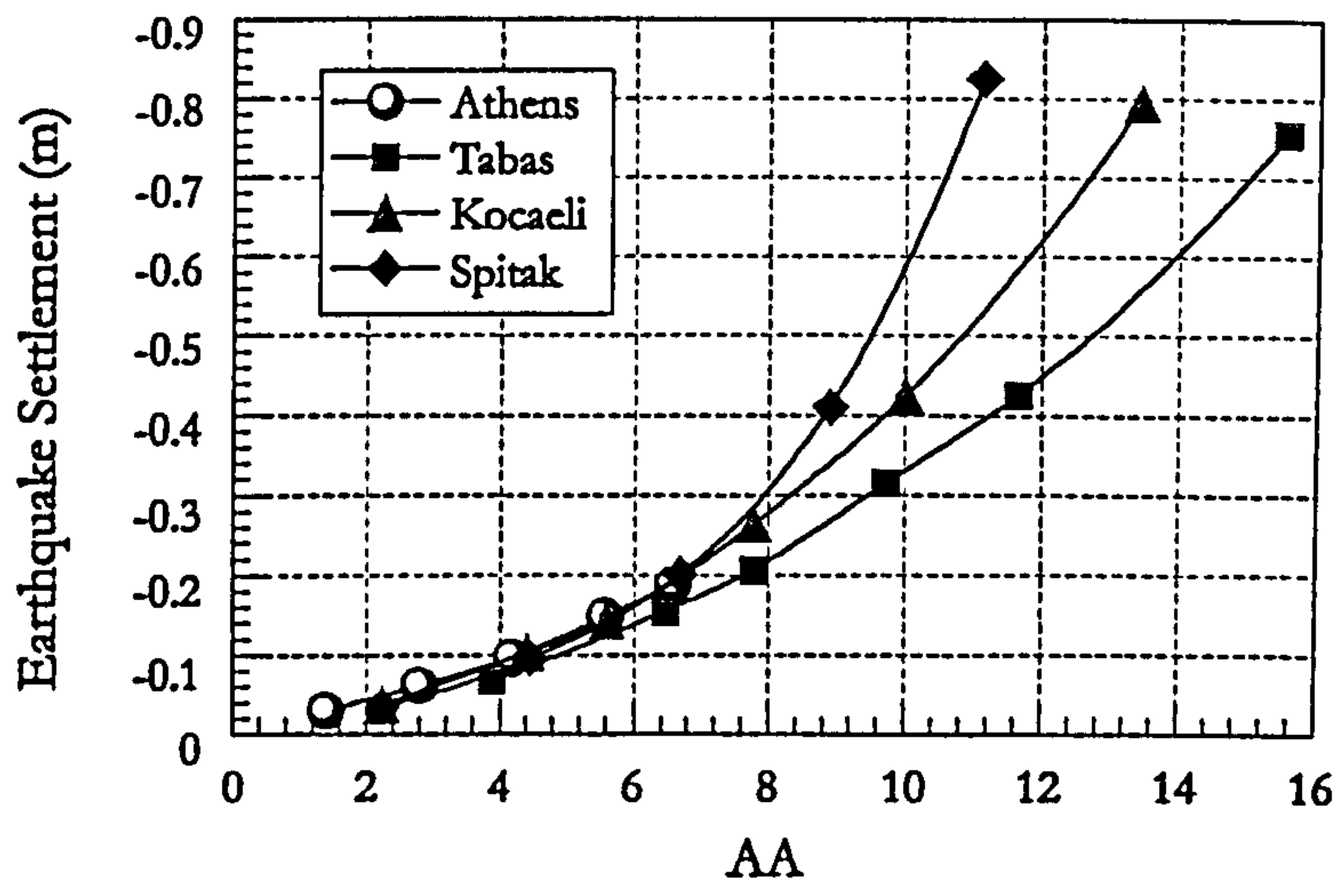

Figure 6.68: AA parameter against earthquake induced settlement

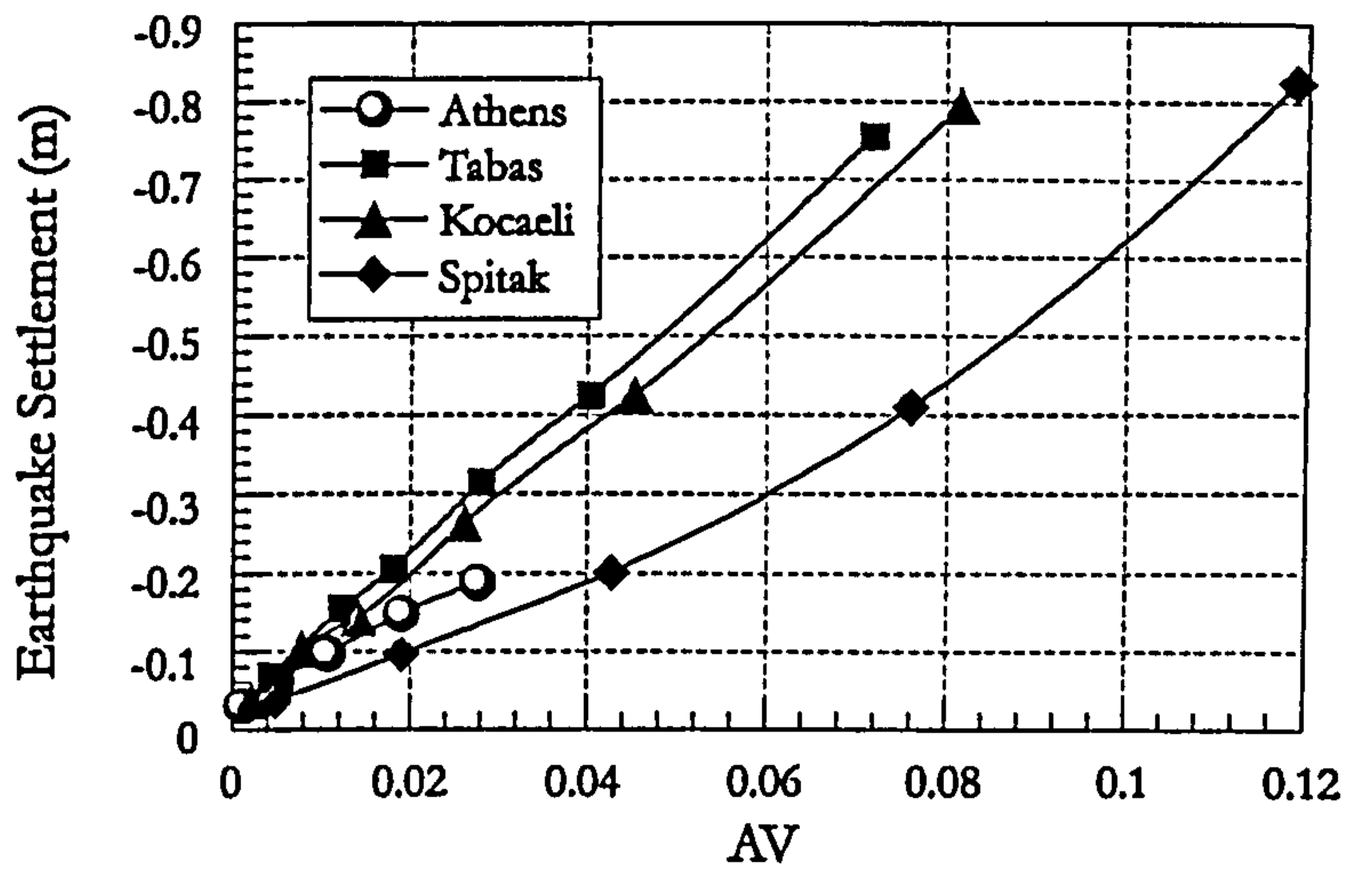

Figure 6.69: AV parameter against earthquake induced settlement

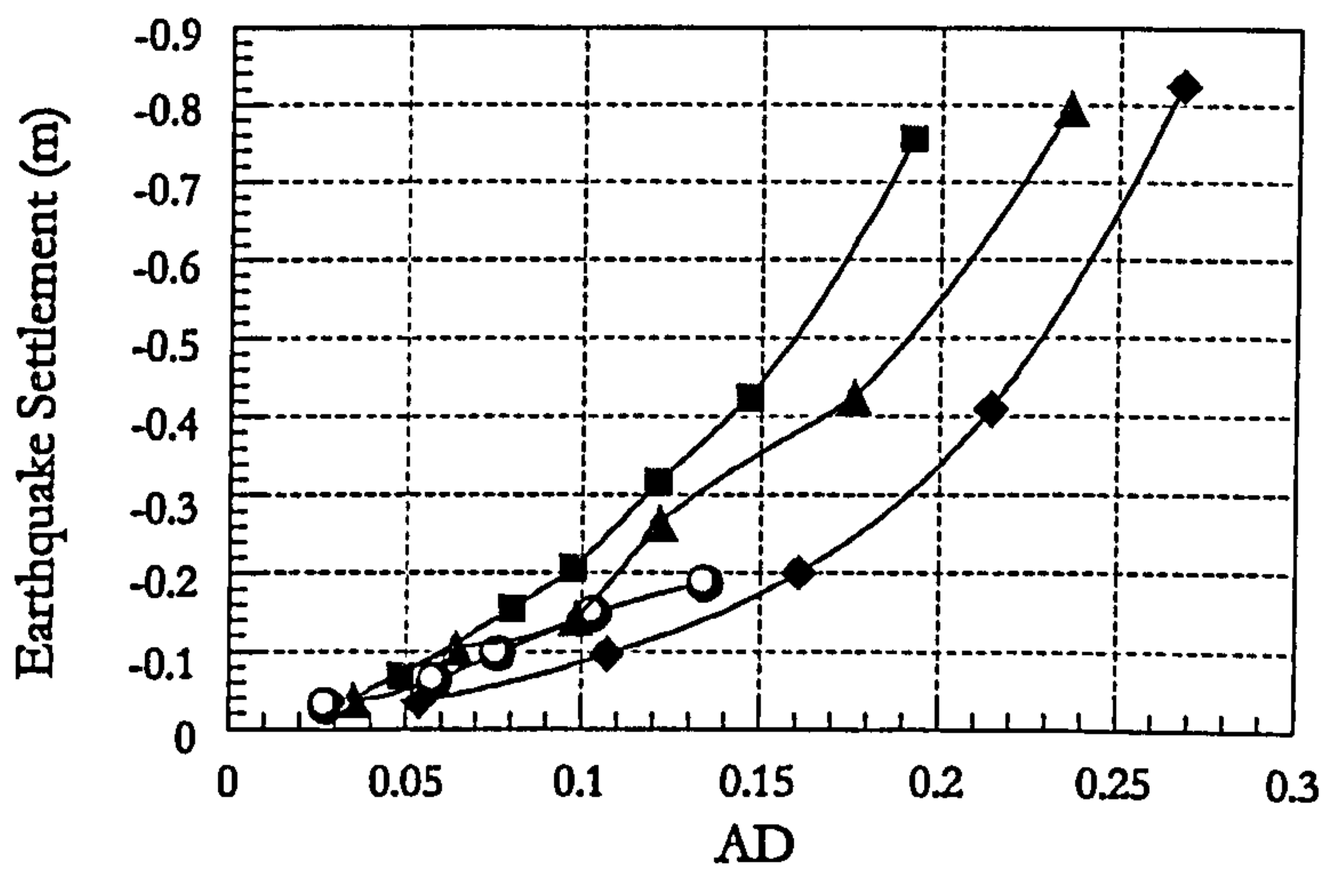

Figure 6.70: AD parameter against earthquake induced settlement

The most successful of all these parameters at normalising the earthquake induced settlement is the AA parameter, which is equivalent to the cumulative absolute velocity defined previously. For AA values below 8.0 m/s*s the parameter normalises the settlements well, although for more damaging earthquakes the lines appear to be diverging. Further investigation of this is clearly needed, although it is important to note that the parameter AS, which is linearly equivalent to the Arias intensity, did not perform a great deal better than the peak ground acceleration at normalising the earthquake induced settlement.

The most damaging of all the earthquake records used for this study was the Spitak record scaled to a maximum acceleration of 0.5*g*. Figure 6.71 shows an enlarged view of the displacement time history for this record.

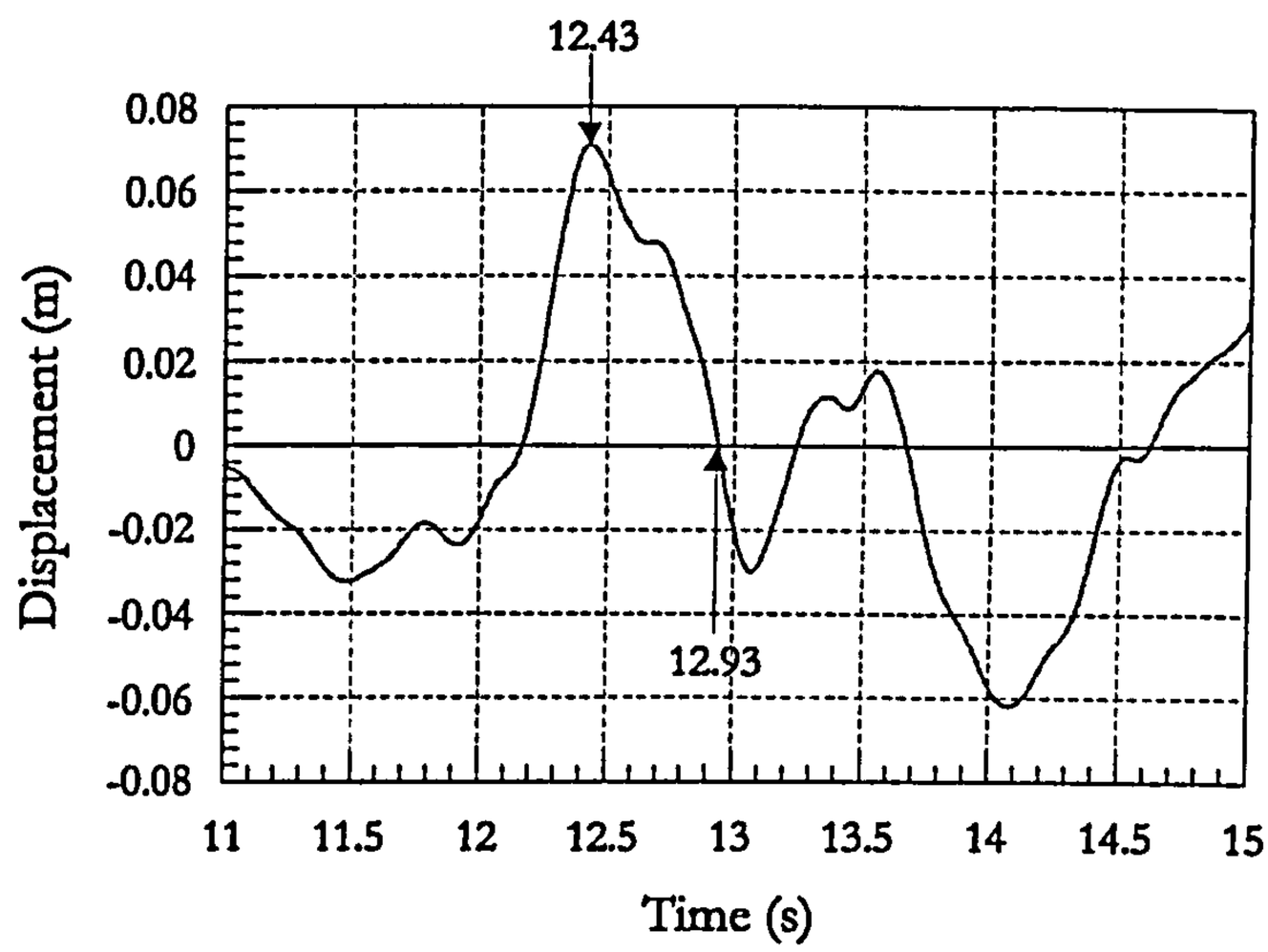

Figure 6.71: Expanded view of the displacement time history for Spitak 0.5*g* record, highlighting important analysis increments

The incremental displacement vectors for the two time increments shown in Figure 6.71 and the final earthquake induced displacement vectors for this analysis are shown in Figure 6.72 to Figure 6.74.

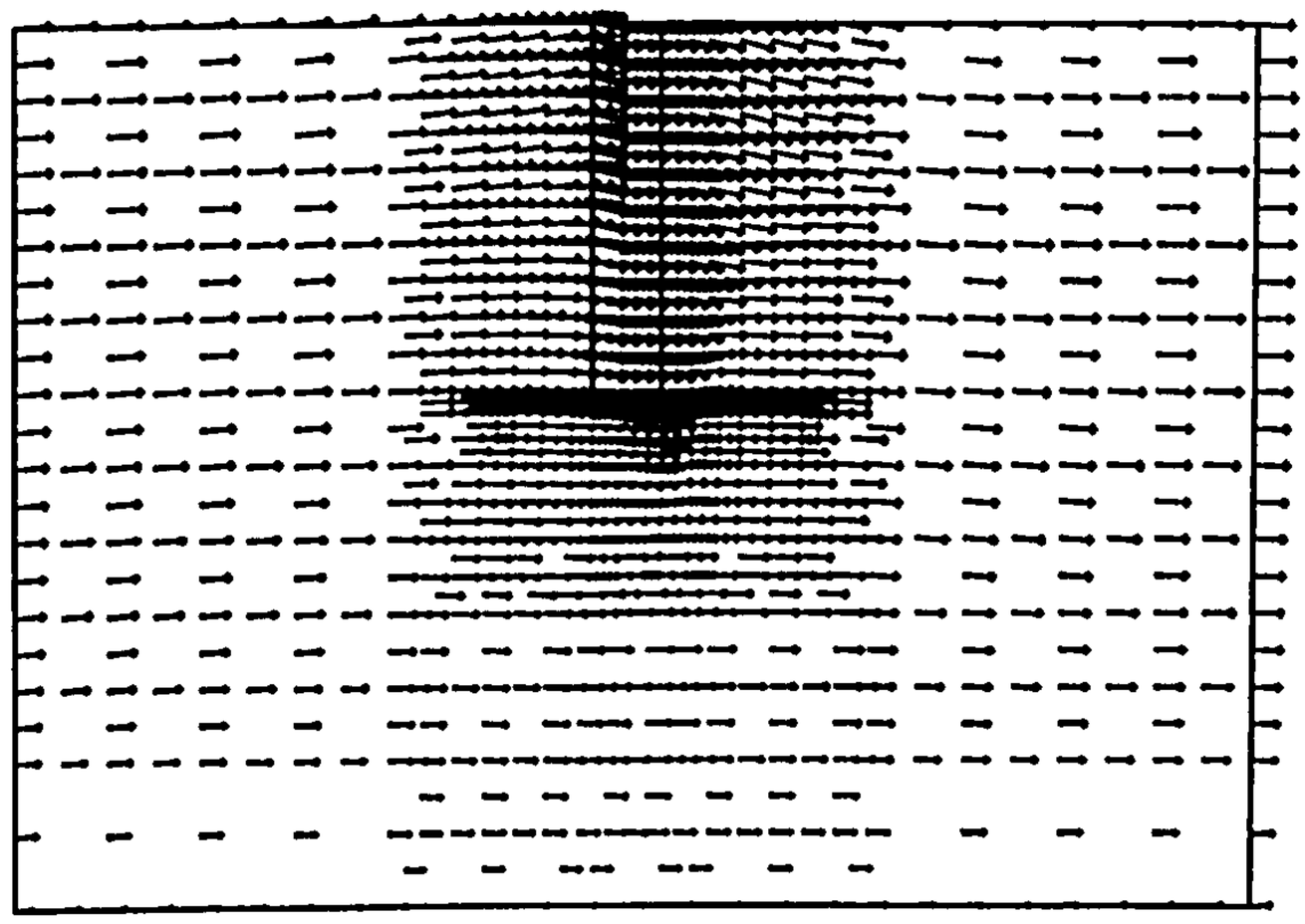

Figure 6.72: Vectors of incremental displacement at time = 12.43 seconds

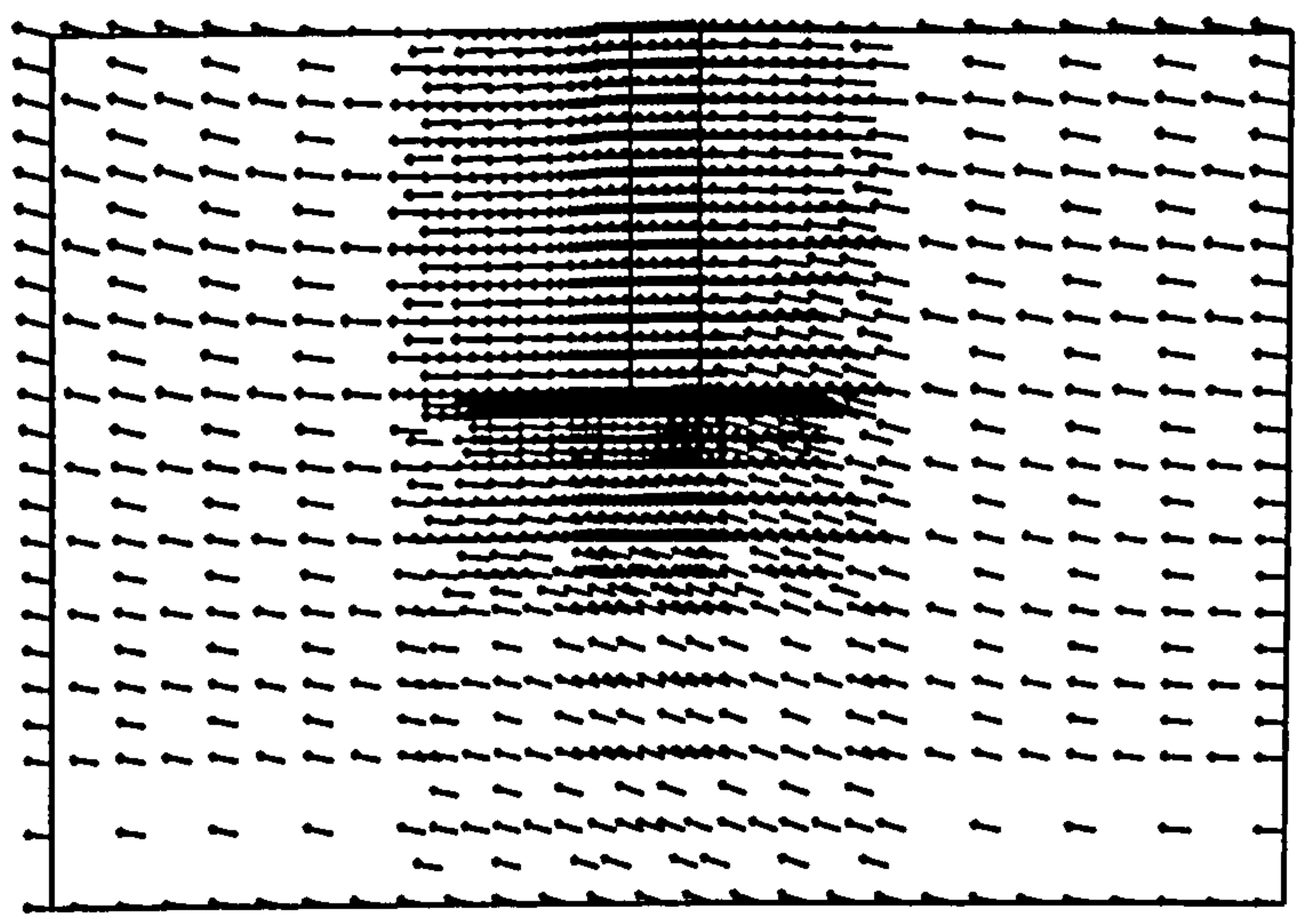

Figure 6.73: Vectors of incremental displacement at time = 12.93 seconds

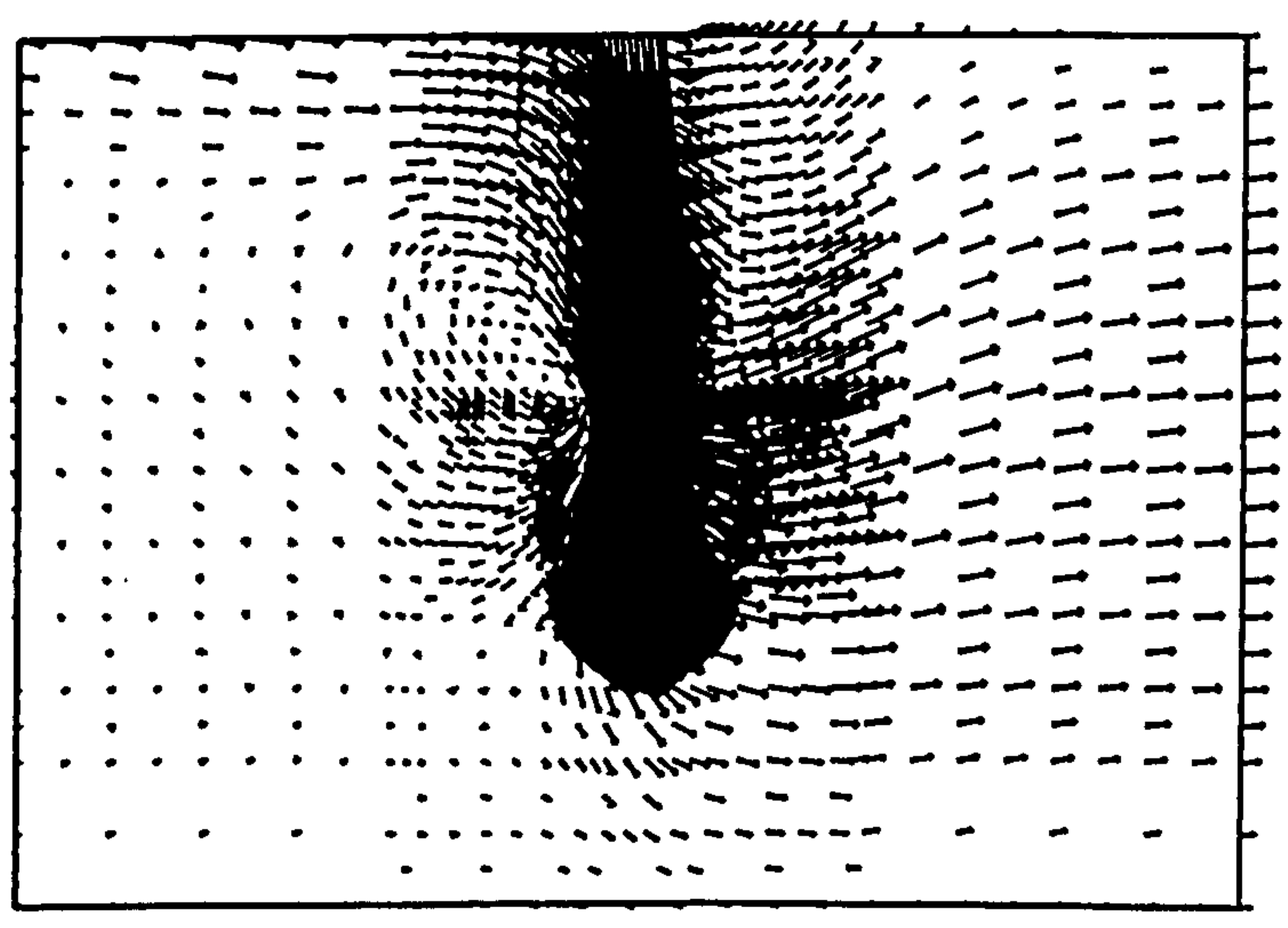

Figure 6.74: Earthquake induced displacement vectors for Spitak 0.5*g* earthquake

The vectors of incremental displacement shown in Figure 6.72 and Figure 6.73 do not show any failure mechanism forming during the analysis. The displacement vectors shown in Figure 6.74 illustrate the settlement of the foundation due to the application of the earthquake motion. This again illustrates that seismically induced forces in the ground to not initiate a bearing capacity type failure, although they do cause the foundation to settle a significant amount.

6.10 Analyses on Foundations at Different Working Loads

6.10.1 Introduction

The results presented in Section 6.9.3 highlighted the importance of including the individual characteristics of each earthquake record in a foundation analysis. The results also illustrated that some of the traditional parameters for defining an earthquake record, namely peak ground acceleration and Arias intensity, do not correlate well with potential earthquake damage.

Potts (2000) demonstrated using pseudo static finite element analysis that the factor of safety (FOS) a foundation is operating at dictates the failure mechanism that develops when the horizontal forces are applied to the foundation. To investigate what effect the factor of safety has on the behaviour of the foundation when an earthquake is applied, the analysis of the foundation subjected to the 0.3*g* Athens earthquake was repeated with the standard foundation taken to different working loads.

6.10.2 Description of Analyses

The working loads and respective factors of safety that were analysed are summarised in Table 6.6. The factors of safety are calculated assuming the bearing capacity of the foundation is 3315kN, which was found from the original finite element analysis.

Analysis	Working Load (kN)	Factor of Safety
1	3013.0	1.1
2	2550.0	1.3
3	1657.5	2.0
4	1228.0	2.7
5	975.0	3.4
6	473.6	7.0

Table 6.6: Summary of analyses undertaken at different working loads

The load-displacement curve of the foundation is shown in Figure 6.75, with the displacement at the different working loads illustrated.

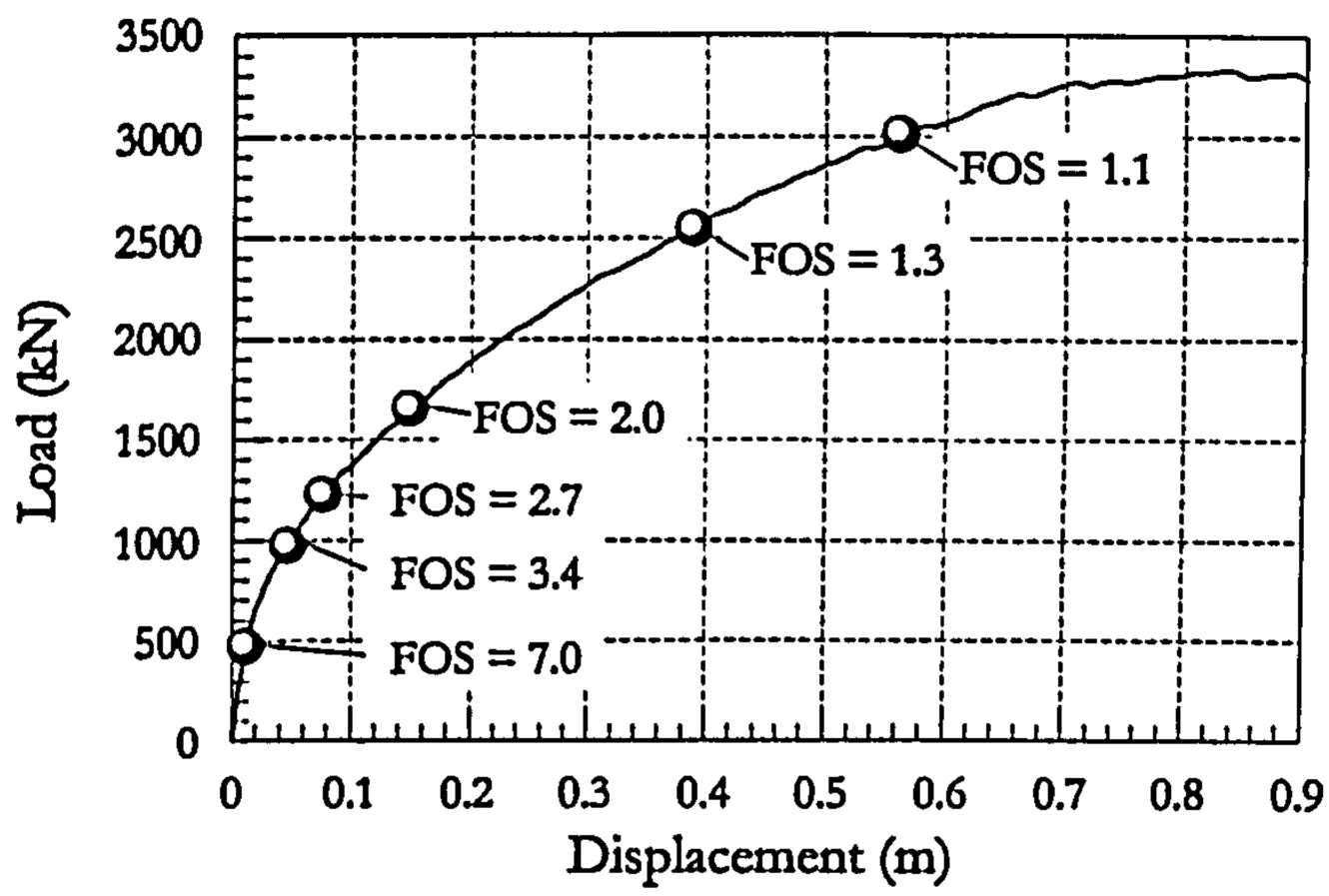

Figure 6.75: Load-displacement curve with different working loads illustrated

The displacement history of point A is shown in Figure 6.76 for each analysis. Due to each analysis starting from a different displacement at working load, only the earthquake induced settlement is shown. After the first 20 seconds of the earthquake record no further settlement is observed and therefore only the first 20 seconds of the displacement curves are shown.

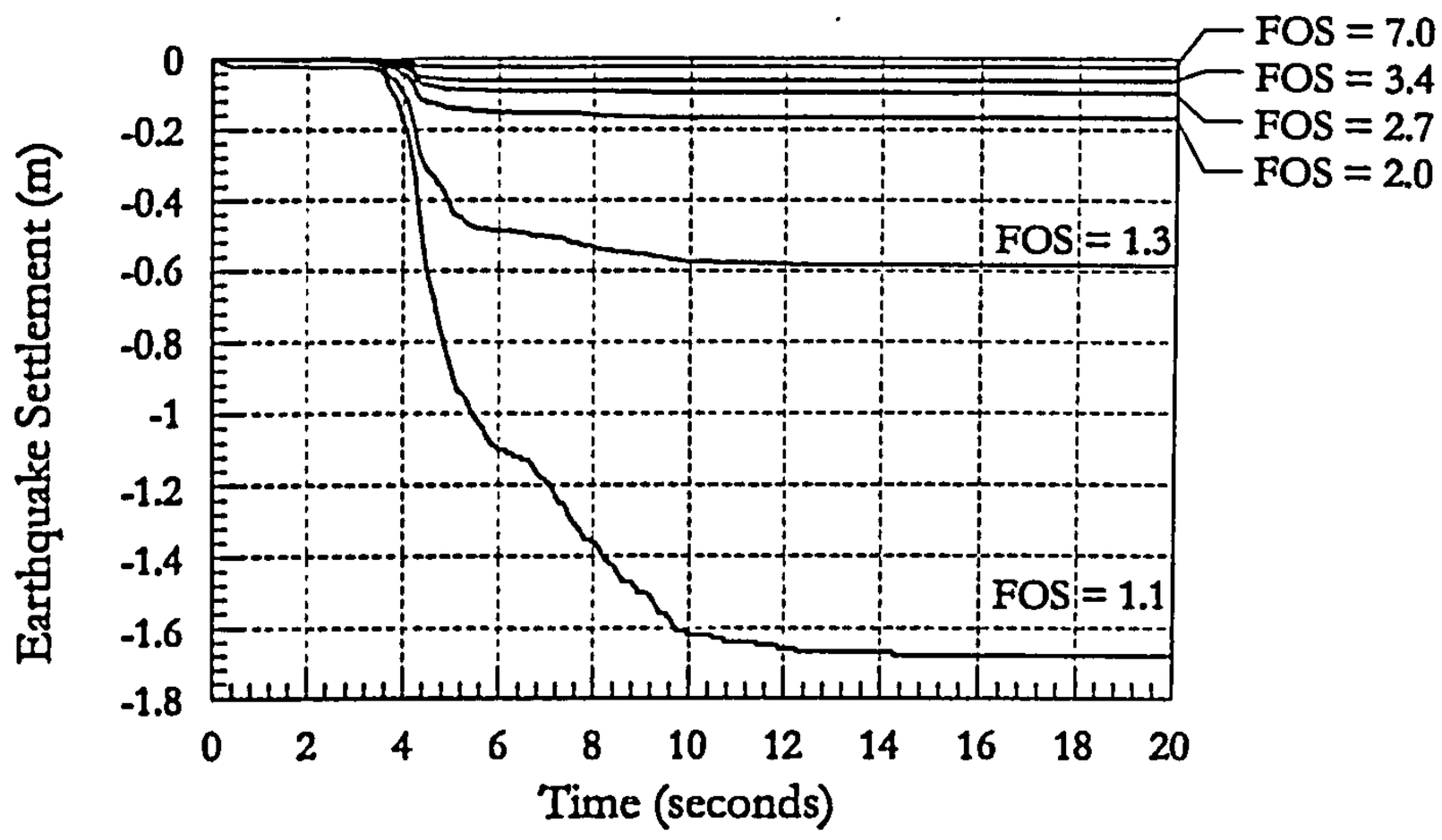

Figure 6.76: Settlement history for the standard foundation at different working loads

As one would intuitively expect, the foundation which is closer to failure at working load experiences more earthquake induced settlement than the foundation which has a lower working load. Whilst the shape of the settlement curve remains approximately the same and the rapid settlement starts at approximately the same time, the foundation with a lower factor of safety experiences significant amounts of settlement for a longer period of time. This implies that when a foundation is closer to failure, the threshold acceleration that causes the foundation to settle is lower. This is a logical result as the plastic strains around the foundation at higher working loads are more wide spread and hence it would take less seismically induced shear strains to create additional plastic deformations. The earthquake induced settlement against static factor of safety is shown in Figure 6.77 with a line of best fit through the data points.

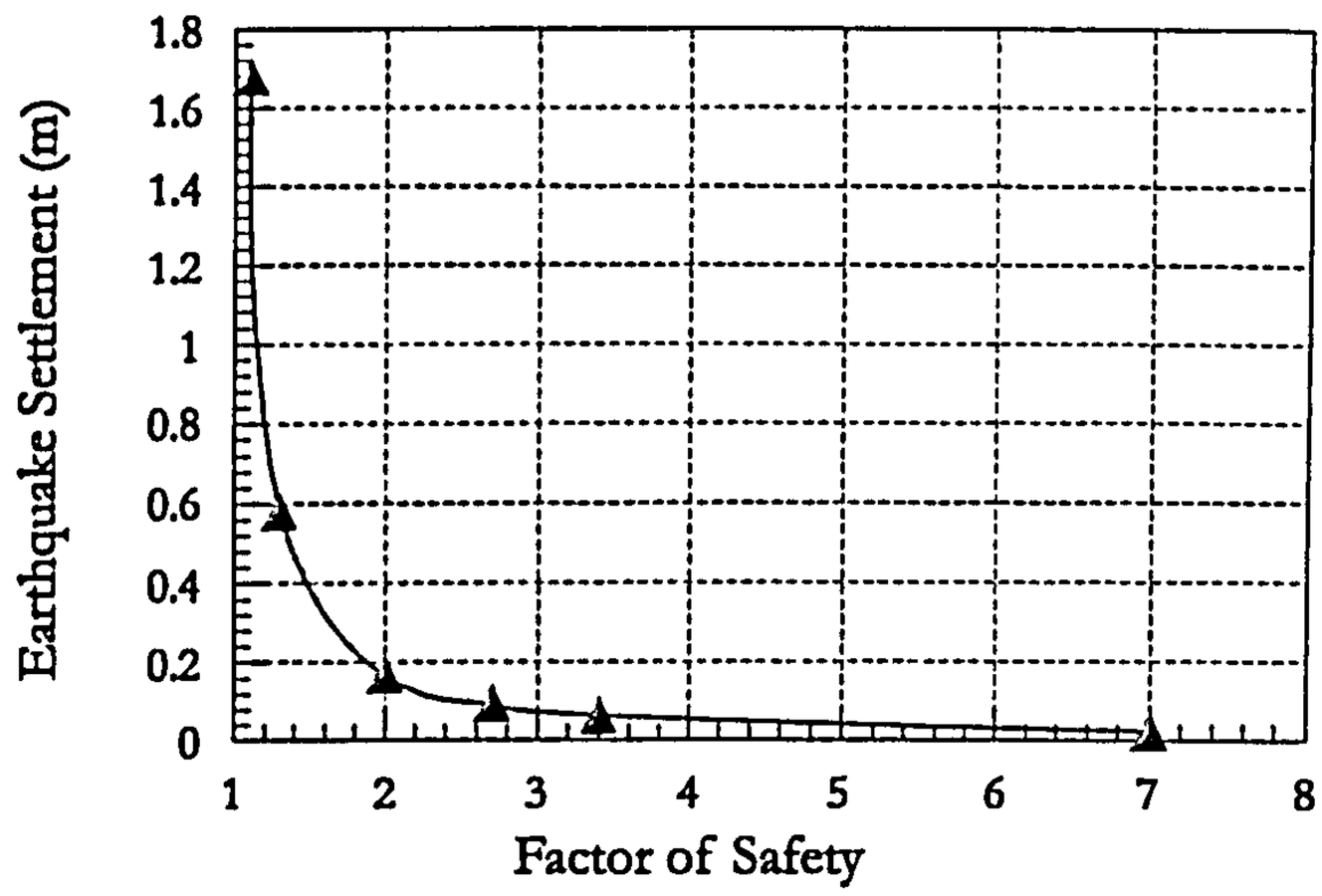

Figure 6.77: Earthquake induced settlement for Athens 0.3*g* record with different working loads

As the factor of safety approaches unity, the earthquake induced settlement tends to infinity. The line of best fit is given by Equation 6.29:

$$d = 0.161(FOS - 1)^{-1.0431} \tag{6.29}$$

where d is the earthquake induced settlement for the 0.3*g* Athens record. This relationship can now be used to predict the earthquake induced settlement that the standard foundation would experience if the limit equilibrium techniques described in Section 6.6 had been used to design it for seismic loading. The magnitude of reduced bearing capacity for the standard foundation subjected to a 0.3*g* earthquake are given in Table 6.7, using the methods proposed by Meyerhof, Hansen and Vesić.

Method	N_q	N_γ	i_q	i_γ	d_q	d_γ	q_{ult}
Meyerhof	18.401	15.668	0.663	0.197	1.866	1.866	2218
Hansen	18.401	15.070	0.444	0.308	1.793	1.000	1435
Vesić	18.401	22.402	0.490	0.343	1.793	1.000	1609

Table 6.7: Seismic bearing capacity of standard foundation subjected to 0.3*g* earthquake

BS 8004 (1986) suggests that a relatively high factor of safety, of 2-3, should be used when calculating acceptable loads for foundations to account for uncertainties in soil conditions and to ensure settlement does not become excessive. For the

purpose of this study a factor of safety of 2.5 will be used. The resultant overall factor safety and earthquake induced settlements predicted by Equation 6.29 are summarised in Table 6.8.

Method	q_{ult}	Working Load (kN)	Overall FOS	Settlement (cm)
Meyerhof	2218	887.36	3.74	5.635
Hansen	1435	573.89	5.78	3.151
Vesić	1609	643.51	5.15	3.647

Table 6.8: Predicted earthquake induced settlement for a foundation designed using limit equilibrium methods

The result of using the limit equilibrium techniques is a reduced ultimate bearing capacity and in the event of an earthquake the lower stresses in the ground causes the foundation to settle less. For the example given here the earthquake induced settlement is around 3-6 cm, which would not cause serious damage to the building constructed on the foundations. The results presented here only relate to the Athens earthquake of 1999 scaled to a maximum acceleration of 0.3*g*. If a more destructive earthquake, like the Kocaeli event were to happen, the results shown in Section 6.9 demonstrate the potential settlement that could occur.

Therefore, it can be concluded that whilst the finite element results demonstrate that the approach of using a limit equilibrium technique for calculating the bearing capacity of a foundation subjected to seismic loading is incorrect, the result is conservative because reducing the working load reduces that amount of settlement the foundation experiences in the event of an earthquake.

6.11 Large Displacement Analyses

6.11.1 Introduction

The analyses presented in the previous sections assumed small displacement finite element theory, which implies the deformation of the mesh remains small during the analysis. This is equivalent to a total Lagrangian frame of reference which is illustrated in Figure 6.78.

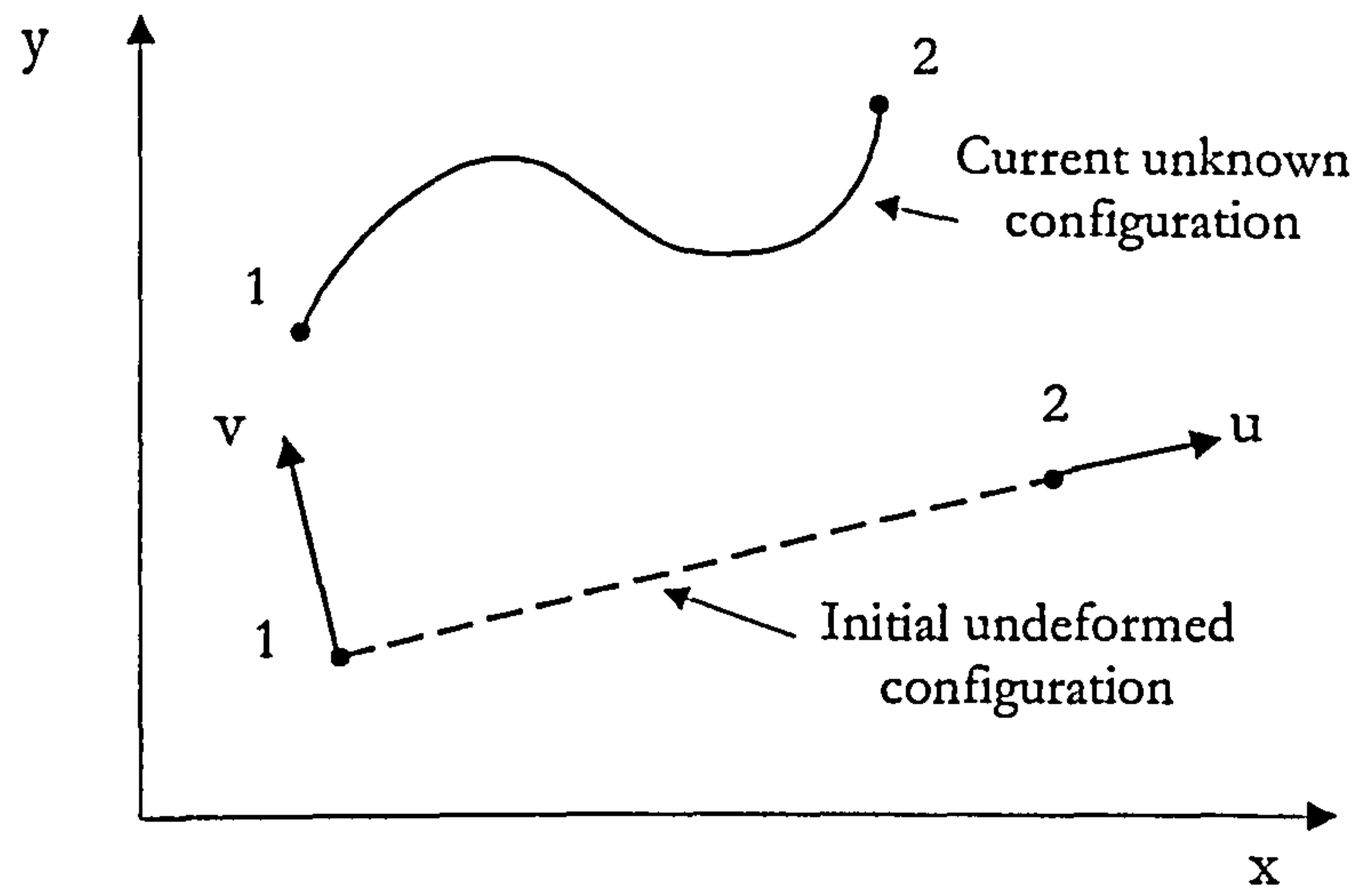

Figure 6.78: Total Lagrangian system (after Izzuddin (1991))

Clearly, the displacements induced in the foundation by some of the more destructive earthquakes are large and may invalidate this assumption. To investigate the effect that this assumption has on the results of the foundation analysis, each one was repeated using large displacement theory. The fundamental assumption of small displacement finite element theory is that any displacement of the mesh during the analysis is small compared to the dimensions of the mesh and therefore the mesh can be assumed not to change during the analysis. Large displacement analyses which use an updated Lagrangian system redefine the mesh at the end of each increment according to the calculated displacements. This is illustrated in Figure 6.79.

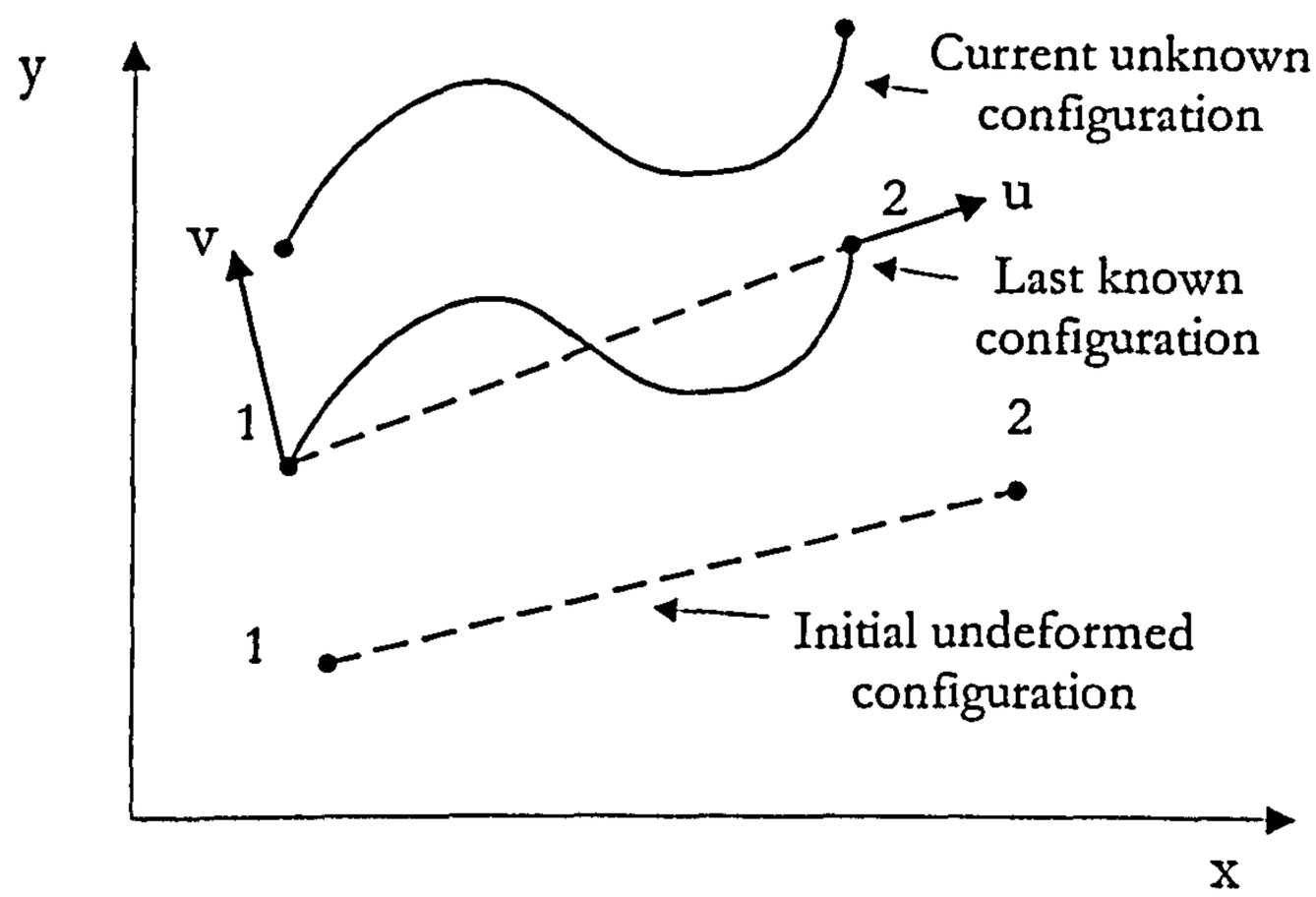

Figure 6.79: Updated Lagrangian system (after Izzuddin (1991))

Large displacements can also be accommodated by adopting an Eulerian reference frame, in which the material moves through the finite element mesh. This approach is more commonly adopted for fluid mechanics problems.

This option is not available in ICFEP and therefore large displacements will be accommodated by employing an updated Lagrangian system. Using the new mesh configuration the stiffness matrix can then be recalculated and the next analysis increment performed on the new mesh. In addition to the stiffness matrix, the mass and damping matrices must also be recalculated for each increment during dynamic large displacement analyses. The Jaumann stress tensor and velocity strain tensor have been implemented into ICFEP to deal with the constantly changing geometry of the finite element mesh. This method is commonly preferred to the 2nd Piola-Kirchoff stress tensor for non-linear materials with path dependant constitutive models. The stresses in the material can be calculated directly from the incremental strains when using the 2nd Piola-Kirchoff stress tensor, whilst the Jaumann stress state is related to the strain rate and therefore the incremental strains must be obtained via an integration process (Bathe (1982)). This implies that the material non-linearity is more accurately accounted for by the Jaumann stress tensor.

6.11.2 Description of Analyses

In theory, the ultimate bearing capacity of the standard foundation should be different when analysed using large displacement analyses, due to the increasing overburden pressure as the foundation is pushed into the ground. This, however, will not be taken into account for these analyses and the same working load of 1228 kN will be used for the large displacement analyses. The displacement of the foundation at working load was practically the same for the large displacement analysis and the small displacement results (7.63mm and 7.66mm respectively), which is to be expected as the soil stiffness does not vary with depth.

The displacement history of point A from the large displacement analysis when subjected to the Spitak earthquake record scaled to a maximum acceleration of 0.5g is compared with equivalent small displacement analysis in Figure 6.80.

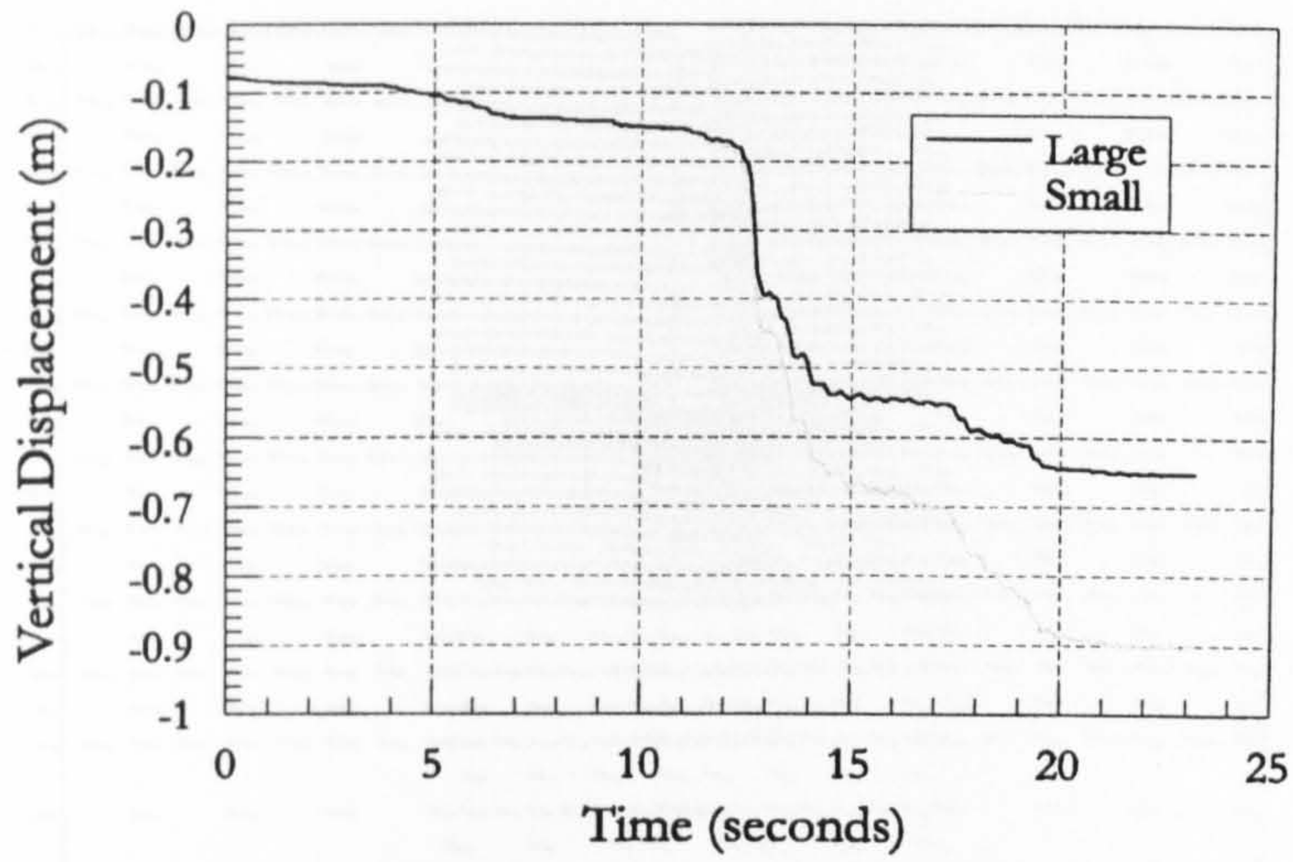

Figure 6.80: Displacement history of point A for Spitak 0.5*g* earthquake for large and small displacement analyses

The two plots follow a very similar path, with the large settlements occurring at the same points in the earthquake record, although the large displacement analysis predicts significantly less earthquake induced settlement (57.6cm compared to 82.5cm for the small displacement analysis).

The vectors of incremental displacement for the time steps highlighted in Figure 6.71 are shown in Figure 6.81 and Figure 6.82 for the large displacement analysis.

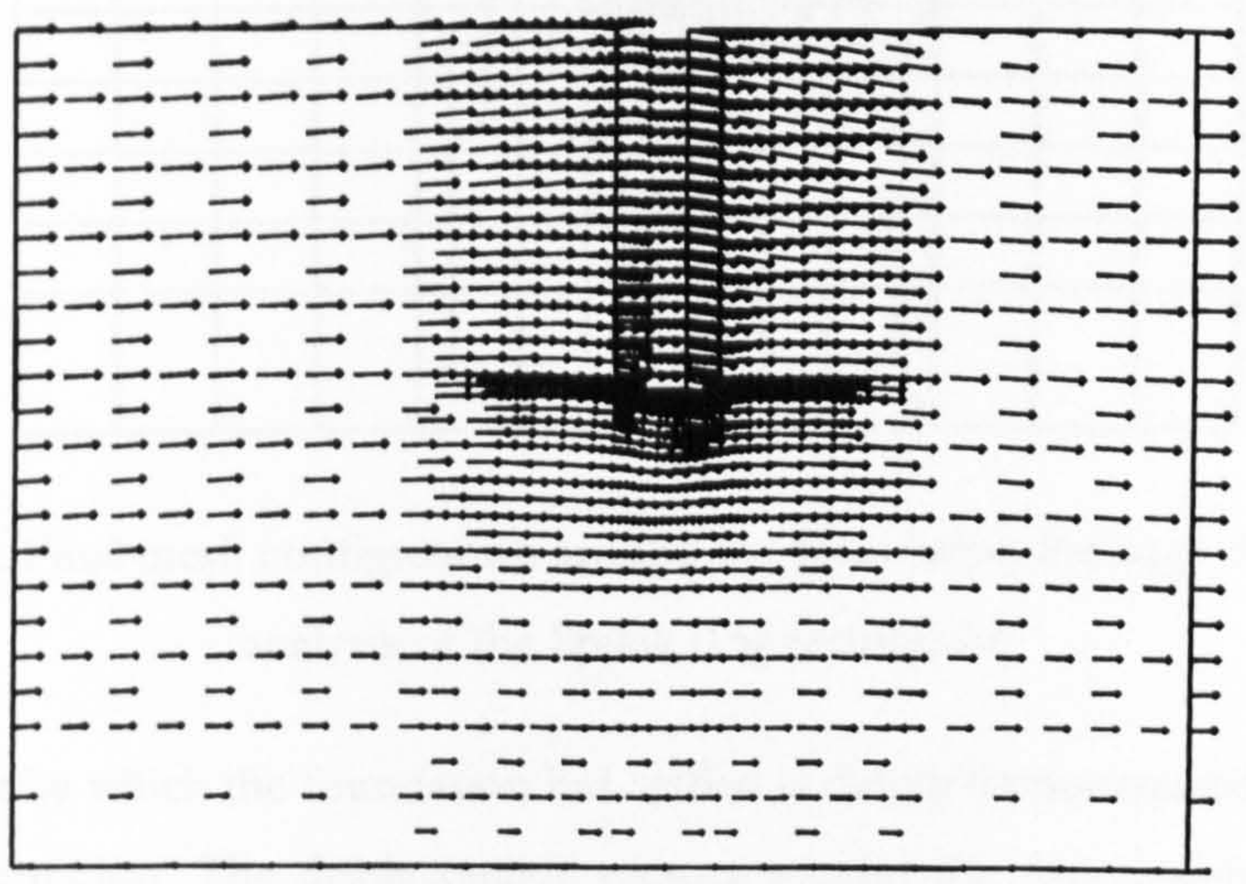

Figure 6.81: Vectors of incremental displacement at time = 12.43 seconds

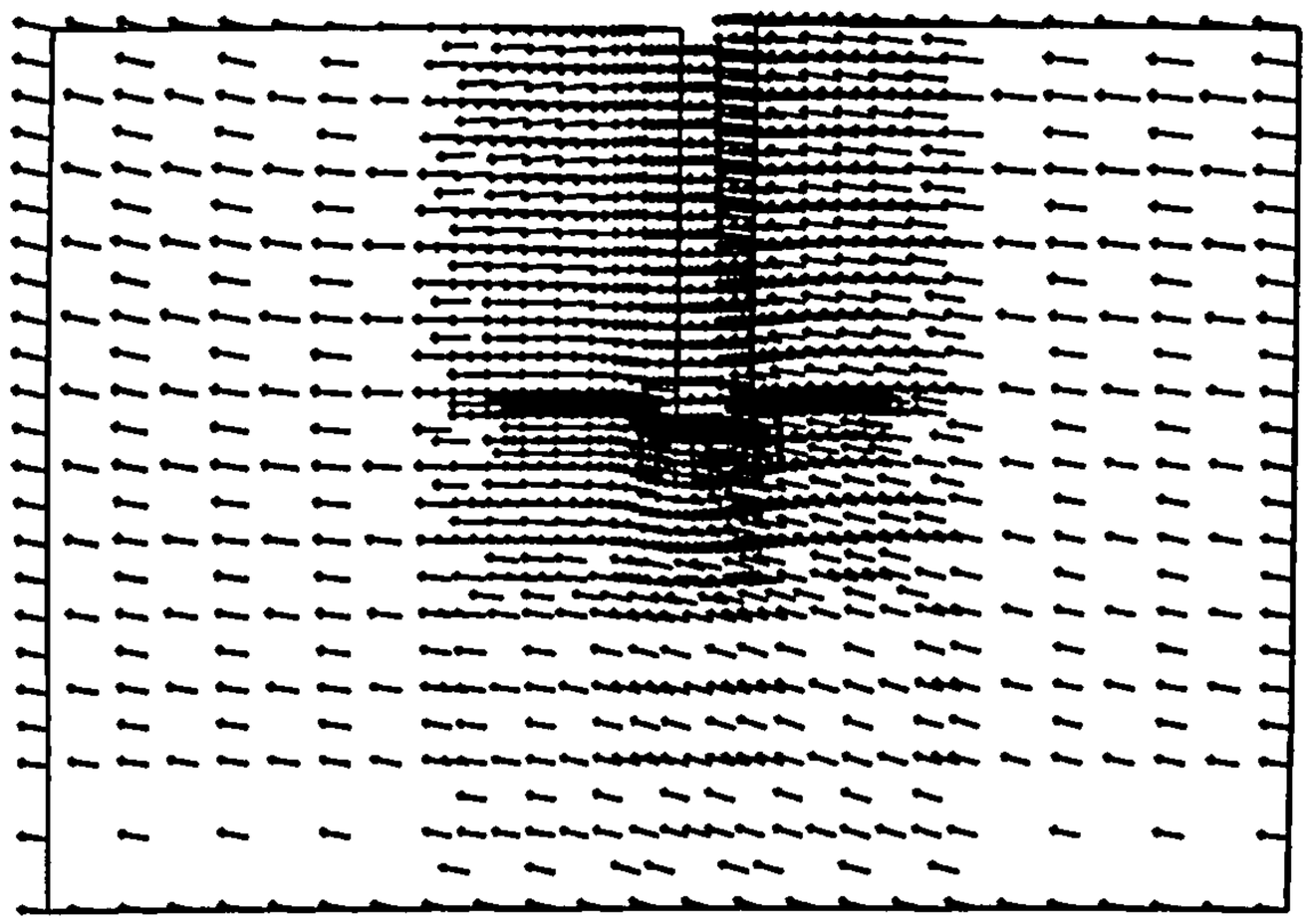

Figure 6.82: Vectors of incremental displacement at time = 12.93 seconds

Figure 6.83 shows an enlarged view of the original and final mesh configurations around the foundation.

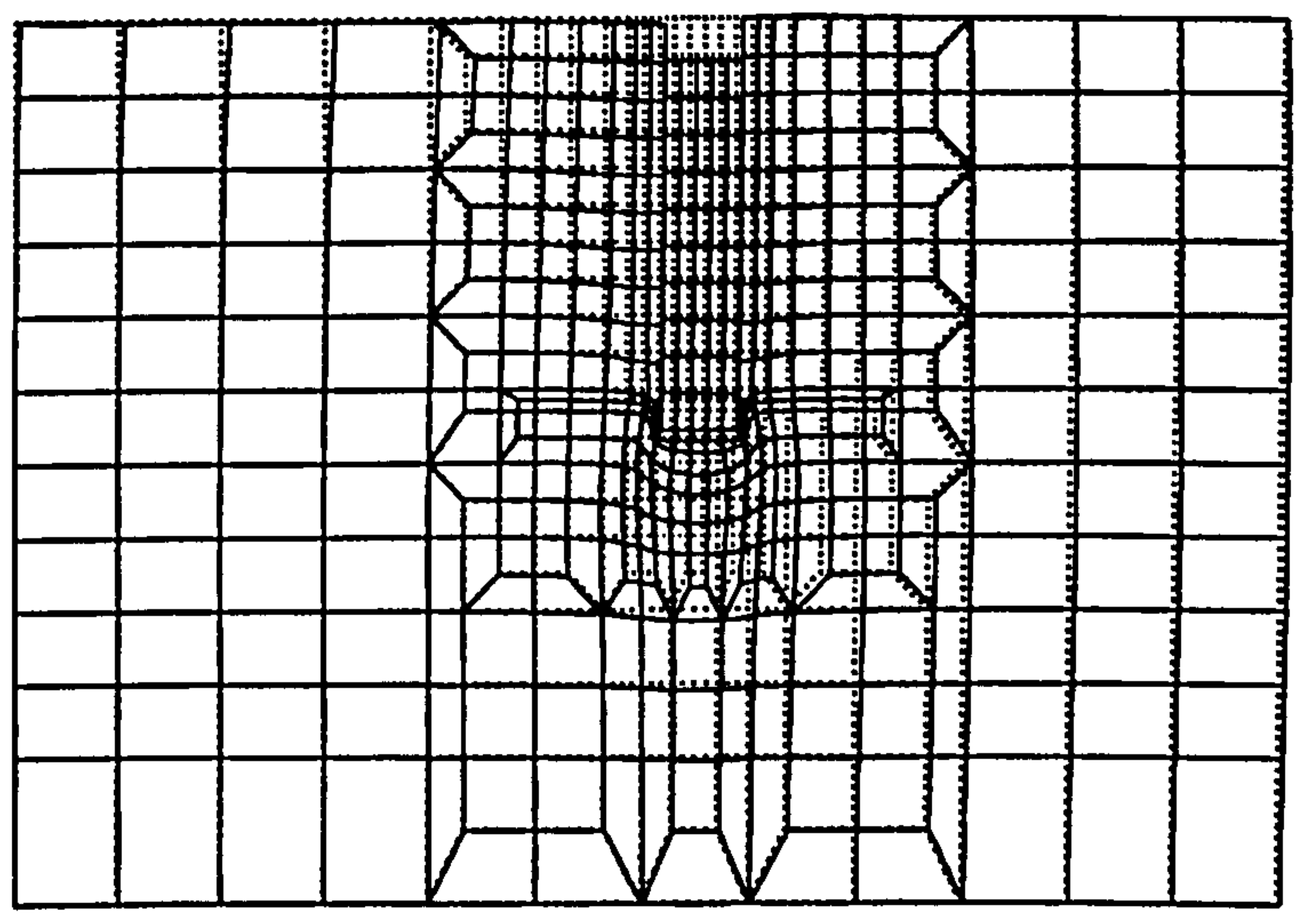

Figure 6.83: Final mesh configuration around the foundation for large displacement analysis of the Spitak 0.5*g* earthquake

The amount by which the foundation has settled is clearly demonstrated by the final mesh configuration. The displacement vectors around the foundation due to the application of the earthquake are shown in Figure 6.84.

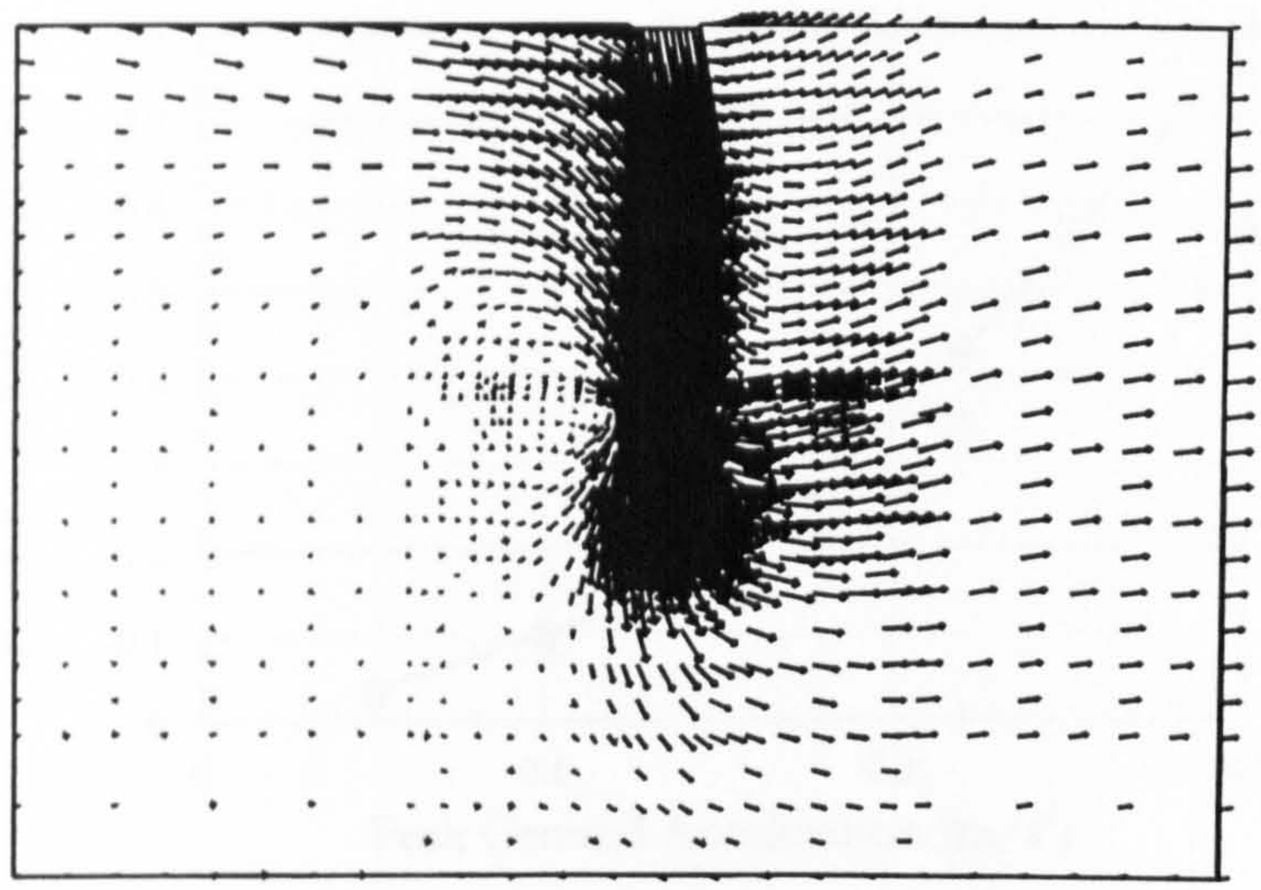

Figure 6.84: Displacement vectors around foundation for Spitak 0.5*g* earthquake

The vectors of incremental displacement and the mode of settlement are similar to those observed from the small displacement analysis and clearly no failure mechanism has been induced by the application of the earthquake.

The earthquake induced settlement for each of the Athens, Kocaeli, Tabas and Spitak earthquake records described in Sections 6.7 and 6.9 are compared for large and small displacement analyses in the following figures

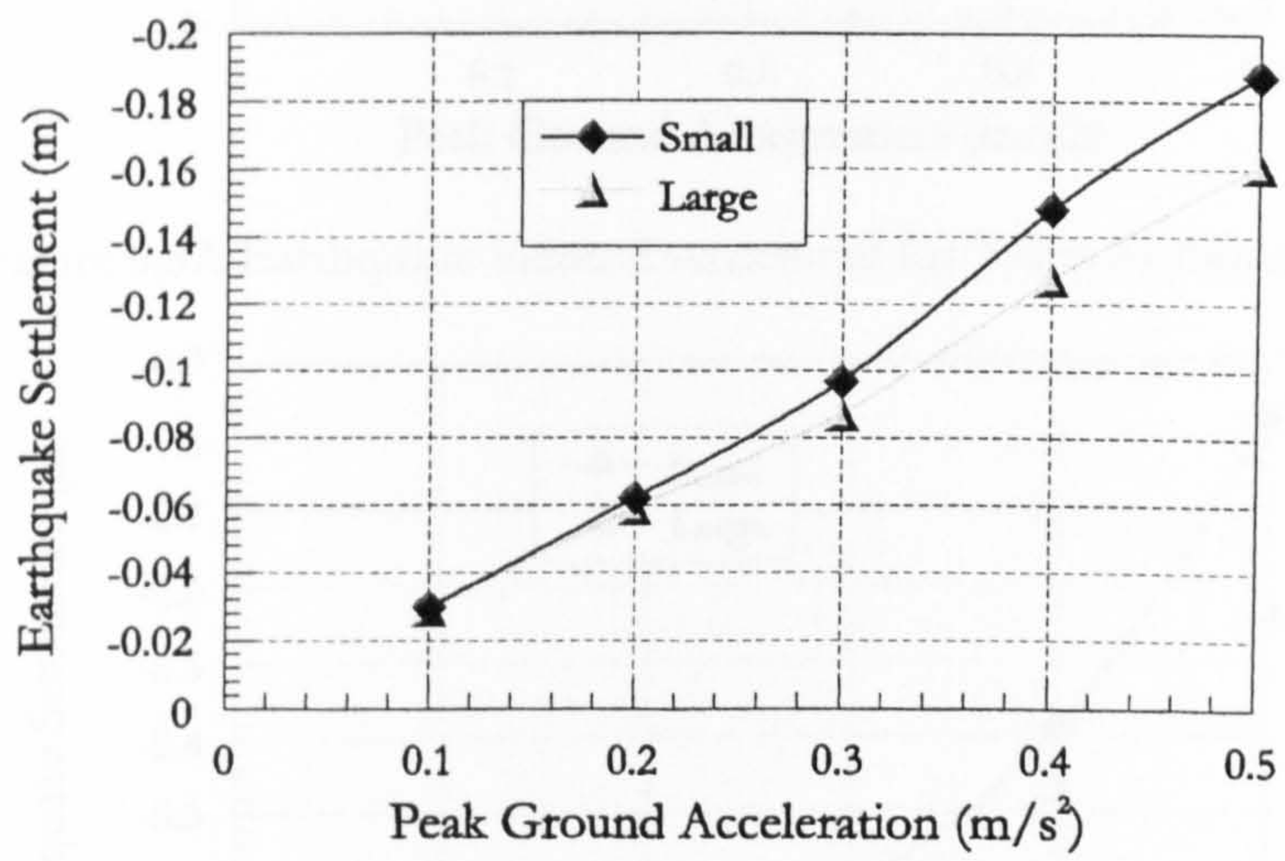

Figure 6.85: Earthquake induced settlement for Athens earthquake

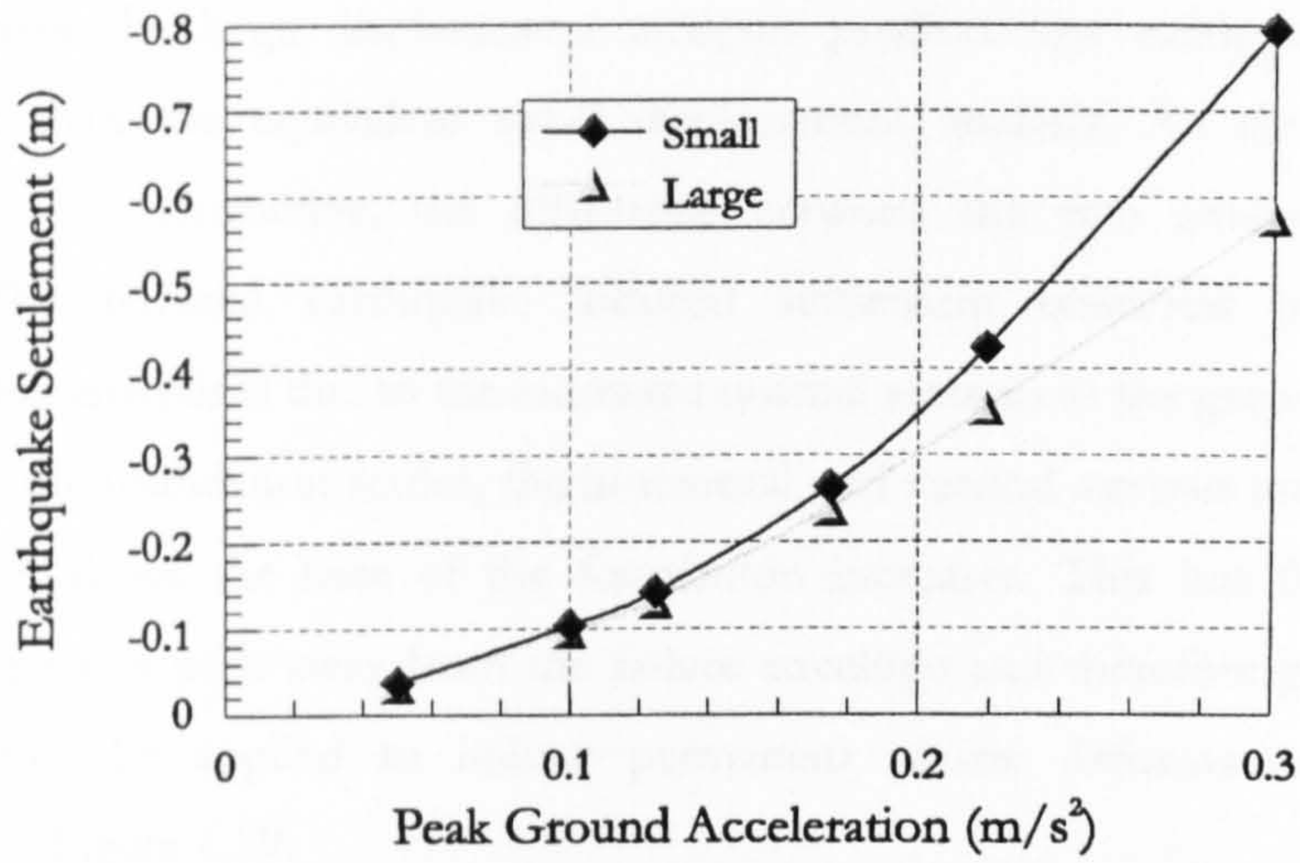

Figure 6.86: Earthquake induced settlement for Kocaeli earthquake

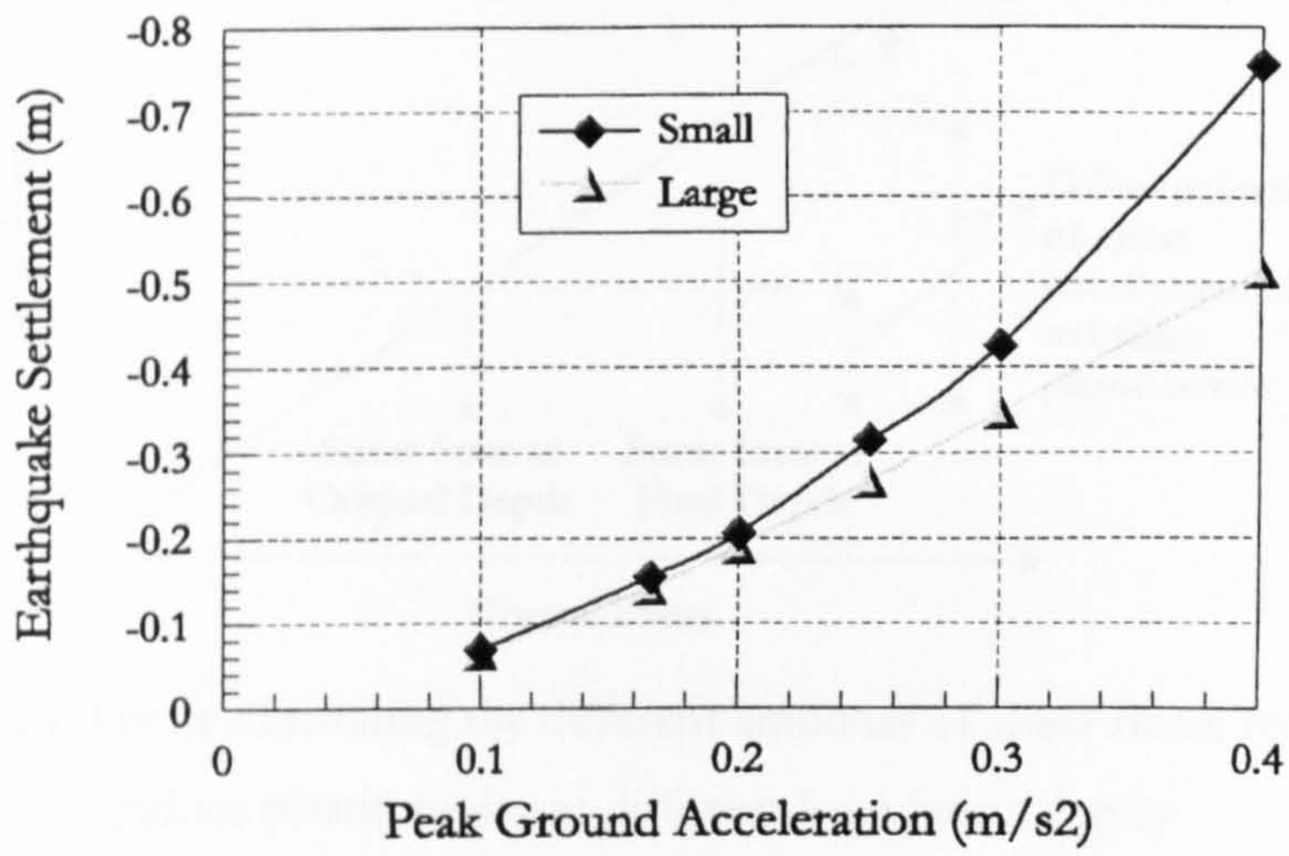

Figure 6.87: Earthquake induced settlement for Tabas earthquake

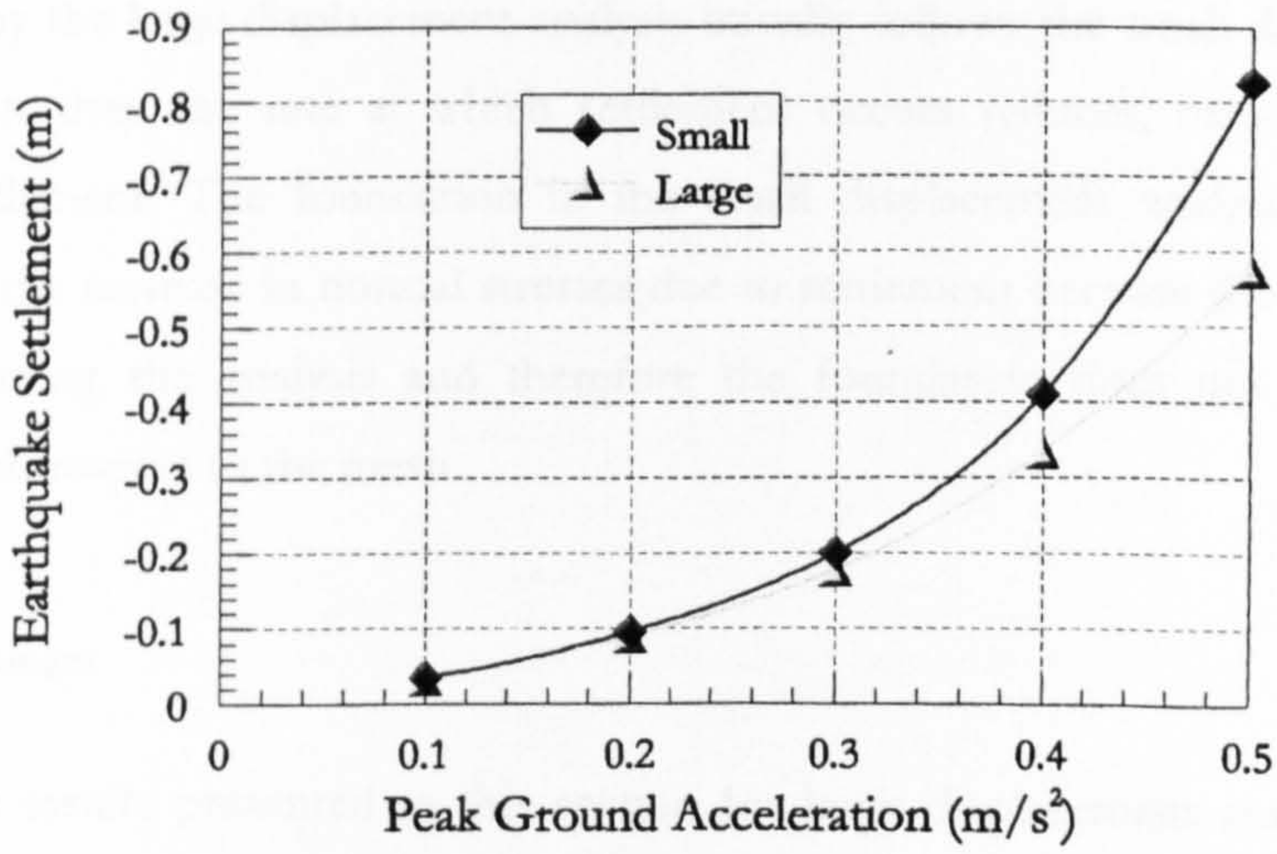

Figure 6.88: Earthquake induced settlement for Spitak earthquake

For all cases the large displacement analyses predicts less earthquake induced settlement than the equivalent small displacement analysis. As the earthquake becomes more destructive, the difference between the two analyses becomes greater. The reduced earthquake induced settlement observed in the large displacement analysis is due to the increased normal stresses in the ground at greater depths. As the foundation settles, the horizontal and vertical stresses increase as the amount soil above the base of the foundation increases. This has the effect of moving the stress path away from the failure envelope and therefore greater shear stresses must be applied to induce permanent plastic deformations. This is illustrated in Figure 6.89.

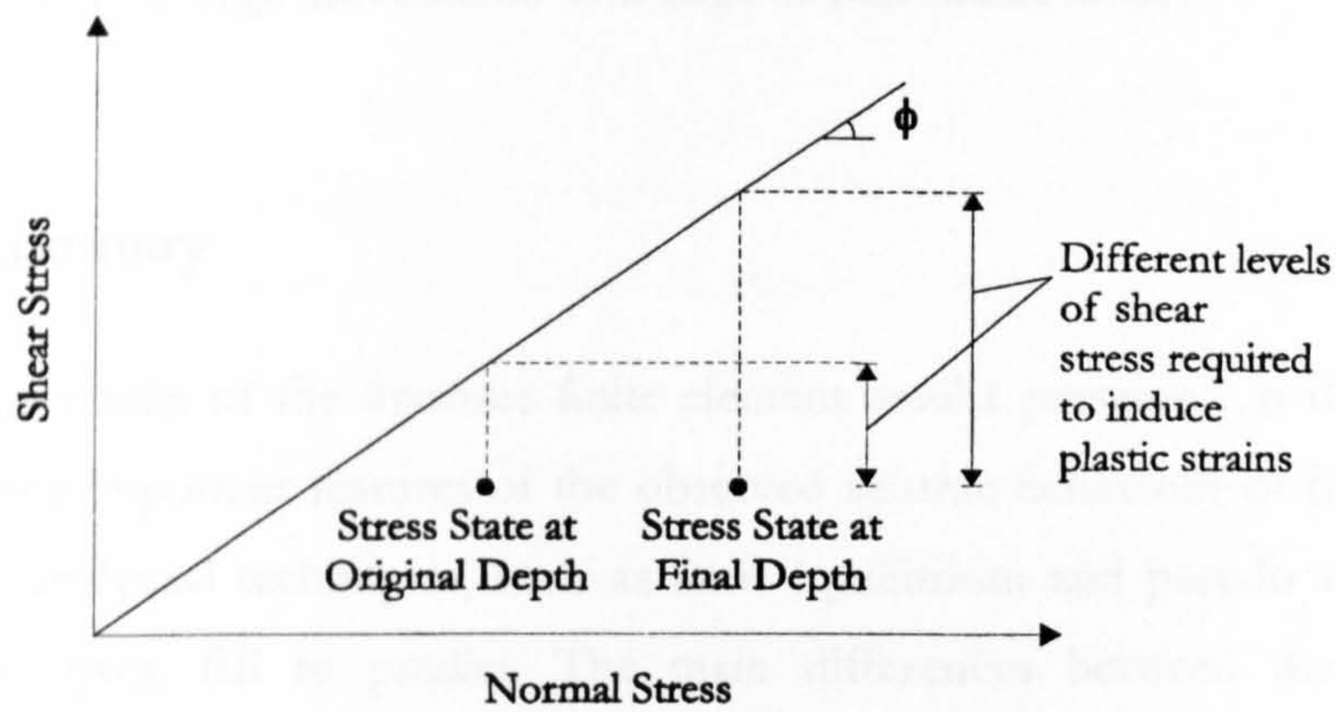

Figure 6.89: Figure illustrating the different amounts of shear stress required to induce plastic strains at different foundation depths

This phenomenon is demonstrated in Figure 6.80 where the amount of settlement predicted by the large displacement analysis initially follows the small displacement analysis, but then the rate at which settlement occurs reduces, resulting in less overall settlement. The foundation in the small displacement analysis does not experience the increase in normal stresses due to settlement because the mesh stays constant during the analysis and therefore the foundation does not change its location with respect to the mesh.

6.11.3 Summary

The results presented in this section for large displacement analyses have demonstrated the importance that large displacements can have on the behaviour of foundations subjected to seismic forces. The application of small displacement finite

element theory to geotechnical problems is normally valid, because the displacements experienced in problems like embankments and tunnels are often small compared to the size of the problem. To take a foundation to failure often requires applying large displacements, for example the 0.9m of displacement used in the capacity analysis of the foundation presented in Section 6.6.3. However, the displacements at working load are usually small and the assumption of small strains is normally valid. The examples of the behaviour of foundations during seismic events presented in Section 6.2 demonstrated that under these conditions the displacements are often large and the finite element results presented in the sections that followed reinforced this fact. It is therefore important to model seismic events which may induce large movements with large displacement theory.

6.12 Summary

The results of the dynamic finite element results presented in this chapter predict some important features of the observed seismic behaviour of foundations that other analytical techniques, such as limit equilibrium and pseudo static finite element analyses, fail to predict. The main differences between the currently available analytical tools and dynamic finite element analysis are summarised below.

The use of a Prandtl type failure mechanism to predict the reduced bearing capacity of a foundation when subjected to seismic loading has been shown to be unrealistic by the results of the pseudo static finite element results first presented by Potts (2000) and partially repeated for this thesis. The failure mechanism induced by the application of a pseudo static horizontal force was found to depend on the static factor of safety the foundation was working at before the application of the horizontal force. However, none of the cases presented by Potts (2000) resembled a Prandtl type failure mechanism and most where dominated by a lateral movement of the foundation.

The results of the dynamic finite element analysis demonstrated that the pseudo static analysis was overly conservative. The peak ground acceleration of an earthquake only occurs once during an earthquake event and therefore to apply a constant horizontal body force equivalent to this inertial loading is over conservative. Four earthquake records (Athens (1999), Spitak (1988), Tabas (1978),

and Kocaeli (1999)) where scaled to a peak ground acceleration of 0.2*g* and applied to a foundation that the pseudo static analysis predicted would fail at this acceleration. No failure of the foundation was observed, although significant amounts of settlement were predicted. The fact that each earthquake record, although scaled to the same peak ground acceleration, predicted different amounts of settlement illustrates that the magnitude of the peak acceleration is not a good indication of earthquake damage potential.

An overall reduction in horizontal stress was observed around the shaft of the foundation, which resulted in the load carried by the shaft being redistributed to the base. This in turn caused an increase in vertical stress under the base of the foundation.

The first set of analyses was undertaken at a constant working load which gave a reasonable factor of safety against static failure. To investigate the influence that the working load has on the behaviour of a foundation subjected to earthquake loading the analysis of the foundation subjected to the Athens 0.3*g* earthquake was repeated for different working loads. The results demonstrated that the practice of reducing the static capacity of a foundation, and therefore increasing its factor of safety, indirectly resulted in a more satisfactory seismic performance of the foundation. The smaller shear strains induced around the foundation at lower working loads result in less permanent plastic deformations when the earthquake loading was applied.

As mentioned previously the peak ground acceleration of an earthquake record did not correlate well with the amount of earthquake induced settlement. To investigate if a parameter could be identified which could be used to predict potential earthquake damage, the four earthquake records used previously (Athens (1999), Kocaeli (1978), Spitak (1988) and Tabas (1978)) were scaled to a range of peak ground acceleration and the foundation analyses repeated for one working load. A single peak value, such as peak acceleration or peak velocity cannot be used to differentiate between earthquake records and therefore a range of parameters were used that integrated different values over the whole earthquake record. Of all the parameters tested none satisfactorily normalised the foundation settlement results, although the most accurate was the absolute velocity integrated over the entire

record. The commonly used Arias intensity was found not to perform any better than the peak ground acceleration.

The standard finite element approximation of small displacement theory is not valid for the magnitude of settlements observed in some of the more destructive earthquakes presented. To investigate the influence that large displacements may have on the behaviour of the foundation, all the analyses were repeated using large displacement analysis. The general behaviour of the foundation was found to be the same as the small displacement analysis. No failure mechanism was developed for any of the earthquake records, although large settlements were still predicted. However, the settlement predicted by the large displacement analysis was always less than that predicted by the small displacement analysis. As the earthquake record became more destructive, the difference became greater. This was found to be due to the normal stresses acting on the foundation increasing in the large displacement analysis as the foundations depth increased. In the small displacement analysis the foundations depth did not change with respect to the mesh and therefore the normal stresses did not change as the foundation settled. At present the density for each element remains constant during the analysis. This implies that the mass of an element will vary during the analysis as its geometry changes. This assumption may affect the results as the elements compressed under the foundation during the application of the earthquake will effectively reduce their mass, and hence their contribution to the inertial forces.

Of course any conclusions drawn from the analyses presented here are limited by the assumptions made. The first and most obvious assumption is the non-inclusion of the building structure in the analysis. As mentioned previously, the cyclic loading caused by the rocking of the structure above will significantly influence the behaviour of the foundation during a seismic event. However, the effects of loading rate on soil behaviour cannot at present be replicated by any soil model in ICFEP and therefore the influence of the cyclic loading would only be negative. It was therefore decided not to include the structure above the foundation in the analysis and to therefore isolate the influence of the seismic shear wave on the foundation from the cyclic loading from the structure above.

To allow comparison of the results with the pseudo static analysis presented by Potts (2000) and the limit equilibrium work by Chen (1997), the presence of a fluid

in the pores of the soil has not been included in the analysis. This is of course unrealistic and would have a major influence of the overall behaviour of the foundation. The analysis presented here is equivalent to a foundation resting on a dry sand which is not a common scenario. Future research should move away from this ideal situation which is a requirement for limit equilibrium analyses and towards modelling the pore pressure build up during a seismic event and the possibility of liquefaction.

The use of a Mohr-Coulomb failure criterion for the analyses was necessary to allow comparison of the results with those obtained by Potts (2000) and Chen (1997). As mentioned in Chapter 4, the Mohr-Coulomb model is not ideally suited to dynamic finite element analyses. The lack of plasticity below the yield surface and the soil becoming elastic upon unloading are not realistic features of the dynamic behaviour of soil which can be recreated by using sophisticated kinematic soil models of the type developed by Al-Tabbaa and Wood (1989) and Stallebrass and Taylor (1997). The behaviour of foundations subjected to earthquake loading should be investigated using this type of model in the future. Despite these limitations the finite element results presented have many similarities with the observed behaviour of foundations described at the beginning of this chapter.

Chapter 7:

CONCLUSIONS AND RECOMMENDATIONS

7.1 Introduction

The aim of this research project was to implement a time marching algorithm into the existing ICFEP program to allow dynamic problems to be analysed. The finite element theory for static geotechnical problems is detailed in Chapter 2 and the changes required to allow dynamic problems to be analysed are given in Chapter 3. The results of the validation exercise performed to ensure these changes had been implemented correctly are presented in Chapter 4. Chapters 5 and 6 give details of two investigations undertaken using the dynamic version of ICFEP. This Chapter gives the conclusions that have been drawn from this study. Sections 7.2 and 7.3 give the conclusions that can be drawn from the finite element implementation and validation respectively. Section 7.4 gives the conclusions that can be made regarding the investigations into the behaviour of bender element tests and deep foundations subjected to earthquake loading. Some comparisons are made between the two problems to highlight their differences and therefore illustrate the diversity of dynamic problems. On the basis of these discussions, the final section gives some suggestions regarding possible directions for further research.

7.2 Finite Element Implementation

To implement the dynamic analysis potential into the existing finite element code, a detailed literature review of existing time discretisation schemes was performed and the most suitable one was then chosen for implementation. This was determined to be the Newmark method due to its ease of implementation and flexibility. The original formulation was modified to include the option of a time discretisation scheme in which the acceleration during an increment is assumed to vary according to a quadratic function. This assumption implies that the third

derivative of displacement with respect to time, or thrust, varies linearly and therefore must be calculated as it appears in the approximations for the incremental velocity and acceleration. It was found, by analysing a single degree of freedom problem, that the thrust could not be calculated by using the displacement, velocity and acceleration values at the previous time step and could only be calculated by considering equilibrium. The third derivative of time does not appear in the equilibrium equation and therefore each term in the dynamic equilibrium equation had to be differentiated with respect to time once to obtain the incremental thrust. This required the derivative of the load vector to be approximated. It was found using the single degree of freedom problem that the simplest possible central difference approximation was sufficient for this purpose. The single degree of freedom problem was used to investigate some properties of the modified Newmark method. It was found that, in the absence of any material damping, the higher order time discretisation scheme was unstable. If no material damping is intended to be included in the material parameters for a given analysis, it was found that sufficient numerical damping could be induced into the analysis by increasing the modified Newmark parameters. This process however, introduced spurious oscillatory modes which did not appear in the closed form solution. Generally, the modified Newmark method did not perform well. The potential increase in accuracy for a comparable time step that was observed for the single degree of freedom problem was lost when the scheme was used for a boundary value analysis. To ensure the analysis remained stable, the time step had to be reduced to a value that if it had been used to analyse the same problem using the original Newmark method, the results would have been very accurate. The boundary value problems that where analysed using the modified Newmark method suffered due to the appearance of spurious oscillatory modes, similar to those observed in the single degree of freedom problem.

7.3 Validation

The implementation of the modified Newmark method was validated by analysing problems for which there are well known closed form solutions. The simplest analysis performed was that of a compression wave travelling through a linear elastic bar. The theoretical wave velocity can be calculated from the elastic

material properties and then compared with that observed in the analysis. The same approach was used to check the velocity of a shear wave and to ensure that wave reflection and refraction occur in the correct proportions at a material boundary.

Quantitative validation was achieved by analysing the application of an impulse load on the interior of a spherical cavity. The displacement time history of the points at known distances away from the centre of the cavity where compared with the closed form solution. The results matched well, although as the radius increased the observed numerical oscillations became more prominent resulting in an unclear wave arrival. It was found that introducing some numerical damping into the problem by altering the Newmark parameters reduced the numerical oscillations, but did not affect the peak displacements observed.

After consideration of the options available from the full Biot solution, it was decided to use the reduced *u-p* approximation to model the pore-fluid soil interaction. The inertia term was not included in the pore fluid equilibrium equation as this would render the final set of equilibrium equations non-symmetrical. It was found by Chan (1988) that this term only became significant in the frequency range at which the *u-p* approximation is no longer valid. The dynamic coupled analyses were validated by analysing a column of fully saturated linear elastic soil subjected to cyclic loading. The solution to this problem was found by Zienkiewicz *et al.* (1980) in terms of two dimensionless parameters Π_1 and Π_2. For a range of values for these parameters the finite element analyses where found to compare well with the closed form solution, until the inertia term in the pore fluid equilibrium equation became significant and the solutions began to diverge.

7.4 Problems Analysed

7.4.1 Comparison of the Problems Analysed

Once the implementation of the time marching scheme had successfully been implemented and validated, two research topics where chosen that would demonstrate the diversity of the potential research topics that this development has made possible. These were the use of bender elements for measuring small strain

stiffness of soils in the laboratory and the behaviour of a deep foundation when subjected to earthquake loading. Whilst the modelling of wave propagation is vital to both problems, they differ in every other way. The generation of the wave in the bender element problem is artificially induced and is therefore of a regular form and input frequency. The input motions for the foundation analyses were measured from actual earthquake events and are therefore random in their nature and contain a wide spectrum of input frequencies.

The most important aspect of the bender element analysis was detecting at which exact moment the shear wave arrived. A parametric analysis was undertaken to determine how fine the mesh has to be and what time step should be used to achieve the necessary accuracy. This resulted in a very fine mesh and small time step. For the example analysis with an input frequency of 10 kHz, the ratio of the meshes fundamental frequency to the time step ($T/\Delta t$) was almost 3500. The point of interest for the foundation analysis was not detecting the exact arrival of the earthquake induced shear wave, but to investigate the effect that the shear wave had upon the behaviour of a deep foundation. The results were then compared to the pseudo static analyses and observations made in the field after actual earthquake events. The ratio of $T/\Delta t$ for the foundation analysis was approximately 70. This is determined by the time step used in the earthquake record. Whilst it is possible by linear interpolation to reduce the time step used in an earthquake record, it was not felt necessary for these analyses as the overall behaviour was of most interest.

To recreate the behaviour of the bender element tests it was necessary to model the soil as linear elastic. This is consistent with the theoretical assumption that bender elements induce strains in the very small range and that the behaviour of soil at this strain level is linear elastic. To capture the behaviour of the deep foundation when subjected to earthquake loading, it was necessary to use a soil model which induced permanent or plastic deformations. To be consistent with the work by Chen (1997) and Potts (2000), a Mohr-Coulomb failure criterion was assigned to the soil. The Mohr-Coulomb framework is not ideally suited to represent dynamic soil behaviour because it cannot model plasticity below the yield surface or upon unloading. The interface between the vertical sides of the foundation and the surrounding soil were modelled using interface elements which obeyed the Mohr-Coulomb failure criterion and allowed relative movement between the foundation and the soil.

The overall scale of the two problems differed considerably. The dimensions of the bender element mesh where chosen to be the same as a standard triaxial sample (76 × 38 mm). The mesh was divided into 100 regular elements along its length and 50 across its width. For the example case with an input frequency of 10 kHz, this results in a mesh density of 23 elements per wavelength. The mesh used for the foundation analysis was chosen to be the same as the one in the previous work by Potts (2000). In reality foundations are built in the infinite earth and therefore the dimensions of the mesh (42 meters wide and 20 meters deep) where chosen so that the artificial boundary conditions that must be applied do not interfere with the results in the areas of interest. The shear wave velocity of the soil and the predominant frequency of the input of the Athens earthquake record (4.5 Hz) give an input wavelength of 25 meters. The mesh used for the foundation analysis is refined around the area of interest and therefore no unique mesh density can be calculated. However, the largest element dimension in the direction of shear wave propagation is 2.9 m and the smallest is 0.5 m resulting in a minimum and maximum mesh density of 8.6 and 50 elements per wavelength respectively. The mesh density used in the bender element analyses lie within this range and both are within the empirical limits derived from the column analysis presented in Section 4.3.5. Therefore, despite the scales of the two problems being so different, the mesh densities used for each analysis are very similar. This confirms the findings from the very simple parametric study undertaken using a cylindrical rod which demonstrated the importance of mesh density upon the accuracy of dynamic finite element results and indicated that a mesh density of 10 elements per wavelength was required.

7.4.2 Conclusions from the Bender Element Analyses

The aim of the bender element investigation was to use dynamic finite element analysis to estimate the inherent errors associated with using bender element tests to determine the small strain stiffness of soils. The most common form of bender element test relies on the user initiating a shear wave to propagate through a soil sample and then measuring the time it takes for that wave to travel through the sample. By knowing the distance the wave travelled and the time it took, the shear wave velocity and shear modulus can then be calculated. It has been found in practice that the wave measured at the receiving bender element is different in form to the input signal and as a result it is difficult to determine

objectively when the shear wave has arrived. To overcome this subjectivity in the bender element test, a new technique has been proposed that uses a continuously cycled input. A standing wave is created between the transmitting and receiving bender elements with a known number of complete wavelengths between them. Knowing the distance between the bender element tips and the input frequency the shear wave velocity can then be calculated. This technique has an advantage over the traditional time of flight method as determining when there are a complete number of wavelengths between the bender element tips is an objective criterion. To allow a comparison between the accuracy of the two methods both were analysed using dynamic finite element analysis. The finite element analysis allows an estimation of the inherent errors to be made because no natural variability or mechanical errors can be introduced.

All the results published to date in the literature have used a plane strain approximation to represent the geometry of a triaxial sample. Usually the axi-symmetry of the problem is utilised to represent a triaxial sample, however, this approximation is not valid for this case due to the out of plane movement of the bender element. Therefore the problem requires a full three dimensional analyses which need a considerable amount of computer resources and analysis run time. Fourier series aided finite element analysis (FSAFEA) offers considerable time savings over traditional three dimensional analyses for problems that have axi-symmetric geometry but non-axi-symmetric material properties and/or boundary conditions. When this assumption is made with regard to this problem, the bender elements are modelled by cylindrical rods rather than flat plates. To allow an assessment of the error associated with the plane strain approximation, all analyses were run using both the Fourier series aided finite element analysis and the plane strain assumption.

The conclusions of bender element tests can be summarised as follows:

- The results from the time of flight method for both the FSAFEA and the plane strain analyses were very similar. They both predicted a near field component which reduced as the input frequency increased. The results from the FSAFEA where less clear due to the necessity of using a coarser mesh.

- Both types of analyses predicted an inherent error in assuming the shear wave arrival is signified by the first inflexion of the output signal.

- The error in the shear modulus back calculated from the finite element analyses of the traditional time of flight method was in the range of +2.72 to +4.66% for the plane strain analyses and -17.36 to +8.79% for the three dimensional Fourier series aided analyses.

- No consistent point could be identified from the analyses that did correspond to the true shear wave arrival.

- The results from the continuously cycled tests showed a similar trend in the FSAFEA and the plane strain approximation, although at some input frequencies the differences where quite significant.

- Both sets of analyses predicted a shear wave velocity for the standing wave that was input frequency dependent.

- The relationship of input frequency to number of wavelengths for both sets of analysis was 'S' shaped which was found to be similar to that which has been found in practice by some researchers.

- The error in the shear modulus back calculated from the finite element analyses of the continuously cycled method was in the range of -19.74 to +60.23% for the plane strain analyses and -21.34 to +144.14% for the three dimensional Fourier series aided analyses.

Overall, it is concluded that the results obtained from continuously cycled bender element tests cannot be relied upon. The large scatter in the results obtained from time of flight bender element tests in the laboratory cannot be attributed to the near field effect. Whilst the initial decrease in the output signal caused by the near field effect does mask the true arrival of the shear wave, the finite element analysis suggests that the error is comparatively small and relatively consistent. The large experimental scatter must therefore be due to effects that cannot be included in the finite element analysis. This may be poor contact between the bender element and the surrounding soil, or possible mechanical problems with the bender element themselves. Anther possible cause of the scatter observed in laboratory tests is the

soil heterogeneity. This feature of true soil behaviour was not modelled in the analyses presented here, although could be included by allowing the soil stiffness properties to be randomised with some given statistical variation. By re-running the same test for differently randomised soil properties, the effect that the standard deviation of the soil stiffness has on the measured shear wave velocity could be investigated.

7.4.3 Conclusions from the Deep Foundation Analyses

The aim of the deep foundation analyses was to assess the applicability of the simplified design methods which have been developed for deep foundations subjected to earthquake loading. The simplest design principle developed for this case is to consider the earthquake induced horizontal inertia forces by designing the foundation for an equivalent inclined load. Including the earthquake induced forces by using an equivalent inclined load, ignores the effect of inertia forces in the ground. Sarma and Issifelis (1990) included these forces by analysing the problem using limit equilibrium principles. They found that for earthquake accelerations above 0.1*g* the assumption of an equivalent inclined loading was non-conservative. The work of Sarma and Issifelis was extended by Chen (1997) to deep foundations subjected to earthquake loads. The results presented were found to be heavily dependent upon the assumption made for the coefficients of earth pressure on the foundation during the earthquake. To check the assumptions made by Chen, Potts (2000) carried out a series of pseudo static finite element analyses. The results demonstrated that the assumption of a Prandtl type failure mechanism may not be correct for foundations subjected to inertia loads. The results also demonstrated that the earth pressures mobilised on the foundation at failure are approximately equal to the limits set by the Mononobe-Okabe equations which were derived for the analysis of retaining walls subjected to earthquake loading.

To allow a comparison to be made between the work presented in this thesis with that of Potts and Chen, a standard foundation was defined which had been used in their analyses. This was a one meter wide and five meters deep foundation in a soil with an angle of internal friction of 30° and an angle of interface friction between the soil and the foundation of 15°. This standard foundation was subjected to four different earthquake records scaled to a range of peak acceleration values. For one

particular earthquake record the analysis was repeated with the foundation operating at a range of working loads.

The conclusions from the foundation analyses can be summarised as follows:

- The limit equilibrium analysis and the pseudo static finite element analysis did not recreate the behaviour of foundations which has been reported after actual earthquake events.

- The dynamic finite element analysis did not predict a failure mechanism forming for any of the earthquake records used.

- Although no failure mechanism developed, the analyses did predict a significant amount of earthquake induced settlement which is more consistent with the behaviour observed in the field.

- The amount of earthquake induced settlement varied considerably depending on the intensity of the earthquake record. The most damaging earthquake modelled (the Spitak record scaled to a maximum acceleration of 0.5*g*) induced 82.5 cm of settlement which represents a 1077% increase in the settlement that was present at working load.

- The settlement was found to be due to the additional plasticity induced in the soil beneath the foundation due to the passage of the seismic wave.

- A transfer of load from the shaft of the foundation to the base was observed during the earthquake analysis. This was found to be due to a reduction of horizontal stress around the foundation.

- This transfer of load from the shaft to the base illustrated why friction piles are avoided in seismic areas.

- The amount of earthquake induced settlement was found to depend heavily on the factor of safety the foundation was operating at before the application of the earthquake.

- This implies that the practice of reducing the bearing capacity of a foundation when earthquake loading is anticipated, results in less earthquake induced settlement.

- All the conclusions drawn from the small displacement analyses where confirmed by repeating each one using large displacement theory. The earthquake induced settlements were found to be consistently less from the large displacement analyses due to the increase in overburden as the foundation settles. This phenomenon does not occur in the small displacement analysis because the foundation does not change its position relative to the rest of the mesh.

Overall, it is concluded that the practice of reducing the bearing capacity of a foundation when considering earthquake loading results in a satisfying performance due to the reduction of shear stresses in the ground. However, it was clearly demonstrated that classifying earthquake by peak ground acceleration does not give an indication of the potential damage an earthquake could cause. The results from this study where used to test different parameters against the earthquake induced settlement with a moderate amount of success. Clearly, finite element results offer a unique opportunity to identify a parameter that correlates with earthquake damage, because the problem can be rerun for many different earthquake records and the exact nature of the input record is known.

7.5 Recommendations for Further Research

The following recommendations for further research are broken down into two parts. The first gives examples of further development work that should be undertaken with ICFEP to make the program more flexible and potentially make the results obtained from dynamic analyses more realistic. The second part discusses further research work that could be carried out on the two research topics investigated in this thesis, namely the use of bender element tests to measure the small strain stiffness of soils and the behaviour of deep foundations subjected to seismic loading.

7.5.1 *Implementation*

As mentioned many times in this thesis, the application of boundary conditions for dynamic analyses poses additional problems to those that exist for static analyses. For a problem such as the bender element analyses presented in Chapter 5, the boundary conditions did not pose any difficulties as they are defined by the restraints applied during a triaxial test. However, the boundary conditions for the foundation analysis presented in Chapter 6 had to be artificially created. In reality the foundation would be built in a semi-infinite half space, and any wave that reflects from the surface or the foundation would be transmitted into the surrounding ground. The process of finite element discretisation however, requires that the solution domain is truncated at a distance great enough so that the artificial zero displacement boundary conditions do not affect the results significantly in the areas of interest. During a dynamic analysis these prescribed boundary conditions, act as a reflecting boundary which can significantly affect the results. The most common solution to this problem is to develop boundary conditions that absorb the out going wave. The earliest and simplest of this type was proposed by Lysmer and Kuhlermeyer (1969). The zero displacement boundary condition is replaced by normal and shear forces which are proportional to the horizontal and vertical velocities respectively. These are equivalent to placing dash-pots around the mesh that absorb the out going energy. This type of absorbing boundary condition is only applicable to problems in which the source of dynamic excitation is not applied on one of the absorbing boundaries. It would not, for example, be applicable to the deep foundation analysis presented in Chapter 6 of this thesis. The earthquake excitation is applied on the bottom of the mesh which is also the boundary through which the reflected waves must be absorbed. This represents two boundary conditions at each node which is inconsistent. Boundary conditions that attempt to solve this problem have been proposed by Ghanooni Mahabadi (1994) and Wolf and Song (1996) and it is this type of boundary condition that should be implemented into ICFEP and its performance investigated.

The time discretisation scheme implemented in ICFEP was a modified version of the Newmark method. The original Newmark method is the most popular and robust time discretisation scheme available in the literature, it is however, generally accepted not be the most accurate. This was clearly demonstrated by the simple

shear wave arrival problem presented in section 5.5.3.1 in which a time step of 1/300th of the input period had to be used before the wave arrival coincided with the theoretical arrival time. The analysis of the single degree of freedom problem presented in Section 4.2 demonstrated the potential increase in accuracy offered by using a higher order approximation, although the following investigation demonstrated that this scheme does not perform satisfactorily. Other time discretisation schemes have been presented in the literature that purport to be as robust and flexible as the Newmark method but obtain a higher degree of accuracy. The most popular of these is the alpha method proposed by Hilbert *et al.* (1977) and it is this kind of three parameter model that should be implemented into ICFEP to determine the potential increase in accuracy offered by these schemes.

7.5.2 Research Topics

7.5.2.1 Bender Element Analyses

All the numerical investigations into the traditional time flight method for using bender elements published in the literature has pointed to a small but well understood error in measuring the shear wave velocity of a soil due to the near field effect. Further work should be carried out using randomised soil properties to investigate the effect soil heterogeneity has on the measured shear wave velocity in time of flight bender element tests. Research attention should also concentrate on understanding why a large scatter still exists in the results obtained in the laboratory. At present this scatter cannot be recreated in numerical simulations and may therefore be due to some practical difficulties. The continuously cycled bender element test does require more numerical investigation to understand why the relationship between the input frequency and number of wavelengths predicted by the finite element analysis and observed in practice is non-linear.

7.5.2.2 Deep Foundation Analyses

This line of work is more in its infancy than that of the bender element investigation and therefore has much more scope for further work. The assumptions made in the investigations presented in this thesis where mainly made to allow comparison to be made with previous researchers. Generally, they had to

be made by these previous researchers due to the restrictions imposed by their chosen analysis tool. For example, Chen (1997) could not use a more complicated soil model than a Mohr-Coulomb failure criterion because he employed the limit equilibrium technique. The soil also had to be assumed dry as including the effect of pore fluid can only be included in a very crude manner or not at all. Whilst the work presented in this thesis has demonstrated the power of dynamic finite element analysis and illustrated some interesting features regarding the behaviour of a deep foundation subjected to earthquake loading, the assumptions made were not realistic. The main areas that should be investigated in future to make the analysis more realistic can be summarised as follows:

- The use of a soil model that can recreate some of the most important characteristics of soil when subjected to cyclic loading. The kinematic hardening models proposed by Al-Tabbaa and Wood (1989) and Stallebrass and Taylor (1997) are particularly well suited to this task.

- The effect of the inclusion of a pore fluid should be investigated. This can be achieved by performing an undrained or coupled analysis.

- The influence of the side boundaries was briefly investigated in this thesis to ensure that their location did not affect the settlement of the foundation. If absorbing boundary conditions of the type discussed in Section 7.5.1 were implemented into ICFEP the influence of all boundaries could be determined.

- Further work should be undertaken to determine a parameter from an earthquake record that could be used to determine the potential damage of an earthquake. Some attempt was made in this thesis to determine such a parameter, although the idea of a threshold acceleration, below which no settlement occurs was not investigated.

- More geometries should be investigated, in particular a single cylindrical pile subjected to horizontal earthquake loading should be modelled using Fourier series aided finite element analysis.

- The presence of a structure above the foundation should also be included in the finite element mesh. This can be achieved using beam elements to represent the structure. The application of the earthquake loading would then include the effects of cyclic loading to the foundation as well as the shear stresses induced in the ground around the foundation due to the passage of the seismic wave.

- If a case study could be found which was fully instrumented and subjected to earthquake loading, an assessment of this type of analysis could be made and recommendations for further developments of soil models etc. made.

- If no real instrumented sites are available then centrifuge data could be used to allow comparisons to be made.

Overall the work presented in the thesis has illustrated the wide applicability of dynamic finite element analyses. The two topics chosen for investigation illustrate that the propagation of waves can be significant on a micro and macro scale and the sources of dynamic waves may be man made and with regular properties or natural and totally random.

REFERENCES

Al-Tabbaa A. & Wood D. (1989), An experimentally based bubble model for clay, NUMOG III, Niagara Falls, 91-99.

Ambraseys N., Smit P., Berardi R., Rinaldis D., Cotton F. & Berge-Thierry C. (2000), *Dissemination of European strong motion data,* CD-ROM collection, European Council, Environment and Climate Research Programme.

Arias A. (1970), A measure of earthquake intensity, in *Seismic design for nuclear power plants,* Editor: Hansen R.J., MIT Press, Cambridge, Massachusetts, pp. 438-483.

Arroyo M., Muir-Wood D. & Greening P.D. (2002), Source near field effects and pulse tests in soil samples, Submitted to *Geotechnique* for publication.

Arulnathan R., Boulanger R.W. and Riemer M.F. (1998), Analysis of bender element tests, Geotechnical testing journal, Vol. 21, No. 2, pp 120-131.

Bathe K.J. (1982), *Finite element procedures in engineering analysis,* Prentice Hall, New Jersey.

Bathe K.J. (1996), *Finite element procedures,* Prentice Hall, New Jersey.

Biot M.A. (1941), General theory of three-dimensional consolidation, *Journal of Applied Physics,* Vol. 12, pp 155-164.

Biot M.A. (1956a), Theory of propagation of elastic waves in a fluid-saturated porous solid. I. Low frequency range, *Journal of the Acoustical Society of America,* Vol. 28, No. 2, pp 168-178.

Biot M.A. (1956b), Theory of propagation of elastic waves in a fluid-saturated porous solid. II. Higher frequency range, *Journal of the Acoustical Society of America,* Vol. 28, No. 2, pp 179-191.

Biot M.A. (1962), Mechanics of deformation and acoustic propagation in porous media, *Journal of Applied Physics,* Vol. 33, No. 4, pp 1482-1498.

Blewett J., Blewett I.J. & Woodward P.K. (1999), Measurement of shear-wave velocity using phase sensitive detection techniques, *Canadian geotechnical journal,* Vol. 36, pp 934-939.

Bowles J.E. (1988), *Foundation analysis and design,* McGraw-Hill, New York.

Bray J.D., Espinoza R.D., Soga K. & Taylor R.L. (1995), *GeoFEAP – Geotechnical finite element analysis program,* Department of Civil and Environmental Engineering, University of California, Berkeley, CA.

Briaud L.J. & Felio G.Y. (1986), Cyclic axial loading of piles: analysis of existing data, *Canadian Geotechnical Journal,* Vol. 23, pp. 362-371.

Brignoli A. & Gotti M. (1992), Misure della velocita di onde elastiche di taglio in laboratorio con l'impiego di transduutori piezoelettrici, *Riv. Ital. Geotech.*, Vol. 26, No. 1, pp 5-16.

Brignoli E.G.M., Gotti M. and Stokoe K.H. II (1996), Measurement of shear waves in laboratory by means of piezoelectric transducers, *Geotechnical testing Journal,* Vol. 19, No. 4, pp 384-397.

Brikgreve R.B.J. & Vermeer P.A. (1998), *Plaxis version 7: part 6: dynamics user's manual,* A.A. Balkema, Rotterdam/Brookfield.

British Standards 8004 (1986), *Code of practice for foundations,* British Standards Institution, London.

Britto A.M & Gunn M.J. (1987), *Critical state soil mechanics via finite elements,* Ellis Horwood Ltd., Chichester.

Chan A.H.C. (1988), *A unified finite element solution to static and dynamic geomechanics problems,* PhD thesis, University College Swansea.

Chen Y.C. (1997), *Seismic bearing capcity of shallow and deep strip foundations,* PhD thesis, Imperial College, London.

Chow F.C. (1997), *Investigations into the behaviour of displacement piles for offshore foundations,* PhD thesis, Imperial College, London.

Crewe A.J., Lings M.L., Taylor C.A., Yeung A.K. & Andrighetto R. (1995), Development of a large flexible shear stack for testing dry sand and simple direct foundations on a shaking table, *Proceedings from the fifth SECED conference on European seismic design practice research and application,* Editor, A.S. Elnashai, A.A. Balkema, Rotterdam.

Day R.A. & Potts D.M. (1990), Curved Mindlin beam and axi-symmetric shell elements – A new approach, *Int. Jnl. Num. Meth. Eng.,* Vol. 30, pp 1263-1274.

Day R.A. (1990), *Finite element analysis of sheet pile retaining walls,* PhD thesis, Imperial College, London.

Dunnavant T.W., Clukey E.C. & Murff J.D. (1990), Affects of cyclic loading and pile flexibility on axial pile capacities in clay, *Proceedings of the XXII offshore technology conference,* OTC 6378, Vol. 3, Houston, Texas, pp. 289-298.

Dyvik R. & Madshus C. (1985), Laboratory measurement of G_{max} using bender elements, *Proceedings of the American Association of Civil Engineers Annual Convention: Advances in the art of testing soils under cyclic conditions,* Detroit.

Fioravante V. (2000), Anisotropy of small strain stiffness of Ticino and Kenya sands from seismic wave propagation in triaxial testing, *Soils and foundations, Japanese Geotechnical Society,* Vol.40, No. 4, pp 129-142.

Focht J.A. and O'Neill M.W. (1985), Piles and other foundations, *11th ICSMFE,* Vol. 1, San Francisco, pp.187-209.

Gajo A. (1996), The effects of inertial coupling in the interpretation of dynamic soil tests, *Geotechnique,* Vol. 46, No. 2, pp 245-257.

Gajo A., Fedel A. & Mongiovi L. (1997), Experimental analysis of the effects of fluid-solid coupling on the velocity of elastic waves in saturated porous media, *Geotechnique,* Vol. 47, No. 5, pp 993-1008.

Genendra D. (1993), *Finite element analysis of laterally loaded piles*, PhD Thesis, Imperial College, London.

Ghanooni Mahabadi S. (1994), *Finite element analysis of earth dam layer systems subjected to strong earthquakes including radiation damping*, PhD thesis, Imperial College, London.

Grosch J.J. & Reese L.C. (1980), Field tests of small scale pile segments in a soft clay deposit under repeated axial loading, *Proceedings 12th offshore technology conference,* OTC 3869, Houston, Texas, pp. 143-151.

Hansen J.B. (1970), A revised and extended formula for bearing capacity, *Danish Geotechnical Bulletin,* No. 28, pp.21.

Hilbert H.M., Hughes T.J.R. & Taylor R.L. (1977), Improved numerical dissipation for time integration algorithms in structural mechanics, *International Journal of Earthquake Engineering and Structural Dynamics,* Vol. 5, pp 283-292.

Houbolt J.C. (1950), *A recurrence matrix solution for the dynamic response of elastic aircraft,* Journal of the Aeronautical Sciences, Vol. 17, pp. 540-550.

Izzuddin B.A. (1991), *Nonlinear dynamic analysis of framed structures*, PhD thesis, Imperial College, London.

Jaime A., Rojas E. & Legorreta H. (1991), Friction piles driven in soft caly: behaviour under static load, *Engineering Institute Publication,* UNAM Mexico.

Jardine R.J. (1991), The cyclic behaviour of large piles with special reference to offshore structures, Chapter 5 in *Cyclic loading of soils,* Edited by M.P. O'Reilly and S.F. Brown, Glasgow.

Jardine R.J., Symes M.J. & Burland J.B. (1986), Studies of the influence of nonlinear stress-strain characteristics in soil-structure interaction, *Geotechnique,* Vol. 36, No. 3, pp 377-396.

Jennings P.C. (1985), Ground motion parameters that influence structural damage, in *Strong ground motion simulation and engineering applications,* Editors: Scholl R.E.

& King J.L., EERI Publications 85-02, Earthquake Engineering Research Institute, Berkeley, California.

Jovičić V. (1997), The measurement and interpretation of small strain stiffness of soils, PhD thesis, The City University.

Jovičić V., Coop M.R. & Simić M. (1996), Objective criteria for determining G_{max} from bender element tests, Geotechnique, Vol. 46, No. 2, pp 357-362.

Joyner W.B. & Boore D.M. (1988), Measurement, characterisation and prediction of strong ground motion, *Earthquake engineering and soil dynamics II – recent advances in ground motion evaluation,* Geotechnical Special Publication 20, ASCE, New York, pp. 43-102.

Karlsrud K. & Haugen T. (1985), Behaviour of piles in clay under cyclic axial loading – results of field model tests, *Behaviour of offshore structures conference,* Amsterdam, Holland, pp. 589-600.

Kolsky H. (1953), *Stress waves in solids,* Clarendon Press, Oxford.

Kraft L.M, Cox W.R. & Verner E.A (1981), Pile load tests: cyclic loads and varying load rates, *Journal of the geotechnical engineering Division,* ASCE, Vol. 107, pp. 1-19.

Kramer S.L. (1996), *Geotechnical earthquake engineering,* Prentice Hall, New Jersey.

Kuwano R. (1999), *The stiffness and yielding of anisotropy of sand,* PhD Thesis, Imperial College, London.

Lawrence F.V. (1963), Propagation of ultrasonic waves through sand, *Research report R63-8,* Massachusetts Institute of Technology, Cambridge, MA.

Lawrence F.V. (1965), Ultrasonic shear wave velocity is sand and clay, *Research report R65-05, Soil publication No. 175,* Massachusetts Institute of Technology, Cambridge, MA.

Lysmer J. & Kuhlemeyer R.L. (1969), Finite dynamic model for infinite media, *ASCE EM,* Vol. 95, No. EM4, pp. 859-877.

Maheetharan A. (1990), *Modelling the seismic response of piles and pile groups,* PhD thesis, Cambridge University.

McAnoy R.P.L., Chasman A.C., &Purvis D. (1982), Cyclic tensile testing of a pile in glacial till, *Recent developments in the design and construction of offshore structures conference,* Institution of Civil Engineers, London.

Mendoza M.J. & Auvinet G. (1988), The Mexico earthquake of September 19, 1985 – Behaviour of building foundations in Mexico City, *Earthquake Spectra,* Vol. 4, No. 14, pp. 835-853.

Mendoza M.J., Romo M.P., Dominguez L., Orozco M. & Noiega I. (2000b), Static and seismic behaviour of frictional pile foundation in Mexico City 5 years after construction, *Proceedings of the XX National Conference on Soil Mechanics,* Oaxaca, Mexico, Vol. 1, pp. 329-340.

Mendoza M.J., Romo M.P., Orozco M. & Dominguez L. (2000a), Static and seismic behaviour of frictional pile-box foundation in Mexico City clay, *Soils and Foundations,* Vol. 40, pp. 143-154.

Menu K.M.H (1986), *Engineering study of near-field earthquake ground motions,* PhD thesis, Imperial College, London

Meyerhof G.G. (1951), The ultimate bearing capacity of foundations, *Geotechnique,* Vol. 2, No. 4, pp. 301-331.

Meyerhof G.G. (1953), The bearing capacity of foundations under eccentric and inclined loads, *3rd ICSMFE,* Vol. 1, pp. 440-445.

Meyerhof G.G. (1963), Some recent research on the bearing capacity of foundations, *Canadian Geotechnical Journal,* Vol. 1, No. 1, pp. 16-26.

Moncaster A. (1997), *The shear modulus of sand at very small strains,* MSc Dissertation, University of Bristol.

Mononobe N. & Matsuo H. (1929), On the determination of earth pressures during earthquakes, *Proceedings World Engineering Conference,* 9, pp. 177-185.

Naylor D.J. (1974), Stresses in nearly incompressible materials by finite elements with application to the calculation of excess pore water pressure, *International journal of numerical methods in engineering,* Vol. 8, pp. 443-460.

Newmark N.M. (1959), A *method of computation for structural dynamics*, ASCE Journal of Engineering Mechanics Division, Vol. 85, pp. 67-94.

Okabe, S. (1924), General theory of earth pressure and seismic stability of retaining wall and dam, *Journal of the Japanese Society of Civil Enginners,* Vol. 10, No. 6.

Pavlides S.B., Papadopoulos G. & Ganas A. (2002), The fault that caused the Athens September 1999 M_s = 5.9 earthquake: field observations, *Natural Hazards,* Vol. 27, pp. 61-84.

Pennington D.S. (1999), The *anisotropic small strain stiffness of Cambridge Gault clay,* PhD Thesis, University of Bristol.

Potts D.M. & Zdravković L.T. (1999), *Finite element analysis in geotechnical engineering: theory,* Thomas Telford, London.

Potts D.M. & Zdravković L.T. (2001), *Finite element analysis in geotechnical engineering: application,* Thomas Telford, London.

Potts V. (2000), *Finite element analyses of the seismic loading of deep foundations,* MSc Dissertation, Imperial College, London.

Puech A. & Jezequel J.F. (1980), The effects of long time cyclic loading on the behaviour of a tension pile, *12th offshore technology conference.* OTC 3870, Houston, Texas, pp.153-162.

Rolo R. (2003), *The study of soil anisotropy and its practical application,* PhD thesis, Imperial College, London.

Saldivar E.E.S (2002), *Investigation into the behaviour of displacement piles under cyclic and seismic loads,* PhD Thesis, Imperial College, London.

Sanches-Salinero I., Rosset J. & Stokoe K.H. (1986), Analytical studies of body wave propagation and attenuation, Report GR 86-15, University of Texas, Austin.

Sarma S.K. & Iossifelis I.S. (1990), Seismic bearing capcity factors of shallow strip foundations, *Geotechnique,* Vol. 40, No. 2, pp. 265-273.

Sarma S.K. (1979), Stability analysis of embankments and slopes, *Journal of soil mechanics and foundation division,* ASCE, Vol. 105, SM 12, pp. 1511-1524.

Sarma S.K. (1994), Analytical solution to the seismic response of visco-elastic soil layers, *Geotechnique,* Vol. 44, No. 2, pp 265-275.

Sharpe J.A. (1942), The production of elastic waves by explosion pressures, *Geophysics,* Vol:7, pp1-26.

Shirley D.J. & Hampton L.D. (1977), Shear-wave measurements in laboratory sediments, *Journal of the Acoustic Society of America,* Vol. 63, No. 2, pp 607-613.

Shyam Sunder S. & Connor J.C. (1982), A new procedure for processing strong motion earthquake signals, *Bulletin of the Seismological Society of America,* Vol. 72, p. 643-661.

Simpson B. (1992), Retaining structures: displacement and design 32nd Rankine lecture, *Geotechnique,* Vol. 42, No. 4, pp 541-576.

Stallebrass S.E. & Taylor R.N. (1997), The development and evaluation of a constitutive model for the prediction of ground movements in over consolidated clay, *Geotechnique,* Vol. 47, No. 2, pp 235-253.

Thomann T.G. & Hryciw R.D. (1990), Laboratory measurement of small strain shear modulus under K_0 conditions, *Geotechnical testing Journal,* Vol. 13, No. 2, pp 97-105.

Tokimatsu K., Mizuno H. & Kakurai M. (1996), Building damage associated with geotechnical problems, *Special issue of Soils and Foundations,* pp. 219-234.

Tsatsanifos C.P. (1982), *Effective stress method for dynamic response of horizontally layered soils,* PhD thesis, Imperial College, London.

Vaghela J.G. & Stokoe K.H. II (1995), Small strain dynamic properties of soils from free-free resonant column testing, *Geotechnical engineering GT95-1,* The university of Texas at Austin.

Van Eekelen H.A.M. & Potts D.M. (1978), The behaviour of Drammen clay under cyclic loading, *Geotechnique*, Vol. 29, No. 1, pp. 99-102.

Vesić A.S. (1973), Analysis of ultimate loads of shallow foundations, *Journal of soil mechanics and foundation division,* ASCE, Vol. 99, SM 1, pp. 45-73.

Vesić A.S. (1974), *Foundation Engineering Handbook,* Van Nostrand Reinhold Book Co., New York, pp.751.

Viggiani G. & Atkinson J.H. (1995), Interpretation of bender element tests, Geotechnique, Vol. 45, No. 1, pp 149-154.

Wilson E.L., Farhoomand I., & Bathe K.J. (1973), *Non-linear dynamic analysis of complex structures,* International Journal of Earthquake Engineering and Structural Dynamics, Vol. 1, pp. 241-252.

Wolf J.P. & Song C. (1996), *Finite element modelling of unbounded media,* John Wiley & Sons, Chichester.

Zienkiewicz O.C., & Taylor R.L. (1991), *The finite element method,* McGraw Hill, London.

Zienkiewicz O.C., Chan A.H.C., Pastor M., Schrefler B.A. & Shiomi T. (1999), *Computational geomechanics with special reference of earthquake engineering,* John Wiley & Sons, Chichester.

Zienkiewicz O.C., Chang C.T. & Bettress P. (1980), Drained, undrained, consolidating and dynamic behaviour assumptions in soils, *Geotechnique,* Vol. 30, No. 4, pp 385-395.

BIBL. LONDIN. UNIV.